Improvements in the design of pendulum absorbers to reduce the vibrations of automotive powertrains

Vincent Mahe

HESAM UNIVERSITÉ

Arts et Métiers Sciences et Technologies

ÉCOLE DOCTORALE SCIENCES ET MÉTIERS DE L'INGÉNIEUR

LISPEN - Campus de Lille

THÈSE

présentée par : **Vincent MAHÉ**
soutenue le : **15 novembre 2022**

pour obtenir le grade de : **Docteur**

préparée à : **École Nationale Supérieure d'Arts et Métiers**

Spécialité : **Mécanique**

Improvements in the design of pendulum absorbers to reduce the vibrations of automotive powertrains

THÈSE DIRIGÉE PAR :
Pr. Olivier THOMAS

ET CO-ENCADRÉE PAR :
Dr. Aurélien GROLET et Dr. Hervé MAHÉ

Jury

Pr. Patrice CARTRAUD	GeM, Ecole Centrale de Nantes	Président
Pr. Steven SHAW	Department of Mechanical and Civil Engineering, FLORIDA TECH	Rapporteur
Pr. Fabrice THOUVEREZ	MSGMGC/LTDS, Ecole Centrale de Lyon	Rapporteur
Dr. Frédéric ABLITZER	LAUM, Le Mans Université	Examinateur
Dr. Soizic TERRIEN	LAUM, Le Mans Université	Examinatrice
Pr. Olivier THOMAS	LISPEN, ENSAM	Examinateur
Dr. Aurélien GROLET	LISPEN, ENSAM	Examinateur
Dr. Alexandre RENAULT	CEPN, Valeo	Invité
Dr. Hervé MAHÉ	CEPN, Valeo	Invité

THÈSE

Remerciements

Le soutient et l'aide reçue au cours de ces trois années de thèse me mènent à remercier de nombreuses personnes.

Tout d'abord, j'aimerai exprimer ma reconnaissance envers mon directeur de thèse Olivier THOMAS et mes co-encadrants Aurélien GROLET et Hervé MAHÉ pour m'avoir offert l'opportunité d'effectuer cette thèse ainsi que pour l'aide et la confiance qu'ils m'ont accordé tout au long de ces trois années. Leur expertise de la dynamique non-linéaire et des systèmes pendulaires m'a beaucoup apporté. Je leur suis également reconnaissant pour les relectures de nombreux articles...

Je remercie bien sûr Valeo pour avoir financé mes travaux, effectués dans le cadre d'une convention CIFRE, et pour m'avoir permis d'avancer dans les meilleurs conditions, notamment sur les aspects expérimentaux.

Je tiens maintenant à remercier les membres de mon jury de thèse, en commençant par Patrice CARTRAUD, qui a accepté de présider ce jury et qui a montré un intérêt pour mes recherches. Je suis très reconnaissant envers Steven W. SHAW et Fabrice THOUVEREZ pour leur lecture approfondie de mon (long) rapport, leur retour très favorable et le partage de leur expertise lors de la discussion fort intéressante qui a suivit ma présentation. Je remercie profondément Soizic TERRIEN et Frédéric ABLITZER d'avoir accepté d'être examinateurs de cette thèse, pour leurs questions et idées très pertinentes et leur bienveillance. Je suis heureux qu'ils aient pu représenter l'Université du Mans, où j'ai effectué deux années de Master extrêmement appréciées et qui m'ont été d'une grande aide pour mener à bien cette thèse. Je remercie également Frédéric pour avoir suivit mes travaux tout au long de ma thèse. Enfin, je remercie profondément Alexandre RENAULT, qui a grandement participé à l'encadrement de ma thèse, et avec qui l'aventure a commencé dès mon stage de Master. C'est en partie puisque c'était un réel plaisir de travailler avec toi que j'ai souhaité pousser plus loin nos recherches avec cette thèse. Merci pour toute l'aide que tu m'as apportée, à la fois au niveau scientifique, notamment avec ton expertise des systèmes pendulaires, mais aussi au niveau gestion de la thèse, en étant le lien parfait entre le laboratoire et l'entreprise.

J'adresse ma reconnaissance à mes collègues de Valeo Thibault, Nicolas, Jérôme, Élodie, Élie, Roël et Anthony, qui m'ont permis de mettre au point et tester des prototypes de pendules dans

les meilleurs conditions. Je tiens aussi à exprimer ma gratitude à toute l'équipe simulation pour leur excellent accueil. J'adresse également une pensée particulière à Alexandre, Benjamin, Yannick, Maxime, Thibault et Guillaume pour les bons moments passés à Amiens.

Ces années de thèse ont également été l'occasion de faire de très belles rencontres. Je remercie ainsi mes collègues doctorants/docteurs/stagiaires Eddy, Zein, Michel, Sebastian, Laurent, Antoine, Mathieu, Arthur, François, Martin, Marielle, Marguerite, Maxime, Lei, Floriane, Tanguy, Shuhan, Dorian, Emre, Guillaume et Hugo ainsi que les membres permanents du laboratoire Simon, Aurélien et Olivier pour tous les bons moments passés à Lille, en conférence et ailleurs. J'ai une pensée spéciale pour Eddy, responsable administratif officieux des doctorants en vibrations, pour François, dont les compétences informatiques m'ont rendu de bons services, et pour Zein et Marguerite, toujours prêts à aller se désaltérer dans cette chaude région qu'est le Nord.

Je tiens maintenant à remercier mes amis Nantais et d'ailleurs pour m'avoir permis de décompresser et prendre du recul quand j'en avais besoin. Je pense également à mon frère, dont l'intérêt pour mes travaux m'a initialement surpris mais était grandement apprécié et motivant. Je tiens maintenant à remercier profondément Tiphaine pour son soutien constant tout au long de ma thèse, mais également lors des années précédentes. Merci pour tous les bons moments passés pendant toutes ces années, malgré ma disponibilité fluctuante... Pour terminer, je remercie mes parents, qui m'ont soutenu et poussé durant toutes mes études, et qui ont toujours été une grande source d'encouragements et de motivation.

Contents

Part I
Introduction and generalities

Chapter 1

Introduction

Content

The work presented in this document is the result of a partnership between the Arts et Métiers Université campus of Lille and the Valeo group. The project is part of a CIFRE agreement and is the result of a collaboration between the Centre d'Etude des Produits Nouveaux (CEPN), which is the R&D centre of Valeo Transmission Systems (based in Amiens) and the Laboratoire d'Ingénieurie des Systèmes Physiques et Numériques (LISPEN) of Lille.

In the context of increasingly stringent environmental standards concerning polluting emissions and fuel consumption of internal combustion engine vehicles, car manufacturers are looking for solutions to design more ecological vehicles [1]. A first step in this direction was to reduce the engine size and operating speeds, but even if this improves the situation, pollution remains too high. Cylinder deactivation, which consists of deactivating one or more cylinders of the engine when at cruising speed, allows to lower gas emissions but this is still not sufficient. This is why, in recent years, attention has turned to the use of electric engines.

Although electric vehicles are more quiet than thermal ones, sources of noise previously dominated by the noise of the combustion engine are coming to the fore. The most disturbing of these sources are the transmission errors that occur in the gearbox. These errors lead to irregularities in the transmitted torque, causing torsional vibrations in the vehicle's drivetrain that generate an unpleasant whining noise radiated by the housing of the gearbox. It is up to the automotive equipment manufacturers to propose means of attenuating torsional vibrations integrated directly into the powertrain.

The transition to electric motorisation and the resulting problems lead to new challenges for the automotive engineers who must ensure an optimum level of comfort and reliability for the consumer. Car manufacturers are therefore asking their suppliers to propose solutions adapted to attenuate the torsional vibrations of electric vehicle powertrains. Hence, there is a need for a supplier such as Valeo Transmission to maintain a constant innovation of its products to meet the demands of its customers. Currently, Valeo only offers solutions to filter the torsional vibrations generated by internal combustion engines. In this thesis, we will focus on one of them, the centrifugal pendulum vibration absorber (CPVA), with two main objectives:

- Adapt centrifugal pendulum systems to electric vehicles;
- Improve the centrifugal pendulums currently used in thermal vehicles.

1.1 Vibrations in automotive powertrains

1.1.1 Sources of vibration

1.1.1.1 Generalities

In this section, we present generalities on the excitation signal encountered in many rotating machines. The machine in question can be an element of an automotive powertrain and the excitation can be due to the acyclism of a thermal engine (*cf.* section 1.1.1.2), transmission errors in the gearbox of an electric vehicle (*cf.* section 1.1.1.3) or the torque ripple of an electric motor (*cf.* section 1.1.1.4) for instance.

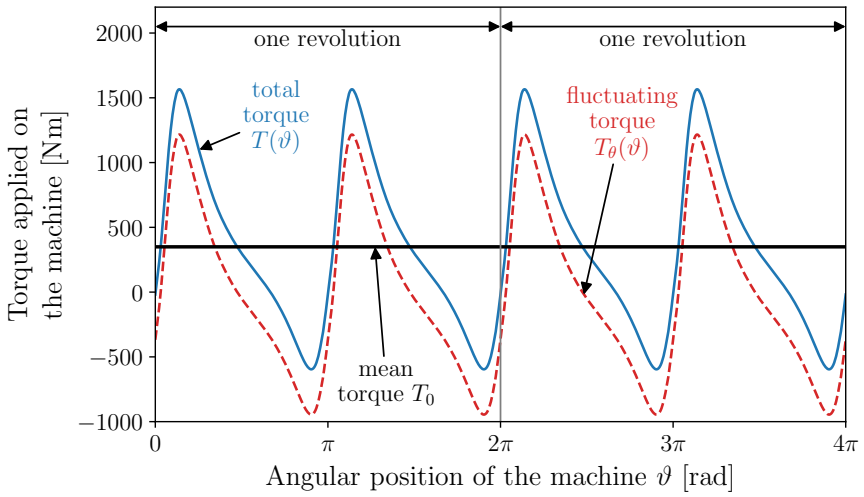

Figure 1.1: Typical torque applied on a rotating machine. This example represents the torque delivered by a four-stroke, four-cylinder internal combustion engine over one engine cycle, for a mean rotational speed $\Omega = 1000$ [rpm].

The torque applied on a rotating machine often takes the form of the signal presented in Fig. 1.1. ϑ is the angular position of the machine and the torque $T(\vartheta)$ applied on it is made of a constant component T_0 and a fluctuating part $T_\theta(\vartheta)$, such that

$$T(\vartheta) = T_0 + T_\theta(\vartheta). \tag{1.1}$$

T_0 sets the machine in motion while $T_\theta(\vartheta)$ is usually undesired because it is a source of vibrations. We can see in Fig. 1.1 that $T_\theta(\vartheta)$ is periodic in ϑ with a period π. The excitation order, written n_e, is defined as the number of fluctuations per revolution of the machine, and the associated period is $2\pi/n_e$. Hence, in the case represented in Fig. 1.1, $n_e = 2$ (and the period is $2\pi/2 = \pi$). When working with rotating machines, we often describe periodic terms using order and angular position in place of frequency and time because the periodicity is in the position rather than the time. $T(\vartheta)$ can be

decomposed into Fourier series of fundamental order n_e such that

$$T(\vartheta) = T_0 + \sum_{k=1}^{\infty} T_{ck}\cos(kn_e\vartheta) + T_{sk}\sin(kn_e\vartheta), \tag{1.2}$$

where T_{ck} and T_{sk} are the Fourier coefficients.

It is convenient to introduce the fundamental angular frequency of the excitation ω_e. To link ω_e to n_e, the fundamental excitation frequency f_e is defined as the number of torque fluctuations per second. Furthermore, the number of cycles per second is given by $\dot{\vartheta}/2\pi$, where we have defined $(\dot{\bullet}) = \partial(\bullet)/\partial t$ and t is the time. $\dot{\vartheta}$ designates the instantaneous rotational speed of the machine. We deduce the fundamental pulsation of the excitation

$$\omega_e = n_e\dot{\vartheta}, \tag{1.3}$$

which shows a proportionality relation between the excitation frequency and the instantaneous speed. Moreover, because of the torque irregularities, the angular position of the machine fluctuates such that

$$\vartheta(t) = \Omega t + \theta(t), \tag{1.4}$$

where Ω is the mean rotational velocity of the machine and $\theta(t)$ captures its vibrations. Hence, the fundamental angular frequency $\omega_e(t) = n_e\Omega + n_e\dot{\theta}(t)$ varies in time. However, in many applications, the fluctuations of the rotational velocity $\dot{\theta}(t)$ are small in front of the mean rotational velocity Ω (i.e. $\dot{\theta}(t) \ll \Omega$), such that it is assumed $\dot{\vartheta}(t) \approx \Omega$ [2]. This allows to rewrite the proportionality relation (1.3) using the mean rotational velocity such that

$$\omega_e \approx n_e\Omega. \tag{1.5}$$

Using this approximation, Eq. (1.2) can be written with time t and the fundamental angular frequency ω_e rather than the angular position of the crankshaft ϑ and the order n_e such that

$$T(t) \approx T_0 + \sum_{k=1}^{\infty} T_{ck}\cos(k\omega_e t) + T_{sk}\sin(k\omega_e t). \tag{1.6}$$

Table 1.1 anticipates sections 1.1.1.2, 1.1.1.3 and 1.1.1.4 by giving orders of magnitude for n_e and detailing the elements usually located by ϑ in the case of thermal engines, gear trains and electric motors. One can see in this table that the order of magnitude of n_e is much larger in electric powertrains than in thermal ones.

1.1.1.2 Acyclism of internal combustion engines

In the case of an internal combustion engine, the source of vibrations is due to the explosions inside the engine. Each explosion causes one of the engine's cylinders to move, which in turn drives the crankshaft, thus setting the drivetrain in motion and making the vehicle move. The explosions

	n_e	ϑ
Thermal engine	0.5 - 6	Crankshaft/flywheel or clutch
Gear train	15 - 60	Driving or driven gear
Electric motors	6 - 48	motor shaft

Table 1.1: Order of magnitude of n_e in thermal and electrical powertrains and rotating element considered.

cause irregularities of the torque delivered by the engine, which takes the form $T(\vartheta) = T_0 + T_\theta(\vartheta)$ discussed in section 1.1.1.1 and generates fluctuations of the crankshaft's rotation $\vartheta(t)$.

Figure 1.1 illustrates these torque irregularities $T_\theta(\vartheta)$, called "acyclism", for a four-stroke, four-cylinder internal combustion engine. For such a configuration, an engine cycle is spread over two crankshaft revolutions and is divided into four phases [3]. Only during the expansion phase, which follows the explosion, does a cylinder provide a significant torque. When using four cylinders, one of them is always in its expansion phase. The successive effect of each of the four cylinders can be seen in the pattern that repeats four times in Fig. 1.1.

For an engine, the excitation order n_e is usually called engine order. It corresponds to the number of strikes per revolution of the crankshaft, so it only depends on the architecture of the engine and typically takes values between 0.5 and 6 (for instance, $n_e = 2$ in Fig. 1.1). The magnitude of the acyclic engine torque $T_\theta(\vartheta)$, responsible for the torsional vibrations of a thermal powertrain [3], is typically several hundreds of Nm. As shown in Fig. 1.1, the acyclic part of the torque is much larger than its constant component, at such point that the torque delivered can become negative.

1.1.1.3 Transmission errors in the gearbox

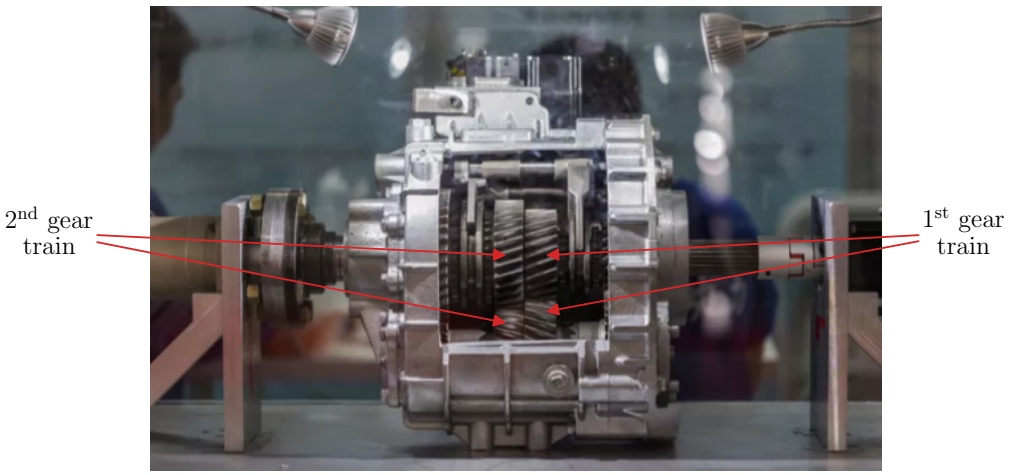

Figure 1.2: Possible architecture for the gearbox of an electric car.

In the case of an electric motor, the acyclism generated by the engine is usually very low. It is

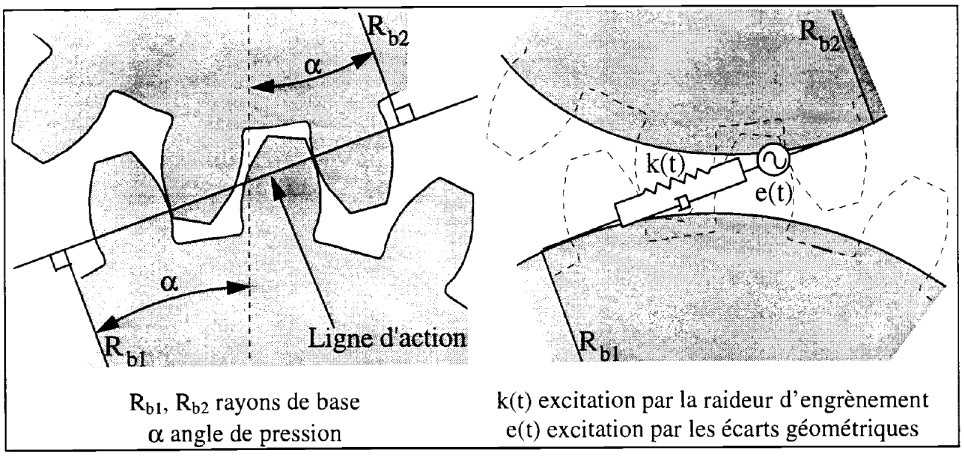

Figure 1.3: Illustration of the transmission error of a gear train (taken from [4]). The meshing between the two gears is shown on the left-hand side and the modelling of the transmission is shown on the right-hand side. R_{b1} and R_{b2} are the base radii of the two gears and α is the pressure angle. The black line tangent to the two base circles is the line of action. On the right-hand side, the transmission is represented as a variable stiffness $k(t)$, a viscous damping element and an imposed displacement $e(t)$ along the line of action.

therefore not the engine that is the main source of the torsional vibrations of the drivetrain, but the transmission errors of the gear trains of the gearbox (*cf.* Fig. 1.2). Note that these errors also exist in thermal vehicles but their effect is negligible in front of the acyclic torque delivered by the engine. A system of two gears is represented in Fig. 1.3. If we call ϑ_1 and ϑ_2 the angular position of the gears, then, in the case of a perfect transmission,

$$R_{b1}\vartheta_1 + R_{b2}\vartheta_2 = 0, \tag{1.7}$$

where R_{b1} and R_{b2} are the base radii of the gears. However, as shown on the right-hand side of Fig. 1.3, the transmission is not perfect. It can be modelled as a time-dependent stiffness $k(t)$, accounting for the variation of the number of teeth in contact and their deformation during the meshing process, and an imposed displacement $e(t)$ along the line of action. A viscous damping c is usually considered in parallel of the stiffness. In this case, the usual kinematic relation between gears (1.7) is no more valid and must be replaced by

$$R_{b1}\vartheta_1 + R_{b2}\vartheta_2 = x(t) \neq 0, \tag{1.8}$$

where $x(t)$ is the dynamic transmission error (DTE). In the case where the torque received by the driving gear is constant, the equation governing the DTE is [5–7]

$$m\ddot{x} + c\dot{x} + k(t)x = k(t)\epsilon(t), \tag{1.9}$$

where $\epsilon(t)$ is the static transmission error (STE) and m is an equivalent mass depending on the

rotational inertia of the gears and their radii. As gears are excited by their own displacement, the system falls into the field of parametric oscillators [7].

If we define Z_1 the number of teeth of the driving gear and neglect the geometrical defaults of the system (i.e. $e(t) = 0,\ \forall t$), then we can say that $\epsilon(\vartheta_1)$ and $k(\vartheta_1)$ fluctuate Z_1 times per revolution of the driving shaft. Hence, $k(\vartheta_1)$ and $\epsilon(\vartheta_1)$ are periodic in ϑ_1 and their fundamental order is the number of teeth $n_e = Z_1$. Thus, from Eq. (1.9), $x(\vartheta_1)$ is also periodic in ϑ_1 and of order n_e. By convention, we chose to look at the gear train from the input, which is why the periodic quantities are expressed in terms of the parameters of the driving gear rather than the driven one. To use the same notations as in section 1.1.1.1, we redefine the angular position of the driving gear as $\vartheta = \vartheta_1$.

After computing $x(\vartheta)$ using for instance one of the methods proposed in [5, 6], one can deduce the fluctuations of the torque transmitted by the driving gear as

$$T_\theta(\vartheta) = R_{b1} x(\vartheta). \tag{1.10}$$

Of course, the gear also transmits a constant torque T_0 such that the total torque $T(\vartheta)$ provided by the driving gear has exactly the same form as the one discussed in section 1.1.1.1. Nevertheless, there are two main differences between the torques delivered by an engine (*cf.* section 1.1.1.2) and transmitted by a gear train:

- The torque order n_e is much larger in a gear train because it corresponds to the number of teeth of the gear, which typically ranges from 15 to 60. In the present report, means to reduce vibrations up to order 20 are proposed (*cf.* section 8.2 and 11.3).
- The order of magnitude of the transmission error is only a few µm [5], so the torque fluctuations generated are only a few Nm, which is much smaller than in thermal engines.

1.1.1.4 Torque ripple in electric motors

Some electric motors generate a fluctuating electromagnetic torque [8] that causes noise and vibrations of the drivetrain [9]. The scientific community studying this topic calls this phenomenon "torque ripple", but this is very similar to the acyclism met in thermal engines. Torque ripple is particularly problematic in synchronous reluctance machines (SynRM), which can be used in electric vehicles due to their low cost, high robustness, high efficiency and compact size [8, 10].

The principle of operation of a SynRM is as follows. Because of its geometry, the rotor provides two flux directions, one along the direct axis d and the other along the quadrature axis q (*cf.* Fig. 1.4). Reluctance is smaller along axis d than axis q and inductance is larger because of the smaller air gap between the rotor and stator. The magnetic flux generated by the current flowing in the stator windings follows the path with the least reluctance. Hence, it generates an electromagnetic torque on the rotor in order to align itself with axis d. As the d axis approaches the flux direction, the stator

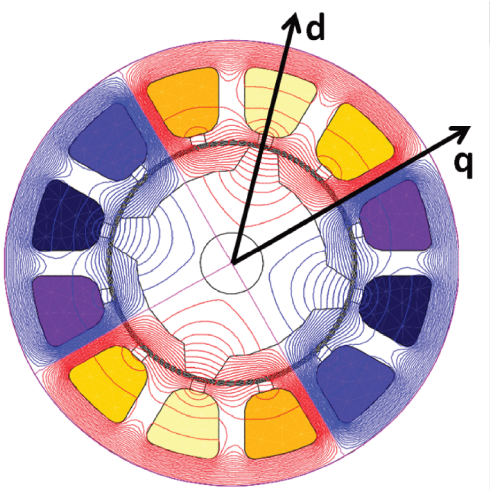

Figure 1.4: Representation of a SynRM with 2 rotor poles and 12 stator slots. Axes d and q are the direct and quadrature axes of the SynRM, respectively. Taken from [11].

currents are adjusted to change the flux direction, which allows to keep the rotation of the rotor going. However, this operation principle generates a periodic torque whose main source of fluctuation is the discrete distribution or the stator windings [9].

If we write ϑ the angular position of the rotor, then the torque produced by the electric motor can be written $T(\vartheta) = T_0 + T_\theta(\vartheta)$, where $T_\theta(\vartheta)$ represents the torque ripple. Hence, the torque produced by the electric motor has the same form as the one produced by a thermal engine (*cf.* Eq. (1.1)). The fundamental torque order corresponds to the number of stator slots, which is usually a multiple of 6 [10, 12, 13]. For instance, a stator made of 12 sots is considered in [10, 11, 14]. The amplitude of the torque fluctuations goes from about 10% of the mean torque to more than 100% [11, 12] and is typically dominated by the amplitude of the fundamental harmonic [11].

The filtering of the torque ripple is not the main aim of this thesis as the most disturbing vibrations in an electric powertrain are usually due to the transmission errors in the gearbox. Still, the adaptation of centrifugal pendulums to the high-order vibrations of gear trains might also find an application in the reduction of the torque ripple.

1.1.2 Specific features of the drivetrain

In the case of thermal vehicles, the powertrain is made of numerous power transmission components, such as the flywheel, the clutch, the gearbox, the transmission shafts and the wheels (*cf.* Fig. 1.9). It is therefore a complex assembly with many torsional modes that are sensitive to engine acyclism. Moreover, the mass and stiffness characteristics of the drivetrain depend on the gear ratio engaged, which implies that the frequencies associated with the torsional modes also depend on it.

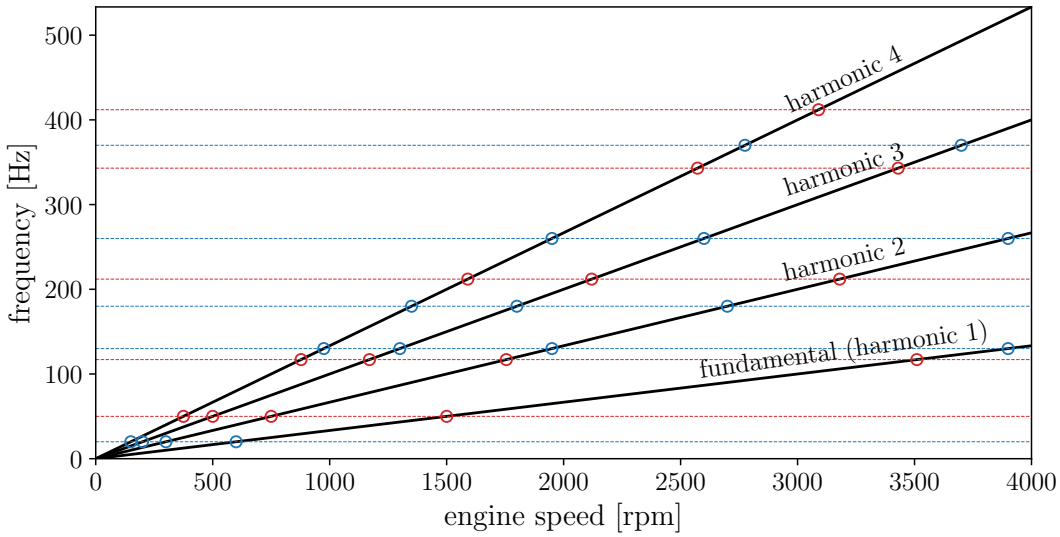

Figure 1.5: Illustration of the numerous critical points (circles) corresponding to a resonance of the drivetrain via the intersection of the harmonics of the excitation (in black) with the modes of the drivetrain (dashed lines). Two drivetrain configurations are shown, one in blue and one in red, corresponding to different gear ratios.

Thus, there are many critical speeds for which the excitation frequency matches one of the natural frequencies of the drivetrain, causing a resonance of the drivetrain (*cf.* Fig. 1.5). During an acceleration phase, these resonances are successively excited, leading to unacceptable vibration levels and bringing discomfort.

Electric drives can have many configurations as the motor can be placed at different locations in the drivetrain and the gearboxes used can be more or less complex. Still, as with internal combustion engines, there are many torsional modes in the drivetrain that can resonate, causing the housing to vibrate and radiate a very unpleasant whining noise [15].

1.2 The centrifugal pendulum vibration absorber

1.2.1 Its function

In response to the vibration problem met in thermal powertrains, described in sections 1.1.1.2 and 1.1.2, automotive manufacturers proposed in the early 1990s the use of the centrifugal pendulum vibration absorber (CPVA), which originates from the aeronautical field. The CPVA is a passive device consisting of several pendular masses (pendulums) distributed around the circumference of a support (rotor), as illustrated in Fig. 1.6.

The operation principle of a CPVA is similar to that of a tuned mass damper (TMD), which is described first. A TMD, illustrated in Fig. 1.7, consists of attaching a resonant system to a primary

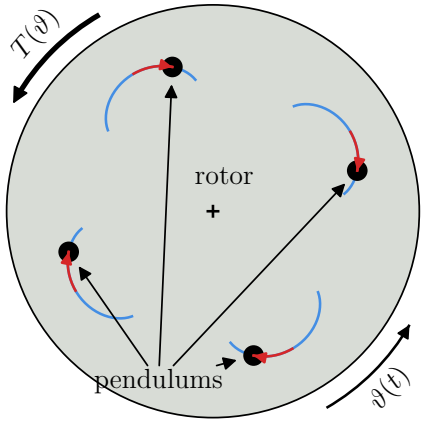

Figure 1.6: Representation of a CPVA with four pendulums. The blue curves are the pendulums' path.

structure in order to counteract its oscillations [16, 17]. The tuning of the TMD is controlled through the appropriate choice of its mass and spring, which determine its natural frequency ω_0. In order to tune the TMD on the natural frequency ω_s of the primary structure, one simply has to set $\omega_0 = \omega_s$. In this configuration, when the primary structure is excited on its resonance, the TMD exerts a force on it that balances the external forcing. As a results, the primary structure remains immobile (in the absence of damping).

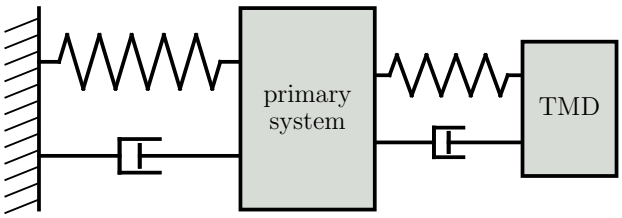

Figure 1.7: Illustration of a tuned mass damper.

The pendulums of a CPVA evolve in a centrifugal acceleration field due to the rotational velocity $\dot{\vartheta}(t)$ of the rotor. The centrifugal acceleration, proportional to $\dot{\vartheta}^2(t)$, plays the role of a stiffness. This way, the natural frequency of the pendulums, ω_p, is proportional to $\dot{\vartheta}(t)$. The proportionality coefficient is the tuning order n_p, controlled through the shape of the pendulums' path. As the excitation frequency ω_e is also proportional to the rotational velocity $\dot{\vartheta}$ (*cf.* Eq. (1.3)), we can tune

the CPVA on the excitation by tuning the pendulums such that:

$$\omega_p = \omega_e, \quad \text{or equivalently} \quad n_p\dot{\vartheta} = n_e\dot{\vartheta} \quad \Rightarrow \quad n_p = n_e. \tag{1.11}$$

Eq. (1.11) shows that a CPVA is tuned on an order, which is independent from the rotational velocity $\dot{\vartheta}$. When $n_p = n_e$, the pendulums exert a torque on the rotor which has the same order (or, equivalently, frequency) and amplitude as the first harmonic of the engine torque $T(\vartheta)$, but is in phase-opposition with it. Thus, the two torques balance and the drivetrain components located after the CPVA are isolated from the fluctuating engine's torque.

Here, we saw that both the TMD and CPVA are tuned absorbers and that they reduce the vibrations of a primary structure. However, there are two main differences: (i) CPVAs are order-tuned absorbers, so that their tuning frequency varies, while TMDs are frequency-tuned absorbers. (ii) TMDs are tuned on the natural frequency of the structure they are attached to, while CPVAs are tuned on the excitation. These differences are discussed in details in the next section.

1.2.2 Advantages of centrifugal pendulums over other absorption means

The number of torsional modes present in the drivetrain, their frequency shift according to the gear engaged (in the case of manual gearboxes, *cf.* Fig. 1.5) and the number of harmonics making up the excitation signal (*cf.* section 1.1.1) imply that filtering solutions must be proposed for a multitude of frequencies and rotation speeds. In this section, we compare the advantages of using CPVAs instead of other absorption means.

CPVA and TMD A CPVA has two main advantages over a TMD. First, TMDs absorb energy around a fixed drivetrain frequency, whereas CPVAs filter-out one of the frequencies of the exciting torque, which variates with the engine speed. CPVAs can therefore operate on a whole speed range. Note that the use of multiple TMDs tuned to slightly different frequencies allows for significant vibration reduction around a small frequency band and makes the absorption of a driveline mode more robust [18]. Another advantage of a CPVA is that it filters the excitation, whereas a TMD reduces the vibrations around a single resonance. This subtle difference has significant consequences as it implies that a CPVA generates an antiresonance on every downstream driveline component. Hence, when placed right after the source of excitation, a CPVA isolates the whole driveline from torque oscillations.

Nonlinear energy sink Nonlinear energy sinks (NES) [19–21] can be effective over a wider frequency band than TMDs as they are more robust to mistuning. Absorption takes place via an irreversible energy transfer from the primary system to the NES. However, this transfer can only be activated for large displacement amplitudes, which prohibits the use of this type of absorber. More-

over, NES do not generate an antiresonance of the primary structure like a TMD or a CPVA, which, in the case of low damping, makes them less efficient.

Metamaterials Metamaterials have been receiving a lot of interest these last years for their interesting properties. Their periodic design leads to the appearance of bandgaps such that any travelling wave with a frequency in this bandgap becomes evanescent. This concept was used in [22] to prevent the propagation of a torsional wave in a beam made of successive heterogeneous cells. However, the frequencies contained in the bandgap are directly related to the cells arrangement of the beam, so it does not seem possible to make this bandgap linearly dependent on the engine speed. Hence, like TMDs, this method can only be used to reduce the vibrations at a fixed drivetrain frequency.

Centrifugated beams The main idea of the CPVA is that it evolves in the centrifugal acceleration field of the rotor, allowing for its auto-tuning (or order-tuning). Nevertheless, other centrifugated systems could exhibit the same feature, as for instance thin beams attached on a rotor. Indeed, above a given rotational velocity of the rotor, the bending stiffness of a beam becomes negligible in front of the tension stiffness, which is proportional to the velocity of the rotor [23, 24]. This defines a critical speed above which the eigenfrequencies of the beam tend to be proportional to the rotor's rotational velocity. The eigenorders (analogous to eigenfrequencies) of a centrifugated beam are derived in Appendix A in the special case of a rotor with a null radius. A possible improvement of the system is to add a mass on the beam, as proposed in [25]. However, this added mass can cause the eigenorders to diminish [26–28], which is detrimental to the high-order tuning required for gear systems. When the mass is large in front of the total mass of the beam, then the system is similar to a CPVA except that the masses are guided via the beam rather than the shape of rolling tracks. The facts that centrifugated beams (with or without added mass) are operational only starting from a given rotor speed and appear to be quite limited in their tuning orders are the two principal drawbacks compared to CPVAs. However, ongoing works should soon provide more details on the limitations of these systems.

Semi-passive systems Another absorption mean is to use electro-mechanical systems, as presented in [17, 29–33]. In these studies, the authors propose to send the mechanical energy related to the torsional vibrations in a resonant shunt circuit where it is absorbed using an electromagnetic transducer. In addition, this shunt circuit can be used together with a passive system (a CPVA or a TMD for instance), leading to a hybrid vibration absorber. These absorbers are out of the scope of the present study, which focuses on fully mechanical absorbers. However, the use of electromagnetic absorbers is very promising as they do not seem to be limited in their tuning order. Moreover, it was theoretically shown that they can improve or even imitate the behaviour of a CPVA [30].

Geometry and control of electric motors In the case of electric motors, several methods are used to reduce the torque ripple. For instance, M. O. Hamiti [9] focused on the geometry of the electric machine and the current sent in the motor. Though these methods can prove efficient, they only apply to electric motors and are out of the scope of this thesis.

As a conclusion, CPVAs appear to be excellent fully passive absorbers for the vibration problem considered due to their auto-tuning property and their filtering efficiency. Two other key features that CPVAs share with other absorbers (the NES and TMD for instance) are the small space required and the small added mass. CPVAs are generally tuned to the fundamental order of the excitation because it has the largest amplitude and therefore generates the most important vibrations. However, this tuning has a limitation: such CPVAs are unable to filter-out the higher torque harmonics, which therefore persist and can be problematic if their amplitude is large. Nevertheless, it is possible to equip a CPVA with pendulums tuned to different orders [34, 35], and thus address the most troublesome higher harmonics. This interesting possibility is not investigated in this report but is left for future works.

1.2.3 History of centrifugal pendulums

The aircraft industry was the first to be concerned about the harmful and potentially disastrous effects of torsional vibrations. The Dragonfly radial engine designed in the UK by G. Bradshaw (ABS Motors) during World War I is a well-known example. The excitation frequency of this engine at nominal flight speed coincided with the frequency of a crankshaft torsional mode, which resulted in its lifespan being limited to only a few hours [36]. CPVAs were invented to prevent such disasters from happening again.

CPVAs can be classified into two categories: monofilar and bifilar systems. To our knowledge, it is B. C. Carter [37] (Royal Aircraft Establishment) who first proposed a monofilar pendulum, in 1929. His design is illustrated in Fig. 1.8(a) and consists of integrating a rolling mass (of cylindrical shape) in a cavity machined directly in the crankshaft. The mass has a single suspension point, hence the name “monofilar”.

Bifilar CPVAs get their name from the fact that the pendulums have two suspension points. It is the French engineer R. R. R. Sarazin (Hispano-Suiza) who patented this concept in 1931 [38], again dedicated to aeronautical applications. He proposed to integrate his system directly in the flywheel, as illustrated in Fig. 1.8(b). The modern bifilar CPVA, which would later inspire the technology adopted by the automotive industry, is the system patented in 1935 by R. Chilton [39] (Pratt & Whitney), shown in Fig. 1.8(c). Like Carter, he proposed to install the pendulums directly on the crankshaft, but in his design the pendulums are guided using two rollers (this architecture is presented in details in the

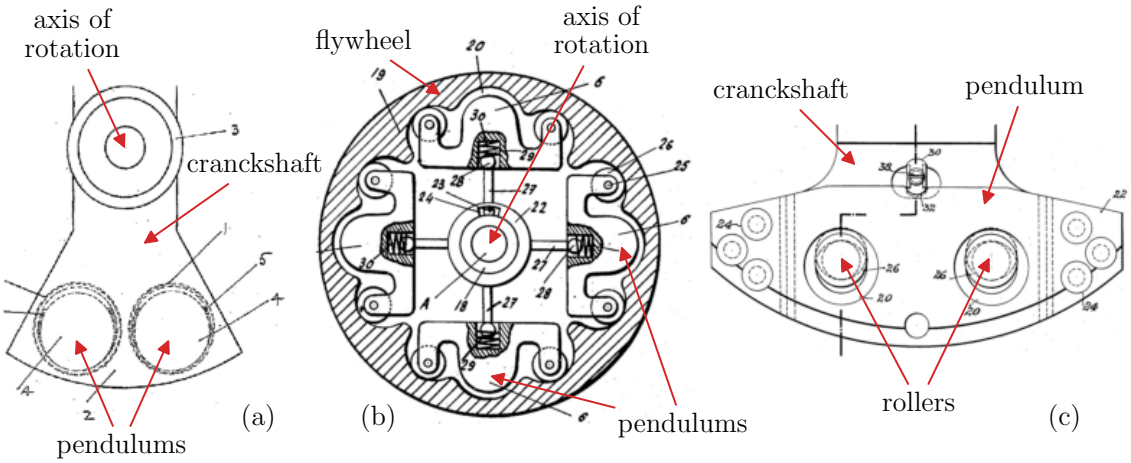

Figure 1.8: Illustrations taken from patents by (a) Carter [37], (b) Sarazin [38] and (c) Chilton [39]. The axis of rotation indicated is that of the rotor.

next section). From then on, the concept proposed by Chilton underwent only minor evolutions and was adapted from the 1970s onwards to helicopter rotors [40, 41]. It was not until the beginning of the 1990s, with the works of Denman [42], that these systems finally appeared in automotive drivetrains. They are generally installed in parallel with the drivetrain, often on the flywheel, as shown in Fig. 1.9.

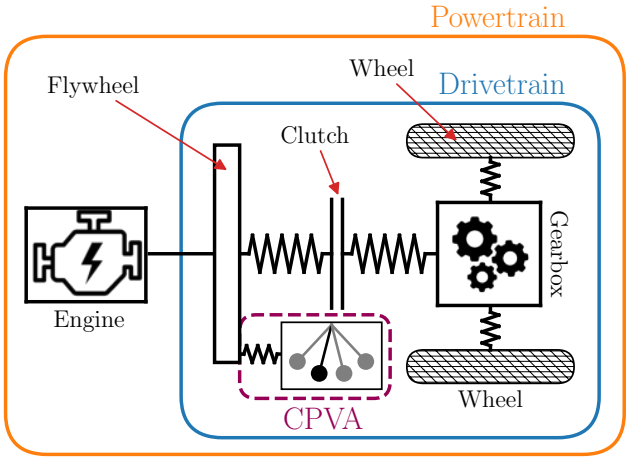

Figure 1.9: Illustration of a centrifugal pendulum vibration absorber (CPVA) attached on a flywheel.

1.2.4 Bifilar pendulums

The bifilar CPVA, which is by far the most used in the industry, is now presented in details. Figure 1.10 shows such a CPVA made of six bifilar pendulums distributed around the circumference of a rotor. The pendulums are made of two thick metal plates arranged on each side of the rotor and acting as masses, and two struts that connect the front and back plates. The movement of a pendulum

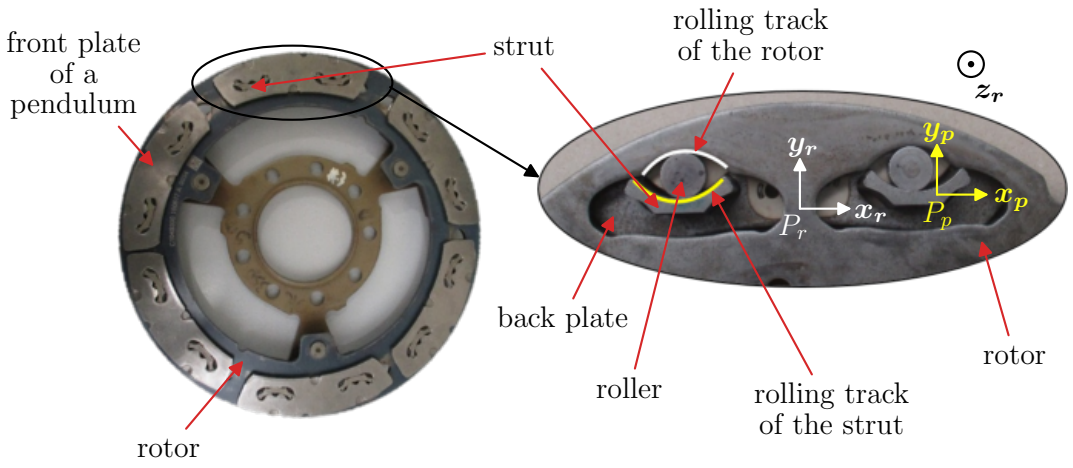

Figure 1.10: Photos of a translated bifilar CPVA with 6 pendulums. The front plate was removed on the zoom in order to observe the rollers and tracks of the CPVA.

is guided by two cylindrical rollers (the two suspension points, hence the name bifilar) rolling without slipping on the tracks of the rotor and the pendulum's struts. The shape of these tracks allows to impose the path followed by the centre of mass of a pendulum during its oscillations.

The CPVA shown in Fig. 1.10 is said to be "translational" because the pendulums only move in translation with respect to the rotor. More precisely, during the pendulums' motion, the frame $\mathscr{R}_p(P_p, \boldsymbol{x_p}, \boldsymbol{y_p}, \boldsymbol{z_r})$ (fixed to the pendulum at point P_p) remains constantly parallel to the frame $\mathscr{R}_r(P_r, \boldsymbol{x_r}, \boldsymbol{y_r}, \boldsymbol{z_r})$ (fixed to the rotor at point P_r). The case of pendulums having a rotational mobility is discussed in section 1.2.5.

Some orders of magnitude regarding the bifilar CPVAs currently used in the automotive sector are given thereafter. The maximum amplitude of motion of a pendulums' centre of mass along its path typically varies from 10 to 15 millimetres. The number of pendulums in a CPVA typically goes from two to eight depending on the application, the performance required and the space available. The same goes for the total pendulums' mass, which typically goes from a few hundreds of grams to more than one kilogram.

1.2.5 Rocking pendulums

In the early developments of CPVAs, some studies considered the case of "rocking" pendulums, i.e. pendulums that rotate relatively to the rotor in addition to their translational motion [43–45], as illustrated in Fig. 1.11. However, after these pioneer works, very few investigations dealing with rocking pendulums were carried out, probably because of early recommendations encouraging the use of purely translated CPVAs [46].

However, J. Mayet *et al.* showed less than ten years ago that the rotational motion can significantly

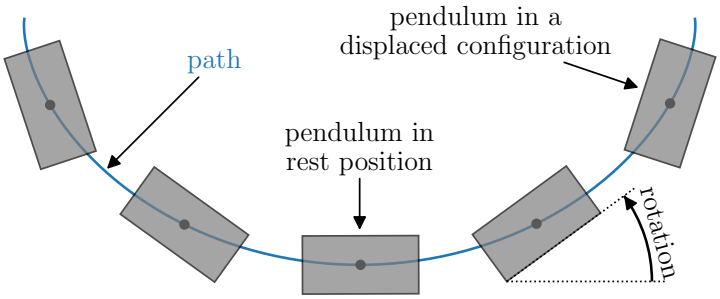

Figure 1.11: Representation of a pendulum (rectangle) in several positions. This pendulum rotates about its centre of mass as it moves on its path.

improve the performance of a CPVA [47, 48]. This is due to the contribution of the pendulums' rotational inertia, which virtually increases their mass, as will be explained in section 2.1.3. These results motivated Valeo to perform in-depth investigations of the rotation law. This was done by A. Renault [2], who proposed original design rules to take maximum advantage of the rotational motion [49, 50]. Since then, Valeo developed a new range of bifilar rocking CPVAs inspired from the concept patented by L. J. Stone in 1945 [45]. An example is shown in Fig. 1.12, where one can see that the yellow frame (attached to the pendulum) rotates relatively to the white frame (attached to the rotor) during the pendulums' motion.

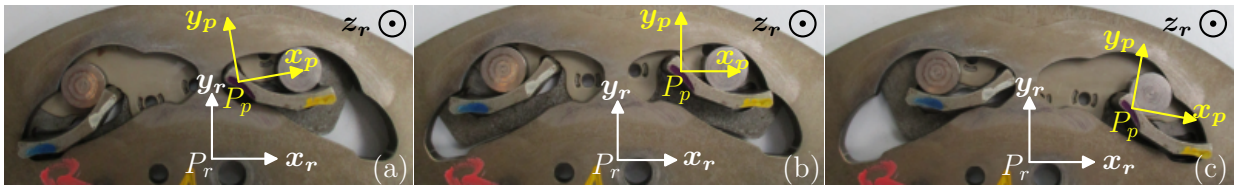

Figure 1.12: Illustration of the motion of a rocking bifilar CPVA.

As for their path, the pendulums' rotation function is controlled by the shape of the rolling tracks. In addition, rotation contributes to the pendulums' tuning order n_p, as detailed in section 2.2.1.1.

Note that rocking bifilar CPVAs are sometimes called "trapezoidal" CPVAs because they can be modelled as a trapezoidal structure [51, 52], as shown in Fig. 1.13.

1.3 Literature review

The study presented in this report is part of a research activity on pendulum absorbers that has been going on for nearly a century. A state of the art of the field is presented in this section.

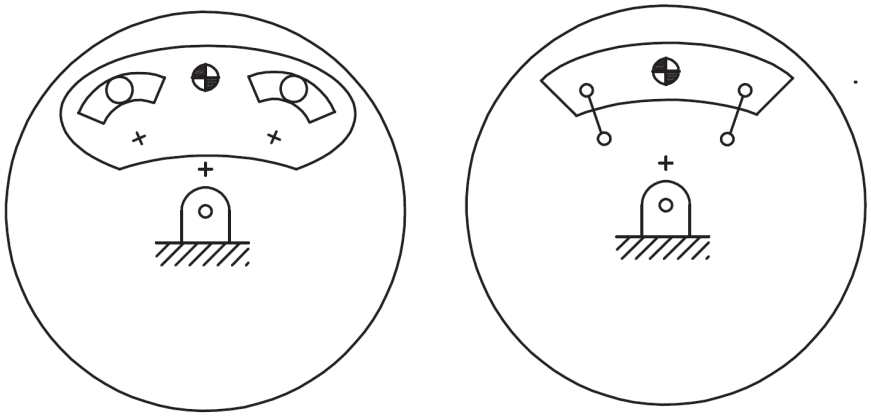

Figure 1.13: Realistic representation of a bifilar CPVA (left) and the associated trapezoidal representation (right). This figure is taken from [52].

Fields of application CPVAs were initially dedicated to the attenuation of torsional vibrations of light aircraft [37, 39, 53]. The first evidence of such applications dates back to World War II [46]. Then, starting from the early 60s, it was proposed to use CPVAs to reduce the torsional vibrations generated by helicopter turbines [40, 41, 54–56]. Actual application examples can be found in [57]. It was only as from the 90s that CPVAs appeared in the automotive sector [42, 58] with the first experimental investigations dedicated to racing cars [59]. More recently, it was also suggested to use CPVAs in ships [60, 61], but no real application is known to the author.

Pendulums' path The choice of the pendulums' path is essential as it determines their proper tuning and contributes to their nonlinear response. D. E. Newland showed that circular paths, which were the first ones to be used, confer the CPVA a softening behaviour leading to jumps of the system's response [62, 63]. This jump is disastrous for performance as it causes the pendulums to oscillate with a much larger amplitude than predicted by linear theory and to act as amplifiers instead of absorbers. In 1980, J. F. Madden patented a CPVA whose pendulums' path is not a circle but a cycloid [56]. This innovation is inspired by the Huygens pendulum [64] whose cycloidal path allows the pendulum to be tautochronic in the gravity acceleration field. This very interesting property means that the pendulum's period of oscillation does not depend on its amplitude of motion. However, cycloidal paths are not the tautochronic paths in a centrifugal acceleration field, but lead to a slightly hardening behaviour. This is still beneficial compared to the circular paths as jumps are avoided, but further improvements can be done to limit the hardening behaviour. This motivated H. H. Denman to propose the epicycloidal path, which is the tautochronic path in a constant centrifugal acceleration field [42]. However, in practice the centrifugal acceleration field fluctuates because of the rotor's vibrations. Moreover, tautochronic pendulums do not allow for maximum performance and are subjected to nonlinear phenomena such as energy localisation (this is discussed further below). This is why many

recent works consider paths close but not equal to the epicycloid, which allows for a nonlinear tuning of the CPVA [2, 65–69]. A circular, cycloidal and epicycloidal path tuned to the same order (hence leading to the same linear response, *cf.* section 2.1.3) are illustrated in Fig. 1.14. One can see that tighter paths lead to more hardening behaviours.

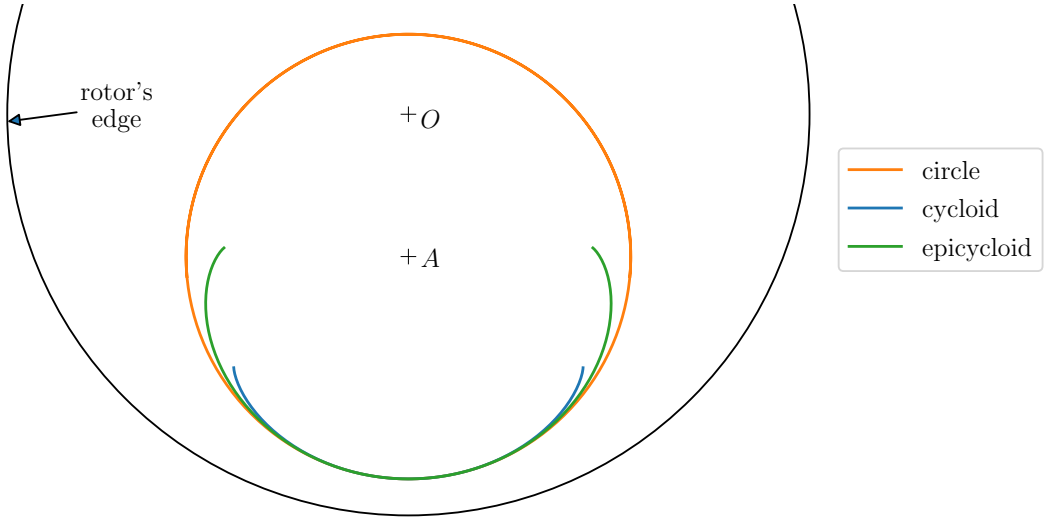

Figure 1.14: Illustration of a circular, cycloidal and epicycloidal path with the same tuning order. O is the centre of the rotor and A is the centre of curvature of the three paths at their vertex. A is also the centre of the circular path as its curvature is constant. The expression of each path can be found in section 2.1.3.

Pendulums' rotation law It is R. Chilton who first investigated the effect of pendulum rotation on the tuning order through his study of a pendulum mass rolling without slipping on a convex surface [43]. Then, R. W. Zdanowich and T. S. Wilson [44] derived the expression of the tuning order of roller-type and ring-type rotating pendulums (note that the ring-type pendulum is a special case of the monofilar pendulum investigated in chapter 3). A similar analysis on a compound pendulum was led by R. G. Mitchiner and R. G. Leonard [70]. However, it was less than ten years ago that J. Mayet and H. Ulbrich provided the first results showing that the rotational motion can significantly improve the performance of a CPVA [47, 48, 68]. In-depth studies of the rotation law of the pendulums were then led by A. Renault [2] and M. A. Acar [71]. A. Renault patented a particular nonlinear rotation law that maximises the vibration reduction over the whole torque range [49, 50]. M. Cera *et al.* proposed to optimise the rotation of a trapezoidal CPVA to reproduce the rotation of a compound pendulum attached at the rotor's centre [72]. As shown in Fig. 1.15, this might permit the use of more voluminous pendulums when the space requirement is very demanding. Another proposition was made by X. Tan *et al.* [73] with the aim to limit the effect of a shock between the pendulum and the rotor. The idea is that if the direction of the force due to the shock is radial, then the associated

momentum about the rotor's centre is null. J. Mayet *et al.* pursued their initial work by proposing a design methodology for robust and efficient rocking CPVAs [74]. The present work, which includes [67, 75, 76], also provides a greater knowledge of the effect of the pendulums' rotation, with a special focus on its nonlinear contribution.

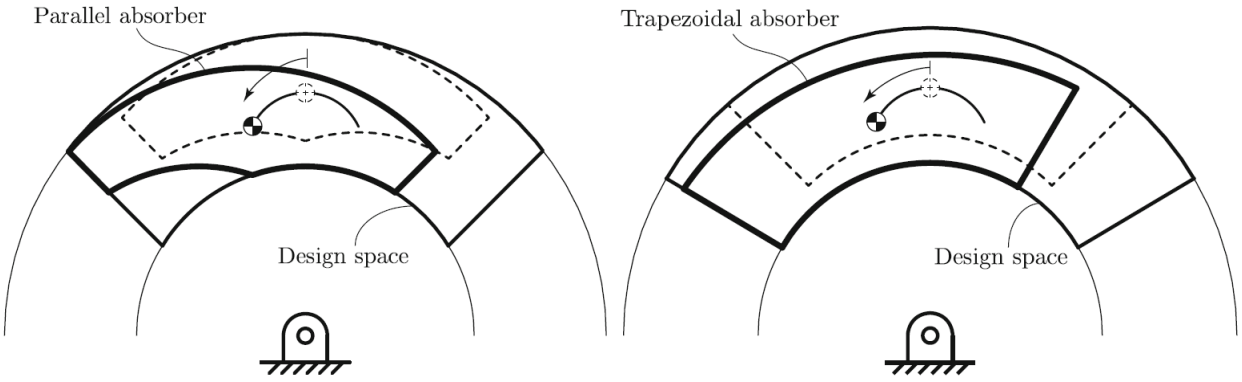

Figure 1.15: Illustration of the benefits of rocking absorbers with respect to space requirements [72].

Localisation in classical tuning The CPVAs currently used in the industry are tuned on (or very close to) the excitation. This is referred-to as the "classical" CPVA tuning (or classical operation), in opposition to the "subharmonic" tuning, discussed in the next paragraph. In classical operation, the desired behaviour of the CPVA is a synchronous motion of the pendulums, so that they act as a single equivalent pendulum. However, due to their cyclic symmetry, CPVAs are subjected to energy localisation phenomena. These phenomena correspond to situations where the stability of the unison solution is broken, leading to a solution where one (or more) pendulums oscillate with an amplitude larger than the others and with a different phase. Energy localisation is known to occur in systems with cyclic symmetry [77–79], and in the case of CPVAs it usually deteriorates the system's performance. Localisation can be caused by an asymmetry in the system, generally due to slight disparities between the pendulums [80–82]. However, a localised response can also exist with identical pendulums, in which case it is due to a nonlinear phenomenon. The first studies on the nonlinear localisation of the pendulums' response, led by C.-P. Chao *et al.* [83, 84], dealt with epicycloidal paths. Then, A. S. Alsuwaiyan *et al.* considered the case of more general paths [65]. This study on general paths was extended by S. W. Shaw *et al.*, who were able to develop an accurate analytical model by taking into account the main nonlinearities coming from both the path and the inertial effects [66]. Other works investigated the localised response itself [85, 86], and it was shown that this asynchronous response can become unstable, leading to quasi-periodic and even chaotic solutions [87, 88]. Moreover, some experimental works led to the observation of localised solutions [89–91]. [67, 76], which were published during this PhD and are included in the present report, also provide a greater understanding of the

localisation phenomenon.

Subharmonic tuning In 1992, Denman discussed the existence of a subharmonic solution [42] which could allow a CPVA operation different form the classical one. The study of this solution was initiated by C.-T. Lee and S. W. Shaw, who focused on a system composed of two pendulums following an epicycloidal path [92]. First, it was shown that the desired subharmonic response corresponds to the pendulums moving in phase-opposition and oscillating at half the excitation frequency. This operation can provide excellent vibration reduction as the pendulums do not generate higher rotor harmonics, contrarily to the classical operation, and they cause a saturation of the rotor's response [93]. A patent was filed [94] and some studies followed, confirming the previous results while analysing the robustness of the solution to the addition of damping [95, 96] and to small modifications of the path [97]. Apart from [75], which was published during this PhD and is included in the present document, the last work dealing in details with the subharmonic solution dates from 2000 [98]. It focused on the stability of the response when several pairs of pendulums are used and it was shown that this solution can be made stable through a judicious choice of the pendulums' path. The phase-opposition motion of two pendulums responding on their subharmonic was observed experimentally in [35].

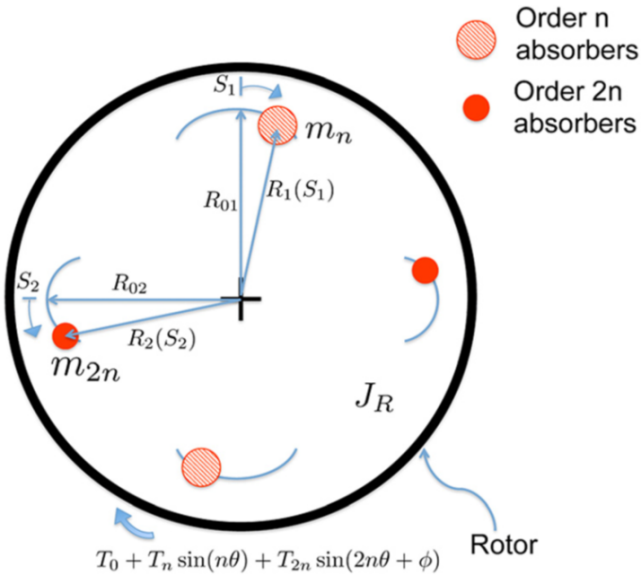

Figure 1.16: Illustration of the CPVA with pendulums tuned on two orders studied by B. J. Vidmar [34, 35].

CPVA designs and CPVA-related concepts The very first CPVA designs had pendulums of the form of rollers [37, 44], as shown in Fig. 1.8(a). The simplicity of roller pendulums led them to be investigated again in the first experimental study dedicated to automotive vehicles [59] and in more recent works [60, 99]. However, the design that received the most attention is by far the bifilar

CPVA (*cf.* section 1.2.4), either purely translated [35, 38, 40, 42, 44, 46, 53, 55, 56, 62, 63, 90, 100–102] or with rocking pendulums [45, 52, 69, 72–74, 103–108]. Note that a purely translated bifilar CPVA with pendulums following circular paths can be modelled using simple pendulums, explaining why several studies focused on this simple design [41, 44, 53, 61, 88, 99, 109–114]. As explained in [115], a significant advantage of the bifilar CPVAs is that their mass and inertia can be controlled more easily than that of roller CPVAs. Though roller-type pendulums and compound pendulums [40, 90] are the most common type of monofilar pendulums, more advanced monofilar designs are also possible [76]. A typical issue of CPVAs in classical operation is the generation of higher rotor harmonics, which led several works to suggest the use of CPVAs with pendulums tuned at different orders [44, 92, 93, 114, 116–118]. This special configuration was particularly studied by B. J. Vidmar [34, 35], who investigated a CPVA made of pendulums tuned on the two first rotor harmonics (*cf.* Fig. 1.16). Another issue of CPVAs is the existence of localised responses, which led J. Mayet *et al.* [47] and M. Cera *et al.* [119] to propose original designs involving an auxiliary body to which the pendulums are all connected and that prevents any asynchronous motion, as shown in Fig. 1.17. The CPVAs used in cars are sometimes combined with other means of vibration reduction such as dual-mass flywheels (DMF) to further reduce the vibrations of the powertrain [105, 120–122]. A different concept of CPVA was proposed by R. W. Zdanowich and T. S. Wilson in [44] where double pendulums are used instead of the simple pendulums, allowing to reduce the rotor's vibrations at two different orders. The system proposed consisted of an absorber (pendulum 2) rolling on a pin (pendulum 1), which itself rolls on the rotor's rolling track. A similar design, shown in Fig. 1.18, was investigated experimentally by J.-G. Duh and M. Wenyong in [123] with the aim to reduce the vibrations due to the blades of a helicopter rotor, which requires a filtering at two distinct orders [124]. Recently, V. Manchi and C. Sujatha proposed an analytical model describing the nonlinear response of a system with double pendulums [125], which they called "centrifugal double pendulum vibration absorber" (CDPVA). They also presented experimental evidence of the vibration reduction with a CDPVA installed directly on the engine shaft of an automotive vehicle.

CPVAs in multi-degree-of-freedom systems Though most studies dealing with CPVAs consider only a rotor and one or several pendulums, these devices are to be used in powertrains, which can have a complex architecture. In a first approach, it can be assumed that a powertrain is made of several inertias connected together by shafts that act as torsional springs, as represented in Fig. 1.19. Some early studies considered systems made of several rotors linked through a torsional stiffness and with a CPVA installed on one of the rotors [53, 62, 63]. More recently, S. W. Shaw, M. A. Acar *et al.* pursued these works and detailed the frequency veering effect which arises when the natural frequency of the pendulums approaches a natural frequency of the drivetrain [118, 126]. This frequency veering phenomenon also occurs with systems made of a single rotor equipped with blades [127]. K. Kadoi *et al.* studied the positioning of a CPVA in a system made of several rotors linked through shafts

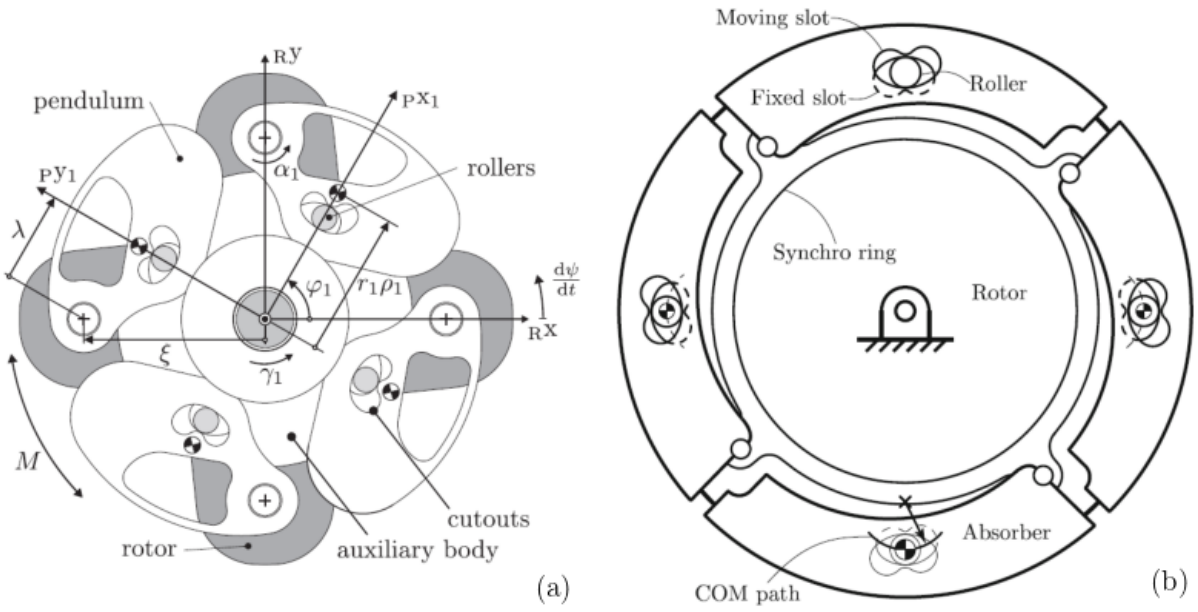

Figure 1.17: Illustration of the CPVAs enforcing a synchronous pendulums' motion proposed by J. Mayet *et al.* [47] (a) and by M. Cera *et al.* [119] (b).

represented as torsional springs and presented a test bench. Another test bench was proposed by T. Inoue *et al.* [128]. In an automotive powertrain, the CPVA is usually placed as close as possible from the engine [107, 108, 129] as this allows to isolate the driveline more efficiently from torque oscillations [2].

Kinematics of bifilar CPVAs When designing a CPVA, one wants to control the path and rotation law of the pendulums. As explained in section 1.2.4 for bifilar CPVAs, this is done through an accurate design of the rolling tracks of both the pendulums and the rotor. The shape of these tracks is not trivial, and a few years ago the designers tried different shapes iteratively until a satisfactory one was obtained. However, much more efficient and time-saving methods were recently proposed by A. Renault [2], X. Tan *et al.* [73] and J. Mayet *et al.* [74]. In each case the path and rotation law are imposed and the goal is to obtain the Cartesian coordinates of the tracks in the rotor's frame, as illustrated in Fig. 1.20.

Effect of gravity When modelling a CPVA, it is usually assumed that the centrifugal acceleration significantly dominates the gravity acceleration, so that the later is neglected (*cf.* section 2.2.1). T. M. Theisen studied this assumption in details and showed that gravity causes the appearance of a harmonic of order 1 in the system's response [130]. However, the effect of gravity is significant only at very low rotation speed, typically at idle speed. M. Mu pursued this work and focused on the gravitational parametric excitation [131], which can perturb the system's response when the engine

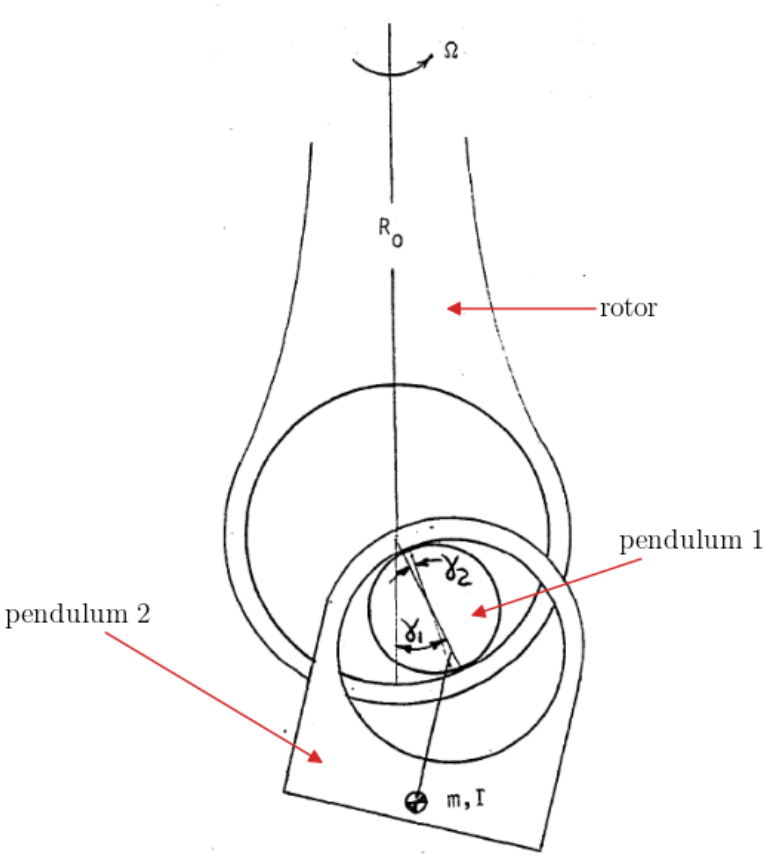

Figure 1.18: Illustration of the CDPVA studied by the NASA [123].

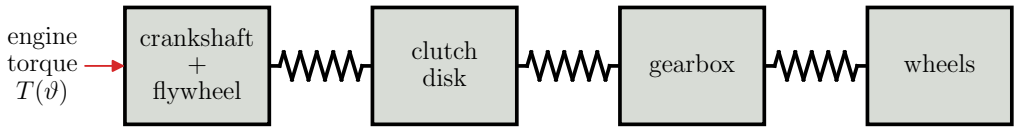

Figure 1.19: Discrete modelling of a drivetrain. The main elements act as inertias while the shafts act as torsional springs.

order is an integer. Recently, D. Tchokogoué *et al.* showed that at low speeds, gravity can cause the pendulums to respond in one or more groups, where the pendulums in each group have the same waveform but different phases [132]. They also investigated in details the direct and parametric excitation arising from gravitational effects. Special care was given to the cases where the engine order is $n_e = 1$ and $n_e = 2$, for which particular resonance effects arise between the gravitational excitation and the external torque.

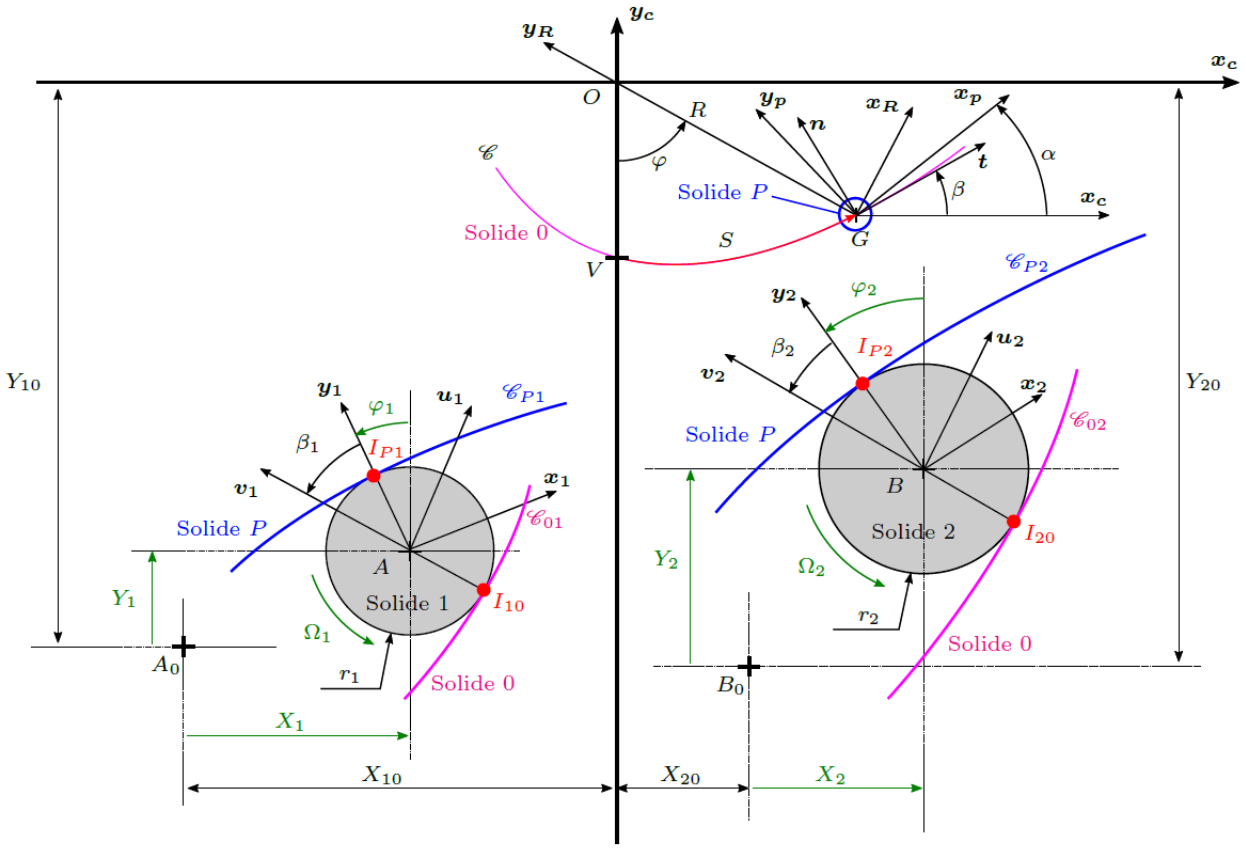

Figure 1.20: Illustration of the method proposed by A. Renault [2] to compute the rolling tracks of a bifilar CPVA. $\mathscr{C}_{P1}$ and $\mathscr{C}_{P2}$ are the rolling tracks of solid P (the pendulum, *cf.* Fig. 1.10) whose centre of mass is G. $\mathscr{C}_{01}$ and $\mathscr{C}_{02}$ are the rolling tracks of solid 0 (the rotor, *cf.* Fig. 1.10). The aim is to determine the shape of $\mathscr{C}_{P1}$, $\mathscr{C}_{P2}$, $\mathscr{C}_{01}$ and $\mathscr{C}_{02}$ such that: (i) the pendulum follows the path $\mathscr{C}$ (ii) the pendulum rotates relatively to the rotor accordingly to the angle $\alpha(S)$ (iii) the rollers (solids 1 and 2) roll without slipping on the rolling tracks.

Damping Damping in CPVAs is desired to be as small as possible (*cf.* section 2.2.4) but it is complex and depends on many physical effects such as material damping, friction, rolling resistance, windage and squeeze film for instance [91]. The influence of Coulomb friction was investigated in [133, 134]. B. J. Vidmar *et al.* [134] showed experimentally and analytically that the presence of Coulomb friction in addition to viscous losses causes the appearance of a threshold torque below which the pendulums are immobile, hence decreasing the filtering efficiency at small excitation levels. E. R. Gomez *et al.* conducted experimental investigations on a bifilar CPVA and showed that the damping could be represented as a combination of viscous losses and Coulomb friction [104]. The influence of hysteretic damping was studied in [58, 84].

Transient response Most studies on CPVAs consider only the steady state response. However, studying the transient response is particularly relevant in some cases, such as cylinder deactivation. Cylinder deactivation consists in deactivating one or more of the engine's cylinder at cruising speed in order to save gas. This deactivation leads to a sudden change in the fundamental order and amplitude of the engine's torque, causing a transient response. Analyses of this response were carried out in [135, 136] where it was shown that an overshoot can occur during the transient, bringing the pendulums to their cusp. Moreover, an experimental set-up aiming for the study of transient responses was proposed by J. Mayet *et al.* [137].

Reduction of translational and tilting rotor vibrations CPVAs are almost exclusively used to reduce torsional vibrations of a rotor. However, another interesting feature of CPVAs investigated mainly by C. Shi and R. G. Parker is their ability to reduce translational [117, 124, 138] and out-of-plane tilting vibrations [113, 114] of the rotor. The translational mobility of the rotor was also accounted for in [58, 82, 100].

Semi-passive and active CPVAs Studies on the active control of CPVAs, whose purpose is to change the pendulums' tuning order as a function of time, were conducted M. Hosek *et al.* [139] and L. Ineichen [140]. Recently, M. Auleley proposed to design a semi-passive system by coupling a CPVA with a resonant electromagnetic shunt circuit (*cf.* Fig. 1.21) to increase the vibration reduction efficiency [17, 29, 30].

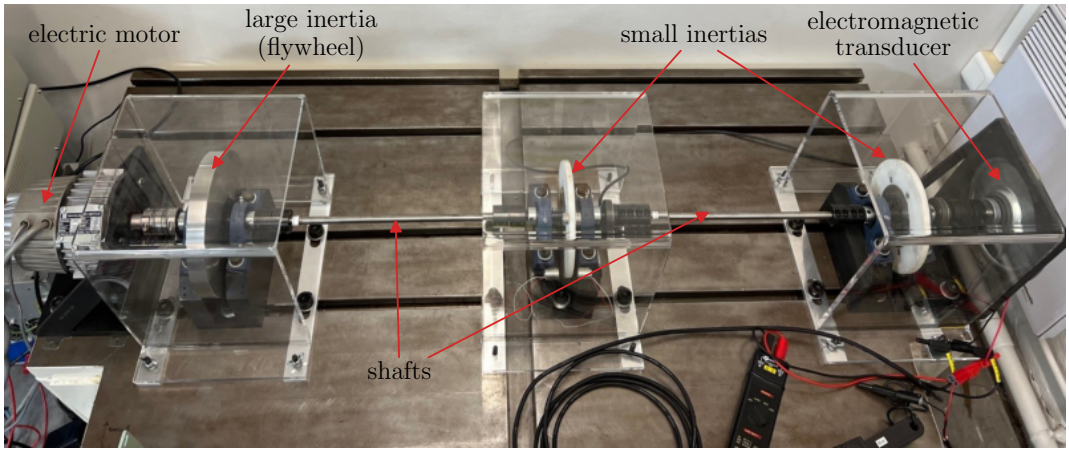

Figure 1.21: Illustration of the test bench proposed by M. Auleley [30], where an electromagnetic transducer is used to reduce the torsional vibrations of a rotating system.

Analysis methods Most of the studies presented in the literature are based on time integrations of the equations of motion and on analytical perturbation methods, usually the averaging method [141] and on rare occasions the method of multiple scales [141]. These analytical methods offer the

advantage of allowing advanced parametric studies but require assumptions and approximations that can become invalid, especially when the amplitudes of motion become large. Recently, A. Renault [2], M. A. Acar [71, 142] and A. Grolet [87] solved the system's dynamics with MANLAB [143, 144], which is a path-following and bifurcation analysis software making use of the numerical asymptotic method coupled with the harmonic balance method and which incorporates a bifurcation detector. Some studies also make use of multibody dynamics software [52, 69, 72, 82, 100, 119] to simulate the response of a CPVA.

Experimental investigations Though early investigations of CPVAs often included experimental approaches due to the limited analytical and numerical methods, A. G. Haddow, T. M. Nester *et al.* were the first to present experimental studies of a CPVA with simple pendulums in a controlled environment [90, 145–147] and obtained results in good agreement with their theoretical predictions. T. M. Nester, S. W. Shaw *et al.* pursued these works by investigating a bifilar CPVA whose pendulums follow epicycloidal paths and are guided using two steel bands wrapping along cheeks instead of two rollers [90, 91]. The acquisition of the pendulums' motion made it possible to observe the localisation of their response. B. J. Vidmar conducted experimental investigations of a CPVA with bifilar pendulums tuned on different orders [35] and obtained good agreements with his theoretical predictions. Moreover, he observed the generation of higher rotor harmonics, which is a known issue of CPVAs. He also captured the localised response and the period-doubling bifurcation leading to a subharmonic response with a CPVA made of two identical pendulums. A comparison between the localised response predicted analytically and observed experimentally was conducted in [76], which is included in the present report.

Research teams It is the automotive industry that is now driving the research activity on CPVAs. In the early 1990s, Ford collaborated with a team of American researchers, mainly S. W. Shaw (Michigan State University/Florida Tech), D. L. Cronin (Missouri University of Science & Technology) and H. H. Denman (Wayne State University). They were particularly interested in a type of centrifugal pendulum mounted directly on the crankshaft. They were soon joined by other manufacturers such as Chrysler and Honda. There was also a great deal of activity in Germany, this time under the impetus of the equipment manufacturer Luk (Shaeffler group) and the manufacturer BMW. These two research groups concentrate the majority of the studies. However, most of the academic work is published by S. W. Shaw and his collaborators, whereas equipment manufacturers such as Luk maintain a high level of secrecy about their developments and generally publish only patents. Valeo also participates to the research through the publication of patents [49, 50, 148, 149], works [2, 150], or the present report, which includes [67, 75, 76]. In addition, a significant academic activity on CPVAs recently emerged from the Italian research team led by E. Pennestrì (University of Rome Tor Vergata).

1.4 Objectives and contributions of the thesis

As explained at the beginning of this chapter, one of the solutions to reduce fuel consumption in thermal vehicles is to reduce the engine size and operating speeds. However, this requires a rise of the operating pressure inside the engine to maintain the same engine power. A direct consequence of this pressure rise is the increase of the engine acyclism, causing larger vibrations of the drivetrain. Hence, more efficient centrifugal pendulums are needed to use engines that reduce fuel consumption while maintaining the same passenger comfort and preventing fatigue of the drivetrain.

Despite the reduction of gas emission of thermal vehicles, the more and more stringent environmental standards bring the automotive industry towards electric vehicles. Though these are less noisy than thermal ones, there are sources of vibration previously masked by the engine that bring discomfort and need to be reduced. The most disturbing one is that related to the transmission errors in the gearbox. The excitation signal generated by these errors is similar to the form of the acyclic torque generated by an engine except that the excitation order is much larger and the excitation amplitude much smaller.

In this context, the main objectives of the thesis are:

1. To adapt to electric vehicles the centrifugal pendulums currently used in thermal vehicles;
2. To investigate ways to improve the efficiency of the centrifugal pendulums used in thermal vehicles

Looking at the literature, it can be seen that most studies on CPVAs consider only purely translated pendulums (this was even more true in 2019, at the beginning of the thesis). However, the works of J. Mayet *et al.* [47, 68, 74], A. Renault [2] and M. A. Acar [71] showed a few years ago that assigning a rotational mobility to the pendulums significantly improves the performance of a CPVA. There is therefore a clear interest in studying in details the effects of this additional rotational motion. The first major contribution of this thesis is thus to include in all investigations the **effect of the rotation of the pendulums**.

Known limitations of centrifugal pendulum vibration absorbers are **instabilities of their periodic response causing jumps and localisation**, the shifting of their antiresonance and the generation of higher rotor harmonics (*cf.* section 1.3). In this thesis, these aspects are investigated analytically, numerically and experimentally on pendulums with a rotational mobility (*cf.* chapters 3, 4, 8). The analytical approach allows to derive original design guidelines optimising the parameters of centrifugal pendulums to minimise their limitations. The numerical and experimental analyses allow to validate the analytical results and to explore phenomena that are too complicated to be captured analytically. In addition, localisation is seen as a limitation because it is thought to systematically

reduce the efficiency of a CPVA. However, we show analytically and numerically that there are cases where localisation is actually beneficial to vibration reduction (*cf.* chapter 5).

The high-order tuning of centrifugal pendulums required for their operation in electric powertrains is a major difficulty (*cf.* section 2.2.3). In this PhD, two solutions to overcome this problem are investigated in detail. The first idea pursued is to use a **subharmonic tuning** (*cf.* section 1.3), which allows to tune the centrifugal pendulums at half the order to be filtered. In this thesis, the subharmonic CPVA operation is investigated analytically, numerically and experimentally on pendulums with a rotational mobility (*cf.* chapters 6, 7 and 8). The experimental study is done on an original CPVA architecture made of spherical pendulums. As for the classical operation, the subharmonic one is subjected to jumps and localisation of the response and to the shifting of the antiresonance. Original guidelines to prevent or minimise these issues are derived.

A second idea for high-order tuning is to use **centrifugal double pendulum vibration absorbers**. Indeed, there is more freedom in the tuning of these devices than for centrifugal pendulums, which allows to reach higher orders without flirting too much with manufacturing tolerances. Centrifugal double pendulums received very little attention until now. In this thesis, the behaviour of such systems is investigated analytically, numerically and experimentally (*cf.* chapters 9, 10 and 11). To our knowledge, it is the first time such an advanced analytical study is led and validated numerically and experimentally. The first difficulty met with CDPVAs is the complexity of the tuning process due to the number of parameters involved. A procedure to facilitate this process is proposed. Moreover, like CPVAs, CDPVAs are subjected to jumps and localisation of their response, a shifting of their antiresonances and the generation of higher rotor harmonics. Original guidelines to prevent or limit these issues are derived.

The contributions of the thesis are represented in Tab. 1.2 along four main themes: (i) the optimisation of linear (if it exists) and nonlinear performance, (ii) the stability analysis, (iii) the study of the localised dynamics and (iv) experimental investigations. For each theme, we consider three different systems: the centrifugal pendulum vibration absorber (CPVA) in classical tuning, the CPVA in subharmonic tuning and the centrifugal double pendulum vibration absorber (CDPVA) in classical operation.

In addition to the work directly related to pendulum absorbers, a python code making use of the SymPy library for symbolic mathematics was developed during the thesis (*cf.* Appendix F). It allows for an automatised implementation of the method of multiple scales (presented in section 2.5.2.1) which saved hundreds of hours of computation during this thesis. It is written in a way such that it can be used with any nonlinear system with polynomial nonlinearities. In its current version, it is able to handle systems with 1:1:...:1 internal resonance. We believe this code could be shared to facilitate

	Optimisation of the performance	Stability analysis	The localised dynamics	Experimental investigation
CPVA in classical tuning	chap. 2 and 4	chap. 3 and 4	chap. 5	chap. 3 and 8
CPVA in subharmonic tuning	chap. 6	chap. 6 and 7	chap. 7	chap. 8
CDPVA in classical tuning	chap. 9	chap. 10	chap. 10	chap. 11

Table 1.2: Main contributions of the PhD.

the analysis of nonlinear systems.

1.5 Organisation of the report

This report is a collection of published or submitted journal articles. It is divided in four parts. Part I is made of two chapters while parts II, III and IV are each made of three chapters, making a total of eleven chapters. The main results of parts II, III and IV are summarised at the beginning of each of these parts in a dedicated summary. In this thesis, we mainly use analytical approaches to investigate centrifugal pendulums. Hence, the structure of most of the articles is similar: an analytical model is developed, it is used to derive design guidelines, and it is verified on a case study.

Part I introduces the subject of the thesis, presents generalities on centrifugal pendulums and details some specificities of nonlinear systems. Part II focuses on the classical tuning of centrifugal pendulums while part III deals with their subharmonic tuning. Finally, part IV investigates the response of centrifugal double pendulums. The content of each part is detailed below.

Part I. Introduction and generalities

The first and present chapter allowed to introduce the vibration problem to be treated and presented the concept and advantages of centrifugal pendulums. A literature review on this subject was proposed and the objectives and contributions of the thesis were detailed.

Chapter 2 introduces generalities. A modelling of the CPVA is proposed and its equations of motion are derived. A linear study is conducted to give a better insight on its operation principle. Means to simplify the equations of motion of a CPVA to prepare their analytical resolution are proposed. The question of the coupling of a CPVA with a drivetrain is also discussed. Finally, some elements on the theory of nonlinear dynamical systems and the methods to study them are described.

Part II. The classical centrifugal pendulum tuning

Chapter 3 proposes a first analytical nonlinear model of the classical CPVA operation and its stability. A case study dealing with a monofilar CPVA is presented and an original visualisation of the stability in the design space of this CPVA is introduced. The analytical model is validated numerically, design guidelines are proposed, and an experimental investigation allows to observe localisation where expected.

Chapter 4 presents a second analytical model describing the unison response of a CPVA and its stability. First, the increased accuracy of this new approach allows to highlight several limitations of the model developed in chapter 3. Then, the unison response and its stability are computed and the results are validated numerically. This chapter also focuses on the performance of a CPVA through the assessment of the shifting of its antiresonance. Guidelines are proposed to lock the antiresonance and to prevent the apparition of localised solutions. These guidelines are represented in the design space, allowing for an efficient identification of the optimal CPVA.

Chapter 5 focuses on the localised response of a CPVA. An original method to compute this response analytically and to assess its stability is presented. This allows to draw the parallel between the asynchronous motion and the modal responses, giving more insight on the localisation phenomenon. The validity of the model is verified numerically on a case study. The numerical resolution of the CPVA's dynamics allows to observe quasi-periodic and even chaotic solutions. Finally, it is shown that in some cases localisation can be beneficial for vibration reduction.

Part III. The subharmonic centrifugal pendulum tuning

The subharmonic operation of a CPVA made of two pendulums is considered in chapter 6. The concept of the subharmonic filtering is explained and its close link with the Coriolis effect is detailed. Then, a nonlinear model of the subharmonic response and its stability is developed and validated numerically. Design guidelines and performance indicators are introduced with the aim of improving the vibration reduction. Finally, the efficiency of a CPVA in subharmonic operation is compared to that of a CPVA in classical operation.

The stability of the subharmonic response in the presence of several pairs of pendulums is assessed in chapter 7. An original procedure to evaluate the stability is presented and verified numerically. Guidelines to avoid localisation of the subharmonic response are proposed and represented in the design space. Moreover, the basin of attraction of the desired subharmonic solution is analysed numerically.

Chapter 8 presents an original CPVA architecture. A prototype is build to investigate experimentally the subharmonic response of the system. Experimental results dealing with the classical behaviour are also provided. These experiments validate several features of the models developed in

chapters 4, 6 and 7. Special care is given to the analysis of the slipping of the pendulums. Then, a CPVA with the same architecture but tuned on a high order is investigated. This highlights the difficulties in realising a subharmonic CPVA to filter-out high orders.

Part IV. The centrifugal double pendulum

Chapter 9 presents the modelling and the unison response of a CDPVA. A procedure for an efficient linear tuning is described. Then, a method to assess analytically the nonlinear unison response of a CDPVA is proposed and validated numerically. Design guidelines to limit the shifting of the antiresonances are derived, which allows to maximise the performance of the system. Moreover, limitations regarding the simultaneous filtering of two orders are highlighted.

The stability of the unison response of a CDPVA is analysed in chapter 10. A numerical resolution of the system's dynamics allows to validate the analytical model and to observe quasi-periodic and chaotic solutions. A guideline to avoid instabilities is proposed and represented in the design space together with the rule from chapter 9 limiting the shifting of one of the antiresonances. This allows to identify the optimal CDPVA designs.

An original CDPVA architecture is presented in chapter 11. A prototype is build and tested experimentally, allowing to validate several features of the models developed in chapters 9 and 10. Then, a CDPVA tuned on a high order is proposed and the difficulties in the practical realisation of such a system are highlighted.

Publications

The work presented in this documents led to the publication of three journal articles [67, 75, 76], whose details are given below:

- V. Mahé, A. Renault, A. Grolet, O. Thomas, H. Mahé, "Dynamic stability of centrifugal pendulum vibration absorbers allowing a rotational mobility", *Journal of Sound and Vibration* (517), 2022,
- V. Mahé, A. Renault, A. Grolet, H. Mahé, O. Thomas, "Subharmonic centrifugal pendulum vibration absorbers allowing a rotational mobility", *Mechanical Systems and Signal Processing* (177), 2022,
- V. Mahé, A. Renault, A. Grolet, H. Mahé, O. Thomas, "On the dynamic stability and efficiency of centrifugal pendulum vibration absorbers with rotating pendulums", *Journal of Sound and Vibration* (536), 2022.

In addition, five journal articles are about to be submitted [151–155]:

- V. Mahé, A. Renault, A. Grolet, H. Mahé, O. Thomas, "Experimental investigation of the direct and subharmonic responses of a new design of centrifugal pendulum vibration absorber", about to be submitted to the *Journal of Sound and Vibration*,
- V. Mahé, A. Renault, A. Grolet, H. Mahé, O. Thomas, "Localised response of a centrifugal pendulum vibration absorber", about to be submitted to *Nonlinear Dynamics*,
- V. Mahé, A. Renault, A. Grolet, H. Mahé, O. Thomas, "On the stability of pairs of subharmonic centrifugal pendulum vibration absorbers allowing a rotational mobility", about to be submitted to *Nonlinear Dynamics*,
- V. Mahé, A. Renault, A. Grolet, H. Mahé, O. Thomas, "Unison response of a centrifugal double pendulum vibration absorber", about to be submitted to the *Journal of Sound and Vibration*,
- V. Mahé, A. Renault, A. Grolet, H. Mahé, O. Thomas, "On the dynamic stability of centrifugal double pendulum vibration absorbers", about to be submitted to the *Journal of Theoretical, Computational and Applied Mechanics*.

The python code presented in Appendix F will also be the subject of an article to come.

In addition, the studies presented in this report led to oral presentations in three national congresses [156–158] and an international one [159], whose details are given below:

- V. Mahé, A. Renault, A. Grolet, H. Mahé, O. Thomas, "Dynamic stability of tuned vibration absorbers allowing a rotational mobility", 10^{th} European Nonlinear Dynamics Conference, Lyon (Nantes), 2022,
- V. Mahé, A. Renault, A. Grolet, H. Mahé, O. Thomas, "Réponse et stabilité d'absorbeurs pendulaires centrifuges sous-harmoniques", 15^{e} Colloque National en Calcul des Structures, Presqu'île de Giens (France), 2022,
- V. Mahé, A. Renault, A. Grolet, H. Mahé, O. Thomas, "Stabilité et performance d'absorbeurs pendulaires centrifuges admettant une mobilité de rotation", 25^{e} Congrès Français de Mécanique, Nantes (France), 2022,
- V. Mahé, A. Renault, A. Grolet, H. Mahé, O. Thomas, "Subharmonic filtration in rotating machines using centrifugal pendulum vibration absorbers", 16^{e} Congrès Français d'Acoustique, Marseille (France), 2022.

Moreover, two patent applications were registered to the INPI (national patent office) and are being processed [148, 149]. Their details are given below:

- V. Mahé, A. Renault, R. Verhoog, H. Mahé, O. Thomas, “Réducteur pour véhicule électrique ou hybride avec au moins un dispositif d’amortissement pendulaire”, FR2101547,
- V. Mahé, A. Renault, A. Grolet, H. Mahé, O. Thomas, “Stabilité dynamique des amortisseurs de vibrations à pendule centrifuge permettant une mobilité rotationnelle”, FR2100397.

Chapter 2

Generalities

Content

This chapter presents the modelling of centrifugal pendulums vibration absorbers (CPVAs) in section 2.1. Then, a linear study of a CPVA is conducted in section 2.2 to highlight its basic features. Means to derive simplified CPVA models amenable to analytical analysis are described in section 2.3. The question of the positioning of a CPVA within the drivetrain and their coupling is addressed in section 2.4. Finally, some elements on the theory of nonlinear dynamical systems and the methods to study them are detailed in section 2.5.

2.1 Modelling of a centrifugal pendulum vibration absorber

2.1.1 Modelling

The aim of the current section is to present the mathematical modelling of CPVAs. In the following, we assume that the rotor and pendulums are rigid bodies. In addition, the pendulum architectures investigated in this report (*cf.* chapters 3 and 8) are made of a single body, so the rollers of bifilar CPVAs are not accounted for in the modelling. However, their effect is usually negligible [66], so the modelling proposed still allows an accurate representation of bifilar CPVAs. For the consideration of rollers in the dynamics of bifilar CPVAs, the reader may refer to [42, 47, 69, 74, 101, 104, 106]. Moreover, it is assumed that the centrifugal acceleration field in which the pendulums evolve is much larger than the acceleration of gravity [84], so the effect of the later is negligible. For the consideration of gravity, the reader is invited to consult [130, 131]. In addition, the system is considered with cyclic symmetry, so that all pendulum related properties are identical. Finally, the only dampings considered are viscous dampings.

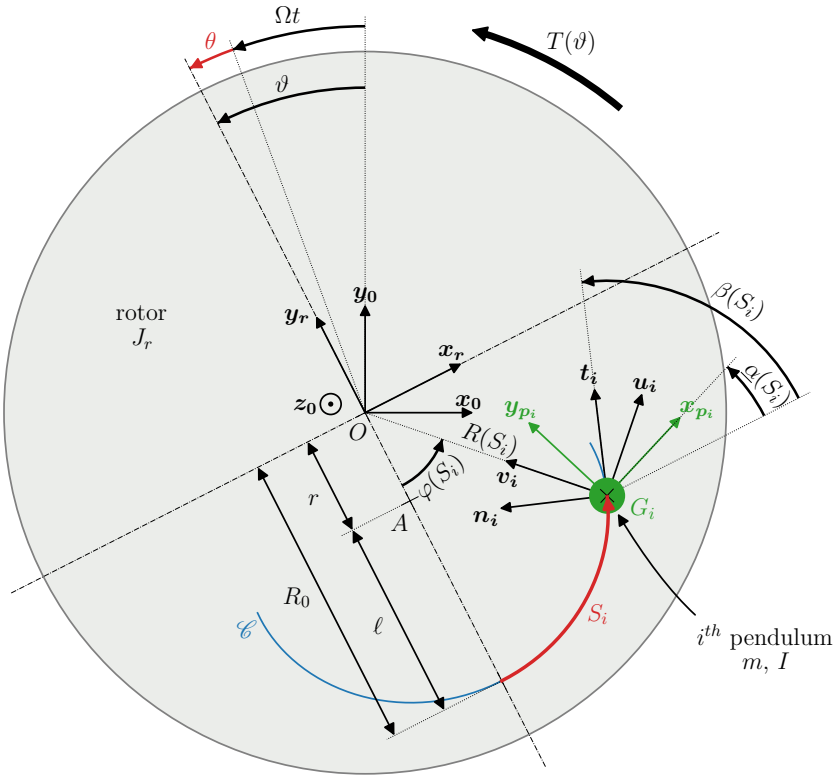

Figure 2.1: Illustration of a CPVA showing the parametrisation of the rotor and the i^{th} pendulum.

The parametrisation of a CPVA is shown in Fig. 2.1. A rotor of inertia J_r rotates about its centre O. The rotating frame $\mathscr{R}_r(O, \boldsymbol{x_r}, \boldsymbol{y_r}, \boldsymbol{z_0})$ is attached to the rotor at point O. The rotation of this frame with respect to the Galilean frame $\mathscr{R}_0(O, \boldsymbol{x_0}, \boldsymbol{y_0}, \boldsymbol{z_0})$ is $\vartheta(t) = \Omega t + \theta(t)$ where Ω is the mean rotational velocity and $\theta(t)$ corresponds to the fluctuating part of the rotation.

N pendulums of mass m and inertia I about their centre of mass G_i oscillate on their path $\mathscr{C}$. The position of G_i along $\mathscr{C}$ is located through the curvilinear abscissa S_i whose origin is taken at the vertex of $\mathscr{C}$. The centre of curvature of $\mathscr{C}$ at $S_i = 0$, denoted A, is located at a distance r from O, and the associated radius of curvature is ℓ. $R_0 = r + \ell$ indicates the distance at rest $OG_i(S_i = 0)$. $\mathscr{R}_{uvi}(G_i, \boldsymbol{u_i}, \boldsymbol{v_i}, \boldsymbol{z_0})$ is an orthonormal frame such that $\boldsymbol{v_i}$ points from G_i to O. $\mathscr{R}_{tni}(G_i, \boldsymbol{t_i}, \boldsymbol{n_i}, \boldsymbol{z_0})$ is an orthonormal frame such that $\boldsymbol{t_i}$ and $\boldsymbol{n_i}$ are vectors tangent and normal to $\mathscr{C}$ at abscissa S_i. The shape of $\mathscr{C}$ can be parametrised relatively to the rotor through the path functions $R(S_i)$ and $\varphi(S_i)$. Indeed, is we use the relations $\boldsymbol{v_i} = -\sin\varphi(S_i)\boldsymbol{x_r} + \cos\varphi(S_i)\boldsymbol{y_r}$, then the curve $\mathscr{C}$ can be described by

$$\mathscr{C}: \{G_i,\, \boldsymbol{OG_i} = -R(S_i)[-\sin\varphi(S_i)\boldsymbol{x_r} + \cos\varphi(S_i)\boldsymbol{y_r}]\}. \tag{2.1}$$

However, in practice, it is much more convenient to introduce the path functions

$$X(S_i) = R(S_i)^2, \tag{2.2a}$$

$$Z(S_i) = R(S_i)^2\left|\frac{d\varphi(S_i)}{dS_i}\right| = \sqrt{X(S_i) - \frac{1}{4}\left(\frac{dX(S_i)}{dS_i}\right)^2}, \tag{2.2b}$$

which can be used to locate G_i using the local frame $\mathscr{R}_{tni}$ such that

$$\boldsymbol{OG_i} = \frac{1}{2}\frac{dX(S_i)}{dS_i}\boldsymbol{t_i} - Z(S_i)\boldsymbol{n_i}. \tag{2.3}$$

Indeed, the path functions Z, R, φ and β can all be expressed in terms of X (*cf.* Appendices A.3 and A.4 of the paper included in section 8.1). Hence, the shape of $\mathscr{C}$ can be controlled using only X. More details on function X are provided in section 2.1.3. The frame $\mathscr{R}_{pi}(G_i, \boldsymbol{x_{pi}}, \boldsymbol{y_{pi}}, \boldsymbol{z_0})$ is attached to the i$^{\text{th}}$ pendulum at point G_i and its rotation with respect to $\mathscr{R}_r$ is $\underline{\alpha}(S_i)$. A linear viscous damping coefficient b is used to model the damping of the pendulums in their motion relative to the rotor.

A torque $T(\vartheta) = T_0 + T_\theta(\vartheta)$ is applied to the rotor where T_0 is a constant component and $T_\theta(\vartheta)$ is periodic with fundamental order of excitation n_e. n_e is a constant depending on the architecture of the exciting system.

2.1.2 Equations of motion

2.1.2.1 Dimensional equations of motion

In this section we set up the equations of motion for a system composed of a rotor and N pendulums. To this end, the Euler-Lagrange equation are used. One therefore needs to first compute the kinetic and potential energies and the generalized forces applied on the system.

The kinetic energy of the system is

$$\mathcal{T} = \frac{1}{2}J_r\dot{\vartheta}^2 + \frac{1}{2}\sum_{i=1}^{N}\left[m\left(\dot{S}_i^2 + X_i(S_i)\dot{\vartheta}^2 + 2\dot{\vartheta}\dot{S}_i Z_i(S_i)\right) + I(\dot{\vartheta} + \dot{S}_i\Gamma(S_i))^2\right], \tag{2.4}$$

where we have introduced the rotation function

$$\Gamma(S_i) = \frac{d\underline{\alpha}(S_i)}{dS_i}. \tag{2.5}$$

As gravity is neglected, the potential energy is $\mathcal{U} = 0$ so that the Lagrangian is simply $\mathcal{L} = \mathcal{T}$. There are three external loads applied on the system:

- A torque $T(\vartheta)\boldsymbol{z_0}$ is applied on the rotor. It is the external forcing.
- A resistive torque $-b_r\dot{\vartheta}\boldsymbol{z_0}$ is applied on the rotor. It represents the damping between the rotor and the ground.
- A resistive force $-b\dot{S}_i\boldsymbol{t_i}$ is applied on the center of mass of the i^{th} pendulum, where $\boldsymbol{t_i}$ is the vector tangent to the path $\mathscr{C}$ at abscissa S_i. It represents the damping of the i^{th} pendulum in the rotor's frame.

Using the Euler-Lagrange equations, one obtains the equations of motion for the rotor and pendulum i:

$$\begin{aligned}&\underbrace{\left[J_r + \sum_{i=1}^{N}(I + mX(S_i))\right]}_{\text{equivalent inertia}}\ddot{\vartheta} + \sum_{i=1}^{N}\underbrace{(mZ(S_i) + I\Gamma(S_i))\,\ddot{S}_i + m\frac{dZ(S_i)}{dS_i}\dot{S}_i^2}_{\substack{\text{torque exerted by}\\ \text{inertial forces}}}\\ &+ \underbrace{I\frac{d\Gamma(S_i)}{dS_i}\dot{S}_i^2}_{\substack{\text{torque exerted during}\\ \text{the accelerated}\\ \text{rotation}}} + \underbrace{m\frac{dX(S_i)}{dS_i}\dot{\vartheta}\dot{S}_i}_{\text{Coriolis effect}} + \underbrace{b_r\dot{\vartheta}}_{\text{damping}} = \underbrace{T(\vartheta)}_{\substack{\text{external}\\ \text{torque}}},\end{aligned} \tag{2.6a}$$

$$\underbrace{(mZ(S_i) + I\Gamma(S_i))\,\ddot{\vartheta}}_{\text{inertial force}} + \underbrace{\left(m + I\Gamma(S_i)^2\right)}_{\text{equivalent mass}}\ddot{S}_i + \underbrace{I\Gamma(S_i)\frac{d\Gamma(S_i)}{dS_i}\dot{S}_i^2}_{\text{force along the path}} - \underbrace{\frac{1}{2}m\frac{dX(S_i)}{dS_i}\dot{\vartheta}^2}_{\text{centripetal force}} + \underbrace{b\dot{S}_i}_{\text{damping}} = 0. \tag{2.6b}$$

Eq. (2.6a) governs the motion of the rotor while the N Eqs. (2.6b) govern the motion of the pendulums. In Eq. (2.6a), the term $J_r + \sum_{i=1}^{N}(I + mX(S_i))$ represents an equivalent inertia of the rotor, due to the fact that it supports all the pendulums. The terms $(mZ(S_i) + I\Gamma(S_i))\ddot{S}_i$ and $mdZ(S_i)/dS_i\dot{S}_i^2$ represent the torque produced on the rotor by the inertial forces of the pendulums. $Id\Gamma(S_i)/dS_i\dot{S}_i^2$ corresponds to the torque exerted on the rotor by a pendulum during its accelerated rotation around its centre of mass. Finally, the term $mdX(S_i)/dS_i\dot{\vartheta}\dot{S}_i$ represents the torque generated via the Coriolis

effect. It is interesting to note that evaluating Eq. (2.6a) at equilibrium (i.e. $T_\theta(\vartheta) = 0\ \forall\vartheta$, such that $\dot{\vartheta} = \Omega$ and $S_i = 0$, $i = 1, ..., N$) leads to

$$b_r\Omega = T_0, \tag{2.7}$$

meaning that the viscous torque exerted on the rotor balances with the constant component of the exciting torque, thus fixing the average rotation speed Ω.

Each of the pendulums' equations (2.6b) involves only the i$^{\text{th}}$ pendulum, meaning that the pendulums are only coupled through the rotor (indeed, every pendulum appears in Eq. (2.6a)). In equation (2.6b), the term $(mZ(S_i) + I\Gamma(S_i))\ddot{\vartheta}$ corresponds to the inertial force of the rotor on the pendulum. $mdX(S_i)/dS_i\vartheta^2$ results from the action of the centripetal force on the pendulum. It is a force that opposes its movement and tends to bring it back to its rest position, so that it plays the role of a restoring force. The term $m + I\Gamma(S_i)^2$ corresponds to an equivalent mass of the pendulum. It shows that the rotation of a pendulum virtually increases its mass, which is the reason why rocking pendulums received an increased interest in the past few years (*cf.* section 1.2.4). Finally, the term $I\Gamma(S_i)d\Gamma(S_i)/dS_i\dot{S}_i^2$ represents a nonlinear force applied along the path of the pendulum during its accelerated rotation.

Note that in several studies [65, 73, 83], it is considered that the pendulums' damping causes a force $b\dot{S}_i\boldsymbol{t_i}$ applied on the rotor at point G_i. This generates a resistive torque $\boldsymbol{OG_i} \times b\dot{S}_i\boldsymbol{t_i} = bZ(S_i)\dot{S}_i\boldsymbol{z_0}$ on the rotor which adds up to the exciting torque. However, this is not accounted for in the modelling proposed in this report as the pendulums' damping is represented as external resistive forces affecting only the pendulums, without any action on the rotor. Moreover, for pendulums following circular paths, the pendulums' damping is introduced as a resistive torque so it does not generate any additional term in the rotor's equation [134]. Furthermore, the resistive torque $bZ(S_i)\dot{S}_i\boldsymbol{z_0}$ is very small such that it is negligible in practice and is not considered in several studies [85, 87, 130]. Hence, both representations of the damping are almost equivalent.

2.1.2.2 Dimensionless equations of motion

In the aim of performing analytical studies, is is convenient to reduce the number of parameters by rewriting the equation of motion under a dimensionless form. To do so, we can introduce the

dimensionless quantities

$$\begin{gathered} s_i = \frac{S_i}{R_0}, \quad \tau = \Omega t, \quad \eta = \frac{I}{mR_0^2}, \quad \mu = \frac{NmR_0^2}{J_r + NI}, \\ \bar{b} = \frac{b}{m\Omega}, \quad \bar{b}_r = \frac{b_r}{(J_r + NI)\Omega}, \quad \bar{T}(\vartheta) = \bar{T}_0 + \bar{T}_\theta(\vartheta) = \frac{T(\vartheta)}{(J_r + NI)\Omega^2}, \\ x(s_i) = \frac{X(R_0 s_i)}{R_0^2}, \quad z(s_i) = \sqrt{x(s_i) - \frac{1}{4}\left(\frac{dx(s_i)}{ds_i}\right)^2}, \\ \alpha(s_i) = \underline{\alpha}(R_0 s_i), \quad \gamma(s_i) = \frac{d\alpha(s_i)}{ds_i}. \end{gathered} \tag{2.8}$$

The s_i are the dimensionless curvilinear abscissa of the pendulums on their paths. τ is a dimensionless time. η is the ratio of a pendulum's rotational inertia over its geometric inertia at rest about O. μ is the ratio of the pendulums' geometric inertias at rest about O over the rotational inertia of the whole system. It is small in practice as J_r is large in front of the pendulums' geometric inertia mR_0^2. $\bar{b}$ and $\bar{b}_r$ are dimensionless damping constants and $\bar{T}(\vartheta)$ is the dimensionless torque applied on the rotor. $x(s_i)$ and $z(s_i)$ are dimensionless path functions while $\alpha(s_i)$ and $\gamma(s_i)$ are dimensionless rotation functions.

Introducing these dimensionless quantities in Eqs. (2.6a) and (2.6b), using the chain rule

$$\frac{\partial(\bullet)}{\partial t} = \Omega \frac{\partial(\bullet)}{\partial \tau}, \tag{2.9}$$

and defining $(\bullet)' = \partial(\bullet)/\partial\tau$, we obtain the dimensionless equations for the rotor and the i$^{\text{th}}$ pendulum

$$\begin{aligned} &\frac{1}{N}\left[\sum_{i=1}^{N}(N + \mu x(s_i))\vartheta'' + \mu\left(z(s_i) + \eta\gamma(s_i)\right)s_i'' + \mu s_i'\left(\frac{dx(s_i)}{ds_i}\vartheta' + \frac{dz(s_i)}{ds_i}s_i' + \eta\frac{d\gamma(s_i)}{ds_i}s_i'\right)\right] \\ &+ \bar{b}_r\vartheta' = \bar{T}(\vartheta), \end{aligned} \tag{2.10a}$$

$$\left(z(s_i) + \eta\gamma(s_i)\right)\vartheta'' + \left(1 + \eta\gamma(s_i)^2\right)s_i'' + \eta\gamma(s_i)\frac{d\gamma(s_i)}{ds_i}s_i'^2 - \frac{1}{2}\frac{dx(s_i)}{ds_i}\vartheta^2 + \bar{b}s_i' = 0, \tag{2.10b}$$

It is interesting to note that the inertia ratio μ, present only in the rotor's equation (2.10a), governs the coupling between the pendulums and the rotor. If the rotor's inertia is much larger than the pendulums', then their effect is negligible. This is well-seen through the limit case $\mu = 0$, corresponding to uncoupled pendulums.

It is important to note that in Eq. (2.10a), the exciting torque does not appear as an external forcing term but as a nonlinear term because of its dependence on ϑ. To tackle this issue, two solutions are possible. They are presented thereafter.

First method to transform the torque into a periodic forcing term A way of transforming the torque into a periodic forcing term, used for instance in [2, 86], is to assume $\theta \ll \tau$ (or equivalently, $\dot{\theta} \ll \Omega$) such that we can approximate $\vartheta \approx \tau$. The assumption $\theta \ll \tau$ makes sense as the aim of the pendulums is to reduce θ to make it as small as possible. The approximation allows to write $T_\theta(\vartheta) \approx T_\theta(\tau)$, so that the external torque is now a periodic forcing term.

Second method to transform the torque into a periodic forcing term Another possibility to transform the torque into a periodic forcing term, is to use the change of variables $\tau \to \vartheta$ initially proposed by S. W. Shaw and S. Wiggins [160]. This change of variables is possible as, in practice, the fluctuations of θ are small such that ϑ increases monotonically. Now that ϑ is the independent variable, $T_\theta(\vartheta)$ is a periodic forcing term. However, one now needs to rewrite the other terms of Eqs. (2.10a) and (2.10b) with ϑ as the independent variable

To introduce the change of variable $\tau \to \vartheta$ in Eqs. (2.10a) and (2.10b), it is convenient to redefine $(\bullet)' = \partial(\bullet)/\partial\vartheta$, to introduce the dimensionless rotor's rotational velocity

$$y = \frac{\dot{\vartheta}}{\Omega} = 1 + \frac{\dot{\theta}}{\Omega} \tag{2.11}$$

and to use the chain rule

$$\dot{(\bullet)} = \Omega y (\bullet)', \quad \ddot{(\bullet)} = \Omega^2 y y' (\bullet)' + \Omega^2 y^2 (\bullet)''. \tag{2.12}$$

Note that with these notations, the rotor acceleration is now $\ddot{\theta} = \Omega^2 y y'$. Introducing the above in Eqs. (2.10a) and (2.10b) and dividing the latter by y, one obtains

$$\begin{aligned} &\frac{1}{N}\left[\sum_{i=1}^{N}(N+\mu x(s_i))yy' + \mu\left(z(s_i)+\eta\gamma(s_i)\right)\left(yy's_i' + y^2 s_i''\right)\right. \\ &\left. + \mu y^2 s_i'\left(\frac{dx(s_i)}{ds_i} + \frac{dz(s_i)}{ds_i}s_i' + \eta\frac{d\gamma(s_i)}{ds_i}s_i'\right)\right] + \bar{b}_r y = \bar{T}(\vartheta), \end{aligned} \tag{2.13a}$$

$$\left[z(s_i)+\eta\gamma(s_i)\right]y' + \left[1+\eta\gamma(s_i)^2\right]\left(y's_i' + ys_i''\right) + \eta\gamma(s_i)\frac{d\gamma(s_i)}{ds_i}ys_i'^2 - \frac{1}{2}\frac{dx(s_i)}{ds_i}y + \bar{b}s_i' = 0. \tag{2.13b}$$

Eqs. (2.13a) and (2.13b) are equivalent to Eqs. (2.10a) and (2.10b), but the independent variable is ϑ rather than τ, which allows to express the torque as a periodic forcing term without any approximation. However, this is done at the expanse of complexity as the change a variable introduced several additional nonlinear terms.

2.1.3 Pendulums' path and rotation

2.1.3.1 Representation of the path and rotation functions

A description of general pendulum paths introduced by Denman [42] uses a one-parameter function to control the radius of curvature $\rho(S)$ of $\mathscr{C}$ such that

$$\rho^2(S) = \ell^2 - \lambda^2 S^2, \tag{2.14}$$

where ℓ is the radius of curvature at the vertex of the path (*cf.* Fig. 2.1) and λ is a parameter taking values between 0 and 1. Equation (2.14) has the advantage to allow for a simple representation of the most common paths. Indeed, the circular, epicycloidal and cycloidal paths simply correspond to $\lambda_{\text{circ}} = 0$, $\lambda_{\text{epi}} = \sqrt{n_t^2/(n_t^2+1)}$, $\lambda_{\text{cyc}} = 1$, where the parameter n_t designates the order of the path. It is defined by

$$n_t = \sqrt{\frac{r}{\ell}}, \tag{2.15}$$

with $r = R_0 - \ell$ (*cf.* Fig. 2.1). Note that index "t" stands for "trajectory". In the case where the pendulums do not rotate about their centre of mass or their inertia is neglected, n_t also corresponds to the natural order of the pendulums (*cf.* section 2.2.1.1).

Despite the convenience of $\rho(S)$, solving the equations of motion (2.6a) and (2.6b) requires a well-defined form of $X(S)$. It can be derived from $\rho(S)$ [42], but the expression then obtained is very complex in the general case. This is why, in this report, it is chosen to represent the path directly through the function X. The expressions of $X(S)$ corresponding to an epicycloid, a circle (centred on A, *cf.* Fig. 2.1) and a cycloid are given by

$$X(S) = R_0^2 - n_t^2 S^2, \tag{2.16a}$$

$$X(S) = r^2 + \ell^2 + 2\ell r \cos\left(\frac{S}{\ell}\right), \tag{2.16b}$$

$$X(S) = (r+\ell)^2 - \left(\frac{r}{\ell} + \frac{3}{4}\right) S^2 + \frac{\ell^2}{4} \arcsin\left(\frac{S}{\ell}\right) \left(\arcsin\left(\frac{S}{\ell}\right) + 2\frac{S}{\ell}\sqrt{1 - \frac{S^2}{\ell^2}}\right), \tag{2.16c}$$

respectively [2, 42]. In order to highlight the similarities between the three paths described in Eq. (2.16), we propose to use Taylor series of $X(S_i)$ in S_i to obtain a polynomial representation of these paths. Doing so and using the relation (2.8) between $X(S)$ and $x(s)$, the expression of the dimensionless path function $x(s)$ for the epicycloid, the circle and the cycloid becomes [2]

$$x(s) = 1 - n_t^2 s^2, \tag{2.17a}$$

$$x(s) = 1 - n_t^2 s^2 + \frac{n_t^2(1+n_t^2)^2}{12} s^4 + \mathcal{O}(s^6), \tag{2.17b}$$

$$x(s) = 1 - n_t^2 s^2 - \frac{(1+n_t^2)^2}{12} s^4 + \mathcal{O}(s^6), \tag{2.17c}$$

respectively. The expression for the epicycloid is exact as its full expression is already a polynomial in s (*cf.* Eq. (2.16a)). However, the circle and the cycloid appear as an epicycloid perturbed by higher even powers of s_i. We conclude that every path of interest can be represented as a perturbed epicycloid. This is why, in this report, we choose to represent $x(s)$ as

$$x(s) = 1 - n_t^2 s^2 + \sum_{k=3}^{N_x} x_{[k]} s^k. \tag{2.18}$$

In practice the paths are symmetric, meaning that $x(s)$ is an even function with only even power monomials. It is also important to note that the paths described by Eq. (2.18) are not defined for all values of s as the dimensionless distance $z(s)$ (*cf.* Eq. (2.8)) must remain real. Hence, the cusp of a path is given by $z(s_{\text{cusp}}) = 0$, which, in the case of the epicycloid, leads to

$$s_{\text{cusp}} = \frac{1}{\sqrt{n_t^2(1+n_t^2)}}. \tag{2.19}$$

Finally, note that there are other ways to parametrise a path, for instance using curvature ratios [52, 69, 72, 103, 119]. However, in the author's opinion, the use of $x(s)$ is much more convenient and provides a provides a clearer explanation of the results.

The rotation function can also be represented as a polynomial such that

$$\alpha(s) = \sum_{k=0}^{N_\alpha} \alpha_{[k]} s^k. \tag{2.20}$$

In practice the rotation is antisymmetric, meaning that $\alpha(s)$ is an odd function with only odd power monomials.

2.1.3.2 Interpretation

In order to interpret the different terms composing the path and rotation functions (2.18) and (2.20), we can consider the generic case

$$x(s) = 1 - n_t^2 s^2 + x_{[4]} s^4, \tag{2.21a}$$

$$\alpha(s) = \alpha_{[1]} s + \alpha_{[3]} s^3. \tag{2.21b}$$

s is typically small because R_0 is usually much larger than S (*cf.* Eq. (2.8)), and because it is limited by the cusp of the path (*cf.* Eq. (2.19)). Hence, it is relevant to limit $x(s)$ to s^4 and $\alpha(s)$ to s^3 in order to capture the dominant phenomena. After inserting Eq. (2.21) into Eq. (2.10b) and considering a CPVA made of a single pendulum, a conservative system and a uniform centrifugal acceleration field (i.e. $N = 1$, $\bar{b} = 0$, $\vartheta' = 1$), the pendulum's equation becomes

$$\left(1 + \eta\alpha_{[1]}^2\right) s'' + n_t^2 s - 2x_{[4]} s^3 + 6\eta\alpha_{[1]}\alpha_{[3]} \left(s^2 s'' + s s'^2\right) + \mathcal{O}(s^5) = 0. \tag{2.22}$$

From Eq. (2.22), one can see that $\eta\alpha_{[1]}^2$ increases the equivalent mass of the pendulum and that n_t^2 plays a role of linear stiffness. $x_{[4]}$ and $\alpha_{[3]}$ determine the nonlinear behaviour of the pendulum at first order. $x_{[4]}$ is a cubic nonlinearity coefficient, showing similarities between pendulums and a Duffing oscillator [161]. The nonlinearity arising from the rotation is more complex as it involves several inertial terms, but it is also cubic.

Pendulums with $x_{[4]} = \alpha_{[3]} = 0$ are said to be tautochronic because their period of oscillation does not depend on their amplitude. $x_{[4]} = 0$ corresponds to the epicycloid, which is thus the tautochronic path of a pendulum in a uniform centrifugal acceleration field [42]. Hence, it is not surprising that $x_{[4]}$, which represents a perturbation of the epicycloid, is the only source of path nonlinearity in Eq. (2.22).

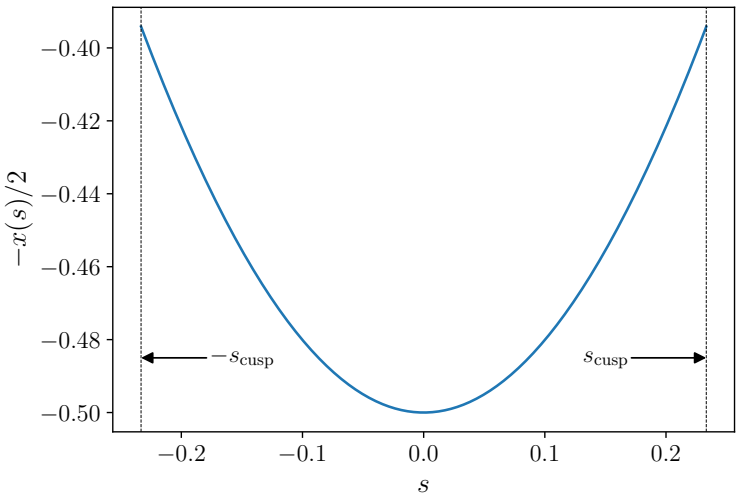

Figure 2.2: Illustration of the potential function $-x(s)/2$. $n_t = 2$, $x_{[4]} = 2$.

In order to provide another interpretation of $x(s)$, we propose to consider for an instant that the pendulum is in pure translation. First, we evaluate again Eq. (2.10b) with a single undamped pendulum evolving in a uniform centrifugal acceleration field. Then, we multiply this equation by s' and integrate it over s [93], leading to

$$\frac{1}{2}s'^2 - \frac{x(s)}{2} = \kappa, \tag{2.23}$$

where κ is an integration constant. Equation (2.23) is typical of a particle evolving in a potential well [162]. This allows to see $-x(s)/2$ as a potential function (this is illustrated in Fig. 2.2) whose quadratic term dictates the linear behaviour of the pendulums while higher order terms determine its nonlinear behaviour [65].

2.2 Linear analysis of a centrifugal pendulum vibration absorber

The aim of this section is to give some insights on the use of a CPVA by presenting its linear modes, its linear response and some linear performance indicators. It is crucial to have a good understanding of these features before studying the nonlinear response.

Introducing the expressions of the path (2.18) and rotation (2.20) functions in the equations of motion (2.10a) and (2.10b), making use of Eq. (2.7) and assuming $\vartheta \approx \tau$ in order to express $\bar{T}_\theta(\vartheta) \approx \bar{T}_\theta(\tau)$ (*cf.* section 2.1.2.2), we obtain, after linearisation, the linear equations

$$(1+\mu)\theta'' + \frac{\mu\Lambda_c}{N}\sum_{i=1}^{N} s_i'' + \bar{b}_r\theta' = \bar{T}_\theta(\tau), \tag{2.24a}$$

$$\Lambda_c\theta'' + \Lambda_m s_i'' + n_t^2 s_i + \bar{b}s_i' = 0, \quad i = 1, ..., N. \tag{2.24b}$$

Here, we have introduced the constants Λ_m and Λ_c, which represent the equivalent mass of a pendulum and the linear coupling term between a pendulum and the rotor. They are given by

$$\Lambda_m = 1 + \eta\alpha_{[1]}^2, \tag{2.25a}$$

$$\Lambda_c = 1 + \eta\alpha_{[1]}, \tag{2.25b}$$

where we remind that $\alpha_{[1]}$ is the linear rotation coefficient (*cf.* Eqs. (2.20) and (2.21)).

2.2.1 Modal analysis

2.2.1.1 The uncoupled pendulums

To better understand pendulum systems, it is interesting to evaluate the pendulums' linear equation (2.24b) in the conservative case and for a uniform centrifugal acceleration field (i.e. $\bar{b} = \theta = 0$). This configuration is often termed "uncoupled pendulums" as the rotor is no longer a degree-of-freedom so that there is no coupling between the pendulums and the rotor, nor between the pendulums. Dividing this uncoupled pendulums' equation by Λ_m, we obtain

$$s_i'' + n_p^2 s_i = 0, \tag{2.26}$$

where n_p is the pendulums' natural order, which we will later call the pendulums' tuning order, and whose expression is

$$n_p = \frac{n_t}{\sqrt{\Lambda_m}}. \tag{2.27}$$

The associated natural frequency is $\omega_p = n_p\Omega$. In the special case where the pendulums are purely translated, this reduces to $\omega_p = \sqrt{r\Omega^2/\ell}$. It is interesting to compare this result to the well-known natural frequency of a simple pendulum of length ℓ in the gravity field, given by $\omega_g = \sqrt{g/\ell}$ [163], as it allows to draw the parallel between the centrifugal acceleration $r\Omega^2$ and the gravity acceleration g.

In the present report the effect of gravity is neglected, meaning that we always assume $r\Omega^2 \gg g$. The differences between a point-mass (or purely translated) pendulum evolving in a gravity field and in a uniform centrifugal acceleration field are summarised in Tab. 2.1.

	acceleration constant	pendulum's natural frequency
Uniform centrifugal acceleration field	$r\Omega^2$	$\omega_p = \Omega\sqrt{r/\ell}$
Gravity field	g	$\omega_g = \sqrt{g/\ell}$

Table 2.1: Differences between a point-mass (or purely translated) pendulum evolving in the gravity field and a uniform centrifugal acceleration field.

2.2.1.2 Coupled system (CPVA)

A modal analysis of a CPVA is now presented. The free, conservative equations associated to system (2.24) can be written as

$$\boldsymbol{M}\ddot{\boldsymbol{q}} + \boldsymbol{K}\boldsymbol{q} = \boldsymbol{0}, \tag{2.28}$$

where $\boldsymbol{q}$, $\boldsymbol{M}$ and $\boldsymbol{K}$ are the vector containing the degrees of freedom and the mass and stiffness matrices, respectively. They are given by

$$\boldsymbol{q} = \begin{bmatrix} \theta \\ s_1 \\ \vdots \\ s_N \end{bmatrix}, \quad \boldsymbol{M} = \begin{bmatrix} N\frac{1+\mu}{\mu} & \Lambda_c & \cdots & \cdots & \Lambda_c \\ \Lambda_c & \Lambda_m & 0 & \cdots & 0 \\ \vdots & 0 & \ddots & \ddots & \vdots \\ \vdots & \vdots & \ddots & \ddots & 0 \\ \Lambda_c & 0 & \cdots & 0 & \Lambda_m \end{bmatrix}, \quad \boldsymbol{K} = \begin{bmatrix} 0 & & & \\ & n_t^2 & & (0) \\ & & \ddots & \\ & (0) & & n_t^2 \end{bmatrix}. \tag{2.29}$$

The associated eigenvalue problem is

$$[\boldsymbol{K} - n^2\boldsymbol{M}]\boldsymbol{\phi} = \boldsymbol{0}, \tag{2.30}$$

whose solutions, composed of an eigenorder n and and eigenshape $\boldsymbol{\phi}$, are the modes of the system. Note that n can be seen as a dimensionless frequency. $[\boldsymbol{K} - n^2\boldsymbol{M}]$ is an arrowhead matrix as it is full of zeros except for its first row, first column and its diagonal. In addition, every term on its diagonal are the same except for the first one. As explained in [164], the eigenvalues of such a matrix are those of a reduced 2×2 matrix (whose computation is trivial) together with the identical terms of the diagonal. Using this procedure, one can easily compute the $N+1$ linear modes $(n_{00}, \boldsymbol{\phi_{00}})$, $(n_{10}, \boldsymbol{\phi_{10_1}})$, ..., $\left(n_{10}, \boldsymbol{\phi_{10_{N-1}}}\right)$, $(n_{20}, \boldsymbol{\phi_{20}})$, whose eigenorders and mode shapes are

$$\begin{gathered} n_{00} = 0, \quad \boldsymbol{\phi_{00}} = [1, 0, ..., 0]^\intercal, \\ n_{10} = n_p, \quad \boldsymbol{\phi_{10_1}} = [0, 1, -1, 0..., 0]^\intercal, \ ..., \ \boldsymbol{\phi_{10_{N-1}}} = [0, 0, ...0, 1, -1]^\intercal, \\ n_{20} = n_p\sqrt{\frac{1+\mu}{1+\mu\left(1-\frac{\Lambda_c^2}{\Lambda_m}\right)}}, \quad \boldsymbol{\phi_{20}} = \left[-\frac{\mu\Lambda_c}{1+\mu}, 1, ..., 1\right]^\intercal, \end{gathered} \tag{2.31}$$

where superscript $^\intercal$ indicates the transpose. These modes are illustrated in Fig. 2.3 for a CPVA made of $N = 2$ pendulums. $(n_{00}, \boldsymbol{\phi_{00}})$ is a rigid body mode for which only the rotor is excited. $(n_{10}, \boldsymbol{\phi_{10_i}})$ are $N-1$ degenerated modes for which only two pendulums are moving in phase-opposition, the others remaining immobile. Their eigenvalue $n_{10} = n_p$ has multiplicity $N-1$ and the rotor is a node of these modes. For a CPVA made of only two pendulums, $(n_{10}, \boldsymbol{\phi_{10}})$ is not degenerated and simply represents a phase-opposition motion of the pendulums. $(n_{20}, \boldsymbol{\phi_{20}})$ is a mode for which the pendulums move in unison but in phase-opposition with respect to the rotor (provided that $\Lambda_c > 0$, which is the case for reasonable parameters). It will be referred-to as the "unison mode" or "mode 2". More details on the modes of a CPVA with more than two pendulums are provided in the paper included in chapter 7.

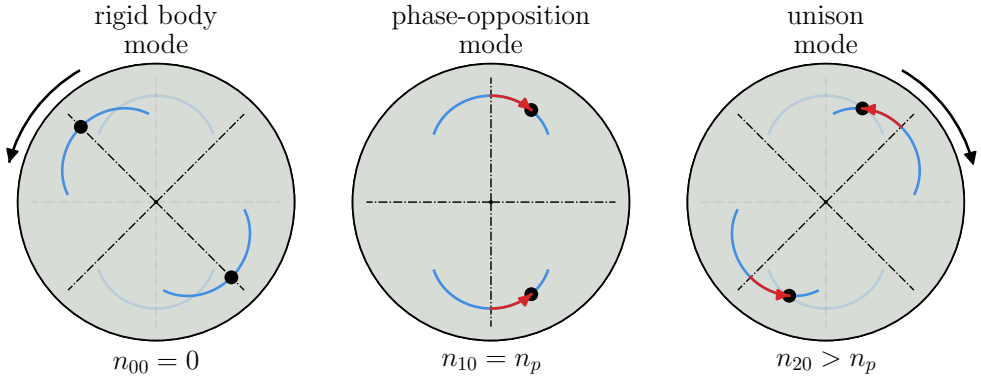

Figure 2.3: Modes of a CPVA made of $N = 2$ pendulums. The rotation of the pendulums about their centre of mass is not represented in this figure.

2.2.2 Linear forced response and tuning of a centrifugal pendulum

In this section, we assume that the torque applied on the rotor contains only the fundamental harmonic such that $\bar{T}_\theta(\tau) = \bar{T}_1 \cos(n\tau)$ and we analyse the linear forced response of the system. Note that in practice, $n = n_e$ is fixed, but it is convenient to make it vary in order to better understand the dynamics of a CPVA by obtaining a curve that can be interpreted as a frequency response function. The computation of the forced CPVA response is detailed in Appendix B and leads to solutions of the form

$$\theta'' = h_1 \cos(n\tau - \psi_1), \quad s_i = s = a\cos(n\tau - \xi), \quad i = 1, ..., N, \tag{2.32}$$

where h_1, ψ_1, a and ξ are the amplitudes and phases of the rotor's acceleration and the pendulums' motion, respectively.

We show in Appendix B that the pendulums generate an antiresonance on the rotor at order $n_{AR} = n_p$ (in the conservative case). This antiresonance is visible in Fig. 2.4(a), which represents the amplitude of the rotor as a function of the excitation order. As the objective is to reduce as much as

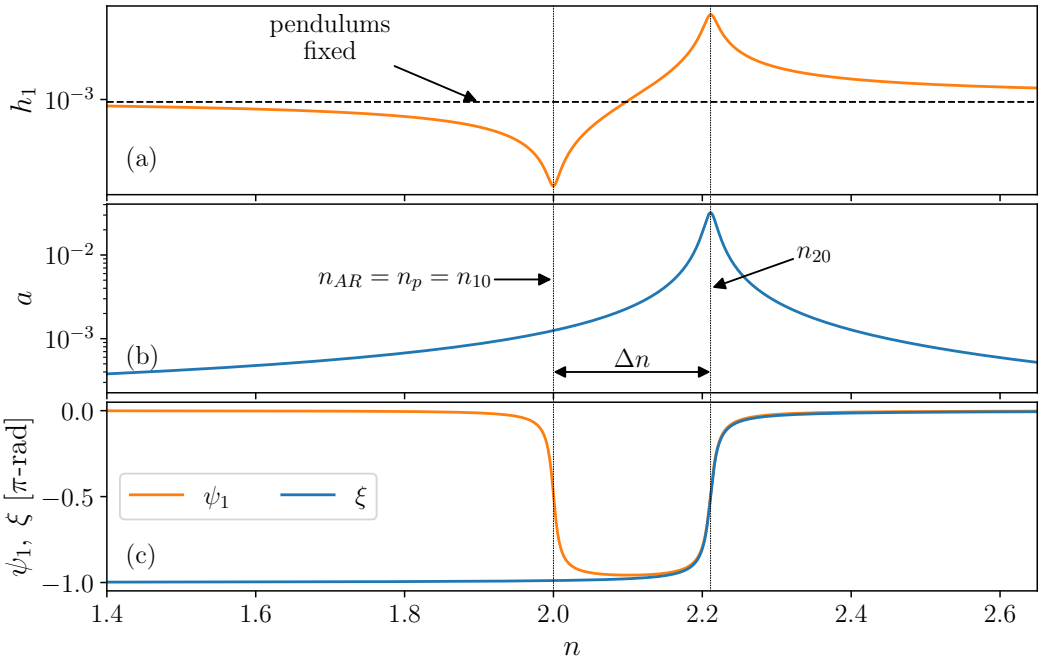

Figure 2.4: Linear response of a CPVA made of two pendulums tuned on order 2. The rotor's and pendulums' amplitudes are represented in (a) and (b), respectively, while their phases are shown in (c). In (a), the horizontal black dashed line corresponds to the rotor's response when the pendulums are fixed. Δn is a performance indicator used in section 2.2.4. $n_p = 2$, $\mu = 0.1$, $\eta = 1$, $\alpha_{[1]} = 1$, $\bar{b} = 0.025$, $\bar{b}_r = 0.002$, $\bar{T}_1 = 0.001$.

possible the amplitude of the fluctuations θ at the operating point $n = n_e$ (we recall that in a real system, the excitation is done at a fixed order n_e, *cf.* section 1.1.1.1), it is judicious to choose to tune the pendulums such that $n_p = n_e$, hence the name "tuning order" attributed to n_p. Furthermore, if $n_p = n_e$ such that the rotor is excited on its antiresonance for all rotation speeds, it is recommended to minimise the damping in the system as much as possible to have almost zero rotor vibrations. In Fig. 2.4(a), the rotor's response is compared to the case with fixed pendulums. Comparing with fixed pendulums allows to account for their added inertia, so it is more relevant than comparing to the case without pendulums.

In Fig. 2.4(b), one can see that the pendulums respond only on the unison mode (indeed, there is no resonance peak close to the natural order $n = n_{10}$). This is because the rotor is a node of modes 1, so that these modes are not excited by the external torque (*cf.* section 2.2.1.2). Looking at Fig. 2.4(a) and (c), one can see that the pendulums reduce the rotor's vibrations when they are in phase-opposition with respect to the external torque (i.e. before the resonance), but they act as amplifiers when they are in phase with it (i.e. after the resonance).

Note that in the presence of relatively small mistuning among the pendulums, the ideal picture of

a unison motion is destroyed and the system's response can be quite complex, as shown in [80, 81]. The sources of mistuning can be manufacturing tolerances, different lubrication or wear for instance. Nevertheless, as mentioned in section 2.1.1, it is considered in this report that the mistuning among the pendulums is small enough to be neglected.

2.2.3 Difficulties of the high-order tuning

We explained in section 1.1.1.3 that the filtering of vibrations related to gears requires a high-order tuning of the CPVA. Reasonable CPVA requirements to reduce torsional vibrations in an electric vehicle are $n_p \sim 20$ and $R_0 < 60$ [mm] (*cf.* section 2.4.1). For instance, if we focus on a purely translated CPVA, we could propose

$$n_t = 20, \quad R_0 = 50 \text{ [mm]} \quad \Rightarrow \quad r = 49.875 \text{ [mm]}, \quad \ell = 124.688 \text{ [µm]}. \tag{2.33}$$

The values of r and ℓ are computed using the definition of n_t (2.15) and the fact that $R_0 = r + \ell$ (*cf.* Fig. 2.1). An error of only 1 [µm] on ℓ would lead to $n_t = 20 \pm 0.08$, which is not acceptable for an accurate tuning. This would get worse for a rocking CPVA as achieving $n_p = 20$ requires $n_t > 20$ (*cf.* Eq. (2.27)).

Moreover, the nonlinear tuning requires a thinner control of the path. Indeed, from the linear point of view, the epicycloidal, circular and cycloid paths are all the same (*cf.* section 2.1.3), but their nonlinear response is completely different (*cf.* section 1.3). For these reasons, we can see that the high-order tuning of a CPVA is very demanding. It is why, in this report, we investigate the subharmonic operation, which allows to divide the tuning order by 2 (*cf.* chapters 6, 7 and 8), and the use of double pendulums, which provide mores flexibility in the tuning (*cf.* chapters 9, 10 and 11).

2.2.4 Linear performance indicators

It is of primary interest to assess the performance of a CPVA as a function of its parameters. To do so, three performance indicators are introduced:

$$G_\theta = \left.\frac{h_1}{h_{1f}}\right|_{n=n_p}, \tag{2.34a}$$

$$\Delta n = n_{20} - n_p, \tag{2.34b}$$

$$G_s = \left.\frac{a}{\bar{T}_1}\right|_{n=n_p}, \tag{2.34c}$$

where h_1 and h_{1f} are the amplitudes of the rotor's acceleration with operating and fixed pendulums, respectively, a is the pendulums' amplitude (*cf.* Fig. 2.4) and $\bar{T}_1$ is the forcing level. G_θ evaluates the reduction of the rotor's vibrations at the operating point. Δn, illustrated in Fig. 2.4, measures the distance between the resonance at n_{20} and the antiresonance at n_p. It is a measure of robustness

as large values of Δn mean that the antiresonance valley is wide such that a small error on n_p does not affect the response much. G_s is related to the torque capacity of the CPVA. Indeed, because the pendulums' path is finite (*cf.* section 2.1.3), there is a critical torque level starting from which the pendulums hit their cusp, causing undesirable noise and preventing the proper operation of the system. This level defines the torque capacity of the CPVA. It is desired to be as large as possible so that the CPVA can filter large torque levels. For a given torque level, the smaller a (hence the smaller G_s), the larger the torque capacity.

The analysis of the linear performance as a function of the system parameters (damping, tuning order n_p, inertia ratio μ, equivalent pendulums' mass Λ_m and coupling term Λ_c) is detailed in Appendix B.2 and a summary is proposed below:

- The best configuration is that with the smallest dampings;
- Performance increases with n_p;
- Increasing μ increases the performance;
- Increasing Λ_m does not affect G_θ and G_s but deteriorates Δn;
- Increasing the linear coupling term Λ_c, which corresponds to choosing positive values of $\alpha_{[1]}$, improves all performance indicators.

As a significant contribution of this thesis is to account for the pendulums' rotation, it is also insightful to assess the evolution of the performance indicators as a function of the linear rotation coefficient $\alpha_{[1]}$, which influences the values of both Λ_m and Λ_c (*cf.* Eqs. (2.25a) and (2.25b)). The computation details of this analysis are given in Appendix B.2 and the evolution of the performance indicators is illustrated in Fig. 2.5.
One can see that using negative values of $\alpha_{[1]}$ leads to a poor linear performance of the system. The worst value is $\alpha_{[1]} = -1/\eta$, for which the pendulums are uncoupled from the rotor ($\Lambda_c = 0$), so that they do not filter the torque at all ($G_\theta|_{\alpha_{[1]}=-1/\eta} = 1$). Decreasing $\alpha_{[1]}$ below this value improves slightly the situation but requires the use of large negative values of $\alpha_{[1]}$, which is difficult to achieve in practice due to design constraints.
On the contrary, using positive values of $\alpha_{[1]}$ leads to significant improvements of the linear response. For $\alpha_{[1]} \in [1, \frac{2}{1-\eta}]$, all performance indicators are improved compared to the case of purely translated pendulums. The particular value $\alpha_{[1]} = 1$, already proposed in [2, 72], is interesting as it maximises Δn. However, one could also choose larger values of $\alpha_{[1]}$ to further improve G_θ and G_s. For instance, $\alpha_{[1]} = 2/(1-\eta)$ is interesting as it improves G_θ and G_s compared to the case $\alpha_{[1]} = 1$ and it does not deteriorate Δn compared to the case of purely translated pendulums.

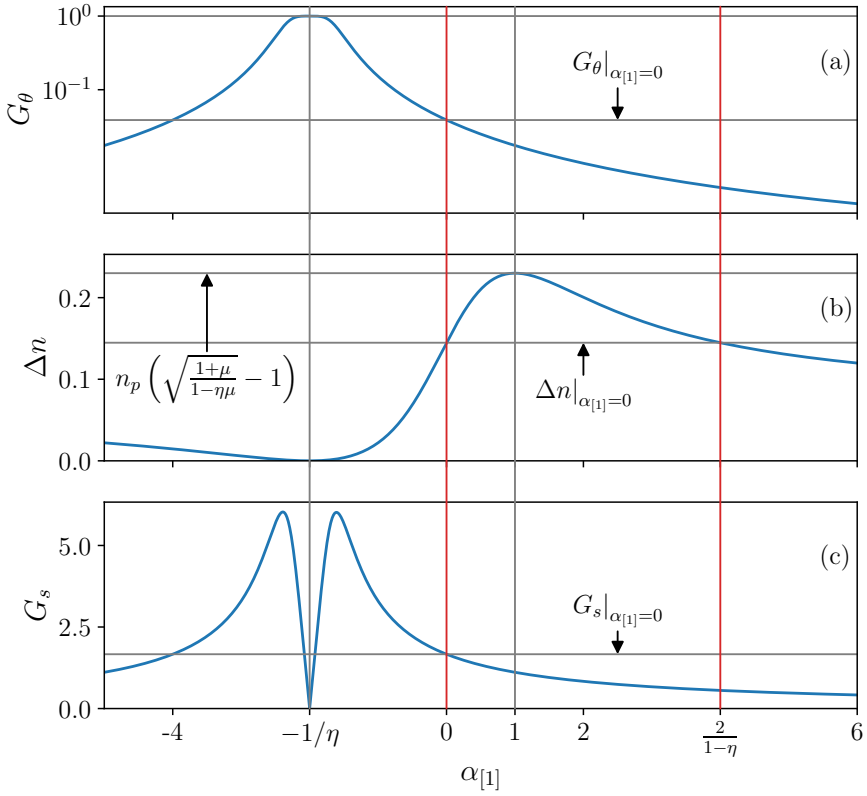

Figure 2.5: Evolution of G_θ (a), Δn (b) and G_s (c) as a function of $\alpha_{[1]}$. $\eta = 0.5$, $n_p = 2$, $\mu = 0.15$, $\bar{b} = 0.01$, $\bar{b}_r = 0.001$.

2.3 Simplified centrifugal pendulum models amenable to nonlinear analytical analysis

One of the main contributions of this thesis is the development of nonlinear analytical models from which design guidelines optimising the efficiency of centrifugal pendulums are obtained. Indeed, CPVAs are subjected to many nonlinearities, so that the linear analysis led in section 2.2 is not sufficient to accurately describe their response. However, the complexity of the equations of motion of a CPVA (*cf.* Eqs. (2.10a) and (2.10b)) prevents the computation of analytical solutions. Hence, there is a need to simplify these equations in order to derive approximate analytical solutions (using for instance the method of multiple scales presented in section 2.5.2.1).

Two simplification methods are described in sections 2.3.1 and 2.3.2. Both of them make use of a small parameter ϵ to scale the parameters and variables according to some remarks and assumptions. For instance, if λ is a parameter of the system that is small in practice, one can introduce the scaled parameter $\tilde{\lambda}$ such that $\lambda = \epsilon^q \tilde{\lambda}$, where q is a scaling coefficient. The scaling allows to express explicitly the "smallness" of some quantities. Once this scaling is done, following the procedure of classical perturbation methods, one can neglect the higher powers of ϵ in the equations of motion (*cf.* Eqs.

(2.10a) and (2.10b)) to obtain simplified equations.

Two scaling choices are investigated, leading to two different simplified models described in the following subsection. The first scaling choice leads to a "simple" model (discussed in section 2.3.1) while the second scaling choice leads to an "accurate" model (discussed in section 2.3.1). As their names indicate, the second model is more accurate than the first one, but it is also more complex. With the first model, we can use either τ or ϑ as the independent variable. However, with the accurate model, the scaling chosen imposes to use ϑ as the independent variable.

The application of analytical methods requires that the path and rotation functions x and α (*cf.* section 2.1.3) be specified explicitly. In the following, we will consider that for $i = 1, \ldots, N$, we have

$$x(s_i) = 1 - n_t^2 s_i^2 + x_{[4]} s_i^4, \tag{2.35a}$$

$$\alpha(s_i) = \alpha_{[1]} s_i + \alpha_{[3]} s_i^3. \tag{2.35b}$$

As explained in section 2.1.3.2, the s_i are typically small so it is relevant to consider only the first nonlinear contribution of $x(s_i)$ and $\alpha(s_i)$. The application of analytical methods also requires to use Taylor series in s_i for the path function $z(s_i)$ defined in Eq. (2.8) (in the following, we will use Taylor series up to s_i^3).

Furthermore, we consider that the excitation signal contains a single harmonic such that $\bar{T}_\theta(\vartheta) = T_1 \cos(n\vartheta)$ where n is the excitation order. As explained in section 2.2.2, in practice, $n = n_e$ is fixed, but it is convenient to make it vary in order to better understand the dynamics of a CPVA. Note that the excitation signals presented in section 1.1.1 all contain several harmonics. Nevertheless, they are dominated by their first harmonic, so in most cases it is an acceptable assumption to consider a single-harmonic torque.

2.3.1 A first simplified model (simple model)

Here, we present a first way of simplifying Eqs. (2.10a) and (2.10b) using a specific scaling of the parameters and variables of the CPVA. The following assumptions and remarks will govern the scaling:

- The optimum system configuration is that with small damping (i.e. $\bar{b}$ and $\bar{b}_r$ are small) so that the rotor's amplitude at its antiresonance is small (*cf.* section 2.2.4);
- The fluctuating torque $T_\theta(\vartheta)$ is small compared to the rotor's kinetic energy (which is $J_r\Omega^2/2$ at equilibrium), so that $\bar{T}_1$ is small (*cf.* Eq. (2.8)).
- The total pendulums' geometric inertia about point O, NmR_0^2, is small compared to the total rotational inertia of the system, $J_r + NI$, so that μ is small (*cf.* Eq. (2.8));

- The rotor's inertia being significant, the fluctuating rotational speed $\dot{\theta}$ is small compared to the mean rotational speed Ω, so that θ' is small (*cf.* Eq. (2.9));
- The pendulums' amplitude of motion is small compared to their distance from the centre of rotation O so that the s_i are small (this was already discussed in section 2.1.3.2);
- The path function is close from an epicycloid so that $x_{[4]}$ is small (*cf.* section 2.1.3);
- The rotation function is close from linear, so that $\alpha_{[3]}$ is small (*cf.* section 2.1.3).

This allows to scale several quantities using a small parameter ϵ such that

$$\begin{gathered} \bar{b} = \epsilon^{\ell}\tilde{b}, \quad \bar{b}_r = \epsilon^{h}\tilde{b}_r, \quad \bar{T}_1 = \epsilon^{r}\tilde{T}_1, \quad \mu = \epsilon^{\phi}\tilde{\mu}, \quad \theta = \epsilon^{w}\tilde{\theta}, \\ s_i = \epsilon^{\nu}\tilde{s}_i, \quad x_{[4]} = \epsilon^{p}\tilde{x}_{[4]}, \quad \alpha_{[3]} = \epsilon^{q}\tilde{\alpha}_{[3]}, \end{gathered} \tag{2.36}$$

where ℓ, h, r, ϕ, w, ν, p and q are scaling coefficients to be determined. Note that in order to give a physical meaning to ϵ, one can choose to set $\epsilon = \mu$ [65]. When substituting the scaled parameters (2.36) in the equations of motion (2.10a) and (2.10b), we obtain terms scaled by different powers of ϵ. These powers are linear combinations of the scaling coefficients, which are chosen to keep some terms at leading orders while discarding others. In this procedure, we would like to keep the effect of the pendulums' damping, the nonlinear contribution of their path and rotation, and the external forcing. We also want to uncouple the pendulums' equation from the rotor's motion as this significantly simplifies the problem (for instance, it allows to take advantage of symmetry properties). To do so, we can choose the set of scaling coefficients

$$\phi = \ell = 1, \quad \nu = 1/2, \quad r = w = \phi + \nu = 3/2, \quad p = q = 0, \quad h > 0. \tag{2.37}$$

Noting that

$$\tilde{T}_1 \cos(n\vartheta) = \tilde{T}_1 \cos[n(\tau + \theta)] = \tilde{T}_1 \cos(n\tau) + \mathcal{O}(\epsilon^w) \tag{2.38}$$

and keeping only the lowest powers of ϵ, we obtain the simplified equations of motion for the rotor and the i$^{\text{th}}$ pendulum

$$\tilde{\theta}'' = \underbrace{\tilde{T}_1 \cos(n\tau)}_{\substack{\text{external} \\ \text{torque}}} + \underbrace{\frac{n_p^2 \tilde{\mu} \Lambda_c}{N} \sum_{i=1}^{N} \tilde{s}_i}_{\substack{\text{torque exerted by} \\ \text{inertial forces}}} + \epsilon^{1/2} \underbrace{\frac{2\tilde{\mu} n_t^2}{N} \sum_{i=1}^{N} \tilde{s}_i \tilde{s}_i'}_{\text{Coriolis effect}}, \tag{2.39a}$$

$$\begin{aligned} \tilde{s}_i'' + n_p^2 \tilde{s}_i = -\frac{\epsilon}{\Lambda_m} \Bigg[& \underbrace{\frac{n_p^2 \tilde{\mu} \Lambda_c^2}{N} \sum_{j=1}^{N} \tilde{s}_j}_{\substack{\text{coupling between} \\ \text{the pendulums}}} + \underbrace{\tilde{b} \tilde{s}_i'}_{\text{damping}} - \underbrace{2\tilde{x}_{[4]} \tilde{s}_i^3}_{\substack{\text{path} \\ \text{nonlinearity}}} + \underbrace{6\eta \alpha_{[1]} \tilde{\alpha}_{[3]} (\tilde{s}_i^2 \tilde{s}_i'' + \tilde{s}_i \tilde{s}_i'^2)}_{\text{rotation nonlinearity}} \\ & + \underbrace{\Lambda_c \tilde{T}_1 \cos(n\tau)}_{\text{external forcing}} \Bigg]. \end{aligned} \tag{2.39b}$$

Equation (2.39a) expresses the rotor's acceleration as a function of the pendulums' motion. The linear term in $\tilde{s}_i$ is obtained using the first-order relation $\tilde{s}_i'' = -n_p^2 \tilde{s}_i$ (*cf.* Eq. (2.39b)) and corresponds to the torque produced by inertial forces. The quadratic term is associated to the Coriolis effect.

Equation (2.39b) expresses the motion of the i^{th} pendulum as a function of every pendulum and the external torque. The rotor's coordinate θ does not appear in this equation because θ'' was substituted by Eq. (2.39a). This substitution is also the reason why the coupling between the pendulums and the external forcing appear explicitly. Eq. (2.39b) contains cubic terms in $\tilde{s}_i$ related to the nonlinear contribution of both $x(\tilde{s}_i)$ and $\alpha(\tilde{s}_i)$.

Note that this first simplified model could also be written using ϑ as the independent variable rather than τ. Indeed, the changes that come out from this change of variable are negligible at the order retained (*cf.* chapter 3).

2.3.2 A second simplified model (accurate model)

To develop the second simplified model, we start from the equations of motion (2.13a) and (2.13b), which are expressed with ϑ as the independent variable rather than τ (*cf.* section 2.1.2.2). It is mandatory to use ϑ as the independent variable with the scaling proposed here. Indeed, it is the only way of uncoupling the rotor's dynamics from the pendulums' equations while keeping the effect of the nonlinear coupling between the rotor and the pendulums. We remind that with ϑ as the independent variable, it is convenient to define $(\bullet)' = \partial(\bullet)/\partial\vartheta$ and to introduce the dimensionless rotor's velocity $y(\vartheta)$ (*cf.* Eq. (2.11)), which we can express

$$y(\vartheta) = 1 + y_\theta(\vartheta), \tag{2.40}$$

where $y_\theta(\vartheta)$ captures the fluctuations of the velocity.

The scaling employed in this second simplified model is governed by the same assumptions and remarks as those listed in the first simplified model. However, in the present case, we choose to define the scaled parameters as

$$\begin{gathered} \bar{b} = \epsilon\tilde{b}, \quad \bar{b}_r = \epsilon\tilde{b}_r, \quad \bar{T}_1 = \epsilon\tilde{T}_1, \quad \mu = \epsilon\tilde{\mu}, \quad y_\theta = \epsilon\tilde{y}_\theta, \\ \theta' = \epsilon\tilde{\theta}', \quad x_{[4]} = \epsilon\tilde{x}_{[4]}, \quad \alpha_{[3]} = \epsilon\tilde{\alpha}_{[3]}, \end{gathered} \tag{2.41}$$

where ϵ is a small parameter. This scaling is different from the one proposed in section 2.3.1 because every small term is scaled by ϵ and the pendulums' motion s_i, $i = 1, ..., N$, is not scaled. Note that if we had chosen this scaling in the first simplified model instead of the choice (2.37), the pendulums' equation would not be uncoupled from the rotor's motion. Furthermore, at first order in ϵ we have

$$1 + \theta' \approx y, \quad \theta'' \approx yy' \approx y' \approx y'/y. \tag{2.42}$$

Hence, at the order retained in this simplified model, we can represent the rotor's acceleration using θ'' instead of y'.

Substituting the scaled quantities (2.41) in the equations of motion (2.13a) and (2.13b), keeping only the lowest powers of ϵ and using Taylor series in s_i for $z(s_i)$, one obtains simplified equations for the rotor and the i$^{\text{th}}$ pendulum

$$\tilde{\theta}'' = \frac{\tilde{\mu}}{N}\left[\sum_{i=1}^{N} \underbrace{n_p^2 \Lambda_c s_i}_{\substack{\text{linear torque}\\ \text{exerted by}\\ \text{inertial forces}}} + \underbrace{2n_t^2 s_i s_i'}_{\text{Coriolis effect}} + \underbrace{n_t^2(1+n_t^2)\left(s_i {s_i'}^2 - \frac{n_p^2}{2}s_i^3\right)}_{\substack{\text{nonlinear (cubic) torque}\\ \text{exerted by inertial forces}}}\right] + \underbrace{\tilde{T}_1 \cos(n\theta)}_{\text{external torque}}, \tag{2.43a}$$

$$\begin{aligned} s_i'' + n_p^2 s_i = -\frac{\epsilon}{\Lambda_m}\Bigg\{ & \underbrace{\frac{\Lambda_c^2 \tilde{\mu}}{N}\sum_{j=1}^{N} n_p^2 s_j}_{\substack{\text{linear coupling}\\ \text{between the pendulums}}} + \underbrace{\tilde{b} s_i'}_{\text{damping}} + \underbrace{\frac{\tilde{\mu} n_t^2 \Lambda_c}{N}\left[\sum_{j=1}^{N} s_j(2s_j' + s_i')\right]}_{\substack{\text{nonlinear (quadratic) coupling}\\ \text{between the pendulums}}} \\ & + \underbrace{\frac{\tilde{\mu} n_t^2}{N}\left[\sum_{j=1}^{N}(1+n_t^2)\Lambda_c\left(s_j {s_j'}^2 - \frac{n_p^2}{2}(s_j^3 + s_j s_i^2)\right) + 2\Lambda_m s_j s_j' s_i'\right]}_{\substack{\text{nonlinear (cubic) coupling between the pendulums}}} - \underbrace{2\tilde{x}_{[4]} s_i^3}_{\substack{\text{path}\\ \text{nonlinearity}}} \\ & + \underbrace{6\eta\alpha_{[1]}\tilde{\alpha}_{[3]}(s_i {s_i'}^2 + s_i^2 s_i'')}_{\text{rotation nonlinearity}} + \underbrace{\left(\Lambda_c + \Lambda_m s_i' - \frac{n_t^2(1+n_t^2)}{2}s_i^2\right)\tilde{T}_1 \cos(n\vartheta)}_{\text{external forcing (direct and parametric)}}\Bigg\}. \end{aligned} \tag{2.43b}$$

Like the first simplified model, this accurate model expresses the rotor's acceleration in terms of the external forcing, the linear torque produced by the pendulums and the torque related to the Coriolis effect (*cf.* Eq. (2.43a)). However, it also accounts the nonlinear torque exerted by the pendulums, which is missed in the first simplified model. This additional nonlinearity allows to capture the generation of the third rotor harmonic (*cf.* chapter 4).

Like Eq. (2.39b), Eq. (2.43b) expresses the motion of the i$^{\text{th}}$ pendulum as a function of every pendulum and the external torque. However, it accounts for the nonlinear coupling (both quadratic and cubic) between the pendulums, which is missed in the first simplified model. In addition, this second simplified model allows to capture the parametric forcing (combination of s_i or its derivatives and $\tilde{T}_1 \cos(n\vartheta)$) exerted on the pendulums.

Clearly, the second simplified model is more accurate than the first one as it accounts for more phenomena. However, it is also significantly more complicated as the equations of motion contain a lot more terms. Note that the additional terms in Eqs. (2.43a) and (2.43b) are all proportional to n_t^q, $q \geq 2$. Hence, it seems that these terms are negligible at low tuning orders, in which case one can get accurate results using the first simplified model. However, for moderate tuning orders (typically $n_p > 1$), one must use the second simplified model. This is discussed further in chapter 4.

2.4 Coupling of a centrifugal pendulum with a drivetrain

2.4.1 Positioning of a centrifugal pendulum in a drivetrain

In thermal vehicles, it is known that the CPVA should be positioned as close as possible from the engine [2]. Indeed, it filters the acyclic torque, so placing it right after the excitation allows to isolate all the driveline components from the torque fluctuations. This way, the antiresonance generated by the pendulums exists on every drivetrain components located after the CPVA [29]. The same reasoning applies to the filtering of the torque ripple generated by an electric motor. However, as explained in section 1.1.1, the main source of excitation in electric vehicles does not come from the motor but the meshing of gears. In that case, the positioning of CPVAs in an electric powertrain is an open question. Recommendations and observations are provided below.

Minimising the tuning order The aim of the gearbox is to adjust the torque and speed of rotation transmitted by the motor to the wheels. Electric motors can spin at very large speeds (up to about 20000 [rpm]), so the gear trains have to reduce the rotational velocity at the gearbox output. This requires driving gears with less teeth than the driven gears. We explained in section 1.1.1.3 that the number of teeth determines the excitation order, and it is known that tuning pendulums at high orders is difficult due to demanding manufacturing tolerances (*cf.* [102] and section 2.2.3). Hence, it seems that the best option is to position the CPVA on the driving gear (or on the shaft supporting it), as illustrated in Fig. 2.6. In this report, the aim is to filter order 20, which is the order of magnitude for the number of teeth of a driving gear in the gearbox of an electric motor.

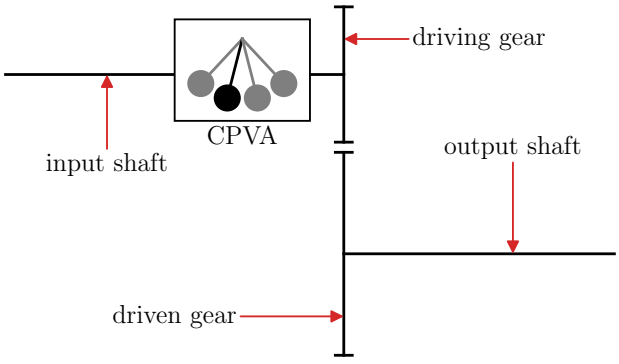

Figure 2.6: Illustration of the optimal positioning of a CPVA in a gear train.

Minimising the pendular mass Another point to consider is the pendular mass required for an efficient filtering. The driving gear has a smaller radius than the driven one, so the torque generated by the transmission errors is smaller (*cf.* Eq. (1.10)). Hence, lighter CPVAs, which have a smaller torque capacity, can be used on the driving gear. Moreover, we saw in section 2.2.4 that the performance of

a CPVA increases when the inertia ratio μ increases. Considering that the connections between the driveline components are perfectly rigid (which is a strong approximation), the rotor's inertia can be replaced by the rotational inertia of the whole drivetrain weighted by the gear ratios and evaluated on the shaft where the CPVA is installed. It is shown in Appendix C that the equivalent inertia of the drivetrain is smaller at the input, where its order of magnitude is only a few [g.m^2]. Hence, less pendulum mass is required at the input to achieve a satisfactory performance.

Considerations on the space available The space available for a CPVA is obviously a major concern. As many different architectures of electric powertrains exist, it is difficult to provide systematic recommendations in this regard. However, the tendency is that there is less space available at the input than at the output of the drivetrain, which could be problematic as it goes against the recommendation of positioning the CPVA at the input. In this report, we consider that the space available on the input shaft does not exceed an external diameter of 120 [mm].

Possible use of several CPVAs Finally, as is visible in Fig. 1.2, a gearbox can contain several gears trains (usually two or three), meaning that there are several sources of vibrations (one per gear train). Thus, introducing a CPVA near the driving gear of the engine shaft would reduce the vibrations caused by the associated gear train, but vibrations due to the other gear trains might require the use of several CPVAs. Nevertheless, for each gear train, the driving gear seems to be the best suited for supporting a CPVA.

As a conclusion, it appears that the best positioning of a CPVA in a gear train is on the driving shaft, as illustrated in Fig. 2.6. Indeed, this allows to minimise the tuning order and the mass of the pendulums. The drawback of this positioning is that, in some cases, there is less room available on the driving shaft than on the driven one. In addition, several CPVAs might need to be used in a gearbox if there are several gear trains.

2.4.2 Modelling of a centrifugal pendulum coupled with a drivetrain

The modelling of a CPVA presented in section 2.1.1 does not account for the complexity of the drivetrain as a single rotor is considered in the model. This simple configuration allows to investigate the intrinsic efficiency of the CPVA, which is useful for the design process. To account for the effect of the full drivetrain, one can use a series of punctual inertias (modelling the massive rotating parts) coupled through torsional springs and dampers (modelling the shafts). This is illustrated in Fig. 2.7 for a thermal powertrain.

In that case, the driveline possesses modes at fixed frequencies. With the introduction of the CPVA, the modal frequencies become dependent on the rotational velocity. Indeed, there is a fre-

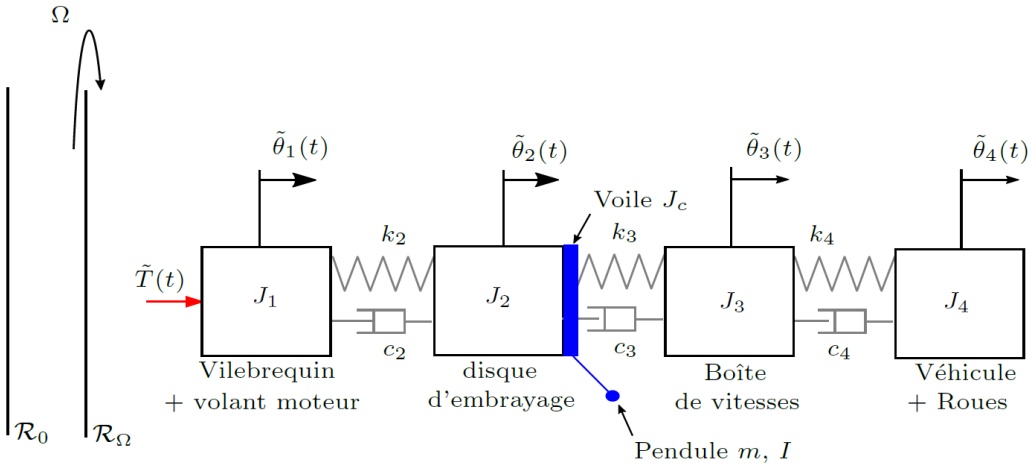

Figure 2.7: Modelling of a drivetrain equipped with a CPVA (taken from [2]). $\mathcal{R}_0$ is a Galilean frame. $\mathcal{R}_\Omega$ is a frame rotating with an angular velocity Ω with respect to $\mathcal{R}_0$. The fluctuating part of the torque delivered by the engine is $\tilde{T}(t)$ where t is the time. Inertias J_1, J_2, J_3 and J_4 represent the crankshaft plus the flywheel, the clutch disk, the gearbox and the wheels, respectively. The fluctuation of their angular position is $\tilde{\theta}_1$, $\tilde{\theta}_2$, $\tilde{\theta}_3$ and $\tilde{\theta}_4$, respectively. The shafts linking these elements are represented through torsional springs and dampers. In the system represented here, the CPVA is mounted directly on the clutch disk.

quency veering effect (*cf.* Fig. 2.8) that prevents the excitation frequency to coincide with a modal frequency, hence avoiding resonances.
In addition, as explained in section 1.2.2, the pendulums filter the excitation to isolate every downstream driveline component. Thus, not only resonances are avoided but an antiresonance is generated on the inertia carrying the pendulums and every inertias that follow [2].

In this report, we only focus on the intrinsic performance of a CPVA, so we do not consider the additional difficulties related to its coupling with a drivetrain (this is left for future work). However, we list some of these difficulties below, which were identified in [2] for a thermal powertrain.

- Due to space requirements, there are situations where the CPVA cannot be placed right after the source of excitation (this is illustrated in Fig. 2.7 where the CPVA is placed on the clutch disk). In that case, the CPVA has no effect on the upstream driveline components (*cf.* section 2.4.1).

- In the presence of several rotors, there are situations where it is not possible to avoid every resonances using the frequency veering effect. This is illustrated in Fig. 2.9, where the natural frequency ω_4^* is repelled by ω_5^*. Because of this, ω_4^* intersects with the excitation frequency ω_e, leading to a resonance. Nevertheless, if the pendulums' mistuning is small enough, the response

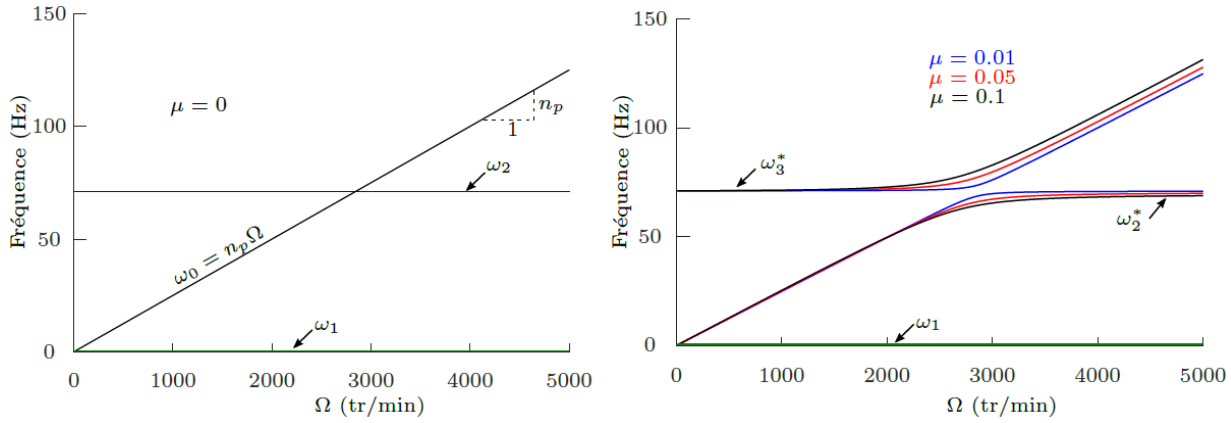

Figure 2.8: Evolution of the natural frequencies with the rotational velocity for a system made of two rotors linked through a torsional spring and with a pendulum attached to the first rotor (taken from [2]). This illustrates the frequency veering effect. Two configurations are represented: the pendulum is uncoupled (on the left) and coupled (on the right) to the rotor. On the right, the natural frequencies corresponding to three different pendulum masses, leading to three different inertia ratios μ (*cf.* Eq. (2.8)), are represented. ω_0 is the natural frequency of the pendulum (written ω_p previously in this report). ω_1 and ω_2 are the natural frequency of the two-rotor system. ω_1, ω_2^* and ω_3^* are the natural frequencies of the coupled system.

of the driveline on this resonance remains acceptable [2].

- The design recommendations derived from the nonlinear study of a CPVA (with a single rotor) are not completely transposable to a realistic drivetrain of a thermal vehicle [2]. There are two main reasons for this. The first one is the effect of the drivetrain on the CPVA, which is ignored in the study of an uncoupled CPVA. The second one is the shape of the excitation signal. Usually, to simplify the analysis, the works dealing with CPVAs consider an external torque of the form $T(\vartheta) = T_0 + T_1 \cos(n\vartheta)$ (as in section 2.3 for instance). However, in practice, the torque contains several harmonics (*cf.* section 1.1.1) whose amplitude depends on the mean rotational velocity Ω [2].

2.5 Nonlinear dynamics and stability

A large contribution of the thesis deals with the nonlinear behaviour of pendulum absorbers. In this section, we present specificities of nonlinear dynamical systems and methods available to analyse their response.

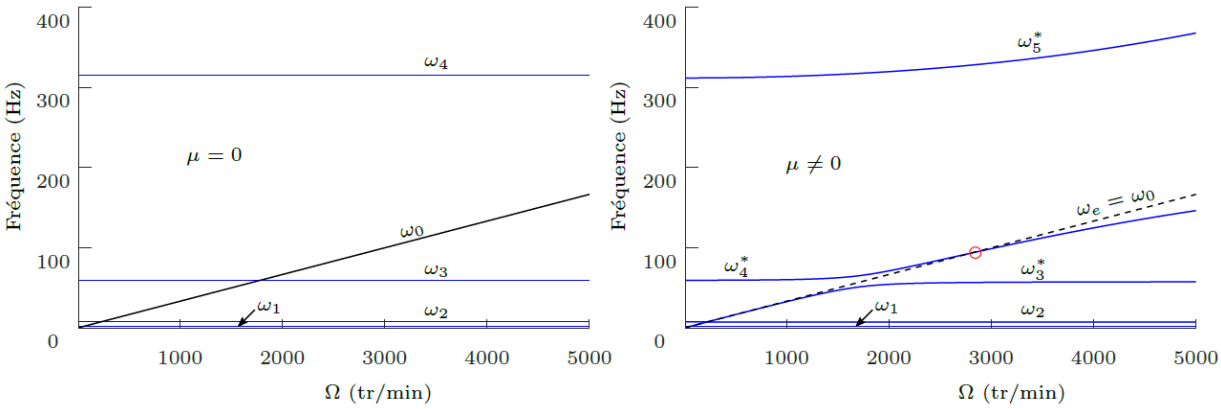

Figure 2.9: Evolution of the natural frequencies of the system represented in Fig. 2.7 as a function of the rotational velocity (taken from [2]). On the left, one can see the natural frequencies ω_i, $= 1, ..., 4$ of the drivetrain uncoupled from the CPVA, and the natural frequency ω_0 corresponding of the pendulum uncoupled from the drivetrain. The diagram shown on the right corresponds to the coupled system. The natural frequencies ω_i^*, $i = 3, 4, 5$ are those subjected to the frequency veering effect.

2.5.1 Theory of nonlinear dynamical systems

2.5.1.1 A typical example: the Duffing oscillator

A famous nonlinear system is the Duffing oscillator [161], whose harmonically forced equation of motion is

$$\ddot{x} + c\dot{x} + \omega_0^2 x + \gamma x^3 = F\cos(\omega t), \tag{2.44}$$

where x, c, ω_0, γ and $F\cos(\omega t)$ are the oscillator's displacement, the viscous damping coefficient, the natural frequency of the oscillator, the cubic nonlinear coefficient and the forcing, respectively.

Nonlinear systems are defined as systems in which the change in the output is not proportional to the change in the input. A simple manifestation of this definition is the fact that if $x(t)$ is the solution for an excitation $F\cos(\omega t)$, then $2x(t)$ will not be a solution for an excitation $2F\cos(\omega t)$. There are a lot more consequences to nonlinearity, some of which are listed below (and discussed further thereafter):

- Nonlinear systems are subjected to harmonic distortion. This means that their response contains higher (and possibly lower) harmonics even when the forcing is harmonic.
- The frequency of free oscillations of a nonlinear system evolves as a function of its amplitude of motion.
- A forced nonlinear systems can possess multiple solutions at the same excitation frequency.
- The response (free of forced) of a nonlinear system might be subjected to instabilities.

- The modes of a nonlinear system can be subjected to internal resonances. This occurs when two modal frequencies are close to integer multiples. These internal resonances lead to nonlinear responses that are completely missed by the linear theory.
- Nonlinear systems might exhibit quasi-periodic responses.
- Nonlinear systems might exhibit chaotic responses. In those cases, the response after a time t is extremely dependent on the initial state of the system.

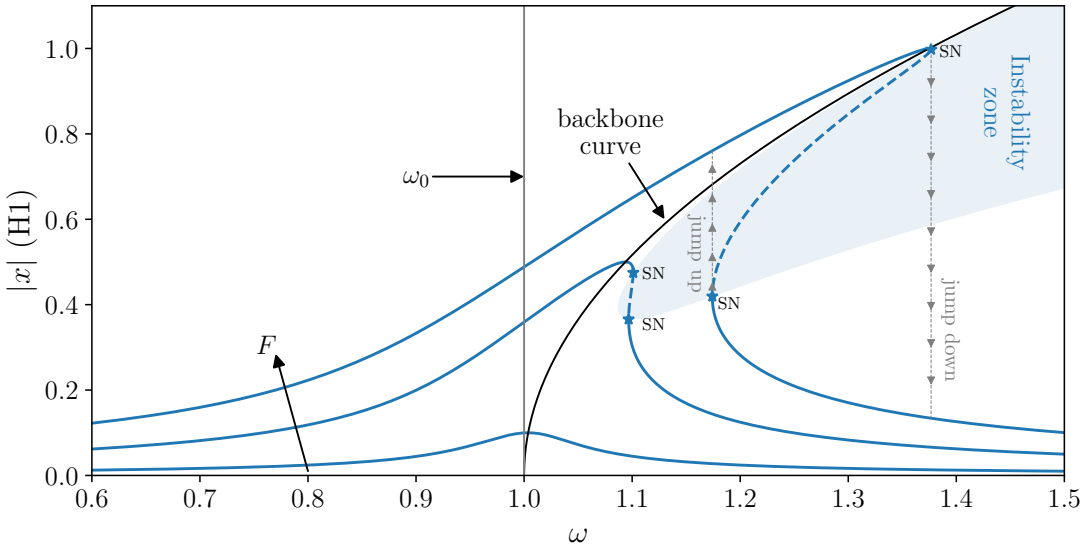

Figure 2.10: Amplitude response of the first harmonic of a Duffing oscillator as a function of the excitation frequency and for three different forcing levels. The solid and dashed lines indicate stable and unstable solutions, respectively. The blue area is an instability zone causing jumps of the response. Blue stars indicate saddle-node (SN) bifurcations. Parameters: $\omega_0 = 1$, $\gamma = 1$, $c = 0.1$, $F = \{0.01,\ 0.05,\ 0.1\}$.

A typical forced response of a Duffing oscillator is represented in Fig. 2.10. It depicts the amplitude of the motion $x(t)$ as a function of the excitation frequency ω and is computed using the method of multiple scales, which is described in section 2.5.2.1. The response is shown for three different forcing levels. For low forcing, the behaviour is almost linear with a resonance near ω_0. However, as the forcing is increased, the response bends to the right and the resonance shifts towards higher frequencies. This bending indicates a hardening behaviour of the system as the frequency of free oscillations, represented by the backbone curve, increases with the amplitude of motion. If the response was to bend to the left, the behaviour would be softening.

Instabilities of the periodic solution appear at moderate forcing amplitudes, when the response enters into the instability zone (blue area). Each intersection between this area and the response corresponds to a saddle-node bifurcation, causing a jump of the response when realising a sweep in ω.

These jumps are a source of hysteresis as the oscillator's response is different whether we are sweeping up or down in ω. More details on the stability and bifurcations are provided in the next section.

2.5.1.2 Fixed points, periodic solutions and their stability

Fixed points Let us consider a free, autonomous nonlinear dynamical system

$$\dot{\boldsymbol{x}} = \boldsymbol{f}(\boldsymbol{x}). \tag{2.45}$$

$\boldsymbol{x}$ is called the *state vector*. The system is autonomous because $\boldsymbol{f}(\boldsymbol{x})$ does not depend explicitly on time. It is generally trivial to express dynamical systems in the form of Eq. (2.45). For instance, Eq. (2.44) can be rewritten in this form by introducing $y = \dot{x}$ such that the state vector be $\boldsymbol{x} = [x, y]^\intercal$. The *phase space* is the space in which $\boldsymbol{x}$ evolves [165]. In the particular case $\boldsymbol{x} = [x, y]^\intercal$, the phase space corresponds to the representation of the system's dynamics in the coordinate system (x, y). The solutions $\boldsymbol{x}^*$ of

$$\boldsymbol{f}(\boldsymbol{x}^*) = \boldsymbol{0} \tag{2.46}$$

are called *fixed points* of the phase space and correspond to static equilibrium points of the system [165].

Stability of fixed points Near a fixed point $\boldsymbol{x}^*$, $\boldsymbol{x}$ can be expressed through a small perturbation $\boldsymbol{u}$ such that

$$\boldsymbol{x} = \boldsymbol{x}^* + \boldsymbol{u},\ \|\boldsymbol{u}\| \ll \|\boldsymbol{x}\|, \quad \Rightarrow \quad \dot{\boldsymbol{u}} = \dot{\boldsymbol{x}} - \underbrace{\dot{\boldsymbol{x}}^*}_{=\boldsymbol{0}} = \dot{\boldsymbol{x}} = \boldsymbol{f}(\boldsymbol{x}) = \boldsymbol{f}(\boldsymbol{x}^* + \boldsymbol{u}). \tag{2.47}$$

Using a Taylor series of $\boldsymbol{f}(\boldsymbol{x}^* + \boldsymbol{u})$ around the fixed point, we obtain

$$\dot{\boldsymbol{u}} = \underbrace{\boldsymbol{f}(\boldsymbol{x}^*)}_{=0} + \boldsymbol{u}\ \left.\frac{\partial \boldsymbol{f}(\boldsymbol{x})}{\partial \boldsymbol{x}}\right|_{\boldsymbol{x}^*} + \mathcal{O}(\|\boldsymbol{u}\|^2). \tag{2.48}$$

Hence, the evolution of the perturbation can be approximated at first order using the *Jacobian matrix* $\boldsymbol{J}$ in order to write

$$\dot{\boldsymbol{u}} \approx \boldsymbol{J}\boldsymbol{u}, \quad \text{where} \quad \boldsymbol{J} = \left.\frac{\partial \boldsymbol{f}(\boldsymbol{x})}{\partial \boldsymbol{x}}\right|_{\boldsymbol{x}^*} \tag{2.49}$$

The general solution of Eq. (2.49) takes the form

$$\boldsymbol{u} = \sum_{i=1}^{N} \kappa_i \boldsymbol{\phi}_i e^{\lambda_i t}, \tag{2.50}$$

where N is the dimension of $\boldsymbol{x}$, κ_i, $i = 1, ..., N$ are constants and $(\lambda_i,\ \boldsymbol{\phi}_i)$ are the eigenvalues and eigenvectors of $\boldsymbol{J}$. If the real part of at least one of the eigenvalues is positive, then $\boldsymbol{u}$ increases exponentially in time. This means that the initially small perturbation grows such that $\boldsymbol{x}$ departs from $\boldsymbol{x}^*$. In this situation, the fixed point is unstable. Contrarily, if both eigenvalues have negative real parts, then the fixed point is stable. Changes of the stability state occur through bifurcations. Some of the most common bifurcation types are described thereafter.

Periodic solutions A periodic solution $\boldsymbol{x}(t)$ with period T of the dynamical system (2.45) is such that $\boldsymbol{x}(t+T) = \boldsymbol{x}(t)$ and $\boldsymbol{x}(t+\tau) \neq \boldsymbol{x}(t)$, $\forall \tau \in]0, T[$. Unlike equilibrium solutions (i.e. fixed points), periodic ones are characterised by time-varying states. In the state space, a periodic solution is a closed orbit (or equivalently a closed trajectory). It is now convenient to discuss *Poincaré maps*, which allow to draw a parallel between periodic solutions and fixed points [165]. In their simplest application, these maps consist in looking at the system's state at time intervals spaced by T. The plot of the points thus obtained in the phase space is a *Poincaré section*. Because of the definition $\boldsymbol{x}(t+T) = \boldsymbol{x}(t)$, a periodic solution is a fixed point of the Poincaré map.

Stability of periodic solutions Previously, we assessed the stability of a fixed point by looking at the effect of a perturbation of the system around this fixed point. We can use the same procedure to study the stability of a periodic solution of a dynamical system. Let us consider the non-autonomous dynamical system

$$\dot{\boldsymbol{x}} = \boldsymbol{f}(\boldsymbol{x}, t) \tag{2.51}$$

where $\boldsymbol{x} \in \mathbb{R}^N$. It is non-autonomous because $\boldsymbol{f}(\boldsymbol{x}, t)$ depends explicitly on t. Let $\boldsymbol{x}_0(t)$ be a periodic solution of the system and $\boldsymbol{u}(t)$ a perturbation around this solution such that

$$\boldsymbol{x}(t) = \boldsymbol{x}_0(t) + \boldsymbol{u}(t). \tag{2.52}$$

Then, using first order Taylor series, we can express [165]

$$\dot{\boldsymbol{u}}(t) \approx \boldsymbol{J}(t)\boldsymbol{u}(t) \quad \text{where} \quad \boldsymbol{J}(t) = \left.\frac{\partial \boldsymbol{f}(\boldsymbol{x})}{\partial \boldsymbol{x}}\right|_{\boldsymbol{x}_0(t)}. \tag{2.53}$$

Note that in this case, the Jacobian $\boldsymbol{J}(t)$ is evaluated on the periodic solution $\boldsymbol{x}_0(t)$, so that it is itself periodic. As a consequence, Eq. (2.53) is a linear differential equation with periodic coefficients, which can be studied using Floquet theory [166, 167]. The solution of this equation takes the form

$$\boldsymbol{y}(t) = \sum_{n=1}^{N} \boldsymbol{y}_n(t), \quad \boldsymbol{y}_n(t) = \boldsymbol{p}_n(t) e^{\alpha_n t}, \tag{2.54}$$

where the α_n are the *Floquet exponents* and the $\boldsymbol{p}_n(t)$ are periodic vector functions. If the real part of one of these exponents is positive, the periodic solution is unstable. As illustrated in Fig. 2.11, the way the Floquet exponents cross the imaginary axis during a change of stability determines the type of bifurcation [165]. Several types of bifurcation are represented in this figure and they are detailed in the subsequent section.

Note that the stability of a periodic solution can also be determined by examining the stability of the fixed point of an associated map [165] (typically, the Poincaré map).

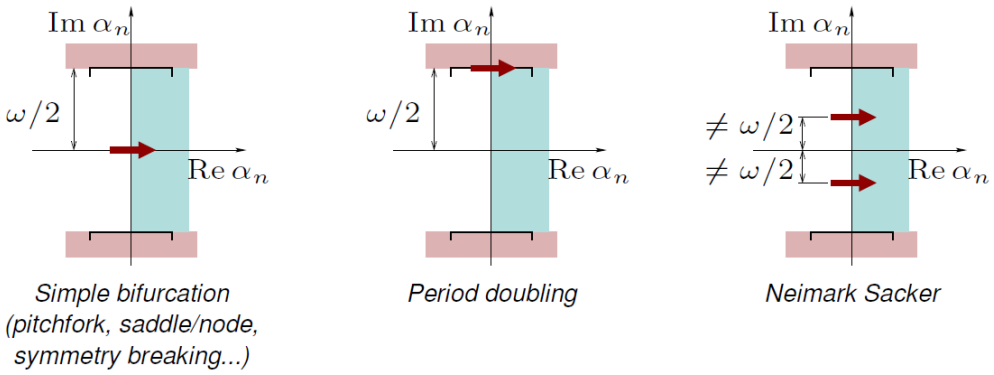

Figure 2.11: Path of Floquet exponents α_n in the complex plane during bifurcations of periodic solutions of angular frequency ω. Taken from [168].

2.5.1.3 Bifurcations

A bifurcation indicates a qualitative change in the features of a system under the variation of one or more control parameters [165]. In practice, a bifurcation point separates a stable part of a solution from an unstable part. Some common types of bifurcation are described briefly thereafter.

Saddle-node bifurcation When a saddle-node bifurcation occurs on a specific branch of solution, its stability changes (from stable to unstable or the opposite). The number of solutions near the bifurcation changes as a function of the control parameter. It goes from two (one stable, one unstable) to zero, which often causes a jump in the response when sweeping in the control parameter. This is illustrated in Fig. 2.10 where the control parameter is ω.

Pitchfork bifurcations When a pitchfork bifurcation occurs, the system transitions from a single periodic solution to three (or more) [169]. These bifurcations can either be supercritical or subcritical, as shown in Fig. 2.12. In the supercritical case, we have a stable solution branch on one side of the bifurcation and three (two stable, one unstable) solution branches on the other side. In the subcritical case, we have three solutions on one side of the bifurcation (one stable, two unstable) and one unstable solution on the other side.

Neimark-Sacker bifurcations When a Neimark-Sacker bifurcation occurs, the periodic solution is replaced by a quasi-periodic one at the crossing of the bifurcation point, with the creation of a new frequency.

Period-doubling bifurcations A period-doubling bifurcation is similar to a pitchfork one except that the top and bottom solutions represented in Fig. 2.12 have a period twice larger than the one of the response before the bifurcation. Like pitchfork bifurcations, period-doubling ones can be super-

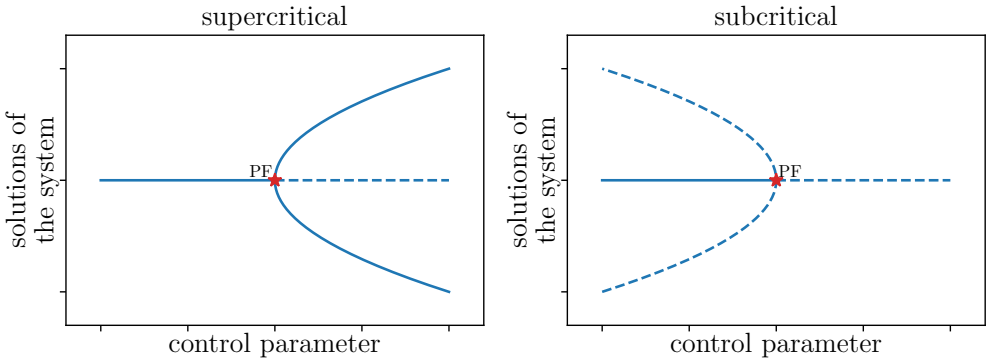

Figure 2.12: Bifurcation diagram representing super- and subcritical pitchfork bifurcations. Dashed lines indicate unstable solutions and the red star corresponds to the pitchfork bifurcation.

or subcritical.

2.5.1.4 Operating regimes

Periodic regime The periodic regime was already discussed in section 2.5.1.2. Here, we simply remind that it corresponds to a system oscillating with a period T, which implies $x(t+T) = x(t)$, and the associated fundamental frequency of the oscillations is ω.

Quasi-periodic regime The quasi-periodic regime corresponds to a situation where a periodic signal of frequency ω is modulated by one or more frequencies. The *Poincaré map*, defined in section 2.5.1.2, is an interesting tool to verify if the response of a system is quasi-periodic. Indeed, because a quasi-periodic signal is a periodically modulated periodic signal, its representation in a Poincaré section takes the form of an orbit [165], as illustrated in Fig. 2.13(a).

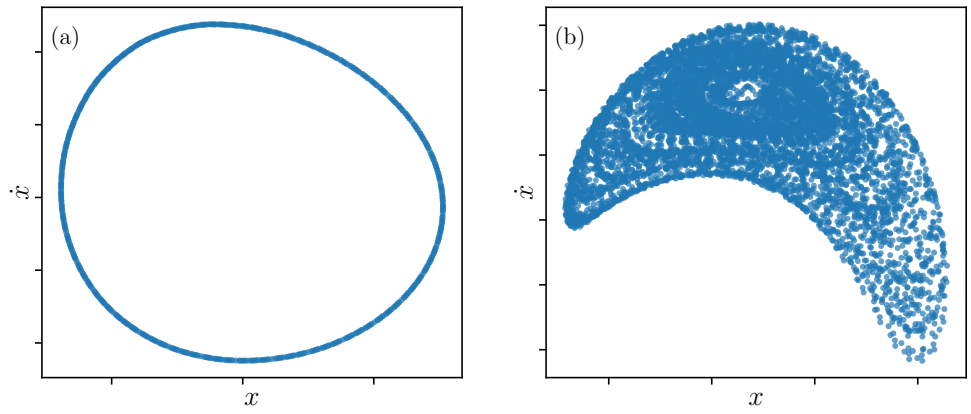

Figure 2.13: Poincaré sections of a nonlinear system in quasi-periodic regime (a) and chaotic regime (b).

Chaotic regime In chaotic regime, the system's response at time t is extremely dependent on the initial state of the system. One often looks at the Lyapunov exponent to determine whether the response is chaotic or not [165]. This exponent quantifies how dependent on the initial conditions the response is. Another way to verify if a response is chaotic is to look at the Poincaré section. Indeed, if the response is chaotic, its representation takes the form of a densely filled closed shape [165], as represented in Fig. 2.13(b).

2.5.2 Tools for the study of nonlinear systems

2.5.2.1 Analytical methods

There are several analytical methods that allow to derive approximate solutions of nonlinear systems, like the harmonic balance method or the averaging method [141]. In this thesis, we choose to use the method of multiple scales (MMS) [141], which is a perturbation method allowing to replace a nonlinear system by a cascade of linear systems which can be solved successively. Some details on the MMS are provided below.

Let us consider a nonlinear dynamical system of the form

$$\ddot{x} + \omega_0^2 x = \epsilon f(x,t), \tag{2.55}$$

where ϵ is a small parameter and $f(x,t)$ is a nonlinear function. This is a very general equation of motion for a weakly damped, weakly forced and weakly nonlinear system. The MMS consists in introducing several independent time scales

$$t_0 = t, \quad t_1 = \epsilon t, \quad ... \quad t_n = \epsilon^n t, \tag{2.56}$$

and looking for an approximated solution for $x(t)$ of the form of an asymptotic expansion such that

$$x(t) \approx x_0(t_0, ..., t_n) + \epsilon x_1(t_0, ..., t_n) + ... + \epsilon^n x_n(t_0, ..., t_n). \tag{2.57}$$

n is the order of the expansion. t_0 is a fast time scale, in opposition to the t_i, $i > 0$, which are slow time scales. Note that the use of several time scales is relevant as a dynamical system typically evolves on different scales: a fast time scale, due to its oscillations, and slower scales, for instance related to the decrease of the oscillation amplitude with time due to damping.

Introducing the time scales (2.56) and the expansion (2.57) in Eq. (2.55) and grouping terms by powers of ϵ, one obtains a set of n linear equations that can be solved successively to express the x_i, $i > 0$, as a function of x_0. If the oscillator is subjected to a forcing of frequency $\omega \approx k\omega_0$, $k \in \mathbb{N}^*$, the general solution for x_0 takes the form

$$x_0(t_0, ..., t_n) = a(t_1, ..., t_n) \cos\left(\frac{\omega}{k} t_0 - \xi(t_1, ..., t_n)\right), \tag{2.58}$$

where a and ξ are the amplitude and the relative phase of x_0 (i.e. the phase between x_0 and the forcing). Notice that a and ξ only depend on the slow time scales. The MMS allows to derive a system governing a and ξ such that, after recombining the slow time scales using their definition (2.56), one obtains

$$\begin{cases} \dfrac{da}{dt} = f_a(a,\xi), & \text{(2.59a)} \\ a\dfrac{d\xi}{dt} = f_\xi(a,\xi). & \text{(2.59b)} \end{cases}$$

$f_a(a,\xi)$ and $f_\xi(a,\xi)$ are known functions. System (2.59) is a slow time system because a and ξ are slow time variables (*cf.* Eq. (2.58)). The periodic solutions of the oscillator correspond to the fixed points of the slow times system, so they must satisfy

$$\begin{cases} f_a(a,\xi) = 0, & \text{(2.60a)} \\ f_\xi(a,\xi) = 0, & \text{(2.60b)} \end{cases}$$

and the stability of these periodic solutions can be assessed through the computation of the Jacobian associated to the slow time system (2.59), as described in section 2.5.1.2.

As an example, the MMS is applied to a Duffing oscillator in Appendix D.

2.5.2.2 Time integration

Sometimes, analytical solutions of nonlinear differential systems cannot be found or require too many approximations. In that case, numerical methods must be used. Here, we present the use of finite differences, which allow to derive solutions using an approach in the time domain.

Let us consider the initial value problem (IVP)

$$\dot{\boldsymbol{x}} = \boldsymbol{f}(\boldsymbol{x},t), \quad \text{(2.61a)}$$
$$\boldsymbol{x}(t=0) = \boldsymbol{x}_0, \quad \text{(2.61b)}$$

where $\boldsymbol{x}$ is a state vector. The basic idea to solve this IVP on the time interval $[0, t_N]$ is to discretise time using time steps Δt such that $t_0 = 0, \ldots, t_n = n\Delta t, \ldots, t_N = N\Delta t$, and to use a finite difference scheme to represent the derivatives. The simplest (but least accurate) scheme is the 2-points Euler forward, which makes use of the simplest definition of the derivative of a function $x(t)$:

$$\dot{x}(t) = \lim_{\Delta t \to 0} \frac{x(t+\Delta t) - x(t)}{\Delta t}. \quad \text{(2.62)}$$

The associated finite-difference scheme is (with Δt small)

$$\dot{x}(t) \approx Dx(t) = \frac{x(t+\Delta t) - x(t)}{\Delta t}. \quad \text{(2.63)}$$

Discretising this scheme and defining $x(t_n) = x_n$, we obtain

$$Dx_n = \frac{x_{n+1} - x_n}{\Delta t}. \tag{2.64}$$

Introducing this in Eq. (2.61), multiplying by Δt and rearranging leads to

$$\boldsymbol{x}_{n+1} = \boldsymbol{x}_n + \Delta t \boldsymbol{f}(\boldsymbol{x}_n, t_n), \tag{2.65a}$$
$$\boldsymbol{x}_0 = \boldsymbol{x}_0. \tag{2.65b}$$

Equation (2.65a) expresses the state of the system at time t_{n+1} as a function of time t_n and Eq. (2.65b) gives the initial state. Hence, one can integrate the system in time to obtain a discrete representation of $\boldsymbol{x}(t)$ on the time interval $[0, t_N]$.

One must be aware that the approximation in Eq. (2.64) generates a truncation error that causes an error in the numerical solution. Indeed, using Taylor series for $x(t + \Delta t)$, we can write

$$x(t + \Delta t) = x(t) + \Delta t \dot{x}(t) + \frac{\Delta t^2}{2}\ddot{x}(t) + \mathcal{O}(\Delta t^3), \tag{2.66}$$

and introducing this in the scheme (2.63), we get

$$Dx(t) = \underbrace{\dot{x}(t)}_{\substack{\text{exact} \\ \text{solution}}} + \underbrace{\frac{1}{2}\Delta t \ddot{x}(t)}_{\substack{\text{leading-order} \\ \text{error}}} + \mathcal{O}(\Delta t^2). \tag{2.67}$$

Here, the numerical error is proportional to powers of Δt [170]. There are much more accurate schemes than the 2-point Euler forward, such as the Runge-Kutta ones for instance [171], for which the truncation error is proportional to Δt^p, $p > 1$. Numerical routines of efficient schemes are already implemented in the `solve_ivp` function from the Python sub-package `scipy.integrate`.

Suppose the function $\boldsymbol{f}(\boldsymbol{x}, t)$ from Eq. (2.61) includes a harmonic forcing term $F\cos(\omega t)$ on one of its components. In that case, it is often desired to obtain the steady state amplitude and phase of the harmonics of $\boldsymbol{x}(t)$ as a function of ω and F. This can be done as follows:

- Choose a finite difference scheme;
- Integrate in time until the steady state is reached to obtain a discrete representation of $\boldsymbol{x}(t)$;
- Use Fourier series to compute the amplitude and phase of the harmonics of $\boldsymbol{x}(t)$;
- Repeat this process for all desired values of ω or F.

Computing a frequency response using finite differences can be time-consuming for several reasons:

- To obtain an accurate numerical solution, one needs a small time step Δt, which implies a large number of time intervals to reach the final time t_N.
- The steady state can take a long time to be reached, especially when a bifurcation occurs. This requires integrating up to a large time t_N.
- Time integrations are required for every desired values of ω (or F). Hence, many integrations must be done to obtain a frequency response with many points.

In addition, time integration does not allow the computation of unstable solutions, which are useful for a batter understanding of the dynamics of a system. For these reasons, numerical methods in the frequency domain are more adapted to the investigation of the steady state solutions of nonlinear systems. One a these methods is presented below.

2.5.2.3 Numerical continuation methods

Several numerical continuation methods exist and allow for a resolution of a system's dynamics in the frequency domain. Some famous software/packages allowing to perform numerical continuation are AUTO [172] and MATCONT [173]. In this report, we will use MANLAB, which is an interactive path-following and bifurcation analysis software implemented in MATLAB environment to compute periodic solutions of a nonlinear dynamical system in the frequency domain [143, 144]. It is developed by the Laboratoire de Mécanique et d'Acoustique (LMA) in Marseille (France) and is based on the harmonic balance method (HBM) coupled with the asymptotic numerical method (ANM, or *MAN* in french). These two methods are briefly presented below.

Consider the nonlinear dynamical system

$$\ddot{\boldsymbol{x}} = \boldsymbol{f}_{nl}(\boldsymbol{x}, \dot{\boldsymbol{x}}) + \boldsymbol{F}\cos(\omega t), \tag{2.68}$$

where $\boldsymbol{x} \in \mathbb{R}^N$. If looking for periodic solutions, we can express x using Fourier series up to harmonic H such that

$$\boldsymbol{x}(t) = \boldsymbol{x}_0 + \sum_{i=1}^{H} \boldsymbol{x}_{ci}\cos(i\omega t) + \boldsymbol{x}_{si}\sin(i\omega t), \tag{2.69}$$

where $\boldsymbol{x}_0$, $\boldsymbol{x}_{ci}$ and $\boldsymbol{x}_{si}$, $i = 1, ..., H$, are N-dimensional vectors containing the Fourier coefficients. Introducing this in Eq. (2.68), ignoring the terms oscillating with a frequency larger than $H\omega$ and grouping the constant terms and the factors of $\cos(i\omega t)$ and $\sin(i\omega t)$, $i = 1, ..., H$, we obtain a system of $N(2H + 1)$ algebraic equations where the $N(2H + 1)$ unknowns are the Fourier coefficients. This is the basic idea of the HBM. The system of $N(2H + 1)$ equations can be written

$$\boldsymbol{R}(\boldsymbol{U}) = \boldsymbol{0}, \tag{2.70}$$

where $\boldsymbol{U}$ is the vector containing the $N(2H+1)$ Fourier coefficients.

We now present the ANM, which is used to compute the solutions of an algebraic system of the form

$$\bar{\boldsymbol{R}}(\boldsymbol{U},\lambda)=\boldsymbol{0}, \tag{2.71}$$

where λ is the continuation parameter, $\boldsymbol{U}$ is the vector of unknowns and $\bar{\boldsymbol{R}}:\mathbb{R}^N\times\mathbb{R}\to\mathbb{R}^N$ is the function governing $\boldsymbol{U}$. In practice, we can use ω or F as the continuation parameter. We want to find a solution branch $\boldsymbol{U}(\lambda)$ for several values of λ. However, these curves can have a complex shape, they can be subjected to bifurcations and there might be values of λ for which several solutions $\boldsymbol{U}$ coexist [168]. This is illustrated in Fig. 2.10 where the control parameter is ω. To overcome these difficulties, it was proposed to re-parametrise the system as a function of a parameter a, which is related to the curvilinear of the solution curve. This way, system (2.71) can be increased and rewritten

$$\tilde{\boldsymbol{R}}(\boldsymbol{U}(a),\lambda(a))=\boldsymbol{0}, \tag{2.72}$$

where the additional equation in $\tilde{\boldsymbol{R}}(\boldsymbol{U}(a),\lambda(a),a)$ compared to $\bar{\boldsymbol{R}}(\boldsymbol{U},\lambda)$ is the definition of a. There are several possible definitions, such as the arc-length or pseudo arc-length ones [174]. The ANM consists in looking for the curve $(\boldsymbol{U}(a),\lambda(a))$ using the high-order asymptotic expansion in a

$$\boldsymbol{U}(a)=\boldsymbol{U}_0+a\boldsymbol{U}_1+...+a^n\boldsymbol{U}_n,\quad \lambda(a)=\lambda_0+a\lambda_1+...+a^n\lambda_n. \tag{2.73}$$

Introducing Eq. (2.73) in system (2.72) and solving leads to an analytic solution for the curve $(\boldsymbol{U}(a),\lambda(a))$ on the interval $[0,a_{\max}]$, where $a_{\max}$ is the maximum value of a for which the norm of $\tilde{\boldsymbol{R}}(\boldsymbol{U}(a),\lambda(a),a)$ remains lower than a given tolerance. Hence, the curve $(\boldsymbol{U},\lambda)$ is known analytically piecewise. More details on the ANM and its implementation in MANLAB can be found in [175].

2.6 Conclusion

We saw that the excitation signal in a thermal powertrain is a periodic torque of the form $T(\vartheta)$, where ϑ is the angular position of the crankshaft. The fundamental frequency of the torque is $\omega_e=n_e\dot{\vartheta}$, where n_e is the engine's order. The modes of the drivetrain are at fixed frequencies, so that they will successively be excited by the engine's torque during an acceleration phase. In an electric powertrain, the problem is very similar except that the fluctuating torque mainly comes from transmission errors in the gear train. In that case, the excitation order n_e corresponds to the number of teeth of the gear considered and ϑ is the angular position of that gear. n_e is typically much larger in electric vehicles than in thermal ones.

The CPVA was presented in sections 2.1 and 2.2. The natural frequency of an uncoupled centrifugated pendulum is $\omega_p = n_p\dot{\vartheta}$, where n_p is the pendulums' tuning order. This dependency of ω_p on $\dot{\vartheta}$ allows the pendulums to remain tuned on the excitation at all speeds if one chooses $n_p = n_e$. In this configuration, the pendulums filter the torque to isolate every downstream driveline component. It is this characteristic that makes the CPVA the best-suited passive absorber to reduce the vibrations of a rotating machine. Simplified CPVA models amenable to nonlinear analysis techniques were presented in section 2.3. The question of the positioning of a CPVA in a drivetrain and their coupling were discussed in section 2.4.

Some elements on the theory of nonlinear dynamical systems were described in section 2.5. This section also presented analytical and numerical methods to study the response of nonlinear dynamical systems. These are helpful to understand the content of the following chapters.

Part II
The classical centrifugal pendulum tuning

Summary of part II

This summary presents a synthesis of the main results of the following three chapters, constituting part II of this report. In this part the system considered is the centrifugal pendulum vibration absorber (CPVA) described in chapters 1 and 2. For the sake of completeness, a brief description of the system is recalled here. It is constituted of a rotor on which are attached N pendulums oscillating along their path and rotating about their centre of mass, as illustrated in Fig. II.1. The system is excited by a torque containing a constant and a periodic part. To simplify the analysis, we consider that the fluctuating torque contains a single harmonic of amplitude $\bar{T}_1$ and order n. Though in this summary we consider a system made of $N = 2$ pendulums for the sake of simplicity, most of the results derived in part II are valid regardless of the number of pendulums.

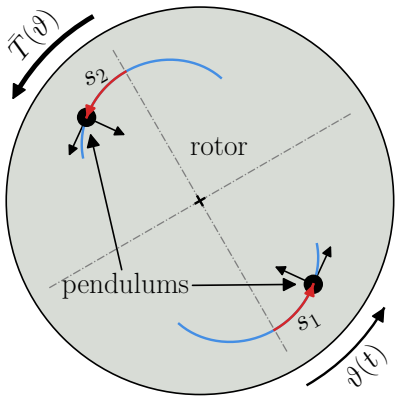

Figure II.1: Illustration of a CPVA made of $N = 2$ pendulums. The black frames attached to the pendulums represent their rotation relatively to the rotor.

The pendulums' path and rotation law are governed by functions

$$x(s_i) = 1 - n_t^2 s_i^2 + x_{[4]} s_i^4, \tag{II.1a}$$

$$\alpha(s_i) = \alpha_{[1]} s_i + \alpha_{[3]} s_i^3, \tag{II.1b}$$

where s_i represents the curvilinear abscissa of the i$^{\text{th}}$ pendulum (*cf.* Fig. II.1), n_t, $x_{[4]}$ are path

parameters and $\alpha_{[1]}$, $\alpha_{[3]}$ are rotation parameters. It turns out that the behaviour of the system can be controlled using only two parameters: the pendulums' tuning order n_p and the nonlinear tuning parameter c_p (*cf.* chapter 4). These two tuning parameters depend on the path and rotation parameters and on the dimensionless pendulums' inertia η such that

$$n_p = \frac{n_t}{\sqrt{1+\eta\alpha_{[1]}^2}}, \quad c_p = 3(x_{[4]} + 2n_p^2\eta\alpha_{[1]}\alpha_{[3]}). \tag{II.2}$$

In the following, we will present the response of CPVAs tuned in different ways in order to highlight the richness of their dynamics.

In part II, we focus on the classical CPVA tuning, which refers to cases where the excitation order is close from the tuning order, i.e. $n \approx n_p$. The classical tuning is the one currently used in automotive vehicles but it still needs improvements (*cf.* chapter 1).

Recall that the system possesses three modes, illustrated in Fig. II.2. Mode 0 is a rigid body mode for which the pendulums are immobile. The phase-opposition mode corresponds to a phase-opposition motion of the pendulums and the rotor is a node of this mode. The associated eigenorder (analogous to an eigenfrequency) is the tuning order n_p of the CPVA. The unison mode represents a unison motion of the pendulums, which are in phase-opposition with the rotor. The associated eigenorder is slightly larger than n_p.

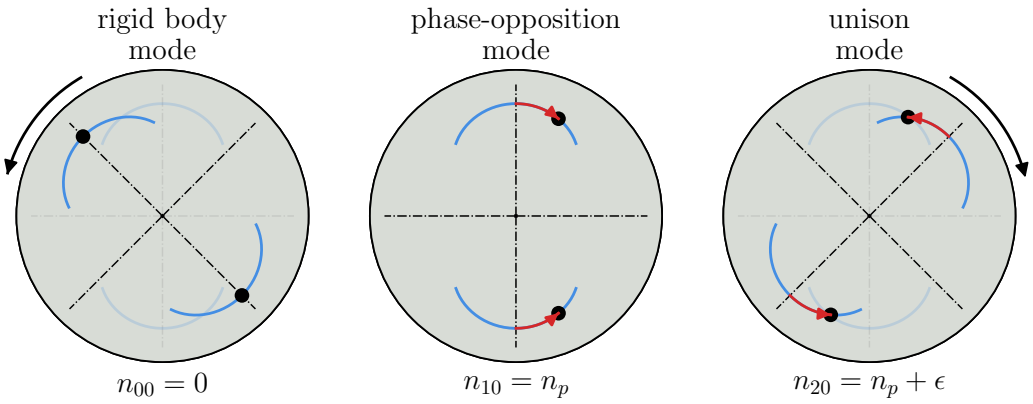

Figure II.2: Modes of a CPVA made of $N = 2$ pendulums. ϵ is a small parameter indicating that the eigenorder of the unison mode is slightly larger than the tuning order. The rotation of the pendulums about their centre of mass is not represented in this figure.

We proposed in chapter 2 to simplify the full equations of motion of a CPVA in order to investigate analytically its nonlinear behaviour. Two different simplification processes were suggested, leading to two different simplified models: one termed "simple" model (used in chapters 3 and 5), and the other termed "accurate" (used in chapter 4). There are three main differences between these models:

- The nonlinearities affecting the pendulums in the simple model are only related to their path and their rotation law. However, the accurate model also accounts for the nonlinear coupling between the pendulums, related to inertial effects.
- In the simple model, the pendulums are excited directly (here, directly means "non-parametrically") by the external torque. The accurate model accounts for both the direct and parametric forcing of the pendulums by the external torque.
- The simple model allows to compute analytically the two first rotor harmonics whereas the accurate one allows to derive its three first harmonics.

The two models are used in the literature (without the contribution of the rotation, see [65, 66, 86] for instance), but they are not compared. A comparison is proposed in chapter 4 and shows that the accurate model should be used in most cases. Nevertheless, there are still cases where the simple model is useful:

- Though the simple model has a much smaller range of validity than the accurate one, it is less complex and provides a proper estimation of the CPVA's behaviour for low values of the tuning order n_p. This is verified in chapter 3.
- The simple model allows to investigate the coupled-mode solution of the system (i.e. the pendulums respond simultaneously on the unison and phase-opposition modes) while the accurate one does not. Indeed, its larger complexity does not allow to derive an analytical solution for the coupled-mode solution consistent with the solution on the unison mode. The simple model is used in chapter 5 to study the coupled-mode solution.

Figure II.3 depicts a typical nonlinear response of the system when submitted to a harmonic torque with variable excitation order n (similar to a frequency response function with a varying excitation frequency). The amplitude of the pendulums is shown in (a) and the amplitude of the rotor's acceleration in (b). The right-hand side of Fig. II.3 deals with the subharmonic CPVA tuning, which is the subject of part III, so it is not detailed here.

The scope of the chapters constituting part II is illustrated on the left-hand side of Fig. II.3. The green curves represent the response of the CPVA for pendulums oscillating at unison. The amplitudes of the pendulums are physically limited due to the finiteness of their path, and this limit is indicated by s_{cusp} in Fig. II.3(a). When the pendulums oscillate on the unison mode and before its resonance, they exert a torque on the rotor that opposes the external torque. This generates the classical antiresonance visible in Fig. II.3(b) near n_p (it is exactly at n_p in the linear, conservative case).

In practice, the excitation order n is fixed, so one would typically tune the pendulums such that $n_p = n$ for the rotor to be excited on its antiresonance, thus reducing its vibrations as much as possible.

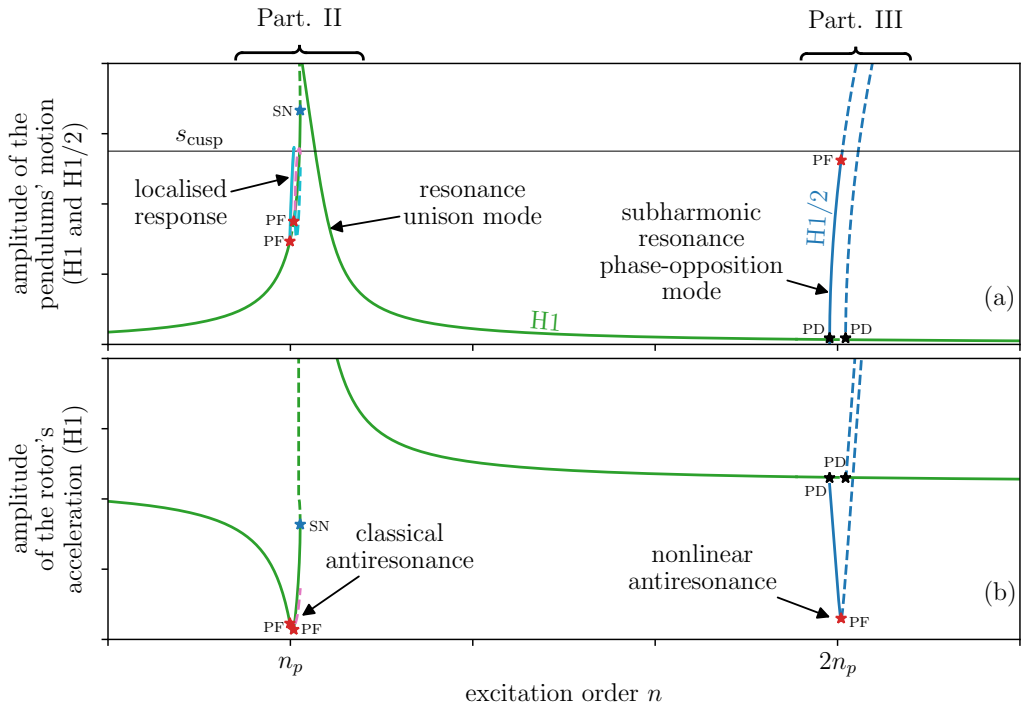

Figure II.3: Typical amplitude response of the pendulums (a) and rotor (b) of a CPVA as a function of the excitation order. The left-hand side of this figure is the scope of part II while the right-hand side is the scope of part III. The green and blue curves correspond to pendulums responding on the unison and phase-opposition modes, respectively, and the dashed lines indicate unstable solutions. Harmonics 1 and 1/2 of the pendulums' response are shown in (a) while only the first rotor harmonic is shown in (b). The horizontal black line in (a) indicates the cusp of the pendulums' path. The red, blue and black stars indicate pitchfork (PF), saddle-node (SN) and period-doubling (PD) bifurcations, respectively.

However, this ideal behaviour is perturbed by nonlinear effects that deteriorate the efficiency of CPVAs. These undesired effects are listed below and discussed in details thereafter:

- The unison response is subjected to several instabilities. This is visible in Fig. II.3 through the presence pitchfork (PF) bifurcations (red stars) and saddle-node (SN) bifurcations (blue stars). PF bifurcations lead to non-unison pendulums' motions (this corresponds to the localised response in pink and cyan in Fig. II.3) and SN bifurcations cause the pendulums to no longer act as absorbers but as amplifiers.

- Because of nonlinear effects, an increase in the amplitude of the external torque causes the classical antiresonance order to shift and depart from n_p. We call this the nonlinear detuning of the antiresonance. In this case, and because in practice the excitation order n is fixed, the rotor is not excited on the minimum of its response over the whole torque range. Hence, the nonlinear

detuning of the antiresonance prevents an optimal reduction of the rotor's vibrations.

In part II, we investigate the unison and localised responses using mainly analytical methods. The analysis of the unison response led to the derivation of original design guidelines allowing to prevent the apparition of instabilities and to limit the shifting of the classical antiresonance. The study of the localised response allowed to gain a better understanding of this phenomenon and to show that, in some cases, it is not detrimental to the filtering efficiency of the CPVA. These points are detailed thereafter.

The development of many of the results discussed in this summary requires elaborate algebraic manipulations, detailed in chapters 3, 4 and 5. Here, we report only the main results of part II, described from a physical point of view.

Stability of the unison solution and localised pendulums' response [chap. 3, 4, 5]

If one now considers that the excitation order n is fixed and that the control parameter is the torque amplitude $\bar{T}_1$, the typical results from chapters 3, 4 and 5 can be summarised in Fig. II.4. This figure depicts the forced response of two different CPVAs excited on their tuning order, i.e. $n = n_p$. The difference between the two CPVAs is their nonlinear tuning c_p, which is controlled through the path and rotation of the pendulums (*cf.* Eq. (II.2)).

We first discuss the response of the CPVA represented in Fig. II.4(a)-(b). When realising an increasing torque sweep (which occurs often in practice, when the car driver accelerates for instance), the amplitude of the pendulums and rotor increases until it reaches the lower SN bifurcation. At this moment, a sudden jump of the response occurs. After this jump, the rotor's oscillations are much larger than if the pendulums were locked. This is because the phase of the pendulums' oscillations changed by π such that the torque they generate on the rotor now adds-up to the external torque instead of balancing it. This situation must absolutely be avoided in practice to prevent the failure of some driveline components.

Figure II.4(c)-(d) shows the response of another CPVA as a function of the forcing amplitude and excited at its tuning order. During an increasing sweep in $\bar{T}_1$, the amplitude of the pendulums and rotor increase until they reach the PF bifurcation. At larger torque levels, the unison response is unstable and the pendulums oscillate with different amplitudes. The energy is localised on the pendulum oscillating with the largest amplitude, hence the name "localised solution". Increasing further the torque amplitude, one can see that localisation causes the pendulums to reach their cusp at a torque level much lower than if they were oscillating at unison. The associated torque level defines the torque capacity, and its reduction is the main drawback of localisation.

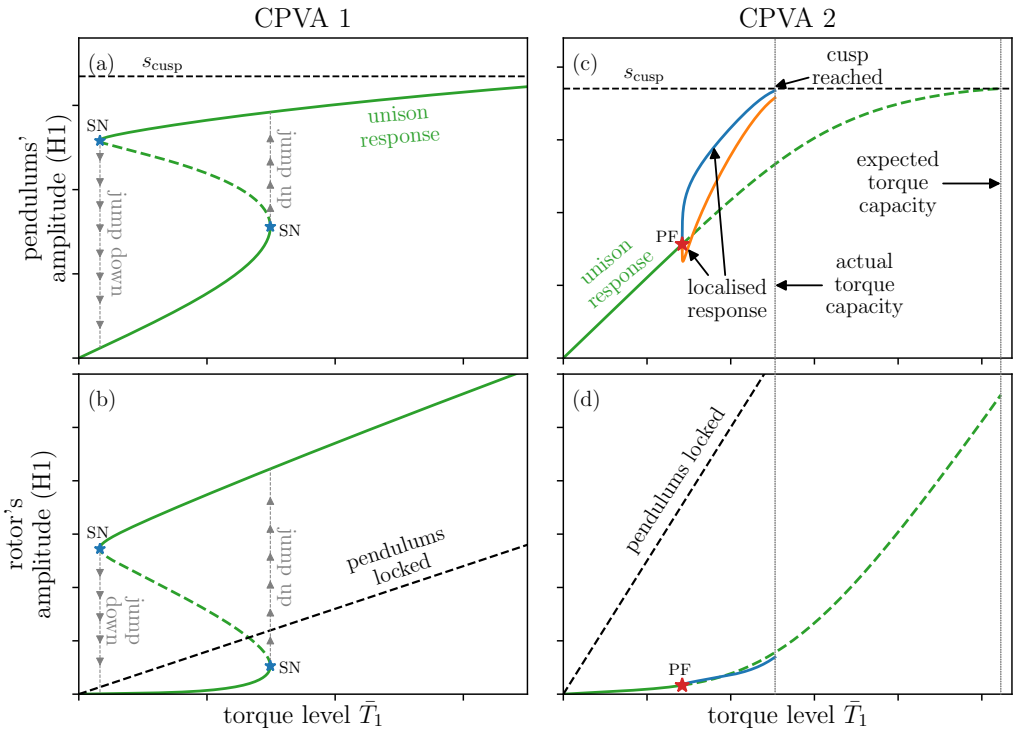

Figure II.4: Torque response of a first CPVA (on the left) and a second one (on the right) as a function of the torque amplitude. (a), (c) and (b), (d) represent the pendulums' and the rotor's amplitudes, respectively. The green curve corresponds to the unison pendulums' motion while the blue and orange ones in (c), (d) correspond to the localised response. Dashed lines indicate unstable solutions. The red and blue stars indicate pitchfork (PF) and saddle-node (SN) bifurcations, respectively. In all plots, $n = n_p$ so that the CPVAs are excited on their tuning order.

One could think that localisation also lowers the filtering efficiency of the CPVA, but it is not necessarily the case. This can be seen in Fig. II.4(d), where the amplitude of the first rotor harmonic is slightly lower with localised pendulums (blue curve) than with a unison motion (green curve). In chapter 5, we even show that in some particular cases localisation does not reduce the torque capacity and lowers the rotor's vibrations, so that it improves the efficiency of the CPVA. Nevertheless, these are unusual scenarios and a common recommendation is that localisation should be avoided.

The cause of the existence of localised solutions, discussed in details in chapter 5, can be understood from the following modal expansion (we consider a CPVA made of $N = 2$ pendulums for simplicity)

$$\begin{bmatrix} s_1 \\ s_2 \end{bmatrix} = \underbrace{\zeta_1 \begin{bmatrix} 1 \\ -1 \end{bmatrix}}_{\substack{\text{phase-opposition} \\ \text{mode}}} + \underbrace{\zeta_2 \begin{bmatrix} 1 \\ 1 \end{bmatrix}}_{\substack{\text{unison} \\ \text{mode}}}. \tag{II.3}$$

s_1 and s_2 are the pendulums' coordinates while ζ_1 and ζ_2 are the modal ones. When only the unison

mode responds (i.e. $\zeta_1 = 0$, $\zeta_2 \neq 0$), the pendulums move at unison. This is the most expected scenario as the phase-opposition mode is not directly excited by the external torque (*cf.* section 2.2). However, because the eigenorders of the unison and phase-opposition modes are close, these modes are in 1:1 internal resonance (*cf.* chapter 5). Hence, there can be energy exchanges between them, and as a consequence the phase-opposition mode can contribute to the pendulums' response (i.e. $\zeta_1 \neq 0$, $\zeta_2 \neq 0$). This nonlinear phenomenon causes the pendulums to oscillate differently as $s_1 = \zeta_1 + \zeta_2 \neq s_2 = -\zeta_1 + \zeta_2$ (*cf.* Eq. (II.3)), leading to energy localisation.
The analytical investigation of the localised solution and its stability in chapter 5 greatly facilitated the numerical observation of quasi-periodic and chaotic CPVA responses. In addition, the experimental analysis presented in chapter 3 allowed to observe localisation where predicted by the analytical model.

Figure II.5 represents the response of the pendulums of three CPVAs as a function of the excitation order. These CPVAs have the same parameters except for their nonlinear tuning.

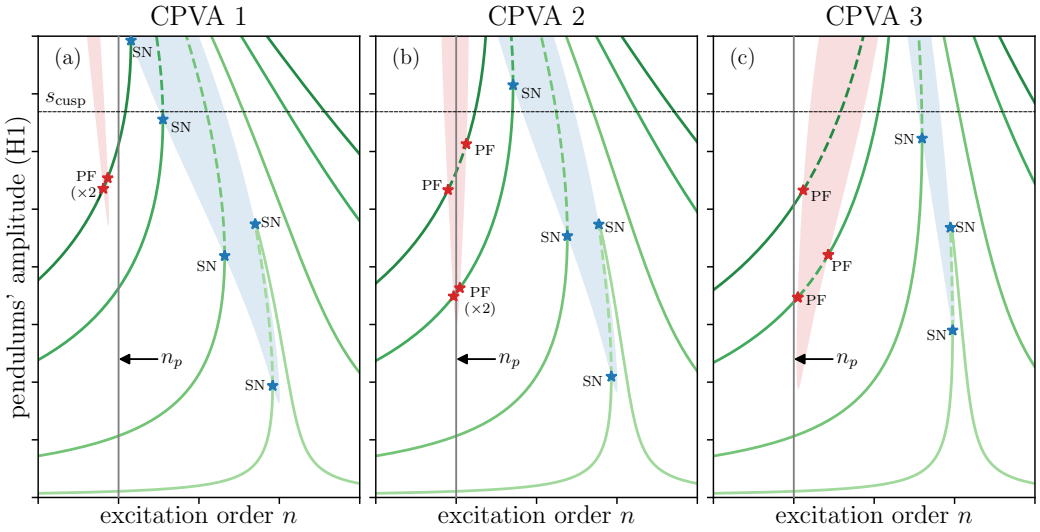

Figure II.5: Amplitude response of the pendulums of three CPVAs with different nonlinear tunings and for several forcing levels. The green curves represents the unison motion and dashed lines indicate unstable solutions. The darker the curve the larger the associated torque level. The red and blue stars indicate pitchfork (PF) and saddle-node (SN) bifurcations, respectively. The red and blue areas are instability zones related to localisation and jumps of the response, respectively. For clarity, the localised responses taking birth at the PF bifurcations are not represented.

The red and blue areas are instability zones. PF and SN bifurcations, which cause localisation and jumps of the response, respectively, are located at the intersections of these zones with the unison response. Hence, to enforce a stable unison motion, one should avoid these intersections.
This can be done via a specific linear and nonlinear tuning of the CPVA, which affects both the hardening/softening behaviour of the response (visible through the bending of the response in Fig. II.5)

and the locus of the instability zones. For instance, the tuning of CPVAs 1 and 3 (*cf.* Fig. II.5(a) and (c)) allows to avoid instabilities at $n = n_p$, which is convenient as the rotor's antiresonance is located near n_p. On the contrary, CPVA 2 (*cf.* Fig. II.5(b)) fails to avoid the apparition of instabilities at $n = n_p$, so the associated nonlinear tuning is not recommended.

Simple tuning guidelines are derived in chapters 3 and 4 to systematically avoid instabilities of the unison response. These guidelines are a major contribution of the thesis.

Shifting of the antiresonance and performance [chap. 4]

Due to the nonlinear nature of the system, the order of the rotor's classical antiresonance depends on the amplitude of the variables, which in turn depends on the amplitude of the forcing torque. Figure II.6(a) illustrates the evolution of the rotor's response around its antiresonance (green curves) as the torque level increases. The pink curve, passing through every antiresonance, is the result of an analytical antiresonance tracking procedure proposed in chapter 4. For the antiresonance to be locked at $n = n_p$, one needs this pink curve to be a straight vertical line. This is used to derive design guidelines and is discussed further thereafter.

Figures II.6(b) and (c) compare the response of two CPVAs as a function of the forcing level and for an excitation order $n = n_p$. The CPVA shown in red is tuned to have tautochronic uncoupled pendulums. This configuration, often discussed in the literature, means that the period of oscillation of the pendulums does not depend on their amplitude of motion when the rotor spins with a constant velocity. It is the evolution of the antiresonance of this CPVA that is represented in Fig. II.6(a). The other CPVA, shown in green in (b)-(c), is tuned to lock the antiresonance at $n = n_p$.

Figure II.6(c) shows that locking the antiresonance lowers the amplitude of the rotor's first harmonic compared to the tautochronic case. This highlights the benefit of locking the antiresonance to reduce the vibrations of the rotor. In Fig. II.6(b) we can see that locking the antiresonance increases slightly the pendulums' amplitude at unison compared to the tautochronic case. However, the tautochronic pendulums are subjected to localisation (due to the presence of the PF bifurcation) way before their cusp, which might significantly decrease their torque capacity. The pendulums locking the antiresonance are not subjected to instabilities before reaching their cusp. Hence, the design rule limiting the shifting of the antiresonance is compatible with the avoidance of instabilities discussed previously.

In Fig. II.6(d) we can see the amplitude of the three first rotor harmonics of the CPVA tuned to lock the antiresonance. The reduction of the first harmonic brings to the fore the contribution of higher rotor harmonics generated because of the nonlinearities introduced by the pendulums. Indeed, near the cusp, the amplitudes of rotor harmonics 2 (in blue) and 3 (in orange) are about 9 and 6 times larger than the amplitude of the fundamental harmonic (in green), respectively. This might be

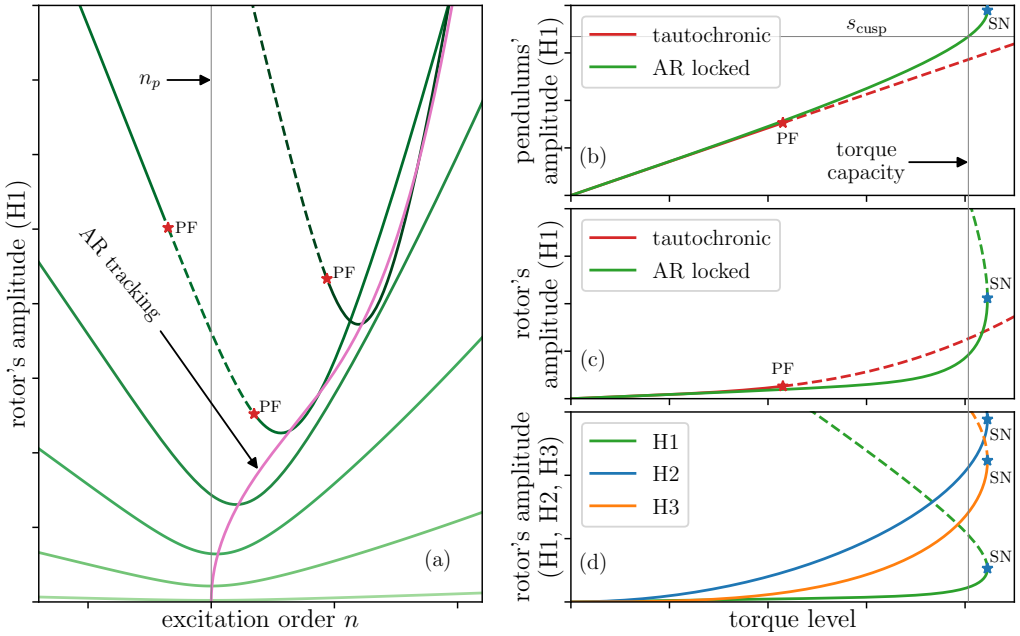

Figure II.6: The response of two different CPVAs is represented in this figure. (a) shows the amplitude of a rotor's first harmonic around its antiresonance and for several forcing levels. This rotor is part of a CPVA with tautochronic pendulums. The darker the line the larger the associated torque level and dashed lines indicate unstable solutions. The pink curve represents the antiresonance locus as the torque amplitude is increased. The pendulums' and rotor's response of two CPVAs are shown in (b) and (c) as a function of the forcing level and for $n = n_p$. One of the CPVAs is the one represented in (a). The other one is tuned to lock the antiresonance at $n = n_p$. (d) represents the three first rotor harmonics of the CPVA tuned to lock the antiresonance as a function of the forcing level. The red and blue stars indicate pitchfork (PF) and saddle-node (SN) bifurcations, respectively.

problematic but it can be avoided using for instance a CPVA in subharmonic operation, which is the subject of part III of this report.

Representation in the design space and optimisation [chap. 3, 4]

In order to carry out a design optimisation of the system, it is proposed in chapters 3 and 4 to represent the design guidelines and the stability state of the unison response in the design space. The coordinates of that space are the parameters of the CPVA. This representation provides an overview of the stability of a range of CPVA designs and indicates which ones satisfy some given characteristics. Thus, one can simultaneously assess the efficiency of these CPVA designs.

Figure II.7 represents the stability information (green-stable, red-unstable and blue-unstable) in a design space with the linear and nonlinear CPVA tuning parameters n_p and c_p as coordinates (which are related to the pendulums' path and rotation function, *cf.* Eq. (II.2)). It also represents the

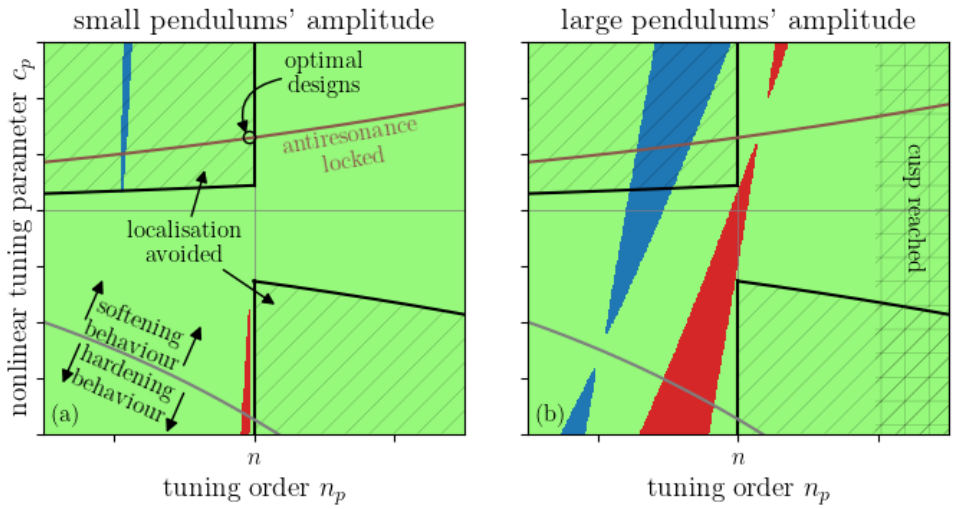

Figure II.7: Maps representing the stability state and some guidelines in the design space. Each map is shown for a given excitation order n and a given pendulums' amplitude. Green, blue and red areas correspond to designs that are stable, subjected to jumps and subjected to localisation, respectively.

guideline locking the antiresonance (brown curve) and another guideline enforcing a straight response of the unison mode such that jumps of the response are avoided (grey line). In addition, the indication of the CPVA designs for which the pendulums have reached their cusp (hatched area in Fig. II.7(b)) provides an information related to the torque capacity. Each map is shown for a given excitation order and a given pendulums' amplitude. The optimal designs are those that are stable over the largest torque range while having their antiresonance fixed and as close as possible from n. In Fig. II.7, these conditions corresponds to the designs located near the intersection of the brown line with the upper hatched area.

Chapter 3

A simple nonlinear model for the unison response of centrifugal pendulums and its stability

This chapter is made of a paper published in the *Journal of Sound and Vibrations* [76]. It focuses on the analytical prediction of the instabilities causing jumps and localisation of the unison response of a centrifugal pendulum vibration absorber (CPVA). Note that the title of the chapter makes reference to a "simple" model because the developments are based on the simplified model described in section 2.3.1, which is less advanced than the simplified model from section 2.3.2, used in chapter 4.

Sections 1 to 4 repeat information from chapters 1 and 2. They present the context of the study, the modelling of a CPVA (*cf.* section 2.1.1), a linear analysis (*cf.* section 2.2) and the simplification of the equations of motion (*cf.* section 2.3). The reader might want to skip these four first sections of the article if he already read chapters 1 and 2.

The novelty of the article starts in section 5, where the nonlinear unison response and its stability are computed analytically using the method of multiple scales (*cf.* section 2.5.2.1). These results are applied to case studies in section 6 and compared to numerical resolutions of the system's dynamics. The CPVAs studied have a particularly low tuning order ($n_p = 0.5$), so it is not relevant for a use in a gear train. Nevertheless, the manufacturing of CPVAs with low tuning orders is of current interest because of the increasing use of cylinder deactivation in thermal engines, which is a mean to reduce fuel consumption. For instance, for four-cylinder, four-stroke engines, which are the most used in the automotive industry, the nominal engine order is $n = 2$ but lowers to $n = 0.5$ if three cylinders are deactivated. The model is seen to match well with the numerical solutions and design guidelines are provided in section 7. In section 8, an experimental investigation on a monofilar CPVA tuned at $n_p = 0.5$ allows to observe localisation where expected.

Journal of Sound and Vibration 517 (2022) 116525

Contents lists available at ScienceDirect

Journal of Sound and Vibration

journal homepage: www.elsevier.com/locate/jsvi

Dynamic stability of centrifugal pendulum vibration absorbers allowing a rotational mobility

V. Mahe [a,b,*], A. Renault [b], A. Grolet [a], O. Thomas [a], H. Mahe [b]

[a] Arts et Metiers Institute of Technology, LISPEN, HESAM Université, F-59000 Lille, France
[b] Valeo Transmissions, Centre d'Étude des Produits Nouveaux, Espace Industriel Nord, Route de Poulainville, 80009 Amiens Cedex 1, France

ARTICLE INFO

Keywords:
Centrifugal pendulum vibration absorber
Non-linear dynamics
Stability
Energy localisation

ABSTRACT

Centrifugal pendulum vibration absorbers (CPVA) are used in the automobile industry to reduce the vibrations of the transmission system. These passive devices are made of several masses oscillating along a given trajectory relative to the rotor. In this paper, the dynamic stability of a new class of CPVA is investigated. The particularity of this new class is that masses now admit a significant rotation motion relative to the rotor, in addition to the traditional translation motion. The efficiency of such devices is optimal for a perfect synchronous motion of the oscillating masses. However, masses unison can be broken for the benefit of energy localisation on a given absorber, leading to a loss of mitigation performances. To assess the stability of such devices, a dynamical model based on an analytic perturbation method is established. The aim of this model is to predict analytically localisation and jumps of the response. The validity of the model is confirmed through a comparison with both a numerical resolution of the system's dynamics and an experimental study.

1. Introduction

In the frame of reduction of polluting emissions and fuel consumption of vehicles using thermal engines, automotive manufacturers try to reduce the cylinder capacity and engine speed of rotation. These evolutions lead to a significant increase of rotation irregularities called "acyclisms", mainly due to higher combustion pressure. One of the main characteristics of these reciprocating engines is the linear dependence of the acyclism frequency to the mean engine speed of rotation. The coefficient of proportionality is called the engine (or firing) order and only depends on the architecture of the engine. For four strokes engines, the engine order is half the number of cylinders. During acceleration phase, the engine sweeps a wide frequency range containing some driveline torsional modes. This situation may lead to significant noise and vibration levels into the passenger compartment and premature wear of the driveline components. Centrifugal pendulum vibration absorbers (CPVA) have been used for many years to minimise acyclisms of automotive powertrains at the engine order. These passive devices consist of oscillating masses (pendulums) moving along particular paths relative to a primary inertia (rotor) as shown in Fig. 1. The operation principle of the CPVA is that of a tuned mass damper whose stiffness is proportional to the mean engine speed. This enables it to remain tuned on the engine order to reduce torsional vibrations of the rotor.

CPVA exhibit strong non-linearities: geometric non-linearities due to the large amplitude of motion, and inertial non-linearities, for instance due to Coriolis effect. The non-linear response of a CPVA is strongly affected by the choice of the pendulums' trajectory. D. E. Newland observed early on that circular trajectories may exhibit unstable periodic responses, leading to jumps of the

* Corresponding author at: Arts et Metiers Institute of Technology, LISPEN, HESAM Université, F-59000 Lille, France.
E-mail addresses: vincent.mahe@ensam.eu (V. Mahe), alexandre.renault@valeo.com (A. Renault), aurelien.grolet@ensam.eu (A. Grolet), olivier.thomas@ensam.eu (O. Thomas), herve.mahe@valeo.com (H. Mahe).

https://doi.org/10.1016/j.jsv.2021.116525
Received 3 May 2021; Received in revised form 6 September 2021; Accepted 2 October 2021
Available online 13 October 2021

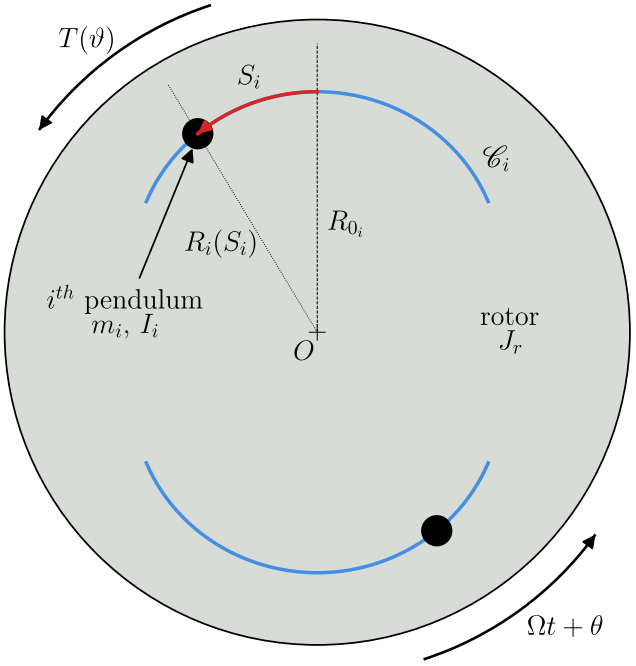

Fig. 1. Representation of the system studied for $N = 2$ pendulums.

response [1]. Since the works of H. H. Denman, the preferred trajectories are epicycloids because they are almost tautochronic [2]. Due to their cyclic symmetry, CPVA are subject to non-linear energy localisation phenomena. Such situations, which might decrease the efficiency of the absorbers, have been studied by S. Shaw et al. [3–7], A. Grolet et al. [8] and K. Nishimura et al. [9] in the case of translated pendulums, i.e. pendulums that do not rotate relatively to the rotor. Until recent times, such pendulums were the only ones used in the industry. However, A. Renault and M. A. Acar showed that adding a rotational mobility of the pendulums may lead to a significant increase of mitigation performances [10–13]. This increase in performance was also observed by J. Mayet and H. Ulbrich [14]. Recent works by M. Cirelli, M. Cera et al. [15–19] confirmed the interest for pendulums with a rotational mobility and introduced a new way a representing the trajectory, using curvature ratios instead of the polynomial coefficients used in most studies (see [4] for instance). M. Cirelli et al. also used a Cartesian representation of the trajectory to derive tuning recommendations consistent with known results of the literature [20]. J. Mayet and H. Ulbrich [21] used Hamilton's formalism to compute the stability of a CPVA with rotating pendulums and gave guidelines regarding the tuning of the system. X. Tan et al. considered a CPVA made of a single pendulum obeying a non-linear rotation law and gave guidelines for the choice of this law [22]. E. R. Gomez et al. investigated theoretically and experimentally the friction losses in a CPVA with rotating pendulums [23]. A new type of CPVA, made of a double pendulum, was studied by V. Manchi and C. Sujatha [24]. The use of CPVA to damp multidegrees-of-freedom systems was considered by K. Kadoi et al. [25]. B. Geist et al. [26] studied the precision requirements and sources of errors associated with the manufacturing process of a bifilar CPVA.

The motivation of this paper is to investigate the stability of CPVA whose pendulums rotate relatively to the rotor. Unlike previous studies [16,18,21], the authors chose to describe the trajectory and rotation functions of a pendulum using polynomials (in [16,18], curvature ratios and a rolling radius are used to describe the trajectory and rotation law, respectively, whilst in [21] the trajectory and rotation are not defined explicitly). This way, the non-linear parts of the trajectory and rotation will appear clearly in the results, allowing for an easier understanding of their impact on the dynamics. To facilitate further this understanding, a tool representing the stability as a function of the trajectory and rotation functions is introduced. New design guidelines are derived from these analysis. Finally, experimental observations of the localised response are used to validate the analytical model. To our knowledge, it is the first time that the analytical prediction of the localisation is compared to experimental results (localisation was observed unexpectedly in [27] and not compared to analytical predictions in [28]).

This paper is organised as follows: Section 2 describes the modelling of the CPVA. Section 3 presents a linear study of the CPVA, setting the basis of the non-linear analysis. This non-linear analysis starts in Section 4 where the simplified pendulums' equation is established. This equation is solved in Section 5 and its stability is assessed. Section 6 presents a case study of the former developments. A numerical validation of the model is shown and an original visualisation of the stability in the design space is introduced. Design rules are proposed in Section 7 and an experimental validation is lead in Section 8. Finally, this paper ends with a conclusion in Section 9.

2. Modelling

The system studied is shown in Fig. 1. It is made of a rotor of inertia J_r rotating about its centre O. Its total angular position is $\vartheta(t) = \Omega t + \theta(t)$ where t is the time, Ω is the mean rotation velocity and θ corresponds to the fluctuating part of the rotation.

A torque $T(\vartheta)$ is applied to this rotor. It can be decomposed into a constant torque T_0 and a periodic one $T_\theta(\vartheta)$. The constant torque balances the torque arising from the rotor's damping, thus setting the mean rotation speed Ω. In the model, an equivalent linear viscous damping b_r is used for the rotor. N pendulums of mass m_i and inertia I_i (about their centre of gravity) oscillate on their trajectory $\mathscr{C}_i$. The position of their centre of gravity on these trajectories is given by the curvilinear abscissa $S_i(t)$ and their distance from the centre of rotation of the rotor is $R_i(S_i)$. The characteristic dimension $R_{0_i} = R_i(S_i = 0)$ represents the position of the pendulums at rest (when $T_\theta = 0$ such that they are perfectly centrifugated). In addition to the traditional translation motion, the present study considers that the pendulums rotate relatively to the rotor according to the rotation function $\alpha_i(S_i)$. As for the rotor, an equivalent linear viscous damping b_i is used to model the damping between the rotor and the i^{th} pendulum. In the later, pendulums and their associated trajectory and rotation functions will be considered identical so that subscript "i" will be dropped when addressing pendulums' parameters. Using the relation between the mean torque, the rotor's damping and the mean rotation speed, $T_0 = b_r\Omega$, and introducing the non-dimensional parameters and variables $s_i = S_i/R_0$, $\eta = I/mR_0^2$, $\bar{b} = b/m\Omega$, $x(s_i) = R(R_0 s_i)^2/R_0^2$, $z(s_i) = \sqrt{x(s_i) - (dx(s_i)/ds_i)^2/4}$, $\gamma(s_i) = R_0 d\alpha(R_0 s_i)/d(R_0 s_i)$, $\mu = NmR_0^2/(J_r + NI)$, $\bar{b}_r = b_r/(J_r + NI)\Omega$, $\bar{T}_0 = T_0/(J_r + NI)\Omega^2$, $\bar{T}_\theta = T_\theta/(J_r + NI)\Omega^2$, $\tau = \Omega t$, the equations of motion can be written as

$$\frac{1}{N}\left[\sum_{i=1}^{N}(N + \mu x(s_i))\theta'' + \mu\left(z(s_i) + \eta\gamma(s_i)\right)s_i'' + \mu s_i'\left(\frac{dx(s_i)}{ds_i}(1+\theta') + \frac{dz(s_i)}{ds_i}s_i' + \eta\frac{d\gamma(s_i)}{ds_i}s_i'\right)\right] + \bar{b}_r\theta' = \bar{T}_\theta(\tau+\theta), \tag{1a}$$

$$\left(z(s_i) + \eta\gamma(s_i)\right)\theta'' + \left(1 + \eta\gamma(s_i)^2\right)s_i'' + \eta\gamma(s_i)\frac{d\gamma(s_i)}{ds_i}s_i'^2 - \frac{1}{2}\frac{dx(s_i)}{ds_i}\left(1+\theta'\right)^2 + \bar{b}s_i' = 0, \quad i = 1, \dots, N \tag{1b}$$

where $(\bullet)'$ denotes derivation with respect to τ. Eq. (1a) is related to the motion of the rotor and the N Eqs. (1b) represent the motion of the pendulums. It is chosen to express the trajectory and rotation functions as polynomials such that

$$x(s_i) = 1 - n_t^2 s_i^2 + \sum_{k=3}^{\infty} x_{[k]} s_i^k, \quad \alpha(s_i) = \sum_{k=0}^{\infty} \alpha_{[k]} s_i^k \tag{2}$$

where n_t is called the trajectory order of the pendulums and $x_{[k]}$, $\alpha_{[k]}$ are trajectory and rotation coefficients. Note that in the case $x_{[k]} = 0\ \forall k$, the pendulums' trajectories are epicycloids, which corresponds to the tautochronic trajectory for $\theta = 0$ [2].

From now on, it is assumed that the fluctuating torque applied to the rotor contains only one harmonic. This is justified by the fact that in reciprocating engines, the fundamental harmonic typically dominates the fluctuating torque. The non-dimensional form of the fundamental torque harmonic is $\bar{T}_1\cos[n(\tau+\theta)]$ where n is the engine order. For a car thermal engine, n corresponds to the number of strikes per revolution of the crankshaft. At this stage, $\bar{T}_1\cos[n(\tau+\theta)]$ is not a periodic forcing term but a non-linear term as it depends on θ. In the following, two methods are proposed to transform it into a periodic forcing term.

Method 1. One can use the change of independent variable $\tau \to \tau + \theta$ proposed by S. Shaw et al. [29] to directly transform $\bar{T}_1\cos[n(\tau+\theta)]$ into a periodic forcing term. This choice is motivated by the fact that the explosions of a car engine do not depend on time but on the angular position of the crankshaft (which is the same as that of the rotor). Though it adds non-linearities to the system, this method is interesting as it does not require any hypothesis, thus keeping the equations exact.

Method 2. Another method is to express the fluctuating torque as a function of τ to write $\bar{T}_1\cos((\omega/\Omega)\tau)$ where ω is the angular frequency of the acyclism. For a car engine, the excitation frequency must correspond to the number of strikes per second, leading to $\omega = n(\Omega + \dot{\theta})$ where $(\dot{\bullet})$ refers to a derivation with respect to time. It can be assumed that the fluctuating rotation velocity of the crankshaft is much smaller than the mean rotation speed, i.e. $\dot{\theta} \ll \Omega$. It follows that $\omega/\Omega \approx n$, leading to a trivial transformation of the torque into a periodic forcing term.

3. Linear vibrations of the system

In this section, a linear analysis of the system is led. After transforming the external torque into a periodic forcing term using *Method 2* (*cf.* Section 2), one can linearise Eqs. (1a) and (1b) and then use a property of arrowhead matrices [30] to find that the eigenorders and eigenvectors of the system are

$$\begin{aligned} &n_{00} = 0, \quad n_{10} = n_p, \quad n_{20} = n_p\sqrt{\frac{1+\mu}{1+\mu\left(1-\frac{\Lambda_c^2}{\Lambda_m}\right)}}, \quad \boldsymbol{\phi_{00}} = [1, 0, \dots, 0]^T, \quad \boldsymbol{\phi_{20}} = \left[-\frac{\mu\Lambda_c}{1+\mu}, 1, \dots, 1\right]^T, \\ &\boldsymbol{\phi}_{\mathbf{10}_i}[i+1] = -\boldsymbol{\phi}_{\mathbf{10}_i}[i+2] = 1, \ \boldsymbol{\phi}_{\mathbf{10}_i}[j \neq \{i+1, i+2\}] = 0, \quad i = 1, \dots, N-1. \end{aligned} \tag{3}$$

Superscript T denotes the transpose. Λ_m and Λ_c are constants representing the equivalent mass of a pendulum and the linear coupling term between a pendulum and the rotor, respectively. They are given by

$$\Lambda_m = 1 + \eta\alpha_{[1]}^2, \quad \Lambda_c = 1 + \eta\alpha_{[1]} \tag{4}$$

where $\alpha_{[1]}$ is the linear rotation coefficient. n_p is the eigenorder of the pendulums when the rotor is spinning at constant speed. Considering the case $\theta = 0$ and linearising Eqs. (1b), one finds that n_p is related to n_t such that

$$n_p = n_t\Lambda_m^{-1/2}. \tag{5}$$

When a fluctuating torque is applied on the rotor, pendulums generate an antiresonance at order n_p (in the conservative case). Thus, for a fluctuating torque of order n, one must choose $n_p = n$ to minimise the vibrations of the rotor (this can be extended to the non-conservative case as damping is small). For this reason, n_p is called the tuning order of the pendulums. It is interesting to note that if $\alpha_{[1]} \neq 0$, then $\Lambda_m > 1$, leading to $n_t > n_p$ (*cf.* Eqs. (4) and (5)). This means that the relative rotation of the pendulums imposes an over-tuning of the trajectory order compared to the case of purely translated pendulums (for which $n_t = n_p$).

$\boldsymbol{\phi_{00}}$ is a rigid body mode for which only the rotor is excited. $\boldsymbol{\phi_{10_i}}$ are $N-1$ degenerated modes for which pendulums i and $i+1$ are out of phase while other pendulums are immobile ($i = 1, \dots, N-1$). They are associated to the eigenvalue n_{10}, which has a multiplicity $N-1$ and the rotor is a node of these modes. Note that in the case $N = 2$, $\boldsymbol{\phi_{10}}$ is not degenerated and simply corresponds to an out-of-phase motion of the pendulums. $\boldsymbol{\phi_{20}}$ is a mode for which pendulums move in unison but in phase-opposition with respect to the rotor (provided that $\Lambda_c > 0$, which is the case in practice).

This section offers a linear analysis of the CPVA. However, it can be seen from Eqs. (1a) and (1b) that the dynamics of the system is subject to several sources of non-linearity. In the following, an analytical model allowing the visualisation and prediction of non-linear phenomena will be derived.

4. Simplification of the equations

Following S. Shaw et al. [4,7,31], the construction of the model starts with a scaling of the parameters, allowing a simplification of the equations of motion such that the dynamics of the pendulums becomes uncoupled from that of the rotor. Since the displacement of the pendulums will be considered small, the trajectory and rotation functions (2) are truncated so that

$$x(s_i) = 1 - n_t^2 s_i^2 + x_{[4]} s_i^4 + \mathcal{O}(s_i^6), \quad \alpha(s_i) = \alpha_{[1]} s_i + \alpha_{[3]} s_i^3 + \mathcal{O}(s_i^5) \tag{6}$$

will be used in the following computations. There are no odd powers of s_i in $x(s_i)$ and no even powers in $\alpha(s_i)$ so that these two functions are symmetric (anti-symmetric, respectively) about $s_i = 0$. It is the case in practice due to design constraints. The fluctuating rotor's rotation is a priori made of several harmonics such that it can be expanded as

$$\theta = \theta^{(1)} + \theta^{(2)} + HOT \tag{7}$$

where $\theta^{(1)}$ and $\theta^{(2)}$ are the first and second harmonics, respectively, and HOT refers to *Higher Order Terms*.

4.1. Scaling

In this subsection, the aim is to scale the weight of some parameters and variables so as to capture the desired physical phenomena. The following hypothesis and remarks will govern the scaling:

- The optimum system configuration is that with small damping (both rotor's and pendulums' dampings). This way, the vibration amplitude of the rotor at its antiresonance is very small.
- The fluctuating torque T_θ is small compared to the rotor's kinetic energy (which is $J_r \Omega^2/2$ at equilibrium). This implies that $\bar{T}_1$ is small.
- The total pendulums' geometric inertia about point O, NmR_0^2, is considered small compared to the inertia of the total rotating system, $J_r + NI$, such that μ is small.
- The rotor's inertia being significant, the fluctuating rotation speed $\dot{\theta}$ is small compared to the mean rotation speed. Note that this hypothesis was already done in Section 3 to transform the external torque into a periodic excitation.
- The pendulums' amplitude of motion is small compared to their distance from the centre of rotation O such that s_i are small.
- The trajectory function chosen (*cf.* Eq. (6)) is an epicycloid perturbed by $x_{[4]} s_i^4$. Considering the perturbation is small, $x_{[4]}$ is a priori small.
- The rotation function chosen (*cf.* Eq. (6)) differs from a linear rotation by the term $\alpha_{[3]} s_i^3$. Considering rotation is mainly linear, $\alpha_{[3]}$ is a priori small.

Accordingly to the above and introducing the small parameter ϵ, the following scaled parameters are introduced

$$\bar{b} = \epsilon^{\ell} \tilde{b}, \quad \bar{b}_r = \epsilon^{h} \tilde{b}_r, \quad \bar{T}_1 = \epsilon^{r} \tilde{T}_1, \quad \mu = \epsilon^{\phi} \tilde{\mu}, \quad \theta^{(1)} = \epsilon^{w_1} \tilde{\theta}^{(1)}, \quad \theta^{(2)} = \epsilon^{w_2} \tilde{\theta}^{(2)}, \quad s_i = \epsilon^{\nu} \tilde{s}_i, \quad x_{[4]} = \epsilon^{p} \tilde{x}_{[4]}, \quad \alpha_{[3]} = \epsilon^{q} \tilde{\alpha}_{[3]} \tag{8}$$

where ℓ, h, r, ϕ, w_1, w_2, ν, p and q are scaling coefficients to be determined. In order to give a physical meaning to ϵ, one can choose to set $\epsilon = \mu$ [4].

4.2. Rotor's dynamics

The aim here is to obtain an equation governing the rotor's dynamics as a function of the pendulums' and the external torque. Introducing the trajectory and rotation functions (6), the expanded form of θ (7) and the scaled parameters (8) in the rotor's Eq. (1a) and setting $r = \phi + \nu$, one can write

$$\epsilon^{w_1} \tilde{\theta}^{(1)\prime\prime} + \epsilon^{w_2} \tilde{\theta}^{(2)\prime\prime} = \epsilon^{r} \left[\tilde{T}_1 \cos(n\tau) + \frac{n_p^2 \tilde{\mu} \Lambda_c}{N} \sum_{i=1}^{N} \tilde{s}_i \right] + \epsilon^{r+\nu} \frac{2\tilde{\mu} n_t^2}{N} \sum_{i=1}^{N} \tilde{s}_i \tilde{s}_i' + \mathcal{O}(\epsilon^{\phi+w_1}, \epsilon^{h+w_1}, \epsilon^{\phi+3\nu}). \tag{9}$$

Note that the external torque was transformed into a periodic forcing term using *Method 2* (*cf.* Section 2). Eq. (9) uses the pendulums' equation at first order $\tilde{s}_i'' = -n_p^2 \tilde{s}_i$ (assuming $\nu < w_1$).

Eq. (9) is similar to that obtained if the change of independent variable $t \to \tau + \Omega$ had been used. The two differences would be that $(\bullet)'$ would denote derivation with respect to $\tau + \theta$ and the torque term which would be $\tilde{T}_1 \cos[n(\tau+\theta)]$. However, using the chain rule, one can observe

$$\frac{\partial}{\partial \tau} = \frac{\partial}{\partial(\tau+\theta)} + \mathcal{O}(\epsilon^{w_1}), \quad \frac{\partial^2}{\partial \tau^2} = \frac{\partial^2}{\partial(\tau+\theta)^2} + \mathcal{O}(\epsilon^{w_1}) \tag{10}$$

so that at the order retained in Eq. (9), derivatives with respect to τ and $\tau+\theta$ are equivalent. Moreover, expanding the torque term, one can notice

$$\tilde{T}_1 \cos[n(\tau+\theta)] = \tilde{T}_1 \cos(n\tau) + \mathcal{O}(\epsilon^{r+w_1}). \tag{11}$$

This means that at the order retained in Eq. (9) and assuming $w_2 < r + w_1$, it is equivalent to transform the torque into a periodic forcing term using the change of independent variables $t \to \tau + \theta$ (*cf. Method 1* in Section 2) or assuming $\omega/\Omega \approx n$ (*cf. Method 2* in Section 2).

4.3. Pendulums' dynamics

The aim here is to uncouple the pendulums' dynamics from the rotor's. To do so, the rotor's simplified Eq. (9) is introduced in the pendulums' Eq. (1b). Then, using the trajectory and rotation functions (6) and choosing the set of scaling coefficients

$$\phi = \ell = 1,\ \nu = 1/2,\ p = q = 0,\ r = 3/2, \tag{12}$$

the pendulums' equation reduces to

$$\tilde{s}_i'' + n_p^2 \tilde{s}_i = -\epsilon \Lambda_m^{-1} \left[-2\tilde{x}_{[4]} \tilde{s}_i^3 + 6\eta \alpha_{[1]} \tilde{\alpha}_{[3]} (\tilde{s}_i^2 \tilde{s}_i'' + \tilde{s}_i \tilde{s}_i'^2) + \tilde{b} \tilde{s}_i' + \Lambda_c \left(\tilde{T}_1 \cos(n\tau) + \frac{n_p^2 \tilde{\mu} \Lambda_c}{N} \sum_{j=1}^{N} \tilde{s}_j \right) \right] + HOT. \tag{13}$$

The set of scaling parameters was chosen to uncouple the pendulums' equation from the rotor's dynamics while keeping the effect of the non-linearities coming from both the trajectory and rotation functions. Eq. (13) contains the influence of the external torque, the coupling between pendulums through the sum over N, and non-linearities coming from both the trajectory and the rotation. It is also interesting to note that because pendulums are identical and coupled, the system exhibits 1:1 internal resonances [32–34]. Eqs. (13) are weakly coupled because pendulums are coupled indirectly through the rotor and their effect on the rotor is small as their relative inertia is small [31]. Moreover, these equations are weakly non-linear because s_i were assumed small and the trajectory and rotation functions chosen (*cf.* Eq. (6)) are close to an epicycloid and a linear rotation, which render a linear behaviour for small fluctuations of the rotational speed. Note that the hypothesis and choice of scaling parameters of this study allows to investigate exclusively the effect of non-linearities due to the trajectory and rotation functions. Other sources of non-linearities, such as those arising from the coupling between the rotor and the pendulums, are missed in the present study. To account for those, other hypothesis can be made, as it is done in [3,5].

5. Solving the simplified equations and stability analysis

5.1. Application of the method of multiple scales

In the present study, the choice is made to solve the pendulums' simplified equations using the method of multiple scales [35]. Two time scales are introduced, $\tau_0 = \tau$ and $\tau_1 = \epsilon\tau$. As it was done previously for the rotor, the pendulums' displacement is expanded such that

$$\tilde{s}_i(\tau) = \tilde{s}_i^{(1)}(\tau_0, \tau_1) + \epsilon \tilde{s}_i^{(3)}(\tau_0, \tau_1) + HOT \tag{14}$$

where $\tilde{s}_i^{(1)}$ and $\tilde{s}_i^{(3)}$ represent the first and third harmonics, respectively. Inserting Eq. (14) in Eq. (13) yields a solution for $\tilde{s}_i^{(1)}$ of the form

$$\tilde{s}_i^{(1)} = a_i(\tau_1) \cos\left(n\tau_0 - \xi_i(\tau_1)\right) \tag{15}$$

where amplitudes a_i and relative phases ξ_i are governed by the $2N$ equations system

$$\begin{cases} D_1 a_i = f_{a_i}(\boldsymbol{a}, \boldsymbol{\xi}), & \text{(a)} \\ a_i D_1 \xi_i = f_{\xi_i}(\boldsymbol{a}, \boldsymbol{\xi}). & \text{(b)} \end{cases} \tag{16}$$

$\boldsymbol{a}$ and $\boldsymbol{\xi}$ are vectors containing the a_i and ξ_i, respectively, and D_1 denotes derivation with respect to τ_1. Functions f_{a_i} and f_{ξ_i} are given by

$$f_{a_i}(\boldsymbol{a}, \boldsymbol{\xi}) = -\frac{1}{2\Lambda_m n_p} \left[\Lambda_c \tilde{T}_1 \sin(\xi_i) + n_p \tilde{b} a_i + \frac{\Lambda_c^2 n_p^2 \tilde{\mu}}{N} \sum_{\substack{j=1 \\ j \neq i}}^{N} a_j \sin(\xi_i - \xi_j) \right], \tag{17a}$$

$$f_{\xi_i}(\boldsymbol{a},\boldsymbol{\xi}) = \sigma a_i - \frac{1}{2\Lambda_m n_p}\left[\Lambda_c \tilde{T}_1 \cos(\xi_i) + \frac{\Lambda_c^2 n_p^2 \tilde{\mu}}{N}\left(a_i + \sum_{\substack{j=1 \\ j\neq i}}^{N} a_j \cos(\xi_i - \xi_j)\right) - \frac{c_p}{2} a_i^3\right], \tag{17b}$$

where σ is a detuning term such that $n = n_p + \epsilon\sigma$ and c_p is a non-linear coefficient related to the perturbation of the trajectory and rotation functions. It is defined as

$$c_p = 3(\tilde{x}_{[4]} + 2n_p^2 \eta \alpha_{[1]} \tilde{\alpha}_{[3]}). \tag{18}$$

In the frame of the study led in this paper, only the steady-state regime is considered. This implies that the pendulums' amplitude and their phase relative to the excitation is time-invariant, such that

$$D_1 a_i = 0, \quad D_1 \xi_i = 0. \tag{19}$$

Introducing Eq. (19) in Eq. (16) leads to the system

$$\begin{cases} 0 = f_{a_i}(\boldsymbol{a},\boldsymbol{\xi}), & \text{(a)} \\ 0 = f_{\xi_i}(\boldsymbol{a},\boldsymbol{\xi}), & \text{(b)} \end{cases} \tag{20}$$

which is to be solved to determine the pendulums' response.

5.2. Reduction to a single mode

It was observed in Section 3 that, in a linear regime, a single mode participates to the pendulums' response. This linear mode, $\boldsymbol{\phi_{20}}$, can be called "unison mode" as it describes a motion for which all pendulums have the same amplitude and phase. As the behaviour considered in this section is weakly non-linear, it can be expected that pendulums will move at unison. Thus, it is assumed that

$$a_i = a, \quad \xi_i = \xi. \tag{21}$$

Introducing Eq. (21) in Eq. (20), one can find the following order response of pendulums at unison

$$\sigma = \frac{1}{2\Lambda_m n_p}\left[\Lambda_c^2 n_p^2 \tilde{\mu} - \frac{c_p}{2} a^2 \pm \sqrt{\Lambda_c^2 \frac{\tilde{T}_1^2}{a^2} - n_p^2 \tilde{b}^2}\right]. \tag{22}$$

The backbone of the non-linear unison mode can be deduced from Eq. (22) as $n_2 = n_p + \epsilon\ \sigma|_{\tilde{T}_1=\tilde{b}=0}$. It is interesting to note that the hardening or softening behaviour of the pendulums is governed by the sign of c_p. This property will later be used to specify design rules (*cf.* Section 7). Introducing Eq. (21) in Eq. (20), one can also find the following torque response

$$\tilde{T}_1 = \frac{a}{\Lambda_c}\left[\frac{c_p^2}{4} a^4 + 2c_p n_p \left(\Lambda_m \sigma - \frac{\Lambda_c^2}{2}\tilde{\mu} n_p\right) a^2 + 4\Lambda_m^2 n_p^2 \sigma^2 + n_p^2 \tilde{b}^2 - n_p^3 \tilde{\mu} \Lambda_c^2 \left(4\Lambda_m \sigma - \Lambda_c^2 n_p \tilde{\mu}\right)\right]^{1/2}. \tag{23}$$

Computing the amplitude response allows accessing the phase response, given by

$$\tan(\xi) = -2n_p \tilde{b}\left[4\Lambda_m n_p \sigma - 2\Lambda_c^2 n_p^2 \tilde{\mu} + c_p a^2\right]^{-1}. \tag{24}$$

Then, using the results for a and ξ and the rotor's simplified Eq. (9), one can compute the amplitude of the two first harmonics of the rotor, given by

$$\left|\tilde{\theta}^{(1)\prime\prime}\right| = \sqrt{\tilde{T}_1^2 + n_p^4 \tilde{\mu}^2 \Lambda_c^2 a^2 + 2\tilde{T}_1 n_p^2 \tilde{\mu} \Lambda_c a \cos(\xi)}, \tag{25}$$

$$\left|\tilde{\theta}^{(2)\prime\prime}\right| = \tilde{\mu} n n_r^2 a^2. \tag{26}$$

Eq. (26) highlights that non-linear effects induced by the pendulums generate higher order harmonics of the rotor (at the order retained, only the 2$^{\text{nd}}$ harmonic, related to Coriolis effects, is present).

5.3. Stability analysis

The stability of the response is now assessed. First, system (16) can be rewritten as

$$\begin{cases} D_1 a_i = f_{a_i}(\boldsymbol{a},\boldsymbol{\xi}), & \text{(a)} \\ D_1 \xi_i = f^*_{\xi_i}(\boldsymbol{a},\boldsymbol{\xi}), & \text{(b)} \end{cases} \tag{27}$$

with $f^*_{\xi_i}(\boldsymbol{a},\boldsymbol{\xi}) = f_{\xi_i}(\boldsymbol{a},\boldsymbol{\xi})/a_i$. Then, the Jacobian of system (27) is computed and evaluated on the unison solution at steady state, yielding a $2N \times 2N$ block circulant matrix such that

$$\boldsymbol{J} = \begin{bmatrix} \boldsymbol{J_1} & \boldsymbol{J_2} & \cdots & \boldsymbol{J_2} \\ \boldsymbol{J_2} & \ddots & \ddots & \vdots \\ \vdots & \ddots & \ddots & \boldsymbol{J_2} \\ \boldsymbol{J_2} & \cdots & \boldsymbol{J_2} & \boldsymbol{J_1} \end{bmatrix}, \quad \boldsymbol{J_1} = \begin{bmatrix} \dfrac{\partial f_{a_i}}{\partial a_i} & \dfrac{\partial f_{a_i}}{\partial \xi_i} \\ \dfrac{\partial f^*_{\xi_i}}{\partial a_i} & \dfrac{\partial f^*_{\xi_i}}{\partial \xi_i} \end{bmatrix}, \quad \boldsymbol{J_2} = \begin{bmatrix} \dfrac{\partial f_{a_i}}{\partial a_j} & \dfrac{\partial f_{a_i}}{\partial \xi_j} \\ \dfrac{\partial f^*_{\xi_i}}{\partial a_j} & \dfrac{\partial f^*_{\xi_i}}{\partial \xi_j} \end{bmatrix}. \tag{28}$$

$\boldsymbol{J_1}$ represents the effect of a perturbation of the ith pendulum on itself while $\boldsymbol{J_2}$ represents the effect that a perturbation of the jth pendulums has on the ith one (with $j \neq i$). The $2N$ eigenvalues of $\boldsymbol{J}$ are given by the 2 eigenvalues of $[\boldsymbol{J_1} + (N-1)\boldsymbol{J_2}]$ and the 2 eigenvalues of $[\boldsymbol{J_1} - \boldsymbol{J_2}]$ with multiplicity $N-1$ [36]. Instabilities appear when the real part of at least one of the eigenvalues of $\boldsymbol{J}$ changes sign. The limits of the instabilities are given by

$$\det[\boldsymbol{J_1} + (N-1)\boldsymbol{J_2}] = 0, \tag{29a}$$

$$\det[\boldsymbol{J_1} - \boldsymbol{J_2}] = 0, \tag{29b}$$

and because the trace of $[\boldsymbol{J_1}+(N-1)\boldsymbol{J_2}]$ and $[\boldsymbol{J_1}-\boldsymbol{J_2}]$ is always negative, the solution is unstable when at least one of the determinants in Eq. (29) is negative.

The determinants in Eq. (29) indicate instabilities of different nature. Consider just for a moment that there is only one pendulum, i.e. $N = 1$. Then, condition (29a) reduces to $\det[\boldsymbol{J_1}] = 0$ and condition (29b) is undefined as $\boldsymbol{J_2}$ is undefined ($\boldsymbol{J_2}$ exists only when $N > 1$). For a given excitation amplitude, $\det[\boldsymbol{J_1}] = 0$ corresponds to a pair of saddle–node bifurcations between which the periodic solution is unstable. This is analogous to a classic Duffing-like bent resonance with jump phenomena [37]. By continuity, when $N > 1$, condition (29a) still indicates saddle–node bifurcations. Instabilities associated to condition (29b) arise only when several pendulums are considered, so that they are related to a loss of unison [4]. Thus, for a given excitation amplitude, condition (29b) corresponds to a pair of pitchfork bifurcations between which the pendulums' response is localised on one or more pendulums.

The critical pendulums' amplitudes corresponding to saddle–node bifurcations are the solutions of condition (29a) and are given by

$$a_{sn} = \sqrt{\frac{-8\sigma\Lambda_m n_p + 4\Lambda_c^2 n_p^2\tilde{\mu} \pm 2n_p\sqrt{\left(2\sigma\Lambda_m - n_p\Lambda_c^2\tilde{\mu}\right)^2 - 3\tilde{b}^2}}{3c_p}}. \tag{30}$$

Similarly, the critical pendulums' amplitudes corresponding to pitchfork bifurcations are the solutions of condition (29b) and are given by

$$a_{pf} = \sqrt{\frac{-8\sigma\Lambda_m n_p \pm 2n_p\sqrt{4\sigma^2\Lambda_m^2 - 3\tilde{b}^2}}{3c_p}}. \tag{31}$$

These critical amplitudes are depicted in Fig. 3. It is interesting to note that the critical amplitudes a_{sn} and a_{pf} tend to infinity as c_p tends to zero. This observation will come useful in Section 7. Moreover, the critical amplitudes are independent of the forcing amplitude $\tilde{T}_1$.

5.4. Limits of the model

It is of importance to bear in mind that the previous analytical computations involve assumptions that limit the range of validity of the model. One of the approximations of the non-linear model is exposed in details below and an order of magnitude of the non-dimensional parameters that can be used in the model is given. The backbone of the unison mode (*cf.* Section 5.2) evaluated for zero pendulums' displacement is a Taylor expansion of the linear eigenvalue n_{20} (*cf.* Eq. (3)) with respect to μ such that

$$n_{20} = \underbrace{n_p + \mu\frac{n_p\Lambda_c^2}{2\Lambda_m}}_{\text{backbone at } a=0} + \mu^2\frac{n_p}{8}\frac{\Lambda_c^2}{\Lambda_m}\left(3\frac{\Lambda_c^2}{\Lambda_m} - 4\right) + \mathcal{O}(\mu^3), \tag{32}$$

where the backbone contains only the two first terms. For the analytical model to be accurate, one needs the third term to be negligible. Eq. (32) allows to write an approximated condition on μ such that the relative error on the backbone at $a = 0$ does not exceed 100χ %. It is given by

$$\mu < \frac{\chi + \sqrt{\chi^2 + 8\chi\left|\frac{3}{4} - \frac{\Lambda_m}{\Lambda_c^2}\right|}}{2\left|\frac{3\Lambda_c^2}{4\Lambda_m} - 1\right|}. \tag{33}$$

In Section 4.1, μ was proposed as the small perturbation parameter of the perturbation analysis. Thus, one can chose $\mu = \epsilon$, yielding an order of magnitude not to be overpassed for every small parameter.

6. Case study and numerical validation

The former developments are now applied on a system of two pendulums. The aim is to present the main assets of the analytical model and to compare them with an exact (numerical) resolution of the equations of motion (1a) and (1b) as a first validation. To perform the numerical resolution, the change of independent variable $\tau \to \tau + \theta$ is introduced in Eqs. (1a) and (1b) to transform the torque into a periodic forcing term while keeping the equations exact (*cf. Method 1* in Section 2). Two different numerical resolutions are used in this paper:

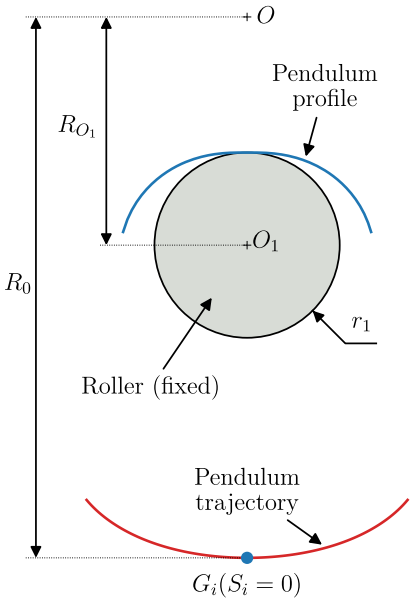

Fig. 2. CPVA studied (only one of the two pendulums is represented, the architecture being symmetric).

Table 1
Parameters of the CPVA studied in this section.

N	n_p	η	μ	$x_{[4]}$	$\alpha_{[1]}$	$\alpha_{[3]}$	$\tilde{b}$	$\tilde{b}_r$
2	0.5	1.4	0.1	−4.2	1.33	0.06	0.16	0.002

- The equations are integrated numerically using a Runge–Kutta algorithm until the steady state is reached. Then, the signals' amplitudes are obtained through a decomposition into Fourier series.
- The equations are solved with MANLAB, which is a path-following and bifurcation analysis software [38].

The CPVA studied in this section is represented in Fig. 2 and its parameters are given in Table 1. Its low tuning order ($n_p = 0.5$) makes it well suited for filtering out vibrations arising from cylinders deactivation. The CPVA is made of two monofilar pendulums (only one is represented in Fig. 2). The profile of a pendulum rolls without slipping on a roller of radius r_1 (fixed on the rotor). The shape of the profile allows to control the trajectory followed by the pendulum's centre of mass. For such pendulums, the rotation function $\alpha(s_i)$ is governed by the functional geometry. The two first rotation coefficients are

$$\alpha_{[1]} = \frac{R_0}{R_0 - R_{O_1} + r_1}, \tag{34}$$

$$\alpha_{[3]} = \alpha_{[1]} \frac{R_{O_1}\left(1+n_t^2\right)^2 - R_0 n_t^2\left(1+n_t^2\right) - \alpha_{[1]} R_{O_1}\left(1+n_t^2\right) + \alpha_{[1]} R_0 n_t^2}{6\left(R_{O_1} - R_0 + \alpha_{[1]} R_0^{-1}\left(\left(R_0 - R_{O_1}\right)^2 - r_1^2\right)\right)}. \tag{35}$$

6.1. Evaluation of the stability as function of mistuning

In practice, the excitation order is fixed such that $n = cte$. However, pendulums may not be tuned exactly to the excitation. This mistuning can be intentional or may arise from material imperfections. Either way, varying the excitation order is similar to introducing mistuning (provided that pendulums are equally mistuned) and is therefore relevant for studying the effect of mistuning on the system's response [8]. The order response of pendulums at unison and their stability is shown in Fig. 3 for several torque amplitudes. The bending of the response indicates that pendulums exhibit a hardening behaviour. The bifurcation zones (unstable unison in red and unstable periodic response in blue), delimited by the bifurcation curves (30) and (31), are shown. The zone corresponding to simultaneous unstable unison and unstable periodic responses is represented in purple while stable responses are represented in green. The same colour code will be used throughout this paper. For small torque amplitudes, the response is almost linear so that no stability changes will occur. As the torque amplitude is increased, the unison response crosses the bifurcation curves, leading to a different stability state.

6.2. Visualisation of the stability in the design space

An original visualisation of the pendulums' stability in the design space is now presented. This space allows to assess the stability of pendulums of the same type but with different sets of parameters $(x_{[4]}, \alpha_{[1]}, \alpha_{[3]})$. In the general case, it is thus a 3D space. However,

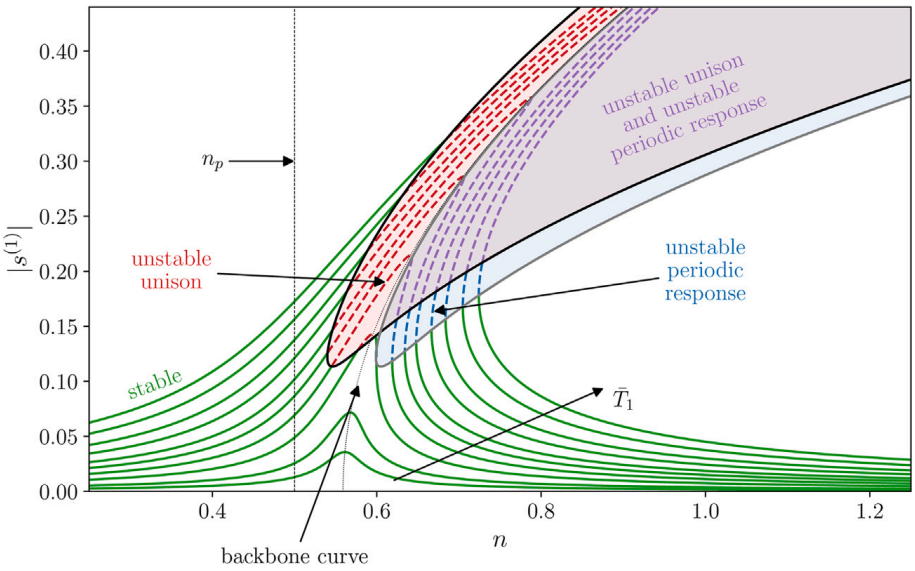

Fig. 3. Order response of the pendulums at unison and their stability. Portions of the response curves corresponding to stable unison, unstable unison and unstable periodic responses are represented in green, red and blue, respectively. Portions where both the unison and the periodic response are unstable are represented in purple. Additionally, all unstable portions are shown as dashed-lines. The black and grey curves represent the pitchfork and saddle–node bifurcations, respectively. $\bar{T}_1 = \{0.1, 0.2, 0.4, 0.6, 0.8, 1, 1.3, 1.6, 2, 2.4\} \times 10^{-2}$.

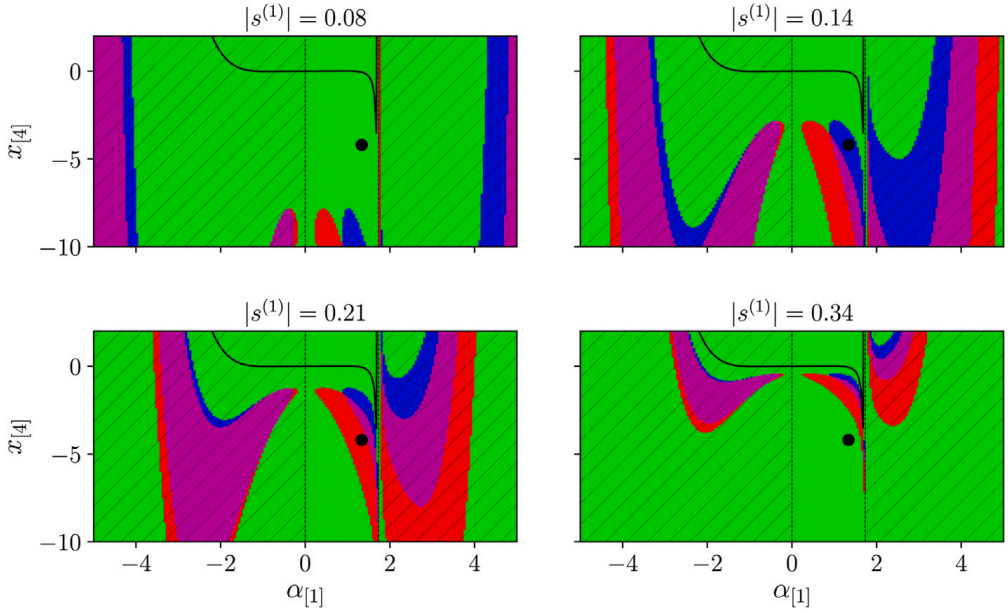

Fig. 4. Representation of the stability in the design space $(\alpha_{[1]}, x_{[4]})$. The colour code is the same as that used in Fig. 3, so that areas corresponding to stable unison, unstable unison and unstable periodic responses are represented in green, red and blue, respectively. Areas where both the unison and the periodic response are unstable are represented in purple. The black dot corresponds to the design represented in Fig. 3. The black curve represents designs rendering a linear behaviour. The hatched regions indicate non-achievable designs. $n = 0.63$, $R_{O_1}/R_0 = 0.422$. (For interpretation of the references to colour in this figure legend, the reader is referred to the web version of this article.)

for the CPVA presented in Fig. 2, the rotation is imposed by the functional geometry causing $\alpha_{[3]}$ to be related to $\alpha_{[1]}$. Moreover, due to space constraints, it is convenient to evaluate designs for a fixed value of the ratio R_{O_1}/R_0. Thus, using Eqs. (34) and (35), one can get $\alpha_{[3]}$ as a function of $\alpha_{[1]}$, which reduces the design space to a 2D space. This method is used to represent the stability of pendulums of the same type as that depicted in Fig. 2 under the form of maps, shown in Fig. 4. Each map is represented for a given amplitude and a given excitation order. Colours represent the stability (the colour code is the same as that used previously). The black line represents designs for which the values of $x_{[4]}$, $\alpha_{[1]}$ and $\alpha_{[3]}$ render the system linear (*cf.* Section 7). The meaning of the hatched regions will be defined later. The black dot corresponds to the design shown in Fig. 3 so that it is fixed in the design space. This specific design passes through several stability states as the amplitude of motion increases. This could already be observed looking at Fig. 3 for $n = 0.63$. The purpose of the representation in the design space is to identify designs which are likely or not

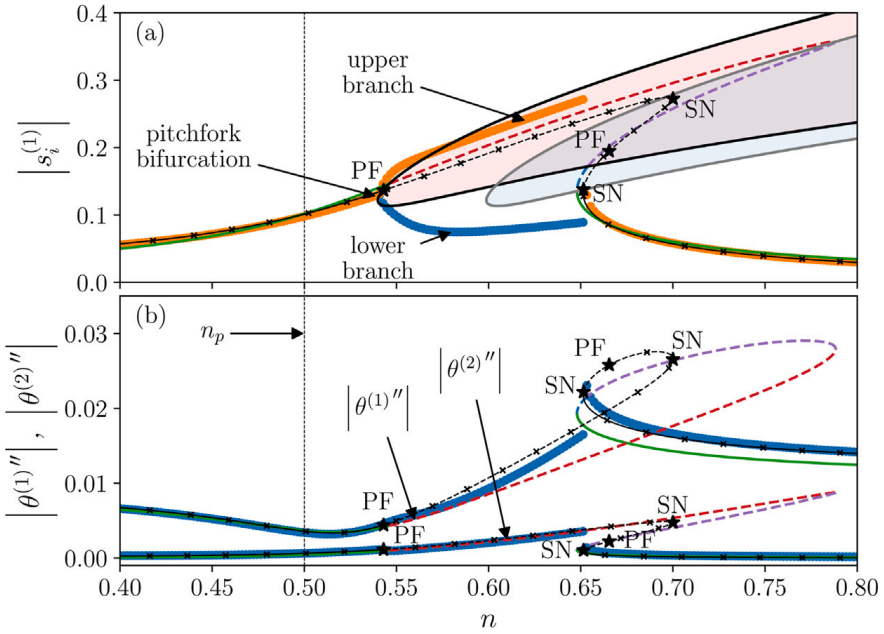

Fig. 5. Comparison of the pendulums' response (a) and rotor's response (b) obtained analytically and numerically. The colour code of the analytical results is the same as that used in Fig. 3. Circles represent the numerical results obtained through temporal integrations. In (a), one of the pendulums is represented by blue circles, the other by orange ones. The MANLAB solution is given as a black line with cross markers. Bifurcation points found with MANLAB are marked as black stars with an associated code name. Code names "PF" and "SN" refer to "pitchfork" and "saddle–node" bifurcations, respectively. $\bar{T}_1 = 0.01$.

to exhibit instabilities. For instance, the upper central region delimited by the black curve on the maps remains stable over the amplitude range represented. This remark will be further discussed in Section 7. Note that there seems to be an artefact on the maps around $\alpha_{[1]} = 1.7$. However, this simply corresponds to a value of $\alpha_{[1]}$ for which r_1 tends to zero, causing $\alpha_{[3]}$ to tend to ∞. Above this threshold value of $\alpha_{[1]}$, r_1 is negative, which is non-physical (remind that r_1 is a radius so that it should not be negative). Similarly, r_1 is negative for $\alpha_{[1]} < 0$. The hatched regions thus correspond to non-achievable designs.

6.3. Comparison with a numerical model

In this section, the analytical model is compared with an exact resolution of Eqs. (1a) and (1b). The pendulums' response obtained through the analytical and numerical models is presented in Fig. 5(a). Like what was observed in the case of absorbers with a pure translation motion [8], the unison mode looses its stability through a pitchfork bifurcation in favour of a localised response. The bifurcation point, theoretically located at the intersection of the black curve and the unison response, is accurately predicted by the model. After this bifurcation, the response divides into two branches so that energy is localised on one of the two pendulums. The pendulum located on the upper branch has a larger amplitude of motion than that predicted by the unison mode, which can be an issue as the maximum amplitude is limited by the nature of the trajectory chosen. This being said, one can see in Fig. 5(a) that the upper branch is close to the (unstable) unison response. Thus, in the case considered here, the risk of reaching the maximum amplitude is not significantly increased by the localisation. The jump located at $n \approx 0.65$ is also well predicted by the model. The amplitude of the stable solution is very well predicted by the analytical model. However, comparing with the MANLAB results, one can see that the analytical model overestimates the unstable solution. Similarly, the bifurcation points located on the unstable solution are not well predicted (especially the saddle–node bifurcation, which is theoretically located at the right intersection of the grey curve and the unison response, around $n \approx 0.69$). The reason for those discrepancies is that the amplitude on the unstable solution is rather large, so that some of the non-linear terms that were dropped in the analytical model have a non-negligible effect. Moreover, the analytical solution is based on a perturbation method around $n = n_p$ (*cf.* Section 5.1), so that less accuracy can be expected as n departs from n_p. This being said, an accurate prediction of the stable solution and the two bifurcation points at $n \approx 0.54$ and $n \approx 0.65$ is the most important point, as only those will be observed in practice. The difference both in phase and amplitude of the pendulums' localised responses is visible on the temporal signals given in Fig. 6(a).

Fig. 5(b) shows a comparison of the rotor's response obtained through the analytical and numerical models. Again, the analytical model allows an accurate prediction of the rotor's response on its stable (green) portions. Surprisingly, portions for which pendulums are not in unison are also well predicted by the model, even though the model uses only the unison mode. This is an interesting point, as it tends to show that localisation does not necessarily impact the rotor's dynamics. Looking at the response of $\theta^{(1)}$, one can see that the non-linearity shifted the antiresonance so that it does not correspond to the linear tuning order n_p. This problem is considered in [39]. The distortion of θ'' coming from the presence of $\theta^{(2)}$ (and in a smaller amount, higher harmonics), can be seen in Fig. 6(b).

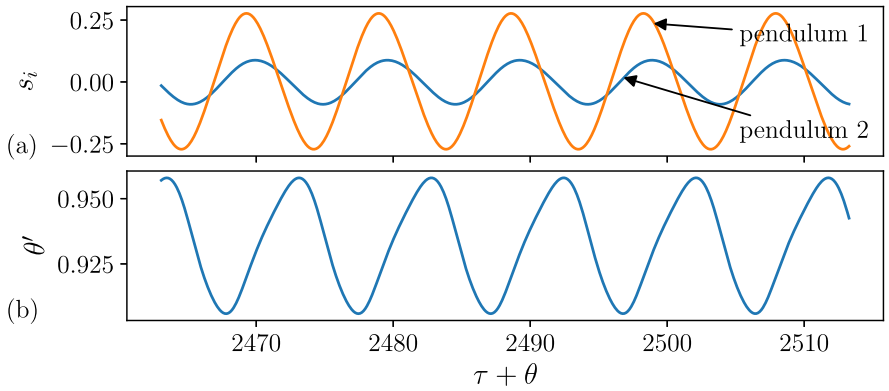

Fig. 6. Temporal signals (truncated) of the pendulums (a) and rotor (b) obtained through a numerical integration of the equations of motion. These signals lead to the amplitudes shown in Fig. 5 at $n = 0.65$.

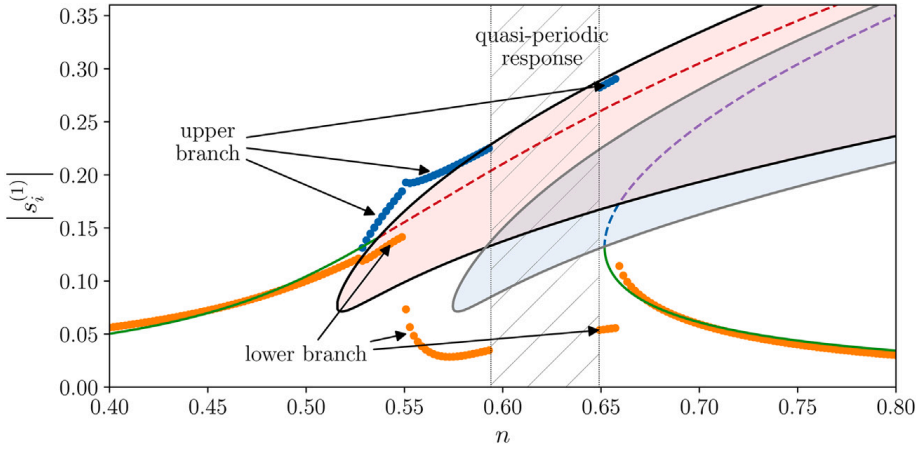

Fig. 7. Pendulums' order response exhibiting non-periodic localised solutions. The colour code of the analytical results is the same as that used in Fig. 3. Circles represent the numerical results. One of the pendulums is represented by blue circles, the other by orange ones. $\bar{b} = 0.063$, $\bar{T}_1 = 0.01$. (For interpretation of the references to colour in this figure legend, the reader is referred to the web version of this article.)

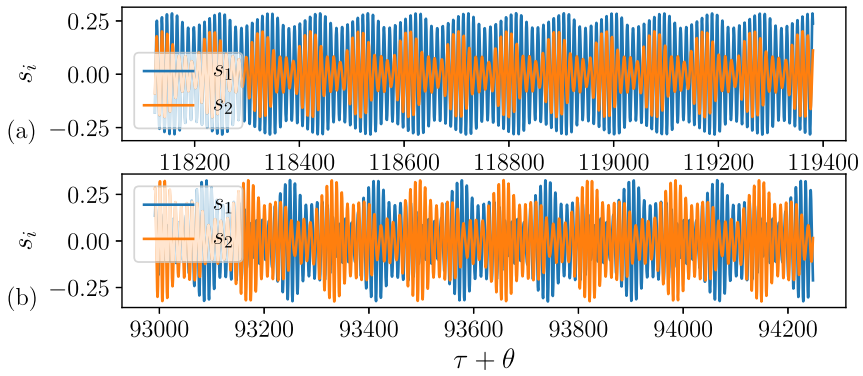

Fig. 8. Temporal signal (truncated) of the pendulums obtained through a numerical integration of the equations of motion. These signals correspond to the quasi-periodic portion of Fig. 7 at (a) $n = 0.621$ and (b) $n = 0.631$.

Other sets of system parameters can lead to solutions more complicated than the ones presented in Fig. 5. For instance, Fig. 7 shows the pendulums' response for a smaller damping than previous simulations, but unchanged other parameters. As in Fig. 5, the response divides into branches through a pitchfork bifurcation. In Fig. 7, those branches are broken into three parts. Localised responses might be subject to instabilities such as jumps of the response [6,7], which explains the discontinuity observed around $n = 0.55$. Between $n \approx 0.59$ and $n \approx 0.65$, no numerical results are shown because the corresponding time signals are not periodic. Two of those temporal signals are represented in Fig. 8. Fig. 8(a) shows a solution for which energy localisation is visible but the amplitude of the two pendulums is modulated. Such quasi-periodic solutions appear through Neimark-Sacker bifurcations [8].

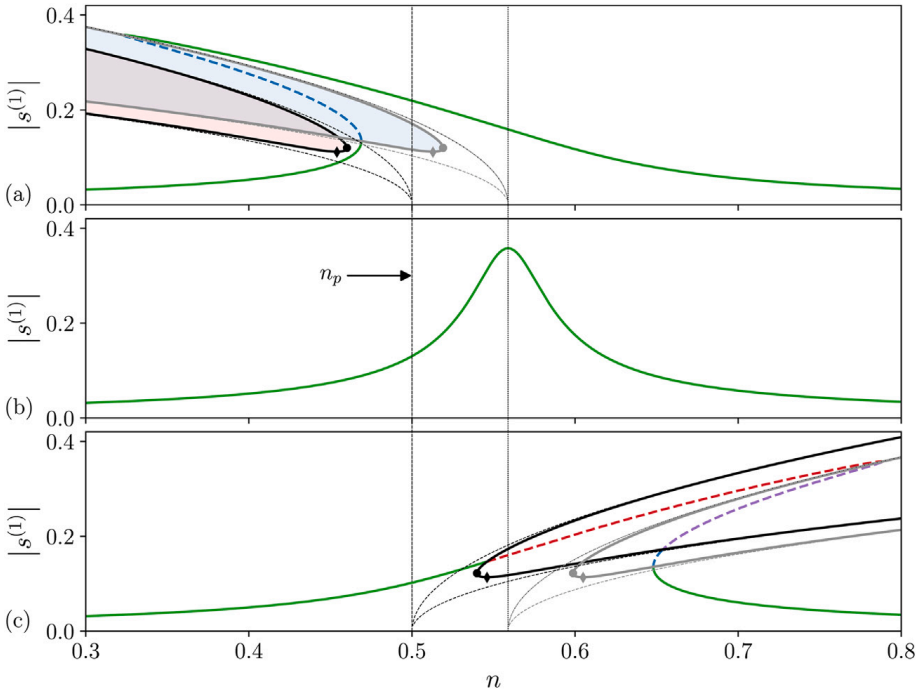

Fig. 9. Behaviour of the response according to the value of $x_{[4]}$. (a) softening, $x_{[4]} = 4.2$, (b) linear, $x_{[4]} = -0.0561$, (c) hardening, $x_{[4]} = -4.2$. The limits of the bifurcation zones in the undamped case are represented with dashed lines. $\tilde{T}_1 = 0.01$ and system parameters are given in Table 1. The colour code is the same as that used in Fig. 3. The black and grey dots indicate the points corresponding to $n_d^{(v)}$ and $n_j^{(v)}$, respectively. The black and grey diamonds indicate the points corresponding to $n_d^{(h)}$ and $n_j^{(h)}$, respectively.

The quasi-periodic solution represented in Fig. 8(b) seems to highlight energy exchanges between the two pendulums, causing the response to be localised successively on each pendulum.

7. Design rules

As discussed in the previous sections, the expected unison motion of pendulums can be broken in favour of more complex regimes. When it arises, desynchronisation leads to an undesired behaviour where one or more pendulums oscillate with an amplitude larger than if they were at unison. This might decrease the efficiency of the vibration absorption and it can lead to impact noise issues if the pendulums hit their cusp point. Additionally, impact non-linearities would greatly change the dynamics of the system. This section proposes several design rules allowing to avoid instabilities of the system.

As seen in Section 5.2, the hardening or softening behaviour of the pendulums is governed by the sign of c_p. Setting this coefficient to zero renders the pendulums' response linear (*cf.* Eqs. (22) and (23)) so that the limits of the instability zones tend towards infinity (*cf.* Eqs. (30) and (31)). Thus, the design rule

$$c_p = 0 \quad \Leftrightarrow \quad x_{[4]} = -2\eta\alpha_{[1]}\alpha_{[3]}n_p^2 \tag{36}$$

is proposed. Physically, this rule means that the non-linearities coming from the trajectory and rotation counterbalance to render the system almost linear. The only non-linearity remaining is that related to Coriolis effects in the rotor's Eq. (9) which generates $\theta^{(2)}$ [40]. Note that the special case $x_{[4]} = \alpha_{[3]} = 0$ is that studied in Section 3: it corresponds to an epicycloidal trajectory and a linear rotation function.

Relation (36) is represented by a black line in the maps of Figs. 4 and 10. The inner region delimited by this line corresponds to softening behaviours whilst the outer region corresponds to hardening ones. For large amplitudes of motion, the instability regions tend to embrace the black curve. This interesting remark will be discussed later in this section. Eq. (36) is also represented in Fig. 9, along with other values of $x_{[4]}$ yielding softening and hardening behaviours.

If Eq. (36) cannot be fulfilled, other recommendations can be proposed. These recommendations use the vertical and horizontal tangents of the bifurcation curves (30) and (31), whose corresponding orders are given by

$$n_j^{(v)} = n_2|_{a=0} \pm \frac{\bar{b}\sqrt{3}}{2\Lambda_m}, \quad n_j^{(h)} = n_2|_{a=0} \pm \frac{\bar{b}}{\Lambda_m}, \quad n_d^{(v)} = n_p \pm \frac{\bar{b}\sqrt{3}}{2\Lambda_m}, \quad n_d^{(h)} = n_p \pm \frac{\bar{b}}{\Lambda_m}. \tag{37}$$

Subscripts j and d are related to the jumps and the desynchronisation of the response, respectively. Superscripts v and h indicate a vertical and horizontal tangent, respectively. + and − solutions correspond to hardening and softening behaviours, respectively. $n_2|_{a=0}$ is the backbone of the unison mode evaluated for zero pendulums' displacement (*cf.* Eq. (22)). Points corresponding to Eq. (37)

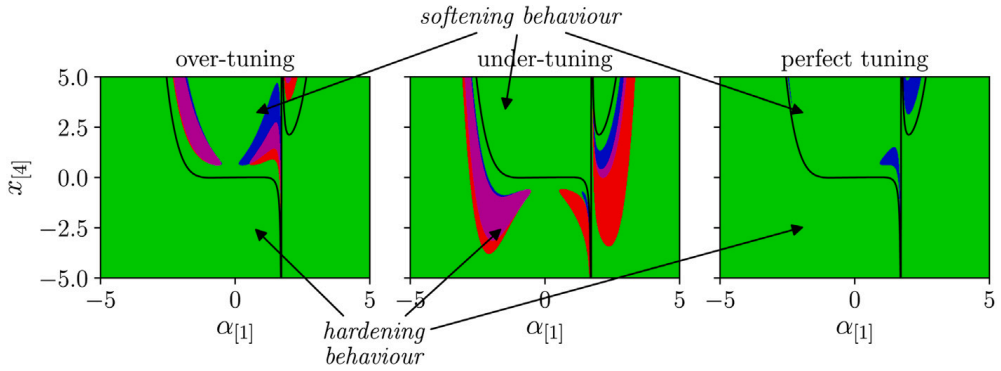

Fig. 10. Representation of the stability in the design space $(\alpha_{[1]}, x_{[4]})$ for three different tuning levels: $n = 0.4$ (over-tuning), $n = 0.6$ (under-tuning) and $n = 0.5$ (perfect tuning). The other system parameters are given in Table 1. The colour code is the same as that used in Fig. 3. The black curve represents designs rendering a linear behaviour. Each map is represented for $|s^{(1)}| = 0.3$ and $R_{O_1}/R_0 = 0.422$.

are represented with black and grey dots and diamonds in Fig. 9. Vertical tangents indicate the minimum level of mistuning for the response to become unstable whilst horizontal tangents indicate the minimum amplitude for which the response enters into an instability zone. Note that the torque level corresponding to these tangents can be obtained using Eqs. (37), (30), (31), and (23). Looking at the vertical tangents, one can see that in the hardening case, $n_p < n_d^{(v)} < n_j^{(v)}$, whilst in the softening case, $n_d^{(v)} < n_p < n_j^{(v)}$ or $n_d^{(v)} < n_j^{(v)} < n_p$. This means that hardening pendulums do not exhibit instabilities as long as $n \leq n_p$ (i.e. they are perfectly tuned or over-tuned). Similarly, softening pendulums do not exhibit unison instabilities as long as $n \geq n_p$ (i.e. they are perfectly tuned or under-tuned). These softening pendulums are however very likely to be subject to jumps even if they are perfectly tuned or under-tuned. This happens if $n_j^{(v)} > n_p$, which is the case in general as damping is small. These remarks are illustrated in Fig. 9 where one can see that the limit of the non-unison zones (black curves) do not cross the vertical line $n = n_p$, whilst the limit of the unstable periodic response (grey curves) crosses it in the softening case. These results are consistent with those obtained considering purely translated undamped pendulums [7]. Moreover, one can see from Eq. (37) that $n_d^{(v)}$ and $n_d^{(h)}$ tend to n_p as damping is reduced. In other words, the small-damping configuration is the most critical one as a very small level of mistuning can lead to a loss of unison. Similarly, $n_j^{(v)}$ and $n_j^{(h)}$ tend to $n_2|_{a=0}$ as damping is reduced. This is visible in Fig. 9, where the limit of the instability zones corresponding to the undamped case are represented with dashed lines.

As remarked previously, the maps presented in Fig. 4 show that the instability regions tend to embrace the black line corresponding to Eq. (36) without crossing it. The situation depicted in those maps corresponds to $n_p < n$, with n sufficiently large so that only hardening pendulums exhibit instabilities, which explains why the instability regions are contained in the outer zone delimited by the black line. Moreover, the instability regions tend towards the black line because, for large amplitudes of motion, the response can be unstable only if the critical amplitudes described by Eqs. (30) and (31) are large. These critical amplitudes get higher as the non-linearity reduces, thus explaining why the instability regions approach the black line at large amplitudes of motion. Indeed, one can see that as $c_p \to 0$, the critical amplitudes a_{pf} and a_{sn} (*cf.* Eqs. (30) and (31)) tend to infinity.

Three different tuning levels (over-tuning, under-tuning and perfect tuning of the pendulums) are represented in the design space in Fig. 10 to illustrate the former developments. For over-tuned pendulums, the instability regions are contained in the inner zone delimited by the black curve. For largely under-tuned pendulums, these instability zones are limited to the outer region delimited by the black curve. Finally, for a perfect tuning, only softening pendulums can be subject to jumps.

8. Experimental validation

An experimental study on the CPVA displayed in Fig. 11 was led to assess the accuracy of the analytical and numerical results. This CPVA is that presented in Fig. 2. It is composed of two identical monofilar pendulums designed especially to exhibit energy localisation. The expanded shape of the pendulums aims at increasing their inertia, thus increasing the impact of rotation. The experimental setup is shown in Fig. 12. The rotor is fixed on a bench of inertia J_b using an adaptation system of inertia J_a. Thus, J_r has to be replaced by the equivalent inertia $J_{eq} = J_r + J_b + J_a$ in the previous developments. The pendulums' amplitude of motion was obtained experimentally as follows:

1. Markers are placed at the pendulums' mass centres.
2. The CPVA is centrifugated and an oscillating torque is applied through the actuator while a fast camera records a movie of the rotating system.
3. The movie recorded is decomposed into frames and each frame is rotated by the opposite of the rotor's angular position. As a consequence, those rotated frames form a movie in which the rotor's position is fixed.
4. A point-tracking algorithm is used to find the position of the pendulums' mass centres. Repeating this operation for each rotated frame yields two time signals corresponding to the two pendulums' positions.
5. The time signals are decomposed into Fourier series to extract the pendulums' amplitudes.

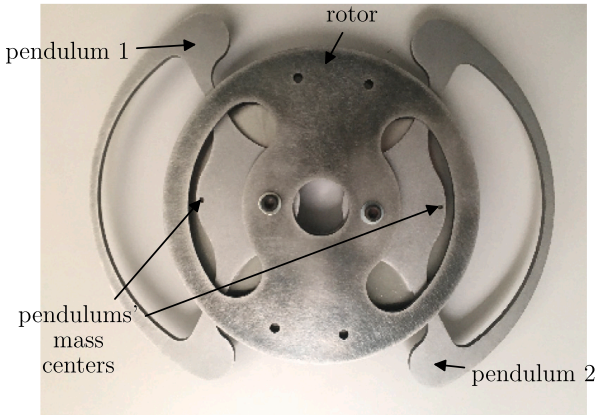

Fig. 11. CPVA used for the experiments.

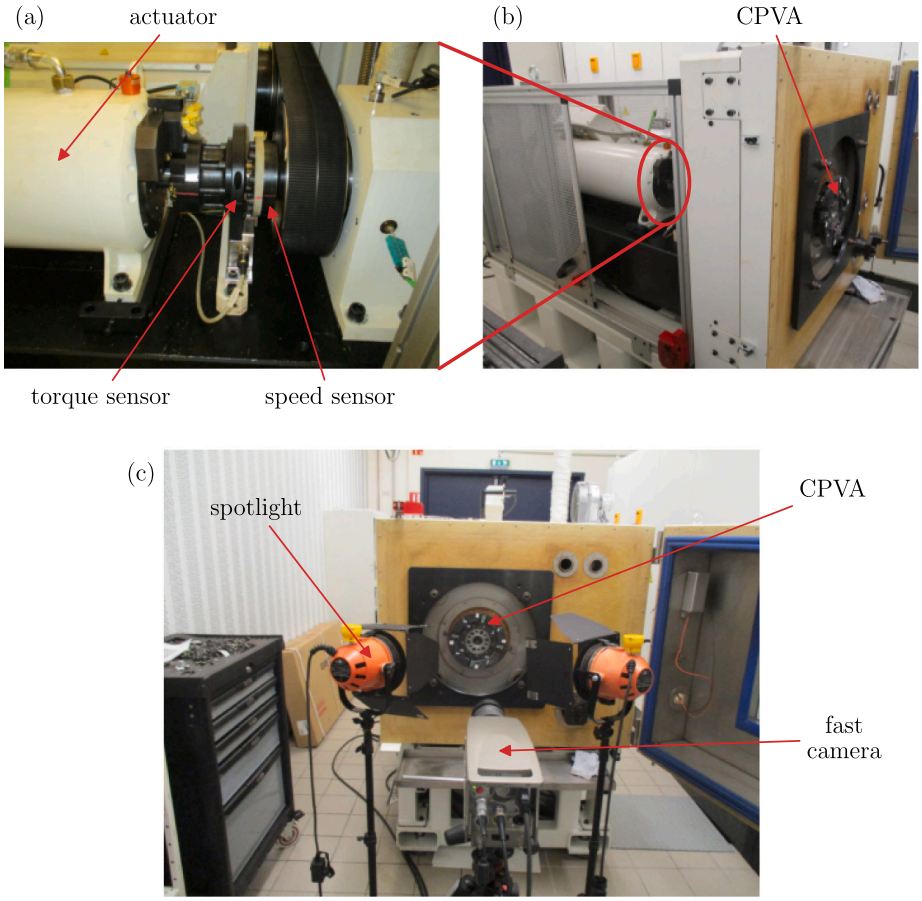

Fig. 12. Experimental setup. (a) zoom on a side view, (b) global view, (c) front view. Note that the CPVA shown in this figure is not the one used for the experiments.

Table 2
Parameters of the CPVA studied experimentally.

N	n_p	η	$x_{[4]}$	$\alpha_{[1]}$	$\alpha_{[3]}$	μ	$\bar{b}$	$\bar{b}_r$
2	0.5	0.88	−4.2	1.33	−0.02	0.167	0.043	0.002

This procedure was repeated for four torque amplitudes, $T_1 = \{3, 6, 10, 12\}$ [Nm], and for $n = 0.568$ and $\Omega = 1500$ [rpm]. The damping coefficients of the CPVA are found experimentally. The parameters of the system are given in Table 2.

A comparison of the experimental results with the analytical and numerical models is shown in Fig. 13. For $T_1 = \{3, 6\}$ [Nm], the pendulums' amplitudes obtained experimentally are significantly different. This indicates energy localisation, in accordance with the analytical and numerical solutions. The accuracy of the localised branches obtained numerically is not extremely good as the

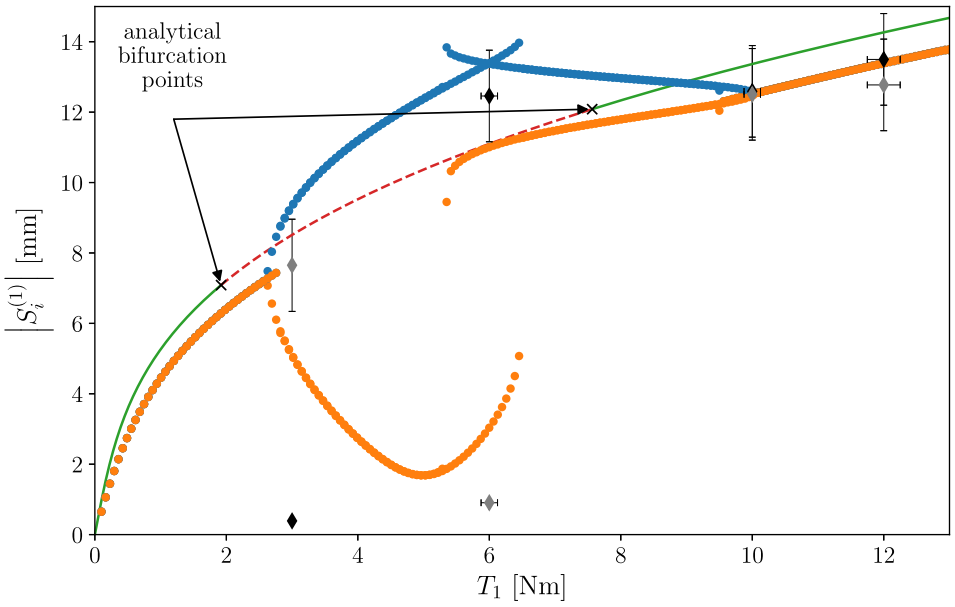

Fig. 13. Comparison of the analytical, numerical and experimental results. Blue and orange circles represent the numerical results (obtained with increasing and decreasing torque sweeps). Diamonds represent the experimental results. One of the pendulums is represented by black diamonds, the other by grey ones. The curve represents the analytical results (stable in green, unstable unison in red). Black crosses indicate the bifurcation points obtained analytically. $n = 0.568$, $\Omega = 1500$ [rpm].

diamonds do not superimpose on the circles. Regarding the upper branch, the difference between the experimental and numerical points almost falls within the measurement errors. However, the difference between numerical and experimental points on the lower branch is rather large. This is mainly due to the fact that, for very small amplitudes, the records of the pendulums' time signals had a low signal to noise ratio, so that the decomposition into Fourier series was inaccurate. This is the reason why no uncertainties along $\left|S_i^{(1)}\right|$ are shown for the two lower points. The discontinuities on the localised branches observed around $T_1 = 5.3$ [Nm] and $T_1 = 6.5$ [Nm] is due to a jump of the response, as observed previously in Fig. 7. The measurement points at $T_1 = \{10, 12\}$ [Nm] agree well with the numerical results. The slight difference of amplitude on the last measurement point is not attributed to a non-linear phenomenon but to measurement errors coming from different sources. The main sources of errors of the experimental results are listed below:

- The torque and speed regulation of the bench do not allow for an exact control of T_1 and Ω. Thus, their values are always slightly different from the prescribed ones.
- Because of manufacturing tolerances and material defects, the geometry of the system cannot perfectly match the prescribed one. Thus, the effective parameters of the system are not exactly those given in Table 2 and the two pendulums are not rigorously identical.
- The point-tracking algorithm requires bright images to accurately find the pendulums' mass centres. Despite the use of spotlights, the images obtained were rather dark.
- The markers used by the point-tracking algorithm are stickers placed by hand as closely as possible to the pendulums' mass centres shown in Fig. 11. The point-tracking algorithm looks for the centre of the markers, which are unlikely to perfectly overlap the mass centres.
- The expected motion is a rolling without slipping of the pendulum profile on the roller. However, because of the almost-flat shape of the middle of the pendulums' profile (see Fig. 2), the odds of slipping when the S_i pass through zero are not insignificant.
- The steady-state regime can take some time to be reached, especially when one expects non-linear behaviours such as localisation. It is possible that some movies were recorded before the steady-state is completely established.

The analytical model, though giving very good qualitative results (localisation is found where expected), slightly overestimates the amplitude at unison and predicts both bifurcation points too early. This highlights limits of the model, which were discussed in Sections 5.4 and 6.3 .

9. Conclusion

The study presented in this paper deals with the stability of centrifugal pendulum vibration absorbers (CPVA) allowing a rotational mobility. Stabilities of two different natures are considered. The instability of the unison response leads to a response localised on one of the pendulums. The instability of the periodic solution leads to a jump of the response. An analytical model

allowing for the prediction of these instabilities was build using a scaling of the parameters, the method of multiple scales and a reduction to a single mode. This model was validated with both numerical and experimental results. An original visualisation of the stability in the design space was presented. This allowed a simultaneous stability assessment of pendulum designs. Moreover, a design rule rendering the pendulums' behaviour linear was proposed. In case this rule cannot be applied, other recommendations were advised. These dealt with the largest mistuning levels leaving the response free of instabilities. Results were interpreted dividing the pendulums in two categories: those exhibiting hardening behaviours and those exhibiting softening ones. Hardening pendulums are stable if they are perfectly or over-tuned. Regarding softening pendulums, the stability of the unison response is preserved as long as they are perfectly or under-tuned. However, jumps can occur whether they are over or under-tuned. Finally, increasing the damping enlarges the range of mistuning for which instabilities are avoided.

CRediT authorship contribution statement

V. Mahe: Formal analysis, Investigation, Validation, Writing – original draft, Investigation, Methodology, Conceptualization, Software. **A. Renault:** Supervision, Conceptualization, Resources, Writing – review & editing. **A. Grolet:** Supervision, Validation, Visualization, Writing – review & editing. **O. Thomas:** Supervision, Validation, Visualization, Writing – review & editing. **H. Mahe:** Supervision, Resources, Funding acquisition.

Declaration of competing interest

The authors declare that they have no known competing financial interests or personal relationships that could have appeared to influence the work reported in this paper.

References

[1] D.E. Newland, Nonlinear problems of centrifugal pendulum vibration absorbers, in: Mechanisms and Machines, Vol. 1, Varna (Bulgaria), 1965.
[2] H.H. Denman, Tautochronic bifilar pendulum torsion absorbers for reciprocating engines, J. Sound Vib. 159 (2) (1992) 251–277, http://dx.doi.org/10.1016/0022-460X(92)90035-V.
[3] C.-P. Chao, S. Shaw, C.-T. Lee, Stability of the unison response for a rotating system with multiple tautochronic pendulum vibration absorbers, J. Appl. Mech. 64 (1) (1997) 149–156, http://dx.doi.org/10.1115/1.2787266.
[4] A.S. Alsuwaiyan, S.W. Shaw, Performance and dynamic stability of general-path centrifugal pendulum vibration absorbers, J. Sound Vib. 252 (5) (2002) 791–815, http://dx.doi.org/10.1006/jsvi.2000.3534.
[5] S.W. Shaw, B. Geist, Tuning for performance and stability in systems of nearly tautochronic torsional vibration absorbers, J. Vib. Acoust. 132 (4) (2010) http://dx.doi.org/10.1115/1.4000840.
[6] A.S. Alsuwaiyan, S.W. Shaw, Non-synchronous and localized responses of systems of identical centrifugal pendulum vibration absorbers, Arab. J. Sci. Eng. 39 (12) (2014) 9205–9217, http://dx.doi.org/10.1007/s13369-014-1464-1.
[7] J.S. Issa, S.W. Shaw, Synchronous and non-synchronous responses of systems with multiple identical nonlinear vibration absorbers, J. Sound Vib. 348 (2015) 105–125, http://dx.doi.org/10.1016/j.jsv.2015.03.021.
[8] A. Grolet, A. Renault, O. Thomas, Energy localisation in periodic structures: application to centrifugal pendulum vibration absorber, in: International Symposium on Transport Phenomena and Dynamics of Rotating Machinery, Maui (Hawaii), 2017.
[9] K. Nishimura, T. Ikeda, Y. Harata, Localization phenomena in torsional rotating shaft systems with multiple centrifugal pendulum vibration absorbers, Nonlinear Dynam. 83 (3) (2016) 1705–1726, http://dx.doi.org/10.1007/s11071-015-2441-2.
[10] A. Renault, Calcul et optimisation d'absorbeurs pendulaires dans une chaîne de traction automobile [Simulation and optimisation of pendular absorbers for automotive powertrain], (Ph.D. thesis), ENSAM, Lille, 2018.
[11] H. Mahé, A. Renault, O. Thomas, Dispositif d'amortissement Pendulaire [Pendular Damping Device], 2018, FR 3 055 037.
[12] H. Mahé, A. Renault, O. Thomas, Dispositif d'amortissement pendulaire [pendular damping device], 2018, FR 3 055 038.
[13] M.A. Acar, Design and tuning of centrifugal pendulum vibration absorbers, (Ph.D. thesis), Michigan State University, Michigan, 2017.
[14] J. Mayet, H. Ulbrich, Tautochronic centrifugal pendulum vibration absorbers: General design and analysis, J. Sound Vib. 333 (3) (2014) 711–729, http://dx.doi.org/10.1016/j.jsv.2013.09.042.
[15] M. Cirelli, J. Gregori, P. Valentini, E. Pennestrí, A design chart approach for the tuning of parallel and trapezoidal bifilar centrifugal pendulum, Mech. Mach. Theory 140 (2019) 711–729, http://dx.doi.org/10.1016/j.mechmachtheory.2019.06.030.
[16] M. Cirelli, M. Cera, E. Pennestrì, P.P. Valentini, Nonlinear design analysis of centrifugal pendulum vibration absorbers: An intrinsic geometry-based framework, Nonlinear Dynam. 102 (3) (2020) 1297–1318, http://dx.doi.org/10.1007/s11071-020-06035-1.
[17] M. Cera, M. Cirelli, E. Pennestrì, P. Valentini, The kinematics of curved profiles mating with a caged idle roller - higher-path curvature analysis, Mech. Mach. Theory 164 (2021) 104414, http://dx.doi.org/10.1016/j.mechmachtheory.2021.104414.
[18] M. Cera, M. Cirelli, E. Pennestrì, P.P. Valentini, Design analysis of torsichrone centrifugal pendulum vibration absorbers, Nonlinear Dynam. 104 (2) (2021) 1023–1041, http://dx.doi.org/10.1007/s11071-021-06345-y.
[19] M. Cera, M. Cirelli, E. Pennestrì, P.P. Valentini, Nonlinear dynamics of torsichrone CPVA with synchroringed form closure constraint, Nonlinear Dynam. (2021) http://dx.doi.org/10.1007/s11071-021-06732-5.
[20] M. Cirelli, E. Capuano, P.P. Valentini, E. Pennestrì, The tuning conditions for circular, cycloidal and epicycloidal centrifugal pendula: A unified cartesian approach, Mech. Mach. Theory 150 (2020) 103859, http://dx.doi.org/10.1016/j.mechmachtheory.2020.103859.
[21] J. Mayet, H. Ulbrich, First-order optimal linear and nonlinear detuning of centrifugal pendulum vibration absorbers, J. Sound Vib. 335 (2015) 34–54, http://dx.doi.org/10.1016/j.jsv.2014.09.017.
[22] X. Tan, S. Yang, J. Yang, J. Li, Study of dynamics of rotational centrifugal pendulum vibration absorbers based on tautochronic design, Meccanica (2021) http://dx.doi.org/10.1007/s11012-021-01340-4.
[23] E.R. Gomez, I.L. Arteaga, L. Kari, Normal-force dependant friction in centrifugal pendulum vibration absorbers: simulation and experimental investigations, J. Sound Vib. 492 (2021) 115815, http://dx.doi.org/10.1016/j.jsv.2020.115815.
[24] V. Manchi, C. Sujatha, Torsional vibration reduction of rotating shafts for multiple orders using centrifugal double pendulum vibration absorber, Appl. Acoust. 174 (2021) 107768, http://dx.doi.org/10.1016/j.apacoust.2020.107768.
[25] K. Kadoi, T. Inoue, J. Kawano, M. Kondo, Nonlinear analysis of a torsional vibration of a multidegrees-of-freedom system with centrifugal pendulum vibration absorbers and its suppression, J. Vib. Acoust. 140 (6) (2018) 061008, http://dx.doi.org/10.1115/1.4040042.

[26] B. Geist, V. Ramakrishnan, P. Attibele, W. Resh, Precision requirements for the bifilar hinge slots of a centrifugal pendulum vibration absorber, Precis. Eng. 52 (2018) 1–14, http://dx.doi.org/10.1016/j.precisioneng.2017.08.001.
[27] T.M. Nester, P.M. Schmitz, A.G. Haddow, S.W. Shaw, Experimental observations of centrifugal pendulum vibration absorbers, in: International Symposium on Transport Phenomena and Dynamics of Rotating Machinery, Honolulu (Hawaii), 2004.
[28] S.W. Shaw, P.M. Schmitz, A.G. Haddow, Tautochronic vibration absorbers for rotating systems, J. Comput. Nonlinear Dyn. 1 (4) (2006) 283–293, http://dx.doi.org/10.1115/1.2338652.
[29] C.-P. Chao, S.W. Shaw, The dynamic response of multiple pairs of subharmonic torsional vibration absorbers, J. Sound Vib. 231 (2) (2000) 411–431, http://dx.doi.org/10.1006/jsvi.1999.2722.
[30] L. Shen, B.W. Suter, Bounds for eigenvalues of arrowhead matrices and their applications to hub matrices and wireless communications, EURASIP J. Adv. Signal Process. 2009 (1) (2009) 379402, http://dx.doi.org/10.1155/2009/379402.
[31] C.-P. Chao, S.W. Shaw, The effects of imperfections on the performance of the subharmonic vibration absorber system, J. Sound Vib. 215 (5) (1998) 1065–1099, http://dx.doi.org/10.1006/jsvi.1998.1634.
[32] O. Thomas, C. Touzé, A. Chaigne, Asymmetric non-linear forced vibrations of free-edge circular plates. part II: Experiments, J. Sound Vib. 265 (5) (2003) 1075–1101, http://dx.doi.org/10.1016/S0022-460X(02)01564-X.
[33] A. Givois, J.-J. Tan, C. Touzé, O. Thomas, Backbone curves of coupled cubic oscillators in one-to-one internal resonance: Bifurcation scenario, measurements and parameter identification, Meccanica 55 (3) (2020) 481–503, http://dx.doi.org/10.1007/s11012-020-01132-2.
[34] A. Grolet, Z. Shami, S. Arabi, O. Thomas, Experimental nonlinear localisation in a system of two coupled beams, in: Dynamical System Theory and Applications, Lodz (Poland), 2019, p. 13.
[35] A.H. Nayfeh, Perturbation Methods, in: Wiley Classics Library, Wiley-VCH, Weinheim, 1973, http://dx.doi.org/10.1002/9783527617609.
[36] M. Golubitsky, I. Stewart, D.G. Schaeffer, in: J.E. Marsden, L. Sirovich (Eds.), Singularities and Groups in Bifurcation Theory, in: Applied Mathematical Sciences, Vol. 2, Springer New York, New York, NY, 1988, http://dx.doi.org/10.1007/978-1-4612-4574-2.
[37] A.H. Nayfeh, D.T. Mook, Nonlinear Oscillations, in: Wiley Classics Library, Wiley-VCH, 1995, http://dx.doi.org/10.1002/9783527617586.
[38] L. Guillot, A. Lazarus, O. Thomas, C. Vergez, B. Cochelin, A purely frequency based Floquet-Hill formulation for the efficient stability computation of periodic solutions of ordinary differential systems, J. Comput. Phys. 416 (2020) 109477, http://dx.doi.org/10.1016/j.jcp.2020.109477.
[39] A. Renault, O. Thomas, H. Mahé, Numerical antiresonance continuation of structural systems, Mech. Syst. Signal Process. 116 (2019) 963–984, http://dx.doi.org/10.1016/j.ymssp.2018.07.005.
[40] C.-T. Lee, S.W. Shaw, On the counteraction of periodic torques for rotating systems using centrifugally driven vibration absorbers, J. Sound Vib. 191 (5) (1996) 695–719, http://dx.doi.org/10.1006/jsvi.1996.0151.

Chapter 4

An accurate nonlinear model for the stability and performance of the unison response of centrifugal pendulums

This chapter is made of a paper published in the *Journal of Sound and Vibrations* [67]. It focuses on the unison response of a centrifugal pendulum vibration absorber (CPVA) through the analytical study of its stability and the optimisation of its performance. The aim is to provide a better understanding of the nonlinear response of a CPVA in order to be able to control it more easily. Note that the title of the chapter makes reference to an "accurate" model because the developments are based on the simplified model described in section 2.3.2, which is more advanced than the simplified model from section 2.3.1, used in chapter 3.

Sections 1 to 3.1 repeat information from chapters 1 and 2. They present the context of the study, the modelling of a CPVA (*cf.* section 2.1.1), a linear analysis (*cf.* section 2.2) and the simplification of the equations of motion (*cf.* section 2.3). The reader might want to skip these sections of the article if he already read chapters 1 and 2.

The novelty of the article starts in sections 3.2 and 3.3, where the nonlinear unison response and its stability are computed analytically using the method of multiple scales (*cf.* section 2.5.2.1). It is shown that these results are more general than the ones obtained in chapter 3, especially at high orders, because the model used is more accurate (*cf.* section 2.3). The results are applied to case studies in section 4 and compared to numerical resolutions of the system's dynamics. Design guidelines allowing to limit the nonlinear detuning of the rotor's antiresonance (hence maximising the performance) while avoiding instabilities are provided.

Journal of Sound and Vibration 536 (2022) 117157

Contents lists available at ScienceDirect

Journal of Sound and Vibration

journal homepage: www.elsevier.com/locate/jsvi

On the dynamic stability and efficiency of centrifugal pendulum vibration absorbers with rotating pendulums

V. Mahé [a,b,*], A. Renault [b], A. Grolet [a], H. Mahé [b], O. Thomas [a]

[a] Arts et Metiers Institute of Technology, LISPEN, HESAM Université, F-59000 Lille, France
[b] Valeo Transmissions, Centre d'Étude des Produits Nouveaux, Espace Industriel Nord, Route de Poulainville, 80009 Amiens Cedex 1, France

ARTICLE INFO

Keywords:
Centrifugal pendulum vibration absorber
Nonlinear dynamics
Energy localisation
Antiresonance locking

ABSTRACT

The automotive industry uses centrifugal pendulum vibration absorbers (CPVAs) to reduce vibrations of the transmission system. These passive devices are made of several masses oscillating along a given path relative to a rotor. This work addresses a recent design of CPVA, in which the pendulums are allowed to rotate relatively to the rotor. The dynamic stability of this CPVA and the shifting of its operating point are investigated in this paper. These two aspects, crucial for an optimal vibration reduction, are assessed using an analytic dynamical model based on a perturbation method. The results obtained allow to propose new design guidelines. The validity of the model is confirmed through a comparison with a numerical resolution of the system's dynamics.

1. Introduction

In the frame of reducing polluting emissions and fuel consumption of vehicles using thermal engines, automotive manufacturers try to reduce the cylinder capacity and engine speed of rotation. These evolutions lead to a significant increase of rotation irregularities called acyclisms, mainly due to higher combustion pressure. One of the main characteristics of these reciprocating engines is the linear dependence of the acyclism frequency to the engine speed of rotation. The coefficient of proportionality is the engine order and only depends on the architecture of the engine. During an acceleration phase, the engine sweeps a wide frequency range containing some driveline torsional modes. This situation may lead to significant noise and vibration levels into the passenger compartment and premature wear of the driveline components. Centrifugal pendulum vibration absorbers (CPVAs) have been used for many years to minimise acyclisms of automotive powertrains at the engine order [1–3]. These passive devices consist of oscillating masses (pendulums) moving along particular paths relative to a primary inertia (rotor) as shown in Fig. 1. Because the pendulums are driven by the centrifugal acceleration field resulting from the rotation of the CPVA, their natural frequency is proportional to the engine speed of rotation. Hence, the CPVA acts like a classical dynamic vibration absorber [4] except that the antiresonance generated on the rotor is located at a fixed[1] order, so that the antiresonance frequency is changing linearly with the engine speed. This allows for a reduction of the vibrations over the whole engine speed range.

CPVAs exhibit nonlinearities of different natures: geometric nonlinearities due to the large amplitude of motion of the pendulums, and inertial nonlinearities, for instance due to Coriolis effects. The pendulums' path plays a key role in the nonlinear response of a CPVA. D. E. Newland showed that circular paths give the CPVA a softening behaviour, which can lead to jumps of the system's

* Corresponding author at: Arts et Metiers Institute of Technology, LISPEN, HESAM Université, F-59000 Lille, France.
E-mail addresses: vincent.mahe@ensam.eu (V. Mahé), alexandre.renault@valeo.com (A. Renault), aurelien.grolet@ensam.eu (A. Grolet), herve.mahe@valeo.com (H. Mahé), olivier.thomas@ensam.eu (O. Thomas).

[1] It is fixed in the linear regime, but it is slightly changing at large pendulum amplitudes due to nonlinear effects. This is explained later in this section.

https://doi.org/10.1016/j.jsv.2022.117157
Received 25 March 2022; Received in revised form 11 June 2022; Accepted 28 June 2022
Available online 30 June 2022
0022-460X/

response [5]. To avoid this jump issue, J. F. Madden recommended the use of a cycloidal path, which confers the CPVA a hardening behaviour [6]. Since the works of H. H. Denman [7], the preferred paths are epicycloids because they are the tautochronic paths of the uncoupled pendulums. The pendulums are uncoupled from the rotor when there are no acyclisms so that the rotor spins at a constant velocity and is not a degree of freedom. However, in the presence of acyclisms, the coupling between the rotor and the pendulums introduces inertial nonlinearities that play an important role in the softening/hardening behaviour of the CPVA, so that jumps of the response can still occur with an epicycloidal path [8].

Moreover, CPVAs are cyclically symmetric structures subject to nonlinear energy localisation phenomena [9,10]. This other kind of instability leads to pendulums oscillating with different phases and/or amplitudes, and it is undesired for two reasons. First, it can decrease the efficiency of the vibration reduction. Secondly, the pendulums' amplitude is limited by the cusp of their path, so that amplitude localisation can reduce the maximum torque amplitude the CPVA can filter-out. The first studies on the localisation of the pendulums' response, led by C.-P. Chao et al. [11,12], dealt with epicycloidal paths. Then, A. S. Alsuwaiyan et al. considered the case of more general paths [13]. This study on general paths was extended by S. Shaw et al., who were able to develop an accurate analytical model by taking into account the main nonlinearities coming from both the trajectory and the inertial effects [8]. B. J. Vidmar et al. investigated localisation in a CPVA made of pendulums tuned at different orders [14]. It was shown in [15–17] that the localised solutions are subjects to saddle-node bifurcations, causing jumps and Hopf bifurcations, leading to quasi-periodic solutions. K. Nishimura et al. showed that the localised response can also bifurcate towards chaotic solutions [18].

In addition to the jumps and the localisation of the response, CPVAs are subject to period-doubling bifurcations leading to a subharmonic solution [19–22]. However, those occur for excitation orders close to twice the CPVA tuning order, so they are not of interest here as this paper focuses on the response near the tuning order.

All the contributions cited above consider purely translated pendulums, probably because early works recommended to use such systems [23]. To the authors' knowledge, it is R. Chilton who first investigated the effect of pendulum rotation on the tuning order through his study of a pendulum mass rolling without slipping on a convex surface [24]. Then, R. W. Zdanowich and T. S. Wilson [25] derived the expression of the tuning order of roller-type and ring-type rotating pendulums (note that the ring-type pendulum is a special case of the monofilar pendulum investigated in [26]). A similar analysis on a pendulum linked to the rotor through a pivot was led by R. G. Mitchiner and R. G. Leonard [27]. However, it was less than ten years ago that J. Mayet and H. Ulbrich provided the first results showing that the rotational motion can significantly improve the performance of a CPVA [28–30]. In-depth studies of the rotation law of the pendulums were also led by A. Renault [31–33] and M. A. Acar [34]. Recent works by M. Cirelli, M. Cera et al. [35–39] confirmed the interest for pendulums with a rotational mobility and introduced a new way of representing the path, using curvature ratios instead of the polynomial functions used in most studies (see [13] for instance). They called "trapezoidal CPVA" systems with rotating pendulums, in opposition to "parallel CPVA", for which the pendulums' motion is a pure relative translation with respect to the rotor. X. Tan et al. considered a CPVA made of a single pendulum obeying a nonlinear rotation law and gave guidelines for the choice of this law [40]. E. R. Gomez et al. investigated theoretically and experimentally the friction losses in a CPVA with rotating pendulums [41]. In addition, they studied numerically and experimentally the behaviour of such a CPVA installed in a detailed powertrain [42]. The filtering of torsional vibrations in multi-degree-of-freedom systems using a CPVA was also investigated by K. Kadoi et al., who dealt with purely translated pendulums [43]. C. Shi et al. showed that CPVAs could be used to reduce translational vibrations and tilting in addition to torsional vibrations [44–48]. V. Mahe et al. considered the effect of rotation on a subharmonic CPVA [49,50] and on a regular CPVA [26]. Some design guidelines were given to choose the path and rotation law in order to avoid instabilities. The authors also studied the filtering effect of the pendulums responding on a localised solution and the stability of that solution [51]. Recently, J. Mayet et al. used a general framework to show how pendulums' relative rotation can increase the performance of a CPVA [52]. They assumed a unison motion of the pendulums and gave guidelines to maximise vibration reduction while avoiding jumps of the response. Other new topics of research dealing with CPVAs include precision requirement in the manufacturing process [53] and the use of double pendulums, which allows to simultaneously filter-out two orders [54].

The motivation of this paper is to investigate the dynamic stability and efficiency of a CPVA with rotating pendulums using analytical perturbation methods. The stability and performance of such systems was investigated in [29,52] without specifying a particular path nor rotation law, and in [36,38], where curvature ratios and a rolling radius were used to describe the path and rotation law. In the present paper, it is chosen to represent the path and rotation law using polynomial functions of the pendulums' positions, like in [26,31–34]. This representation gives a clear physical meaning to the coefficients of those polynomials, which are the parameters that control the linear and nonlinear tuning of the CPVA. In addition, this representation allows designers to easily adjust the tuning in practice as one simply has to change the value of the polynomial coefficients. The analytical model developed in this paper uses different assumptions than those of [26], which allows to capture the nonlinearities arising from inertial terms, hence making the model more accurate. The efficiency of a CPVA is closely related to the features of the antiresonance generated by the pendulums on the rotor. If the rotor's amplitude at the antiresonance is low and the antiresonance order does not shift much as the torque amplitude is increased, the CPVA will significantly reduce the vibrations over the whole torque range. D. E. Newland observed early on that the antiresonance order generated by bifilar pendulums following a circular path diminishes as the torque amplitude is increased [55]. This shifting of the operating point for circular path pendulums was also studied by M. Sharif-Bakhtiar et al. [56] and observed experimentally by A. G. Haddow [57]. Over-tuning the pendulums was recommended to minimise the decrease in performance due to the antiresonance shifting, but it is limited by the occurrence of jumps of the system's response [55,56]. A. Renault proposed a procedure to track the locus of the antiresonance and applied his method to Euler's pendulum [58]. He observed that the antiresonance does not necessarily shift in the same direction as the resonance of the system. This is of great importance for CPVAs and will be investigated in this paper.

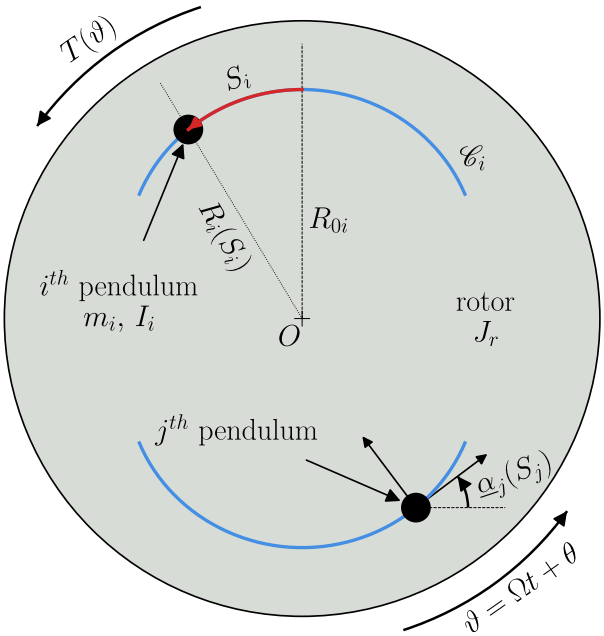

Fig. 1. Representation of the system studied. It is made of $N = 2$ pendulums.

This paper is organised as follows. Section 2 describes the modelling of the CPVA and presents a linear analysis. The response of a CPVA and its stability are derived in Section 3. Case studies and design guidelines allowing to reduce the shifting of the antiresonance and to avoid instabilities are presented in Section 4. This paper ends with a conclusion in Section 5.

2. Modelling and linear analysis

2.1. Modelling

The system studied is shown in Fig. 1. A rotor of inertia J_r rotates about its centre O. Its total angular position is $\vartheta(t) = \Omega t + \theta(t)$ where t is the time, Ω is the mean rotational velocity and $\theta(t)$ corresponds to the fluctuating part of the rotation. A torque $T(\vartheta) = T_0 + T_\theta(\vartheta)$ is applied to the rotor where T_0 is its constant part and $T_\theta(\vartheta)$ is periodic. At equilibrium, $T_0 = b_r\Omega$ where b_r is the linear viscous damping coefficient of the rotor, such that the constant torque balances with the damping to set the mean rotational speed Ω. N pendulums of mass m_i and inertia I_i (about their centre of mass) oscillate on their path $\mathscr{C}_i$. Their position on these paths is given by the curvilinear abscissa $S_i(t)$ and their distance from O is $R_i(S_i)$. The characteristic dimension $R_{0i} = R_i(S_i = 0)$ is the distance between O and the vertex of the path. In addition to the traditional translation motion, the present study considers that the pendulums rotate about their centre of mass according to the rotation function $\underline{\alpha}_i(S_i)$. As for the rotor, an equivalent linear viscous damping coefficient b_i is used to model the damping between the ith pendulum and the rotor. In the later, pendulums and their associated path and rotation functions will be considered identical so that subscript "i" will be dropped when addressing pendulums' parameters.

In order to write the equations of motion in a non-dimensional form, the following parameters and variables are introduced:

$$
\begin{gathered}
s_i = \frac{S_i}{R_0}, \quad y = \frac{\dot{\vartheta}}{\Omega} = 1 + \frac{\dot{\theta}}{\Omega}, \quad \eta = \frac{I}{mR_0^2}, \quad \mu = \frac{NmR_0^2}{J_r + NI}, \quad \bar{b} = \frac{b}{m\Omega}, \quad \bar{b}_r = \frac{b_r}{(J_r + NI)\Omega}, \\
\bar{T}(\vartheta) = \bar{T}_0 + \bar{T}_\theta(\vartheta) = \frac{T(\vartheta)}{(J_r + NI)\Omega^2}, \quad x(s_i) = \frac{R(R_0 s_i)^2}{R_0^2}, \quad z(s_i) = \sqrt{x(s_i) - \frac{1}{4}\left(\frac{dx(s_i)}{ds_i}\right)^2}, \\
\alpha(s_i) = \underline{\alpha}(R_0 s_i), \quad \gamma(s_i) = \frac{d\alpha(s_i)}{ds_i},
\end{gathered}
\tag{1}
$$

where $(\dot{\bullet}) = \partial(\bullet)/\partial t$. The s_i and y are the $N + 1$ degree-of-freedom of the system. They correspond to the dimensionless relative position of the pendulums and rotational velocity of the rotor, respectively. η and μ are inertia ratios, $\bar{b}$ and $\bar{b}_r$ are non-dimensional damping constants and $\bar{T}(\vartheta)$ is the non-dimensional torque applied on the rotor. $x(s_i)$ and $z(s_i)$ are path functions while $\alpha(s_i)$ and $\gamma(s_i)$ are rotation functions. In this paper, $x(s_i)$ and $\alpha(s_i)$ are written as polynomials in the curvilinear abscissa s_i such that

$$
x(s_i) = 1 - n_t^2 s_i^2 + \sum_{k=3}^{N_x} x_{[k]} s_i^k, \quad \alpha(s_i) = \sum_{k=0}^{N_\alpha} \alpha_{[k]} s_i^k,
\tag{2}
$$

where n_t is the order of the pendulums' path and $x_{[k]}$, $\alpha_{[k]}$ are path and rotation coefficients. In the special case $x_{[k]} = 0, \forall k$, the pendulums' path are epicycloids of order n_t, which are the tautochronic paths when the rotor spins at a constant speed [7]. Note that paths defined as in Eq. (2) have a cusp point [7]. For small $x_{[k]}, \forall k$, the cusp point can be approximated by the cusp of the epicycloid, given by

$$s_{\text{cusp}} = \frac{1}{n_t\sqrt{1+n_t^2}}. \tag{3}$$

In order to give $\bar{T}(\vartheta)$ the meaning of an external forcing term, we replace the independent variable t by the rotor's position ϑ [59], which can be seen as a non-dimensional time. Using the chain rule, one can show that

$$\dot{(\bullet)} = \Omega y(\bullet)', \quad \ddot{(\bullet)} = \Omega^2 yy'(\bullet)' + \Omega^2 y^2(\bullet)'', \tag{4}$$

where $(\bullet)' = \partial(\bullet)/\partial\vartheta$ (the details can be found in [49]). Hence, the non-dimensional rotor's acceleration is now $\ddot{\vartheta}/\Omega^2 = \dot{y}/\Omega = yy'$. Using the non-dimensional quantities (1) and the chain rule (4), one can write the equations of motion as

$$\frac{1}{N}\left[\sum_{i=1}^{N}(N+\mu x(s_i))yy' + \mu\left(z(s_i)+\eta\gamma(s_i)\right)(yy's_i' + y^2s_i'') + \mu y^2 s_i'\left(\frac{dx(s_i)}{ds_i} + \frac{dz(s_i)}{ds_i}s_i' + \eta\frac{d\gamma(s_i)}{ds_i}s_i'\right)\right] + \bar{b}_r y = \bar{T}(\vartheta), \tag{5a}$$

$$\left[z(s_i)+\eta\gamma(s_i)\right]y' + \left[1+\eta\gamma(s_i)^2\right](y's_i' + ys_i'') + \eta\gamma(s_i)\frac{d\gamma(s_i)}{ds_i}ys_i'^2 - \frac{1}{2}\frac{dx(s_i)}{ds_i}y + \bar{b}s_i' = 0, \qquad i = 1,\dots,N. \tag{5b}$$

Computation details can be found in [49]. Eq. (5a) governs the motion of the rotor while the N Eqs. (5b) govern the motion of the pendulums.

From now on, it is assumed that the fluctuating torque applied on the rotor contains only one harmonic whose non-dimensional form is $\bar{T}_1\cos(n\vartheta)$, where n is the excitation order. For a car engine, n corresponds to the number of strikes per revolution of the crankshaft.

2.2. Linear analysis

First of all, one can use Eq. (4) to show that, at first order, $1+\theta' \approx y$ and $\theta'' \approx yy' \approx y'$ (the demonstration can be found in [49]). Hence, it is possible to represent the motion of the rotor with position θ instead of velocity y. This way, all the degree-of-freedom of the system are positions, which facilitates the representation of the mode shapes. Using θ instead of y and the balance between the constant torque and the damping $\bar{b}_r = \bar{T}_0$ (*cf.* Section 2.1), one can linearise Eqs. (5a) and (5b). This leads to the free, conservative, linear equations

$$(1+\mu)\theta'' + \frac{\mu\Lambda_c}{N}\sum_{i=1}^{N}s_i'' = 0, \tag{6a}$$

$$\Lambda_c\theta'' + \Lambda_m s_i'' + n_t^2 s_i = 0, \quad i = 1,\dots,N. \tag{6b}$$

Λ_m and Λ_c are constants representing the equivalent mass of a pendulum due to the effect of the rotatory inertia and the linear coupling term between a pendulum and the rotor, respectively. They are given by

$$\Lambda_m = 1+\eta\alpha_{[1]}^2, \quad \Lambda_c = 1+\eta\alpha_{[1]}, \tag{7}$$

where $\alpha_{[1]}$ is the linear rotation coefficient (*cf.* Eq. (2)).

The linearised equations of motions (6) can be written as a matrix equation. Solving the associated eigenvalue problem requires to find the eigenvalues of an arrowhead matrix whose diagonal terms are all identical except for the first one. As explained in [60], the eigenvalues of such a matrix are those of a reduced 2×2 matrix together with the identical terms of the diagonal. Applying this procedure, one can find that the eigenorders and mode shapes of the system are

$$\begin{aligned}
&n_{00} = 0, \quad n_{10} = n_p, \quad n_{20} = n_p\sqrt{\frac{1+\mu}{1+\mu\left(1-\frac{\Lambda_c^2}{\Lambda_m}\right)}}\\
&\boldsymbol{\phi_{00}} = [1,0,\dots,0]^\intercal, \quad \boldsymbol{\phi_{20}} = \left[-\frac{\mu\Lambda_c}{1+\mu},1,\dots,1\right]^\intercal,\\
&\boldsymbol{\phi_{10}}_i[i+1] = -\boldsymbol{\phi_{10}}_i[i+2] = 1, \quad \boldsymbol{\phi_{10}}_i[j\neq\{i+1,i+2\}] = 0, \quad i = 1,\dots,N-1.
\end{aligned} \tag{8}$$

The eigenorders can be seen as non-dimensional eigenfrequencies and superscript $^\intercal$ indicates the transpose. n_p is the pendulums' tuning order, which is related to the path order n_t such that

$$n_p = \frac{n_t}{\sqrt{\Lambda_m}}, \tag{9}$$

and it corresponds to the eigenorder of the pendulums when they are uncoupled from the rotor. The value inside the brackets after $\boldsymbol{\phi_{10}}_i$ is used to refer to one of its components.

$(n_{00}, \boldsymbol{\phi_{00}})$ is a rigid body mode for which only the rotor is excited. $\left(n_{10}, \boldsymbol{\phi_{10_i}}\right)$ are $N-1$ degenerated modes for which two pendulums are moving in phase-opposition. Their eigenvalue n_{10} has multiplicity $N-1$ and the rotor is a node of these modes. For a CPVA made of only two pendulums, $(n_{10}, \boldsymbol{\phi_{10}})$ is not degenerated and simply represents a phase-opposition motion of the pendulums. $(n_{20}, \boldsymbol{\phi_{20}})$ is a mode for which the pendulums move in unison but in phase-opposition with respect to the rotor (provided that $\Lambda_c > 0$, which is the case for reasonable parameters). It will be referred-to as the "unison mode" or "mode 2". To filter-out a fluctuating torque, one typically chooses $n_p \approx n$ to generate an antiresonance on the rotor at $n_{AR} \approx n_p$ using the unison mode.

Note that in the case of a real automotive driveline (a simple model of which consists in successive rotors linked through torsional springs [61]), the CPVA should be placed as close as possible from the source of excitation (i.e. the engine). Doing so, the antiresonance generated by the pendulums exists on every driveline components located after the CPVA [62], which allows to isolate the whole driveline from the torque fluctuations.

3. Response and stability of the CPVA

3.1. Scaling and simplification of the equations

The first step to derive approximate analytical solutions of Eqs. (5a) and (5b) is to simplify those equations. The full procedure is detailed in [49], so only the main steps are reminded here. The path and rotation functions followed by the pendulums, whose general form are given by Eq. (2), are chosen to be

$$x(s_i) = 1 - n_t^2 s_i^2 + x_{[4]} s_i^4, \quad \alpha(s_i) = \alpha_{[1]} s_i + \alpha_{[3]} s_i^3, \tag{10}$$

and the rotor's rotational velocity is expanded such that

$$y(\vartheta) = 1 + y_\theta(\vartheta). \tag{11}$$

Following S. Shaw et al. [8], we assume small damping, small fluctuations of the rotor's rotational velocity, small external torque amplitudes, small ratio of the pendulums' geometric inertia over the CPVA's inertia and a path close to an epicycloid. In addition, we assume a rotational law close from a linear one. Hence, we can scale the parameters such that

$$\bar{b} = \epsilon\tilde{b}, \quad \bar{b}_r = \epsilon\tilde{b}_r, \quad \bar{T}_1 = \epsilon\tilde{T}_1, \quad \mu = \epsilon\tilde{\mu}, \quad y_\theta = \epsilon\tilde{y}_\theta, \quad \theta' = \epsilon\tilde{\theta}', \quad x_{[4]} = \epsilon\tilde{x}_{[4]}, \quad \alpha_{[3]} = \epsilon\tilde{\alpha}_{[3]}, \tag{12}$$

where ϵ is a small parameter that can for instance be chosen to be μ. In the following, only first-order terms will be retained in the rotor's equation. Hence, like in Section 2.2, the approximation $\tilde{\theta}' \approx \tilde{y}_\theta$ can be used in order to represent the degree-of-freedom of the rotor through its position rather than its velocity [49].

Using Eqs. (10), (11) and (12) and Taylor series for $z(s_i)$, Eqs. (5a) and (5b) can be simplified such that

$$\tilde{\theta}'' = \frac{\tilde{\mu}}{N}\left[\sum_{i=1}^{N} n_p^2 \Lambda_c s_i + 2n_t^2 s_i s_i' + n_t^2(1+n_t^2)\left(s_i s_i'^2 - \frac{n_p^2}{2} s_i^3\right)\right] + \tilde{T}_1 \cos(n\theta), \tag{13a}$$

$$\begin{aligned} s_i'' + n_p^2 s_i = -\epsilon \Lambda_m^{-1} \Bigg\{ & \frac{\Lambda_c^2 \tilde{\mu}}{N} \sum_{j=1}^{N} n_p^2 s_j + \tilde{b} s_i' + \frac{\tilde{\mu} n_t^2 \Lambda_c}{N}\left[\sum_{j=1}^{N} s_j (2s_j' + s_i')\right] \\ & + \frac{\tilde{\mu} n_t^2}{N}\left[\sum_{j=1}^{N} (1+n_t^2)\Lambda_c \left(s_j s_j'^2 - \frac{n_p^2}{2}(s_j^3 + s_j s_i^2)\right) + 2\Lambda_m s_j s_j' s_i'\right] \\ & + 6\eta\alpha_{[1]}\tilde{\alpha}_{[3]}(s_i s_i'^2 + s_i^2 s_i'') - 2\tilde{x}_{[4]} s_i^3 + \left(\Lambda_c + \Lambda_m s_i' - \frac{n_t^2(1+n_t^2)}{2} s_i^2\right)\tilde{T}_1 \cos(n\vartheta) \Bigg\}, \quad i = 1, \ldots, N. \end{aligned} \tag{13b}$$

Eq. (13a) expresses the rotor's acceleration as a function of the pendulums' motion. The first, second and third terms are linear, quadratic and cubic in s_i, respectively. The pendulums' equations (13b) are uncoupled from the rotor's dynamics, so that one can solve them to obtain the s_i and then inject the results in Eq. (13a) to retrieve the rotor's response. Eqs. (13b) contain the effect of the external torque, the damping, the coupling between pendulums (both linear and nonlinear) through the sums over N, and the perturbations of the path and rotation functions. Eqs. (13b) are weakly coupled because pendulums are coupled indirectly through the rotor and their effect on the rotor is small as their relative inertia is small [21]. These equations are also weakly nonlinear because the path and rotation functions chosen are close to an epicycloid and a linear rotation (indeed, $x_{[4]}$ and $\alpha_{[3]}$ were assumed to be of order ϵ, *cf.* Eq. (12)), which render a quasi-linear behaviour for small fluctuations of the rotational speed.

3.2. Solutions of the simplified equations

The method of multiple scales [63] is used to find the solutions of Eqs. (13b). Two rotation scales are introduced, $\vartheta_0 = \vartheta$ and $\vartheta_1 = \epsilon\vartheta$, and pendulums coordinates are expanded such that

$$s_i(\vartheta) = s_{i1}(\vartheta_0, \vartheta_1) + \epsilon s_{i2}(\vartheta_0, \vartheta_1). \tag{14}$$

As the excitation order n is close from n_p, it is convenient to define the detuning term σ as

$$n = n_p + \epsilon\sigma. \tag{15}$$

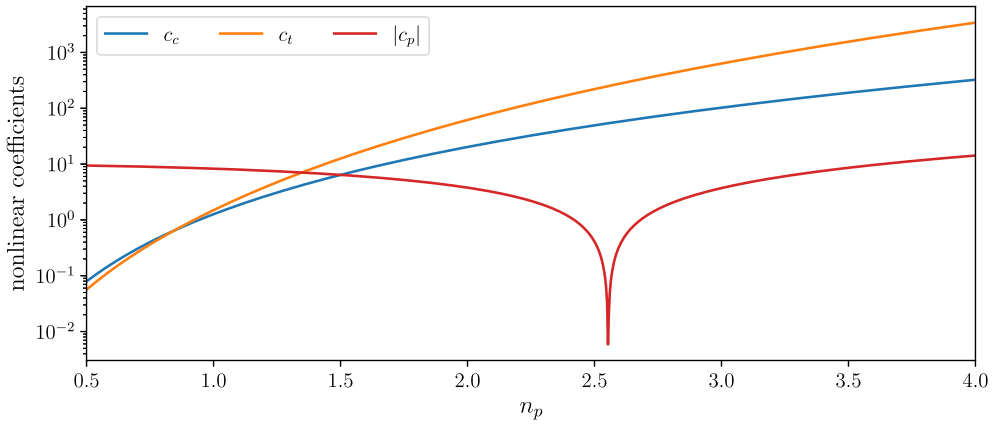

Fig. 2. Evolution of the nonlinear coefficients c_c, c_t and c_p as a function of the tuning order n_p. The other parameters are given in Table 1.

$\sigma > 0$ and $\sigma < 0$ correspond to under-tuned and over-tuned pendulums, respectively. Applying the method of multiple scales yields first-order solutions of the form

$$s_{i1}(\vartheta_0, \vartheta_1) = a_i(\vartheta_1)\cos\left(n\vartheta_0 - \xi_i(\vartheta_1)\right). \tag{16}$$

Amplitudes a_i and phases ξ_i are governed by the system

$$\begin{cases} D_1 a_i &= f_{a_i}(\boldsymbol{a}, \boldsymbol{\xi}), \ \text{(a)} \\ a_i D_1 \xi_i &= f_{\xi_i}(\boldsymbol{a}, \boldsymbol{\xi}), \ \text{(b)} \end{cases} \tag{17}$$

where $D_1(\bullet) = \partial(\bullet)/\partial\vartheta_1$ and $\boldsymbol{a}, \boldsymbol{\xi}$ are vectors containing the a_i and ξ_i, respectively. Functions f_{a_i} and f_{ξ_i} are given in Appendix A. The solutions sought are those at steady-state, meaning that the amplitudes and phases are invariant with ϑ such that

$$D_1 a_i = D_1 \xi_i = 0, \quad \forall i. \tag{18}$$

Moreover, we look for a response of the pendulums on the unison mode, which implies

$$a_i = a, \quad \xi_i = \xi, \quad \forall i. \tag{19}$$

The pendulums' response is obtained by introducing the steady-state (18) and unison (19) conditions in system (17) and solving for σ, $\tilde{T}_1$ and ξ. The solutions obtained are given in Appendix B. For readability, it is convenient to introduce the nonlinear coefficients

$$\begin{aligned} &c_2 = -c_c + 2c_t + c_p, \quad c_c = \tilde{\mu} n_t^4, \\ &c_t = \frac{\Lambda_c}{2}\tilde{\mu} n_p^2 n_t^2 (1 + n_t^2), \quad c_p = 3(\tilde{x}_{[4]} + 2n_p^2 \eta \alpha_{[1]} \tilde{\alpha}_{[3]}). \end{aligned} \tag{20}$$

c_2 is the nonlinear coefficient governing the hardening/softening behaviour of mode 2 (i.e. the unison mode). c_c, c_t and c_p are nonlinear coefficients related to Coriolis effects, the large displacements along the path, and the perturbation of the path and rotation functions, respectively. The backbone curve of the unison mode is obtained by cancelling the damping and forcing in the forced order response (*cf.* Eq. (B.1a)), leading to

$$n_2 = n_p + \frac{\Lambda_c^2 n_p^2 \mu}{2\Lambda_m n_p} - \epsilon \frac{c_2}{4\Lambda_m n_p} a^2. \tag{21}$$

n_2 is the resonance order of mode 2. It is interesting to note that even with an epicycloidal path and a linear rotation law (i.e. $c_p = 0$), the behaviour of mode 2 is hardening or softening, depending on the sign of $c_c - 2c_t$ (*cf.* Eq. (20)). These two coefficients are due to the nonlinear coupling between the rotor and pendulums, and their presence shows that the epicycloid is the tautochronic path of the pendulums only if they are uncoupled from the rotor. This was previously remarked by H. H. Denman [7]. Moreover, for reasonable parameters and tuning orders larger than 1, we have $2c_t > c_c > 0$ (*cf.* Fig. 2), so that the unison mode is typically softening. One can choose c_p to increase (decrease) this softening behaviour, resulting in softened (hardened) pendulums. Hence, c_p can be seen as the nonlinear tuning parameter of the CPVA while n_p is the linear tuning parameter. Note that c_c and c_t depend linearly on μ. Hence, for small values of μ, c_p dominates so that only small negative c_p values yield a hardening behaviour. c_c, c_t and c_p also depend on n_p, as illustrated in Fig. 2. It is very interesting to realise that for small n_p values, the contribution of c_c and c_t is negligible, even for reasonable μ values. Small n_p values can be encountered when dealing with cylinder deactivation, in which case a model simpler than the one presented in this paper can be used [26].

The response of the first three harmonics of the rotor's acceleration are obtained by substituting the pendulums' solutions in Eq. (13a). Their amplitude and phase are given in Appendix B.

3.3. Stability analysis

The procedure to determine the stability is the same as that used in [26], so only the main steps are reminded here. First, system (17) is rewritten as

$$\begin{cases} D_1 a_i = f_{a_i}(\boldsymbol{a}, \boldsymbol{\xi}), & \text{(a)} \\ D_1 \xi_i = f^*_{\xi_i}(\boldsymbol{a}, \boldsymbol{\xi}), & \text{(b)} \end{cases} \tag{22}$$

where we define $f^*_{\xi_i} = f_{\xi_i}/a_i$. Then, the Jacobian $\boldsymbol{J}$ of system (22) is computed and evaluated on the unison solution at steady state. $\boldsymbol{J}$ is a block-circulant matrix of size $2N \times 2N$ such that

$$\boldsymbol{J} = \begin{bmatrix} \boldsymbol{J_1} & \boldsymbol{J_2} & \cdots & \boldsymbol{J_2} \\ \boldsymbol{J_2} & \ddots & \ddots & \vdots \\ \vdots & \ddots & \ddots & \boldsymbol{J_2} \\ \boldsymbol{J_2} & \cdots & \boldsymbol{J_2} & \boldsymbol{J_1} \end{bmatrix}, \quad \boldsymbol{J_1} = \begin{bmatrix} \dfrac{\partial f_{a_i}}{\partial a_i} & \dfrac{\partial f_{a_i}}{\partial \xi_i} \\ \dfrac{\partial f^*_{\xi_i}}{\partial a_i} & \dfrac{\partial f^*_{\xi_i}}{\partial \xi_i} \end{bmatrix}, \quad \boldsymbol{J_2} = \begin{bmatrix} \dfrac{\partial f_{a_i}}{\partial a_j} & \dfrac{\partial f_{a_i}}{\partial \xi_j} \\ \dfrac{\partial f^*_{\xi_i}}{\partial a_j} & \dfrac{\partial f^*_{\xi_i}}{\partial \xi_j} \end{bmatrix}. \tag{23}$$

$\boldsymbol{J_1}$ represents the effect of a perturbation of the ith pendulum on itself, while $\boldsymbol{J_2}$ represents the effect of a perturbation of the jth pendulum on the ith one with $i \neq j$. The unison solution is subjected to a jump of the response if $\det[\boldsymbol{J_1} + (N-1)\boldsymbol{J_2}] < 0$, and it is subjected to localisation if $\det[\boldsymbol{J_1} - \boldsymbol{J_2}] < 0$ [26,64]. The limits of those instability regions define two bifurcation curves, which represent the bifurcation points of the unison solution for every forcing amplitude. The bifurcations leading to a jump are saddle-node bifurcations, hence the associated bifurcation curve is called a_{sn}. The other curve is called a_{pf} as localisation arises through a pitchfork bifurcation. Each crossing between a and a_{sn} or a_{pf} leads to a change of stability of the unison solution. The expression of the bifurcation curves is given in Appendix C under the form $\sigma_{sn}(a)$ and $\sigma_{pf}(a)$.

4. Case studies and design guidelines

The aim here is to present the main assets of the analytical model and to assess the accuracy of this model by comparing it to numerical resolutions of the initial equations of motion (5a) and (5b). These equations will be solved numerically using MANLAB, which is a path-following and bifurcation analysis software [65,66].

4.1. Response of the CPVA as a function of linear mistuning

In practice, the excitation order is fixed such that n is a constant. However, pendulums may not be tuned exactly to the excitation. This mistuning can be intentional or may arise from material imperfections. Either way, varying the excitation order is similar to introducing mistuning (provided that pendulums are equally mistuned) and is therefore relevant for studying the effect of mistuning on the system's response [17].

The order response of pendulums at unison and their stability is shown in Fig. 3 for several torque amplitudes. The bending of the response to the left indicates that pendulums exhibit a softening behaviour. The unison response computed analytically (green curves) fits quite well with the numerical results (green lines with square markers). There are however discrepancies at large amplitudes and at the resonance. At large amplitudes, the behaviour is more hardening than expected for $n < 1.56$ and more softening for $n > 1.56$. The amplitude at the resonance is not well estimated, but this was to be expected for two reasons. First, the analytical method uses a perturbation around $n = n_p$, which is not close from the resonance. Secondly, the system has very small damping, making the amplitude at the resonance difficult to predict accurately. Note that the analytical solutions above s_{cusp} exist only because of the use of Taylor series to approximate $z(s_i)$ in Section 3.1, so they are not physically relevant. The unstable zones leading to localisation (red) and jumps (blue) are shown. Each crossing between the unison solution and the limit of those zones leads to a change of stability. This is verified by MANLAB results, which indicate stability changes with red and blue stars. The position of the unstable zones is quite accurate as their limits fit well with the stars. Finally, note that Eq. (3) is a good approximation of the cusp of the path as it almost corresponds to the maximum amplitude that can be computed with numerical methods.

Fig. 4 displays the rotor's response associated to the pendulums' response shown in Fig. 3. Again, the overall response and its stability are well predicted, though discrepancies arise at large amplitudes. The strange shape of the response around the resonance for $\bar{T}_1 > 0.005$ can simply be ignored as it occurs for pendulums way above their cusp, which is non-physical. The zoom included in the figure allows to better see the evolution of the antiresonance with $\bar{T}_1$. For low torque amplitudes, the antiresonance order is $n_{AR} \approx n_p$, but as $\bar{T}_1$ is increased, n_{AR} shifts to the right. It is interesting to note that contrarily to the antiresonance, the resonance is shifting to the left, so the softening/hardening behaviour of the antiresonance is completely different from that of the resonance. This was previously observed for Euler's pendulum by A. Renault et al. [58] and is investigated further in the next section. One can see in the zoom in Fig. 4 that the antiresonance gets narrower as $\bar{T}_1$ is increased (this is because the amplitude at the antiresonance remains very small over the whole torque range, while the rest of the response considerably increase with $\bar{T}_1$). This makes n_{AR} harder to predict for large $\bar{T}_1$ values, as seen in the zoom in Fig. 4 for $\bar{T}_1 = 0.075$.

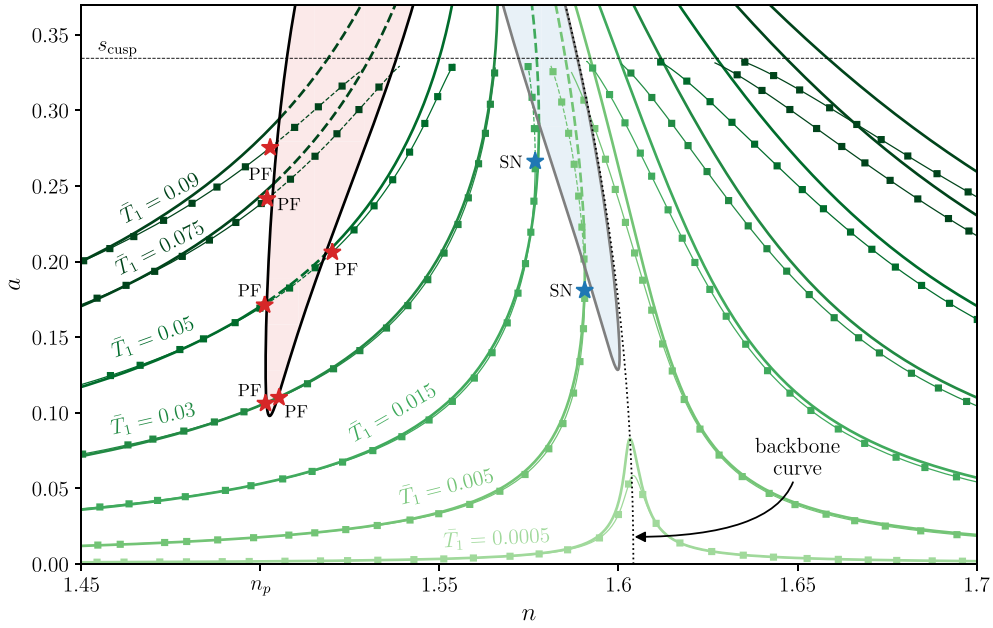

Fig. 3. Order response of the pendulums for several torque amplitudes. The analytical results representing the pendulums' response at unison are represented as green lines. The darker the line the larger the associated torque amplitude. For each analytical response there is an associated numerical result, computed with MANLAB, shown as a green line with square markers. Dashed lines indicate unstable solutions. The unstable zones obtained analytically are coloured in red (associated to localisation) and blue (associated to the jumps). Bifurcation points are also computed with MANLAB. Pitchfork and saddle-node bifurcations are represented as red and blue stars, respectively. The cusp of the path, approximated using Eq. (3), is shown as a black dashed line. The backbone curve of the unison mode is the black dotted line. The parameters of the CPVA are given in Table 1. (For interpretation of the references to colour in this figure legend, the reader is referred to the web version of this article.)

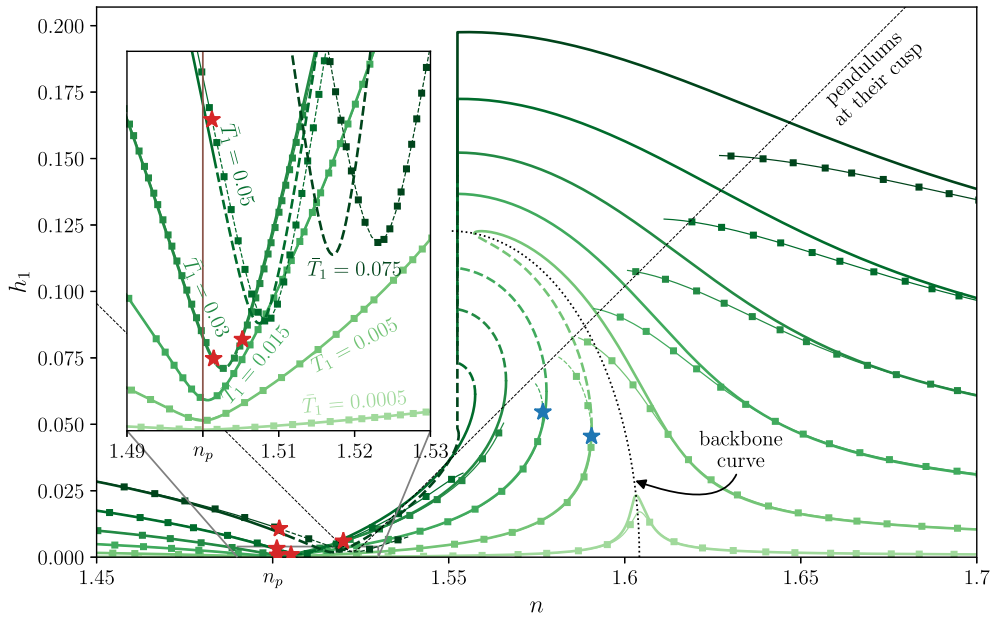

Fig. 4. Order response of the rotor for several torque amplitudes. The associated pendulums' response is given in Fig. 3 (however, for clarity, the curve corresponding to $\bar{T}_1 = 0.09$ is not shown in the present figure). The analytical results representing the pendulums' response at unison are represented as green lines. The darker the line the larger the associated torque amplitude. For each analytical response there is an associated numerical result, computed with MANLAB, shown as a green line with square markers. Dashed lines indicate unstable solutions. Pitchfork and saddle-node bifurcations computed with MANLAB are represented as red and blue stars, respectively. The value of h_1 for which the pendulums reach their cusp is shown as a black dashed line. It is computed using Eqs. (3), (B.1b) and (B.2a). The backbone curve of the unison mode is the black dotted line. A zoom around the antiresonance is included in the figure. The parameters of the CPVA are given in Table 1. (For interpretation of the references to colour in this figure legend, the reader is referred to the web version of this article.)

Table 1
Parameters of the CPVA studied in this section.

N	n_p	η	μ	$x_{[4]}$	$\alpha_{[1]}$	$\alpha_{[3]}$	$\bar{b}$	$\bar{b}_r$
2	1.5	0.5	0.1	−0.2	0.5	−0.1	0.005	0.008

4.2. Antiresonance locking

The filtering is optimal if the excitation order n coincides with the antiresonance order n_{AR} over the whole torque range. However, as seen in the previous section, nonlinear effects cause n_{AR} to be amplitude-dependent, so it is crucial to assess its evolution to ensure the CPVA achieves good performance over the whole torque range. The analytical model can be used to obtain a design rule minimising the shift of the antiresonance so it remains close from n_p. The procedure is described below.

The rotor's acceleration can be approximated by

$$\theta'' = h_1\cos(n\vartheta - \psi_1) + h_2\cos(2n\vartheta - \psi_2) + h_3\cos(3n\vartheta - \psi_3), \tag{24}$$

where the harmonics' amplitudes h_i and phases ψ_i $(i = 1,2,3)$ are given in Appendix B. Neglecting the effect of damping and considering excitation orders smaller than the order at resonance, the pendulums are in phase-opposition with the external torque so that $\cos(\xi) = -1$. Using this in Eq. (B.2a) leads to the expression of the amplitude of the rotor's first harmonic

$$h_1 = \left|\bar{T}_1 - \mu n_p^2\Lambda_c a - \frac{\mu(2n^2 - 3n_p^2)n_t^2(1+n_t^2)}{8}a^3\right|. \tag{25}$$

Using Eq. (B.1b) to perform a Taylor series of $\bar{T}_1$ in a leads to

$$\bar{T}_1 = a\left|\Lambda_c\tilde{\mu}n_p^2 - \frac{2\Lambda_m n_p\sigma}{\Lambda_c} + \left(\frac{3c_t - 2c_2}{4\Lambda_c} - \frac{3\Lambda_m n_p c_f\sigma}{4\Lambda_c^2}\right)a^2\right| + \mathcal{O}(a^4), \tag{26}$$

where c_f is a nonlinear coefficient representing the nonlinear forcing on the pendulums (*cf.* Appendix A). It is defined as

$$c_f = n_t^2(1+n_t^2). \tag{27}$$

In Eq. (26), the term inside the absolute value can fairly be assumed positive as $\mu\Lambda_c n_p^2$ is positive for reasonable parameters, a^2 is negligible for small values of a, σ is assumed small and $\bar{T}_1$ increases monotonically with a if there is no jump. Introducing Eq. (26) in Eq. (25) leads to

$$h_1 = \frac{a}{2\Lambda_c}\left|4\Lambda_m n_p\sigma + \left(\frac{3\Lambda_m n_p c_f\sigma}{2\Lambda_c} + c_2 - 2c_t\right)a^2\right|. \tag{28}$$

Because there is no damping in our reasoning, the amplitude of the rotor's first harmonic must be null at the antiresonance. Hence, the antiresonance locus is obtained by solving $h_1 = 0$ for σ, leading to

$$n_{AR} = n_p + \epsilon\frac{c_c - c_p}{4\Lambda_m n_p}a^2 + \mathcal{O}(a^4). \tag{29}$$

Thus, the condition to lock the antiresonance at n_p is

$$c_p = c_c > 0. \tag{30}$$

It is of great importance to note that rule (30) is different from the one rendering a tautochronic response of the pendulums. Indeed, one can see from Eq. (21) that the condition yielding a constant value of n_2 is

$$c_2 = 0 \Leftrightarrow c_p = c_c - 2c_t. \tag{31}$$

Rule (30) also requires the pendulums' path not to be the tautochronic path of the uncoupled system (this would correspond to $c_p = 0$, *cf.* Appendix D). Hence, despite the large focus on tautochronic designs [28,38,67,68], these are not the preferred ones. This highlights the importance of studying the antiresonance locus and not only the pendulums' response.

Fig. 5 shows the response of a CPVA tuned to fulfil condition (30). The rotor's response (b) is very well predicted by the model up to $\bar{T}_1 = 0.03$. For $\bar{T}_1 = 0.05$, the analytical model predicts a small shift of the antiresonance to the left while MANLAB shows that it actually shifts to the right. This shifting is amplified for $\bar{T}_1 = 0.075$, which highlights limits of the analytical model.

Looking at the pendulums' response (a), one can clearly see the softening behaviour for $\bar{T}_1 = 0.03$, with a jump at $n = 1.544$. However, at higher torque amplitudes, the MANLAB solutions show that the behaviour becomes less softening. Moreover, for $\bar{T}_1 = 0.075$, there are two pitchfork bifurcations that are not predicted by the analytical model. This confirms that the accuracy of the model is limited to small torque amplitudes. Note also that even though rule (30) requires a softening behaviour, it is much less softening than for a circular path. Indeed, in the case presented in Fig. 5, $x_{[4]} = 0.3261$, while for the same parameters but a circular path, $x_{[4]} = 2.6303$ [13]. Moreover, values of $\eta\alpha_{[1]}\alpha_{[3]}$ larger than those given in Table 1 would require smaller values of $x_{[4]}$ to fulfil rule (30).

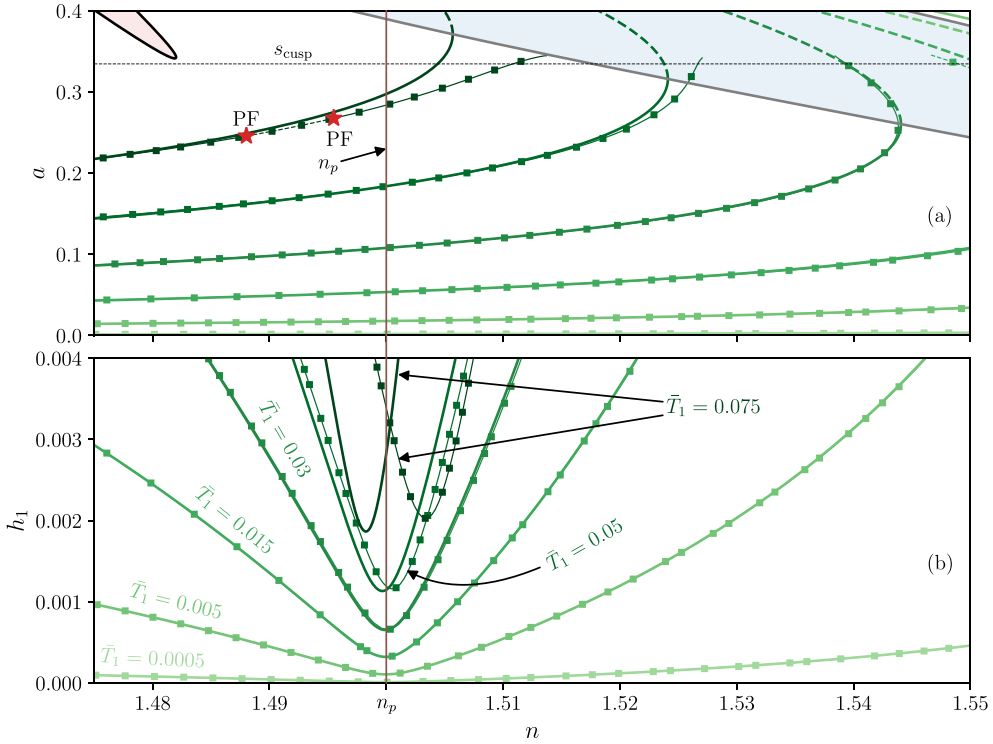

Fig. 5. Order response of the pendulums (a) and the rotor (b) for several torque amplitudes. The pendulums are tuned to lock the antiresonance at n_p. The unison response is represented in green and its unstable parts are dashed. The darker the line the larger the torque amplitude. The red and blue areas are the instability regions related to localisation and jumps, respectively. MANLAB solutions are represented as thin lines with square markers. The red stars indicate the pitchfork bifurcations obtained with MANLAB. The vertical brown line indicates n_p. $\bar{T}_1 = \{0.0005, 0.005, 0.015, 0.03, 0.05, 0.075\}$ and the other parameters are given in Table 1 except for $x_{[4]} = 0.3261$. (For interpretation of the references to colour in this figure legend, the reader is referred to the web version of this article.)

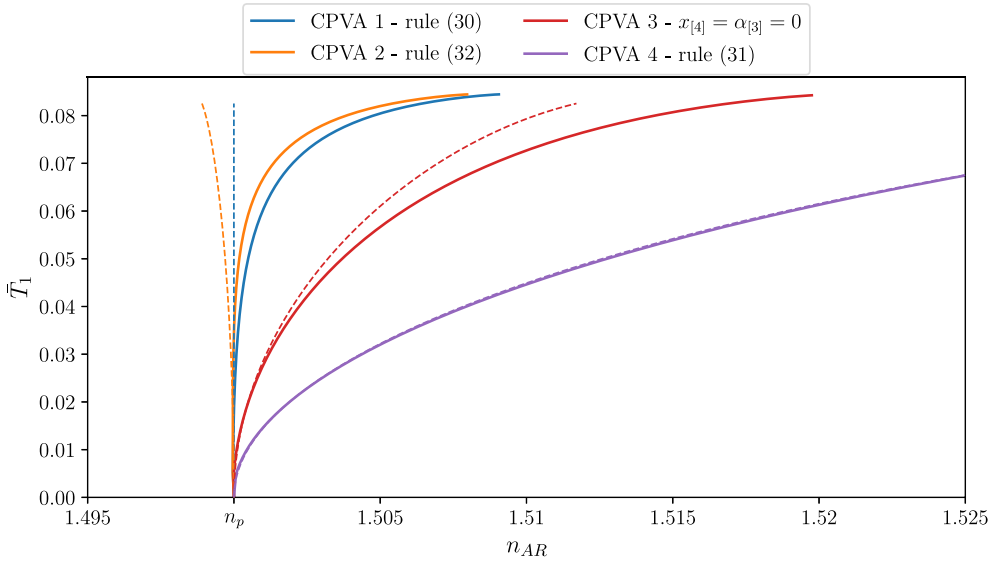

Fig. 6. Evolution of the antiresonance order as a function of the torque amplitude for four different designs. The parameters of the three CPVAs are given in Table 1 expect for $x_{[4]} = \{0.3261, 0.3460, 0, -0.5119\}$ for CPVAs 1, 2, 3 and 4, respectively, and $\alpha_{[3]} = 0$ for CPVA 3. The dashed lines represent the analytical approximation of n_{AR} obtained using Eq. (29), while the solid lines correspond to the antiresonance continuation procedure implemented in MANLAB [58].

Another rule limiting the shifting of the antiresonance was proposed by A. Renault [31–33]. It is derived from a regular perturbation solution of Eqs. (5a) and (5b) without damping, as presented in Appendix E, and leads to the recommendation

$$c_p = \frac{3\Lambda_m}{3(1+\mu)\Lambda_m - 4\mu\Lambda_c^2} c_c. \tag{32}$$

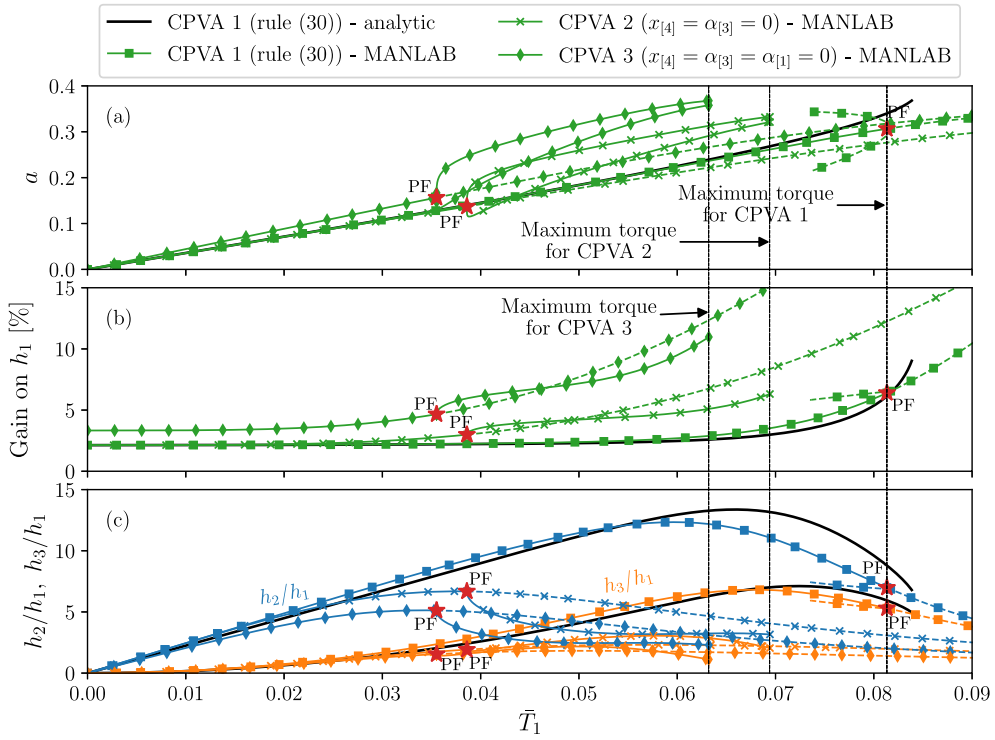

Fig. 7. Torque response of three different CPVAs at $n = n_p$. The solutions associated to the first, second and third CPVAs are shown as lines with square, cross and diamond markers, respectively. The first harmonic of the pendulums is shown in (a), the gain on the first harmonic of the rotor is shown in (b), and higher rotor harmonics are shown in (c). The gain shown in (b) is defined as $h_1/\bar{T}_1$, as the amplitude of the rotor with fixed pendulums is $\bar{T}_1$. Analytical results are shown in black for CPVA 1 (they are not shown for CPVAs 2 and 3 for clarity). Pitchfork bifurcations are indicated as red stars. Dashed lines indicate unstable solutions. The parameters of the three CPVAs are given in Table 1 expect for $x_{[4]} = \{0.3261, 0, 0\}$, $\alpha_{[3]} = \{-0.1, 0, 0\}$ and $\alpha_{[1]} = \{0.5, 0.5, 0\}$ for CPVAs 1, 2 and 3, respectively.

It is interesting to note that the design rule (30) is the same as Eq. (32) where the contribution of μ is neglected. These two rules are compared by computing the antiresonance order as a function of the excitation amplitude, as shown in Fig. 6. This computation is performed using MANLAB together with an antiresonance continuation procedure [58]. For comparison purposes, Fig. 6 also represents $n_{AR}(\bar{T}_1)$ for a CPVA tuned accordingly to rule (31) and for a reference CPVA for which no nonlinear mistuning is introduced (i.e. $x_{[4]} = \alpha_{[3]} = 0$, so that the rotation law is linear and the pendulums follow an epicycloidal path). We can see that rules (30) and (32) both limit efficiently the shifting of the antiresonance. Rule (32) is slightly more effective as it is the one keeping n_{AR} closest from n_p. In the case of the CPVA with no nonlinear mistuning, the antiresonance is largely shifting to the right, which shows that the antiresonance naturally has a hardening behaviour. The case of the CPVA with pendulums following the tautochronic path of the coupled system leads to the worst results. This is logical as the antiresonance is initially shifting to the right, and rule (31) increases even more this hardening behaviour. The analytical prediction of n_{AR} fits well with the numerical results for small torque amplitudes (around $\bar{T}_1 = 0.03$). For larger amplitudes the differences become significant, especially for designs that limit well the shifting of the antiresonance.

A torque response at $n = n_p$ of three different CPVAs is shown in Fig. 7.

- CPVA 1 is tuned using rule (30),
- The pendulums of CPVA 2 follow an epicycloid and a linear rotation law,
- The pendulums of CPVA 3 follow an epicycloid and do not rotate.

Note that no CPVA tuned accordingly to rule (32) is shown as it results in a response very close from that of CPVA 1 and the stability information is not provided by the analytical procedure detailed in Appendix E. The torque for which the pendulums reach their cusp is indicated for the three CPVAs. The pendulums of CPVA 3 cannot filter-out large torque amplitudes because localisation leads to a significant increase in amplitude, brining one of the pendulums to its cusp at $\bar{T}_1 \approx 0.0632$. A similar situation occurs for CPVA 2, with one of the pendulums reaching its cusp at $\bar{T}_1 \approx 0.0693$. The torque range of CPVA 1 is much larger than that of CPVAs 2 and 3. It is limited by the appearance of a subcritical pitchfork bifurcation, leading to a jump of the pendulums that brings them to their cusp. At small torque amplitudes, the gain on h_1 is the same for CPVAs 1 and 2, but it is larger for CPVA 3. This highlights the benefit of the added rotational motion of the pendulums. Starting from $\bar{T}_1 \approx 0.0265$, the gain for CPVAs 2 and 3 increases significantly compared to that of CPVA 1. In spite of the pendulums responding on a localised solution starting from $\bar{T}_1 = 0.0385$, CPVA 2 leads to a satisfying vibration reduction, with a gain of 6.4% when the pendulums reach their cusp. Still, one should be careful about the localised solution since a larger number of pendulums would likely reduce even more the torque

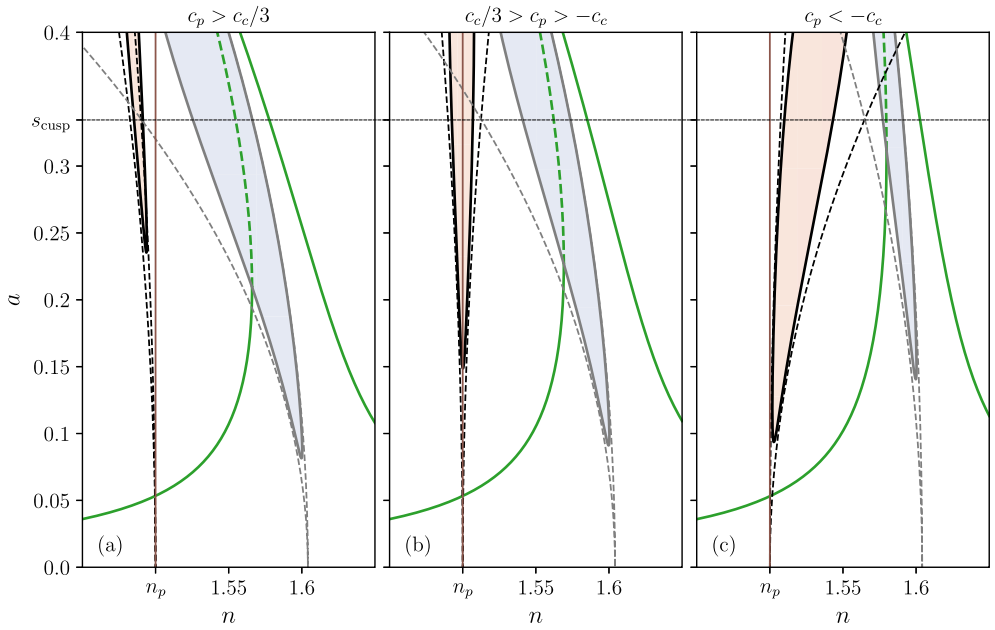

Fig. 8. Order response of the pendulums for three different values of nonlinear tuning. The unison response is represented in green and its unstable parts are dashed. The red and blue areas are the instability regions related to localisation and jumps, respectively. The dashed black and grey lines are 2nd order approximations of the limits of those regions in the conservative case. The vertical brown line indicates n_p. $\bar{T}_1 = 0.015$ and $x_{[4]} = \{0.25, 0.1, -0.25\}$ in (a), (b) and (c), respectively, while the other parameters are given in Table 1. (For interpretation of the references to colour in this figure legend, the reader is referred to the web version of this article.)

range [11]. The filtering with CPVA 3 is rather poor, with a gain exceeding 10% starting from as soon as $\bar{T}_1 = 0.0610$. Despite the small shift of the antiresonance visible in Figs. 5(b) and 6, the filtering of the 1st harmonic is extremely satisfying with CPVA 1. Indeed, Fig. 7(b) shows that the gain on most of the torque range is of 2.4%, and it does not exceed 6.4%. Though the pendulums are efficient in filtering the harmonic excitation, they generate higher rotor harmonics. Fig. 7(c) shows that this effect is absolutely not negligible as the amplitude of the 2nd and 3rd harmonics equals up to 12.4 and 7 times h_1, respectively, for CPVA 1. This issue is less visible for CPVAs 2 and 3, mostly because h_1 is larger. A possibility to limit the apparition of higher harmonics is to use pendulums tuned at different orders [14]. Another solution is to use another filtering principle of the CPVA, based on a subharmonic response [49,50,69]. Finally, the analytical model predicts accurately most of the response even though it indicates a shifting of the antiresonance in the wrong direction (*cf.* Fig. 5(b)). This is because the shifting predicted by the analytical model is roughly the opposite of the actual shifting.

4.3. Avoidance of the instabilities

As explained in Section 1, instabilities of the unison solution are to be avoided as they reduce the torque range of the CPVA and might decrease the vibration reduction. Hence, it is interesting to have a simple information on the position of the instability zones to know how to avoid them. This can be done by neglecting the damping and using Taylor series in a in the expression of $\sigma_{sn}(a)$ and $\sigma_{pf}(a)$, leading to

$$\sigma_{sn} = \frac{\Lambda_c^2 \tilde{\mu} n_p}{2\Lambda_m} + \frac{-2c_2 \pm c_2}{4\Lambda_m n_p} a^2 + \mathcal{O}(a^4), \tag{33a}$$

$$\sigma_{pf} = \frac{-2c_p \pm |c_2 - 2c_t|}{4\Lambda_m n_p} a^2 + \mathcal{O}(a^4) = \frac{-2c_p \pm |c_p - c_c|}{4\Lambda_m n_p} a^2 + \mathcal{O}(a^4) \tag{33b}$$

There are important remarks to be done about Eqs. (33a) and (33b):

- The bifurcation curve related to saddle-node bifurcations emanates from $\sigma = \Lambda_c^2 \tilde{\mu} n_p / 2\Lambda_m$, which corresponds to $n = n_{20} > n_p$. However, the bifurcation curve related to pitchfork bifurcations emanates from $\sigma = 0$, which corresponds to $n = n_p$.
- σ_{sn} increases with the amplitude if $c_2 < 0$ and decreases if $c_2 > 0$. It is logical that this bifurcation curve follows the sign of c_2 as jumps are due to the hardening/softening behaviour, and c_2 is the parameter that controls this behaviour (*cf.* Eq. (21)).
- σ_{pf} increases with the amplitude if $-2c_p - |c_p - c_c| > 0$ and decreases if $-2c_p + |c_p - c_c| < 0$. The case $-2c_p - |c_p - c_c| < 0 < -2c_p + |c_p - c_c|$ is highly undesired as σ_{pf} would remain around 0, causing the instability zone to exist at the operating point $n \approx n_p$. This is illustrated in Fig. 8.

In order to avoid instabilities while keeping $n_p \approx n$, the best options are to choose

$$2c_p > |c_p - c_c| \Leftrightarrow c_p > c_c/3 \text{ and } n_p < n, \text{ or} \tag{34a}$$

$$2c_p < -|c_p - c_c| \Leftrightarrow c_p < -c_c \text{ and } n_p > n. \tag{34b}$$

Conditions (34a) and (34b) correspond to the part of Fig. 8(a) where $n > n_p$ and to the part of Fig. 8(c) where $n < n_p$, respectively. Because of damping, the localisation zone does not start from $n = n_p$, so one can still use conditions (34a) and (34b) with $n_p = n$. In [29], linear over-tuning together with a hardening behaviour was recommended to avoid localisation. This is in agreement with condition (34b). In [8], which considered purely translated pendulums, it was proposed to use an over-tuned epicycloidal trajectory in order to keep the unison solution stable. The disadvantage of this method is that the level of detuning must be chosen depending on the maximum pendulums' amplitude desired, whereas conditions (34) prevent the appearance of a localised solution no matter the pendulums' amplitude. Moreover, the linear over-tuning required in [8] is relatively large, which decreases the efficiency of the vibration reduction (*cf.* Section 4.2). Finally, note that in the special case $c_p = c_c$ (which is recommended to keep the antiresonance locked, *cf.* Section 4.2), condition (34a) can be satisfied but not condition (34b). Hence, recommendation (34a) is compatible with recommendations (30) and (32).

In order to avoid the jumps up to the cusp, one must ensure that

$$\sigma < \min[\sigma_{sn}(s_{\text{cusp}})]. \tag{35}$$

4.4. Visualisation of the preferred design in the design space

Fig. 9 represents the stability of the unison solution at a given excitation order and as a function of the linear and nonlinear tuning parameters, n_p and $\bar{c}_p$, where the later is simply the unscaled version of c_p, i.e.

$$\bar{c}_p = 3(x_{[4]} + 2n_p^2\eta\alpha_{[1]}\alpha_{[3]}). \tag{36}$$

For convenience, we also introduce the unscaled coefficient $\bar{c}_c = \mu n_t^4$. Fig. 9 contains four maps, all corresponding to a different pendulums' amplitude. Each set $(n_p, \bar{c}_p)$ corresponds to a given design, making the maps useful to assess simultaneously the stability of different designs. The designs subjected to jumps (localisation) at amplitude a are shown in blue (red). The stable designs are shown in green. The guidelines limiting the shifting of the antiresonance (30) and preventing the appearance of localisation (34) are also represented, so one can see the designs that allow performance and stability. The hatched areas indicate the designs for which the pendulums have reached their cusp, so the instability zones should be avoided until the design becomes hatched. The black dot corresponds to the design presented in Figs. 5 and 7 (CPVA 1 in Fig. 7).

The designs leading to the best vibration reduction are those located around the brown line and close to $n_p = n$. Fig. 9 shows that a small over-tuning could lead to localisation while a small under-tuning might cause a jump. Moreover, as explained in Section 4.3, the lower the damping the closer the instability zone is from n_p. Hence, to have an efficient and robust CPVA, the best choice is to choose $\bar{c}_p \approx \bar{c}_c$ and n_p equal or very slightly smaller than n.

5. Conclusion

This paper deals with the filtering efficiency of CPVAs and their dynamic stability. To consider modern CPVA designs, the N identical pendulums are allowed to rotate relatively to the rotor. The dynamic response of the system and its stability are computed using a perturbation method, and the validity of this analytical model is validated through comparisons with numerical solutions. Because the system is nonlinear, the resonance and antiresonance orders can increase/decrease with the excitation amplitude. We showed that in the case of pendulums following an epicycloidal path and a linear rotation law, the resonance order tends to diminish with the exciting torque amplitude, revealing a softening behaviour. This softening is due to nonlinearities arising through the coupling between the rotor and the pendulums. However, contrarily to the resonance, the antiresonance order increases with the excitation amplitude. Hence, to design an efficient CPVA, it is not sufficient to assess only the behaviour of the pendulums, which does not contain information regarding the evolution of the antiresonance order. In this paper, we derived design guidelines that allow to minimise the shifting of the antiresonance, thus leading to a maximised filtering over the whole torque range. These guidelines require the use of paths/rotation laws that slightly soften the system's response compared to the case of an epicycloid and a linear rotation. The accuracy of these guidelines was assessed using an antiresonance tracking procedure and a torque sweep confirmed the efficiency of such nonlinear tunings. This torque sweep also highlighted that the amplitude of higher rotor harmonics is not negligible at the operating point. Then, two other design guidelines preventing the apparition of localised solutions were proposed. One of them is highly relevant as it is compatible with the rule locking the antiresonance. Finally, a representation of the stability and design rules in the design space allowed to identify the CPVA tuning parameters leading to a stable response and a maximum vibration reduction.

CRediT authorship contribution statement

V. Mahé: Formal analysis, Investigation, Validation, Writing – original draft, Investigation, Methodology, Conceptualisation, Software. **A. Renault:** Supervision, Conceptualisation, Resources, Software. **A. Grolet:** Supervision, Validation, Visualisation. **H. Mahé:** Supervision. **O. Thomas:** Supervision, Validation, Visualisation, Writing – review & editing.

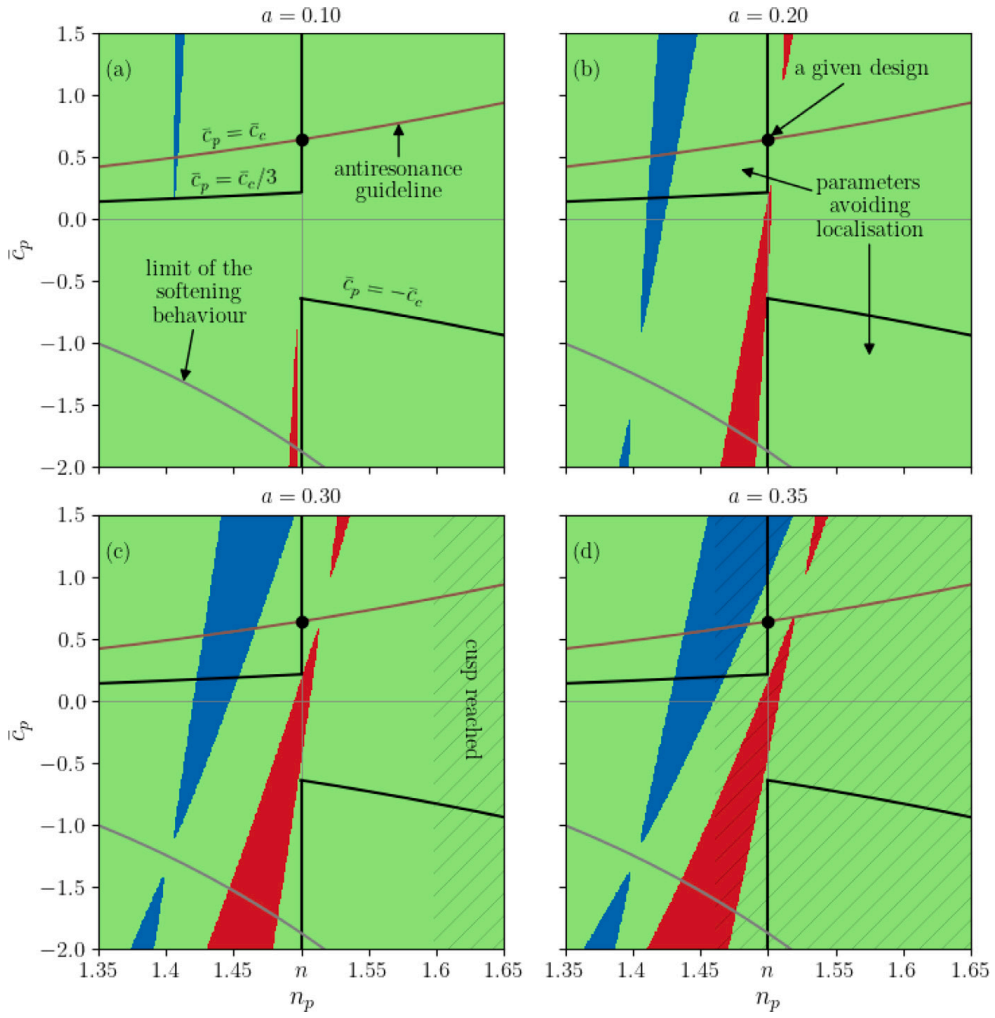

Fig. 9. Maps representing the stability of the response as a function of the tuning parameters n_p and $\bar{c}_p$. Each map is shown for a given order n and a given pendulums' amplitude a. Stable designs are depicted in green while designs subjected to localisation or jumps are shown in red or blue, respectively. The parameters avoiding localisation are delimited by black lines. The brown line corresponds to recommendation (30), locking the antiresonance. The grey line shows the limit between the hardening and softening behaviour of the unison mode. Designs below this line are hardening. The hatched areas indicate the designs for which amplitude a is larger than s_{cusp}. $n = 1.5$ and the parameters that are not varied are given in Table 1. (For interpretation of the references to colour in this figure legend, the reader is referred to the web version of this article.)

Declaration of competing interest

The authors declare that they have no known competing financial interests or personal relationships that could have appeared to influence the work reported in this paper.

Appendix A. System obtained through the method of multiple scales

The system of equations obtained through the application of the method of multiple scales is given by Eq. (17) where functions f_{a_i} and f_{ξ_i} are

$$f_{a_i}(\boldsymbol{a},\boldsymbol{\xi}) = \left[-2n_p\tilde{b}a_i + \frac{2\Lambda_c^2 n_p^2\tilde{\mu}}{N}\sum_{j=1}^{N} a_j \sin(\Delta\xi_{ij}) + \frac{1}{N}\sum_{j=1}^{N}\left[c_c a_i a_j^2 \sin(2\Delta\xi_{ij}) - \frac{c_t}{2}(a_j^3 + a_j a_i^2)\sin(\Delta\xi_{ij})\right] - \left(2\Lambda_c - \frac{c_f}{4}a_i^2\right)\tilde{T}_1 \sin(\xi_i)\right] \left[4\Lambda_m n_p\right]^{-1}, \tag{A.1}$$

$$f_{\xi_i}(\boldsymbol{a},\boldsymbol{\xi}) = \sigma a_i - \left[\frac{2\Lambda_c^2 n_p^2\tilde{\mu}}{N}\sum_{j=1}^{N} a_j \cos(\Delta\xi_{ij}) - c_p a_i^3 + \frac{1}{N}\sum_{j=1}^{N}\left[c_c a_i a_j^2 \cos(2\Delta\xi_{ij}) - \frac{c_t}{2}(a_j^3 + 3a_j a_i^2)\cos(\Delta\xi_{ij})\right] + \left(2\Lambda_c - \frac{3c_f}{4}a_i^2\right)\tilde{T}_1 \cos(\xi_i)\right] \left[4\Lambda_m n_p\right]^{-1}. \tag{A.2}$$

Constants c_p, c_c, c_t and c_f are defined in Eqs. (20) and (27) and $\Delta\xi_{ij}$ is defined as

$$\Delta\xi_{ij} = \xi_j - \xi_i. \tag{A.3}$$

Appendix B. Response of the systems with pendulums at unison

The amplitude and phase response of the pendulums at unison is given by

$$\sigma = \frac{2\Lambda_c^2 n_p^2 \tilde{\mu} - c_2 a^2}{4\Lambda_m n_p} \pm \frac{8\Lambda_c - 3c_f a^2}{16\Lambda_m n_p} \sqrt{\frac{\tilde{T}_1^2}{a^2} - \frac{64 n_p^2 \tilde{b}^2}{(8\Lambda_c - c_f a^2)^2}}, \tag{B.1a}$$

$$\tilde{T}_1 = 4a \left[\frac{\left(2n_p(2\Lambda_m\sigma - \Lambda_c^2 n_p \tilde{\mu}) + c_2 a^2\right)^2}{\left(8\Lambda_c - 3c_f a^2\right)^2} + \frac{4n_p^2 \tilde{b}^2}{\left(8\Lambda_c - c_f a^2\right)^2} \right]^{1/2}, \tag{B.1b}$$

$$\tan(\xi) = -\frac{2n_p \tilde{b}}{4\Lambda_m n_p \sigma - 2\Lambda_c^2 n_p^2 \tilde{\mu} + c_2 a^2} \frac{8\Lambda_c - 3c_f a^2}{8\Lambda_c - c_f a^2}. \tag{B.1c}$$

Eqs. (B.1a) and (B.1b) are used to compute the amplitude response as a function of the excitation order and excitation amplitude, respectively.

The rotor's response can be approximated by Eq. (24). The amplitudes h_i and phases ψ_i $(i = 1, 2, 3)$ of its harmonics are given by

$$h_1^2 = \bar{T}_1^2 + \mu \bar{T}_1 a \cos(\xi) \left(2n_p^2 \Lambda_c + \frac{n_t^2(1+n_t^2)}{4}(2n^2 - 3n_p^2)a^2 \right) + \frac{\mu^2 a^2}{4} \left(2n_p^2 \Lambda_c + \frac{n_t^2(1+n_t^2)}{4}(2n^2 - 3n_p^2)a^2 \right)^2, \tag{B.2a}$$

$$\tan(\psi_1) = \frac{\mu a \left(8n_p^2 \Lambda_c + n_t^2(1+n_t^2)(2n^2 - 3n_p^2)a^2 \right) \sin(\xi)}{\mu a \left(8n_p^2 \Lambda_c + n_t^2(1+n_t^2)(2n^2 - 3n_p^2)a^2 \right) \cos(\xi) + 8\bar{T}_1}, \tag{B.2b}$$

$$h_2 = \mu n n_t^2 a^2, \tag{B.2c}$$

$$\tan(\psi_2) = \frac{-\cos(2\xi)}{\sin(2\xi)}, \tag{B.2d}$$

$$h_3 = \frac{n_t^2(1+n_t^2)}{8}(n_p^2 + 2n^2)\mu a^3, \tag{B.2e}$$

$$\tan(\psi_3) = \frac{-\sin(3\xi)}{-\cos(3\xi)}. \tag{B.2f}$$

Appendix C. Expression of the bifurcation curves

The bifurcation curves $a_{sn}(\sigma)$ and $a_{pf}(\sigma)$ can be written as $\sigma_{sn}(a)$ and $\sigma_{pf}(a)$ such that

$$\sigma_{sn} = \frac{1}{4\Lambda_m n_p (8\Lambda_c + 3c_f a^2)} \left[\varpi_{sn_1} \pm \frac{\sqrt{\varpi_{sn_2}}}{(-8\Lambda_c + c_f a^2)^3} \right], \tag{C.1a}$$

$$\sigma_{pf} = \frac{1}{4\Lambda_m n_p (8\Lambda_c + 3c_f a^2)(-8\Lambda_c + c_f a^2)} \left[\varpi_{pf_1} \pm \frac{\sqrt{\varpi_{pf_2}}}{(-8\Lambda_c + c_f a^2)^2} \right], \tag{C.1b}$$

with

$$\varpi_{sn_1} = 12\Lambda_c c_t a^2 + 16\Lambda_c(\Lambda_c^2 n_p^2 \tilde{\mu} - c_2 a^2), \tag{C.2a}$$

$$\begin{aligned} \varpi_{sn_2} = {} & (-8\Lambda_c + c_f a^2)^3 (-8\Lambda_c + 3c_f a^2)^2 \Big[c_f a^2 \Big(-4n_p^2 \tilde{b}^2 (9c_f (8\Lambda_c + c_f a^2) a^2 - 64\Lambda_c^2) \\ & + c_2^2 a^4 \left((-24\Lambda_c + c_f a^2) c_f a^2 + 192\Lambda_c^2 \right) \Big) + 512\Lambda_c^3 (2n_p \tilde{b} + c_2 a^2)(2n_p \tilde{b} - c_2 a^2) \Big], \end{aligned} \tag{C.2b}$$

$$\varpi_{pf_1} = -c_f \left(6c_f c_c a^6 + 16\Lambda_c (c_t + 2c_p - c_2) a^4 \right) + 128\Lambda_c^2 c_p a^2, \tag{C.2c}$$

$$\begin{aligned} \varpi_{pf_2} = {} & (-8\Lambda_c + c_f a^2)^3 (-8\Lambda_c + 3c_f a^2)^2 \\ & \Big[c_f a^2 \Big[c_f a^2 \Big[c_f a^2 \left((3c_c - c_t + c_p)^2 a^4 - 36 n_p^2 \tilde{b}^2 \right) - 8\Lambda_c (36 n_p^2 \tilde{b}^2 + (c_c - c_t + 3c_p)(3c_c - c_t + c_p) a^4) \Big] \\ & - 64\Lambda_c^2 \left(-4n_p^2 \tilde{b}^2 + (9c_c c_t - 5c_c c_2 - 2c_t^2 + 7c_t c_p + c_t c_2 - 3c_p c_2) a^4 \right) \Big] - 512\Lambda_c^3 (2c_t - c_2)^2 a^4 + 2048\Lambda_c^3 n_p^2 \tilde{b}^2 \Big]. \end{aligned} \tag{C.2d}$$

Appendix D. Study of the uncoupled system

In this section, we focus on the case of where no fluctuating torque is applied on the rotor so that is spins at a constant speed. Hence, it is not a degree-of-freedom and the pendulums are uncoupled from the rotor. Setting $y = 1, y' = 0$ in Eq. (5b) and ignoring the damping leads to

$$\left[1 + \eta\gamma(s_i)^2\right] s_i'' + \eta\gamma(s_i)\frac{d\gamma(s_i)}{ds_i} s_i'^2 - \frac{1}{2}\frac{dx(s_i)}{ds_i} = 0, \qquad i = 1, \dots, N. \tag{D.1}$$

Considering that the paths and rotation functions are given by Eq. (10), Eq. (D.1) can be rewritten as

$$\Lambda_m s_i'' + n_t^2 s_i - 2x_{[4]} s_i^3 + 6\eta\alpha_{[1]}\alpha_{[3]}\left(s_i^2 s_i'' + s_i s_i'^2\right) + 9\eta\alpha_{[3]}^2\left(s_i^4 s_i'' + 2s_i^3 s_i'^2\right) = 0, \qquad i = 1, \dots, N. \tag{D.2}$$

In the special case $x_{[4]} = \alpha_{[3]} = 0$, Eq. (D.2) becomes a linear equation, meaning that the configuration $x_{[4]} = \alpha_{[3]} = 0$ yields a tautochronic behaviour of the pendulums. In the following, we look for other sets $(x_{[4]}, \alpha_{[3]})$ that approximately lead to a tautochronic behaviour. Like in Section 3, this is done using the scaling $x_{[4]} = \epsilon\tilde{x}_{[4]}$, $\alpha_{[3]} = \epsilon\tilde{\alpha}_{[3]}$ and the method of multiple scales with the fast time $\vartheta_0 = \vartheta$ and the slow one $\vartheta_1 = \epsilon\vartheta$. Using the expansion (14) and the steady state condition (18), one finds that the backbone curve of the ith uncoupled pendulum is

$$n_{uc} = n_p - \frac{c_p}{4\Lambda_m n_p} a^2. \tag{D.3}$$

Hence, for the period of oscillation of the pendulums to be independent on their amplitude, one must have

$$c_p = 0. \tag{D.4}$$

Note that Eq. (D.3) can also be retrieved by setting $\mu = 0$ in the backbone curve of the unison mode (21).

Appendix E. Application of a regular perturbation method on the equations of motion

Here we present the application of a regular perturbation method on Eqs. (5a) and (5b) without damping. Only one pendulum is considered, but the procedure is exactly the same with N pendulums. First, variables y and s are expanded such that

$$s = \epsilon s_1 + \epsilon^2 s_2 + \epsilon^3 s_3 + \mathcal{O}(\epsilon^4), \tag{E.1a}$$

$$y = 1 + \epsilon y_{\theta 1} + \epsilon^2 y_{\theta 2} + \epsilon^3 y_{\theta 3} + \mathcal{O}(\epsilon^4). \tag{E.1b}$$

Note that because damping is neglected, the constant part of the torque must not be considered. Indeed, in practice it balances with the rotor's damping such that $\bar{b}_r = \bar{T}_0$ (*cf.* Section 2.1). Introducing the expansions in the equations of motion leads to three systems of two equations, the ith system appearing at order ϵ^i. These systems are given by

$$\begin{cases} (1+\mu)y_{\theta 1}' + \mu\Lambda_c s_1'' &= \bar{T}_1\cos(n\vartheta), \quad \text{(a)} \\ \Lambda_c y_{\theta 1}' + \Lambda_m s_1'' + n_t^2 s_1 &= 0 \quad \text{(b)} \end{cases}$$
$$\begin{cases} (1+\mu)y_{\theta 2}' + \mu\Lambda_c s_2'' &= f_{\theta 2}(y_{\theta 1}, s_1), \quad \text{(c)} \\ \Lambda_c y_{\theta 2}' + \Lambda_m s_2'' + n_t^2 s_2 &= f_{s2}(y_{\theta 1}, s_1), \quad \text{(d)} \end{cases} \tag{E.2}$$
$$\begin{cases} (1+\mu)y_{\theta 3}' + \mu\Lambda_c s_3'' &= f_{\theta 3}(y_{\theta 1}, s_1, y_{\theta 2}, s_2), \quad \text{(e)} \\ \Lambda_c y_{\theta 3}' + \Lambda_m s_3'' + n_t^2 s_3 &= f_{s3}(y_{\theta 1}, s_1, y_{\theta 2}, s_2), \quad \text{(f)} \end{cases}$$

with

$$f_{\theta 2}(y_{\theta 1}, s_1) = -\mu[\Lambda_c y_{\theta 1}' s_1' - 2n_t^2 s_1 s_1' + (2\Lambda_c s_1'' + y_{\theta 1}')y_{\theta 1}] - y_{\theta 1} y_{\theta 1}', \tag{E.3a}$$

$$f_{s2}(y_{\theta 1}, s_1) = -\Lambda_m(y_{\theta 1}' s_1' + y_{\theta 1} s_1'') - n_t^2 y_{\theta 1} s_1 \tag{E.3b}$$

$$\begin{aligned} f_{\theta 3}(y_{\theta 1}, s_1, y_{\theta 2}, s_2) = -\mu \Bigg[& \left(\Lambda_c y_{\theta 1}^2 + 2\Lambda_c y_{\theta 2}\right) s_1'' + \left(\Lambda_c y_{\theta 2}' - 2n_t^2 s_2\right) s_1' + \left(3\alpha_{[3]}\eta s_1'' - \frac{n_t^2(1+n_t^2)}{2} s_1''\right) s_1^2 \\ & + \left(\Lambda_c s_2' - n_t^2 s_1^2 + y_{\theta 2}\right) y_{\theta 1}' + \left(6\alpha_{[3]}\eta s_1'^2 - n_t^2(1+n_t^2)s_1'^2 - 2n_t^2 s_2'\right) s_1 \\ & + \left(2\Lambda_c s_2'' - 4n_t^2 s_1 s_1' + \Lambda_c y_{\theta 1}' s_1' + y_{\theta 2}'\right) y_{\theta 1} \Bigg] - y_{\theta 1} y_{\theta 2}' - y_{\theta 2} y_{\theta 1}', \end{aligned} \tag{E.3c}$$

$$\begin{aligned} f_{s3}(y_{\theta 1}, s_1, y_{\theta 2}, s_2) = & -6\alpha_{[1]}\alpha_{[3]}\eta s_1^2 s_1'' + 2x_{[4]} s_1^3 - \Lambda_m y_{\theta 2} s_1'' - \Lambda_m y_{\theta 2}' s_1' - \left(6\alpha_{[1]}\alpha_{[3]}\eta s_1'^2 + n_t^2 y_{\theta 2}\right) s_1 \\ & - \left(\Lambda_m s_2' + \left(3\alpha_{[3]}\eta - \frac{n_t^2(1+n_t^2)}{2}\right) s_1^2\right) y_{\theta 1}' - \left(\Lambda_m s_2'' + n_t^2 s_2\right) y_{\theta 1}. \end{aligned} \tag{E.3d}$$

Looking at the nature of the forcing terms in the three systems of equations, it makes sense to look for solutions of the form

$$y_{\theta 1} = \mathfrak{R}[\hat{h}_{1(1)} e^{jn\vartheta}], \quad s_1 = \mathfrak{R}[\hat{a}_{1(1)} e^{jn\vartheta}], \tag{E.4a}$$

$$y_{\theta 2} = \mathfrak{R}[\hat{h}_{2(2)} e^{2jn\vartheta}], \quad s_2 = a_{2(0)} + \mathfrak{R}[\hat{a}_{2(2)} e^{2jn\vartheta}], \tag{E.4b}$$

$$y_{\theta 3} = \mathfrak{R}[\hat{h}_{3(1)} e^{jn\vartheta}] + \mathfrak{R}[\hat{h}_{3(3)} e^{3jn\vartheta}], \quad s_3 = \mathfrak{R}[\hat{a}_{3(1)} e^{jn\vartheta}] + \mathfrak{R}[\hat{a}_{3(3)} e^{3jn\vartheta}], \tag{E.4c}$$

where $\hat{\bullet}$ denotes a complex quantity and the index in brackets refers to the number of the harmonic. Inserting these general forms of solution in the three systems of equations and assuming $n = n_p$ leads to

$$\hat{h}_{1(1)} = 0, \quad \hat{a}_{1(1)} = -\frac{\bar{T}_1}{\mu \Lambda_c n_p^2}, \tag{E.5a}$$

$$\hat{h}_{2(2)} = \frac{3\mu \Lambda_m^2 n_p^2 \hat{a}_{1(1)}^2}{2(3(1+\mu)\Lambda_m) - 4\mu\Lambda_c^2}, \quad \hat{a}_{2(2)} = -j \frac{\mu \Lambda_m \Lambda_c n_p \hat{a}_{1(1)}^2}{3(1+\mu)\Lambda_m - 4\mu\Lambda_c^2}, \tag{E.5b}$$

$$\hat{h}_{3(1)} = j \frac{2n_p^3 \Lambda_m \hat{h}_{2(2)} - 3n_p (x_{[4]} + 2n_p^2 \eta \alpha_{[1]} \alpha_{[3]}) \hat{a}_{1(1)}^2}{2\Lambda_c n_p^2}. \tag{E.5c}$$

The expressions for $\hat{h}_{3(3)}$, $\hat{a}_{3(1)}$ and $\hat{a}_{3(3)}$ are not necessary to study the position of the antiresonance. As $\hat{h}_{1(1)} = 0$, the condition to lock the antiresonance at n_p is $\hat{h}_{3(1)} = 0$. Solving this leads to condition (32).

References

[1] B.C. Carter, Improvements in or relating to damping of oscillation-checking devices, 1929, 337 466.
[2] R.R.R. Sarazin, Means adapted to reduce the torsional oscillations of crankshafts, 1931, 2 079 226.
[3] R. Chilton, Pendulum counterweight, 1935, 2 112 984.
[4] M. Auleley, O. Thomas, C. Giraud-Audine, H. Mahé, Enhancement of a dynamic vibration absorber by means of an electromagnetic shunt, J. Intell. Mater. Syst. Struct. 32 (3) (2021) 331–354, http://dx.doi.org/10.1177/1045389X20957097.
[5] D.E. Newland, Nonlinear problems of centrifugal pendulum vibration absorbers, in: Mechanisms and Machines, Vol. 1, Varna (Bulgaria), 1965, pp. 39–62.
[6] J.F. Madden, Constant frequency bifilar vibration absorber, 1980, 4 218 187.
[7] H.H. Denman, Tautochronic bifilar pendulum torsion absorbers for reciprocating engines, J. Sound Vib. 159 (2) (1992) 251–277, http://dx.doi.org/10.1016/0022-460X(92)90035-V.
[8] S.W. Shaw, B. Geist, Tuning for performance and stability in systems of nearly tautochronic torsional vibration absorbers, J. Vib. Acoust. 132 (4) (2010) http://dx.doi.org/10.1115/1.4000840.
[9] A. Givois, J.-J. Tan, C. Touzé, O. Thomas, Backbone curves of coupled cubic oscillators in one-to-one internal resonance: Bifurcation scenario, measurements and parameter identification, Meccanica 55 (3) (2020) 481–503, http://dx.doi.org/10.1007/s11012-020-01132-2.
[10] A. Grolet, Z. Shami, S. Arabi, O. Thomas, Experimental nonlinear localisation in a system of two coupled beams, in: Dynamical System Theory and Applications, Lodz (Poland), 2019, p. 13.
[11] C.-P. Chao, C.-T. Lee, S. Shaw, Non-unisson dynamics of multiple centrifugal pendulum vibration absorbers, J. Sound Vib. 204 (5) (1997) 769–794, http://dx.doi.org/10.1006/jsvi.1997.0960.
[12] C.-P. Chao, S.W. Shaw, C.-T. Lee, Stability of the unison response for a rotating system with multiple tautochronic pendulum vibration absorbers, J. Appl. Mech. 64 (1) (1997) 149–156, http://dx.doi.org/10.1115/1.2787266.
[13] A. Alsuwaiyan, S.W. Shaw, Performance and dynamic stability of general-path centrifugal pendulum vibration absorbers, J. Sound Vib. 252 (5) (2002) 791–815, http://dx.doi.org/10.1006/jsvi.2000.3534.
[14] B.J. Vidmar, S.W. Shaw, B.F. Feeny, B.K. Geist, Nonlinear interactions in systems of multiple order centrifugal pendulum vibration absorbers, J. Vib. Acoust. 135 (6) (2013) http://dx.doi.org/10.1115/1.4024969.
[15] A.S. Alsuwaiyan, S.W. Shaw, Non-synchronous and localized responses of systems of identical centrifugal pendulum vibration absorbers, Arab. J. Sci. Eng. 39 (12) (2014) 9205–9217, http://dx.doi.org/10.1007/s13369-014-1464-1.
[16] J.S. Issa, S.W. Shaw, Synchronous and non-synchronous responses of systems with multiple identical nonlinear vibration absorbers, J. Sound Vib. 348 (2015) 105–125, http://dx.doi.org/10.1016/j.jsv.2015.03.021.
[17] A. Grolet, A. Renault, O. Thomas, Energy localisation in periodic structures: Application to centrifugal pendulum vibration absorber, in: International Symposium on Transport Phenomena and Dynamics of Rotating Machinery, Maui (Hawaii), 2017.
[18] K. Nishimura, T. Ikeda, Y. Harata, Localization phenomena in torsional rotating shaft systems with multiple centrifugal pendulum vibration absorbers, Nonlinear Dynam. 83 (3) (2016) 1705–1726, http://dx.doi.org/10.1007/s11071-015-2441-2.
[19] C.-T. Lee, S.W. Shaw, The non-linear dynamic response of paired centrifugal pendulum vibration absorbers, J. Sound Vib. 203 (5) (1997) 731–743, http://dx.doi.org/10.1006/jsvi.1996.0707.
[20] C.-T. Lee, S.W. Shaw, V.T. Coppola, A subharmonic vibration absorber for rotating machinery, J. Vib. Acoust. 119 (4) (1997) 590–595, http://dx.doi.org/10.1115/1.2889766.
[21] C.-P. Chao, S.W. Shaw, The effects of imperfections on the performance of the subharmonic vibration absorber system, J. Sound Vib. 215 (5) (1998) 1065–1099, http://dx.doi.org/10.1006/jsvi.1998.1634.
[22] C.-P. Chao, S.W. Shaw, The dynamic response of multiple pairs of subharmonic torsional vibration absorbers, J. Sound Vib. 231 (2) (2000) 411–431, http://dx.doi.org/10.1006/jsvi.1999.2722.
[23] Les amortisseurs dynamiques de vibrations [dynamic vibration dampers], Rev. Tech. Hispano Suiza (3) (1939).
[24] R. Chilton, Rocking dynamic damper, 1939, 2184734.
[25] R.W. Zdanowich, T.S. Wilson, The elements of pendulum dampers, Proc. Inst. Mech. Eng. 143 (1) (1940) 182–210, http://dx.doi.org/10.1243/PIME_PROC_1940_143_028_02.
[26] V. Mahe, A. Renault, A. Grolet, O. Thomas, H. Mahe, Dynamic stability of centrifugal pendulum vibration absorbers allowing a rotational mobility, J. Sound Vib. 517 (2022) 116525, http://dx.doi.org/10.1016/j.jsv.2021.116525.
[27] R.G. Mitchiner, R.G. Leonard, Centrifugal pendulum vibration absorbers—theory and practice, J. Vib. Acoust. 113 (4) (1991) 503–507, http://dx.doi.org/10.1115/1.2930214.

[28] J. Mayet, H. Ulbrich, Tautochronic centrifugal pendulum vibration absorbers: General design and analysis, J. Sound Vib. 333 (3) (2014) 711–729, http://dx.doi.org/10.1016/j.jsv.2013.09.042.
[29] J. Mayet, H. Ulbrich, First-order optimal linear and nonlinear detuning of centrifugal pendulum vibration absorbers, J. Sound Vib. 335 (2015) 34–54, http://dx.doi.org/10.1016/j.jsv.2014.09.017.
[30] J.A.C. Mayet, Centrifugal Vibration Absorbers: Theory and Application (Ph.D. thesis), Technische Universität München, München, 2015.
[31] A. Renault, Calcul et Optimisation d'Absorbeurs Pendulaires Dans une Chaîne de Traction Automobile [Simulation and Optimisation of Pendular Absorbers for Automotive Powertrain] (Ph.D. thesis), ENSAM, Lille, France, 2018.
[32] H. Mahé, A. Renault, O. Thomas, Dispositif d'amortissement pendulaire [pendular damping device], 2018, FR 3 055 038.
[33] H. Mahé, A. Renault, O. Thomas, Dispositif d'amortissement pendulaire [pendular damping device], 2018, FR 3 055 037.
[34] M.A. Acar, Design and Tuning of Centrifugal Pendulum Vibration Absorbers (Ph.D. thesis), Michigan State University, Michigan, 2017.
[35] M. Cirelli, J. Gregori, P. Valentini, E. Pennestrí, A design chart approach for the tuning of parallel and trapezoidal bifilar centrifugal pendulum, Mech. Mach. Theory 140 (2019) 711–729, http://dx.doi.org/10.1016/j.mechmachtheory.2019.06.030.
[36] M. Cirelli, M. Cera, E. Pennestrì, P.P. Valentini, Nonlinear design analysis of centrifugal pendulum vibration absorbers: An intrinsic geometry-based framework, Nonlinear Dynam. 102 (3) (2020) 1297–1318, http://dx.doi.org/10.1007/s11071-020-06035-1.
[37] M. Cera, M. Cirelli, E. Pennestrì, P. Valentini, The kinematics of curved profiles mating with a caged idle roller - higher-path curvature analysis, Mech. Mach. Theory 164 (2021) 104414, http://dx.doi.org/10.1016/j.mechmachtheory.2021.104414.
[38] M. Cera, M. Cirelli, E. Pennestrì, P.P. Valentini, Design analysis of torsichrone centrifugal pendulum vibration absorbers, Nonlinear Dynam. 104 (2) (2021) 1023–1041, http://dx.doi.org/10.1007/s11071-021-06345-y.
[39] M. Cera, M. Cirelli, E. Pennestrì, P.P. Valentini, Nonlinear dynamics of torsichrone CPVA with synchroringed form closure constraint, Nonlinear Dynam. (2021) http://dx.doi.org/10.1007/s11071-021-06732-5.
[40] X. Tan, S. Yang, J. Yang, J. Li, Study of dynamics of rotational centrifugal pendulum vibration absorbers based on tautochronic design, Meccanica (2021) http://dx.doi.org/10.1007/s11012-021-01340-4.
[41] E.R. Gomez, I.L. Arteaga, L. Kari, Normal-force dependant friction in centrifugal pendulum vibration absorbers: Simulation and experimental investigations, J. Sound Vib. 492 (2021) 115815, http://dx.doi.org/10.1016/j.jsv.2020.115815.
[42] E.R. Gomez, J. Sjöstrand, L. Kari, I.L. Arteaga, Torsional vibrations in heavy-truck powertrains with flywheel attached centrifugal pendulum vibration absorbers, Mech. Mach. Theory 167 (2022) 104547, http://dx.doi.org/10.1016/j.mechmachtheory.2021.104547.
[43] K. Kadoi, T. Inoue, J. Kawano, M. Kondo, Nonlinear analysis of a torsional vibration of a multidegrees-of-freedom system with centrifugal pendulum vibration absorbers and its suppression, J. Vib. Acoust. 140 (6) (2018) 061008, http://dx.doi.org/10.1115/1.4040042.
[44] C. Shi, R.G. Parker, Modal properties and stability of centrifugal pendulum vibration absorber systems with equally spaced, identical absorbers, J. Sound Vib. 331 (21) (2012) 4807–4824, http://dx.doi.org/10.1016/j.jsv.2012.05.018.
[45] C. Shi, R.G. Parker, Modal structure of centrifugal pendulum vibration absorber systems with multiple cyclically symmetric groups of absorbers, J. Sound Vib. 332 (18) (2013) 4339–4353, http://dx.doi.org/10.1016/j.jsv.2013.03.009.
[46] C. Shi, R.G. Parker, S.W. Shaw, Tuning of centrifugal pendulum vibration absorbers for translational and rotational vibration reduction, Mech. Mach. Theory 66 (2013) 56–65, http://dx.doi.org/10.1016/j.mechmachtheory.2013.03.004.
[47] C. Shi, R.G. Parker, Vibration modes and natural frequency veering in three-dimensional, cyclically symmetric centrifugal pendulum vibration absorber systems, J. Vib. Acoust. 136 (1) (2014) 011014, http://dx.doi.org/10.1115/1.4025678.
[48] C. Shi, S.W. Shaw, R.G. Parker, Vibration reduction in a tilting rotor using centrifugal pendulum vibration absorbers, J. Sound Vib. 385 (2016) 55–68, http://dx.doi.org/10.1016/j.jsv.2016.08.035.
[49] V. Mahe, A. Renault, A. Grolet, H. Mahe, O. Thomas, Subharmonic centrifugal pendulum vibration absorbers allowing a rotational mobility, Mech. Syst. Signal Process. 177 (2022) 109125, http://dx.doi.org/10.1016/j.ymssp.2022.109125.
[50] V. Mahé, A. Renault, A. Grolet, H. Mahe, O. Thomas, On the stability of pairs of subharmonic centrifugal pendulum vibration absorbers allowing a rotational mobility, Nonlinear Dyn. (2022) submitted for publication.
[51] V. Mahé, A. Renault, A. Grolet, H. Mahé, O. Thomas, Localised response of a centrifugal pendulum vibration absorber, Nonlinear Dyn. (2022) submitted for publication.
[52] J. Mayet, M.A. Acar, S.W. Shaw, Effective and robust rocking centrifugal pendulum vibration absorbers, J. Sound Vib. 527 (2022) 116821, http://dx.doi.org/10.1016/j.jsv.2022.116821.
[53] B. Geist, V. Ramakrishnan, P. Attibele, W. Resh, Precision requirements for the bifilar hinge slots of a centrifugal pendulum vibration absorber, Precis. Eng. 52 (2018) 1–14, http://dx.doi.org/10.1016/j.precisioneng.2017.08.001.
[54] V. Manchi, C. Sujatha, Torsional vibration reduction of rotating shafts for multiple orders using centrifugal double pendulum vibration absorber, Appl. Acoust. 174 (2021) 107768, http://dx.doi.org/10.1016/j.apacoust.2020.107768.
[55] D.E. Newland, Nonlinear aspects of the performance of centrifugal pendulum vibration absorbers, J. Eng. Ind. 86 (3) (1964) 257–263, http://dx.doi.org/10.1115/1.3670529.
[56] M. Sharif-Bakhtiar, S.W. Shaw, Effects of nonlinearities and damping on the dynamic response of a centrifugal pendulum vibration absorber, J. Vib. Acoust. 114 (3) (1992) 305–311, http://dx.doi.org/10.1115/1.2930262.
[57] A.G. Haddow, S.W. Shaw, Centrifugal pendulum vibration absorbers: An experimental and theoretical investigation, Nonlinear Dynam. 34 (3/4) (2003) 293–307, http://dx.doi.org/10.1023/B:NODY.0000013509.51299.c0.
[58] A. Renault, O. Thomas, H. Mahé, Numerical antiresonance continuation of structural systems, Mech. Syst. Signal Process. 116 (2019) 963–984, http://dx.doi.org/10.1016/j.ymssp.2018.07.005.
[59] S.W. Shaw, S. Wiggins, Chaotic dynamics of a whirling pendulum, Physica D 31 (2) (1988) 190–211, http://dx.doi.org/10.1016/0167-2789(88)90076-0.
[60] L. Shen, B.W. Suter, Bounds for eigenvalues of arrowhead matrices and their applications to hub matrices and wireless communications, EURASIP J. Adv. Signal Process. 2009 (1) (2009) 379402, http://dx.doi.org/10.1155/2009/379402.
[61] S.W. Shaw, M.A. Acar, B.F. Feeny, B.K. Geist, Modal properties of rotating shafts with order-tuned absorbers, in: J. De Clerck (Ed.), Topics in Modal Analysis I, Vol. 7, Springer International Publishing, Cham, 2014, pp. 181–189, http://dx.doi.org/10.1007/978-3-319-04753-9_18.
[62] M. Auleley, C. Giraud-Audine, H. Mahé, O. Thomas, Tunable electromagnetic resonant shunt using pulse-width modulation, J. Sound Vib. 500 (2021) 116018, http://dx.doi.org/10.1016/j.jsv.2021.116018.
[63] A.H. Nayfeh, Perturbation Methods, in: Wiley Classics Library, Wiley-VCH, Weinheim, 1973, http://dx.doi.org/10.1002/9783527617609.
[64] M. Golubitsky, I. Stewart, D.G. Schaeffer, in: J.E. Marsden, L. Sirovich (Eds.), Singularities and Groups in Bifurcation Theory, in: Applied Mathematical Sciences, vol. 2, Springer New York, New York, NY, 1988, http://dx.doi.org/10.1007/978-1-4612-4574-2.
[65] L. Guillot, A. Lazarus, O. Thomas, C. Vergez, B. Cochelin, A purely frequency based Floquet-Hill formulation for the efficient stability computation of periodic solutions of ordinary differential systems, J. Comput. Phys. 416 (2020) 109477, http://dx.doi.org/10.1016/j.jcp.2020.109477.
[66] L. Guillot, B. Cochelin, C. Vergez, A taylor series-based continuation method for solutions of dynamical systems, Nonlinear Dynam. 98 (4) (2019) 2827–2845, http://dx.doi.org/10.1007/s11071-019-04989-5.
[67] S.W. Shaw, P.M. Schmitz, A.G. Haddow, Tautochronic vibration absorbers for rotating systems, J. Comput. Nonlinear Dyn. 1 (4) (2006) 283–293, http://dx.doi.org/10.1115/1.2338652.
[68] R.J. Monroe, S.W. Shaw, A.H. Haddow, B.K. Geist, Accounting for roller dynamics in the design of bifilar torsional vibration absorbers, J. Vib. Acoust. 133 (6) (2011) http://dx.doi.org/10.1115/1.4003942.
[69] C.-T. Lee, S.W. Shaw, On the counteraction of periodic torques for rotating systems using centrifugally driven vibration absorbers, J. Sound Vib. 191 (5) (1996) 695–719, http://dx.doi.org/10.1006/jsvi.1996.0151.

Chapter 5

The localised response of centrifugal pendulums

This chapter is made of a paper about to be submitted to *Nonlinear Dynamics* [152]. It focuses on predicting the localised response of a centrifugal pendulum vibration absorber (CPVA) which arises through instabilities of the classical CPVA operation. The aim to provide a better understanding of this localised behaviour. This study makes use of the simplified CPVA model described in section 2.3.1.

Sections 1 to 3.1 repeat information from chapters 1 and 2. They present the context of the study, the modelling of a CPVA (*cf.* section 2.1.1), a linear analysis (*cf.* section 2.2) and the simplification of the equations of motion (*cf.* section 2.3). The reader might want to skip these sections of the article if he already read chapters 1 and 2.

The novelty of the article starts in section 3.2, where the simplified equations of a CPVA (*cf.* section 2.3.1) are projected on the modal basis. In section 4, the modal responses are computed and the stability of the coupled-mode solution is assessed using the method of multiple scales (*cf.* section 2.5.2.1). The modal approach highlights that the localised response is due to this coupled-mode response for which both the unison and phase-opposition modes contribute to the pendulums' response, causing them to oscillate differently. The results are applied to case studies in section 5 and verified using numerical resolutions of the system's dynamics. Bifurcations towards quasi-periodic solutions are captured both analytically and numerically. The numerical investigation of these quasi-periodic solutions showed that they can also become unstable and lead to chaotic responses of the CPVA. We also show that, in some particular cases, the localisation does not limit the torque capacity of the system and improves the vibration reduction. In such situations, localisation is beneficial to the performance of the CPVA.

The localised response of centrifugal pendulum vibration absorbers allowing a rotational mobility

Vincent Mahé[1,2*], Alexandre Renault[2], Aurélien Grolet[1], Hervé Mahé[2] and Olivier Thomas[1]

[1*]Arts et Metiers Institute of Technology, LISPEN, HESAM Université, Boulevard Louis XIV, Lille, F-59000, France.
[2]Centre d'Étude des Produits Nouveaux, Valeo Transmissions, Espace Industriel Nord, Route de Poulainville, Amiens Cedex 1, 80009, France.

*Corresponding author(s). E-mail(s): vincent.mahe@ensam.eu;
Contributing authors: alexandre.renault@valeo.com;
aurelien.grolet@ensam.eu; herve.mahe@valeo.com;
olivier.thomas@ensam.eu;

Abstract

Rotating machines are often subjected to fluctuating torques, leading to vibrations of the rotor and finally to premature fatigue and noise pollution. These vibrations can be reduced using centrifugal pendulum vibration absorbers (CPVA). These passive devices are made of several masses (pendulums) oscillating along a given trajectory and rotating relatively to the rotor. Previous studies showed that the dynamics of these devices is subject to instabilities leading to localisation of the motion of the masses. In this paper, the localised behaviour of a CPVA made of two pendulums allowed to rotate about their center of mass is investigated. To this aim, a dynamical model based on an analytic perturbation method is established. The aim of this model is to highlight some special features of the localised response, such as the appearance of quasi-periodic regimes. The case studies showed that in some special cases, localisation can improve the filtration as compared to a unison motion. The validity of the model was confirmed through a comparison with a numerical resolution of the system's dynamics.

Keywords: centrifugal pendulum vibration absorber, nonlinear dynamics, stability, energy localisation, Neimark-Sacker bifurcation

1 Introduction

Centrifugal pendulum vibration absorbers (CPVAs) are passive devices that have been used for many years to reduce the torsional vibrations of rotating machines [1–3]. They consist of oscillating masses (pendulums) moving along particular paths relative to a primary inertia (rotor), as shown in Fig. 1. Contrarily to tuned mass damper systems (TMD) [4, 5], CPVAs are tuned to an order[1], not a frequency. This enables CPVAs to reduce the vibrations at every rotational speed while a TMD can operate only around a resonance of the rotating machine [6].

CPVAs exhibit strong nonlinearities: geometric nonlinearities due to the large amplitude of motion, and inertial nonlinearities, for instance due to Coriolis effect. The nonlinear response of a CPVA is strongly affected by the choice of the pendulums' trajectory. D. E. Newland observed early on that circular trajectories yield a softening response of the system, leading to jumps of the response [2]. J. F. Madden proposed to use cycloidal trajectories [7], which were earlier shown by C. Huygens to be the tautochronic trajectories of pendulums oscillating in the gravity field [8]. However, cycloids confer a hardening behaviour to the response of centrifugal pendulums. Still, this has the benefit of preventing the jumps of the response. It is H. H. Denman who demonstrated that the tautochronic trajectory of pendulums oscillating in a constant centrifugal acceleration field is an epicycloid [9]. Nevertheless, in the case of a CPVA, there are additional nonlinearities coming from the coupling between the rotor and the pendulums [10–12] so that epicycloidal trajectories no longer yield a tautochronic response [13].
Less than ten years ago, J. Mayet and H. Ulbrich showed that pendulums allowed to rotate about their center of mass could reduce the vibrations more efficiently thanks to the contribution of their rotational inertia [14]. Since this work, many studies on CPVAs consider the rotation of the pendulums [15–19]. A. Renault [20–22] and M. A. Acar [23] were the first to investigate in details the effect of rotation on the linear and nonlinear response of the system. Since their works, new studies on rotation law were led by M. Cirelli *et al.* [24], M. Cera *et al.* [25], X. Tan *et al.* [26], J. Mayet *et al.* [27] and V. Mahé *et al.* [13, 28–31].

Due to their cyclic symmetry, CPVAs are subjected to nonlinear energy localisation phenomena, causing the pendulums to oscillate with different

[1] An order is the proportionality coefficient between a frequency and the rotational speed of the rotating machine

phases and amplitudes. The first studies on such instabilities of the unison response were led by C.-P. Chao *et al.* [10], who considered pendulums following an epicycloidal path. The case of more general paths was then investigated by A. S. Alsuwaiyan *et al.* [32], S. Shaw *et al.*[12] and A. Grolet *et al.* [33]. The localisation phenomenon was also observed in several experimental studies [28, 34–36]. Localisation in the presence of rotating pendulums was studied in [13, 25, 37]. V. Mahé *et al.* showed that the rotation law can be chosen such that the nonlinearities it generates balance with those coming from the trajectory, resulting in a linear pendulums' response and preventing the apparition of instabilities [28]. Furthermore, several papers focused on the localised solution itself. Symmetric bifurcation theory was used in [11] to study N perfectly-tuned pendulums riding along an epicycloidal path. The case of mistuned pendulums following more general trajectories was investigated in [38, 39]. [40] focused on simple pendulums (thus following a circular path) with a torsional stiffness at their pivot point. Localised solutions were computed using numerical methods and bifurcations leading to quasi-periodic and chaotic responses were observed.

The motivation of this paper is to present an analytical procedure to compute the localised solution of a CPVA and to assess its stability. The CPVA considered in this paper is made of two pendulums following a general path and allowed to rotate relatively to the rotor. To our knowledge, the only analytical study of the localised solution considered purely translated pendulums following an epicycloidal path [11], and the case of other trajectories was investigated solely numerically [38–41]. Analytic computations allow for easier (though less accurate) simulations than numerical methods, making them well-suited to explore the large particularities the localised solution. The non-unison response is usually undesired for two reasons. Firstly, it is believed to decrease the filtration performances, though some studies revealed a slight increase of performance due to localisation [40, 41]. Secondly, localisation causes one (or more) pendulum to oscillate with a larger amplitude than if it were responding at unison. Because the trajectories are limited by a cusp point, this increase of amplitude is problematic as it reduces the torque capacity of the system. In this paper, we will show that localisation can lead to a large increase in performance while not affecting the torque capacity. Finally, in addition to the saddle-node bifurcations of the localised solution, we use the Routh-Hurwitz criterion to find analytically Neimark-Sacker bifurcations leading to quasi-period regimes.

This paper is organised as follows: section 2 describes the modelling of the CPVA and presents its linear characteristics. The complete equations of motion are simplified in section 3 and the modal equations are derived. Analytical solutions of the modal and physical coordinates together with their stability are derived in section 4. Case studies are presented in section 5 and the paper ends with a conclusion in section 6.

2 Modelling and linear analysis

2.1 Modelling

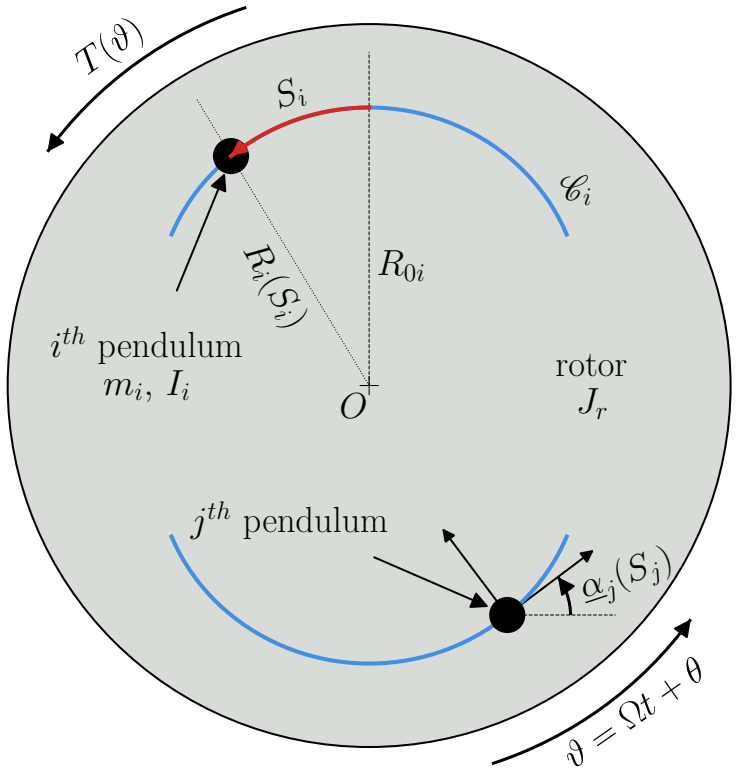

Figure 1: Representation of the system studied for $N = 2$ pendulums.

The system studied is shown in Fig. 1. It is made of a rotor of inertia J_r rotating about its centre O. Its total angular position is $\vartheta(t) = \Omega t + \theta(t)$ where t is the time, Ω is the mean rotational velocity and $\theta(t)$ corresponds to the fluctuating part of the rotation. A torque $T(\vartheta) = T_0 + T_\theta(\vartheta)$ is applied to the rotor where T_0 is its constant part and $T_\theta(\vartheta)$ is periodic. At equilibrium, $T_0 = b_r\Omega$ where b_r is the linear viscous damping coefficient of the rotor, such that the constant torque balances with the damping to set the mean rotational speed Ω. N pendulums of mass m_i and inertia I_i (about their centre of gravity) oscillate on their trajectory $\mathscr{C}_i$. The position of their center of gravity on these trajectories is given by the curvilinear abscissa $S_i(t)$ and their distance from O is $R_i(S_i)$. The characteristic dimension $R_{0i} = R_i(S_i = 0)$ is the distance between O and the vertex of the trajectory. In addition to the traditional translation motion, the present study considers that the pendulums rotate about their centre of mass according to the rotation function $\underline{\alpha}_i(S_i)$. As for the rotor, an equivalent linear viscous damping b_i is used to model the damping between the rotor and the i^{th} pendulum. In the later, pendulums and

their associated trajectory and rotation functions will be considered identical so that subscript "i" will be dropped when addressing pendulums' parameters.

In order to write the equations of motion in a non-dimensional form, the following parameters and variables are introduced:

$$\begin{gathered} s_i = \frac{S_i}{R_0}, \quad \eta = \frac{I}{mR_0^2}, \quad \mu = \frac{NmR_0^2}{J_r + NI}, \\ \bar{b} = \frac{b}{m\Omega}, \quad \bar{b}_r = \frac{b_r}{(J_r + NI)\Omega}, \quad \bar{T}(\vartheta) = \bar{T}_0 + \bar{T}_\theta(\vartheta) = \frac{T(\vartheta)}{(J_r + NI)\Omega^2}, \\ x(s_i) = \frac{R(R_0 s_i)^2}{R_0^2}, \quad z(s_i) = \sqrt{x(s_i) - \frac{1}{4}\left(\frac{dx(s_i)}{ds_i}\right)^2}, \\ \alpha(s_i) = \underline{\alpha}(R_0 s_i), \quad \gamma(s_i) = \frac{d\alpha(s_i)}{ds_i}, \quad \tau = \Omega t, \end{gathered} \tag{1}$$

where τ is a dimensionless time. Moreover, it is chosen to express the trajectory and rotation functions as polynomials such that

$$x(s_i) = 1 - n_t^2 s_i^2 + \sum_{k=3}^{\infty} x_{[k]} s_i^k, \quad \alpha(s_i) = \sum_{k=1}^{\infty} \alpha_{[k]} s_i^k, \tag{2}$$

where n_t is the order of the pendulums' trajectory (also called geometric tuning order [17]), and $x_{[k]}$ and $\alpha_{[k]}$ are trajectory and rotation coefficients. In the case $x_{[k]} = 0$, $\forall k$, the pendulums' trajectories are epicycloids, which are the tautochronic trajectories when the rotor spins at a constant speed [9]. Hence, for $k > 1$, $x_{[k]}$ and $\alpha_{[k]}$ represent the deviation from an epicycloid and a linear rotation law, respectively. In case the $x_{[k]}$ are small $\forall k$, the cusp of the trajectory can be approximated by the cusp of the epicycloid, given by [9]

$$s_{\text{cusp}} = \frac{1}{n_t\sqrt{1 + n_t^2}}. \tag{3}$$

Using the dimensionless quantities (1), the equations of motion can be written as [29]

$$\frac{1}{N}\left[\sum_{i=1}^{N}(N+\mu x(s_i))\theta'' + \mu\left(z(s_i)+\eta\gamma(s_i)\right)s_i'' + \mu s_i'\left(\frac{dx(s_i)}{ds_i}(1+\theta') + \frac{dz(s_i)}{ds_i}s_i' + \eta\frac{d\gamma(s_i)}{ds_i}s_i'\right)\right] + \bar{b}_r\theta' = \bar{T}_\theta(\vartheta), \tag{4a}$$

$$\left(z(s_i)+\eta\gamma(s_i)\right)\theta'' + \left(1+\eta\gamma(s_i)^2\right)s_i'' + \eta\gamma(s_i)\frac{d\gamma(s_i)}{ds_i}s_i'^2 - \frac{1}{2}\frac{dx(s_i)}{ds_i}(1+\theta')^2 + \bar{b}s_i' = 0, \quad i=1,...,N, \tag{4b}$$

where $(\bullet)' = \partial(\bullet)/\partial\tau$. Equation (4a) is related to the motion of the rotor and the N Eqs. (4b) represent the motion of the pendulums. From now on, it is assumed that the fluctuating torque applied to the rotor contains only one harmonic. Its non-dimensional form is $\bar{T}_1\cos(n\vartheta)$ where n is the engine order. To transform this torque into a periodic forcing term, one can simply assume $\vartheta \approx \tau$ [28]. Moreover, this paper focuses on the analysis of a CPVA made of two pendulums, so that $N=2$ in the following.

2.2 Linear vibrations of the system

In this section, a linear analysis of the system is led. One can linearise Eqs. (4a) and (4b) to find that the eigenorders[1] and eigenvectors of the system are

$$n_{00}=0, \quad n_{10}=n_p, \quad n_{20}=n_p\sqrt{\frac{1+\mu}{1+\mu\left(1-\frac{\Lambda_c^2}{\Lambda_m}\right)}}$$
$$\boldsymbol{\phi_0}=[1,0,0]^\intercal, \quad \boldsymbol{\phi_1}=[0,1,-1]^\intercal, \quad \boldsymbol{\phi_2}=\left[-\frac{\mu\Lambda_c}{1+\mu},1,1\right]^\intercal. \tag{5}$$

Superscript $^\intercal$ denotes the transpose. Λ_m and Λ_c are constants representing the equivalent mass of a pendulum and the linear coupling term between a pendulum and the rotor, respectively. They are given by

$$\Lambda_m = 1+\eta\alpha_{[1]}^2, \quad \Lambda_c = 1+\eta\alpha_{[1]}, \tag{6}$$

where $\alpha_{[1]}$ is the linear rotation coefficient. n_p is the tuning order of the pendulums and corresponds to their eigenorder when they are uncoupled from the rotor (i.e. the rotor is spinning at constant speed and is no longer a degree of

[1] The eigenorders are analogous to eigenfrequencies. They can even be seen as dimensionless eigenfrequencies.

freedom). Considering the case $\theta = 0$ and linearising Eqs. (4b), one finds that n_p is related to n_t such that

$$n_p = n_t/\sqrt{\Lambda_m}. \tag{7}$$

$(n_{00}, \boldsymbol{\phi_0})$, $(n_{10}, \boldsymbol{\phi_1})$ and $(n_{20}, \boldsymbol{\phi_2})$ will be referred-to as modes 0, 1 and 2, respectively. They are represented in Fig. 2. Mode 0 is a rigid body mode for which only the rotor is excited. Mode 1 corresponds to an phase-opposition motion of the pendulums and the rotor is a node of this mode. Mode 2 is a mode for which pendulums move in unison and in phase-opposition with respect to the rotor (provided that $\Lambda_c > 0$, which is the case in practice).

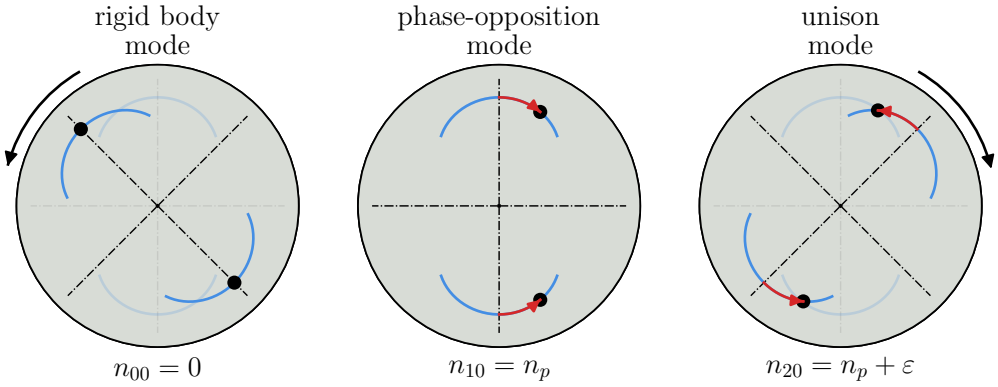

Figure 2: Modes of a CPVA made of $N = 2$ pendulums. The rotation of the pendulums about their centre of mass is not represented in this figure. ε indicates that n_{20} is slightly larger than n_p.

When a fluctuating torque is applied, the pendulums respond on mode 2 and generate an antiresonance on the rotor at order n_p. Thus, for a fluctuating torque of order n, one typically chooses $n_p \approx n$ to minimise the vibrations of the rotor. However, nonlinear effects can cause mode 1 to participate to the response. If $n \approx 2n_p$, a subharmonic response of mode 1 exists [29, 30, 42], but this is out of the scope of this paper as we will focus on $n \approx n_p$. In this case, the contribution of mode 1 to the systems' response is manifested through the apparition of a localised solution.

3 Simplified equations

Following S. Shaw *et al.* [32], the construction of the model starts with a scaling of the parameters, allowing a simplification of the equations of motion such that the dynamics of the pendulums becomes uncoupled from that of the rotor. The beginning of the procedure is detailed in [28], so only the main steps are reminded here. Then, simplified modal equations will be derived. The

trajectory and rotation functions followed by the pendulums, whose general form is given by Eq. (2), are chosen to be

$$x(s_i) = 1 - n_t^2 s_i^2 + x_{[4]} s_i^4, \quad \alpha(s_i) = \alpha_{[1]} s_i + \alpha_{[3]} s_i^3. \tag{8}$$

There are no odd powers of s_i in $x(s_i)$ and no even powers in $\alpha(s_i)$ so that these two functions are symmetric (anti-symmetric, respectively) about $s_i = 0$. It is the case in practice due to design constraints. In addition, we only consider low powers of s_i in $x(s_i)$ and $\alpha(s_i)$ as s_i will be considered small in the following (*cf.* section 3.1). The fluctuating rotor's rotation can be expanded as

$$\theta = \theta_1 + \theta_2 + HOT, \tag{9}$$

where θ_1 and θ_2 have different orders of magnitude (*cf.* section 3.1), and *HOT* refers to *Higher Order Terms*.

3.1 Scaling and simplified physical equations

According to relevant remarks and assumptions [28], the parameters and variables can be scaled as

$$\begin{aligned} &\bar{b} = \epsilon^{\ell} \tilde{b}, \quad \bar{b}_r = \epsilon^{h} \tilde{b}_r, \quad \bar{T}_1 = \epsilon^{r} \tilde{T}_1, \quad \mu = \epsilon^{\phi} \tilde{\mu}, \quad \theta_1 = \epsilon^{w_1} \tilde{\theta}_1, \\ &\theta_2 = \epsilon^{w_2} \tilde{\theta}_2, \quad s_i = \epsilon^{\nu} \tilde{s}_i, \quad x_{[4]} = \epsilon^{p} \tilde{x}_{[4]}, \quad \alpha_{[3]} = \epsilon^{q} \tilde{\alpha}_{[3]}, \end{aligned} \tag{10}$$

where ℓ, h, r, ϕ, w_1, w_2, ν, p and q are scaling coefficients to be determined and ϵ is a small parameter. Then, the simplified equations of the rotor and the pendulums are obtained using the trajectory and rotation functions (8), the expanded form of θ (9), the scaled parameters (10), and choosing the set of scaling coefficients

$$\phi = \ell = 1, \quad \nu = 1/2, \quad p = q = 0, \quad r = w_1 = 3/2, \quad w_2 = 2, \quad h > \nu. \tag{11}$$

This set was chosen to match the assumptions while uncoupling the pendulums' equation from the rotor's dynamics and keeping the desired terms at first order. The same scaling was used in [32, 38, 39, 43, 44] for purely translated

pendulums. The rotor's and pendulums' simplified equations are

$$\tilde{\theta}_1'' + \epsilon^{1/2}\tilde{\theta}_2'' = \left[\tilde{T}_1\cos(n\tau) + \frac{n_p^2\tilde{\mu}\Lambda_c}{N}\sum_{i=1}^{N}\tilde{s}_i\right] + \epsilon^{1/2}\frac{2\tilde{\mu}n_t^2}{N}\sum_{i=1}^{N}\tilde{s}_i\tilde{s}_i' + HOT, \tag{12a}$$

$$\tilde{s}_i'' + n_p^2\tilde{s}_i = -\epsilon\Lambda_m^{-1}\left[-2\tilde{x}_{[4]}\tilde{s}_i^3 + 6\eta\alpha_{[1]}\tilde{\alpha}_{[3]}(\tilde{s}_i^2\tilde{s}_i'' + \tilde{s}_i\tilde{s}_i'^2) + \tilde{b}\tilde{s}_i' + \Lambda_c\tilde{T}_1\cos(n\tau) + \frac{n_p^2\tilde{\mu}\Lambda_c^2}{N}\sum_{j=1}^{N}\tilde{s}_j\right] + HOT, \quad i = 1, 2, \tag{12b}$$

respectively. At the order retained in the rotor's equation (12a), only linear and quadratic terms in s_i are present. The pendulums' equations (12b) contain the influence of the external torque, the pendulums' damping, the coupling between pendulums through the sum over N, and nonlinearities coming from both the trajectory and the rotation. Equations (12b) are weakly coupled because pendulums are coupled indirectly through the rotor and their effect on the rotor is small as their relative inertia is small [45]. Moreover, these equations are weakly nonlinear because s_i were assumed small and the trajectory and rotation functions chosen are close to an epicycloid and a linear rotation, which render a linear behaviour for small fluctuations of the rotational speed. Note that at the order retained, the nonlinearities coming from the coupling between the rotor and the pendulums are missed [10, 12, 13, 29], so that the only nonlinearities of the system are due to the perturbation of the trajectory and rotation functions.

3.2 Simplified modal equations

Equations (12b) can be written in matrix form using the vector of unknowns

$$\boldsymbol{q} = [\tilde{s}_1, \tilde{s}_2] = \sum_{k=1}^{2}\zeta_k\boldsymbol{\psi}_k, \tag{13}$$

where $\boldsymbol{\psi}_k$ are the reduced eigenvectors

$$\boldsymbol{\psi}_1 = [1, -1], \quad \boldsymbol{\psi}_2 = [1, 1]. \tag{14}$$

They simply correspond to the eigenvectors of the full system without the rotor's component (*cf.* Eq. (5)). It is possible to use only those two modes because mode 0 is a rigid body mode that does not affect the pendulums' response (*cf.* section 2.2). ζ_1 and ζ_2 are the modal coordinates associated to the reduced modes $(n_{10}, \boldsymbol{\psi}_{10})$ and $(n_{20}, \boldsymbol{\psi}_{20})$, respectively. Projecting the pendulums' matrix equation on the reduced modes leads to the two modal equations

$$\zeta_1'' + n_p^2 \zeta_1 = f_1(\zeta_1, \zeta_2, \tau), \tag{15a}$$
$$\zeta_2'' + n_p^2 \zeta_2 = f_2(\zeta_1, \zeta_2, \tau). \tag{15b}$$

where functions f_1 and f_2 are given by

$$\begin{aligned} f_1(\zeta_1, \zeta_2, \tau) = &- \epsilon \Lambda_m^{-1} \Big[\tilde{b}\zeta_1' - 2\tilde{x}_{[4]}(\zeta_1^3 + 3\zeta_1\zeta_2^2) + 6\eta\alpha_{[1]}\tilde{\alpha}_{[3]}(\zeta_1 {\zeta_1'}^2 \\ &+ 2\zeta_2\zeta_1'\zeta_2' + \zeta_1{\zeta_2'}^2 + \zeta_1^2\zeta_1'' + 2\zeta_1\zeta_2\zeta_2'' + \zeta_2^2\zeta_1'') \Big], \end{aligned} \tag{16a}$$

$$\begin{aligned} f_2(\zeta_1, \zeta_2, \tau) = &- \epsilon \Lambda_m^{-1} \Big[\tilde{b}\zeta_2' - 2\tilde{x}_{[4]}(\zeta_2^3 + 3\zeta_1^2\zeta_2) + 6\eta\alpha_{[1]}\tilde{\alpha}_{[3]}(\zeta_2 {\zeta_2'}^2 \\ &+ 2\zeta_1\zeta_1'\zeta_2' + \zeta_2{\zeta_1'}^2 + \zeta_2^2\zeta_2'' + 2\zeta_1\zeta_2\zeta_1'' + \zeta_1^2\zeta_2'') \\ &+ \Lambda_c \left(\tilde{T}_1 \cos(n\tau) + n_p^2 \tilde{\mu} \Lambda_c \zeta_2 \right) \Big]. \end{aligned} \tag{16b}$$

One can see that the external torque only appears in f_2, which is consistent with pendulums oscillating at unison in the linear regime. However, nonlinearities induce a strong modal coupling such that ζ_2 can exchange energy with ζ_1 through a 1:1 internal resonance [46, 47]. This situation results in a coupled-mode solution leading to energy localisation on a pendulum. Indeed, the pendulums' coordinates are

$$\tilde{s}_1 = \zeta_2 + \zeta_1, \tag{17a}$$
$$\tilde{s}_2 = \zeta_2 - \zeta_1, \tag{17b}$$

and one can see that when $\zeta_1 \neq 0$, the pendulums oscillate with different amplitudes and/or phases.

4 Modal and physical solutions and stability analysis

4.1 Application of the method of multiple scales

Now, the simplified modal equations are solved using the method of multiple scales [48]. Two time scales are introduced, $\tau_0 = \tau$ and $\tau_1 = \epsilon\tau$, and the modal coordinates are expanded such that

$$\zeta_1(\tau) = \zeta_{11}(\tau_0, \tau_1) + \epsilon\zeta_{12}(\tau_0, \tau_1), \tag{18a}$$
$$\zeta_2(\tau) = \zeta_{21}(\tau_0, \tau_1) + \epsilon\zeta_{22}(\tau_0, \tau_1). \tag{18b}$$

Applying the method of multiple scales yields solutions of the form

$$\zeta_{11}(\tau_0, \tau_1) = u_1(\tau_1)\cos(n\tau_0 - \beta_1(\tau_1)), \tag{19a}$$
$$\zeta_{21}(\tau_0, \tau_1) = u_2(\tau_1)\cos(n\tau_0 - \beta_2(\tau_1)). \tag{19b}$$

Amplitudes u_1, u_2 and phases β_1, β_2 are governed by the system

$$\begin{cases} D_1 u_1 = f_{u_1}(\boldsymbol{u}, \boldsymbol{\beta}), & \text{(20a)} \\ u_1 D_1 \beta_1 = f_{\beta_1}(\boldsymbol{u}, \boldsymbol{\beta}), & \text{(20b)} \\ D_1 u_2 = f_{u_2}(\boldsymbol{u}, \boldsymbol{\beta}), & \text{(20c)} \\ u_2 D_1 \beta_2 = f_{\beta_2}(\boldsymbol{u}, \boldsymbol{\beta}), & \text{(20d)} \end{cases}$$

where $D_1(\bullet) = \partial(\bullet)/\partial\tau_1$, $\boldsymbol{u} = [u_1, u_2]^\intercal$ and $\boldsymbol{\beta} = [\beta_1, \beta_2]^\intercal$. Functions f_{u_1}, f_{β_1}, f_{u_2} and f_{β_2} are given in Appendix A. The solutions sought are those at steady state, which corresponds to

$$D_1 u_1 = D_1 u_2 = D_1 \beta_1 = D_1 \beta_2 = 0. \tag{21}$$

The form of system (20) can lead to two types of solutions :

- $(u_1 = 0,\ u_2 \neq 0)$ corresponds to the unison solution for which all pendulums move in a synchronous motion.
- $(u_1 \neq 0,\ u_2 \neq 0)$ corresponds to the coupled-mode solution leading to localisation on a pendulum.

4.2 Unison solution

The unison solution is obtained by solving Eqs. (20c) and (20d) for $u_1 = 0$. This leads to

$$\sigma = \frac{1}{2\Lambda_m n_p}\left[\Lambda_c^2 n_p^2 \tilde{\mu} - \frac{c_p}{2}u_2^2 \pm \sqrt{\Lambda_c^2 \frac{\tilde{T}_1^2}{u_2^2} - n_p^2 \tilde{b}^2}\right], \tag{22a}$$

$$\tilde{T}_1 = \frac{u_2}{\Lambda_c}\left[\left(\frac{c_p}{2}u_2^2 + 2\Lambda_m n_p \sigma - n_p^2 \tilde{\mu}\Lambda_c^2\right)^2 + n_p^2 \tilde{b}^2\right]^{1/2}, \tag{22b}$$

$$\tan(\beta_2) = -2n_p\tilde{b}\left[4\Lambda_m n_p \sigma - 2\Lambda_c^2 n_p^2 \tilde{\mu} + c_p u_2^2\right]^{-1}, \tag{22c}$$

where σ and c_p are a detuning term and a nonlinear coefficient related to the perturbations of the trajectory and rotation law, respectively. They are defined as

$$n = n_p + \epsilon\sigma, \tag{23}$$

$$c_p = 3(x_{[4]} + 2n_p^2 \eta \alpha_{[1]}\alpha_{[3]}). \tag{24}$$

The backbone curve of mode 2 is obtained by setting $\tilde{b} = \tilde{T}_1 = 0$ in Eq. (22a), leading to

$$n_2 = n_p - \frac{c_p}{4\Lambda_m n_p}u_2^2. \tag{25}$$

Equation (25) shows that the hardening/softening behaviour of mode 2 is governed by c_p. As c_p can be controlled through the values of $x_{[4]}$ and $\alpha_{[3]}$, it

can be seen as the nonlinear tuning parameter of the system.

The stability of the unison solution is not easy to assess with the current coordinates. To compute it, one should first rewrite system (20) using cartesian coordinates, as done in [29]. Then, the stability can be assessed by computing the Jacobian of the cartesian system and evaluating the sign of the real part of its eigenvalues. An easier way is to analyse the Jacobian of the system of physical coordinates. This was done in [28] and led to the bifurcation curves

$$u_{2sn} = \sqrt{\frac{-8\sigma\Lambda_m n_p + 4\Lambda_c^2 n_p^2 \tilde{\mu} \pm 2n_p\sqrt{\left(2\sigma\Lambda_m - n_p\Lambda_c^2\tilde{\mu}\right)^2 - 3\tilde{b}^2}}{3c_p}} \tag{26}$$

and

$$u_{2pf} = \sqrt{\frac{-8\sigma\Lambda_m n_p \pm 2n_p\sqrt{4\sigma^2\Lambda_m^2 - 3\tilde{b}^2}}{3c_p}}. \tag{27}$$

u_{2sn} and u_{2pf} define the saddle-node and pitchfork bifurcations of the unison solution for every torque amplitude $\bar{T}_1$. In other words, each crossing between u_{2sn} and u_2 leads to a jump of the response, while the crossings between u_{2pf} and u_2 lead to the localised solution.

4.3 Localised solution

To start the computation of the localised solution, one needs to express the response of mode 1 in terms of mode 2 using Eqs. (20a) and (20b). This leads to

$$u_1 = -\frac{4n_p\Lambda_m\sigma + 2c_p u_2^2 \pm \sqrt{c_p^2 u_2^4 - 4n_p^2\tilde{b}^2}}{c_p}, \tag{28a}$$

$$\sin(2\Delta\beta) = \frac{2n_p\tilde{b}}{c_p u_2^2}, \quad \cos(2\Delta\beta) = \pm\text{sign}(c_p)\sqrt{1 - \frac{4n_p^2\tilde{b}^2}{c_p^2 u_2^4}}, \tag{28b}$$

where the phase difference $\Delta\beta$ is defined as

$$\Delta\beta = \beta_1 - \beta_2. \tag{29}$$

Now, a solution for mode 2 in terms of the excitation parameters is sought. As u_1 depends on σ, one has to introduce Eq. (28a) in Eqs. (20c) and (20d)

to find $\sigma(u_2)$. This leads to

$$\begin{aligned}\sigma = \Bigg[& -2\tilde{\mu}n_p^2\Lambda_c^2 - 5c_p u_2^2 \mp 3\sqrt{c_p^2u_2^4 - 4n_p^2\tilde{b}^2} + \frac{2n_p\tilde{b}\sin(2\Delta\beta)}{1+\cos(2\Delta\beta)} \\ & \pm \frac{\sqrt{2}}{1+\cos(2\Delta\beta)}\Bigg[4\left(\frac{\tilde{T}_1^2}{u_2^2}\Lambda_c^2 - n_p^2\tilde{b}^2\right)(1+\cos(2\Delta\beta)) + \sin^2(2\Delta\beta) \\ & \left(4n_p^2\tilde{b}^2 - 2n_p^4\tilde{\mu}^2\Lambda_c^4 - \left(2n_p^2\tilde{\mu}\Lambda_c^2 + c_p u_2^2\right)\left(c_p u_2^2 \pm \sqrt{c_p^2u_2^4 - 4n_p^2\tilde{b}^2}\right)\right) \\ & - n_p\tilde{b}\left(2n_p^2\tilde{\mu}\Lambda_c^2 + c_p u_2^2 \pm \sqrt{c_p^2u_2^4 - 4n_p^2\tilde{b}^2}\right) \\ & (2\sin(2\Delta\beta) + \sin(4\Delta\beta))\Bigg]^{1/2}\Bigg][8n_p\Lambda_m]^{-1}.\end{aligned} \tag{30}$$

In the contrary, as u_1 is independent on $\tilde{T}_1$, one can just use Eqs. (20c) and (20d) to obtain $\tilde{T}_1(u_2)$. This leads to

$$\begin{aligned}\tilde{T}_1^2 = & \frac{u_2^2}{\Lambda_c^2}\Bigg[\left(\frac{c_p}{2}u_2^2 + 2\Lambda_m n_p\sigma - n_p^2\tilde{\mu}\Lambda_c^2\right)^2 + n_p^2\tilde{b}^2 + u_1^2c_p\Bigg(n_p\tilde{b}\sin(2\Delta\beta) \\ & + \left(u_2^2c_p + 4n_p\sigma\Lambda_m - 2n_p^2\tilde{\mu}\Lambda_c^2\right)\left(1 + \frac{\cos(2\Delta\beta)}{2}\right) \\ & + u_1^2c_p\left(\cos(2\Delta\beta) + \frac{5}{4}\right)\Bigg)\Bigg].\end{aligned} \tag{31}$$

Finally, the phase of mode 2 is given by

$$\tan(\beta_2) = \frac{c_p u_1^2\sin(-2\Delta\beta) - 2n_p\tilde{b}}{4n_p\Lambda_m\sigma + c_p\left(2u_1^2 + u_2^2 + u_1^2\cos(2\Delta\beta)\right) - 2\tilde{\mu}n_p^2\Lambda_c^2}. \tag{32}$$

The stability of this localised solution is assessed in section 4.4.

4.4 Stability of the localised solution

On the localised solution, $u_1 \neq 0$ and $u_2 \neq 0$ so that system (20) can be rewritten as

$$\begin{cases} D_1u_1 = f_{u_1}(\boldsymbol{u},\boldsymbol{\beta}), & \text{(33a)} \\ D_1\beta_1 = f^*_{\beta_1}(\boldsymbol{u},\boldsymbol{\beta}), & \text{(33b)} \\ D_1u_2 = f_{u_2}(\boldsymbol{u},\boldsymbol{\beta}), & \text{(33c)} \\ D_1\beta_2 = f^*_{\beta_2}(\boldsymbol{u},\boldsymbol{\beta}), & \text{(33d)} \end{cases}$$

where $f^*_{\beta_1}$ and $f^*_{\beta_2}$ simply correspond to f_{β_1}/u_1 and f_{β_2}/u_2, respectively. Next, the Jacobian $\boldsymbol{J}$ of system (33) is computed and evaluated on the localised

solution. Looking for a change in the sign of $\det[\boldsymbol{J}]$ indicates a change in the sign of the real part of one of its eigenvalues, hence a change of stability. However, these instabilities are only related to saddle-node bifurcations. In order to obtain the Neimark-Sacker bifurcations as well, one needs to analyse the characteristic polynomial of $\boldsymbol{J}$, written as

$$P(\lambda) = k_4\lambda^4 + k_3\lambda^3 + k_2\lambda^2 + k_1\lambda + k_0. \tag{34}$$

The roots λ_i, $i = 1, ...4$ of $P(\lambda)$ are the eigenvalues of $\boldsymbol{J}$ and coefficients k_i are given in B.1. The stability state depends on the form of the eigenvalues:

- If $\Re(\lambda_i) < 0$, $\forall i$, the localised solution is stable.
- If $\Re(\lambda_i) > 0$ for at least one $i \in \{1, ..., 4\}$, the localised solution is unstable. The instability at stake here is that arising through saddle-node bifurcations and leading to a jump a the system's response.
- If $\lambda_i = \lambda_j^*$ and $\Re(\lambda_i) = 0$ for at least one $i, j \in \{1, ..., 4\}$, $i \neq j$, where $*$ indicates the complex conjugate, a Neimark-Sacker bifurcation occurs and leads to a quasi-periodic solution.

There are no closed-form solutions for the roots of $P(\lambda)$ but one can analyse them using the Routh-Hurwitz criterion [49] and conclude on the stability state. The full procedure is presented in B.

4.5 Physical solutions

The pendulums' response at first order can be written

$$\tilde{s}_i = a_i \cos(n\tau - \xi_i), \quad i = 1, 2, \tag{35}$$

where the scaled amplitudes a_i and the phases ξ_i are obtained in terms of u_1, u_2 and β_1, β_2 through Eqs. (17) and (19) evaluated at steady state. This leads to

$$a_1 = \sqrt{u_1^2 + u_2^2 + 2u_1u_2\cos(\Delta\beta)}, \tag{36a}$$

$$a_2 = \sqrt{u_1^2 + u_2^2 - 2u_1u_2\cos(\Delta\beta)}, \tag{36b}$$

$$\tan\xi_1 = \frac{u_1\sin\beta_1 + u_2\sin\beta_2}{u_1\cos\beta_1 + u_2\cos\beta_2}, \tag{36c}$$

$$\tan\xi_2 = \frac{-u_1\sin\beta_1 + u_2\sin\beta_2}{-u_1\cos\beta_1 + u_2\cos\beta_2}. \tag{36d}$$

Using Eqs. (35) and (36) in Eq. (12a), one obtains the unscaled amplitude of the first two rotors harmonics, written $h_1 = |\theta_1''|$ and $h_2 = |\theta_2''|$,

$$h_1^2 = \epsilon^2 \left[\frac{\tilde{\mu}^2 n_p^4 \Lambda_c^2}{4} \left(a_1^2 + a_2^2 + 2a_1 a_2 \cos(\xi_1 - \xi_2) \right) + \tilde{\mu} n_p^2 \Lambda_c \tilde{T}_1 (a_1 \cos \xi_1 + a_2 \cos \xi_2) + \tilde{T}_1^2 \right], \tag{37a}$$

$$h_2^2 = \epsilon^3 \frac{\tilde{\mu}^2 n^2 n_t^4}{4} \left[\left(a_1^2 \sin 2\xi_1 + a_2^2 \sin 2\xi_2 \right)^2 + \left(a_1^2 \cos 2\xi_1 + a_2^2 \cos 2\xi_2 \right)^2 \right]. \tag{37b}$$

5 Case studies

The aim of this section is to visualise some interesting features of the localised solution and to compare the analytical results with numerical ones in order to validate the model. Two different numerical resolutions are used in this paper:

- Eqs. (4a) and (4b) are integrated numerically using a Runge-Kutta algorithm until the steady state is reached. Then, the signals' amplitudes are obtained through a decomposition into Fourier series.
- Eqs. (4a) and (4b) are solved with MANLAB, which is a path-following and bifurcation analysis software [50, 51].

For convenience, the dimensionless pendulums' amplitudes $\bar{a}_i$ are introduced. They simply correspond to the unscaled version of a_i, i.e. $\bar{a}_i = \epsilon^{1/2} a_i$. Similarly, we introduce the unscaled modal amplitudes $\bar{u}_i = \epsilon^{1/2} u_i$.

5.1 Modal and physical response

In practice, the excitation order is fixed such that n is a constant. However, pendulums may not be tuned exactly to the excitation. This mistuning can be intentional or may arise from material imperfections. Either way, varying the excitation order is similar to introducing mistuning (provided that pendulums are equally mistuned) and is therefore relevant for studying the effect of mistuning on the system's response [33, 52].

Figure 3 represents the order response of modes 1 and 2 as a function of the excitation order n. The green curve corresponds to the response on mode 2 only (i.e. the unison response), while the brown and pink curves represent the coupled response of modes 1 and 2 (i.e. the localised response). The blue and red are the unstable zones delimited by the bifurcation curves u_{2sn} and u_{2pf}. We can see that when the green curve enters into the red zone, mode 1 starts responding and the response of mode 2 is no longer that of unison.

Figure 4 represents the pendulums' amplitude and phase response associated to the modal response depicted in Fig. 3. The comparison between the numerical and experimental results is in good agreement, both for the unison and the localised solutions. The discrepancies are larger at large amplitudes,

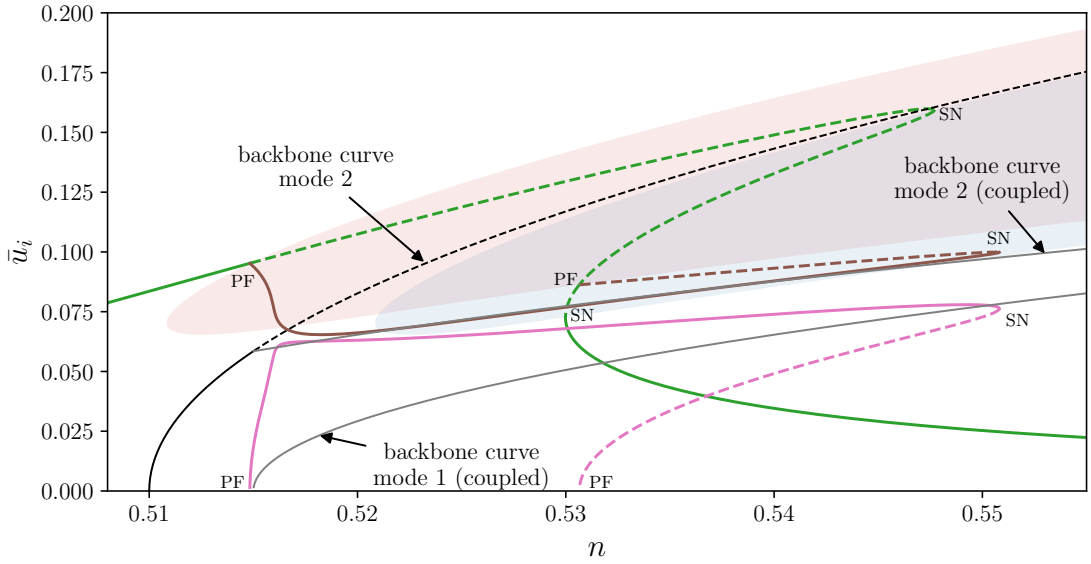

Figure 3: Amplitude of modes 1 and 2 as a function of the excitation order. The single-mode solution (mode 2) is depicted in green and its backbone curve is shown in black. For the coupled-mode solution, modes 1 and 2 are represented in pink and brown, respectively. The backbone curve of the coupled-mode solution projected on modes 1 and 2 is shown in grey. Dashed lines indicate unstable solutions. The red and blue areas correspond to unstable zones of the unison response leading to a localised solution and a jump of the response, respectively. The pitchfork and saddle-node bifurcations obtained analytically are indicated with code names "PF" and "SN", respectively. $\bar{T}_1 = 0.001$ and the other parameters are given in Tab. 1.

which was to be expected from the assumptions used to simplify the equations (*cf.* section 3.1). The time required to reach the steady state during the temporal integrations was very long near the bifurcation points. The small differences between the time integration and MANLAB results are due to the steady state not yet established.
A time signal reconstructed from the analytical model is compared to that obtained through time integration in Fig. 5. As expected, the signals match almost perfectly.

Figure 6 shows the amplitude response of the two first rotor harmonics. Again, the predictions of the analytical model are quite good, though less accurate that in the case of the pendulums, especially for harmonic 1. This is due to the fact only the linear pendulums' contribution was taken into account in h_1 (*cf.* Eq. (12a)). Interestingly, we can see that the amplitude of the first two rotor harmonics is lower on the localised solution than on the unison one. Further discussion on that matter is provided in section 5.3.

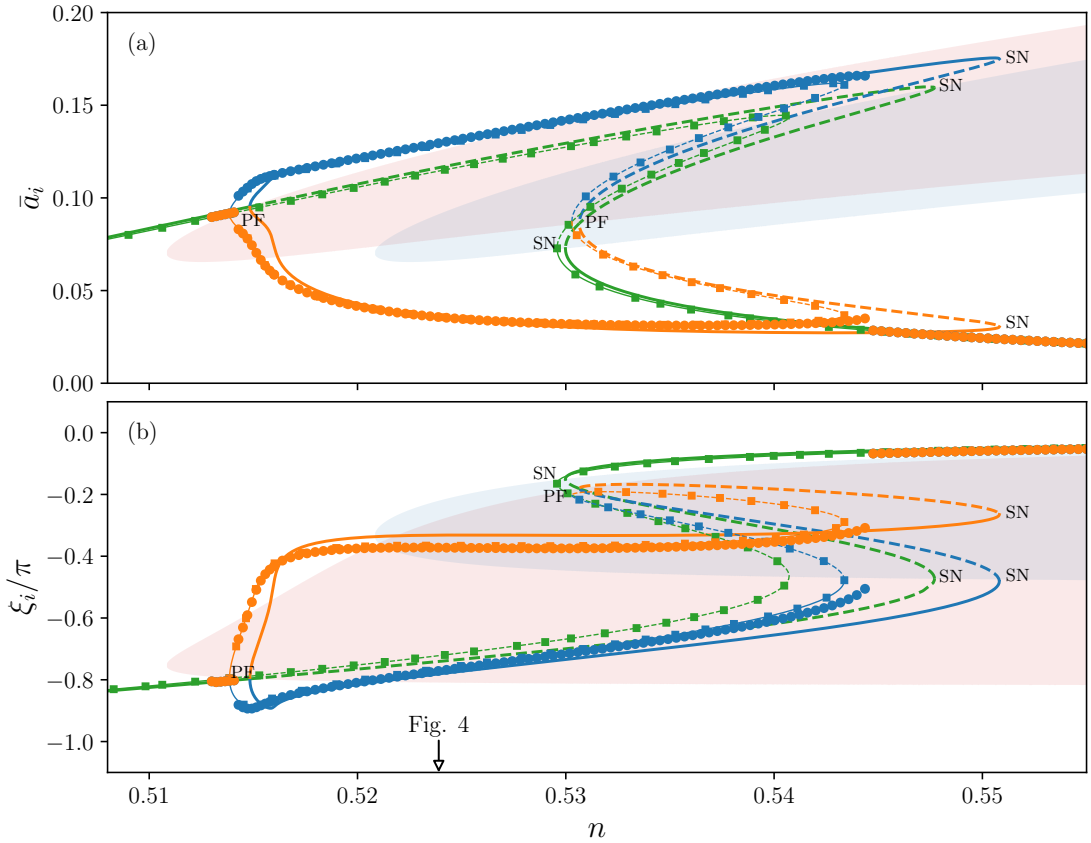

Figure 4: Amplitude (a) and phase (b) of the pendulums as a function of the excitation order. The analytical and MANLAB unison solutions are depicted in green while the localised branches of pendulums 1 and 2 are shown in orange and blue, respectively. Dashed lines indicate unstable solutions. The solutions obtained using MANLAB are represented as lines with square markers. The coloured circles are the solutions obtained through time integration. The red and blue areas correspond to unstable zones of the unison response leading to a localised solution and a jump of the response, respectively. The pitchfork and saddle-node bifurcations obtained analytically are indicated with code names "PF" and "SN", respectively. The arrow at the bottom of (b) indicates the order for which Fig. 5 is represented. $\bar{T}_1 = 0.001$ and the other parameters are given in Tab. 1.

N	n_p	η	μ	$x_{[4]}$	$\alpha_{[1]}$	$\alpha_{[3]}$	b	b_r
2	0.5	1	0.02	-2	1	0.1	0.025	0.0015

Table 1: Parameters of the CPVA studied in this section.

5.2 Non-periodic solutions

Figure 7 shows the amplitude and phase response of the pendulums of a CPVA whose parameters are given in Tab. 2. The response undergoes Neimark-Sacker bifurcations leading to a quasi-periodic response. The range of orders for which the numerical solution is not periodic was assessed by looking at the time

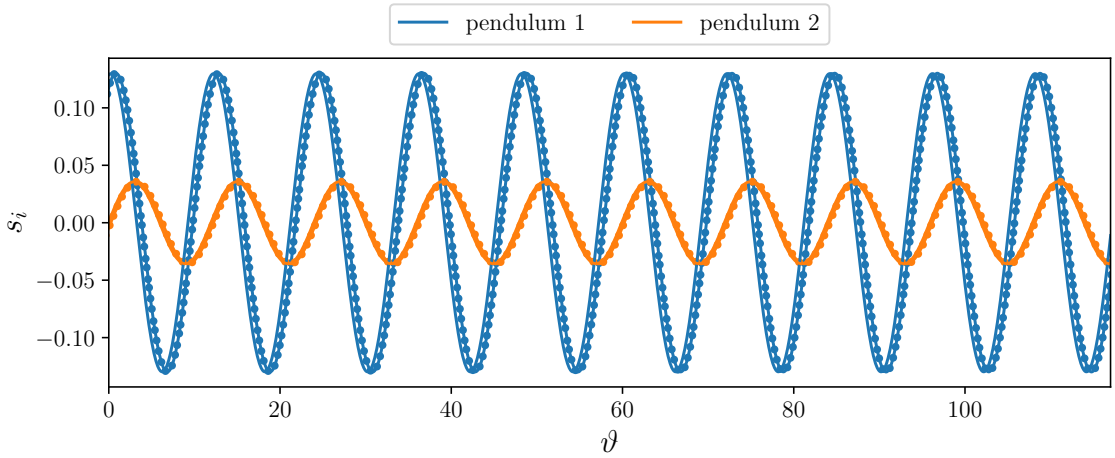

Figure 5: Time signals of the pendulums for the excitation parameters $n = 0.5239$ and $\bar{T}_1 = 0.001$. The amplitude and phase of these signals are shown Fig. 4. Both analytic and time integration signals are shown. The time integration ones are shown as lines with dot markers. The system parameters are given in Tab. 1.

integration signals at different orders, as shown in Fig. 8. This range of non-periodic solutions fits very well with the Neimark-Sacker bifurcations obtained analytically (red stars). Fig. 9 shows the Poincare sections associated to the signals given in Fig. 8(b) and (c). From Fig. 9(a), we can see that the signal in Fig. 8(b) is quasi-periodic. However, from Fig. 9(b), it seems that the quasi-periodic solution at $n = 0.5265$ is unstable and bifurcates towards a chaotic solution [53]. Bifurcations from the localised solution leading to a chaotic response was also observed in [40]. Chaotic motions can also appear in CPVAs made of a single pendulum (in which case localisation cannot occur), as shown in [54, 55].

N	n_p	η	μ	$x_{[4]}$	$\alpha_{[1]}$	$\alpha_{[3]}$	$\bar{b}$	$\bar{b}_r$
2	0.5	1	0.02	-1	1	0.1	0.0075	0.0015

Table 2: Parameters of the CPVA studied in this section.

5.3 Filtration improvement

Though some studies showed that localisation can improve the filtration performance [40, 41], it is not desired as it generally decreases the torque capacity. In this section, it is shown that one can use localisation to increase the filtration will not decreasing the torque capacity. In other words, localisation can improve the efficiency of the filtration as compared to the unison solution.

Figure 10 shows an amplitude response of the pendulums and the two first rotor harmonics as a function of the torque amplitude and for an order very

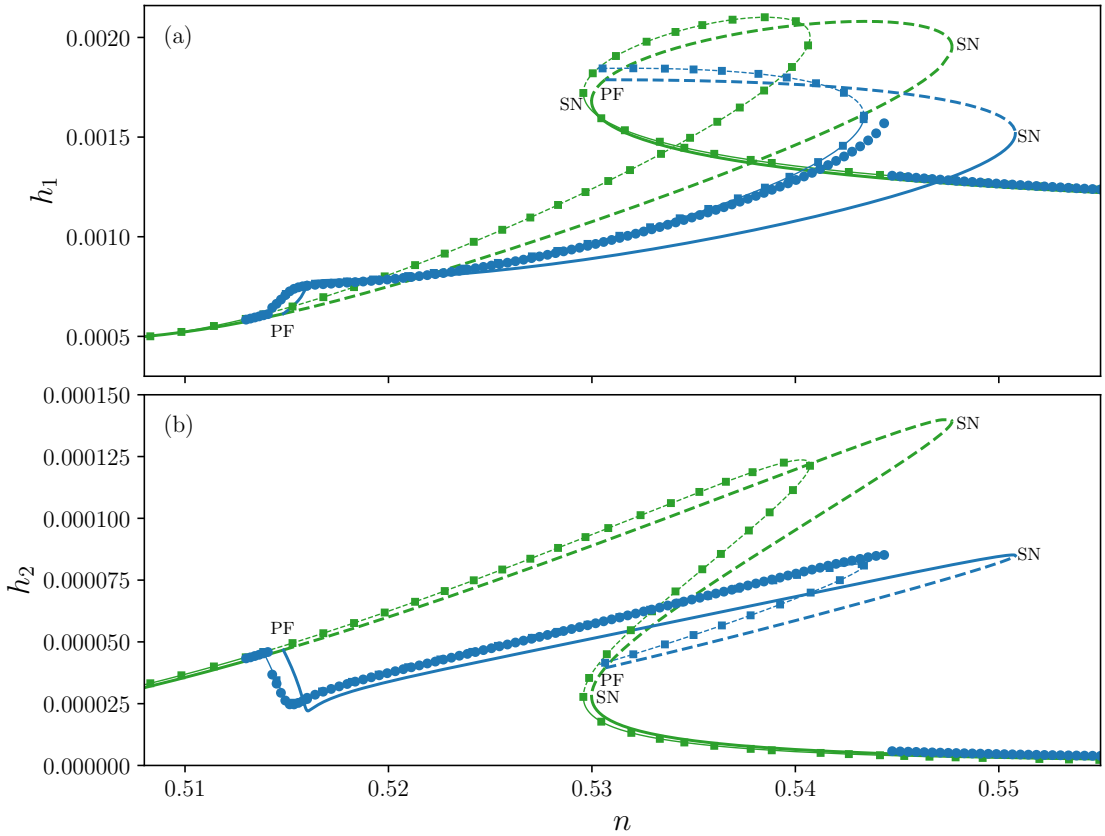

Figure 6: Amplitude of the first (a) and second (b) harmonics of the rotor's acceleration as a function of the excitation order. The analytical and MANLAB unison solutions are depicted in green while the localised solution is shown in blue. Dashed lines indicate unstable solutions. The pitchfork and saddle-node bifurcations obtained analytically are indicated with code names "PF" and "SN", respectively. The solutions obtained using MANLAB are represented as lines with square markers. The blue circles are the solutions obtained through time integration. $\bar{T}_1 = 0.001$ and the other parameters are given in Tab. 1.

slightly above the tuning order. Both analytical and MANLAB results are shown. The solutions match well for small torque amplitudes but they become more different as the amplitude is increased. It is not surprising to observe differences in the solutions as the analytical model assumed small pendulums amplitudes, whereas they are certainly not small. Indeed, one of the pendulums reaches an amplitude close from 1. Though the analytical prediction is not perfect, it describes well the shape of the localised solution. Figure 10(a) shows that the pendulums do not hit their cusp because of localisation, hence the torque range is the same as if localisation did not occur. Moreover, looking at Fig. 10(b) and (c), one can see that there is a significant torque range over which the localised solution leads to a smaller amplitude of the two first rotor harmonic than the unison solution. The MANLAB results show that above $\bar{T}_1 \approx 0.006$, the filtration of harmonic 1 achieved through the localised

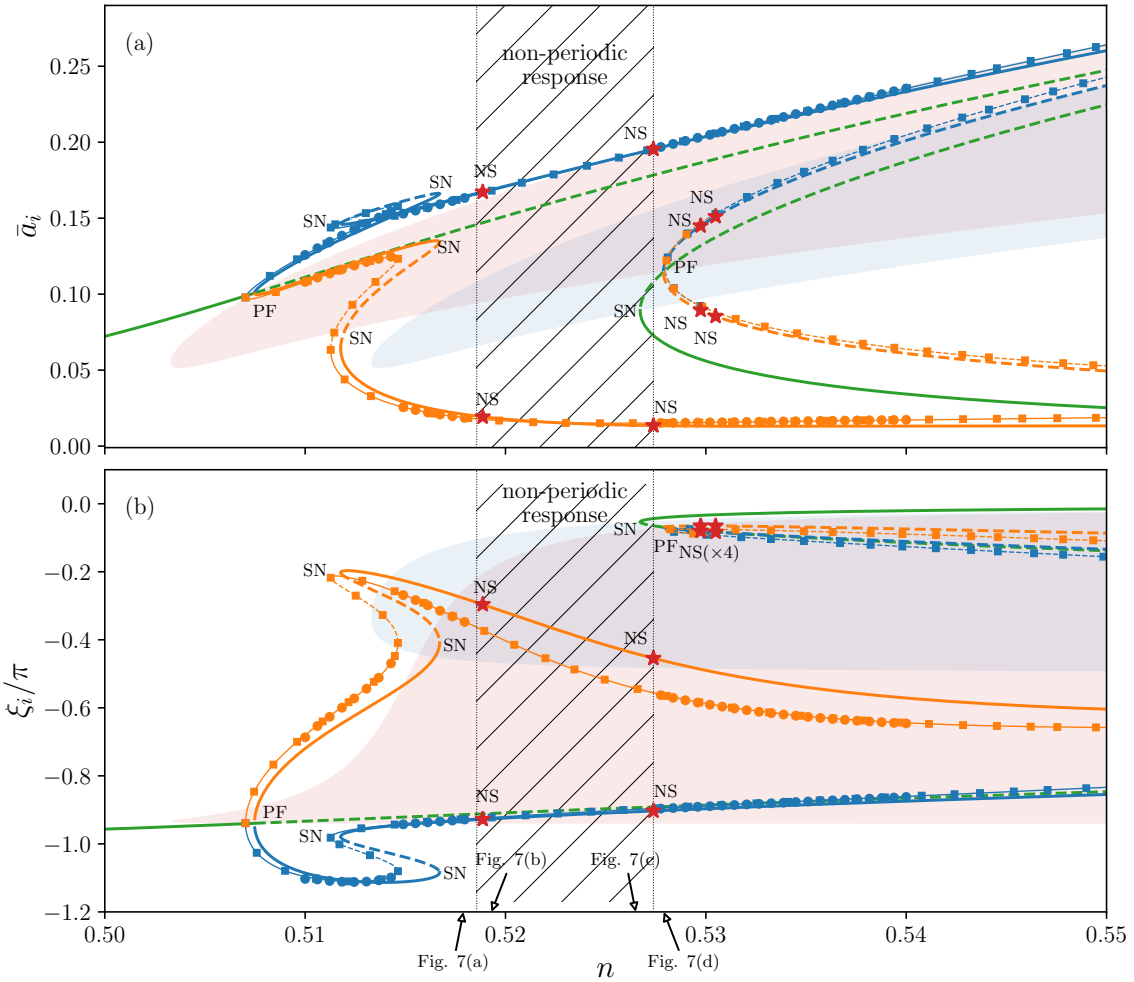

Figure 7: Amplitude (a) and phase (b) of the pendulums as a function of the excitation order. The analytical and MANLAB unison solutions are depicted in green while the localised branches of pendulums 1 and 2 are shown in orange and blue, respectively. Dashed lines indicate unstable solutions. The solutions obtained using MANLAB are represented as lines with square markers. The coloured circles are the solutions obtained through time integration. The red stars with code name "NS" are the Neimark-Sacker bifurcations predicted analytically. The pitchfork and saddle-node bifurcations obtained analytically are indicated with code names "PF" and "SN", respectively. The dashed area corresponds to the range of excitation orders for which non-periodic responses were observed on time integration signals. The red and blue areas correspond to unstable zones of the unison response leading to a localised solution and a jump of the response, respectively. The arrow at the bottom of (b) indicates the orders for which the time signals in Fig. 8 are represented. $\bar{T}_1 = 0.001$ and the other parameters are given in Tab. 2.

solution is less efficient than predicted. However, the filtration of the 2$^{\text{nd}}$ harmonic is better than expected. Overall, localisation reduces the amplitude of the rotor's two first harmonics, and as it does not reduce the torque capacity, it provides a better filtration than the unison solution. Hence, one should not

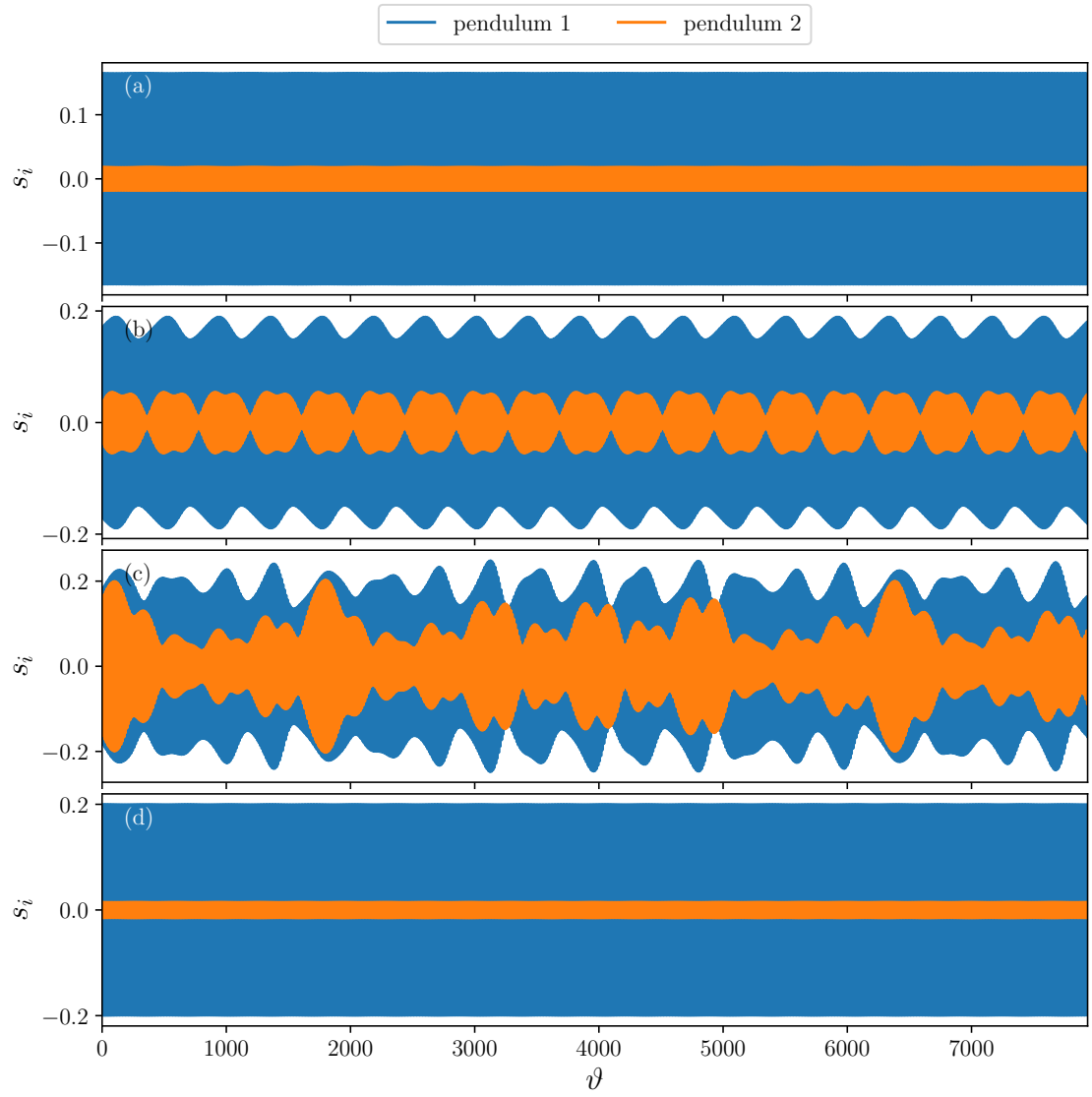

Figure 8: Time signals of the pendulums for the four excitation orders indicated by arrows at the bottom of Fig. 7(b). (a), (b), (c) and (d) correspond to $n = \{0.5179, 0.5193, 0.5265, 0.5279\}$, respectively. (a) and (d) are at the outer limit of the non-periodic response zone, while (b) and (c) are in the inner limit. $\bar{T}_1 = 0.001$ and the system parameters are given in Tab. 2.

systematically aim to avoid the localised solution. Instead, it should be investigated to determine whether it decreases the efficiency of the CPVA or not.

Finally, an interesting feature of the unison response shown in Fig. 10(b) is that between the two pitchfork bifurcations h_1 diminishes as $\bar{T}_1$ increases. It is shown in C that the local maximum at $\bar{T}_1 \approx 0.0036$ and the local minimum at $\bar{T}_1 \approx 0.0084$ indeed correspond to pitchfork bifurcations. In addition, it is also shown that the antiresonance locus is

$$n_{AR} = n_p - \epsilon \frac{c_p}{4\Lambda_m n_p} a^2. \tag{38}$$

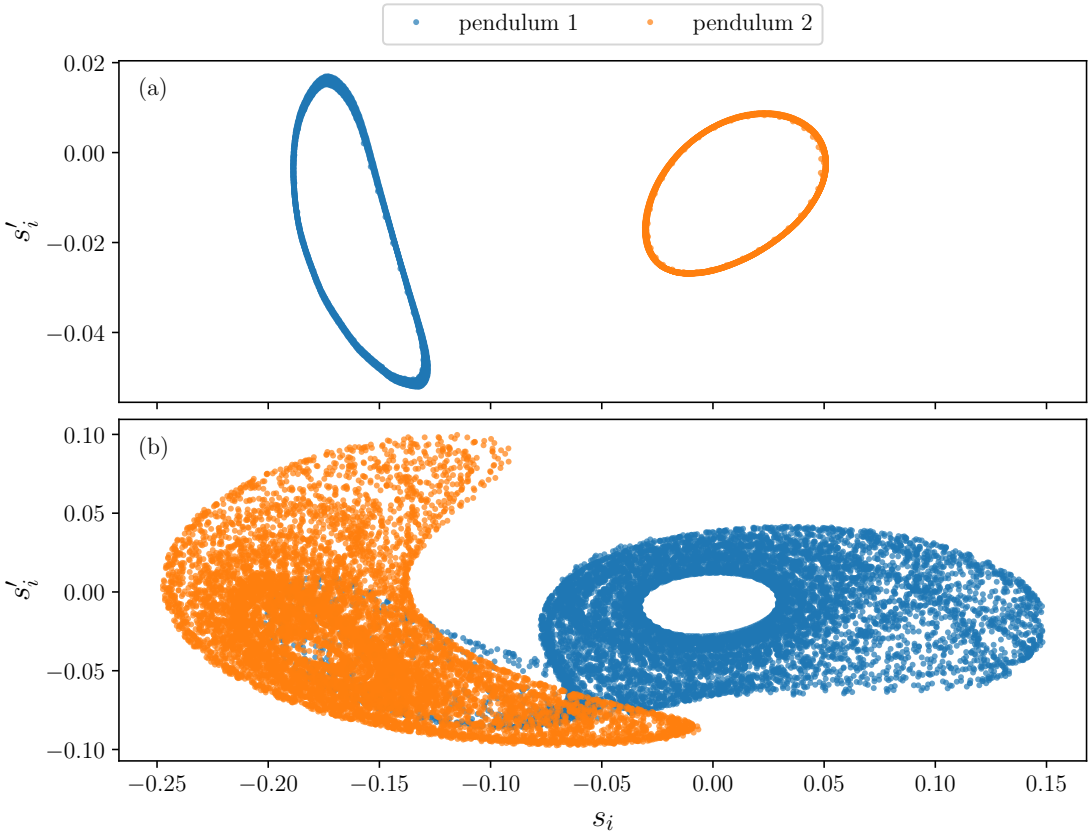

Figure 9: (a) and (b) are Poincaré maps associated to the non-periodic signals represented in Fig. 8(b) and (c), respectively. $n = \{0.5193, 0.5265\}$ for (a) and (b), respectively, $\bar{T}_1 = 0.001$ and the system parameters are given in Tab. 2.

For the CPVA shown in Fig. 10, $c_p < 0$ so that the antiresonance shifts to the right as $\bar{T}_1$ increases. As the excitation order is $n = 0.504 > n_p$, the antiresonance gets closer from the excitation order until $n = n_{AR}$, which corresponds to the local minimum.

N	n_p	η	μ	$x_{[4]}$	$\alpha_{[1]}$	$\alpha_{[3]}$	b	b_r
2	0.5	1	0.02	0.01	1	-0.035	0.001	0.0015

Table 3: Parameters of the CPVA studied in this section.

6 Conclusion

This paper deals with the nonlinear dynamics of CPVAs made of two identical pendulums that are allowed to rotate relatively to the rotor. Analytical procedures to compute the localised solution and assess its stability are proposed. The stability analysis allows the prediction of saddle-node bifurcations, leading to jumps of the response, and Neimark-Sacker bifurcations, leading

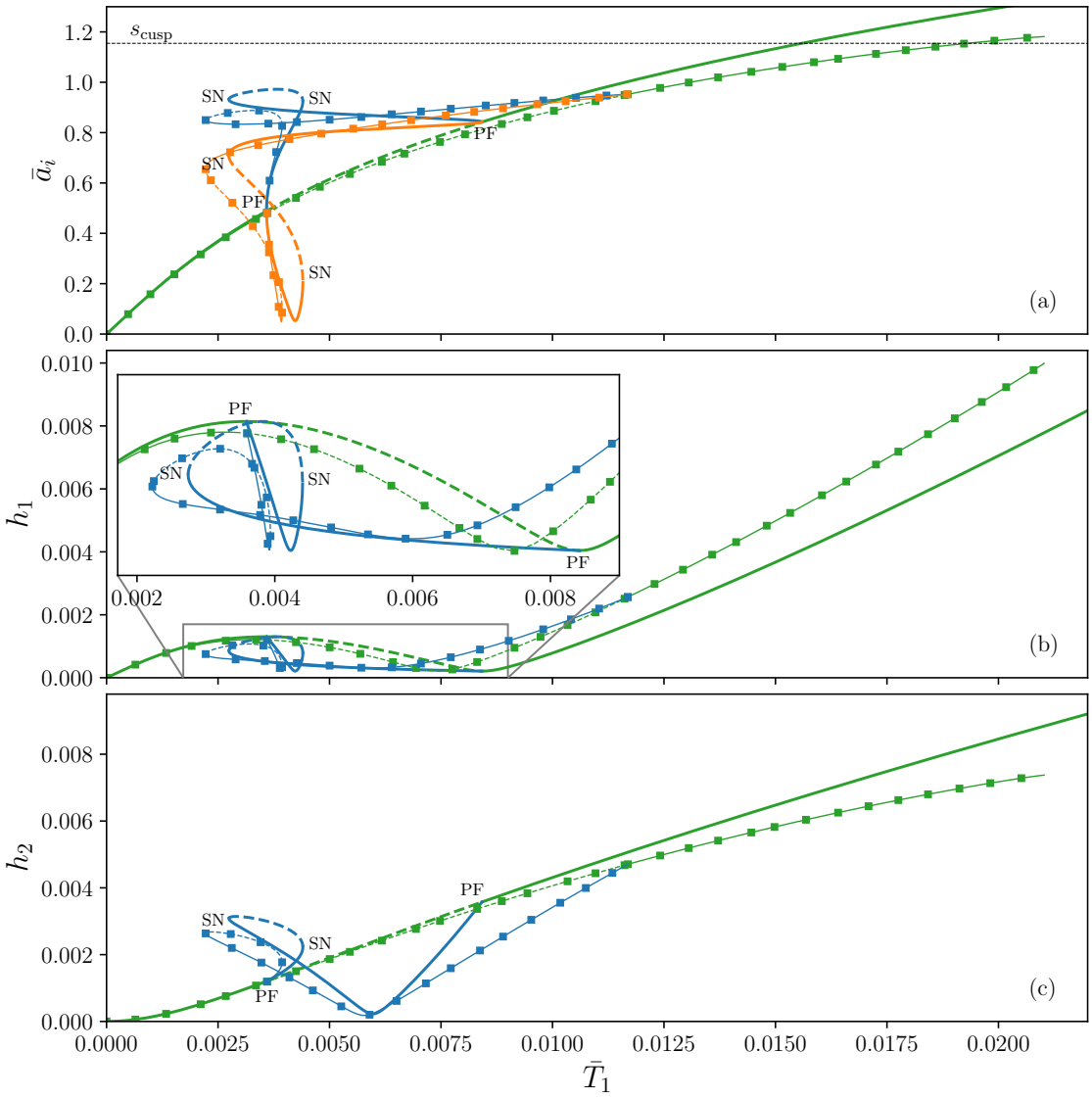

Figure 10: Amplitude of the pendulums (a) and the first (b) and second (c) harmonics of the rotor's acceleration as a function of the excitation amplitude. The analytical and MANLAB unison solutions are depicted in green while the localised branches of pendulums 1 and 2 are shown in orange and blue, respectively. The localised rotor response is shown in blue. Dashed lines indicate unstable solutions. The pitchfork and saddle-node bifurcations obtained analytically are indicated with code names "PF" and "SN", respectively. The solutions obtained using MANLAB are represented as lines with square markers. $n = 0.504$ and the other parameters are given in Tab. 3.

to non-periodic solutions. Numerical resolutions of the systems' dynamics validated the accuracy of the analytical predictions and allowed to visualise quasi-periodic and chaotic solutions. Finally, it was shown that the localised response can provide a better filtration than the unison one while not affecting the torque range. Hence, one should not systematically aim to avoid localisation.

Statements and declarations

Funding. The authors declare that no funds, grants, or other support were received during the preparation of this manuscript.

Competing interests. The authors have no relevant financial or non-financial interests to disclose.

Author Contributions. All authors contributed to the study conception and design. Material preparation, data collection and analysis were performed by V. Mahé. The first draft of the manuscript was written by V. Mahé and all authors commented on previous versions of the manuscript. All authors read and approved the final manuscript.

Appendix A System obtained through the method of multiple scales

The system of equations obtained through the application of the method of multiple scales is given by Eq. (20) where functions f_{u_1}, f_{β_1}, f_{u_2} and f_{β_2} are

$$f_{u_1}(\boldsymbol{u},\boldsymbol{\beta}) = \left[c_p u_2^2 u_1 \sin(2\Delta\beta) - 2n_p\tilde{b}u_1\right][4n_p\Lambda_m]^{-1}, \tag{A1}$$

$$f_{\beta_1}(\boldsymbol{u},\boldsymbol{\beta}) = \sigma u_1 + \left[c_p\left(u_1^3 + 2u_2^2u_1 + u_2^2u_1\cos(2\Delta\beta)\right)\right][4n_p\Lambda_m]^{-1}, \tag{A2}$$

$$f_{u_2}(\boldsymbol{u},\boldsymbol{\beta}) = \left[c_p u_1^2 u_2 \sin(-2\Delta\beta) - 2n_p\tilde{b}u_2 - 2\Lambda_c\tilde{T}_1\sin(\beta_2)\right][4n_p\Lambda_m]^{-1}, \tag{A3}$$

$$\begin{aligned} f_{\beta_2}(\boldsymbol{u},\boldsymbol{\beta}) = \sigma u_2 + \Big[&c_p\left(u_2^3 + 2u_1^2u_2 + u_1^2u_2\cos(2\Delta\beta)\right) \\ &- 2\Lambda_c\tilde{T}_1\cos(\beta_2) - 2\tilde{\mu}n_p^2\Lambda_c^2u_2\Big][4n_p\Lambda_m]^{-1}, \end{aligned} \tag{A4}$$

where c_p and $\Delta\beta$ are defined in Eqs. (24) and (29), respectively.

Appendix B Stability analysis of the localised solution

B.1 Coefficients of $P(\lambda)$

The coefficients of the characteristic polynomial given in Eq. (34) are

$$\begin{aligned}
k_0 =& -u_1^2\Big[-32n_p^4(u_1^2+u_2^2)\tilde{b}^4-4n_p^2c_pu_2^2\tilde{b}^2\\
&\Big(4n_p(2\Lambda_m\sigma-\Lambda_c^2n_p\tilde{\mu})(-u_1^2+u_2^2\cos(2\Delta\beta)+2u_2^2)\\
&+c_p\big(-u_1^4\cos(2\Delta\beta)-4u_1^4+4u_1^2u_2^2\cos^2(2\Delta\beta)+12u_1^2u_2^2\cos(2\Delta\beta)\\
&+6u_1^2u_2^2+2u_2^4\cos^2(2\Delta\beta)+5u_2^4\cos(2\Delta\beta)+4u_2^4\big)\Big)\\
&+c_p^2u_2^6(4\Lambda_mn_p\sigma-2\Lambda_c^2n_p^2\tilde{\mu}+c_pu_1^2\cos(2\Delta\beta)+2c_pu_1^2+c_pu_2^2)\\
&(4\Lambda_mn_p\sigma-2\Lambda_c^2n_p^2\tilde{\mu}+c_pu_1^2\cos(2\Delta\beta)+2c_pu_1^2-2c_pu_2^2\cos^2(2\Delta\beta)\\
&-8c_pu_2^2\cos(2\Delta\beta)-5c_pu_2^2)\cos(2\Delta\beta)\Big]\left[8\Lambda_m^2n_p^2u_2^2\right]^{-2},
\end{aligned} \tag{B5}$$

$$\begin{aligned}
k_1 =&\tilde{b}\Big[-4n_p^2\tilde{b}^2(u_1^4-8u_1^2u_2^2-u_2^4)\\
&+u_2^4\big(4n_p^2(2\Lambda_m\sigma-\Lambda_c^2n_p\tilde{\mu})^2+8c_pn_p(u_1^2+u_2^2)(2\Lambda_m\sigma-\Lambda_c^2n_p\tilde{\mu})\\
&+c_p^2(-u_1^4\cos^2(2\Delta\beta)+4u_1^4+8u_1^2u_2^2\cos^2(2\Delta\beta)\\
&+10u_1^2u_2^2\cos(2\Delta\beta)+8u_1^2u_2^2+3u_2^4)\big)\Big]\left[16\Lambda_m^3n_p^2u_2^4\right]^{-1},
\end{aligned} \tag{B6}$$

$$k_2 = k_1\frac{\Lambda_m}{\tilde{b}}+\frac{\tilde{b}^2}{\Lambda_m^2}, \tag{B7}$$

$$k_3 = \frac{2\tilde{b}}{\Lambda_m}, \tag{B8}$$

$$k_4 = 1. \tag{B9}$$

B.2 The Routh table

The use of the Routh-Hurwitz criterion requires the construction of a Routh table. The Routh table corresponding to the characteristic polynomial (34) is given in Tab. B1 and the expression of the elements of this table are

$$\begin{aligned}
&r_{40}=k_4,\quad r_{41}=k_2,\quad r_{42}=k_0,\quad r_{30}=k_3,\quad r_{31}=k_1,\\
&r_{20}=\frac{k_1}{k_3}+\frac{k_3^2}{4},\quad r_{21}=k_0,\quad r_{10}=\frac{(k_1+k_3^3/4)k_1-k_0k_3^2}{k_1+k_3^3/4},\quad r_{00}=k_0.
\end{aligned} \tag{B10}$$

The stability state of the system is obtained by analysing Tab. B1. Cases of interest are briefly presented below and other special cases can be found in [56].

- The number of roots with positive real parts equals the number of sign changes in the first column of Tab. B1 (provided that none of the coefficients in this column are null).
- There is at least one pair of complex conjugate eigenvalues if a row $\mathcal{R}_i$, $i > 0$, is full of zeros. In this case, one has to recompute the coefficients of the Routh table based on the row preceding the row of zeros. The real part of the pair(s) of complex conjugate eigenvalues can be determined by analysing the first column of the table, starting from the row preceding the row of zeros.

Row $\mathcal{R}_4$	r_{40}	r_{41}	r_{42}
Row $\mathcal{R}_3$	r_{30}	r_{31}	0
Row $\mathcal{R}_2$	r_{20}	r_{21}	0
Row $\mathcal{R}_1$	r_{10}	0	0
Row $\mathcal{R}_0$	r_{00}	0	0

Table B1: Routh table for a polynomial of degree 4. The r_{ij} are the elements of the Routh table.

B.3 Application of the Routh-Hurwitz criterion

To apply the Routh-Hurwitz criterion to the CPVA, it is first useful to note that

$$k_3 > 0, \quad k_4 > 0 \quad \Rightarrow \quad r_{30} > 0, \quad r_{40} > 0. \tag{B11}$$

Thus, there are never sign changes between rows $\mathcal{R}_4$ and $\mathcal{R}_3$, which indicates that there is always at least one eigenvalue with a negative real part. Moreover, Eq. (B11) implies that $\mathcal{R}_4$ and $\mathcal{R}_3$ are never full of zeros. Then, there are three cases to consider.

Case 1: no rows are full of zeros

There are no Neimark-Sacker bifurcations and the response is unstable if the r_{i0}, $i = 0, ..., 3$ do not all have the same sign.

Case 2: row $\mathcal{R}_2$ is full of zeros

The Routh table has to be modified as explained in [56], leading to Tab. B2. The fact that the zero row is even means that $P(\lambda)$ has a zero root. This root does not need to be studied, which explains why Tab. B2 has one row less than Tab. B1. The expression of the modified elements $\bar{r}_{ij}$ is

$$\bar{r}_{20} = 2r_{30}, \quad \bar{r}_{10} = r_{31}. \tag{B12}$$

The real part of the pair of complex conjugate roots is analysed by looking at the sign changes in the first column from $\mathcal{R}_3$ to $\mathcal{R}_1$.

- There are no sign changes if $k_1 > 0$. In that case, $P(\lambda)$ has a pair of purely imaginary complex conjugate roots. This is the condition for a Neimark-Sacker bifurcation to occur. The other two eigenvalues are 0 and a complex number with a negative real part, so that the Neimark-Sacker bifurcation occurs on a stable part of the localised response.
- There is one change of sign if $k_1 < 0$, so that $P(\lambda)$ has two negative roots, a zero root and a positive root. Hence, the response is unstable.

Row $\mathcal{R}_4$	r_{40}	r_{41}	r_{42}
Row $\mathcal{R}_3$	r_{30}	r_{31}	0
Row $\mathcal{R}_2$	$\bar{r}_{20}$	0	0
Row $\mathcal{R}_1$	$\bar{r}_{10}$	0	0

Table B2: Routh table if $\mathcal{R}_2$ is full of zeros. The r_{ij} are the same elements as in Tab. B1 and the $\bar{r}_{ij}$ are the modified elements.

Case 3: row $\mathcal{R}_1$ is full of zeros

As in the previous case, the Routh table has to be modified, leading to Tab. B3. The expression of the modified elements $\bar{\bar{r}}_{ij}$ is

$$\bar{\bar{r}}_{10} = 2r_{20}, \quad \bar{\bar{r}}_{00} = r_{21}. \tag{B13}$$

The sign of the real part of one of the eigenvalues is assessed by analysing the first column of rows $\mathcal{R}_3$ and $\mathcal{R}_2$.

- There is no change of sign if $r_{20} > 0$. In this case, $P(\lambda)$ has at least a second root with a negative real part.
- There is a change of sign if $r_{20} < 0$. In this case, $P(\lambda)$ has at least one root with a positive real part, meaning that the solution is unstable.

The real part of the pair of complex conjugate roots is analysed by looking at the sign changes in the first column from $\mathcal{R}_2$ to $\mathcal{R}_0$.

- There are no sign changes if $\text{sign}(r_{20}) = \text{sign}(r_{21})$, so that $P(\lambda)$ has a pair of purely imaginary complex conjugate roots. This is the condition for a Neimark-Sacker bifurcation to occur.
- There is one change of sign if $\text{sign}(r_{20}) \neq \text{sign}(r_{21})$, so that the pair of complex conjugate roots is not purely imaginary.

Row $\mathcal{R}_4$	r_{40}	r_{41}	r_{42}
Row $\mathcal{R}_3$	r_{30}	r_{31}	0
Row $\mathcal{R}_2$	r_{20}	r_{21}	0
Row $\mathcal{R}_1$	$\bar{\bar{r}}_{10}$	0	0
Row $\mathcal{R}_0$	$\bar{\bar{r}}_{00}$	0	0

Table B3: Routh table if $\mathcal{R}_1$ is full of zeros. The r_{ij} are the same elements as in Tab. B1 and the $\bar{\bar{r}}_{ij}$ are the modified elements.

Appendix C Analysis of the local minimum and maximum of the rotor's torque response

Neglecting the damping and assuming the excitation order is below n_2, the pendulums' response at unison is in phase-opposition with the exciting torque such that $\cos(\beta_2) = -1$. Hence, the amplitude of the first harmonic of mode 2 and the rotor is

$$\tilde{T}_1 = \frac{u_2}{\Lambda_c}\left|n_p^2\tilde{\mu}\Lambda_c^2 - \frac{c_p}{2}u_2^2 - 2\Lambda_m n_p\sigma\right|, \tag{C14a}$$

$$h_1 = \epsilon^{3/2}\left|\tilde{T}_1 - n_p^2\tilde{\mu}\Lambda_c u_2\right|. \tag{C14b}$$

We can assume $n_p^2\tilde{\mu}\Lambda_c^2 > c_p u_2^2/2 + 2\Lambda_m n_p\sigma$ when σ is small as u_2^2 is negligible for small values of u_2 and $\bar{T}_1$ increases monotonically with u_2 if there is no jump. Hence, one can write

$$\tilde{T}_1 = \frac{u_2}{\Lambda_c}\left(n_p^2\tilde{\mu}\Lambda_c^2 - \frac{c_p}{2}u_2^2 - 2\Lambda_m n_p\sigma\right), \tag{C15a}$$

$$h_1 = \epsilon^{3/2}\left|\frac{c_p}{2}u_2^2 + 2\Lambda_m n_p\sigma\right|. \tag{C15b}$$

Local minimum

The antiresonance locus is obtained by solving Eq. (C15b) for σ, leading to

$$n_{AR} = n_p - \epsilon\frac{c_p}{4\Lambda_m n_p}u_2^2. \tag{C16}$$

Note that this corresponds to the eigenorder of the uncoupled pendulums [13]. If $c_p \neq 0$, the amplitude at the antiresonance is given by

$$u_{2AR} = \sqrt{\frac{-4\Lambda_m n_p\sigma}{c_p}}, \tag{C17}$$

which is equal to the upper branch of u_{2pf} (*cf.* Eq. (27)). Hence, in the absence of damping, there is always a pitchfork bifurcation at the antiresonance.

Local maximum

The amplitude of mode 2 at the local maximum is obtained by solving $\partial h_1/\partial u_2 = 0$ for u_2, leading to

$$u_2 = \sqrt{\frac{-4\Lambda_m n_p \sigma}{3c_p}}. \tag{C18}$$

This corresponds to the lower branch of u_{2pf} (*cf.* Eq. (27)), so that in the absence of damping there is always a pitchfork bifurcation at the local maximum.

References

[1] Taylor, E.S.: Crankshaft torsional vibration in radial aircraft engines. S.A.E. JOURNAL **38**(3), 9 (1936)

[2] Newland, D.E.: Nonlinear problems of centrifugal pendulum vibration absorbers. In: Mechanisms and Machines, vol. 1. Varna (Bulgaria), pp. 39–62 (1965)

[3] Mitchiner, R.G., Leonard, R.G.: Centrifugal Pendulum Vibration Absorbers—Theory and Practice. Journal of Vibration and Acoustics **113**(4), 503–507 (1991). https://doi.org/10.1115/1.2930214

[4] Frahm, H.: Device for Damping Vibrations of Bodies. 989,958, 1911

[5] Auleley, M., Thomas, O., Giraud-Audine, C., Mahé, H.: Enhancement of a dynamic vibration absorber by means of an electromagnetic shunt. Journal of Intelligent Material Systems and Structures **32**(3), 331–354 (2021). https://doi.org/10.1177/1045389X20957097

[6] Shaw, S.W., Garg, V., Chao, C.-P.: Attenuation of Engine Torsional Vibrations Using Tuned Pendulum Absorbers. In: SAE Noise and Vibration Conference and Exposition, p. 971961 (1997). https://doi.org/10.4271/971961

[7] Madden, J.F.: Constant Frequency Bifilar Vibration Absorber. 4218187, 1980. 4 218 187

[8] Huygens, C.: Horologium Oscillatorium Sive de Motu Pendulorum Ad Horologia Aptato. Demostrationes Geometricae, (1673)

[9] Denman, H.H.: Tautochronic bifilar pendulum torsion absorbers for reciprocating engines. Journal of Sound and Vibration **159**(2), 251–277 (1992). https://doi.org/10.1016/0022-460X(92)90035-V

[10] Chao, C.-P., Shaw, S.W., Lee, C.-T.: Stability of the Unison Response for a Rotating System With Multiple Tautochronic Pendulum Vibration Absorbers. Journal of Applied Mechanics **64**(1), 149–156 (1997). https://doi.org/10.1115/1.2787266

[11] Chao, C.-P., Lee, C.-T., Shaw, S.W.: Non-unisson dynamics of multiple centrifugal pendulum vibration absorbers. Journal of Sound and Vibration **204**(5), 769–794 (1997). https://doi.org/10.1006/jsvi.1997.0960

[12] Shaw, S.W., Geist, B.: Tuning for Performance and Stability in Systems of Nearly Tautochronic Torsional Vibration Absorbers. Journal of Vibration and Acoustics **132**(4) (2010). https://doi.org/10.1115/1.4000840

[13] Mahé, V., Renault, A., Grolet, A., Mahé, H., Thomas, O.: On the dynamic stability and efficiency of centrifugal pendulum vibration absorbers with rotating pendulums. Journal of Sound and Vibration **536**, 117157 (2022). https://doi.org/10.1016/j.jsv.2022.117157

[14] Mayet, J., Ulbrich, H.: Tautochronic centrifugal pendulum vibration absorbers: General design and analysis. Journal of Sound and Vibration **333**(3), 711–729 (2014). https://doi.org/10.1016/j.jsv.2013.09.042

[15] Mayet, J., Ulbrich, H.: First-order optimal linear and nonlinear detuning of centrifugal pendulum vibration absorbers. Journal of Sound and Vibration **335**, 34–54 (2015). https://doi.org/10.1016/j.jsv.2014.09.017

[16] Cera, M., Cirelli, M., Pennestrì, E., Valentini, P.P.: Nonlinear dynamics of torsichrone CPVA with synchroringed form closure constraint. Nonlinear Dynamics (2021). https://doi.org/10.1007/s11071-021-06732-5

[17] Gomez, E.R., Arteaga, I.L., Kari, L.: Normal-force dependant friction in centrifugal pendulum vibration absorbers: Simulation and experimental investigations. Journal of Sound and Vibration **492**, 115815 (2021). https://doi.org/10.1016/j.jsv.2020.115815

[18] Gomez, E.R., Sjöstrand, J., Kari, L., Arteaga, I.L.: Torsional vibrations in heavy-truck powertrains with flywheel attached centrifugal pendulum vibration absorbers. Mechanism and Machine Theory **167**, 104547 (2022). https://doi.org/10.1016/j.mechmachtheory.2021.104547

[19] Inoue, T., Okumura, R., Yabui, S., Jiang, X.: Evaluation of Relationship Between Shape of a Rigid Body Unifilar Centrifugal Pendulum Vibration Absorber and Vibration Suppression Performance. Journal of Vibration and Acoustics **143**(3), 031014 (2021). https://doi.org/10.1115/1.4050273

[20] Mahé, H., Renault, A., Thomas, O.: Dispositif D'amortissement Pendulaire [Pendular Damping Device]. 3055038, 2018. FR 3 055 038

[21] Mahé, H., Renault, A., Thomas, O.: Dispositif D'amortissement Pendulaire [Pendular Damping Device]. 3055037, 2018. FR 3 055 037

[22] Renault, A.: Calcul et optimisation d'absorbeurs pendulaires dans une chaîne de traction automobile [Simulation and optimisation of pendular absorbers for automotive powertrain]. PhD thesis, ENSAM, Lille, France (2018)

[23] Acar, M.A.: Design and tuning of centrifugal pendulum vibration absorbers. PhD thesis, Michigan State University, Michigan (2017)

[24] Cirelli, M., Gregori, J., Valentini, P.P., Pennestrí, E.: A design chart approach for the tuning of parallel and trapezoidal bifilar centrifugal pendulum. Mechanism and Machine Theory **140**, 711–729 (2019). https://doi.org/10.1016/j.mechmachtheory.2019.06.030

[25] Cera, M., Cirelli, M., Pennestrì, E., Valentini, P.P.: Design analysis of torsichrone centrifugal pendulum vibration absorbers. Nonlinear Dynamics **104**(2), 1023–1041 (2021). https://doi.org/10.1007/s11071-021-06345-y

[26] Tan, X., Yang, S., Yang, J., Li, J.: Study of dynamics of rotational centrifugal pendulum vibration absorbers based on tautochronic design. Meccanica (2021). https://doi.org/10.1007/s11012-021-01340-4

[27] Mayet, J., Acar, M.A., Shaw, S.W.: Effective and robust rocking centrifugal pendulum vibration absorbers. Journal of Sound and Vibration **527**, 116821 (2022). https://doi.org/10.1016/j.jsv.2022.116821

[28] Mahe, V., Renault, A., Grolet, A., Thomas, O., Mahe, H.: Dynamic stability of centrifugal pendulum vibration absorbers allowing a rotational mobility. Journal of Sound and Vibration **517**, 116525 (2022). https://doi.org/10.1016/j.jsv.2021.116525

[29] Mahe, V., Renault, A., Grolet, A., Mahe, H., Thomas, O.: Subharmonic centrifugal pendulum vibration absorbers allowing a rotational mobility. Mechanical Systems and Signal Processing **177**, 109125 (2022). https://doi.org/10.1016/j.ymssp.2022.109125

[30] Mahé, V., Renault, A., Grolet, A., Mahe, H., Thomas, O.: On the stability of pairs of subharmonic centrifugal pendulum vibration absorbers allowing a rotational mobility. , *Submitted to Nonlinear Dynamics*

[31] Mahé, V., Renault, A., Grolet, A., Mahé, H., Thomas, O.: Experimental investigation of the direct and subharmonic responses of a new design of centrifugal pendulum vibration absorber. , *Submitted to the Journal of Sound and Vibration*

[32] Alsuwaiyan, A.S., Shaw, S.W.: Performance and dynamic stability of general-path centrifugal pendulum vibration absorbers. Journal of Sound and Vibration **252**(5), 791–815 (2002). https://doi.org/10.1006/jsvi.2000.3534

[33] Grolet, A., Renault, A., Thomas, O.: Energy Localisation in Periodic Structures: Application to Centrifugal Pendulum Vibration Absorber. In: International Symposium on Transport Phenomena and Dynamics of Rotating Machinery, Maui (Hawaii) (2017)

[34] Nester, T.M., Schmitz, P.M., Haddow, A.G., Shaw, S.W.: Experimental observations of centrifugal pendulum vibration absorbers. In: International Symposium on Transport Phenomena and Dynamics of Rotating Machinery, Honolulu (Hawaii) (2004)

[35] Shaw, S.W., Schmitz, P.M., Haddow, A.G.: Tautochronic Vibration Absorbers for Rotating Systems. Journal of Computational and Nonlinear Dynamics **1**(4), 283–293 (2006). https://doi.org/10.1115/1.2338652

[36] Vidmar, B.J.: Analysis and Design of Multiple Order Centrifugal Pendulum Vibration Absorbers. PhD thesis, American Society of Mechanical Engineers, Chicago, Illinois, USA (August 2012)

[37] Cirelli, M., Cera, M., Pennestrì, E., Valentini, P.P.: Nonlinear design analysis of centrifugal pendulum vibration absorbers: An intrinsic geometry-based framework. Nonlinear Dynamics **102**(3), 1297–1318 (2020). https://doi.org/10.1007/s11071-020-06035-1

[38] Alsuwaiyan, A.S., Shaw, S.W.: Non-synchronous and Localized Responses of Systems of Identical Centrifugal Pendulum Vibration Absorbers. Arabian Journal for Science and Engineering **39**(12), 9205–9217 (2014). https://doi.org/10.1007/s13369-014-1464-1

[39] Issa, J.S., Shaw, S.W.: Synchronous and non-synchronous responses of systems with multiple identical nonlinear vibration absorbers. Journal of Sound and Vibration **348**, 105–125 (2015). https://doi.org/10.1016/j.jsv.2015.03.021

[40] Nishimura, K., Ikeda, T., Harata, Y.: Localization phenomena in torsional rotating shaft systems with multiple centrifugal pendulum vibration absorbers. Nonlinear Dynamics **83**(3), 1705–1726 (2016). https://doi.org/10.1007/s11071-015-2441-2

[41] Acar, M.A., Shaw, S.W.: Application of the Harmonic Balance Method to Centrifugal Pendulum Vibration Absorbers. In: Di Miao, D., Tarazaga, P., Castellini, P. (eds.) Special Topics in Structural Dynamics, Volume 6, pp. 243–252. Springer International Publishing, Cham (2016). https:

//doi.org/10.1007/978-3-319-29910-5_25

[42] Lee, C.-T., Shaw, S.W., Coppola, V.T.: A Subharmonic Vibration Absorber for Rotating Machinery. Journal of Vibration and Acoustics **119**(4), 590–595 (1997). https://doi.org/10.1115/1.2889766

[43] Theisen, T.M.: Gravity's effect on centrifugal pendulum vibration absorbers. Master's thesis, Michigan State University, Michigan (2011)

[44] Vidmar, B.J., Feeny, B.F., Shaw, S.W., Haddow, A.G., Geist, B.K., Verhanovitz, N.J.: The effects of Coulomb friction on the performance of centrifugal pendulum vibration absorbers. Nonlinear Dynamics **69**(1-2), 589–600 (2012). https://doi.org/10.1007/s11071-011-0289-7

[45] Chao, C.-P., Shaw, S.W.: The effects of imperfections on the performance of the subharmonic vibration absorber system. Journal of Sound and Vibration **215**(5), 1065–1099 (1998). https://doi.org/10.1006/jsvi.1998.1634

[46] Thomas, O., Touzé, C., Chaigne, A.: Asymmetric non-linear forced vibrations of free-edge circular plates. Part II: Experiments. Journal of Sound and Vibration **265**(5), 1075–1101 (2003). https://doi.org/10.1016/S0022-460X(02)01564-X

[47] Givois, A., Tan, J.-J., Touzé, C., Thomas, O.: Backbone curves of coupled cubic oscillators in one-to-one internal resonance: Bifurcation scenario, measurements and parameter identification. Meccanica **55**(3), 481–503 (2020). https://doi.org/10.1007/s11012-020-01132-2

[48] Nayfeh, A.H.: Perturbation Methods. Wiley Classics Library. Wiley-VCH, Weinheim (1973). https://doi.org/10.1002/9783527617609

[49] Routh, E.J.: Dynamics of a System of Rigid Bodies, 6th edn. Macmillan, London (1905)

[50] Guillot, L., Lazarus, A., Thomas, O., Vergez, C., Cochelin, B.: A purely frequency based Floquet-Hill formulation for the efficient stability computation of periodic solutions of ordinary differential systems. Journal of Computational Physics **416**, 109477 (2020). https://doi.org/10.1016/j.jcp.2020.109477

[51] Guillot, L., Cochelin, B., Vergez, C.: A Taylor series-based continuation method for solutions of dynamical systems. Nonlinear Dynamics **98**(4), 2827–2845 (2019). https://doi.org/10.1007/s11071-019-04989-5

[52] Haddow, A.G., Shaw, S.W.: Torsional Vibration Absorbers: A Testing

and Evaluation Apparatus. In: SAE 2001 Noise & Vibration Conference & Exposition, pp. 2001–011577 (2001). https://doi.org/10.4271/2001-01-1577

[53] Nayfeh, A.H., Balachandran, B.: Applied Nonlinear Dynamics: Analytical, Computational and Experimental Methods. Wiley Series in Nonlinear Science. Wiley-VCH, Weinheim (2004)

[54] Shaw, S.W., Wiggins, S.: Chaotic Motions of a Torsional Vibration Absorber. Journal of Applied Mechanics **55**(4), 952–958 (1988). https://doi.org/10.1115/1.3173747

[55] Sharif-Bakhtiar, M., Shaw, S.W.: The dynamic response of a centrifugal pendulum vibration absorber with motion-limiting stops. Journal of Sound and Vibration **126**(2), 221–235 (1988). https://doi.org/10.1016/0022-460X(88)90237-4

[56] Nise, N.S.: Control Systems Engineering, (2015)

Part III
The subharmonic centrifugal pendulum tuning

Summary of part III

This summary presents a synthesis of the main results of the following three chapters, constituting part III of this report. In this part the system considered is the centrifugal pendulum vibration absorber (CPVA) described in chapters 1 and 2. For the sake of completeness, a brief description of the system is recalled here. It is constituted of a rotor on which are attached N pendulums oscillating along their path and rotating about their centre of mass, as illustrated in Fig. III.1. The system is excited by a torque containing a constant and a periodic part. To simplify the analysis, we consider that the fluctuating torque contains a single harmonic of amplitude $\bar{T}_1$ and order n.

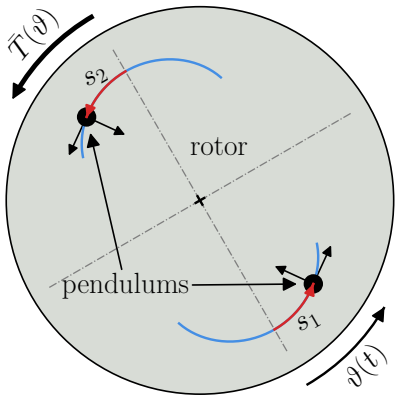

Figure III.1: Illustration of a CPVA made of $N = 2$ pendulums. The black frames attached to the pendulums represent their rotation relatively to the rotor.

The pendulums' path and rotation law are governed by functions

$$x(s_i) = 1 - n_t^2 s_i^2 + x_{[4]} s_i^4, \tag{III.1a}$$

$$\alpha(s_i) = \alpha_{[1]} s_i + \alpha_{[3]} s_i^3, \tag{III.1b}$$

where s_i represents the curvilinear abscissa of the i$^{\text{th}}$ pendulum (*cf.* Fig. III.1), n_t, $x_{[4]}$ are path parameters and $\alpha_{[1]}$, $\alpha_{[3]}$ are rotation parameters. It turns out that the behaviour of the system can be controlled by the pendulums' tuning order n_p and the nonlinear tuning parameter c_p (*cf.* chapter 7).

These two tuning parameters depend on the path and rotation parameters and on the dimensionless pendulums' inertia η such that

$$n_p = \frac{n_t}{\sqrt{1+\eta\alpha_{[1]}^2}}, \quad c_p = 3(x_{[4]} + 2n_p^2\eta\alpha_{[1]}\alpha_{[3]}). \tag{III.2}$$

In the following, we will present the behaviour of CPVAs tuned in different ways in order to highlight the richness of their dynamics.

Recall that for $N = 2$ pendulums, the system possesses three modes, illustrated in Fig. III.2. Mode 0 is a rigid body mode for which the pendulums are immobile. The phase-opposition mode corresponds to a phase-opposition motion of the pendulums and the rotor is a node of this mode. The associated eigenorder (analogous to an eigenfrequency) is the tuning order n_p of the CPVA. The unison mode represents a unison motion of the pendulums, which are in phase-opposition with the rotor. The associated eigenorder is slightly larger than n_p.

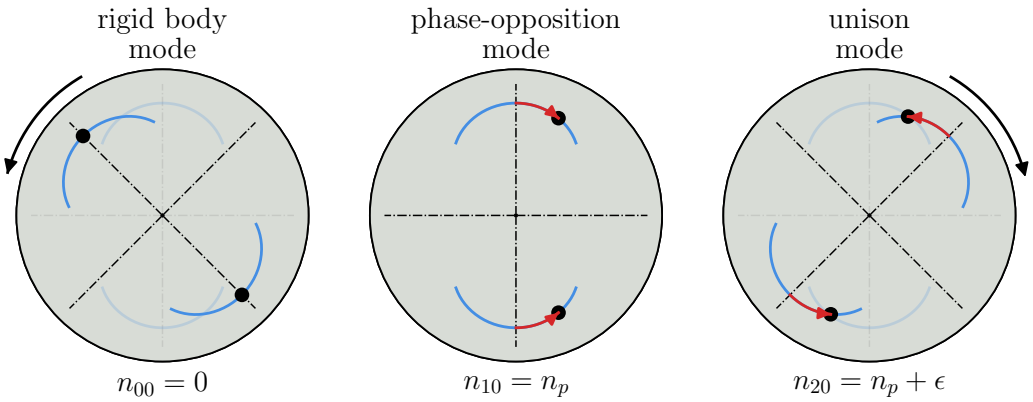

Figure III.2: Modes of a CPVA made of $N = 2$ pendulums. ϵ is a small parameter indicating that the eigenorder of the unison mode is slightly larger than the tuning order. The rotation of the pendulums about their centre of mass is not represented in this figure.

In this part, we focus on the subharmonic CPVA tuning, which refers to cases where the excitation order is close from twice the tuning order, i.e. $n \approx 2n_p$. This tuning condition can be realised only due to the nonlinear nature of the system. Indeed, it will be shown that the solution with pendulums oscillating at unison presents a period-doubling bifurcation, which allows the pendulums to vibrate at half the excitation order.

This factor two between the tuning and the excitation allows to filter the high-order torques encountered in electric vehicles (*cf.* section 1.1.1.3) without tuning the pendulums at such high orders. This is convenient as high-order tuning is difficult to achieve in practice due to manufacturing tolerances (*cf.* section 2.2.3).

Chapter 6 deals with the computation of the subharmonic response and its stability for a CPVA made of $N = 2$ pendulums. In the case N even but larger than 2, the phase-opposition mode illustrated in Fig. III.2 becomes degenerated. This significantly complicates the analysis of the subharmonic response and is addressed in chapter 7. Chapter 8 presents an experimental investigation on a prototype designed to work in subharmonic regime following the recommendations exposed in chapters 6 and 7.

Figure III.3 depicts a typical nonlinear response of the system when submitted to a harmonic torque with variable excitation order n (similar to a frequency response function with a varying excitation frequency). The amplitude of the pendulums is shown in (a) and the amplitude of the rotor's acceleration in (b). The left-hand side of Fig. III.3 deals with the classical CPVA tuning, which is the subject of part II, so it is not detailed here.

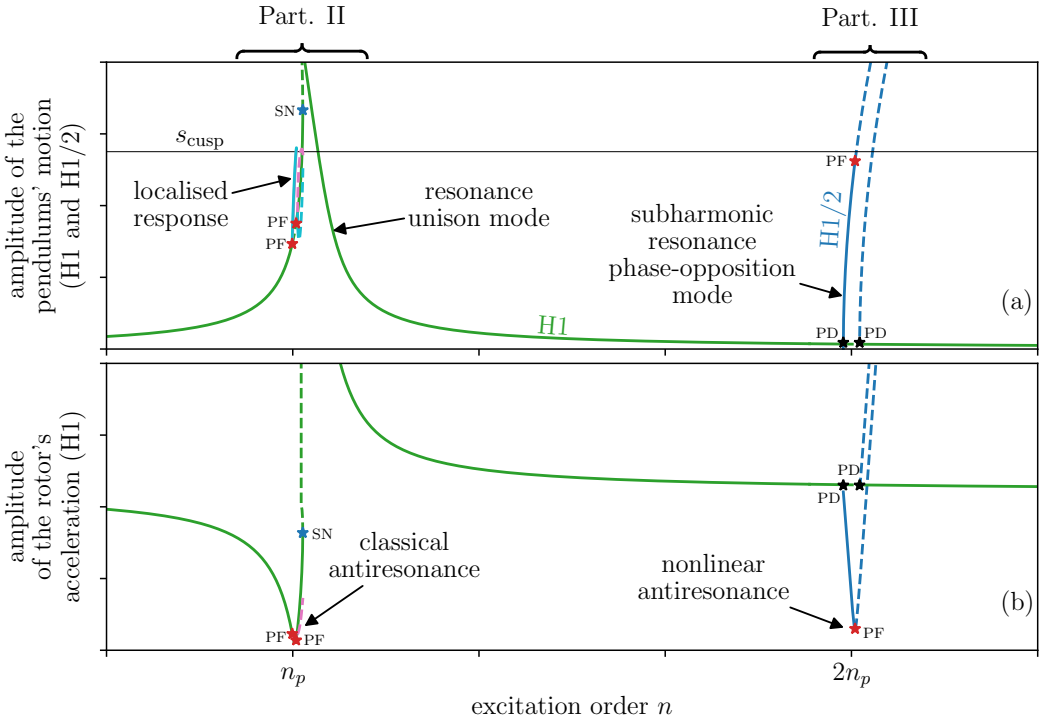

Figure III.3: Typical amplitude response of the pendulums (a) and rotor (b) of a CPVA as a function of the excitation order. The left-hand side of this figure is the scope of part II while the right-hand side is the scope of part III. The green and blue curves correspond to pendulums responding on the unison and phase-opposition modes, respectively, and the dashed lines indicate unstable solutions. Harmonics 1 and 1/2 of the pendulums' response are shown in (a) while only the first rotor harmonic is shown in (b). The horizontal black line in (a) indicates the cusp of the pendulums' path. The red, blue and black stars indicate pitchfork (PF), saddle-node (SN) and period-doubling (PD) bifurcations, respectively.

The scope of the chapters constituting part III is illustrated on the right-hand side of Fig. III.3.

The amplitudes of the pendulums are physically limited due to the finiteness of their path, and this limit is indicated by s_{cusp} in Fig. III.3(a). The green curves represent the response of the CPVA for pendulums oscillating at unison. This response is subjected to instabilities at $n \approx 2n_p$. Indeed, one can see two period-doubling (PD) bifurcations (black stars) giving birth to a subharmonic response of the pendulums on the phase-opposition mode. This subharmonic (of order 2) motion means that the pendulums oscillate at half the torque order. This is why the blue curves in (a) represent harmonic 1/2 of the pendulums' motion. The subharmonic pendulums' motion exerts a torque on the rotor that opposes the external torque, leading to the generation of the nonlinear rotor antiresonance visible in (b) around $2n_p$.

In practice, the excitation order n is fixed, so one could tune the pendulums such that $n_p = n/2$ for the rotor to be excited on its nonlinear antiresonance, thus reducing its vibrations as much as possible. However, this ideal behaviour is perturbed by nonlinear effects that deteriorate the efficiency of the subharmonic CPVA operation. These undesired effects are listed below and discussed in details thereafter:

- Because of nonlinear effects, an increase in the amplitude of the external torque causes the nonlinear antiresonance order to shift and depart from $2n_p$. In this case, and because in practice the excitation order n is fixed, the rotor is not excited on the minimum of its response over the whole torque range. Hence, the nonlinear detuning of the antiresonance prevents an optimal reduction of the rotor's vibrations.

- The subharmonic response is subjected to several sources of instabilities. The most concerning one is related to the pitchfork (PF) bifurcation (red star) which is located exactly on the nonlinear antiresonance (*cf.* Fig. III.3(b)). This PF bifurcation leads to a response different from the desired phase-opposition motion of the pendulums. Other instabilities, not visible in Fig. III.3, are due to a subharmonic response of the unison mode which also perturbs the phase-opposition motion.

In part III, we investigate the subharmonic response using mainly analytical methods. This allowed to gain a better understanding of this particular solution. It also led to the derivation of original design guidelines allowing to prevent the apparition of instabilities and to limit the shifting of the nonlinear antiresonance. These points, which maximise the efficiency of the CPVA, are detailed thereafter.

The development of many of the results discussed in this summary requires elaborate algebraic manipulations, detailed in chapters 6, 7 and 8. Here, we report only the main results of part III, described from a physical point of view.

Basics of the subharmonic response [chap. 6]

For a CPVA made of two absorbers, the desired subharmonic operation is a pendulums' response on the subharmonic of the phase-opposition mode such that they oscillate at half the torque order and with opposite phases. Taking into account this phase-opposition motion, the rotor's acceleration can be expressed at first order as (*cf.* chapter 6)

$$\underbrace{\theta''}_{\substack{\text{acceleration}\\ \text{of the rotor}}} = \underbrace{\bar{T}_1 \cos(n\vartheta)}_{\substack{\text{external}\\ \text{torque}}} + \underbrace{\mu n_t^2 \left(s_1 s_1' + s_2 s_2'\right)}_{\text{Coriolis effect}} = \bar{T}_1 \cos(n\vartheta) + 2\mu n_t^2 s s', \quad s = s_1 = -s_2, \tag{III.3}$$

where s_1 and s_2 are the coordinates of pendulums 1 and 2, respectively, and μ and n_t are an inertia ratio and the order of the pendulums' path (*cf.* sections 2.1.2.2 and 2.1.3). The only term balancing the external torque in Eq. (III.3) is due to the Coriolis effect and has a quadratic nonlinearity. A consequence of this nonlinearity is that the term ss' oscillates at twice the frequency of s. This explains how subharmonic pendulums' oscillations at $n_p = n/2$ generate a torque of order n that can reduce the rotor's vibrations. Moreover, no higher rotor harmonics are generated by the subharmonic operation because every term in the rotor's acceleration (III.3) oscillates at order n. This is a significant advantage compared to the classical operation.

A typical subharmonic response for a CPVA made of $N = 2$ pendulums is shown in Fig. III.4. This CPVA is said to be "perfectly tuned" because the path and rotation functions of the pendulums are an epicycloid and a linear rotation, so they do not generate additional nonlinearities in the system (*cf.* section 2.1.3).

Let us first look at Fig. III.4(c)-(d), which represent a forced response of the CPVA at twice its tuning order (i.e. $n = 2n_p$). The subharmonic response (blue curves) appears through a PD bifurcation from a trivial solution (green curves). This trivial solution is actually an approximation of the response on the unison mode far from its resonance (*cf.* Fig. III.3 and chapter 6). The PD bifurcation is not located at zero torque, meaning that there is a torque threshold to trigger the subharmonic response. This is one of the drawbacks of the subharmonic operation as it makes it inefficient at low torque levels. This threshold exists because the phase-opposition mode is excited parametrically by the external torque (*cf.* chapter 6). The torque level bringing the pendulums to the cusp of their path is defined as the torque capacity, which is represented in Fig. III.4(c).

Another particularity of the subharmonic operation is the saturation phenomenon. This is visible in Fig. III.4(d), where the rotor's amplitude is independent of the forcing level. The fact that the vibrations do not increase with the forcing is an extremely interesting particularity to use for vibration reduction.
The saturation phenomenon is also visible in Fig. III.4(b), which represents the rotor's response around

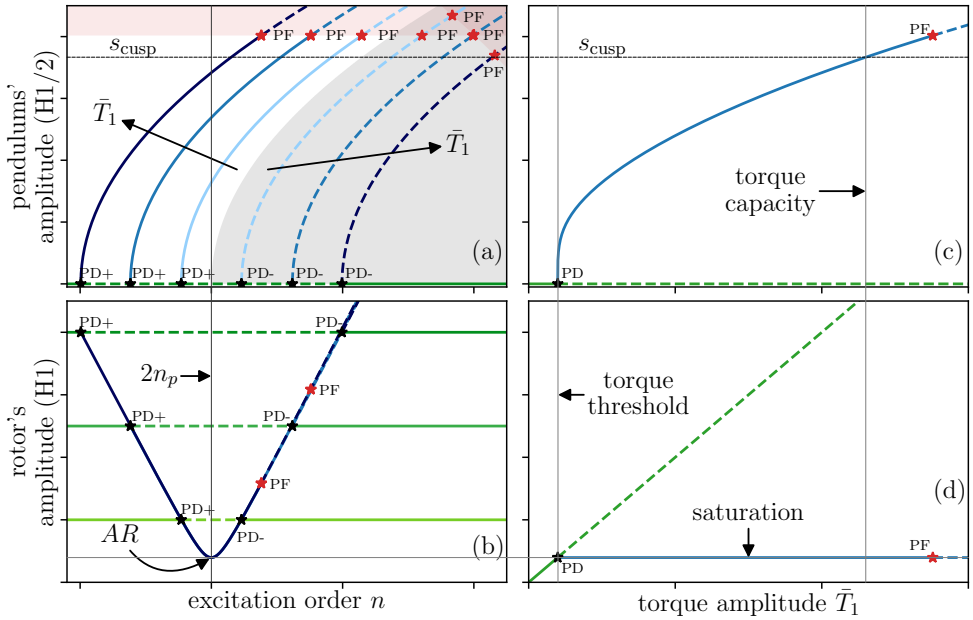

Figure III.4: On the left, we represent the amplitude of the pendulums (a) and the rotor (b) as a function of the excitation order and for three torque levels. The darker the line the larger the associated torque level. On the right, we also represent the amplitude of the pendulums (c) and the rotor(d), but as a function of the forcing level and at order $n = 2n_p$. Green and blue curves correspond to the solution with immobile pendulums and the subharmonic operation, respectively. Dashed lines indicate unstable solutions. Red and black stars correspond to pitchfork (PF) and period-doubling (PD+ for supercritical, PD- for subcritical) bifurcations, respectively. The red and grey areas indicate instability zones related to localisation of the subharmonic solution and to jumps, respectively.

its antiresonance for three different torque levels. In this figure, the unstable and stable branches of the response overlap, so they cannot be distinguished. In addition, the responses associated to the three torque levels represented (each taking birth at two PD bifurcations) overlap so only the one corresponding to the largest forcing, shown in dark blue, is visible. The fact that the responses are overlapped means that the antiresonance (AR) does not move with the forcing, which illustrates the saturation phenomenon.

Furthermore, the subharmonic response is subjected to several instabilities. The PD bifurcations can be subcritical (PD-) (*cf.* section 2.5.1.3), in which case they give birth to unstable subharmonic solutions. These unstable solutions are located in the grey area in Fig. III.4(a). Note that they correspond to the lower branches of the subharmonic response, which bends to the right, hence exhibiting a hardening behaviour.

The red area in Fig. III.4(a) indicates another instability zone of the subharmonic solution. PF bifurcations occur at the crossings of the response with this zone. They give rise to coupled-mode solutions

for which the unison mode contributes to the subharmonic response (*cf.* chapter 6). This is the opposite of the situation encountered in classical operation, where the response at unison is perturbed by the contribution of phase-opposition mode (*cf.* part II). These coupled-mode solutions cause the pendulums to oscillate differently and lower the filtering efficiency of the CPVA.
Note that every PF bifurcation in Fig. III.4 occurs above the cusp, so they are not an issue because the pendulums cannot oscillate at such amplitudes. Nevertheless, there can cases other than the one depicted in Fig. III.4 for which these instabilities are problematic. Hence, guidelines are provided in chapter 6 to ensure that the subharmonic solution remains stable up until the pendulums reach their cusp.

Stability of the subharmonic solution in the presence of several pairs of pendulums and nonlinear mistuning [chap. 6, 7]

In a CPVA made of several pairs of pendulums, the phase-opposition mode is degenerated, and the desired subharmonic solution, denoted "SH1", corresponds to particular combinations of these degenerated modes (*cf.* chapter 7). These combinations should be such that the N pendulums oscillate with the same amplitude, but $N/2$ pendulums are in phase-opposition with the other $N/2$. One of these configurations is illustrated in Fig. III.5. SH1 is the preferred subharmonic solution because it prevents one or more pendulums to oscillate with a larger amplitude than the others (i.e. it avoids localisation), which maximises the torque capacity of the CPVA.

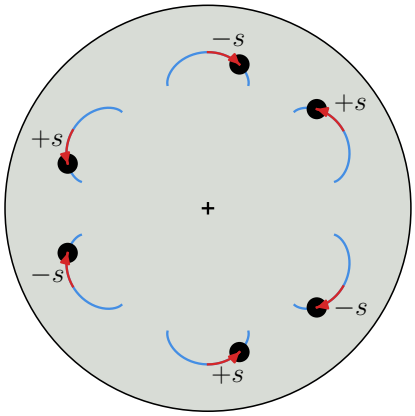

Figure III.5: Illustration of the desired motion in subharmonic operation for a CPVA made of six pendulums. This desired motion corresponds to the solution called "SH1". Note that here we represent only one configuration satisfying SH1, but there are others (three successive pendulums in unison and in phase-opposition with the next three for instance).

The response of a nonlinearly mistuned CPVA (i.e. the pendulums' path and/or rotation functions are different from an epicycloid and a linear rotation law) made of several pairs of pendulums is shown

in Fig. III.6.

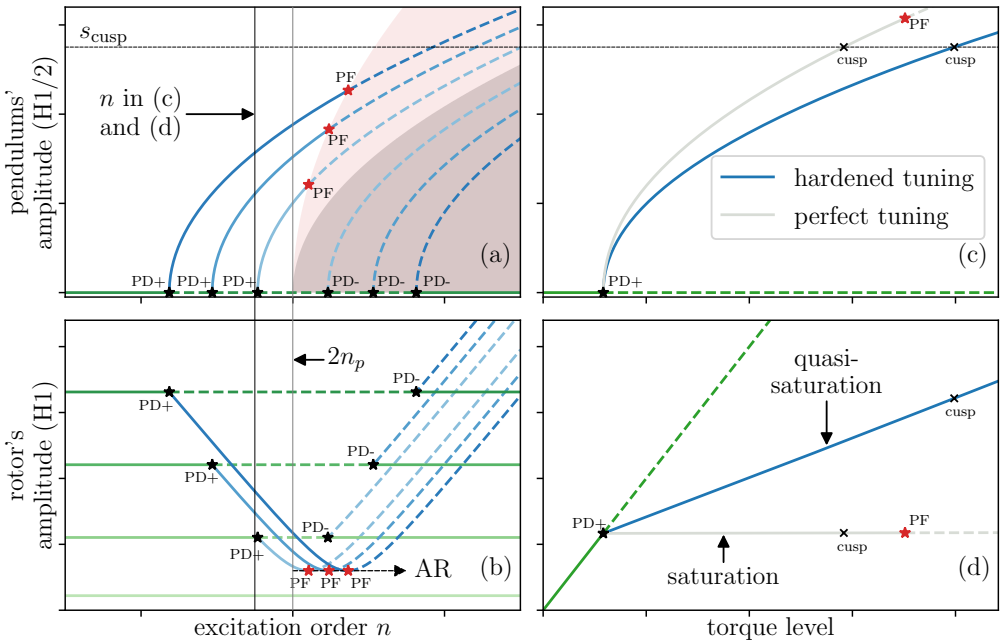

Figure III.6: Amplitude of the pendulums (harmonic 1/2) and the rotor (harmonic 1) as a function of the excitation order ((a), (b), respectively) and as a function of the torque level ((c), (d), respectively). Four torque levels are represented in (a) and (b), and the darker the curves the larger the torque level. Green and blue curves correspond to the solution with immobile pendulums and the subharmonic operation, respectively. Note that the CPVA whose subharmonic response is shown in blue is intentionally nonlinearly mistuned. Dashed lines indicate unstable solutions. Red and black stars correspond to pitchfork (PF) and period-doubling (PD) bifurcations, respectively. The red and grey areas indicate instability zones related to localisation of the subharmonic solution and to jumps, respectively. In (a) and (b), the vertical grey line indicates the excitation order corresponding to the torque response shown in (c) and (d).

First, one can notice the presence of a red area starting from $n = 2n_p$ in Fig. III.6(a), which did not exist in the presence of only two pendulums (*cf.* Fig. III.4(a)). It corresponds to an additional instability zone which exists only when several pairs of pendulums are used. Indeed, in that case, the degenerated phase-opposition modes are all in 1:1 internal resonance, so they can exchange energy and thus cause instabilities of the desired SH1 solution.

The PF bifurcations, located at the intersections of SH1 and the instability zone, give birth to localised subharmonic solutions. In such a case, the pendulums have different motions and at least one of them oscillates with an amplitude larger than SH1. Hence, when the torque increases, it reaches its cusp at forcing level smaller than expected, which reduces the torque capacity of the CPVA. In addition, this localised subharmonic solution usually leads to an increase in the rotor's vibrations (*cf.* chapter 7). For these reasons, these instabilities are undesired. Moreover, they are particularly bothering

because the PF bifurcations giving birth to the localised solution are located exactly at the rotor's antiresonance, as visible in Fig. III.6(b).
A design guidelines allowing to avoid these instabilities is proposed in chapter 7. This is a major contribution to the study of centrifugal pendulums in subharmonic operation.

In Fig. III.6(a), the red instability zone is located at $n \geq 2n_p$ because the nonlinear CPVA mistuning is chosen to harden SH1 (i.e. to make the response more hardening than with perfect tuning). If the nonlinear mistuning was chosen to soften SH1, the instability zone would be located at $n \leq 2n_p$. Perfect tuning never happens in practice, due to manufacturing tolerances for instance. Hence, to know where the instability zone is located and be able to avoid it, one has to use a minimum level of nonlinear mistuning. However, this causes the antiresonance to shift as the torque level increases, as shown in Fig. III.6(b). Because of this shifting, the saturation of the rotor's response, visible in Fig. III.6(d), is no longer perfect.

There is a balance to be found between the avoidance of instabilities and the limitation of the antiresonance shifting. The most recommended configuration is a hardened CPVA with overtuned (i.e. $2n_p > n$) pendulums, which corresponds to the configuration shown in Fig. III.6. This has the advantage of slightly increasing the torque capacity compared to the perfectly-tuned case (*cf.* Fig. III.6(c)-(d)). Nevertheless, for a given application, the use of a subharmonic CPVA tuning leads to a much lower torque capacity than a classical tuning (*cf.* chapter 6). This is one of the main drawbacks of the subharmonic operation.

Finally, it is important to note that there is an infinity of possible combinations of the degenerated phase-opposition modes that take birth at the PD bifurcations. However, we want the pendulums to respond on an SH1 combination (we recall that there are several equivalent configurations, *cf.* chapter 7, as for instance the one illustrated in Fig. III.5). This is why we verified numerically in chapter 7 that the basin of attraction of SH1 is large enough for the PD bifurcations to lead the pendulums to respond on SH1. This was verified for a hardened overtuned CPVA, which is the configuration recommended previously to render SH1 stable while maximising the torque capacity.

Experimental investigation of an original centrifugal pendulum design [chap. 8]

The theoretical results obtained in this thesis are based on very general CPVA models. This way, these results can be used to design any architecture of CPVA. Nevertheless, it must be kept in mind that the main goal of the thesis is to propose solutions to adapt pendulum absorber systems to electric vehicles, which requires the filtering of high orders (*cf.* section 1.1.1.3). This is why an original CPVA design, dedicated to high-order tuning, is proposed and investigated in this thesis. This design, studied in chapter 8 and shown in Fig. III.7, is made of spherical pendulums. Its simplicity allows to

overcome issues encountered with bifilar CPVAs at high orders (*cf.* chapter 8).

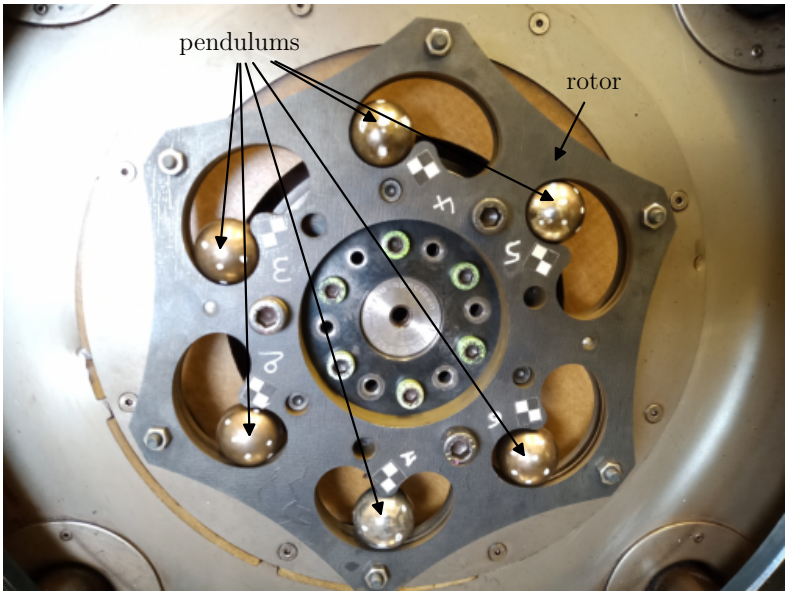

Figure III.7: Prototype of a CPVA with spherical pendulums

The prototype was tested in subharmonic operation, but also in classical operation. One of the aims of the tests in classical operation was to validate the CPVA design (identification of the linear and nonlinear tuning parameters, the damping coefficients, ...) using a tuning configuration that is well known, and thus easier to study.

The main results are shown in Fig. III.8. Figure III.8(a) shows an order sweep near the pendulums' tuning order. The good fitting of the model with the experimental data allowed to validate the pendulums' tuning and to identify their damping coefficient (note that the discrepancy around the resonance is due to a failure in the input torque control, *cf.* Fig. III.8(b)). The particularly large 28 [dB] attenuation highlights the high filtering performance of the prototype. However, the slipping of the pendulums, investigated in chapter 8, was seen to significantly reduce the torque capacity of the CPVA. This slipping issue is a major drawback of this architecture.

The subharmonic filtering can be observed in Fig. III.8(c), where a torque response of the rotor is represented for n slightly lower than $2n_p$. As explained previously, this overtuning is chosen to avoid instabilities. The analytical results match relatively well with the experimental data up to a given torque level, above which the pendulums start to slip. Unfortunately, the slipping of the pendulums significantly reduces the torque capacity of the CPVA (the torque at the adherence limit is about 50% of the torque at the cusp). To our knowledge, Fig. III.8(c) shows the first evidence of subharmonic filtering with a CPVA.

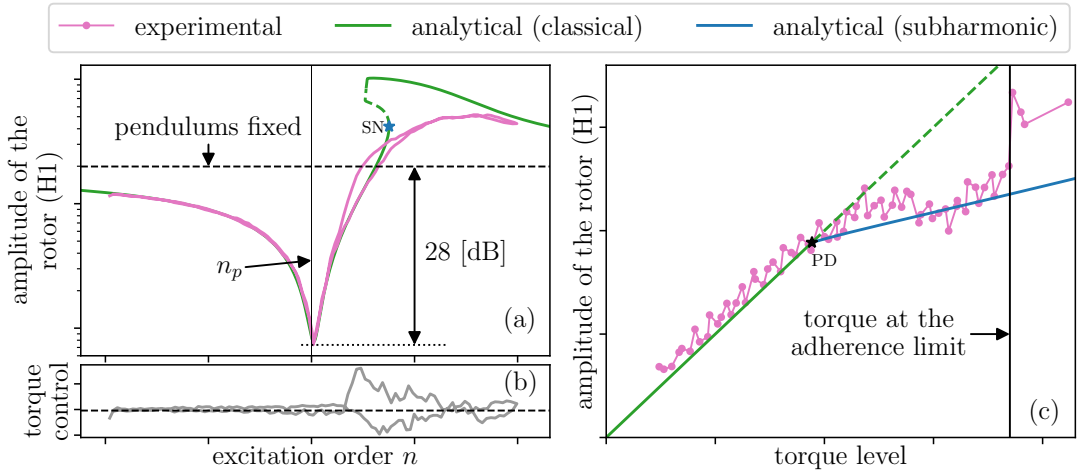

Figure III.8: Experimental (pink) and analytical (green and blue) responses of the CPVA prototype in classical (a) and subharmonic (c) operations. The torque response in (c) is represented for an excitation order n slightly lower than $2n_p$. The blue and black stars indicate saddle-node (SN) and period-doubling (PD) bifurcations, respectively. (b) indicates the control of the torque level during the order sweep in classical operation. The dashed black line indicates the target torque while the grey line indicates the actual torque.

A CPVA prototype tuned at order 10 is proposed in chapter 8 to filter order 20 when in subharmonic operation. However, the nonlinear tuning of such a high-order CPVA requires too demanding manufacturing tolerances. In addition, the reduced torque capacity due to the slipping of the pendulums is too detrimental for a satisfactory performance. For these reasons, the subharmonic tuning does not seem sufficient to adapt centrifugal pendulums to electric powertrains.

Chapter 6

The subharmonic operation of centrifugal pendulums

This chapter is made of a paper published in the *Journal of Sound and Vibrations* [75]. It focuses on the subharmonic response of a centrifugal pendulum vibration absorber (CPVA). This could prove useful to adapt CPVAs to gear trains as it allows to divide by two the tuning order required for the pendulums. In this chapter, the analytical results are obtained starting from the simplified CPVA model proposed in section 2.3.2.

Sections 1 to 3 repeat information from chapters 1 and 2. They present the context of the study, the modelling of a CPVA (*cf.* section 2.1.1) and a linear analysis (*cf.* section 2.2). In addition, sections 5.1 and 5.2 repeat the derivation of simplified CPVA equations, which was already detailed in section 2.3.2 of chapter 2. The reader might want to skip these sections of the article if he already read chapters 1 and 2.

The novelty of the article starts in section 4, where the basic principles of the subharmonic operation are presented. The computation of simplified modal equations is detailed in section 5 (we remind that the content of sections 5.1 and 5.2 was already discussed in chapter 2, so the reader might only want to look at section 5.3). In section 6, the associated modal solutions and their stability are computed using the method of multiple scales (*cf.* section 2.5.2.1). In addition, they are validated through comparisons with numerical resolutions of the system's dynamics. The model is applied to case studies in section 7, and the link between the shifting of the nonlinear antiresonance and the saturation of the rotor's response is investigated. Design rules allowing to maximise the performance while avoiding instabilities are provided. Finally, in section 8, the performance in subharmonic operation is compared to that in classical operation.

Mechanical Systems and Signal Processing 177 (2022) 109125

Contents lists available at ScienceDirect

Mechanical Systems and Signal Processing

journal homepage: www.elsevier.com/locate/ymssp

Subharmonic centrifugal pendulum vibration absorbers allowing a rotational mobility

V. Mahe [a,b,*], A. Renault [b], A. Grolet [a], H. Mahe [b], O. Thomas [a]

[a] Arts et Metiers Institute of Technology, LISPEN, HESAM Université, F-59000 Lille, France
[b] Valeo Transmissions, Centre d'Étude des Produits Nouveaux, Espace Industriel Nord, Route de Poulainville, 80009 Amiens Cedex 1, France

ARTICLE INFO

Communicated by X. Jing

Keywords:
Centrifugal pendulum vibration absorber
Non-linear dynamics
Subharmonic absorber

ABSTRACT

Rotating machines are often subjected to fluctuating torques, leading to vibrations of the rotor and finally to premature fatigue and noise pollution. This work addresses a new design of centrifugal pendulum vibration absorbers (CPVAs), used to reduce the vibrations in an automotive transmission line. These passive devices, composed of several masses oscillating along a trajectory relative to the rotor, are here tuned at a subharmonic of the targeted harmonic torque frequency. Thanks to the inherent non-linearities, a CPVA with two masses oscillating in phase opposition is able to efficiently counteract the input torque, with particular features such as saturation phenomena. This work particularly extends previous works to a new class of CPVA, whose peculiarity is that masses admit a significant rotation motion relative to the rotor, thus adding the benefit of their rotatory inertia. Results on the system's subharmonic response and its stability are obtained thanks to an analytical perturbation method, and design guidelines are proposed. The validity of those results is also confirmed through comparisons with numerical solutions and the performance of this subharmonic system is compared to that of a classical CPVA tuned at the torque frequency.

1. Introduction

In the frame of reducing polluting emissions and fuel consumption of vehicles using thermal engines, automotive manufacturers try to reduce the cylinder capacity and engine speed of rotation. These evolutions lead to a significant increase of rotation irregularities called "acyclisms", mainly due to higher combustion pressure. One of the main characteristics of these reciprocating engines is the linear dependence of the acyclism frequency to the mean engine speed of rotation. The coefficient of proportionality is called the engine order and only depends on the architecture of the engine. For four strokes engines, the engine order is half the number of cylinders. During an acceleration phase, the engine sweeps a wide frequency range containing some driveline torsional modes. This situation may lead to significant noise and vibration levels into the passenger compartment and premature wear of the driveline components. Centrifugal pendulum vibration absorbers (CPVAs) have been used for many years to minimise acyclisms of automotive powertrains at the engine order [1–3]. These passive devices consist of oscillating masses (pendulums) moving along particular paths relative to a primary inertia (rotor) as shown in Fig. 1. Because the pendulums are driven by the centrifugal acceleration field resulting from the rotation of the CPVA, their natural frequency is proportional to the mean engine speed of rotation. The coefficient of proportionality is the pendulums' tuning order, which can be chosen to filter out vibrations at the engine order.

* Corresponding author at: Arts et Metiers Institute of Technology, LISPEN, HESAM Université, F-59000 Lille, France.
E-mail addresses: vincent.mahe@ensam.eu (V. Mahe), alexandre.renault@valeo.com (A. Renault), aurelien.grolet@ensam.eu (A. Grolet), herve.mahe@valeo.com (H. Mahe), olivier.thomas@ensam.eu (O. Thomas).

https://doi.org/10.1016/j.ymssp.2022.109125
Received 26 November 2021; Received in revised form 7 February 2022; Accepted 31 March 2022
Available online 27 April 2022

The classical way of choosing the pendulums' tuning order, used in industrial solutions, is to tune the pendulums at the engine order. Similarly to usual dynamic vibration absorbers [4], this tuning generates an antiresonance of the rotor at the engine order, allowing for significant vibration reduction. However, CPVAs are non-linear systems that include geometric and inertial non-linearities. At large excitation amplitudes, this can lead to jumps of the response [5], localisation of the pendulums' response [6–17], a shift of the antiresonance [18] and the generation of higher rotor harmonics [19–24].

Another tuning possibility is to set the pendulums' tuning order to half the engine order. To our knowledge, this was first mentioned in [25], but studies on this topic were led by S. Shaw et al. [19,26–30]. With such a tuning, the pendulums oscillate at half the engine order so that the solution is a subharmonic of order 2. The study of subharmonic oscillations has many fields of application, such as energy harvesting [31,32], the creation of models for the design of pedestrian structures [33], and, of interest here, vibration reduction [28]. In two degree-of-freedom systems with quadratic non-linearities, solutions with one mode oscillating at half the frequency of the other one can lead to a saturation phenomenon where the amplitude of the higher mode becomes independent of the forcing amplitude [34]. This phenomenon, due to a 2:1 internal resonance, can be an efficient way to reduce vibrations. It is for instance used in [35,36] to reduce the vibrations of a beam through a nonlinear piezoelectric shunt. In the case of a CPVA with two pendulums, quadratic non-linearity exists through Coriolis effects and the pendulums' phase-opposition mode is in a 2:1 resonance relation with respect to the excitation [29]. This allows a pair of pendulums oscillating in phase-opposition at half the engine frequency to generate a saturation of the rotor's response [28]. The stability of that response and the effects of pendulums mistuning are addressed in [29]. If the CPVA comprises N pendulums (with N even), the desired behaviour is that where two groups of $N/2$ in phase pendulums are moving in phase-opposition, so that each group acts as an equivalent pendulum. Such a system is subject to additional instabilities [30]. Contrarily to the classical tuning, the subharmonic one does not generate higher rotor harmonics [19], which is a significant advantage. In addition, the subharmonic tuning allows for a saturation of the rotor's response while in classical CPVAs the rotor's amplitude increases with the torque amplitude. Another benefit of subharmonic CPVAs is that tuning pendulums at lower orders results in wider trajectories that require less demanding manufacturing tolerances [37].

Studies dealing with subharmonic CPVAs are restricted to the case of translated pendulums, i.e. pendulums that do not rotate relatively to the rotor. This is probably due to the fact that early works recommended the use of purely translated pendulums [38]. However, A. Renault [39–41] and M. A. Acar [42] recently showed that adding a rotational mobility of the pendulums leads to a significant increase of mitigation performances. This increase in performance was also observed in [43] and the effect of rotation is a current topic of research [15–17,44–47]. The motivation of this paper is to investigate the subharmonic response of CPVAs with two pendulums that are allowed to rotate relatively to the rotor. Two tools aiming at helping designing subharmonic CPVAs are introduced. They allow to visualise the evolution of the torque capacity[1] and the efficiency of the absorption as a function of the linear and non-linear tunings. Additionally, a new design guideline intended to improve the efficiency of the filtration is given. Finally, to the author's knowledge, this paper presents the first comparison between the classical and subharmonic tunings.

This paper is organised as follows. Section 2 describes the modelling of the CPVA and a linear analysis is led in Section 3. The basic mechanisms of the subharmonic filtration are exposed in Section 4. The construction of the analytical model starts in Section 5 with the simplification of the equations of motion and their expansion on the modal basis. The modal and physical solutions along with their stability are derived in Section 6. Case studies and design guidelines are presented in Section 7 and the subharmonic filtration is compared to the classical one in Section 8.

2. Modelling

The system studied is shown in Fig. 1. A rotor of inertia J_r rotates about its centre O. Its total angular position is $\vartheta(t) = \Omega t + \theta(t)$ where t is the time, Ω is the mean rotation velocity and θ corresponds to the fluctuating part of the rotation. A torque $T(\vartheta) = T_0 + T_\theta(\vartheta)$ is applied to the rotor where T_0 is its constant part and $T_\theta(\vartheta)$ is periodic. The constant torque balances the damping, thus setting the mean rotational speed Ω such that $T_0 = b_r\Omega$, where b_r is the linear viscous damping coefficient of the rotor. N pendulums of mass m_i and inertia I_i (about their centre of mass) oscillate on their trajectory $\mathscr{C}_i$. Their position on these trajectories is given by the curvilinear abscissa S_i and their distance from O is $R_i(S_i)$. The characteristic dimension $R_{0i} = R_i(S_i = 0)$ represents the position of the pendulums at rest (when $T_\theta = 0$ such that they are perfectly centrifugated). In addition to the traditional translation motion, the present study considers that the pendulums rotate about their centre of mass according to the angle $\alpha_i(S_i)$. This function can be chosen by the designer, just like the trajectory $\mathscr{C}_i$. As for the rotor, an equivalent linear viscous damping coefficient b_i is used to model the damping between the rotor and the ith pendulum. In the later, pendulums and their associated trajectory and rotation functions will be considered identical so that subscript "i" will be dropped when addressing pendulums' parameters.

In order to write the equations of motion in a non-dimensional form, the following parameters and variables are introduced:

$$s_i = \frac{S_i}{R_0}, \quad y = \frac{\dot\vartheta}{\Omega} = 1 + \frac{\dot\theta}{\Omega}, \quad \eta = \frac{I}{mR_0^2}, \quad \mu = \frac{NmR_0^2}{(J_r + NI)}, \quad x(s_i) = \frac{R(R_0 s_i)^2}{R_0^2}, \quad z(s_i) = \sqrt{x(s_i) - \frac{1}{4}\left(\frac{dx(s_i)}{ds_i}\right)^2},$$
$$\gamma(s_i) = \frac{d\alpha(s_i)}{ds_i}, \quad \bar b = \frac{b}{m\Omega}, \quad \bar b_r = \frac{b_r}{(J_r + NI)\Omega}, \quad \bar T(\vartheta) = \bar T_0 + \bar T_\theta(\vartheta) = \frac{T(\vartheta)}{(J_r + NI)\Omega^2}, \tag{1}$$

where $\dot{(\bullet)} = \partial(\bullet)/\partial t$. The s_i and y are the $N+1$ degree-of-freedom of the system. They correspond to the relative position of the pendulums and the non-dimensional rotation velocity of the rotor, respectively. η is the ratio of the pendulums' inertia about their

[1] The torque capacity is the maximum level of torque applied on the rotor for which the system can operate as desired.

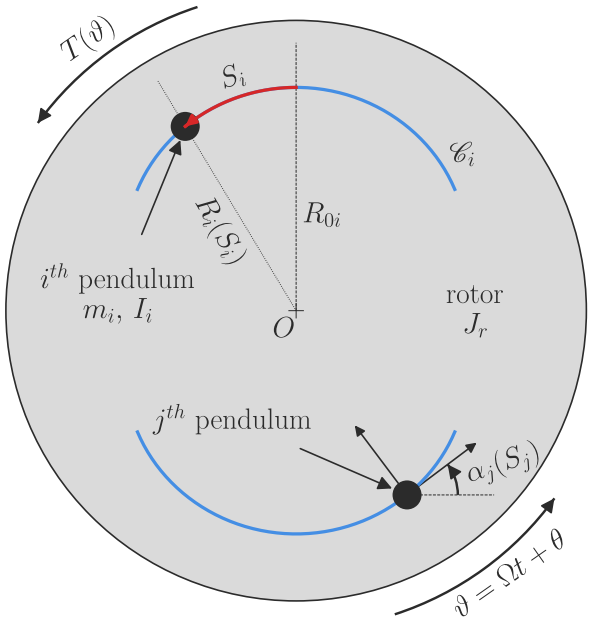

Fig. 1. Representation of the system studied. It is made of $N = 2$ pendulums.

centre of mass over their geometric inertia about O. μ is the ratio of all the pendulums' geometric inertias about O over the rotatory inertia of the whole system about O. $x(s_i)$ and $z(s_i)$ are trajectory functions while $\alpha(s_i)$ and $\gamma(s_i)$ are rotation functions. In this paper, $x(s_i)$ and $\alpha(s_i)$ are written as polynomials in the curvilinear abscissa s_i such that

$$x(s_i) = 1 - n_t^2 s_i^2 + \sum_{k=3}^{\infty} x_{[k]} s_i^k, \quad \alpha(s_i) = \sum_{k=0}^{\infty} \alpha_{[k]} s_i^k, \tag{2}$$

where n_t is the order of the pendulums' trajectory (called geometric tuning order in [45]) and $x_{[k]}$, $\alpha_{[k]}$ are trajectory and rotation coefficients. Note that in the case $x_{[k]} = 0, \forall k$, the pendulums' trajectories are epicycloids, which corresponds to the tautochronic trajectory for $\theta = 0$ [25]. $\bar{b}$ and $\bar{b}_r$ are non-dimensional damping constants and $\bar{T}(\vartheta)$ is the non-dimensional torque applied on the rotor.

In order to give $\bar{T}(\vartheta)$ the meaning of an external forcing term, we replace the independent variable t by the rotor's position ϑ [48], which can be seen as a non-dimensional time. Using the chain rule, one can show that

$$\dot{(\bullet)} = \Omega y (\bullet)', \quad \ddot{(\bullet)} = \Omega^2 y y' (\bullet)' + \Omega^2 y^2 (\bullet)'', \tag{3}$$

where $(\bullet)' = \partial(\bullet)/\partial\vartheta$ (computation details are given in Appendix A). Hence, the non-dimensional rotor's acceleration is now $\ddot{\vartheta}/\Omega^2 = \dot{y}/\Omega = y y'$. Using the non-dimensional quantities (1) and the chain rule (3), one can write the equations of motion as

$$\frac{1}{N}\left[\sum_{i=1}^{N}(N + \mu x(s_i)) y y' + \mu\left(z(s_i) + \eta\gamma(s_i)\right)(y y' s_i' + y^2 s_i'') + \mu y^2 s_i'\left(\frac{dx(s_i)}{ds_i} + \frac{dz(s_i)}{ds_i}s_i' + \eta\frac{d\gamma(s_i)}{ds_i}s_i'\right)\right] + \bar{b}_r y = \bar{T}(\vartheta), \tag{4a}$$

$$\left[z(s_i) + \eta\gamma(s_i)\right] y' + \left[1 + \eta\gamma(s_i)^2\right](y' s_i' + y s_i'') + \eta\gamma(s_i)\frac{d\gamma(s_i)}{ds_i} y s_i'^2 - \frac{1}{2}\frac{dx(s_i)}{ds_i} y + \bar{b} s_i' = 0, \qquad i = 1, \dots, N. \tag{4b}$$

Computation details are given in Appendix B. Eq. (4a) governs the motion of the rotor while the N Eqs. (4b) govern the motion of the pendulums. These equations are difficult to interpret at this stage as one cannot distinguish the linear and non-linear terms that are hidden in functions $x(s_i), z(s_i)$ and $\gamma(s_i)$ and in variable y.

From now on, it is assumed that the fluctuating torque applied to the rotor contains only one harmonic whose non-dimensional form is $\bar{T}_1 \cos(n\vartheta)$ where n is the engine order. For a car engine, n corresponds to the number of strikes per revolution of the crankshaft.

3. Linear analysis of the system

In this section, a linear analysis of the system with $N = 2$ pendulums is led. First of all, one can use Eq. (3) to show that, at first order,

$$1 + \theta' \approx y, \quad \theta'' \approx y y' \approx y'. \tag{5}$$

The demonstration is provided in Appendix C. Relations (5) allow to represent the motion of the rotor with position θ instead of velocity y. This way, all the degree-of-freedom of the system are positions, which facilitates the representation of the mode shapes.

In addition, the balance between the constant torque and the mean rotational velocity (*cf.* Section 2) can be written in terms of the non-dimensional variables such that

$$\bar{T}_0 = \bar{b}_r. \tag{6}$$

Using relations (5) and (6), one can linearise Eqs. (4a) and (4b) to obtain

$$(1+\mu)\theta'' + \frac{\mu\Lambda_c}{N}\sum_{i=1}^{N} s_i'' + \bar{b}_r\theta' = \bar{T}_\theta(\vartheta), \tag{7a}$$

$$\Lambda_c\theta'' + \Lambda_m s_i'' + n_t^2 s_i + \bar{b}s_i' = 0, \tag{7b}$$

where Λ_m and Λ_c are constants representing the equivalent mass of a pendulum due to the effect of the rotatory inertia and the linear coupling term between a pendulum and the rotor, respectively. They are given by

$$\Lambda_m = 1 + \eta\alpha_{[1]}^2, \quad \Lambda_c = 1 + \eta\alpha_{[1]}, \tag{8}$$

where $\alpha_{[1]}$ is the linear rotation coefficient (*cf.* Eq. (2)). The eigenorders and mode shapes of the conservative system are

$$n_{00} = 0, \quad n_{10} = n_p, \quad n_{20} = n_p\sqrt{\frac{1+\mu}{1+\mu\left(1-\frac{\Lambda_c^2}{\Lambda_m}\right)}} \tag{9a}$$

$$\boldsymbol{\phi_{00}} = [1,0,0]^T, \quad \boldsymbol{\phi_{10}} = [0,1,-1]^T, \quad \boldsymbol{\phi_{20}} = \left[-\frac{\mu\Lambda_c}{1+\mu}, 1, 1\right]^T. \tag{9b}$$

The eigenorders can be seen as non-dimensional eigenfrequencies and the three components of the eigenvectors correspond to θ, s_1 and s_2, respectively. n_p is the pendulums' tuning order, which is related to the trajectory order n_t such that

$$n_p = \frac{n_t}{\sqrt{\Lambda_m}}, \tag{10}$$

and it corresponds to the eigenorder of the pendulums when they are uncoupled from the rotor. Superscript "T" denotes the transpose.

$\boldsymbol{\phi_{00}}$ is a rigid-body mode for which only the rotor is excited. $\boldsymbol{\phi_{10}}$ represents a phase-opposition motion of the pendulums with an immobile rotor. As the rotor is a node of $\boldsymbol{\phi_{10}}$, this mode does not respond in the linear regime. $\boldsymbol{\phi_{20}}$ describes a mode for which pendulums move in unison but in phase-opposition with respect to the rotor. Modes associated to $\boldsymbol{\phi_{00}}$, $\boldsymbol{\phi_{10}}$ and $\boldsymbol{\phi_{20}}$ will be called mode 0, 1 and 2, respectively.

When a fluctuating torque is applied, the pendulums respond on mode 2 and generate an antiresonance on the rotor at order n_p (in the conservative case). Thus, for a fluctuating torque of order n, one typically chooses $n_p \approx n$ to minimise the vibrations of the rotor. Note that n_p is not strictly equal to n as mistuning is usually desired to increase the torque range of the system and/or to prevent the apparition of instabilities [8,10,17]. In the case of a real automotive driveline (a simple model of which consists in successive rotors linked through torsional springs [49]), the CPVA should be placed as close as possible from the source of excitation (i.e. the engine). Doing so, the antiresonance generated by the pendulums exists on every driveline components located after the CPVA [50], which allows to isolate the whole driveline from the torque fluctuations.

Although classical CPVAs are currently the only ones used by the industry, there exists another mean of reducing the rotor's vibrations using a non-linear subharmonic response of the pendulums [28]. This is explained in the next section.

4. Basis of the subharmonic filtration

4.1. Filtration principle

The aim here is to show that there exists a solution to filter out the vibrations of the rotor other than the classical one with $n_p \approx n$ and pendulums oscillating in unison. To do so, the simple case of a CPVA with two undamped pendulums following epicycloidal trajectories and with a linear rotation law is considered. Moreover, the solution sought is that of perfect filtration so that the rotor spins at a constant speed (i.e. $y = 1$, $y' = 0$).

One can see that if the pendulums are in phase-opposition (i.e. $s_1 = s = -s_2$), most of the non-linearities they generate on the rotor will balance each other as $x(s) = x(-s)$, $z(s) = z(-s)$ and $\gamma(s) = \gamma(-s)$. Thus, Eqs. (4a) and (4b) simplify to

$$-2\mu n_t^2 s s' = \bar{T}_1\cos(n\vartheta), \tag{11a}$$

$$s'' - n_p^2 s = 0. \tag{11b}$$

These equations have an exact solution, given by

$$s = \frac{1}{n_t}\sqrt{\frac{\bar{T}_1}{\mu n_p}}\cos(n_p\vartheta + \varphi), \quad n_p = n/2, \quad \varphi = \frac{\pi}{4} \text{ or } \frac{\pi}{4} + \pi. \tag{12}$$

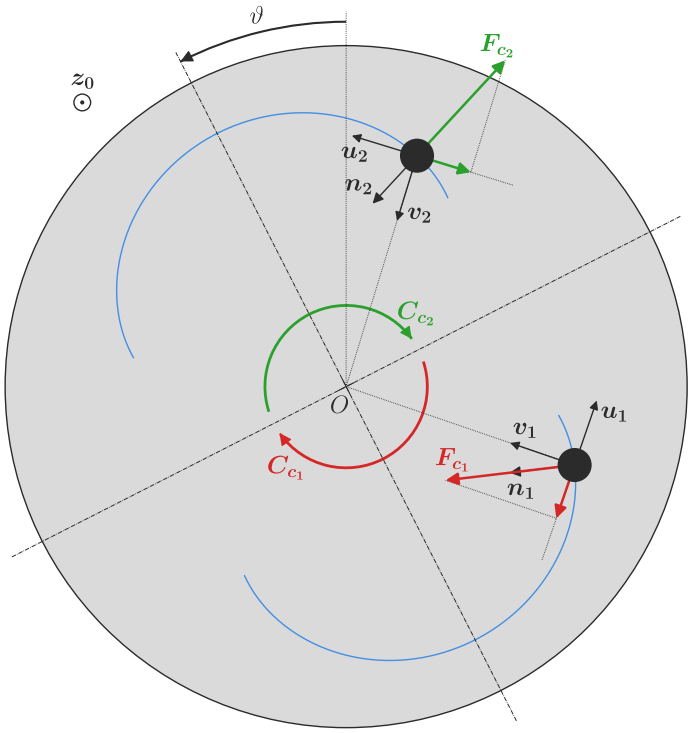

Fig. 2. Representation of the Coriolis forces and torques generated by two pendulums in phase-opposition. The projection of the Coriolis forces on vectors $\boldsymbol{u}_1$ and $\boldsymbol{u}_2$ is also given, as it indicates the sign of the torque produced.

Eq. (12) represents a motion of the pendulums (we remind that $s_1 = s = -s_2$) such that they perfectly counterbalance the external torque to eliminate the vibrations of the rotor. The fact that $n_p = n/2$ shows that the desired pendulums' response is a subharmonic of order 2 as they oscillate at half the excitation order. The reason why a subharmonic oscillation of order 2 is needed is that the term balancing the external torque in Eq. (11a) is quadratic. Thus, if s is harmonic and oscillating at $n/2$, ss' will generate a purely harmonic torque oscillating at n that can cancel the external torque. The fact that ss' is purely harmonic implies that the pendulums counterbalance the external torque without producing higher rotor harmonics, contrarily to the classical tuning (this was already pointed out in [19]).

It is interesting to see how the pendulums can generate a torque on the rotor even though they are in phase-opposition. In Eq. (11a), the term balancing the external torque arises from Coriolis effects. One can compute the Coriolis acceleration of the ith pendulum and the associated force $\boldsymbol{F}_{c_i}$ to find

$$\boldsymbol{F}_{c_i} = -2\dot{\vartheta} m \dot{S}_i \boldsymbol{n}_i, \tag{13}$$

where $\boldsymbol{n}_i$ is the normal to the ith pendulum's trajectory at abscissa S_i. The torque produced by $\boldsymbol{F}_{c_i}$ on the rotor is given by $\boldsymbol{C}_{c_i} = -R_i \boldsymbol{v}_i \times \boldsymbol{F}_{c_i}$ where $\boldsymbol{v}_i$ is a unitary vector pointing from the ith pendulum's centre of mass to the rotor's. Using geometric relations, one can show that the Coriolis torque arising from the ith pendulum is given by

$$\boldsymbol{C}_{c_i} = -\dot{\vartheta} m \dot{S}_i \frac{dX(S_i)}{dS_i} \boldsymbol{z}_0, \tag{14}$$

where $X(S_i) = R_0^2 x(S_i/R_0)$ is a dimensional trajectory function and $\boldsymbol{z}_0$ is such that $(\boldsymbol{u}_i, \boldsymbol{v}_i, \boldsymbol{z}_0)$ forms a right-handed orthonormal basis (*cf.* Fig. 2). Assuming $X(S_i)$ is even (it is the case in practice due to design constraints), the Coriolis torques produced by the two pendulums add up even though they are in phase-opposition. This is illustrated in Fig. 2.

4.2. Typical response of a subharmonic CPVA

A typical response of a subharmonic CPVA is depicted in Fig. 3. It corresponds to approximate analytical solutions of Eqs. (4a) and (4b) (*cf.* Sections 5 and 6.3). Fig. 3 represents the fundamental harmonic of the rotor's acceleration in (a) and (b) and the subharmonic motion of the pendulums in (c) and (d). An order response of the CPVA is shown in (a) and (c) while a torque response is shown in (b) and (d). Green curves represent the system's response for immobile pendulums while blue curves correspond to the pendulums' subharmonic solution and the associated rotor's response. Dashed lines indicate unstable solutions.

Fig. 3(a) shows the non-linear antiresonance generated by the pendulums on the rotor. In Fig. 3(b), one can see that the amplitude at the antiresonance is independent from the forcing amplitude, thus leading to a saturation phenomenon. This saturation is effective

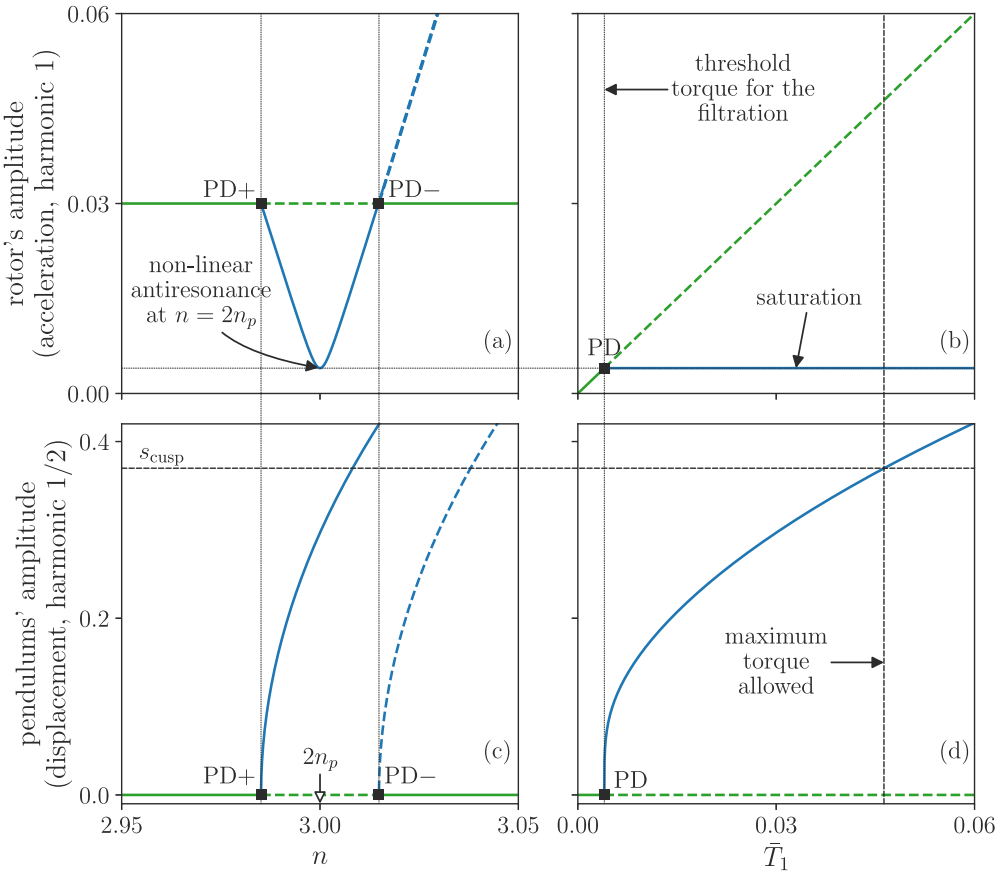

Fig. 3. Typical order (left) and torque (right) responses of a CPVA. Pendulums' responses are shown in (c) and (d) while rotor's responses are shown in (a) and (b). (a) and (c) are order responses for $\bar{T}_1 = 0.03$ while (b) and (d) are torque responses for $n = 2n_p = 3$. Green curves represent the system's response for immobile pendulums while blue curves correspond to the pendulums' subharmonic solution and the associated rotor's response. Dashed lines indicate unstable solutions. Black squares with code names "PD" indicate period doubling bifurcations. PD+ and PD-correspond to supercritical and subcritical bifurcations, respectively. $n_p = 1.5$, $\mu = 0.1$, $\bar{b} = 0.002$, $\eta = \alpha_{[k]} = x_{[k]} = 0, \forall k$.

starting from a threshold torque amplitude and up to a maximum torque. This upper torque limit exists because the pendulums' trajectory has a cusp that pendulums cannot overpass.

Fig. 3 depicts some essential features of the subharmonic filtration, but considers only purely translated pendulums following an epicycloidal trajectory. In the following, an analytical model allowing for the study of more general CPVAs is developed. It takes into account the rotation of the pendulums and perturbations of the epicycloidal trajectory.

5. Simplified modal equations

Following Chao et al. [29], the first step in the construction of an analytical model is to scale the parameters. This allows to simplify the equations of motion such that the dynamics of the pendulums becomes uncoupled from that of the rotor. These simplified equations of motion will then be projected on a modal basis to obtain modal equations.

Since the displacement of the pendulums will be considered small (*cf.* Section 5.2), higher orders of $x(s_i)$ and $\alpha(s_i)$ have a negligible effect. Thus, it is relevant to keep only their first non-linear contributions such that

$$x(s_i) = 1 - n_t^2 s_i^2 + x_{[4]} s_i^4, \quad \alpha(s_i) = \alpha_{[1]} s_i + \alpha_{[3]} s_i^3. \tag{15}$$

These functions are taken to be symmetric (respectively anti-symmetric) about $s_i = 0$ as it is the case in practice due to design constraints [40,41]. Like what was done previously for the torque, the non-dimensional rotor's velocity can be split into a constant term 1 and fluctuating component $y_\theta(\vartheta)$ such that

$$y(\vartheta) = 1 + y_\theta(\vartheta). \tag{16}$$

5.1. Scaling

In this subsection, the aim is to scale the weight of some parameters and variables so as to capture the desired physical phenomena. The following remarks will govern the scaling:

- The optimum system configuration is that with small damping. In Section 4, it was shown that the absence of damping could lead to a perfect filtration.
- The fluctuating torque T_θ is small compared to the rotor's kinetic energy (which is $J_r\Omega^2/2$ at equilibrium). This implies that $\tilde{T}_1$ is small.
- The total pendulums' geometric inertia about point O, NmR_0^2, is considered small compared to the total inertia of the rotating system about O, $J_r + NI$, such that μ is small.
- The rotor's inertia being significant, the fluctuating rotational speed y_θ is small against 1. This means that θ' is small as, at first order, $y_\theta \approx \theta'$ (*cf.* Appendix C).
- The trajectory and rotation functions chosen (*cf.* Eq. (15)) are an epicycloid perturbed by $x_{[4]}$ and a linear law perturbed by $\alpha_{[3]}$, respectively. Considering those perturbations are small, $x_{[4]}$ and $\alpha_{[3]}$ are small.

In accordance with those remarks and introducing the small parameter ϵ, the following scaled parameters are introduced:

$$\bar{b} = \epsilon\tilde{b}, \quad \bar{b}_r = \epsilon\tilde{b}_r, \quad \bar{T}_1 = \epsilon\tilde{T}_1, \quad \mu = \epsilon\tilde{\mu}, \quad y_\theta = \epsilon\tilde{y}_\theta, \quad \theta' = \epsilon\tilde{\theta}', \quad x_{[4]} = \epsilon\tilde{x}_{[4]}, \quad \alpha_{[3]} = \epsilon\tilde{\alpha}_{[3]}. \tag{17}$$

In order to give a physical meaning to ϵ, one can choose to set $\epsilon = \mu$ [8]. Moreover, in the following, only first order terms will be retained in the rotor's equation (*cf.* Section 5.2). Hence, one can use the first order approximations (5) to express the rotor's dynamics using the scaled position $\tilde{\theta}$ instead of the scaled rotational velocity $\tilde{y}_\theta$. Approximations (5) can be written in terms of those scaled variables, leading to

$$\tilde{y}_\theta \approx \tilde{\theta}', \quad \tilde{y}'_\theta \approx \tilde{\theta}''. \tag{18}$$

5.2. Simplified physical equations

The aim here is to obtain an equation governing the rotor's dynamics as a function of the pendulums' motion and the external torque while uncoupling the pendulums' dynamics from the rotor's. Introducing Eqs. (15), (16) and (17) in the equations of motion (4a) and (4b) and using Taylor series for $z(s_i)$, one obtains

$$\tilde{\theta}'' = \frac{\tilde{\mu}}{N}\left[\sum_{i=1}^{N} n_p^2\Lambda_c s_i + 2n_t^2 s_i s_i' + n_t^2(1+n_t^2)\left(s_i s_i'^2 - \frac{n_p^2}{2}s_i^3\right)\right] + \tilde{T}_1\cos(n\theta), \tag{19a}$$

$$\begin{aligned} s_i'' + n_p^2 s_i = {} & -\epsilon\Lambda_m^{-1}\left\{\frac{\Lambda_c^2\tilde{\mu}}{N}\sum_{j=1}^{N} n_p^2 s_j + \tilde{b}s_i' + \frac{\tilde{\mu}n_t^2\Lambda_c}{N}\left[\sum_{j=1}^{N} s_j(2s_j' + s_i')\right] + \frac{\tilde{\mu}n_t^2}{N}\left[\sum_{j=1}^{N}(1+n_t^2)\Lambda_c\left(s_j s_j'^2 - \frac{n_p^2}{2}(s_j^3 + s_j s_i^2)\right)\right.\right. \\ & \left.\left. +2\Lambda_m s_j s_j' s_i'\right] + 6\eta\alpha_{[1]}\tilde{\alpha}_{[3]}(s_i s_i'^2 + s_i^2 s_i'') - 2\tilde{x}_{[4]}s_i^3 + \left(\Lambda_c + \Lambda_m s_i' - \frac{n_t^2(1+n_t^2)}{2}s_i^2\right)\tilde{T}_1\cos(n\vartheta)\right\} + HOT, \\ & i = 1, \ldots, N. \end{aligned} \tag{19b}$$

Eq. (19a) expresses the rotor's acceleration as a function of the pendulums' motion. It makes use of the pendulums' equation at first order $s_i'' = -n_p^2 s_i$. The rotor's acceleration contains linear, quadratic and cubic terms. As seen in Section 4, the quadratic term is the one responsible of the subharmonic filtration.

The N coupled Eqs. (19b) govern the pendulums' motion. They are uncoupled from the rotor's dynamics and contain the effect of the external torque, the damping, the coupling between pendulums (both linear and non-linear) through the sums over N, and the perturbations of the trajectory and rotation functions (i.e. $\tilde{x}_{[4]}$ and $\tilde{\alpha}_{[3]}$). These N equations are weakly non-linear because the trajectory and rotation functions chosen (*cf.* Eq. (15)) are close to an epicycloid and a linear rotation, which render a quasi-linear behaviour for small fluctuations of the rotational speed. The external torque appears under three different forms in Eqs. (19b). $\tilde{T}_1\cos(n\vartheta)$ alone has the meaning of a direct forcing while $s_i'\tilde{T}_1\cos(n\vartheta)$ is a parametric forcing, which can be interpreted as a variable damping. The torque also appears as a non-linear term through $s_i^2\tilde{T}_1\cos(n\vartheta)$.

As stated previously, Taylor series of $z(s_i)$ were used to obtain the simplified equations. This is relevant as the trajectory has a cusp that pendulums cannot overpass, so their motions s_i are restricted to be small. In the special case of the epicycloid (i.e. $x_{[4]} = 0$), the amplitude at the cusp is

$$s_{\text{cusp}} = \frac{1}{\sqrt{n_t^2(1+n_t^2)}}. \tag{20}$$

5.3. Modal equations

The aim here is to derive the modal equations. From now on, we consider that the system is made of $N = 2$ pendulums. Eqs. (19a) and (19b) can be written in matrix form using the vector of unknowns

$$\boldsymbol{q} = [\tilde{\theta}, s_1, s_2]^T = \sum_{k=0}^{2}\zeta_k\boldsymbol{\phi_{k0}}, \tag{21}$$

where ζ_0, ζ_1 and ζ_2 are the modal coordinates associated to modes 0, 1 and 2, respectively. The matrix equation obtained can then be projected on the modes of the system, leading to the following three modal equations:

$$\zeta_0'' = f_0(\zeta_1, \zeta_2, \vartheta), \tag{22a}$$

$$\zeta_1'' + n_p^2\zeta_1 = f_1(\zeta_1, \zeta_2, \vartheta), \tag{22b}$$

$$\zeta_2'' + n_p^2\zeta_2 = f_2(\zeta_1, \zeta_2, \vartheta). \tag{22c}$$

The full form of functions f_0, f_1 and f_2 is given in Appendix D. It is of importance to note that only ζ_1 and ζ_2 appear in Eqs. (22b) and (22c). This means that modes 1 and 2 are uncoupled from mode 0. The reason for this is that those two modes are due to the presence of the pendulums, whose equations were uncoupled from the rotor's dynamics (*cf.* Section 5.2).

We remind that the desired situation for the subharmonic filtration is that with pendulums oscillating in phase-opposition, which corresponds to $\zeta_1 \neq 0, \zeta_2 = 0$. In that case, Eqs. (22a) and (22b) become

$$\zeta_0'' = 2\tilde{\mu}n_t^2\zeta_1\zeta_1' + \tilde{T}_1\cos(n\vartheta), \tag{23a}$$

$$\zeta_1'' + n_p^2\zeta_1 \quad = -\epsilon\Lambda_m^{-1}\left[\Lambda_m\zeta_1'\tilde{T}_1\cos(n\vartheta) + 2\tilde{\mu}n_t^2\Lambda_m\zeta_1\zeta_1'^2 + 6\eta\alpha_{[1]}\tilde{\alpha}_{[3]}(\zeta_1\zeta_1'^2 + \zeta_1^2\zeta_1'') - 2\tilde{x}_{[4]}\zeta_1^3 + \tilde{b}\zeta_1'\right], \tag{23b}$$

and mode 0 exactly corresponds to the rotor's motion as $\zeta_0'' = \tilde{\theta}''$. It is clear from Eq. (23a) that there is an energy transfer between the rigid-body mode (i.e. the rotor) and the phase-opposition mode (i.e. the pendulums). In Eq. (23b), f_1 captures the parametric excitation, the damping and cubic non-linearities arising from Coriolis effects and perturbations of the trajectory and rotation functions.

6. Modal and physical solutions

6.1. Application of the method of multiple scales

The method of multiple scales [51] is now used to solve Eqs. (22b) and (22c). Two rotation scales are introduced, $\vartheta_0 = \vartheta$ and $\vartheta_1 = \epsilon\vartheta$. Modal coordinates are expanded such that

$$\zeta_1(\vartheta) = \zeta_{11}(\vartheta_0, \vartheta_1) + \epsilon\zeta_{12}(\vartheta_0, \vartheta_1), \tag{24a}$$

$$\zeta_2(\vartheta) = \zeta_{21}(\vartheta_0, \vartheta_1) + \epsilon\zeta_{22}(\vartheta_0, \vartheta_1). \tag{24b}$$

Because the solution sought is a subharmonic of order 2, it is convenient to introduce the detuning term σ such that

$$n = 2n_p + \epsilon\sigma. \tag{25}$$

$\sigma > 0$ and $\sigma < 0$ correspond to under-tuned and over-tuned pendulums, respectively. Applying the method of multiple scales yields first order solutions of the form

$$\zeta_{11}(\vartheta_0, \vartheta_1) = u_1(\vartheta_1)\cos\left(\frac{n\vartheta_0 - \beta_1(\vartheta_1)}{2}\right), \tag{26a}$$

$$\zeta_{21}(\vartheta_0, \vartheta_1) = u_2(\vartheta_1)\cos\left(\frac{n\vartheta_0 - \beta_2(\vartheta_1)}{2}\right). \tag{26b}$$

Amplitudes u_1, u_2 and phases β_1, β_2 are governed by the system

$$\begin{cases} D_1u_1 & = f_{u_1}(\boldsymbol{u}, \boldsymbol{\beta}), & \text{(a)} \\ u_1D_1\beta_1 & = f_{\beta_1}(\boldsymbol{u}, \boldsymbol{\beta}), & \text{(b)} \\ D_1u_2 & = f_{u_2}(\boldsymbol{u}, \boldsymbol{\beta}), & \text{(c)} \\ u_2D_1\beta_2 & = f_{\beta_2}(\boldsymbol{u}, \boldsymbol{\beta}), & \text{(d)} \end{cases} \tag{27}$$

where $D_1(\bullet) = \partial(\bullet)/\partial\vartheta_1$ and $\boldsymbol{u}, \boldsymbol{\beta}$ are vectors containing u_1, u_2 and β_1, β_2, respectively. Functions f_{u_1}, f_{β_1}, f_{u_2} and f_{β_2} are given in Appendix E.

The solutions sought are those at steady-state, meaning that the amplitudes and phases are invariant with ϑ such that

$$D_1u_1 = D_1u_2 = D_1\beta_1 = D_1\beta_2 = 0. \tag{28}$$

Four types of solutions are possible for system (27):

- $(u_1 = u_2 = 0)$ corresponds to the trivial solution for which pendulums are immobile.
- $(u_1 \neq 0, u_2 = 0)$ corresponds to the desired behaviour as pendulums respond only on mode 1. This solution will be called "SH1" where "SH" stands for "subharmonic".
- $(u_1 = 0, u_2 \neq 0)$ corresponds to a solution with in phase pendulums and will be called "SH2".
- $(u_1 \neq 0, u_2 \neq 0)$ corresponds to coupled-mode solutions that will be called "SH12".

6.2. Stability of the trivial solution

The trivial solution simply corresponds to immobile pendulums. It is interesting to assess its stability as bifurcations will lead to one of the non-linear solutions. As the equations of system (27) are singular when either u_1 or u_2 is zero, it is convenient to use a

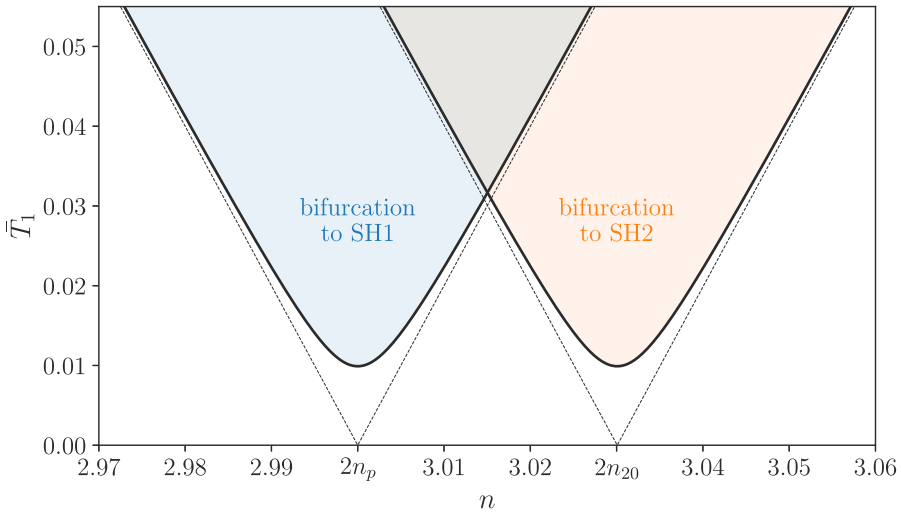

Fig. 4. Arnold tongues representing the range of excitation parameters for which the trivial solution bifurcates to SH1 or SH2. Dashed lines represent the limit of the tongues in the absence of damping. Parameters used are those given in Table 1, except for $\bar{b} = 0.005$.

change from polar to Cartesian coordinates [29]. To this aim, the new variables

$$p_1 = u_1 \cos\left(\frac{\beta_1}{2}\right), \quad q_1 = u_1 \sin\left(\frac{\beta_1}{2}\right), \quad p_2 = u_2 \cos\left(\frac{\beta_2}{2}\right), \quad q_2 = u_2 \sin\left(\frac{\beta_2}{2}\right) \tag{29}$$

are defined and system (27) is rewritten under the form

$$\begin{cases} D_1 p_1 &= f_{p_1}(\boldsymbol{p}, \boldsymbol{q}), \quad \text{(a)} \\ D_1 q_1 &= f_{q_1}(\boldsymbol{p}, \boldsymbol{q}), \quad \text{(b)} \\ D_1 p_2 &= f_{p_2}(\boldsymbol{p}, \boldsymbol{q}), \quad \text{(c)} \\ D_1 q_2 &= f_{q_2}(\boldsymbol{p}, \boldsymbol{q}). \quad \text{(d)} \end{cases} \tag{30}$$

$\boldsymbol{p}$ and $\boldsymbol{q}$ are vectors containing p_1, p_2 and q_1, q_2, respectively. f_{p_1}, f_{q_1}, f_{p_2} and f_{q_2} are functions given in Appendix G. The Jacobian of system (30) evaluated on the trivial response has the special form

$$\boldsymbol{J} = \begin{bmatrix} \boldsymbol{A} & \boldsymbol{0} \\ \boldsymbol{0} & \boldsymbol{B} \end{bmatrix}, \quad \boldsymbol{A} = \begin{bmatrix} \frac{\partial f_{p_1}}{\partial p_1} & \frac{\partial f_{p_1}}{\partial q_1} \\ \frac{\partial f_{q_1}}{\partial p_1} & \frac{\partial f_{q_1}}{\partial q_1} \end{bmatrix}, \quad \boldsymbol{B} = \begin{bmatrix} \frac{\partial f_{p_2}}{\partial p_2} & \frac{\partial f_{p_2}}{\partial q_2} \\ \frac{\partial f_{q_2}}{\partial p_2} & \frac{\partial f_{q_2}}{\partial q_2} \end{bmatrix}, \tag{31}$$

so that the eigenvalues of $\boldsymbol{J}$ are the eigenvalues of $\boldsymbol{A}$ and $\boldsymbol{B}$. $\boldsymbol{A}$ and $\boldsymbol{B}$ represent the effect of a perturbation of modes 1 and 2 on the system, respectively. Thus, if the real part of one of the eigenvalues of $\boldsymbol{A}$ ($\boldsymbol{B}$) becomes positive, the system's response bifurcates to SH1 (SH2). The eigenvalues of $\boldsymbol{A}$ and $\boldsymbol{B}$ are given by

$$\lambda_{1,2} = -\frac{2\tilde{b} \pm \Lambda_m \sqrt{\tilde{T}_1^2 - 4\sigma^2}}{4\Lambda_m}, \tag{32a}$$

$$\lambda_{3,4} = -\frac{2\tilde{b} \pm \sqrt{\tilde{T}_1^2 \Lambda_m^2 - 4(\Lambda_m \sigma - \Lambda_c^2 n_p \tilde{\mu})^2}}{4\Lambda_m}, \tag{32b}$$

respectively. From Eq. (32), one can conclude that the trivial solution is unstable if

$$\tilde{T}_1^2 - \frac{4\tilde{b}^2}{\Lambda_m^2} - 4\sigma^2 > 0, \quad \text{or} \tag{33a}$$

$$\tilde{T}_1^2 - \frac{4\tilde{b}^2}{\Lambda_m^2} - 4\left(\sigma - n_p \tilde{\mu} \frac{\Lambda_c^2}{\Lambda_m}\right)^2 > 0. \tag{33b}$$

Conditions (33a) and (33b) are associated to a pitchfork bifurcation[2] towards SH1 and SH2, respectively. The bifurcation sets of the trivial solution are shown in Fig. 4.

[2] It is a pitchfork bifurcation of the slow scale system (30), which corresponds to a period doubling bifurcation of the initial dynamical system, since a harmonic 1 response bifurcates to a harmonic 1/2 response. (*cf.* Appendix F).

6.3. Solution on the phase-opposition mode

Pendulums in phase-opposition is the desired behaviour of the system. Using Eqs. (27a) and (27b) with $u_2 = 0$, one can find that SH1 is given by

$$u_1^2 = n_p \frac{2\Lambda_m \sigma \pm \sqrt{\Lambda_m^2 \tilde{T}_1^2 - 4\tilde{b}^2}}{c_c - c_p}, \tag{34a}$$

$$\tan\beta_1 = \mp\sqrt{\frac{\Lambda_m^2 \tilde{T}_1^2}{4\tilde{b}^2} - 1}. \tag{34b}$$

c_c and c_p are non-linear coefficients related to Coriolis effects and to the perturbations of the trajectory and rotation functions, respectively. They are defined as

$$c_c = \tilde{\mu} n_t^4, \quad c_p = 3(\tilde{x}_{[4]} + 2n_p^2 \eta \alpha_{[1]} \tilde{\alpha}_{[3]}). \tag{35}$$

The backbone curve of SH1 is

$$n_1^{(SH)} = 2n_p + \epsilon \frac{c_c - c_p}{2n_p \Lambda_m} u_1^2, \tag{36}$$

so that for reasonable values of c_p, mode 1 is hardening.

SH1 is not defined for every parameter as u_1 must be real. Evaluating Eq. (34a) for $u_1 = 0$, one finds that the torque or order at the bifurcation are

$$\tilde{T}_1^{*^2} = 4\sigma^2 + \frac{4\tilde{b}^2}{\Lambda_m^2}, \quad n_{1,2}^* = 2n_p \pm \frac{1}{2}\sqrt{\tilde{T}_1^2 - \frac{4\tilde{b}^2}{\Lambda_m^2}}. \tag{37}$$

Superscript $*$ indicates that the quantity is that at the bifurcation. Eq. (37) corresponds to the limit of condition (33a), thus confirming that this condition is associated to SH1. One typically wants $\tilde{T}_1^*$ to be as small as possible for SH1 to exist at small torque amplitudes. This would correspond to a configuration with small damping, small mistuning and maximum equivalent mass.

The stability information of SH1 is given by the eigenvalues of the Jacobian of system (30) evaluated on SH1. It has the same form as shown in Eq. (31), but matrices $\boldsymbol{A}$ and $\boldsymbol{B}$ have a slightly different meaning. As $\boldsymbol{J}$ is evaluated on SH1, $\boldsymbol{A}$ represents the effect of a perturbation of mode 1 on itself. Thus, stability changes computed from $\boldsymbol{A}$ indicate saddle–node bifurcations, leading to a jump of the response. $\boldsymbol{B}$ represents the effect of a perturbation of mode 2 on mode 1. Hence, stability changes computed from $\boldsymbol{B}$ indicate pitchfork bifurcations leading to SH12. The eigenvalues of $\boldsymbol{A}$ and $\boldsymbol{B}$ are given by

$$\lambda_{1,2} = -\frac{n_p \tilde{b} \pm \sqrt{2n_p \Lambda_m (c_c - c_p)\sigma u_1^2 + n_p^2 \tilde{b}^2 - (c_c - c_p)^2 u_1^4}}{2n_p \Lambda_m}, \tag{38a}$$

$$\lambda_{3,4} = -\frac{1}{2\Lambda_m n_p}\left[n_p \tilde{b} \pm \sqrt{\left(\Lambda_c^2 n_p^2 \tilde{\mu} - (c_p + 3c_t/2)u_1^2\right)\left(2\Lambda_m n_p \sigma - \Lambda_c^2 n_p^2 \tilde{\mu} + (c_p + c_t/2)u_1^2\right) + n_p^2 \tilde{b}^2} \right], \tag{38b}$$

respectively. Instabilities occur when the real part of at least one of the eigenvalues becomes positive. The limit case $\Re[\lambda_2] = 0$ corresponds exactly to the backbone of SH1 (*cf.* Eq. (36)), while $\Re[\lambda_4] = 0$ leads to

$$u_{1a}^2 = \frac{n_p^2 \tilde{\mu} \Lambda_c^2 - 2n_p \Lambda_m \sigma}{c_p + c_t/2}, \tag{39a}$$

$$u_{1b}^2 = \frac{n_p^2 \tilde{\mu} \Lambda_c^2}{c_p + 3c_t/2}. \tag{39b}$$

Eqs. (39a) and (39b) correspond to the limit of stability regions and will be called "bifurcation curves". Each crossing between one of those curves and SH1 leads to a change of stability. This is illustrated in Fig. 5, where the order response of SH1 and its stability are presented. u_{1a} is shown in black in Fig. 5 while u_{1b} does not exist for the set of parameters used. The crossings between the black curve and SH1 lead to pitchfork bifurcations, indicated by code names PF. The instability zones are the coloured red (for the bifurcations to SH12) and blue (for the saddle–node bifurcations) areas. The purple area corresponds to the superposition of the two instabilities. Unstable parts of the response are shown as dashed-lines. The trivial solution is represented in green. SH2 is not shown in this figure. Note that the part of the response above s_{cusp} can help understanding the solution but is not physically relevant as it exists only because of approximations (*cf.* Section 5.2). A numerical response, obtained with the MANLAB[3] software [52,53], is shown as thin blue lines with dot markers. It is almost superimposed with the analytical computations, which exhibits the accuracy of the model. The pitchfork bifurcation obtained numerically (red star) is not exactly the same as that predicted analytically (PF), but it is close.

[3] MANLAB is a path-following and bifurcation analysis software.

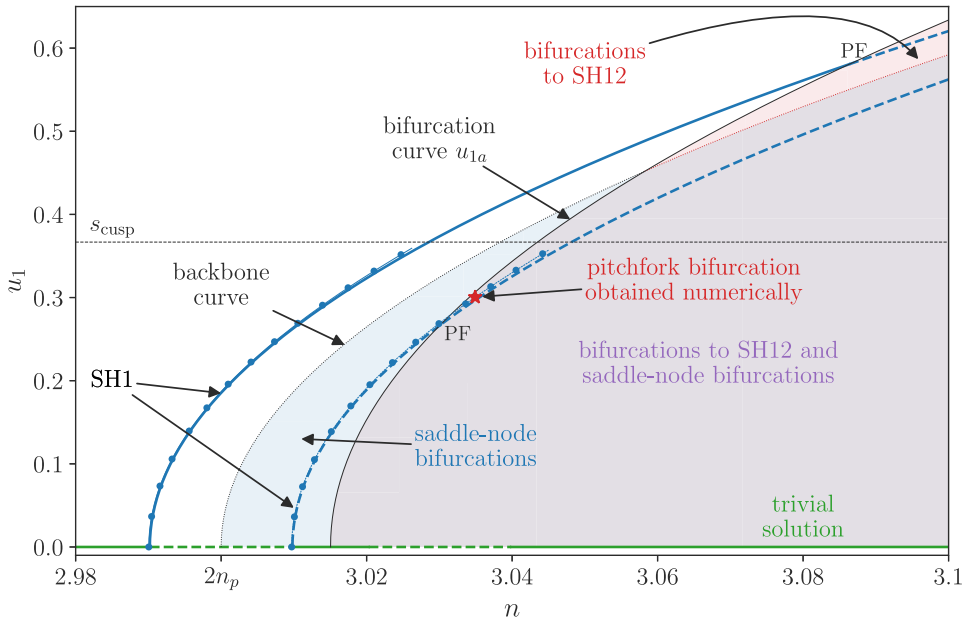

Fig. 5. Order response of mode 1 and its stability. Dashed lines indicate an unstable response. The black line represents one of the bifurcation curves. Coloured areas correspond to the instability zones. Numerical solutions are represented as thin blue lines with dot markers. PF indicates a pitchfork bifurcation. $\bar{T}_1 = 0.02$, and other parameters are given in Table 1.

Table 1
Parameters of the CPVA presented in this section. These parameters are chosen to favour the apparition of instabilities.

N	n_p	η	μ	$x_{[4]}$	$\alpha_{[1]}$	$\alpha_{[3]}$	$\bar{b}$	$\bar{b}_r$
2	1.5	1	0.025	−0.2	−0.1	0.1	0.002	0.002

6.4. Solution on the unison mode

Solution SH2 is now analysed. Using Eqs. (27c) and (27d) with $u_1 = 0$, one can find that SH2 is given by

$$u_2^2 = n_p \frac{2\Lambda_m\sigma - 2n_p\tilde{\mu}\Lambda_c^2 \pm \sqrt{\Lambda_m^2\tilde{T}_1^2 - 4\tilde{b}^2}}{c_c - c_p - 2c_t}, \tag{40a}$$

$$\tan\beta_2 = \mp\sqrt{\frac{\Lambda_m^2\tilde{T}_1^2}{4\tilde{b}^2} - 1}. \tag{40b}$$

c_t is a non-linear coefficient related to large pendulums displacements along their trajectories. It is defined as

$$c_t = \frac{\Lambda_c}{2}\tilde{\mu}n_p^2 n_t^2(1 + n_t^2). \tag{41}$$

The backbone curve of SH2 is

$$n_2^{(SH)} = 2n_p + \epsilon n_p\tilde{\mu}\frac{\Lambda_c^2}{\Lambda_m} + \epsilon\frac{c_c - c_p - 2c_t}{2n_p\Lambda_m}u_2^2. \tag{42}$$

Because of the term $-2c_t$, mode 2 is more softening than mode 1 (provided $\Lambda_c > 0$, which is the case for reasonable parameters).

Like SH1, SH2 is not defined for every parameter as u_2 must be real. Evaluating Eq. (40a) for $u_2 = 0$, one finds that the torque or order at the bifurcation are

$$\tilde{T}_1^{*2} = 4\left(\sigma - n_p\tilde{\mu}\frac{\Lambda_c^2}{\Lambda_m}\right)^2 + \frac{4\tilde{b}^2}{\Lambda_m^2}, \quad n_{1,2}^* = n_2^{(SH)}\big|_{u_2=0} \pm \frac{1}{2}\sqrt{\tilde{T}_1^2 - \frac{4\tilde{b}^2}{\Lambda_m^2}}. \tag{43}$$

Eq. (43) corresponds to the limit of condition (33b), thus confirming that this condition is associated to SH2. Comparing Eqs. (37) and (43), one can see that there is a difference on $\tilde{T}_1^*$ between SH1 and SH2. This difference is due to the presence of $n_p\tilde{\mu}\Lambda_c^2/\Lambda_m$, which is directly related to the fact that the linear resonance of mode 2 is higher than that of mode 1 (*cf.* Eq. (9)). For small mistunings, this difference implies that the system will bifurcate to SH1 before SH2, thus achieving the desired behaviour. Levels of mistuning for which the system would bifurcate to SH2 before SH1 are relatively large. Corresponding orders must be greater

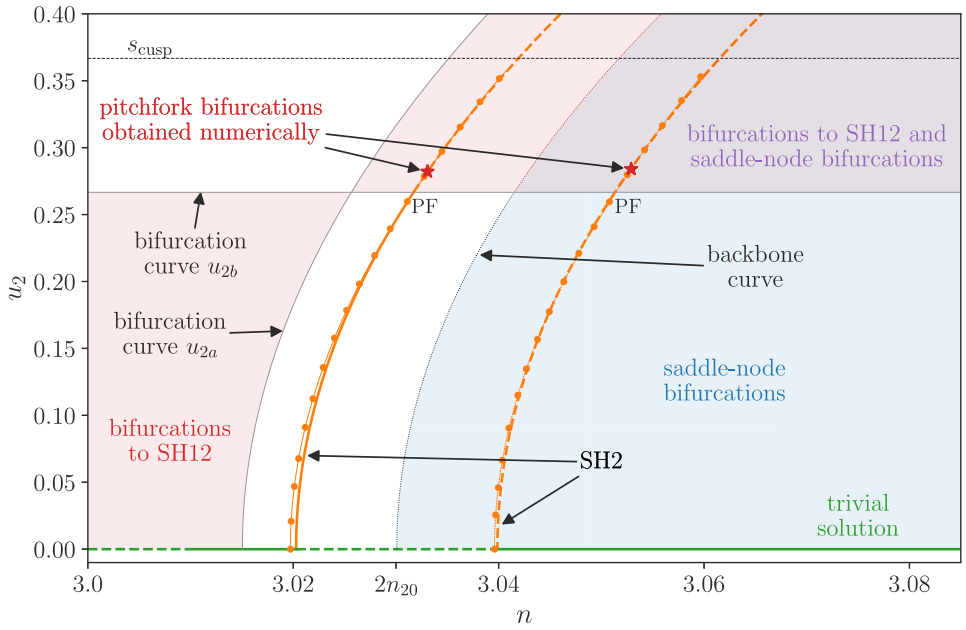

Fig. 6. Order response of mode 2 and its stability. Dashed lines indicate an unstable response. Bifurcation curves are shown in grey. Coloured areas correspond the instability zones. Numerical solutions are represented as thin orange lines with dot markers. PF indicates a pitchfork bifurcation. $\tilde{T}_1 = 0.02$, and other parameters are given in Table 1.

than the critical order n_{cr}, given by

$$n_{cr} = n_p\left(2 + \mu\frac{\Lambda_c^2}{2\Lambda_m}\right) \approx n_{10} + n_{20}. \tag{44}$$

The stability of SH2 is determined in the same way as that of SH1. The eigenvalues of the Jacobian of system (30) evaluated on SH2 are

$$\lambda_{1,2} = -\frac{1}{2\Lambda_m n_p}\left[\, n_p\tilde{b} \pm \sqrt{-\left(\Lambda_c^2 n_p^2\tilde{\mu} + \left(c_1 + c_t/2\right)u_2^2\right)\left(2\Lambda_m n_p\sigma - \Lambda_c^2 n_p^2\tilde{\mu} + \left(c_p + 3c_t/2\right)u_2^2\right) + n_p^2\tilde{b}^2}\,\right], \tag{45a}$$

$$\lambda_{3,4} = -\frac{1}{2\Lambda_m n_p}\left[\, n_p\tilde{b} \pm \sqrt{2n_p\Lambda_m(\sigma - n_p\tilde{\mu}\Lambda_c^2/\Lambda_m)(c_c - c_p - 2c_t)u_2^2 - (c_c - c_p - 2c_t)^2u_2^4 + n_p^2\tilde{b}^2}\,\right]. \tag{45b}$$

$\Re[\lambda_2]$ is related to a bifurcation towards SH12 while $\Re[\lambda_4]$ is related to jumps of the response. The limit case $\Re[\lambda_4] = 0$ corresponds exactly to the backbone of SH2 (*cf.* Eq. (42)), while $\Re[\lambda_2] = 0$ leads to the bifurcation curves defined as

$$u_{2a}^2 = \frac{n_p^2\tilde{\mu}\Lambda_c^2 - 2n_p\Lambda_m\sigma}{c_p + 3c_t/2}, \tag{46a}$$

$$u_{2b}^2 = -\frac{n_p^2\tilde{\mu}\Lambda_c^2}{c_p + c_t/2}. \tag{46b}$$

This is illustrated in Fig. 6, where the bifurcation curves are shown as grey lines and the instability zones are indicated with the same colour code as in Fig. 5. Crossings between the grey curves and SH2 lead to pitchfork bifurcations. Unstable parts of the response are shown as dashed-lines. The trivial solution is represented in green. SH1 is not shown in this figure. A numerical response is shown as thin orange lines with dot markers. As for SH1, it is almost superimposed with the analytical computations. The pitchfork bifurcations obtained numerically (red stars) are close to those predicted analytically (PF).

6.5. Coupled mode solution

The coupled-mode solutions are now investigated. The forced solutions cannot be computed analytically without additional assumptions. Chao et al. [29] computed them for pendulums that do not rotate relatively to the rotor and assuming a special phase relation between modes 1 and 2. In this paper, the backbones of the SH12 solutions are computed.

Using system (27) with $\tilde{b} = \tilde{T}_1 = 0$, one can find two free responses for SH12. The first one, called "SH12a", corresponds to the case where modes 1 and 2 are in phase-quadrature. It is given by

$$u_1^2 = \frac{2\Lambda_m n_p\sigma + (c_p + c_t + c_c)u_2^2}{c_c - c_p}, \tag{47a}$$

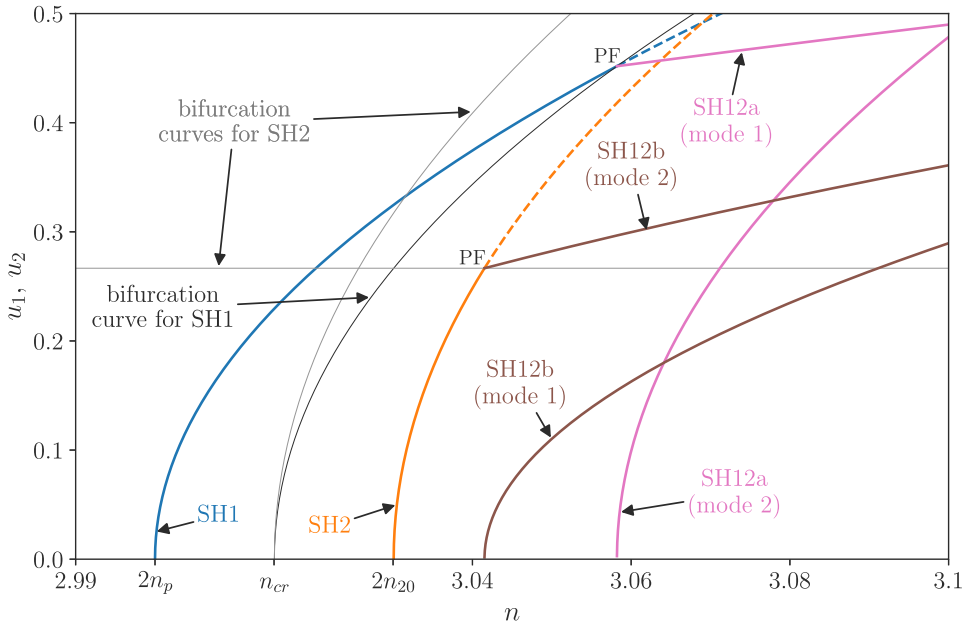

Fig. 7. Free responses of SH1 (blue), SH2 (orange), SH12a (pink) and SH12b (brown). Bifurcation curves associated to SH1 and SH2 are shown in black and grey, respectively. Dashed lines indicate unstable responses. PF indicates a pitchfork bifurcation. Parameters are given in Table 1.

$$\sin(\beta_1 - \beta_2) = 0, \quad \cos(\beta_1 - \beta_2) = -1, \tag{47b}$$

$$u_2^2 = 2n_p \frac{n_p \tilde{\mu} \Lambda_c^2 (c_c - c_p) - \Lambda_m \sigma (2c_c + c_t)}{4c_p c_c + c_t^2 + 4c_c c_t}. \tag{47c}$$

The second solution, called "SH12b", corresponds to the case where modes 1 and 2 are in phase or in phase-opposition. Whether these modes are in phase or in phase-opposition will not change the pendulums' response. SH12b is given by

$$u_1^2 = \frac{2\Lambda_m n_p \sigma + (3c_p + 3c_t - c_c) u_2^2}{c_c - c_p}, \tag{48a}$$

$$\sin(\beta_1 - \beta_2) = 0, \quad \cos(\beta_1 - \beta_2) = 1, \tag{48b}$$

$$u_2^2 = 2n_p \frac{n_p \tilde{\mu} \Lambda_c^2 (c_c - c_p) - \Lambda_m \sigma (2c_p + 3c_t)}{8c_p^2 + 16c_p c_t - 4c_p c_c + 9c_t^2 - 4c_t c_c}. \tag{48c}$$

SH12a and SH12b can arise through pitchfork bifurcations either from SH1 or SH2, as shown in Fig. 7 for free responses.

6.6. Physical solutions

Trivial solution. As stated earlier, the trivial solution at first order corresponds to immobile pendulums, i.e. $s_1^{(1/2)} = s_2^{(1/2)} = 0$, where superscripts in brackets indicate the number of the harmonic considered. Using Eq. (19a), one simply finds

$$\left|\tilde{\theta}^{(1)''}\right| = \tilde{T}_1. \tag{49}$$

It is interesting to note that if one goes up to the second order in the multiple scales developments, the trivial solution corresponds to pendulums responding linearly to the excitation (this is shown in Appendix F). In that case, they act as amplifiers and will slightly increase the amplitude of $\tilde{\theta}^{(1)}$. This was also observed in [28].

Phase-opposition solution. If pendulums respond on SH1, then $s_1^{(1/2)} = \zeta_1 = -s_2^{(1/2)}$, leading to

$$\left|\tilde{\theta}^{(1)''}\right|^2 = \tilde{T}_1^2 + \tilde{\mu}^2 n_t^4 \frac{n^2 u_1^4}{4} + \tilde{T}_1 \tilde{\mu} n_t^2 n u_1^2 \sin\beta_1. \tag{50}$$

Replacing u_1 and β_1 with their expressions in the case of perfect tuning (i.e. $\sigma = c_p = 0$, *cf.* Section 7.1), Eq. (50) reduces to

$$\left|\tilde{\theta}^{(1)''}\right| = \frac{2\tilde{b}}{\Lambda_m}. \tag{51}$$

This corresponds to a saturation of the rotor's response as it is independent of the forcing amplitude. The saturation level is desired to be as small as possible, which corresponds to a configuration with small damping and maximum equivalent mass. As damping is difficult to control in practice, designers should aim at maximising the equivalent mass, which implies to maximise the pendulums' inertia and their linear rotation rate (*cf.* Eq. (8)). Note that it does not matter whether this linear rotation rate is positive or negative.

Table 2
Parameters of the hardened-CPVA.

n_p	η	μ	$x_{[4]}$	$\alpha_{[1]}$	$\alpha_{[3]}$	$\bar{b}$	$\bar{b}_r$
1.5	1	0.1	−0.2	−0.1	0.1	0.002	0.002

In phase solution. If pendulums respond on SH2, then $s_1^{(1/2)} = \zeta_2 = s_2^{(1/2)}$, leading to

$$\left|\tilde{\theta}^{(1/2)''}\right| = \tilde{\mu}\left(n_p^2\Lambda_c + \frac{(n^2-6n_p^2)n_t^2(1+n_t^2)}{16}u_2^2\right)u_2, \tag{52a}$$

$$\left|\tilde{\theta}^{(1)''}\right|^2 = \tilde{T}_1^2 + \tilde{\mu}^2 n_t^4 \frac{n^2u_2^4}{4} + \tilde{T}_1\tilde{\mu}n_t^2 n u_2^2 \sin\beta_2, \tag{52b}$$

$$\left|\tilde{\theta}^{(3/2)^Prime}\right| = \frac{\tilde{\mu}n_t^2(1+n_t^2)(2n_p^2+n^2)u_2^3}{16}. \tag{52c}$$

From Eq. (52), one can see that pendulums generate 1/2 and 3/2 rotor harmonics whose amplitudes do not seem negligible, especially at high orders. This is problematic as pendulums will, at best, shift the vibration issues to orders $n/2$ and $3n/2$. Moreover, there is no set of parameters σ and c_p for which $\left|\tilde{\theta}^{(1)''}\right|$ perfectly saturates. For those reasons, pendulums responding on mode 2 is undesired.

Coupled solution. If the two pendulums respond on SH12a, then their free responses are given by

$$a_1 = a_2 = \sqrt{u_1^2 + u_2^2}. \tag{53}$$

Thus, SH12a corresponds to a solution for which the pendulums oscillate with the same amplitudes. If the pendulums respond on SH12b, their free responses are

$$a_1 = u_1 + u_2, \quad a_2 = |u_1 - u_2|, \tag{54}$$

respectively. Thus, SH12b leads to a response localised on one of the pendulums.

7. Case studies and design guidelines

7.1. Effect of linear and non-linear mistunings

As explained in Section 3, n_p is the tuning order of the pendulums and the linear eigenorder of mode 1, so it can be seen as the linear tuning parameter of the CPVA. Moreover, Eq. (36) shows that the subharmonic response of mode 1 is hardening but can be hardened even more or softened a little using c_p. Hence, c_p can be seen as the non-linear tuning parameter, and $c_p < 0$ and $c_p > 0$ correspond to hardened and softened tunings, respectively. The special case $n_p = n/2$ and $c_p = 0$ is called the "perfectly-tuned case". In practice, one can choose the value of the trajectory order n_t and the linear rotation coefficient $\alpha_{[1]}$ to set n_p (*cf.* Eq. (10)). Similarly, c_p is set by choosing the value of the perturbation coefficients of the trajectory and the rotation functions, that is $x_{[4]}$ and $\alpha_{[3]}$, respectively (*cf.* Eq. (35)).

The former developments are now applied to a CPVA whose parameters are given in Table 2. It has a hardened behaviour as $c_p < 0$. That CPVA will be compared to a reference-CPVA corresponding to the perfectly-tuned case. The parameters of that perfectly-tuned CPVA are the same except for $x_{[4]} = 0.045$, which renders $c_p = 0$.

Fig. 8 shows an order response of the two CPVAs for three torque amplitudes. In practice, the excitation order is a constant, but varying it is an efficient way to study the pendulums' linear mistuning, provided that all pendulums are equally mistuned [14]. The subharmonic and trivial responses are depicted as blue and green lines, respectively. The darker the line the higher the associated torque amplitude. Dashed lines indicate unstable responses and stars with code names PF indicate pitchfork bifurcations.

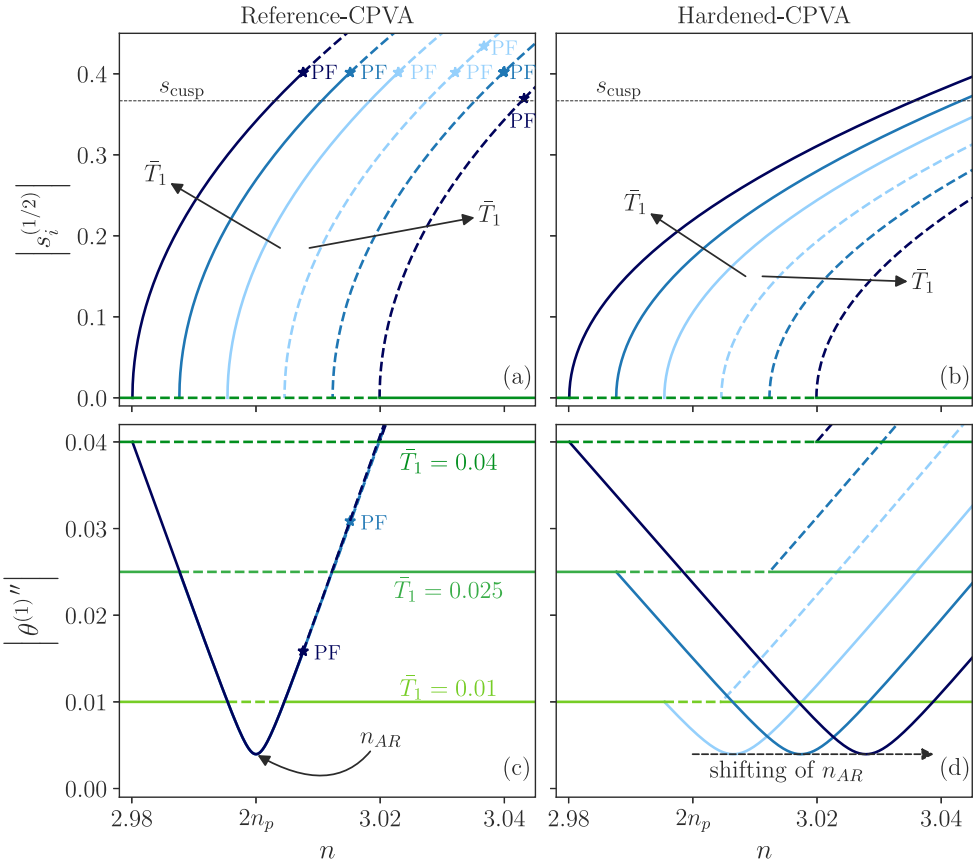

Fig. 8. Order response of the hardened- and reference-CPVA for three torque amplitudes. The associated pendulums' response are shown in (a) and (b) and the associated rotor's response are given in (c) and (d), respectively. The subharmonic and trivial responses are depicted as blue and green lines, respectively. The darker the line the higher the associated torque amplitude. Dashed lines indicate unstable responses and stars with code names PF indicate pitchfork bifurcations. Only one trivial response is shown in (a) and (b) as it overlaps with the other ones (only the unstable part is different). n_{AR} is the order at the non-linear antiresonance. $\bar{T}_1 = \{0.01, 0.025, 0.04\}$.

As remarked in [29], Figs. 8(a) and (b) confirm that one can use the non-linear mistuning to increase the torque capacity of the CPVA. Indeed, the pendulums' amplitude is always smaller in Fig. 8(b) than in Fig. 8(a), so that the hardened-pendulums will hit their cusp for a larger torque level. Moreover, a linear over-tuning (which corresponds to $n < 3$) allows for a decrease in the pendulums' amplitude and thus an increase in the torque capacity.

The evolution of the rotors' response is given in Figs. 8(c) and (d). For the reference-CPVA, the response at the three torque levels overlaps so that $\min\left|\theta^{(1)''}\right|$ is fixed both in order (at n_{AR}) and in amplitude. This is the saturation phenomenon as increasing the forcing does not change the amplitude's response. A small linear mistuning still leads to a saturation,[4] but at a larger amplitude. This can be seen looking at Fig. 8(c) at $n = 2.99$ for instance. The rotor's behaviour is significantly different for the hardened-CPVA shown in Fig. 8(d). Indeed, increasing the torque level shifts the antiresonance order to the right. Because of this shifting, the rotor's amplitude at a given order will evolve with the torque level instead of saturating. This can be seen looking at Fig. 8(d) at $n = 3$ for instance. An interesting point is that the rotor's amplitude at the antiresonance does not change, only n_{AR} is shifted. Hence, the CPVA remains efficient in reducing vibrations but its maximum efficiency is shifted to higher orders. This feature will be used for the design guideline proposed in Section 7.2. As $\min\left|\theta^{(1)''}\right|$ is tuning-independent, the recommendations on $\tilde{b}$ and Λ_m proposed earlier in the case of perfect tuning (*cf.* Section 6.6) also apply in the presence of mistunings.

In the case of a CPVA with a softened behaviour (i.e. $c_p > 0$), the rotor's response would not shift to the right but to the left, leading to similar qualitative results as those of the hardened-CPVA. However, the amplitude of softened pendulums is larger than that of perfectly-tuned ones, so that their torque range is reduced. Those two remarks are illustrated in Appendix H.

The pros and cons of intentional mistuning have now been exposed, and the results are in accordance with [29], where pendulums with a purely translational motion were considered. However, to our knowledge, no directions were given regarding how to choose those mistunings efficiently. This is discussed in the next section.

[4] Actually, the saturation is not perfect in that case. Zooming on Fig. 8(c) around $n = 2.997$, one would see that there is a small difference on $\left|\theta^{(1)''}\right|$ between the three torque levels. However, this difference seems negligible.

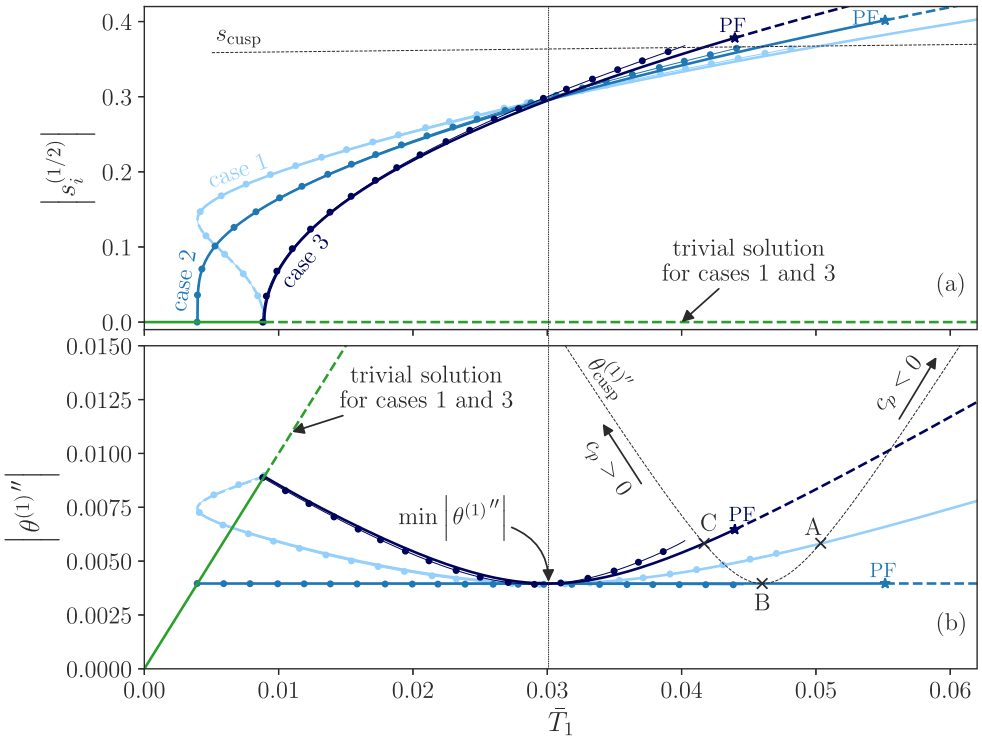

Fig. 9. Torque response of cases 1, 2 and 3. Pendulums and rotor's responses are shown in (a) and (b), respectively. Cases 1, 2 and 3 are represented as light, regular and dark blue lines, respectively. The trivial solution for cases 1 and 3 is depicted in green. That of case 2 is not shown as it overlaps the others (only the unstable part is different). Dashed lines indicate unstable responses and stars with code names PF indicate pitchfork bifurcations. Numerical solutions are shown as thin lines with dot markers. Dashed black lines indicate the cusp amplitudes for CPVAs that minimise the rotor's vibrations at $\bar{T}_1 = 0.03$ using relation (55). A, B and C indicate the rotor's amplitude at cusp point corresponding to cases 1, 2 and 3, respectively. $n = 3$ and other parameters are given in Table 2 except for n_p, $x_{[4]}$ and $\alpha_{[3]}$. $n_p = \{1.498, 1.5, 1.502\}$, $x_{[4]} = \{-0.037, 0, 0.0556\}$ and $\alpha_{[3]} = \{0.02, 0, 0.02\}$ in cases 1, 2 and 3, respectively.

7.2. Control of the detuning

It is interesting to study how $\left|\tilde{\theta}^{(1)''}\right|$ evolves in the presence of mistuning. It reaches a minimum (corresponding to the non-linear antiresonance) equal to the perfectly-tuned case (*cf.* Eq. (51)) for a specific value of σ, given by

$$\sigma_{AR} = -\frac{c_p}{c_c}\sqrt{\frac{\tilde{T}_1^2}{4} - \frac{\tilde{b}^2}{\Lambda_m^2}}. \tag{55}$$

Eq. (55) is an interesting relation as it allows one to select σ and c_p to minimise the rotor's vibrations at a given torque level. Of course, it is possible to choose $\sigma = c_p = 0$ for the rotor to perfectly saturate, but this choice cannot be achieved exactly in practice due to manufacturing tolerances, and it can lead to instabilities when the system is made of more than two pendulums [30].

Relation (55) is illustrated in Fig. 9 with three different cases, all aiming to minimise the rotor's amplitude at $\bar{T}_1 = 0.03$. Those cases correspond to CPVAs whose parameters are the same as those of Table 2, except for the values of n_p, $x_{[4]}$ and $\alpha_{[3]}$. Here are the characteristics of the three cases considered:

- case 1: $n_p < n/2$, $c_p < 0$, where $n = 3$ is the order corresponding to the torque response depicted in Fig. 9. This is the under-tuned, hardened case.
- case 2: $n_p = n/2$, $c_p = 0$. This is the perfectly-tuned case.
- case 3: $n_p > n/2$, $c_p > 0$. This is the over-tuned, softened case.

Fig. 9(b) clearly shows that it is possible to minimise the rotor's amplitude for a desired torque, and that minimum corresponds to the perfectly-tuned case. It is interesting to note that the amplitude of the pendulums at $\bar{T}_1 = 0.03$ is the same in all three cases. Before and after that $\bar{T}_1$ value, the filtration is not optimal as the excitation order does not coincide with the antiresonance order (*cf.* Fig. 8). This being said, the overall rotor's amplitude in case 1 is not too far from the perfectly-tuned case, thus allowing for a good filtration over the whole torque range.

Fig. 9(a) shows that the pendulums hit their cusp point at different values, thus changing the torque range. This is also observed in Fig. 9(b) where the cusp amplitude of cases 1, 2 and 3 is represented by points A, B and C, respectively. The torque range of case 1 is larger than for the two other cases, which is an advantage. This is discussed in details in Section 7.3.

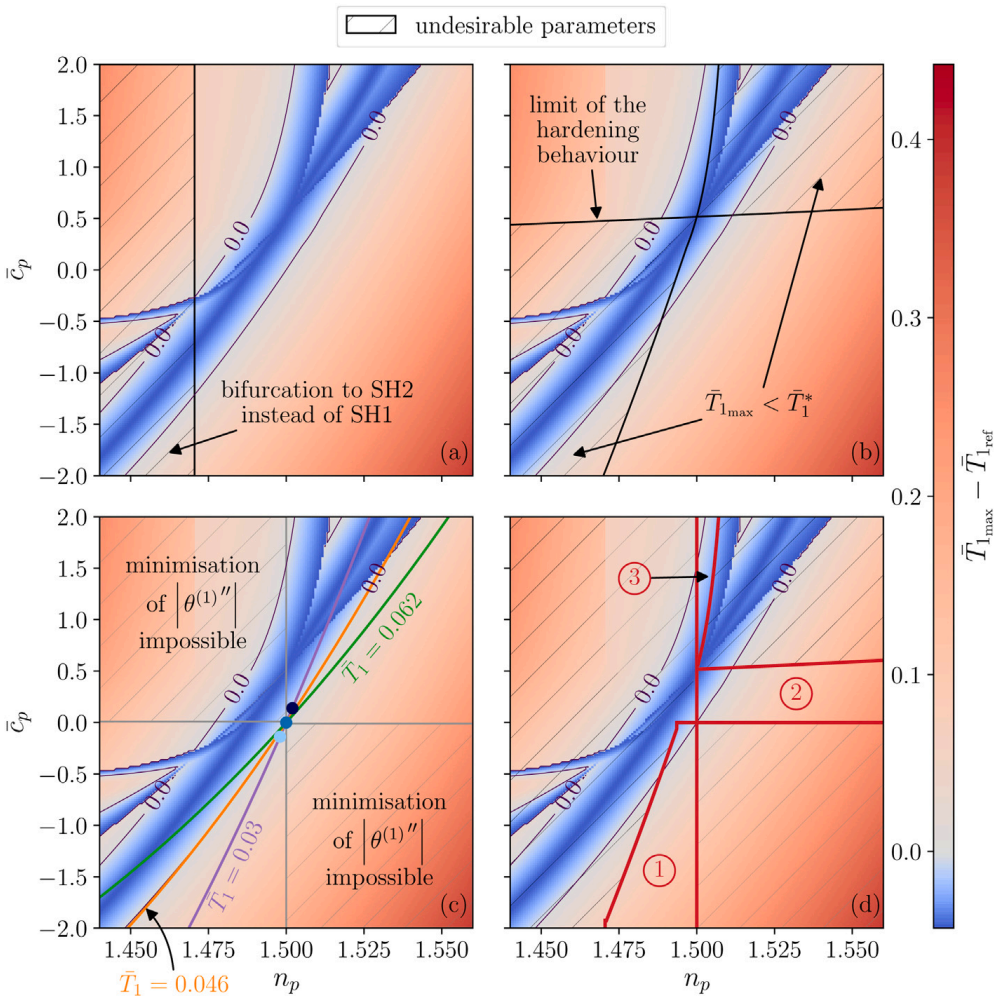

Fig. 10. Representation of the torque capacity as a function of tuning parameters for $n = 3$. The torque capacity is compared to the maximum torque of perfectly-tuned pendulums, called $\bar{T}_{1_{\text{ref}}}$. The hatched regions describe undesirable sets of parameters. The three coloured curves in (c) correspond to the use of relation (55) for three different $\bar{T}_1$. The blue dots along the purple curve represent the cases shown in Fig. 9. The three zones delimited by red lines in (d) represent parameter sets that are a priori not undesirable. System parameters that are not varied are given in Table 2.

7.3. Torque capacity

It is important to have an information on the torque capacity of pendulums responding on SH1. The maximum torque is limited either by pendulums reaching their cusp or by SH1 becoming unstable. A good approximation of the torque driving the pendulums to their cusp is obtained by equating the amplitude on SH1 (*cf.* Eq. (34a)) with the cusp point of an epicycloid (*cf.* Eq. (20)), leading to

$$\tilde{T}_{1_{\text{cusp}}}^2 = \left(2\sigma - \frac{c_c - c_p}{2c_t} n_p \tilde{\mu} \frac{\Lambda_c}{\Lambda_m}\right)^2 + \frac{4\tilde{b}^2}{\Lambda_m^2}. \tag{56}$$

The torque at which SH1 bifurcates to SH12 is obtained by equating the amplitude on SH1 with one of the bifurcation curves given by Eqs. (39a) and (39b). In the case where those bifurcation curves exist and cross SH1, the torques leading to a bifurcation towards SH12a and SH12b are given by

$$\tilde{T}_{1_a}^2 = \left(2\sigma - \frac{c_c - c_p}{c_p + c_t/2}\left(n_p \tilde{\mu} \frac{\Lambda_c^2}{\Lambda_m} - 2\sigma\right)\right)^2 + \frac{4\tilde{b}^2}{\Lambda_m^2}, \tag{57a}$$

$$\tilde{T}_{1_b}^2 = \left(2\sigma - \frac{c_c - c_p}{c_p + 3c_t/2} n_p \tilde{\mu} \frac{\Lambda_c^2}{\Lambda_m}\right)^2 + \frac{4\tilde{b}^2}{\Lambda_m^2}, \tag{57b}$$

respectively. The torque capacity is $\bar{T}_{1_{\max}} = \min\left[\bar{T}_{1_{\text{cusp}}}, \bar{T}_{1_a}, \bar{T}_{1_b}\right]$, and from Eqs. (56) and (57) it is clear that $\bar{T}_{1_{\max}}$ is affected by the tuning parameters σ and c_p.

The torque capacity is shown in Fig. 10 for an excitation order $n = 3$ and as a function of the tuning parameters n_p and $\bar{c}_p$. $\bar{c}_p$ is the unscaled equivalent of c_p, i.e.

$$\bar{c}_p = \epsilon c_p = 3(x_{[4]} + 2n_p^2 \eta \alpha_{[1]} \alpha_{[3]}). \tag{58}$$

It is compared to a reference torque $\bar{T}_{1_{\text{ref}}}$, which simply corresponds to the torque capacity for perfectly-tuned pendulums (i.e. $\bar{T}_{1_{\text{ref}}} = \bar{T}_{1_{\max}}\big|_{\sigma=c_p=0}$). Fig. 10 contains four maps representing the torque capacity and additional information. On every of those maps, the areas coloured in red represent sets of tuning parameters that increase the torque capacity in comparison to perfectly-tuned pendulums. On the contrary, blue areas represent sets of parameters that diminish the torque capacity.

In Fig. 10(a), the hatched area corresponds to undesirable values of n_p for which the trivial solution will bifurcate to SH2 instead of SH1. The limit value of n_p is given in Appendix I.

In Fig. 10(b), the hatched areas correspond to sets $(n_p, \bar{c}_p)$ for which the torque at bifurcation is larger than the maximum torque. This highly undesirable situation occurs when pendulums are subject to a large jump at the bifurcation point. In those cases, the pendulums directly hit their cusp point or respond on SH12 when the trivial solution becomes unstable (*cf.* Fig. I.14). The limits of the hatched regions are obtained by equating Eqs. (56) or (57) with Eq. (37) (more details are given in Appendix I). Note that the issue discussed here deals only with under-tuned pendulums if SH1 has a hardening behaviour, which is the case for reasonable parameters.

In Fig. 10(c), the hatched areas correspond to parameters that prevent the minimisation of $\left|\tilde{\theta}^{(1)''}\right|$ at a given torque amplitude using relation (55). Those hatched regions are not as undesirable as those depicted in Figs. 10(a) and (b) as they do not prevent the system from responding on SH1 (this is why those regions are represented in grey rather than black). However, it was shown in Fig. 9 that relation (55) can come very useful in minimising the rotor's vibrations over the whole torque range. Three coloured curves are shown in Fig. 10(c). Each of them corresponds to sets $(n_p, \bar{c}_p)$ that minimise the rotor's vibrations for three different torque amplitudes. The purple curve represents situations where the torque at minimum is smaller than $\bar{T}_{1_{\max}}$. Three such examples were depicted in Fig. 9 and are shown here as light, regular and dark blue dots along the purple curve. The orange (green) curve corresponds to situations where the torque minimising the rotor's vibrations is equal to (larger than) the torque capacity of perfectly-tuned pendulums. This means that the minimum seen at $\bar{T}_1 = 0.03$ in Fig. 9 would be shifted to $\bar{T}_1 = 0.046$ ($\bar{T}_1 = 0.062$). These situations do not allow for a good use of the minimisation of $\left|\tilde{\theta}^{(1)''}\right|$ as the torque at minimum is close to or larger than the torque capacity.

Finally, the undesirable areas described in Figs. 10(a), (b) and (c) are superimposed in Fig. 10(d). This reduces the parameters choice to the three zones delimited by thick red lines. Zone 3 does not seem to be a good choice as it reduces the torque capacity. The red part of zone 2 might seem acceptable but it was explained previously that it does not allow for a good use of relation (55). This makes zone 1 the most suitable one, so that under-tuned, hardened pendulums should be preferred to other configurations.

7.4. Global vibration reduction

Section 7.3 introduced several guidelines about how to choose the tuning parameters for optimal performance. Different criteria were considered, including the possibility to use relation (55) because it is assumed from the observations of Fig. 9 that this relation can reduce the overall vibrations of the rotor. The aim of the present section is to validate this assumption.

Computing the area below $\left|\tilde{\theta}^{(1)''}\right|$ between $\bar{T}_1^*\big|_{\sigma=c_p=0}$ and $\bar{T}_{1_{\max}}$ is a good indicator of the overall vibration level. Small areas should indicate a small overall vibration. However, one also needs to take into account the size of the torque range in the assessment of the overall vibration as small torque ranges will necessarily lead to a small area below the curve. Thus, the global vibration reduction indicator G is defined as

$$G = \frac{\left(\bar{T}_{1_{\text{ref}}} - \bar{T}_1^*\big|_{\sigma=0}\right)^2}{A_{\text{ref}}} \times \begin{cases} \dfrac{A}{\left(\bar{T}_{1_{\max}} - \bar{T}_1^*\big|_{\sigma=0}\right)^2} & \text{if} \quad \bar{T}_{1_{\max}} > \bar{T}_1^* \\ \dfrac{A}{\left(\bar{T}_1^* - \bar{T}_1^*\big|_{\sigma=0}\right)^2} & \text{if} \quad \bar{T}_{1_{\max}} < \bar{T}_1^* \end{cases} \tag{59}$$

A is the area below $\left|\tilde{\theta}^{(1)''}\right|^2$ between $\bar{T}_1^*\big|_{\sigma=0}$ and $\bar{T}_{1_{\max}}$ or $\bar{T}_1^*$. If two stable solutions exist simultaneously on a part of that interval, the average area is considered. Finally, A_{ref} is just A for perfectly-tuned pendulums.

G is represented in Fig. 11 as a function of the tuning parameters. The smaller G, the better the filtration. The hatched areas, their limits and the three zones of Fig. 10 are also shown, together with the purple curve of Fig. 10(c). It is interesting to see that the smallest values of G are located along this purple curve. This confirms that relation (55) is useful in reducing the rotor's vibrations over the whole torque range. Moreover, Fig. 11 indicates that designs from zone 1 (which were recommended in Section 7.3) are efficient in reducing the overall vibrations.

Figs. 10 and 11 form a powerful design tool that helps choosing wisely the tuning parameters of a CPVA to maximise the torque range while keeping the overall vibrations of the rotor as small as possible.

7.5. Avoidance of the SH12 solutions

As stated in Section 7.3, bifurcations from SH1 to SH12a or SH12b should be avoided in order to increase the torque range. The aim of this section is to provide guidelines regarding the choice of the tuning parameters in order to avoid those bifurcations.

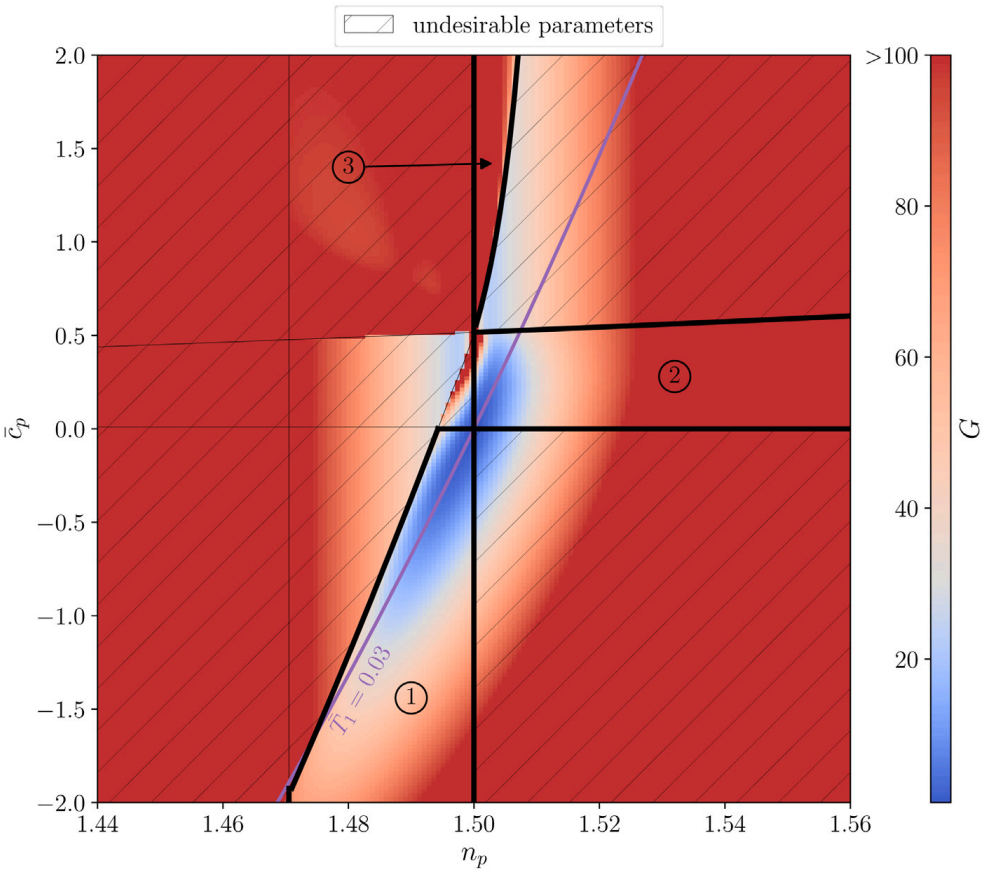

Fig. 11. Representation of indicator G as a function of tuning parameters for $n = 3$. Values $G \geq 100$ are represented with the same colour. The hatched regions describe undesirable sets of parameters. The purple curve corresponds to the use of relation (55) for $\bar{T}_1 = 0.03$. The three zones delimited by thick black lines represent parameter sets that are a priori not undesirable. System parameters that are not varied are given in Table 2.

Avoidance of SH12a. Using the definition of σ (25), the bifurcation curve (39a) can be rearranged such that

$$n_{1a} = 2n_p + \mu n_p \frac{\Lambda_c^2}{2\Lambda_m} - \epsilon \frac{c_p + c_t/2}{2\Lambda_m n_p} u_1^2. \tag{60}$$

To avoid bifurcations, one should have $n < n_{1a}$ over the whole torque range, that is up to $u_1 = s_{\text{cusp}}$. This is satisfied if

$$n_p > n\left(2 + \mu \frac{\Lambda_c^2}{2\Lambda_m}\right)^{-1} \quad \text{and} \tag{61a}$$

$$c_p < -2\Lambda_m n_p n_t^2 (1 + n_t^2)\sigma + \left(2\Lambda_c - \frac{1}{2}\right) c_t. \tag{61b}$$

Note that condition (61a) was already mandatory to prevent the trivial solution from bifurcating to SH2 instead of SH1 (see Eq. (44)).

Avoidance of SH12b. As the bifurcation curve (39b) is independent of σ, it is easier to treat. This curve should either not exist (i.e. be imaginary) or be above s_{cusp}. This is satisfied if

$$c_p < \left(-\frac{3}{2} + 2\Lambda_c\right) c_t. \tag{62}$$

If conditions (61) and (62) are fulfilled, one ensures that the SH1 solution will not bifurcate to one of the SH12 solutions before it reaches its cusp.

8. Comparison of the subharmonic filtration with a standard filtration

The subharmonic filtration is now compared to the classical one that uses $n_p \approx n$. To this aim, two different CPVAs are considered. Their parameters are given in Table 3. The subharmonic CPVA corresponds to the case 1 shown in Fig. 9, while the classical CPVA is slightly over-tuned to avoid pendulums' localisation [17].

Fig. 12 shows a torque response of the two CPVAs for $n = 3$, computed with MANLAB [52,53]. Solutions related to the subharmonic and classical CPVAs are shown as lines with dot and cross markers, respectively. Harmonics 1/2, 1, 2 and 3 are depicted in red, blue, orange and pink, respectively. Dashed lines represent unstable responses.

Table 3
Parameters of the subharmonic and classical CPVAs.

	n_p	η	μ	$x_{[4]}$	$\alpha_{[1]}$	$\alpha_{[3]}$	$\bar{b}$	$\bar{b}_r$
Subharmonic CPVA	1.498	1	0.1	−0.037	−0.1	0.02	0.002	0.002
Classical CPVA	3.02	1	0.1	0	−0.1	0	0.002	0.002

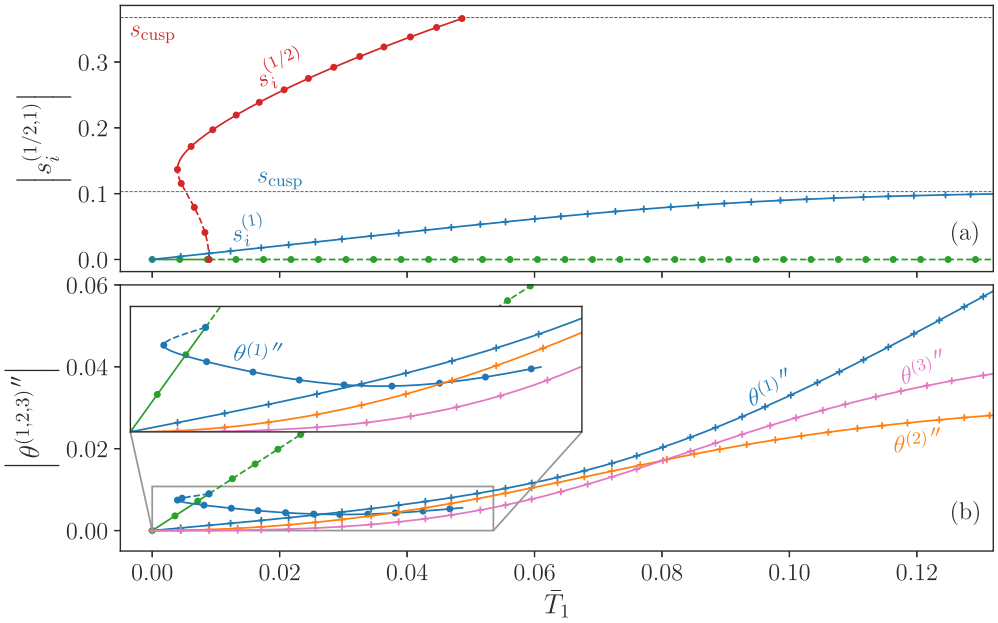

Fig. 12. Comparison of a torque response at $n = 3$ between a subharmonic CPVA (lines with dot markers) and a classical one (lines with cross markers). Pendulums' and rotors' responses are shown in (a) and (b), respectively. The trivial subharmonic solution is shown in green. Horizontal blue and red dashed lines represent the cusp point of the pendulums in the classical and subharmonic case, respectively. Parameters are given in Table 3.

From Fig. 12(a), one can see that the classical pendulums reach their cusp at a much larger torque than the subharmonic ones (the cusp point of the classical pendulums is not visible in Fig. 12(a), it is around $\bar{T}_1 = 0.192$). This is the main drawback of subharmonic CPVAs, as it means that their torque range is smaller than that of classical ones. It is possible to use more than one pair of pendulums to increase the torque range, but one has to be careful about the additional instabilities that might appear [30].

In Fig. 12(b), one can see that pendulums with a classical tuning generate higher order rotor harmonics (only higher harmonics 2 and 3 are shown here). This is a known issue [19] that limits the efficiency of the system as it generates vibration problems at higher orders. On the contrary, pendulums with a subharmonic tuning do not generate higher order harmonics, which is a clear advantage. In addition, the zoom in Fig. 12(b) shows that above $\bar{T}_1 = 0.026$, the subharmonic CPVA allows for a better filtration of $\theta^{(1)''}$ than the classical one. However, for small torque amplitudes, the filtration from the classical CPVA is superior.

Another advantage of the subharmonic CPVA over the classical one is that lower tuning orders require less demanding manufacturing tolerances [37].

9. Conclusion

The study presented in this paper deals with the subharmonic response of CPVAs made of two pendulums allowing a rotational mobility. First, the physical origin of the subharmonic filtration was explained. Next, an analytical model allowing for the prediction of this non-linear response and its stability was build using a scaling of the parameters, a modal decomposition and the method of multiple scales. The validity of the model was verified numerically and design guidelines were presented. First, it was advised to maximise the inertia and linear rotation of the pendulums to minimise the vibrations of the rotor. Then, a special relation between the pendulums' tuning parameters was introduced. It allows to minimise the rotor's amplitude for a desired torque amplitude. This relation increases the robustness of the CPVA as perfect tuning is impossible to achieve due to manufacturing tolerances. Moreover, it can be used to increase the torque range. Then, two design tools were introduced. They take the form of maps where two performance criteria and additional information are shown as a function of the tuning parameters. These two criteria represent the torque range and the global vibration level of the rotor over that torque range. The additional information are related to the proper operation of the CPVA. From the design tools it was observed that under-tuned pendulums with a hardened behaviour provide the best compromise between a large torque range and a satisfying vibration reduction. Additional guidelines were given regarding the choice of the tuning parameters so that the subharmonic solution remains stable over the whole operating range of

the CPVA. Finally, it was shown that the subharmonic tuning can provide a better filtration than the classical tuning for medium torque amplitudes, but at the cost of a reduced torque range. This enhanced filtration is rendered possible by the saturation of the rotor's first harmonic and the non-generation of higher nor lower rotor harmonics.

Declaration of competing interest

The authors declare that they have no known competing financial interests or personal relationships that could have appeared to influence the work reported in this paper.

Appendix A. Chain rule for a change of variable from t to ϑ

Using the chain rule, one can write

$$\frac{\partial(\bullet)}{\partial t} = \frac{\partial \vartheta}{\partial t}\frac{\partial(\bullet)}{\partial \vartheta}. \tag{A.1}$$

Computing the second derivative with respect to time leads to

$$\begin{aligned}\frac{\partial^2(\bullet)}{\partial t^2} &= \frac{\partial}{\partial t}\left(\frac{\partial(\bullet)}{\partial t}\right)\\ &= \frac{\partial}{\partial t}\left(\frac{\partial \vartheta}{\partial t}\frac{\partial(\bullet)}{\partial \vartheta}\right)\\ &= \frac{\partial}{\partial t}\left(\frac{\partial \vartheta}{\partial t}\right)\frac{\partial(\bullet)}{\partial \vartheta} + \frac{\partial \vartheta}{\partial t}\frac{\partial}{\partial t}\left(\frac{\partial(\bullet)}{\partial \vartheta}\right)\\ &= \frac{\partial \vartheta}{\partial t}\frac{\partial}{\partial \vartheta}\left(\frac{\partial \vartheta}{\partial t}\right)\frac{\partial(\bullet)}{\partial \vartheta} + \frac{\partial \vartheta}{\partial t}\frac{\partial \vartheta}{\partial t}\frac{\partial}{\partial \vartheta}\left(\frac{\partial(\bullet)}{\partial \vartheta}\right)\\ &= \frac{\partial \vartheta}{\partial t}\frac{\partial}{\partial \vartheta}\left(\frac{\partial \vartheta}{\partial t}\right)\frac{\partial(\bullet)}{\partial \vartheta} + \left(\frac{\partial \vartheta}{\partial t}\right)^2\frac{\partial^2(\bullet)}{\partial \vartheta^2}.\end{aligned} \tag{A.2}$$

Using the definition of y (1) and the notations $\dot{(\bullet)} = \partial(\bullet)/\partial t$, $(\bullet)' = \partial(\bullet)/\partial\vartheta$, Eqs. (A.1) and (A.2) can be written as Eq. (3).

Appendix B. Details on the computation of the equations of motion

The kinetic energy of the system represented in Fig. 1 is

$$\mathcal{T} = \frac{1}{2}J_r\dot{\vartheta}^2 + \frac{1}{2}\sum_{i=1}^{N}\left[m_i\dot{S}_i^2 + m_iX_i(S_i)\dot{\vartheta}^2 + 2m_i\dot{\vartheta}\dot{S}_iZ_i(S_i) + I_i(\dot{\vartheta}+\dot{\alpha}_i(S_i))^2\right] \tag{B.1}$$

and the potential energy $\mathcal{U}$ is neglected as the gravitational acceleration is assumed negligible in front of the centrifugal acceleration. Hence, the Lagrangian is $\mathcal{L} = \mathcal{T}$. There are three external loads applied on the system:

- A torque $T(\vartheta)\boldsymbol{z_0}$ is applied on the rotor, where $\boldsymbol{z_0}$ is the out-of-plane unit vector (*cf.* Fig. 2). It is the external forcing.
- A resistive torque $-b_r\dot{\vartheta}\boldsymbol{z_0}$ is applied on the rotor. It represents the damping between the rotor and the ground.
- A resistive force $-b_i\dot{S}_i\boldsymbol{t_i}$ is applied on the centre of mass of the ith pendulum, where $\boldsymbol{t_i}$ is the vector tangent to the trajectory C_i at abscissa S_i. It represents the damping between the rotor and the ith pendulum.

Using the Euler–Lagrange equations together with the principle of virtual power, one obtains the equations of motion

$$\left[J_r + \sum_{i=1}^{N} I_i + m_iX_i(S_i)\right]\ddot{\vartheta} + \sum_{i=1}^{N}\left(m_iZ_i(S_i) + I_i\Gamma_i(S_i)\right)\ddot{S}_i + \dot{S}_i\left[I_i\frac{\Gamma_i(S_i)}{dS_i}\dot{S}_i + m_i\left(\frac{dX_i(S_i)}{dS_i}\dot{\vartheta} + \frac{dZ_i(S_i)}{dS_i}\dot{S}_i\right)\right] + b_r\dot{\vartheta} = T(\vartheta), \tag{B.2a}$$

$$\left(m_iZ_i(S_i) + I_i\Gamma_i(S_i)\right)\ddot{\vartheta} + \left(m_i + I_i\Gamma_i(S_i)^2\right)\ddot{S}_i + I_i\Gamma_i(S_i)\frac{d\Gamma_i(S_i)}{dS_i}\dot{S}_i^2 - \frac{1}{2}m_i\frac{dX_i(S_i)}{dS_i}\dot{\vartheta}^2 + b_i\dot{S}_i = 0, \quad i = 1,\dots,N. \tag{B.2b}$$

Eq. (B.2a) governs the motion of the rotor while the N Eqs. (B.2b) govern the motion of the pendulums. Those equations can be written in a non-dimensional form using the non-dimensional parameters and variables (1) and the chain rule (3). In addition, if the pendulums are assumed identical, one obtains Eqs. (4a) and (4b).

Appendix C. Relations between coordinates y and θ

From Section 2, we have

$$y = \frac{\dot{\vartheta}}{\Omega} = \frac{1}{\Omega}\frac{\partial(\Omega t+\theta)}{\partial t} = 1 + \frac{\dot{\theta}}{\Omega}, \tag{C.1a}$$

$$yy' = \frac{\ddot{\vartheta}}{\Omega^2} = \frac{1}{\Omega^2}\frac{\partial^2(\Omega t+\theta)}{\partial t^2} = \frac{\ddot{\theta}}{\Omega^2}. \tag{C.1b}$$

Using Eq. (3) at first order, we can write

$$\frac{\dot{\theta}}{\Omega} = y\theta' \approx \theta', \tag{C.2a}$$

$$\frac{\ddot{\theta}}{\Omega^2} = yy'\theta' + y^2\theta'' \approx \theta''. \tag{C.2b}$$

From Eqs. (C.1) and (C.2), we have the first order relations

$$\theta' = y - 1, \tag{C.3a}$$

$$\theta'' = yy'. \tag{C.3b}$$

Appendix D. Expression of the simplified modal equations

The system of modal Eqs. (22) uses functions f_0, f_1 and f_2, which are given by

$$\begin{aligned} f_0(\zeta_1,\zeta_2,\vartheta) = {} & \frac{\tilde{\mu}\Lambda_c}{1+\tilde{\mu}}\zeta_2'' + \tilde{\mu}n_p^2\left(\Lambda_c\zeta_2 - \frac{n_t^2(1+n_t^2)}{2}(3\zeta_1^2\zeta_2+\zeta_2^3)\right) + 2\tilde{\mu}n_t^2(\zeta_1\zeta_1' + \zeta_2\zeta_2') \\ & + \tilde{\mu}n_t^2(1+n_t^2)(2\zeta_1\zeta_1'\zeta_2' + \zeta_2\zeta_1'^2 + \zeta_2\zeta_2'^2) + \tilde{T}_1\cos(n\vartheta), \end{aligned} \tag{D.1}$$

$$\begin{aligned} f_1(\zeta_1,\zeta_2,\vartheta) = {} & -\epsilon\Lambda_m^{-1}\Big[(\Lambda_m\zeta_1' - n_t^2(1+n_t^2)\zeta_1\zeta_2)(\tilde{\mu}n_p^2\Lambda_c\zeta_2 + \tilde{T}_1\cos(n\vartheta)) \\ & + 2\tilde{\mu}n_t^2\Lambda_m\zeta_1'(\zeta_1\zeta_1' + \zeta_2\zeta_2') + 6\eta\alpha_{[1]}\tilde{\alpha}_{[3]}(\zeta_1\zeta_1'^2 + 2\zeta_2\zeta_1'\zeta_2' \\ & + \zeta_1\zeta_2'^2 + \zeta_1^2\zeta_1'' + 2\zeta_1\zeta_2\zeta_2'' + \zeta_2^2\zeta_1'') - 2\tilde{x}_{[4]}(\zeta_1^3 + 3\zeta_1\zeta_2^2) + \tilde{b}\zeta_1'\Big], \end{aligned} \tag{D.2}$$

$$\begin{aligned} f_2(\zeta_1,\zeta_2,\vartheta) = {} & -\epsilon\Lambda_m^{-1}\Bigg[\left(\Lambda_c + \Lambda_m\zeta_2' - \frac{n_t^2(1+n_t^2)}{2}(\zeta_1^2+\zeta_2^2)\right)(\tilde{\mu}n_p^2\Lambda_c\zeta_2 + \tilde{T}_1\cos(n\vartheta)) + 2\tilde{\mu}n_t^2(\Lambda_c + \Lambda_m\zeta_2')(\zeta_1\zeta_1' + \zeta_2\zeta_2') \\ & - \Lambda_c\tilde{\mu}n_p^2\frac{n_t^2(1+n_t^2)}{2}(3\zeta_1^2\zeta_2+\zeta_2^3) + \Lambda_c\tilde{\mu}n_t^2(1+n_t^2)(2\zeta_1\zeta_1'\zeta_2' + \zeta_2\zeta_1'^2 + \zeta_2\zeta_2'^2) + 6\eta\alpha_{[1]}\tilde{\alpha}_{[3]}(2\zeta_1\zeta_1'\zeta_2' + \zeta_2\zeta_1'^2 + \zeta_2\zeta_2'^2 \\ & + 2\zeta_1\zeta_1''\zeta_2 + \zeta_2''\zeta_1^2 + \zeta_2''\zeta_2^2) - 2\tilde{x}_{[4]}(3\zeta_1^2\zeta_2 + \zeta_2^3) + \tilde{b}\zeta_2'\Bigg]. \end{aligned} \tag{D.3}$$

Appendix E. System obtained through the method of multiple scales

The system of equations obtained through the application of the method of multiple scales is given by Eq. (27) where functions f_{u_1}, f_{β_1}, f_{u_2} and f_{β_2} are

$$f_{u_1}(\boldsymbol{u},\boldsymbol{\beta}) = \left[(c_p - c_c + c_t)u_1u_2^2\sin(\beta_1-\beta_2) + n_p\Lambda_m u_1\tilde{T}_1\cos(\beta_1) - 2n_p\tilde{b}u_1\right][4n_p\Lambda_m]^{-1}, \tag{E.1}$$

$$f_{\beta_1}(\boldsymbol{u},\boldsymbol{\beta}) = u_1\sigma - 2\left[-(c_p - c_c + c_t)u_1u_2^2\cos(\beta_1-\beta_2) - (c_p - c_c)u_1^3 - 2(c_p + c_t)u_1u_2^2 + n_p\Lambda_m u_1\tilde{T}_1\sin(\beta_1)\right][4n_p\Lambda_m]^{-1}, \tag{E.2}$$

$$f_{u_2}(\boldsymbol{u},\boldsymbol{\beta}) = \left[(c_p - c_c + c_t)u_1^2u_2\sin(\beta_2-\beta_1) + n_p\Lambda_m u_2\tilde{T}_1\cos(\beta_2) - 2n_p\tilde{b}u_2\right][4n_p\Lambda_m]^{-1}, \tag{E.3}$$

$$f_{\beta_2}(\boldsymbol{u},\boldsymbol{\beta}) = u_2\sigma - 2\left[-(c_p - c_c + c_t)u_1^2u_2\cos(\beta_2-\beta_1) - (c_p - c_c + 2c_t)u_2^3 - 2(c_p + c_t)u_1^2u_2 + n_p\Lambda_m u_2\tilde{T}_1\sin(\beta_2) + 2n_p^2\tilde{\mu}\Lambda_c^2u_2\right][4n_p\Lambda_m]^{-1}. \tag{E.4}$$

Constants c_p, c_c and c_t are defined in Eqs. (35) and (41).

Appendix F. Details on the trivial solution

The application of the method of multiple scales to Eqs. (22b) and (22c) yields two equations of order 1, governing ζ_{11} and ζ_{21}, and two equations of order ϵ, governing ζ_{12} and ζ_{22}. The trivial solution at second order is given by ζ_{22} and ζ_{12}. Introducing the expansion (24a) in the modal Eqs. (22b) and (22c) and evaluating this on the trivial solution (i.e. for $\zeta_{11} = \zeta_{21} = 0$), one finds that

$$\zeta_{12} = 0, \tag{F.1a}$$

$$\zeta_{22} = \frac{\Lambda_c}{3\Lambda_m n_p^2}\tilde{T}_1\cos n\vartheta. \tag{F.1b}$$

The associated pendulums' motion is

$$s_1 = s_2 = \epsilon\zeta_{22} = \frac{\Lambda_c}{3\Lambda_m n_p^2}\tilde{T}_1\cos n\vartheta. \tag{F.2}$$

Solving the linear system (7), one can show that Eq. (F.2) corresponds to the linear solution at $n = 2n_p$ when the contributions of μ and the damping are neglected. Hence, the trivial solution at second order is an approximation of the pendulums' linear response.

It is possible to determine the trivial response of the rotor at order 2 by introducing the pendulums' solution (F.2) in the simplified rotor's Eq. (19a). Neglecting terms of order higher than ϵ and the damping, one finds

$$\tilde{\theta}'' = \left(1 + \mu\frac{\Lambda_c^2}{3\Lambda_m}\right)\tilde{T}_1 \cos n\vartheta. \tag{F.3}$$

This indicates that pendulums generate a torque on the rotor that adds up with the external torque, so that they do not act as absorbers but as amplifiers. Hence, they slightly increase the rotor's amplitude compared to the case of immobile pendulums. Eq. (F.3) corresponds to the results found in [28] if one considers purely translated pendulums and neglects higher order terms in μ. Note that the amplification effect of the pendulums diminishes as Λ_c diminishes, so that the use of negative linear rotation rates limits the amplification effect (*cf.* Eq. (8)). This makes sense as Λ_c is related to the linear coupling between the pendulums and the rotor, so reducing this coupling diminishes the action of the pendulums on the rotor.

Appendix G. System from the method of multiple scales with Cartesian coordinates

The Cartesian form of the system obtained from the method of multiple scales is given by Eq. (30) where functions f_{p_1}, f_{q_1}, f_{p_2} and f_{q_2} are

$$\begin{aligned} f_{p_1}(\boldsymbol{p},\boldsymbol{q}) = \big[&-2n_p\tilde{b}p_1 - (c_p - c_c)(p_1^2+q_1^2)q_1 - 2(c_p+c_t)(p_2^2+q_2^2)q_1 + (c_p - c_c + c_t)\left(q_1(p_2^2-q_2^2) - 2p_1p_2q_2\right)\\ &+n_p\Lambda_m\tilde{T}_1p_1 - 2n_p\Lambda_m\sigma q_1\big]\,[4n_p\Lambda_m]^{-1}, \end{aligned} \tag{G.1}$$

$$\begin{aligned} f_{q_1}(\boldsymbol{p},\boldsymbol{q}) = \big[&-2n_p\tilde{b}q_1 + (c_p - c_c)(p_1^2+q_1^2)p_1 + 2(c_p+c_t)(p_2^2+q_2^2)p_1 + (c_p - c_c + c_t)\left(p_1(p_2^2-q_2^2) + 2q_1p_2q_2\right)\\ &-n_p\Lambda_m\tilde{T}_1q_1 + 2n_p\Lambda_m\sigma p_1\big]\,[4n_p\Lambda_m]^{-1}, \end{aligned} \tag{G.2}$$

$$\begin{aligned} f_{p_2}(\boldsymbol{p},\boldsymbol{q}) = \big[&-2n_p\tilde{b}p_2 - (c_p - c_c + 2c_t)(p_2^2+q_2^2)q_2 - 2(c_p+c_t)(p_1^2+q_1^2)q_2 + 2n_p^2\tilde{\mu}\Lambda_c^2q_2 - (c_p - c_c + c_t)\left(2p_1q_1p_2 - q_2(p_1^2-q_1^2)\right)\\ &+n_p\Lambda_m\tilde{T}_1p_2 - 2n_p\Lambda_m\sigma q_2\big]\,[4n_p\Lambda_m]^{-1}, \end{aligned} \tag{G.3}$$

$$\begin{aligned} f_{q_2}(\boldsymbol{p},\boldsymbol{q}) = \big[&-2n_p\tilde{b}q_2 + (c_p - c_c + 2c_t)(p_2^2+q_2^2)p_2 + 2(c_p+c_t)(p_1^2+q_1^2)p_2 - 2n_p^2\tilde{\mu}\Lambda_c^2p_2 + (c_p - c_c + c_t)\left(2p_1q_1q_2 + p_2(p_1^2-q_1^2)\right)\\ &-n_p\Lambda_m\tilde{T}_1q_2 + 2n_p\Lambda_m\sigma p_2\big]\,[4n_p\Lambda_m]^{-1}. \end{aligned} \tag{G.4}$$

Appendix H. Effect of a softened behaviour on SH1

Fig. H.13 represents the order response of a perfectly-tuned CPVA (left) and a softened-CPVA (right). The parameters of the two CPVAs are the same as in Section 7.1, except for the softened-CPVA for which $x_{[4]} = 0.1$, leading to $c_p > 0$.

From (a) and (b), one can see that the pendulums' amplitude at a given torque and order is always larger for the softened-CPVA. Hence, it has a smaller torque capacity compared to the perfectly-tuned CPVA. The other important feature, visible in (d), is that the antiresonance shift to the left as the torque amplitude is increased. This is opposite to hardened-CPVAs for which the antiresonance shifts to the right (*cf.* Fig. 8).

Appendix I. Additional information regarding the torque capacity

As explained in Section 7.3, there are some sets of parameters that are undesired as they do not allow for a desired operation of the CPVA.

In Fig. 10(a), the hatched area corresponds to values of n_p for which the trivial solution bifurcates to SH2 instead of SH1. The corresponding limit value of n_p, computed using Eq. (44), is

$$n_p = n\left(2 + \mu\frac{\Lambda_c^2}{2\Lambda_m}\right)^{-1}. \tag{I.1}$$

In Fig. 10(b), the hatched areas correspond to cases where $\bar{T}_{1_{\max}} < \bar{T}_1^*$. An example of this situation is depicted in Fig. I.14. The solutions of $\bar{T}_{1_{\max}} = \bar{T}_1^*$ are

$$c_p = c_c, \tag{I.2a}$$

$$c_p = c_c - \frac{8\sigma c_t\Lambda_m}{\tilde{\mu}n_p\Lambda_c} \quad \text{if} \quad \bar{T}_{1_{\max}} = \bar{T}_{1_{\text{cusp}}}, \tag{I.2b}$$

$$c_p = \left[-2\sigma c_t + c_c\left(\frac{n_p\tilde{\mu}\Lambda_c^2}{\Lambda_m} - 2\sigma\right)\right]\left(2\sigma + \frac{n_p\tilde{\mu}\Lambda_c^2}{\Lambda_m}\right)^{-1} \quad \text{if} \quad \bar{T}_{1_{\max}} = \bar{T}_{1_a}, \tag{I.2c}$$

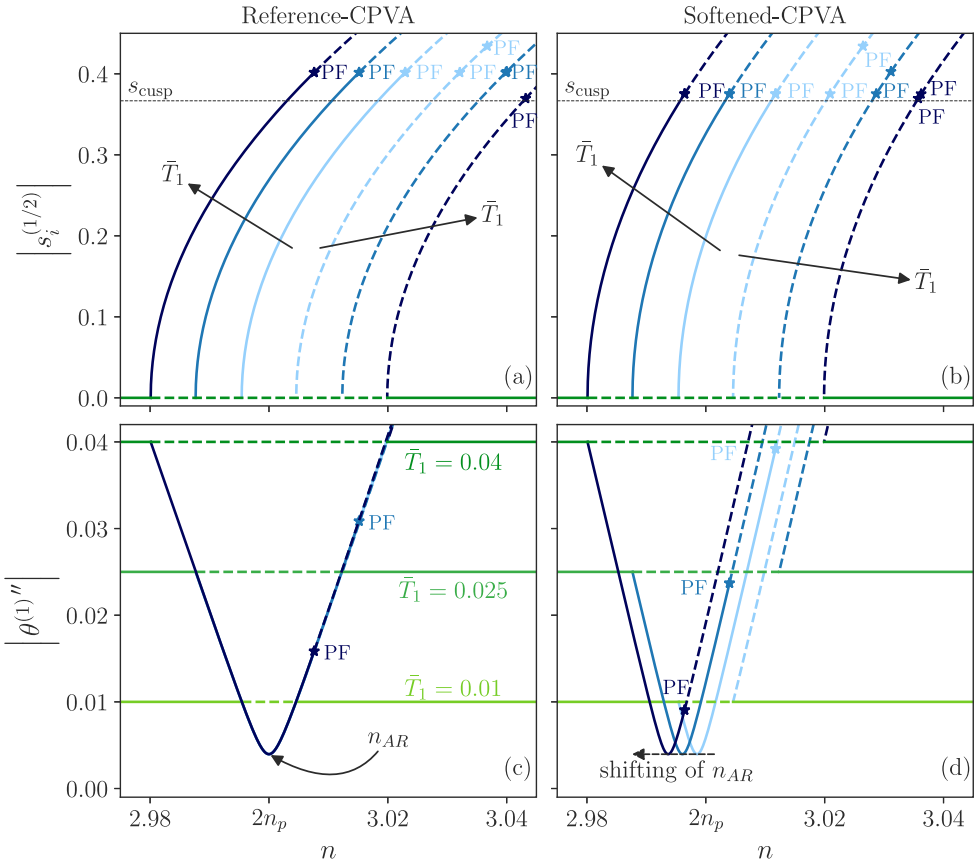

Fig. H.13. Order response of the softened- and reference-CPVA for three torque amplitudes. The associated pendulums' response are shown in (a) and (b) and the associated rotor's response are given in (c) and (d), respectively. The subharmonic and trivial responses are depicted as blue and green lines, respectively. The darker the line the higher the associated torque amplitude. Dashed lines indicate unstable responses and stars with code names PF indicate pitchfork bifurcations. Only one trivial response is shown in (a) and (b) as it overlaps with the other ones (only the unstable part is different). n_{AR} is the order at the non-linear antiresonance. $\bar{T}_1 = \{0.01, 0.025, 0.04\}$.

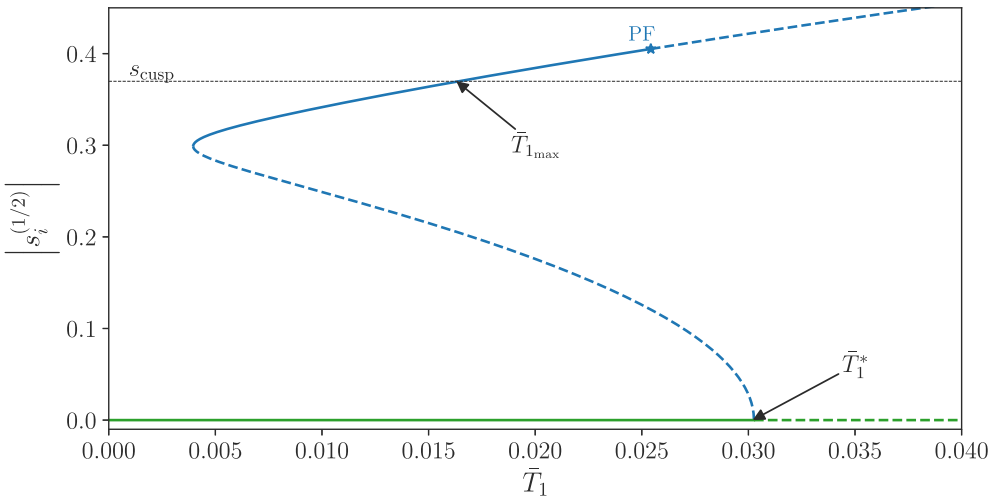

Fig. I.14. Torque response of the pendulums for $n = 3$. Blue and green curves correspond to SH1 and the trivial solution, respectively. Dashed lines indicate unstable solutions. The star with code name "PF" indicates a pitchfork bifurcation. Parameters: $n_p = 1.4925$, $\mu = 0.1$, $\eta = 1$, $\alpha_{[1]} = -0.1$, $\bar{c}_p = 0$, $\bar{b} = 0.002$.

$$c_p = \left[-6\sigma c_t + c_c \frac{n_p \tilde{\mu} \Lambda_c^2}{\Lambda_m}\right] \left(4\sigma + \frac{n_p \tilde{\mu} \Lambda_c^2}{\Lambda_m}\right)^{-1} \quad \text{if} \quad \bar{T}_{1_{\max}} = \bar{T}_{1_b}, \tag{I.2d}$$

$$n_p = n\left(2 + \mu\frac{\Lambda_c^2}{2\Lambda_m}\right)^{-1} \quad \text{if} \quad \bar{T}_{1_{\max}} = \bar{T}_{1_a}. \tag{I.2e}$$

Note that condition (I.2a) corresponds to SH1 being neither hardening nor softening (*cf.* Eq. (36)). In that case, the backbone curve of SH1 is a vertical line and when the trivial solution bifurcates to SH1, the pendulums' amplitude tends to infinity.

References

[1] B.C. Carter, Improvements in or relating to damping of oscillation-checking devices, 337 (1929) 466.
[2] R.R.R. Sarazin, Means adapted to reduce the torsional oscillations of crankshafts, 2079 (1931) 226.
[3] R. Chilton, Pendulum counterweight 2 (112) (1935) 984.
[4] M. Auleley, O. Thomas, C. Giraud-Audine, H. Mahé, Enhancement of a dynamic vibration absorber by means of an electromagnetic shunt, J. Intell. Mater. Syst. Struct. 32 (3) (2021) 331–354, http://dx.doi.org/10.1177/1045389X20957097.
[5] D.E. Newland, Nonlinear problems of centrifugal pendulum vibration absorbers, in: Mechanisms and Machines, vol. 1, Varna (Bulgaria), 1965, pp. 39–62.
[6] C.-P. Chao, C.-T. Lee, S. Shaw, Non-unisson dynamics of multiple centrifugal pendulum vibration absorbers, J. Sound Vib. 204 (5) (1997) 769–794, http://dx.doi.org/10.1006/jsvi.1997.0960.
[7] C.-P. Chao, S.W. Shaw, C.-T. Lee, Stability of the unison response for a rotating system with multiple tautochronic pendulum vibration absorbers, J. Appl. Mech. 64 (1) (1997) 149–156, http://dx.doi.org/10.1115/1.2787266.
[8] A. Alsuwaiyan, S.W. Shaw, Performance and dynamic stability of general-path centrifugal pendulum vibration absorbers, J. Sound Vib. 252 (5) (2002) 791–815, http://dx.doi.org/10.1006/jsvi.2000.3534.
[9] S.W. Shaw, P.M. Schmitz, A.G. Haddow, Tautochronic vibration absorbers for rotating systems, J. Comput. Nonlin. Dynam. 1 (4) (2006) 283–293, http://dx.doi.org/10.1115/1.2338652.
[10] S.W. Shaw, B. Geist, Tuning for performance and stability in systems of nearly tautochronic torsional vibration absorbers, J. Vib. Acoust. 132 (4) (2010) http://dx.doi.org/10.1115/1.4000840.
[11] A.S. Alsuwaiyan, S.W. Shaw, Non-synchronous and localized responses of systems of identical centrifugal pendulum vibration absorbers, Arab. J. Sci. Eng. 39 (12) (2014) 9205–9217, http://dx.doi.org/10.1007/s13369-014-1464-1.
[12] J.S. Issa, S.W. Shaw, Synchronous and non-synchronous responses of systems with multiple identical nonlinear vibration absorbers, J. Sound Vib. 348 (2015) 105–125, http://dx.doi.org/10.1016/j.jsv.2015.03.021.
[13] K. Nishimura, T. Ikeda, Y. Harata, Localization phenomena in torsional rotating shaft systems with multiple centrifugal pendulum vibration absorbers, Nonlinear Dynam. 83 (3) (2016) 1705–1726, http://dx.doi.org/10.1007/s11071-015-2441-2.
[14] A. Grolet, A. Renault, O. Thomas, Energy localisation in periodic structures: application to centrifugal pendulum vibration absorber, in: International Symposium on Transport Phenomena and Dynamics of Rotating Machinery, Maui (Hawaii), 2017.
[15] M. Cirelli, M. Cera, E. Pennestrì, P.P. Valentini, Nonlinear design analysis of centrifugal pendulum vibration absorbers: An intrinsic geometry-based framework, Nonlinear Dynam. 102 (3) (2020) 1297–1318, http://dx.doi.org/10.1007/s11071-020-06035-1.
[16] M. Cera, M. Cirelli, E. Pennestrì, P.P. Valentini, Design analysis of torsichrone centrifugal pendulum vibration absorbers, Nonlinear Dynam. 104 (2) (2021) 1023–1041, http://dx.doi.org/10.1007/s11071-021-06345-y.
[17] V. Mahe, A. Renault, A. Grolet, O. Thomas, H. Mahe, Dynamic stability of centrifugal pendulum vibration absorbers allowing a rotational mobility, J. Sound Vib. 517 (2022) 116525, http://dx.doi.org/10.1016/j.jsv.2021.116525.
[18] A. Renault, O. Thomas, H. Mahé, Numerical antiresonance continuation of structural systems, Mech. Syst. Signal Process. 116 (2019) 963–984, http://dx.doi.org/10.1016/j.ymssp.2018.07.005.
[19] C.-T. Lee, S.W. Shaw, On the counteraction of periodic torques for rotating systems using centrifugally driven vibration absorbers, J. Sound Vib. 191 (5) (1996) 695–719, http://dx.doi.org/10.1006/jsvi.1996.0151.
[20] S.W. Shaw, V. Garg, C.-P. Chao, Attenuation of engine torsional vibrations using tuned pendulum absorbers, in: SAE Noise and Vibration Conference and Exposition, 1997, 971961, http://dx.doi.org/10.4271/971961.
[21] Y. Ishida, T. Inoue, T. Fukami, M. Ueda, Torsional vibration suppression by roller type centrifugal vibration absorbers, J. Vib. Acoust. 131 (5) (2009) 051012, http://dx.doi.org/10.1115/1.3147124.
[22] B.J. Vidmar, S.W. Shaw, B.F. Feeny, B.K. Geist, Nonlinear interactions in systems of multiple order centrifugal pendulum vibration absorbers, J. Vib. Acoust. 135 (6) (2013) http://dx.doi.org/10.1115/1.4024969.
[23] M. Cirelli, E. Capuano, P.P. Valentini, E. Pennestrì, The tuning conditions for circular, cycloidal and epicycloidal centrifugal pendula: A unified cartesian approach, Mech. Mach. Theory 150 (2020) 103859, http://dx.doi.org/10.1016/j.mechmachtheory.2020.103859.
[24] M. Cera, M. Cirelli, E. Pennestrì, P.P. Valentini, Nonlinear dynamics of torsichrone CPVA with synchroringed form closure constraint, Nonlinear Dynam. (2021) http://dx.doi.org/10.1007/s11071-021-06732-5.
[25] H.H. Denman, Tautochronic Bifilar pendulum torsion absorbers for reciprocating engines, J. Sound Vib. 159 (2) (1992) 251–277, http://dx.doi.org/10.1016/0022-460X(92)90035-V.
[26] C.-T. Lee, S.W. Shaw, Torsional vibration reduction in internal combustion engines using centrifugal pendulums, 1995.
[27] C.-T. Lee, S.W. Shaw, The non-linear dynamic response of paired centrifugal pendulum vibration absorbers, J. Sound Vib. 203 (5) (1997) 731–743, http://dx.doi.org/10.1006/jsvi.1996.0707.
[28] C.-T. Lee, S.W. Shaw, V.T. Coppola, A subharmonic vibration absorber for rotating machinery, J. Vib. Acoust. 119 (4) (1997) 590–595, http://dx.doi.org/10.1115/1.2889766.
[29] C.-P. Chao, S.W. Shaw, The effects of imperfections on the performance of the subharmonic vibration absorber system, J. Sound Vib. 215 (5) (1998) 1065–1099, http://dx.doi.org/10.1006/jsvi.1998.1634.
[30] C.-P. Chao, S.W. Shaw, The dynamic response of multiple pairs of subharmonic torsional vibration absorbers, J. Sound Vib. 231 (2) (2000) 411–431, http://dx.doi.org/10.1006/jsvi.1999.2722.
[31] T. Huguet, M. Lallart, A. Badel, Orbit jump in bistable energy harvesters through buckling level modification, Mech. Syst. Signal Process. 128 (2019) 202–215, http://dx.doi.org/10.1016/j.ymssp.2019.03.051.
[32] L.-Q. Chen, W.-A. Jiang, M. Panyam, M.F. Daqaq, A broadband internally resonant vibratory energy harvester, J. Vib. Acoust. 138 (6) (2016) 061007, http://dx.doi.org/10.1115/1.4034253.
[33] M. García-Diéguez, V. Racic, J. Zapico-Valle, Complete statistical approach to modelling variable pedestrian forces induced on rigid surfaces, Mech. Syst. Signal Process. 159 (2021) 107800, http://dx.doi.org/10.1016/j.ymssp.2021.107800.
[34] A.H. Nayfeh, D.T. Mook, Nonlinear Oscillations, in: Wiley Classics Library, Wiley-VCH, 1995, http://dx.doi.org/10.1002/9783527617586.
[35] Z.A. Shami, C. Giraud-Audine, O. Thomas, A nonlinear piezoelectric shunt absorber with a 2:1 internal resonance: theory, Mech. Syst. Signal Process. 170 (2022) 108768, http://dx.doi.org/10.1016/j.ymssp.2021.108768.

[36] Z.A. Shami, C. Giraud-Audine, O. Thomas, A nonlinear piezoelectric shunt absorber with 2:1 internal resonance: Experimental proof of concept, Smart Mater. Struct. 31 (3) (2022) 035006, http://dx.doi.org/10.1088/1361-665X/ac4ab5.
[37] B. Geist, V. Ramakrishnan, P. Attibele, W. Resh, Precision requirements for the bifilar hinge slots of a centrifugal pendulum vibration absorber, Precis. Eng. 52 (2018) 1–14, http://dx.doi.org/10.1016/j.precisioneng.2017.08.001.
[38] Les amortisseurs dynamiques de vibrations [dynamic vibration dampers], Rev. Tech. Hispano Suiza (3) (1939).
[39] A. Renault, Calcul et optimisation d'absorbeurs pendulaires dans une chaîne de traction automobile [simulation and optimisation of pendular absorbers for automotive powertrain], (Ph.D. thesis), ENSAM, Lille, 2018.
[40] H. Mahé, A. Renault, O. Thomas, Dispositif d'amortissement pendulaire [pendular damping device], FR 3 055 037 (2018).
[41] H. Mahé, A. Renault, O. Thomas, Dispositif d'amortissement pendulaire [Pendular damping device], FR 3 055 038 (2018).
[42] M.A. Acar, Design and tuning of centrifugal pendulum vibration absorbers, (Ph.D. thesis), Michigan State University, Michigan, 2017.
[43] J. Mayet, H. Ulbrich, Tautochronic centrifugal pendulum vibration absorbers: General design and analysis, J. Sound Vib. 333 (3) (2014) 711–729, http://dx.doi.org/10.1016/j.jsv.2013.09.042.
[44] M. Cirelli, J. Gregori, P. Valentini, E. Pennestrí, A design chart approach for the tuning of parallel and trapezoidal bifilar centrifugal pendulum, Mech. Mach. Theory 140 (2019) 711–729, http://dx.doi.org/10.1016/j.mechmachtheory.2019.06.030.
[45] E.R. Gomez, I.L. Arteaga, L. Kari, Normal-force dependant friction in centrifugal pendulum vibration absorbers: simulation and experimental investigations, J. Sound Vib. 492 (2021) 115815, http://dx.doi.org/10.1016/j.jsv.2020.115815.
[46] X. Tan, S. Yang, J. Yang, J. Li, Study of dynamics of rotational centrifugal pendulum vibration absorbers based on tautochronic design, Meccanica (2021) http://dx.doi.org/10.1007/s11012-021-01340-4.
[47] E.R. Gomez, J. Sjöstrand, L. Kari, I.L. Arteaga, Torsional vibrations in heavy-truck powertrains with flywheel attached centrifugal pendulum vibration absorbers, Mech. Mach. Theory 167 (2022) 104547, http://dx.doi.org/10.1016/j.mechmachtheory.2021.104547.
[48] S.W. Shaw, S. Wiggins, Chaotic dynamics of a whirling pendulum, Physica D 31 (2) (1988) 190–211, http://dx.doi.org/10.1016/0167-2789(88)90076-0.
[49] S.W. Shaw, M.A. Acar, B.F. Feeny, B.K. Geist, Modal properties of rotating shafts with order-tuned absorbers, in: J. De Clerck (Ed.), Topics in Modal Analysis I, Vol. 7, Springer International Publishing, Cham, 2014, pp. 181–189, http://dx.doi.org/10.1007/978-3-319-04753-9_18.
[50] M. Auleley, C. Giraud-Audine, H. Mahé, O. Thomas, Tunable electromagnetic resonant shunt using pulse-width modulation, J. Sound Vib. 500 (2021) 116018, http://dx.doi.org/10.1016/j.jsv.2021.116018.
[51] A.H. Nayfeh, Perturbation Methods, in: Wiley Classics Library, Wiley-VCH, Weinheim, 1973, http://dx.doi.org/10.1002/9783527617609.
[52] L. Guillot, A. Lazarus, O. Thomas, C. Vergez, B. Cochelin, A purely frequency based floquet-hill formulation for the efficient stability computation of periodic solutions of ordinary differential systems, J. Comput. Phys. 416 (2020) 109477, http://dx.doi.org/10.1016/j.jcp.2020.109477.
[53] L. Guillot, B. Cochelin, C. Vergez, A taylor series-based continuation method for solutions of dynamical systems, Nonlinear Dynam. 98 (4) (2019) 2827–2845, http://dx.doi.org/10.1007/s11071-019-04989-5.

Chapter 7

Stability of the subharmonic response of centrifugal pendulums

This chapter is made of a paper about to be submitted to *Nonlinear Dynamics* [154]. It focuses on the stability of the subharmonic response of a centrifugal pendulum vibration absorber (CPVA) made of several pairs of pendulums. More specifically, it aims to predict analytically the apparition of localised subharmonic responses and to provide guidelines to avoid them using the simplified CPVA model detailed in section 2.3.2. It is the logical continuity of chapter 6, which investigated the subharmonic response of a CPVA made of a single pair of pendulums. Hence, like chapter 6, the present chapter can prove useful in the adaptation of CPVAs to electric vehicles.

Sections 1 and 2 repeat information from chapters 1 and 2. They present the context of the study, the modelling of a CPVA (*cf.* section 2.1.1) and a linear analysis (*cf.* section 2.2). In addition, section 3.2 repeats the derivation of simplified CPVA equations, which was already detailed in section 2.3.2 of chapter 2. The reader might want to skip these sections of the article if he already read chapters 1 and 2.

The novelty of the article starts in section 3.1, where the desired subharmonic solution in the presence of several pairs of pendulums is detailed. This desired solution corresponds to pendulums moving with the same amplitude, but with half of them in phase-opposition with the other half. Thus, they act as two equivalent pendulums in phase-opposition. This special solution is discussed further in the rest of section 3, which is a summary of the results from chapter 6. Hence, the reader might want to skip sections 3.2, 3.3 and 3.4 if he already read chapter 6. The stability of the desired solution is evaluated in section 4 using the method of multiple scales (*cf.* section 2.5.2.1) and an original procedure. It is found that great care must be taken in the tuning of the pendulums as localisation might easily occur. The analytical results are applied to case studies in section 5 and validated through comparisons with numerical resolutions of the system's dynamics. Guidelines to enforce a bifurcation towards the desired response and to make this response stable are proposed.

On the stability of pairs of subharmonic centrifugal pendulum vibration absorbers allowing a rotational mobility

Vincent Mahé[1,2*], Alexandre Renault[2], Aurélien Grolet[1], Hervé Mahé[2] and Olivier Thomas[1]

[1*]Arts et Metiers Institute of Technology, LISPEN, HESAM Université, Boulevard Louis XIV, Lille, F-59000, France.
[2]Centre d'Étude des Produits Nouveaux, Valeo Transmissions, Espace Industriel Nord, Route de Poulainville, Amiens Cedex 1, 80009, France.

*Corresponding author(s). E-mail(s): vincent.mahe@ensam.eu;
Contributing authors: alexandre.renault@valeo.com;
aurelien.grolet@ensam.eu; herve.mahe@valeo.com;
olivier.thomas@ensam.eu;

Abstract

Centrifugal pendulum vibration absorbers (CPVAs) are passive devices used to reduce torsional vibrations in rotating machines. Previous works showed that a CPVA configuration with two pendulums oscillating in phase-opposition and at half the excitation frequency is efficient in reducing the rotor's vibrations. This paper deals with a new generation of CPVAs, in which the pendulums admit a rotational motion relative to the rotor in addition to the traditional translational motion. The aim of this study is to assess the dynamic stability of a particular subharmonic solution of CPVAs composed of several pairs of pendulum. To do so, a new method based on an analytical perturbation technique is proposed. It leads to more general conclusions than previous studies as the results are derived for CPVAs with any even number of pendulums. The validity of the analytical model is confirmed through a comparison with a numerical resolution of the system's dynamics, and new design guidelines are proposed.

Keywords: centrifugal pendulum vibration absorber, non-linear dynamics, subharmonic absorber, stability

1 Introduction

In the frame of reducing polluting emissions and fuel consumption of vehicles using thermal engines, automotive manufacturers try to reduce the cylinder capacity and engine speed of rotation. These evolutions lead to a significant increase of rotation irregularities called "acyclisms", mainly due to higher combustion pressure. One of the main characteristics of these reciprocating engines is the linear dependence of the acyclism frequency to the engine mean speed of rotation. The coefficient of proportionality is called the engine order and only depends on the architecture of the engine. During an acceleration phase, the engine sweeps a wide frequency range containing some driveline torsional modes. This situation may lead to significant noise and vibration levels into the passenger compartment and premature wear of the driveline components. Centrifugal pendulum vibration absorbers (CPVAs) have been used for many years to minimise acyclisms of automotive powertrains at the engine order [1–3]. These passive devices consist of oscillating masses (pendulums) moving along particular paths relative to a primary inertia (rotor) as shown in Fig. 1. Because the pendulums move in the centrifugal acceleration field resulting from the rotation of the CPVA, their natural frequency is proportional to the mean engine speed of rotation. The coefficient of proportionality is the pendulums' tuning order, which can be chosen to filter out vibrations at the engine order.

There are two ways of choosing the pendulums' tuning order. The "classical" way, used in industrial solutions, is to tune the pendulums on the engine order. This generates an antiresonance of the rotor at the engine order, allowing for significant vibration reduction. However, because of non-linearities inherent to CPVA systems, several dysfunctions occur at large excitation amplitudes, such as jumps of the response [4], localisation of the pendulums' response [5–17], a shift of the antiresonance [17, 18] and the generation of higher rotor harmonics [17, 19–24].
An alternative tuning, studied by S. Shaw *et al.* [19, 25–29] and V. Mahé *et al.* [30], is to set the pendulums' tuning order to half the engine order. In this case, the pendulums oscillate at half the engine order so that the solution is a subharmonic of order 2 [31]. This generates a non-linear antiresonance of the rotor at the engine order. Moreover, in the case of perfect-tuning, the amplitude at the antiresonance is saturated, which allows for an efficient reduction of the rotor's vibrations [27]. This saturation effect is a known consequence of subharmonic solutions and proved useful in other fields of application (see e.g. [32, 33] and references therein).

Most studies dealing with CPVAs consider purely translated pendulums, i.e. pendulums that do not rotate relatively to the rotor. However, several works recently showed that adding a rotational mobility to the pendulums can significantly increase the efficiency of the CPVA [34–38]. These works encouraged researchers to investigate the impacts of rotation [14, 15, 39–43], including the authors of the present paper [16, 17, 30], who extended former results on the subharmonic solution by considering pendulums that can rotate relatively to the rotor.

In [19, 25–28, 30], the subharmonic solution is studied for CPVAs made of only two pendulums. If the CPVA is made of several pairs of pendulums, the ideal solution is obtained when half of these pendulums are in phase opposition with the other half. Hence, the two half act as equivalent pendulums. However, C.-P. Chao *et al.* showed that the presence of several pairs of pendulums leads to additional instabilities [29]. The motivation of this paper is to investigate the stability of the subharmonic response of CPVAs made of N pendulums (N even) that are allowed to rotate relatively to the rotor. In [29], concepts from group theory and symmetric bifurcation theory were used to assess the stability of CPVAs made of 4 and 6 pendulums. Though giving very interesting results, the method used gets more complex as one considers CPVAs with larger numbers of pendulums. In the present study, an alternative method is proposed. It leads to more general conclusions as the results obtained are valid for any even value of N. In addition, this new method allows to derive an analytical expression for the limits of the instability zones, resulting in more accurate design guidelines. Another major contribution of the present paper is that the rotational motion of the pendulums is taken into account.

This paper is organised as follows. The modelling and a linear analysis of a CPVA are conducted in section 2. The subharmonic solution of interest is computed in section 3 and its stability is assessed in section 4. Case studies and design guidelines are presented in section 5.

2 Modelling and linear analysis

2.1 Modelling

The system studied is shown in Fig. 1. A rotor of inertia J_r rotates about its centre O. Its total angular position is $\vartheta(t) = \Omega t + \theta(t)$ where t is the time, Ω is the mean rotational velocity and $\theta(t)$ corresponds to the fluctuating part of the rotation (with zero mean). A torque $T(\vartheta) = T_0 + T_\theta(\vartheta)$ is applied to the rotor where T_0 is its constant part and $T_\theta(\vartheta)$ is periodic (with zero mean). For constant torque and constant rotation speed, one has $T_0 = b_r\Omega$ where b_r is the linear viscous damping coefficient of the rotor, such that the constant torque balances with the damping to set the mean rotation speed Ω. N pendulums of mass m_i and inertia I_i (about their centre of mass) oscillate on their path $\mathscr{C}_i$. Their position on these paths is given by the curvilinear

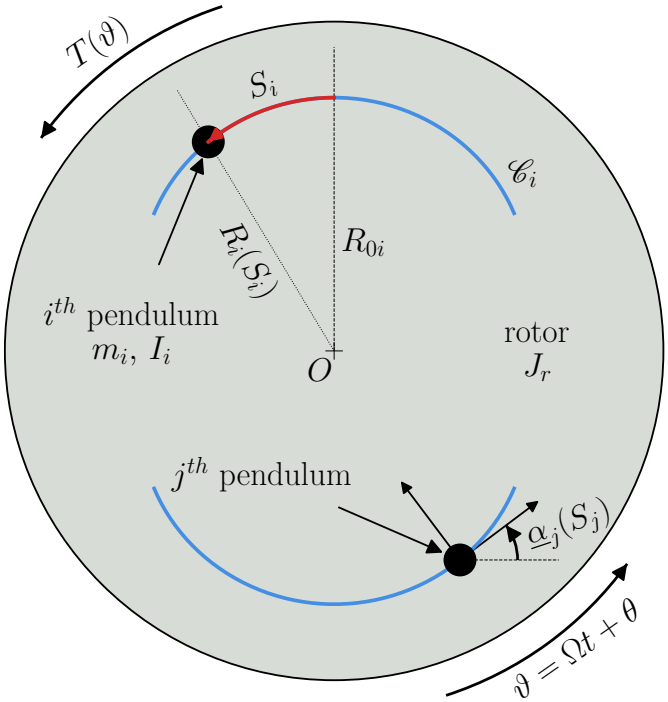

Figure 1: Representation of the system studied with $N = 2$ pendulums.

abscissa $S_i(t)$ and their distance from O is $R_i(S_i)$. The characteristic dimension $R_{0i} = R_i(S_i = 0)$ is the distance between O and the vertex of the path. In addition to the traditional translation motion, the present study considers that the pendulums rotate about their centre of mass according to the rotation function $\underline{\alpha}_i(S_i)$. As for the rotor, an equivalent linear viscous damping coefficient b_i is used to model the damping between the i^{th} pendulum and the rotor. In the later, pendulums and their associated path and rotation functions will be considered identical so that subscript "i" will be dropped when addressing pendulums' parameters.

In order to write the equations of motion in a non-dimensional form, the following parameters and variables are introduced:

$$
\begin{gathered}
s_i = \frac{S_i}{R_0}, \quad y = \frac{\dot{\vartheta}}{\Omega} = 1 + \frac{\dot{\theta}}{\Omega}, \quad \eta = \frac{I}{mR_0^2}, \quad \mu = \frac{NmR_0^2}{(J_r + NI)}, \\
x(s_i) = \frac{R(R_0 s_i)^2}{R_0^2}, \quad z(s_i) = \sqrt{x(s_i) - \frac{1}{4}\left(\frac{dx(s_i)}{ds_i}\right)^2}, \\
\alpha(s_i) = \underline{\alpha}(R_0 s_i), \quad \gamma(s_i) = \frac{d\alpha(s_i)}{ds_i}, \\
\bar{b} = \frac{b}{m\Omega}, \quad \bar{b}_r = \frac{b_r}{(J_r + NI)\Omega}, \quad \bar{T}(\vartheta) = \bar{T}_0 + \bar{T}_\theta(\vartheta) = \frac{T(\vartheta)}{(J_r + NI)\Omega^2},
\end{gathered}
\tag{1}
$$

where $\dot{(\bullet)} = \partial(\bullet)/\partial t$. The s_i and y are the $N+1$ degrees of freedom of the system. They correspond to the relative position of the pendulums and the non-dimensional rotation velocity of the rotor, respectively. η and μ are inertia ratios and $x(s_i)$ and $z(s_i)$ are path functions while $\alpha(s_i)$ and $\gamma(s_i)$ are rotation functions. In this paper, $x(s_i)$ and $\alpha(s_i)$ are written as polynomials in the curvilinear abscissa s_i such that

$$x(s_i) = 1 - n_t^2 s_i^2 + \sum_{k=3}^{\infty} x_{[k]} s_i^k, \quad \alpha(s_i) = \sum_{k=0}^{\infty} \alpha_{[k]} s_i^k, \tag{2}$$

where n_t is the order of the pendulums' path and $x_{[k]}$, $\alpha_{[k]}$ are path and rotation coefficients. Note that in the case $x_{[k]} = 0, \forall k$, the pendulums' paths are epicycloids, which corresponds to the tautochronic path when the rotor spins at a constant speed [44]. $\bar{b}$ and $\bar{b}_r$ are non-dimensional damping constants and $\bar{T}(\vartheta)$ is the non-dimensional torque applied on the rotor.

In order to give $\bar{T}(\vartheta)$ the meaning of an external forcing term, we replace the independent variable t by the rotor's position ϑ [45], which can be seen as a non-dimensional time. The condition to use this change of variables is that ϑ be strictly monotonic, which is the case in practice. Using the chain rule, one can show that

$$\dot{(\bullet)} = \Omega y (\bullet)', \quad \ddot{(\bullet)} = \Omega^2 y y' (\bullet)' + \Omega^2 y^2 (\bullet)'', \tag{3}$$

where $(\bullet)' = \partial(\bullet)/\partial\vartheta$ (the demonstration can be found in [30]). Hence, the non-dimensional rotor's acceleration is now $\ddot{\vartheta}/\Omega^2 = \dot{y}/\Omega = y y'$. Using the non-dimensional quantities (1) and the chain rule (3), one can write the equations of motion as

$$\begin{aligned} &\frac{1}{N}\left[\sum_{i=1}^{N}(N+\mu x(s_i))yy' + \mu\left(z(s_i)+\eta\gamma(s_i)\right)\left(yy's_i' + y^2 s_i''\right)\right. \\ &\left. + \mu y^2 s_i'\left(\frac{dx(s_i)}{ds_i} + \frac{dz(s_i)}{ds_i}s_i' + \eta\frac{d\gamma(s_i)}{ds_i}s_i'\right)\right] + \bar{b}_r y = \bar{T}(\vartheta), \end{aligned} \tag{4a}$$

$$\begin{aligned} &\left[z(s_i)+\eta\gamma(s_i)\right]y' + \left[1+\eta\gamma(s_i)^2\right]\left(y's_i' + ys_i''\right) + \eta\gamma(s_i)\frac{d\gamma(s_i)}{ds_i}y{s_i'}^2 \\ &- \frac{1}{2}\frac{dx(s_i)}{ds_i}y + \bar{b}s_i' = 0, \qquad i = 1, ..., N. \end{aligned} \tag{4b}$$

Computation details can be found in [30]. Equation (4a) governs the motion of the rotor while the N Eqs. (4b) govern the motion of the pendulums.

From now on, it is assumed that the fluctuating torque applied on the rotor contains only one harmonic whose non-dimensional form is $\bar{T}_1 \cos(n\vartheta)$, where

n is the excitation order. For a car engine, n corresponds to the number of strikes per revolution of the crankshaft.

2.2 Linear analysis

First of all, one can use Eq. (3) to show that, at first order, $1 + \theta' \approx y$ and $\theta'' \approx yy' \approx y'$ (the demonstration can be found in [30]). Hence, it is possible to represent the motion of the rotor with position θ instead of velocity y. This way, all the degrees of freedom of the system are positions, which facilitates the representation of the mode shapes. Using θ instead of y and the balance between the constant torque and the damping (*cf.* section 2.1), one can linearise Eqs. (4a) and (4b). This leads to the free, conservative, linear, matrix equation

$$\boldsymbol{M}\ddot{\boldsymbol{q}} + \boldsymbol{K}\boldsymbol{q} = \boldsymbol{0}, \tag{5}$$

where $\boldsymbol{q}$, $\boldsymbol{M}$ and $\boldsymbol{K}$ are the vector containing the degrees of freedom and the mass and stiffness matrices, respectively. They are given by

$$\boldsymbol{q} = \begin{bmatrix} \theta \\ s_1 \\ \vdots \\ s_N \end{bmatrix}, \ \boldsymbol{M} = \begin{bmatrix} N\frac{1+\mu}{\mu} & \Lambda_c & \cdots & \cdots & \Lambda_c \\ \Lambda_c & \Lambda_m & 0 & \cdots & 0 \\ \vdots & 0 & \ddots & \ddots & \vdots \\ \vdots & \vdots & \ddots & \ddots & 0 \\ \Lambda_c & 0 & \cdots & 0 & \Lambda_m \end{bmatrix}, \ \boldsymbol{K} = \begin{bmatrix} 0 & & & \\ & n_t^2 & & \\ & & \ddots & \\ & & & n_t^2 \end{bmatrix}. \tag{6}$$

Λ_m and Λ_c are constants representing the equivalent mass of a pendulum due to the effect of the rotatory inertia and the linear coupling term between a pendulum and the rotor, respectively. They are given by

$$\Lambda_m = 1 + \eta\alpha_{[1]}^2, \quad \Lambda_c = 1 + \eta\alpha_{[1]}, \tag{7}$$

where $\alpha_{[1]}$ is the linear rotation coefficient (*cf.* Eq. (2)).

The eigenvalue problem $[\boldsymbol{K} - n^2\boldsymbol{M}]\boldsymbol{\phi} = \boldsymbol{0}$ can be solved using a property of arrowhead matrices [46], leading to the eigenorders[1] and mode shapes of

[1] Eigenorders can be seen as nondimensional eigenfrequencies.

the system. These are given by

$$
\begin{aligned}
&n_{00} = 0, \quad n_{10} = n_p, \quad n_{20} = n_p \sqrt{\frac{1+\mu}{1+\mu\left(1-\frac{\Lambda_c^2}{\Lambda_m}\right)}} \\
&\boldsymbol{\phi_{00}} = [1, 0, ..., 0]^\intercal, \quad \boldsymbol{\phi_{20}} = \left[-\frac{\mu\Lambda_c}{1+\mu}, 1, ..., 1\right]^\intercal, \\
&\boldsymbol{\phi_{1_i}}[i+1] = -\boldsymbol{\phi_{1_i}}[i+2] = 1, \quad \boldsymbol{\phi_{1_i}}[j \neq \{i+1, i+2\}] = 0, \\
&i = 1, ..., N-1.
\end{aligned}
\tag{8}
$$

Superscript $\intercal$ indicates the transpose and $\boldsymbol{\phi_{1_i}}[j]$ refers to the j^{th} component of $\boldsymbol{\phi_{1_i}}$. n_p is the pendulums' tuning order, which is related to the path order n_t such that

$$
n_p = \frac{n_t}{\sqrt{\Lambda_m}}. \tag{9}
$$

It corresponds to the eingenorder of the pendulums when they are uncoupled from the rotor.
$(n_{00}, \boldsymbol{\phi_{00}})$, $(n_{10}, \boldsymbol{\phi_{1_i}})$ and $(n_{20}, \boldsymbol{\phi_{20}})$ will be referred to as modes 0, 1_i and 2, respectively. For simplicity, modes 1 will refer to the set containing all modes 1_i. The modes are illustrated in Fig. 2 for a CPVA made of $N = 4$ pendulums. Mode 0 is a rigid body mode for which only the rotor is excited. Modes 1 are $N-1$ degenerated modes for which two pendulums are moving in phase-opposition. Their eigenvalue n_{10} has a multiplicity $N-1$ and the rotor is a node of these modes. For a CPVA made of only two pendulums, mode 1 is not degenerated and simply represents a phase-opposition motion of the pendulums. Note that there are many ways to write modes 1 (they are not unique), the only conditions being that

- the rotor's component is null,
- the sum of all the components is null,
- modes 0, 1 and 2 form a complete basis of $\mathbb{R}^{N+1}$.

More details on this matter are presented in Appendix A. Mode 2 is a mode for which pendulums move in unison but in phase-opposition with respect to the rotor (provided that $\Lambda_c > 0$, which is the case for reasonable parameters).

When a fluctuating torque is applied, one can choose to tune the pendulums such that $n_p \approx n$ or $n_p \approx n/2$ to filter-out the rotor's vibrations using mode 2 or modes 1, respectively.

3 The desired subharmonic solution

3.1 The undamped, perfectly-tuned case

The aim here is to show that the solution with half the pendulums oscillating in unison and in phase-opposition with the other half allows for an efficient

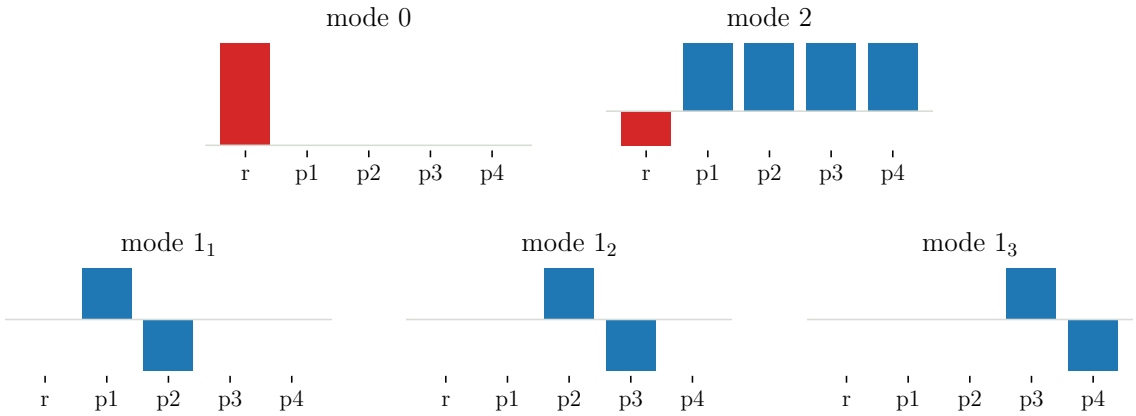

Figure 2: Representation of the modes of a CPVA made of $N = 4$ pendulums. "r" indicates the rotor's component (in red) while "pi" indicates the component of the i^{th} pendulum (in blue).

reduction of the rotor's vibrations (note that the special case of $N = 2$ pendulums was already treated in [30]). To do so, the case of a CPVA with undamped pendulums following epicycloidal paths and with a linear rotation law $\alpha(s_i) = \alpha_{[1]} s_i$ is considered. Moreover, the solution sought is that of perfect filtration, i.e. with $y' = 0$, $y = 1$ so that the rotor spins at a constant speed. In this case, the pendulums' response is of the form

$$s_i = a_i \cos(n_p \vartheta + \varphi_i), \quad i = 1, ..., N. \tag{10}$$

The pendulums can be split into two groups by introducing the sets of integers

$$\mathcal{G}_1 = \{1, 2, ..., N/2\} \quad \text{and} \quad \mathcal{G}_2 = \{N/2 + 1, N/2 + 2, ..., N\}. \tag{11}$$

These sets are chosen to be of the same size so that the N pendulums split into two groups of $N/2$ pendulums, each group acting as an equivalent pendulum with mass $Nm/2$ and inertia $NI/2$. It is now assumed that the pendulums in $\mathcal{G}_1$ oscillate in phase, but their amplitudes are not necessarily the same. Pendulums in $\mathcal{G}_2$ oscillate with the same amplitudes as those in $\mathcal{G}_1$ but in phase-opposition. Under these assumptions, the rotor's equation (4a) reduces to

$$\frac{2n_t^2 n_p \mu}{N} \sum_{i=1}^{N/2} a_i^2 \cos\left[2(n_p \vartheta + \varphi_i) - \pi/2\right] = \bar{T}_1 \cos(n\vartheta), \tag{12}$$

and is verified under the conditions

$$n_p = n/2, \quad \varphi_i = \pi/4, \ i \in \mathcal{G}_1, \quad \varphi_i = \pi/4 + \pi, \ i \in \mathcal{G}_2, \tag{13a}$$

$$\sum_{i=1}^{N/2} a_i^2 = \frac{N\bar{T}_1}{2n_t^2 n_p \mu}. \tag{13b}$$

Because of condition (13b), there is an infinity of solutions for the pendulums' responses. However, in addition to the efficiency of the filtration, one should keep in mind that CPVAs have a limited torque range due to the nature of the pendulums' path. Indeed, the paths have a cusp that pendulums cannot overpass. For instance, the cusp of an epicycloid is

$$s_{\text{cusp}} = \frac{1}{\sqrt{n_t^2(1+n_t^2)}}. \tag{14}$$

In order to maximise the torque range, one should aim for the solution minimising the amplitude of all the absorbers. From Eq. (13b), it can be seen that this is achieved when all the absorbers oscillate with the same amplitude (i.e. $a_i = a \ \forall i$), which corresponds to a particular solution, called "SH1"[1]. This special solution corresponds to a combination of modes 1 such that

$$\boldsymbol{\phi_{SH1}} = \sum_{i=1}^{N/2} i\boldsymbol{\phi_{1_{0i}}} + \sum_{i=N/2+1}^{N-1} (N-i)\boldsymbol{\phi_{1_{0i}}} = [0, \underbrace{1, ..., 1}_{N/2}, \underbrace{-1, ..., -1}_{N/2}]^{\mathsf{T}}. \tag{15}$$

SH1 allows for a complete filtration of the rotor's vibrations while maximising the torque range, which makes it the desired subharmonic solution.

Notations from group theory [47] define $\boldsymbol{S}_M$ as a group with symmetry M, that is to say a set that is invariant under any permutation of its M elements. In the case of a CPVA, $\boldsymbol{S}_M$ refers to a solution for which a subgroup of M absorbers have the exact same motion, so that any permutation of these M absorbers results in the same response. Hence, SH1 can be seen as a special $\boldsymbol{S}_{N/2} \times \boldsymbol{S}_{N/2}$ solution where the amplitudes in the two $\boldsymbol{S}_{N/2}$ groups are equal but the phases are shifted by π.

3.2 Discussion on the mode shapes obtained through combinations of modes 1

Modes 1 are degenerated modes, so they are all in 1:1:...:1 internal resonance (*cf.* Eq. (8)) [48]. Hence, any combination of these modes can also be seen as a mode of the system (it could actually have been defined as a mode in place of one of the modes 1_i, *cf.* section 2.2). In section 3.1, we discussed SH1, defined as the ideal combination of modes 1 to filter the rotor's torsional vibrations while minimising the pendulums' amplitude of motion. However, this is not the only optimal combination of modes 1. Indeed, instead of defining $\mathcal{G}_1$ and $\mathcal{G}_2$ as the sets containing the first and last $N/2$ pendulums, respectively, we could have defined them as $\mathcal{G}_1 = \{2, 3, ..., N/2+1\}$ and $\mathcal{G}_2 = \{1, N/2+2, N/2+3, ..., N\}$. Then, if we make the same assumptions as in section 3.1 (the pendulums all have the same amplitude but those in $\mathcal{G}_1$ are in phase-opposition with those

[1] "SH" stands for "subharmonic" and "1" refers to the response being on modes 1.

in $\mathcal{G}_2$), we obtain a mode shape SHR of the form

$$\text{SHR}: \quad [0, -1, \underbrace{1, ..., 1}_{N/2}, \underbrace{-1, ..., -1}_{N/2-1}]^\intercal. \tag{16}$$

Note that SHR is just a rotation by 1 of SH1. As the pendulums are identical, their response on SHR leads to the same rotor's response as SH1. Moreover, the pendulums' responses are also identical except for that of the first and last pendulums which are swapped. There are $N-1$ rotations of SH1, and instead of studying them all it is relevant to study only SH1.

There are also combinations of modes 1 that satisfy "all pendulums oscillate with the same amplitude but half of them are in phase opposition with the other half" while not being rotations of SH1. For instance, this is the case of the mode shape

$$\text{SHX}: \quad [0, \underbrace{1, -1, 1, -1, ..., 1, -1}_{N}]^\intercal, \tag{17}$$

obtained by defining $\mathcal{G}_1 = \{1, 3, 5, ..., N-1\}$ and $\mathcal{G}_2 = \{2, 4, 6, ..., N\}$. Again, as the pendulums are all identical, their response on SHX leads to the same rotor's response as SH1. The pendulums' responses are also the same as with SH1 except that they are swapped. There is however a difference between mode shapes of the form of SHR, which are rotations of SH1, and those like SHX, which are not. Indeed, the pendulums' distribution does not affect the torque they generate on the rotor, but it affects the resulting force they apply on it. This is illustrated in Appendix B, where one can see that SH1 and its rotations generate shaking forces on the rotor while SHX does not. This is of small importance in the present study as the translational mobility of the rotor is not taken into account, so these shaking forces are of no consequence. However, if this mobility was to be accounted for, the shaking forces would be a source of translational rotor vibrations. Such vibrations are investigated in [49–56] but are out of the scope of this paper.

Dropping the assumption that all pendulums have the same amplitude (this was assumed in section 3.1 to maximise the torque capacity of the CPVA), one can generate mode shapes different from the ones discussed above. Among these different-amplitude mode shapes, one can find all modes 1 but also combinations such as

$$[0, 1, 1, -1, -1, \underbrace{0, ..., 0}_{N-4}]^\intercal \quad \text{and} \quad [0, 3, -1, -1, -1, \underbrace{0, ..., 0}_{N-4}]^\intercal \tag{18}$$

for instance. Though such solutions are not desired as they decrease the torque capacity and might not allow for an efficient filtering of the rotor's vibrations, they exist and it will be shown thereafter (*cf.* section 5 and Appendices A, G

and H) that they significantly complicate the dynamics of the system.

To conclude this brief discussion on the different combinations of modes 1, one has to be aware that:

- SH1 is not the only optimal pendulums' response.
- Every optimal pendulums' response leads to a system's response very similar to SH1 (provided that the rotor does not have a translational mobility), so it is sufficient to study only SH1.
- Non-ideal pendulums' responses exist and complicate the dynamics of the system.

3.3 Scaling and simplification of the equations

Now that SH1 has been identified as (one of) the desired response, it is essential to study it further by taking into account the damping and considering more general path and rotation functions. To do so, the first step is to simplify Eqs. (4a) and (4b) in order to obtain equations of motion that can be solved analytically. The full procedure is detailed in [30], so only the main steps are reminded here. The path and rotation functions followed by the pendulums are chosen to be

$$x(s_i) = 1 - n_t^2 s_i^2 + x_{[4]} s_i^4, \quad \alpha(s_i) = \alpha_{[1]} s_i + \alpha_{[3]} s_i^3, \tag{19}$$

and the rotor's rotational velocity is expanded such that

$$y(\vartheta) = 1 + y_\theta(\vartheta). \tag{20}$$

According to physically relevant assumptions [17, 30], some parameters and variables are scaled such that

$$\begin{aligned} &\bar{b} = \epsilon\tilde{b}, \quad \bar{b}_r = \epsilon\tilde{b}_r, \quad \bar{T}_1 = \epsilon\tilde{T}_1, \quad \mu = \epsilon\tilde{\mu}, \quad y_\theta = \epsilon\tilde{y}_\theta, \\ &\theta' = \epsilon\tilde{\theta}', \quad x_{[4]} = \epsilon\tilde{x}_{[4]}, \quad \alpha_{[3]} = \epsilon\tilde{\alpha}_{[3]}, \end{aligned} \tag{21}$$

where ϵ is a small parameter. In order to give it a physical meaning, one can choose $\epsilon = \mu$ [7]. In the following, only first-order terms will be retained in the rotor's equation. Hence, like in section 2.2, the approximation $\tilde{\theta} \approx \tilde{y}_\theta$ can be used in order to represent the degree of freedom of the rotor through its position rather than its velocity.

Using Eqs. (19), (20) and (21) and using Taylor series for $z(s_i)$, Eqs. (4a) and (4b) can be simplified such that

$$\tilde{\theta}'' = \frac{\tilde{\mu}}{N}\left[\sum_{i=1}^{N} n_p^2 \Lambda_c s_i + 2n_t^2 s_i s_i' + n_t^2(1+n_t^2)\left(s_i {s_i'}^2 - \frac{n_p^2}{2} s_i^3\right)\right] + \tilde{T}_1 \cos(n\theta), \tag{22a}$$

$$\begin{aligned} s_i'' + n_p^2 s_i = -\epsilon \Lambda_m^{-1} \Bigg\{ & \frac{\Lambda_c^2 \tilde{\mu}}{N} \sum_{j=1}^{N} n_p^2 s_j + \tilde{b} s_i' + \frac{\tilde{\mu} n_t^2 \Lambda_c}{N}\left[\sum_{j=1}^{N} s_j (2s_j' + s_i')\right] \\ & + \frac{\tilde{\mu} n_t^2}{N}\left[\sum_{j=1}^{N} (1+n_t^2)\Lambda_c \left(s_j {s_j'}^2 - \frac{n_p^2}{2}(s_j^3 + s_j s_i^2)\right)\right. \\ & \left. + 2\Lambda_m s_j s_j' s_i'\right] + 6\eta \alpha_{[1]} \tilde{\alpha}_{[3]} (s_i {s_i'}^2 + s_i^2 s_i'') - 2\tilde{x}_{[4]} s_i^3 \\ & + \left(\Lambda_c + \Lambda_m s_i' - \frac{n_t^2(1+n_t^2)}{2} s_i^2\right) \tilde{T}_1 \cos(n\vartheta) \Bigg\}, \\ & i = 1, ..., N. \end{aligned} \tag{22b}$$

Equation (22a) expresses the rotor's acceleration as a function of the pendulums' motion. As seen in section 3.1, the quadratic terms $s_i s_i'$ are the ones responsible of the subharmonic filtration. The pendulums' equations (22b) are uncoupled from the rotor's dynamics, so that one can solve them to obtain the s_i and then inject the results in Eq. (22a) to retrieve the rotor's response. Equations (22b) contain the effect of the external torque, the damping, the coupling between pendulums (both linear and non-linear) through the sums over N, and the perturbations of the path and rotation functions. Equations (22b) are weakly coupled because pendulums are coupled indirectly through the rotor and their effect on the rotor is small as their relative inertia is small [28]. These equations are also weakly non-linear because the path and rotation functions chosen are close to an epicycloid and a linear rotation, which render a quasi-linear behaviour for small fluctuations of the rotational speed.

3.4 The subharmonic solutions

The method of multiple scales [57] is used to find the subharmonic solutions of Eqs. (22b). Two rotation scales are introduced, $\vartheta_0 = \vartheta$ and $\vartheta_1 = \epsilon\vartheta$ and pendulums coordinates are expanded such that

$$s_i(\vartheta) = s_{i1}(\vartheta_0, \vartheta_1) + \epsilon s_{i2}(\vartheta_0, \vartheta_1). \tag{23}$$

Because the solution sought is a subharmonic of order 2, it is convenient to define the detuning term σ as

$$n = 2n_p + \epsilon\sigma. \tag{24}$$

$\sigma > 0$ and $\sigma < 0$ correspond to under-tuned and over-tuned pendulums, respectively. Applying the method of multiple scales to Eq. (22b) yields first-order solutions of the form

$$s_{i1}(\vartheta_0, \vartheta_1) = a_i(\vartheta_1) \cos\left(\frac{n\vartheta_0 - \xi_i(\vartheta_1)}{2}\right), \quad i = 1, ..., N \tag{25}$$

Amplitudes a_i and phases ξ_i are governed by the system

$$\begin{cases} D_1 a_i = f_{a_i}(\boldsymbol{a}, \boldsymbol{\xi}), & i = 1, ..., N \quad (26a) \\ a_i D_1 \xi_i = f_{\xi_i}(\boldsymbol{a}, \boldsymbol{\xi}), & i = 1, ..., N, \quad (26b) \end{cases}$$

where $D_1(\bullet) = \partial(\bullet)/\partial\vartheta_1$ and $\boldsymbol{a}, \boldsymbol{\xi}$ are vectors containing the a_i and ξ_i, respectively. Functions f_{a_i} and f_{ξ_i} are given in Appendix C. The solutions sought are those at steady-state, meaning that the amplitudes and phases are invariant with ϑ such that

$$D_1 a_i = D_1 \xi_i = 0, \quad \forall i. \tag{27}$$

Phase-opposition solution

The desired solution SH1 corresponds to

$$a_i = a_j = a, \quad \xi_i = \xi, \quad \xi_j = \xi + 2\pi, \quad \forall i \in \mathcal{G}_1, \quad \forall j \in \mathcal{G}_2. \tag{28}$$

Introducing Eqs. (27) and (28) in system (26) and solving for a and ξ leads to

$$a^2 = n_p \frac{2\Lambda_m \sigma \pm \sqrt{\Lambda_m^2 \tilde{T}_1^2 - 4\tilde{b}^2}}{c_c - c_p}, \tag{29a}$$

$$\tan(\xi) = \mp \sqrt{\frac{\Lambda_m^2 \tilde{T}_1^2}{4\tilde{b}^2} - 1}. \tag{29b}$$

c_c and c_p are non-linear coefficients related to Coriolis effects and to the perturbations of the path and rotation functions, respectively. They are defined as

$$c_c = \tilde{\mu} n_t^4, \quad c_p = 3(\tilde{x}_{[4]} + 2n_p^2 \eta \alpha_{[1]} \tilde{\alpha}_{[3]}). \tag{30}$$

As expected, Eqs. (29) have exactly the same form as the results obtained in [30], where only two pendulums were considered. The fact that there are more

than two pendulums appears only through the increase of $\tilde{\mu}$, which is involved in c_c (*cf.* Eqs. (30), (21) and (1)). The backbone of SH1 is given by

$$n_1^{(SH)} = 2n_p + \epsilon \frac{c_c - c_p}{2n_p \Lambda_m} a^2, \tag{31}$$

so that in the special case $c_p = 0$, SH1 is hardening. One can choose c_p to increase (decrease, respectively) this hardening behaviour, resulting in hardened (softened) pendulums. Hence, c_p can be seen as the non-linear tuning parameter.
Introducing Eqs. (25) and (29) in Eq. (22a) leads to the rotor's response

$$\left|\theta^{(1)\,\prime\prime}\right|^2 = \bar{T}_1^2 + \mu^2 n_t^4 \frac{n^2 a^4}{4} + \bar{T}_1 \mu n_t^2 n a^2 \sin\xi. \tag{32}$$

Superscripts in brackets indicate the number of the harmonic considered so that Eq. (32) represents the amplitude of the first harmonic of the rotor's acceleration. At the order retained here, all the other rotor harmonics are null. In the case of perfect-tuning (i.e. $n_p = n/2$ and $c_p = 0$), Eq. (32) reduces to

$$\left|\theta^{(1)\,\prime\prime}\right| = \frac{2\bar{b}}{\Lambda_m}, \tag{33}$$

which highlights the saturation phenomenon as the rotor's amplitude is independent from the forcing amplitude $\bar{T}_1$.

Trivial solution

System (26) also has a trivial solution (TS) for which pendulums are immobile, i.e. $a_i = 0, \forall i$. The associated rotor's response is simply

$$\left|\theta^{(1)\,\prime\prime}\right| = \bar{T}_1, \tag{34}$$

and the conditions under which TS is unstable (*cf.* [30]) are

$$\tilde{T}_1^2 - \frac{4\tilde{b}^2}{\Lambda_m^2} - 4\sigma^2 > 0, \quad \text{or} \tag{35a}$$

$$\tilde{T}_1^2 - \frac{4\tilde{b}^2}{\Lambda_m^2} - 4\left(\sigma - n_p\tilde{\mu}\frac{\Lambda_c^2}{\Lambda_m}\right)^2 > 0. \tag{35b}$$

Conditions (35a) and (35b) are associated to period-doubling bifurcations towards modes 1 (a single mode or a combination of modes, like SH1), and mode 2, respectively [30].

Other solutions

System (26) allows many other solutions than the two discussed previously. A response on mode 2 and a coupled-mode solution involving modes 1 and 2 were studied in [30]. Solutions on a single mode 1_i and combinations of modes 1 different from SH1 are also possible. Some of them are derived in Appendix A.

3.5 Typical response of a subharmonic CPVA

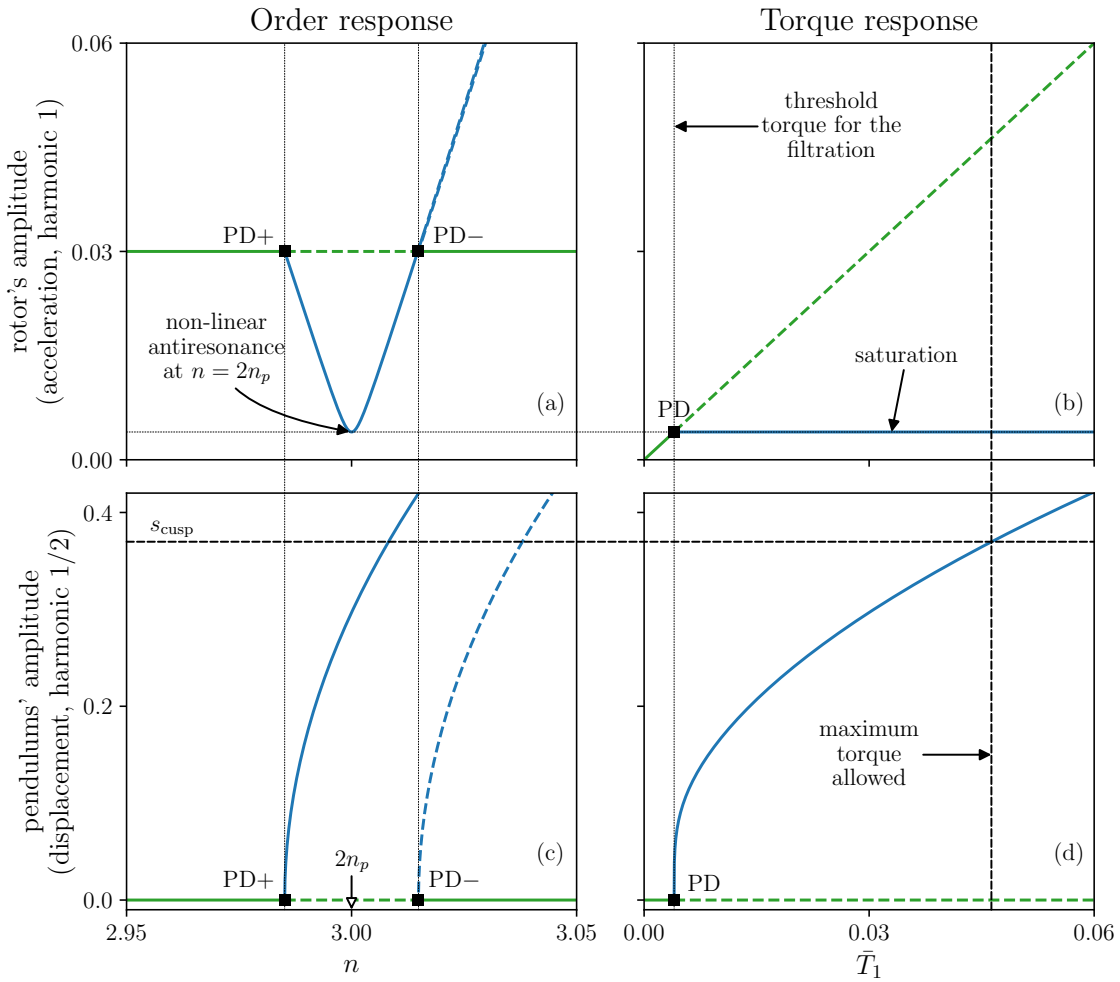

Figure 3: Typical order (left) and torque (right) responses of a CPVA. Pendulums' responses are shown in (c) and (d) while rotor's responses are shown in (a) and (b). (a) and (c) are order responses for $\bar{T}_1 = 0.03$ while (b) and (d) are torque responses for $n = 2n_p = 3$. Green curves represent the system's response for immobile pendulums while blue curves correspond to SH1. Dashed lines indicate unstable solutions. $n_p = 1.5$, $\mu = 0.1$, $\bar{b} = 0.002$, $\eta = \alpha_{[1]} = \alpha_{[3]} = x_{[4]} = 0$.

A typical response of a subharmonic CPVA is depicted in Fig. 3. Its parameters are chosen such that $c_p = 0$, which corresponds to perfect non-linear tuning. Figure 3 shows an order response[1] (left) and a torque response[2] (right) at and excitation order such that $n = 2n_p$. The fundamental harmonic of the rotor's acceleration is given in (a) and (b) and the subharmonic motion of the pendulums is given in (c) and (d). Green and blue curves represent the trivial and SH1 solutions, respectively. Dashed lines indicate unstable solutions (the stability of SH1 is evaluated in section 4). PD+ and PD- indicate supercritical and subcritical period-doubling bifurcations, respectively. Note that in (a), the unstable part of the rotor's response almost overlaps with the part of the stable response located on the right of the PD- bifurcation. This is why the unstable branch is not clearly visible in (a).
Figure 3(a) shows the non-linear antiresonance generated by the pendulums on the rotor. In Fig. 3(b), one can see that the amplitude at the antiresonance is independent from the forcing amplitude, thus leading to a saturation phenomenon. This saturation is effective starting from a threshold torque amplitude and up to a maximum torque. This upper torque limit exists because of the cusp of the pendulums' path (*cf.* Eq. (14)).

The saturation visible in Fig. 3(b) is perfect (i.e. the amplitude is rigorously constant) because the CPVA has perfect non-linear tuning. In the case $c_p \neq 0$, the antiresonance shifts as the forcing is increased, leading to imperfect saturation [30]. This is illustrated in Fig. 4 on a CPVA for which $c_p < 0$, so that SH1 is hardened, causing a shift of the antiresonance towards higher orders. The red line indicates the rotor's amplitude at a given order (here $n = 2n_p$). The increase of the amplitude with $\bar{T}_1$ on the red line shows that the rotor does not perfectly saturates.

4 Stability analysis

4.1 Jacobian of the system

The first step to evaluate the stability of SH1 is to compute the Jacobian of system

$$\begin{cases} D_1 a_i = f_{a_i}(\boldsymbol{a}, \boldsymbol{\xi}), & \text{(36a)} \\ D_1 \xi_i = f^*_{\xi_i}(\boldsymbol{a}, \boldsymbol{\xi}), & \text{(36b)} \end{cases}$$

and to evaluate this Jacobian on SH1. System (36) simply corresponds to system (26) with Eq. (26b) divided through by a_i ($f^*_{\xi_i}$ is defined as f_{ξ_i}/a_i). The Jacobian $\boldsymbol{J}$ evaluated on SH1 has the form

$$\boldsymbol{J} = \begin{bmatrix} \boldsymbol{U} & \boldsymbol{H} \\ \boldsymbol{H} & \boldsymbol{U} \end{bmatrix}, \tag{37}$$

[1] This is analogous to a frequency response.
[2] This corresponds to the response as a function of the excitation amplitude.

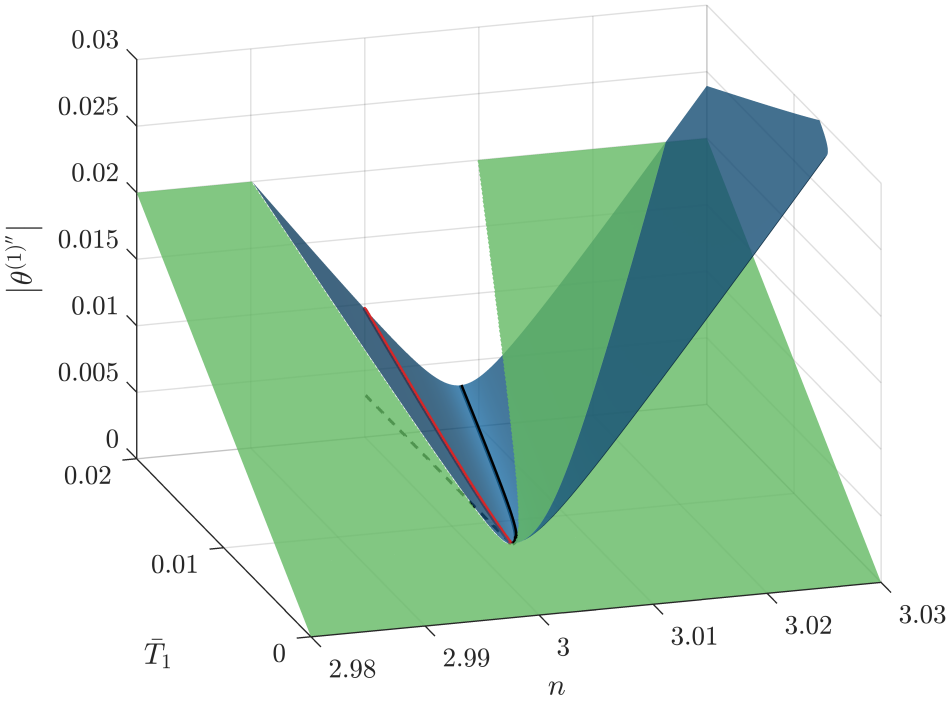

Figure 4: Response of the rotor of a hardened CPVA as a function of the torque order and amplitude. Blue and green surfaces correspond to SH1 and TS, respectively. The solid black line indicates the locus of the antiresonance which, in the present case, shifts towards higher orders as the torque increases. The dashed black and the red lines are both in the plane $n = 2n_p = 3$. The dashed line represents the saturated amplitude in the case of perfect tuning. It remains constant as the torque increases due to $c_p = 0$. The red line represents the rotor's amplitude of the present design, which increases with the torque level due to $c_p \neq 0$, which causes the antiresonance to shift. For readability reasons, the unstable solutions are not shown. The parameters are those given in Tab. 1, except for $\alpha_{[3]} = -0.1$.

where $\boldsymbol{U}$ and $\boldsymbol{H}$ are block-circulant matrices given by

$$\boldsymbol{U} = \begin{bmatrix} \boldsymbol{J_1} & \boldsymbol{J_{2_a}} & \cdots & \boldsymbol{J_{2_a}} \\ \boldsymbol{J_{2_a}} & \ddots & \ddots & \vdots \\ \vdots & \ddots & \ddots & \boldsymbol{J_{2_a}} \\ \boldsymbol{J_{2_a}} & \cdots & \boldsymbol{J_{2_a}} & \boldsymbol{J_1} \end{bmatrix}, \quad \boldsymbol{H} = \begin{bmatrix} \boldsymbol{J_{2_b}} & \boldsymbol{J_{2_b}} & \cdots & \boldsymbol{J_{2_b}} \\ \boldsymbol{J_{2_b}} & \boldsymbol{J_{2_b}} & \cdots & \boldsymbol{J_{2_b}} \\ \vdots & \vdots & \ddots & \vdots \\ \boldsymbol{J_{2_b}} & \boldsymbol{J_{2_b}} & \cdots & \boldsymbol{J_{2_b}} \end{bmatrix}, \tag{38}$$

and matrices $\boldsymbol{J_1}$, $\boldsymbol{J_{2_a}}$ and $\boldsymbol{J_{2_b}}$ are

$$\begin{aligned}
\boldsymbol{J_1} &= \begin{bmatrix} \frac{\partial f_{a_i}}{\partial a_i} & \frac{\partial f_{a_i}}{\partial \xi_i} \\ \frac{\partial f^*_{\xi_i}}{\partial a_i} & \frac{\partial f^*_{\xi_i}}{\partial \xi_i} \end{bmatrix}, \quad \boldsymbol{J_{2_a}} = \begin{bmatrix} \frac{\partial f_{a_i}}{\partial a_j} & \frac{\partial f_{a_i}}{\partial \xi_j} \\ \frac{\partial f^*_{\xi_i}}{\partial a_j} & \frac{\partial f^*_{\xi_i}}{\partial \xi_j} \end{bmatrix}, \quad i,j \in \mathcal{G}_1 \text{ or } i,j \in \mathcal{G}_2 \\
\boldsymbol{J_{2_b}} &= \begin{bmatrix} \frac{\partial f_{a_i}}{\partial a_j} & \frac{\partial f_{a_i}}{\partial \xi_j} \\ \frac{\partial f^*_{\xi_i}}{\partial a_j} & \frac{\partial f^*_{\xi_i}}{\partial \xi_j} \end{bmatrix}, \quad i \in \mathcal{G}_1,\ j \in \mathcal{G}_2 \text{ or } i \in \mathcal{G}_2,\ j \in \mathcal{G}_1.
\end{aligned} \tag{39}$$

This makes $\boldsymbol{J}$ a block-circulant matrix whose blocks are themselves block-circulant matrices. Block $\boldsymbol{U}$ is related to the effect that absorbers from the same group have on each other, while block $\boldsymbol{H}$ is related to the effect that absorbers from one group have on the other group. More specifically:

- $\boldsymbol{J_1}$ represents the effect of a perturbation of absorber i on itself,
- $\boldsymbol{J_{2_a}}$ represents the effect of a perturbation of an absorber j on absorber i, provided these two are in the same group,
- $\boldsymbol{J_{2_b}}$ represents the effect of a perturbation of an absorber j on absorber i, provided these two are in different groups.

4.2 Determinant of the Jacobian

As in [58, 59], the Schur determinant formula

$$\begin{bmatrix} \boldsymbol{U} & \boldsymbol{H} \\ \boldsymbol{H} & \boldsymbol{U} \end{bmatrix} \begin{bmatrix} \boldsymbol{I} & \boldsymbol{0} \\ -\boldsymbol{U}^{-1}\boldsymbol{H} & \boldsymbol{I} \end{bmatrix} = \begin{bmatrix} \boldsymbol{U} - \boldsymbol{H}\boldsymbol{U}^{-1}\boldsymbol{H} & \boldsymbol{H} \\ \boldsymbol{0} & \boldsymbol{U} \end{bmatrix} \tag{40}$$

can be used to express the determinant of $\boldsymbol{J}$ as

$$\det(\boldsymbol{J}) = \det(\boldsymbol{U}) \det(\boldsymbol{U} - \boldsymbol{H}\boldsymbol{U}^{-1}\boldsymbol{H}) = \det(\boldsymbol{U}) \det(\boldsymbol{G}), \tag{41}$$

where $\boldsymbol{I}$ and $\boldsymbol{0}$ are the identity and zero matrices of the appropriate size and

$$\boldsymbol{G} = \boldsymbol{U} - \boldsymbol{H}\boldsymbol{U}^{-1}\boldsymbol{H} \tag{42}$$

is the Schur complement of $\boldsymbol{U}$ in $\boldsymbol{J}$ [60]. $\det(\boldsymbol{U})$ can be easily computed using properties of block-circulant matrices [47], so the difficulty is to compute $\det(\boldsymbol{G})$, which involves $\boldsymbol{U}^{-1}$.

The procedure to invert a block-circulant matrix is explained in [61]. It involves product of block matrices, which is trivial as all the matrices involved here are comfortably partitioned [62]. The procedure to compute $\boldsymbol{U}^{-1}$ also requires to invert a sum of matrices, which was studied in [63]. Using results from those papers together with some properties about the roots of unity (see Appendix D), it is possible, after lengthy computations, to obtain matrix $\boldsymbol{U}^{-1}$. It is a

block-circulant matrix that has the same shape as $\boldsymbol{U}$. It is useful to note that $\boldsymbol{H}$ is a special block-circulant matrix as its blocks are all the same. Thus, the blocks of $\boldsymbol{H}\boldsymbol{U}^{-1}\boldsymbol{H}$ are all the same, and because $\boldsymbol{U}$ is block-circulant, $\boldsymbol{G}$ will also be block-circulant such that

$$\boldsymbol{G} = \begin{bmatrix} \boldsymbol{G_1} & \boldsymbol{G_2} & \cdots & \boldsymbol{G_2} \\ \boldsymbol{G_2} & \ddots & \ddots & \vdots \\ \vdots & \ddots & \ddots & \boldsymbol{G_2} \\ \boldsymbol{G_2} & \cdots & \boldsymbol{G_2} & \boldsymbol{G_1} \end{bmatrix}, \tag{43}$$

where $\boldsymbol{G_1}$ and $\boldsymbol{G_2}$ are 2×2 blocks. Finally, the determinant of the Jacobian can be computed using results from [47]. It is given by

$$\det(\boldsymbol{J}) = \det(\boldsymbol{U}) \det(\boldsymbol{G}) = \det(\boldsymbol{A_U}) \det(\boldsymbol{B_U})^{\frac{N}{2}-1} \det(\boldsymbol{A_G}) \det(\boldsymbol{B_G})^{\frac{N}{2}-1}, \tag{44}$$

where matrices $\boldsymbol{A_U}$, $\boldsymbol{B_U}$, $\boldsymbol{A_G}$ and $\boldsymbol{B_G}$ are defined as

$$\begin{aligned} \boldsymbol{A_U} &= \boldsymbol{J_1} + \left(\frac{N}{2} - 1\right) \boldsymbol{J_{2_a}}, \quad \boldsymbol{B_U} = \boldsymbol{J_1} - \boldsymbol{J_{2_a}}, \\ \boldsymbol{A_G} &= \boldsymbol{G_1} + \left(\frac{N}{2} - 1\right) \boldsymbol{G_2}, \quad \boldsymbol{B_G} = \boldsymbol{G_1} - \boldsymbol{G_2}. \end{aligned} \tag{45}$$

Since those four matrices are 2×2, the computation of $\det(\boldsymbol{J})$ becomes trivial. Moreover, matrices $\boldsymbol{B_U}$ and $\boldsymbol{B_G}$ are the same, so that $\boldsymbol{B} = \boldsymbol{B_U} = \boldsymbol{B_G}$ will be used in the following, and one can write

$$\det(\boldsymbol{J}) = \det(\boldsymbol{A_U}) \det(\boldsymbol{A_G}) \det(\boldsymbol{B})^{N-2}. \tag{46}$$

4.3 Instability zones

SH1 is unstable when at least one eigenvalue λ_i of $\boldsymbol{J}$ has a positive real part. Changes in $\text{sign}(\Re[\lambda_i])$ occur either when $\det(\boldsymbol{J})$ changes sign (that is, $\det(\boldsymbol{A_U})$ or $\det(\boldsymbol{A_G})$ changes sign) or when $\det(\boldsymbol{J})$ passes singularly through zero without becoming negative (that is, $\det(\boldsymbol{B})$ changes sign or $\det(\boldsymbol{A_U})$ and $\det(\boldsymbol{A_G})$ change sign simultaneously). $\det(\boldsymbol{J}) < 0$ always indicate unstable solutions as it means that the number of eigenvalues with negative real part is not even (hence it is not $2N$). It is however not possible to conclude on the stability state when $\det(\boldsymbol{J}) > 0$. Indeed, these situations could correspond to any even number of eigenvalues with a positive real part (including 0). Finally, instabilities arising from Neimark-Sacker bifurcations do not correspond to $\det(\boldsymbol{J}) = 0$, so they cannot be captured through the analysis led in this paper. This being said, numerical resolutions of Eqs. (4a) and (4b) never revealed quasi-periodic solutions.

The determinants of matrices $\boldsymbol{A_U}$, $\boldsymbol{A_G}$ and $\boldsymbol{B}$ are given in Appendix E. One can solve $\det(\boldsymbol{A_U}) = 0$, $\det(\boldsymbol{A_G}) = 0$ and $\det(\boldsymbol{G}) = 0$ for a to find the limits of the instability regions. This yields bifurcation curves, that is to say curves defining the bifurcation points for any forcing amplitude [16]. Each crossing between one of those curves and SH1 leads to a change of stability. Excluding the curves equal to zero, the bifurcation curves are

$$a_{pf_1}^2 = \frac{\Lambda_c^2 \tilde{\mu} n_p^2 - 2\Lambda_m n_p \sigma}{c_p + \frac{c_t}{2}}, \tag{47a}$$

$$a_{pf_2}^2 = \frac{\Lambda_c^2 \tilde{\mu} n_p^2}{c_p + \frac{3c_t}{2}}, \tag{47b}$$

$$a_{sn}^2 = \frac{2\Lambda_m n_p \sigma}{c_c - c_p}, \tag{47c}$$

$$a_{pf_3}^2 = -\frac{2\Lambda_m \sigma n_p}{c_p}, \tag{47d}$$

$$a_{pf_4}^2 = \frac{\Lambda_c^2 \tilde{\mu} n_p^2 - 4\Lambda_m n_p \sigma}{-c_c + 2c_p + \frac{c_t}{2}}, \tag{47e}$$

$$a_{pf_5}^2 = \frac{\Lambda_c^2 \tilde{\mu} n_p^2}{-c_c + 2c_p + \frac{3c_t}{2}}. \tag{47f}$$

c_t is a non-linear coefficient related to large pendulums displacements along their paths and is defined as

$$c_t = \frac{\Lambda_c}{2} \tilde{\mu} n_p^2 n_t^2 (1 + n_t^2). \tag{48}$$

Indices "pf" and "sn" stand for "pitchfork" and "saddle-node" bifurcations, respectively. a_{pf_1}, a_{pf_2} and a_{sn} are associated to $\det(\boldsymbol{A_G}) = 0$ and are exactly the same bifurcation curves as those obtained for a CPVA with two pendulums [30]. In this former work, a_{pf_1} and a_{pf_2} defined pitchfork bifurcations leading to a coupled-mode solution in which modes 1 (not degenerated) and 2 responded simultaneously. By extension, in the presence of N pendulums, those bifurcations lead to a coupled-mode solution involving SH1 and mode 2. a_{sn} defines saddle-node bifurcations leading to a jump of the response. As noticed in [30], this bifurcation curve is equal to the backbone curve of SH1. a_{pf_3}, a_{pf_4} and a_{pf_5} arise when the CPVA is made of several pairs of pendulums. They define pitchfork bifurcations leading to combinations of modes 1 different from SH1. a_{pf3} corresponds to $\det(\boldsymbol{B}) = 0$ while a_{pf4} and a_{pf5} are associated to $\det(\boldsymbol{A_U}) = 0$ and $\det(\boldsymbol{A_G}) \to \pm\infty$.

All the bifurcation curves are shown in Fig. 5 together with the pendulums' response. SH1 and TS are shown in blue and green, respectively. Pitchfork bifurcations are indicated by a blue star with code name "PF". Note that the part of the response above s_{cusp} can help understanding the solution but is

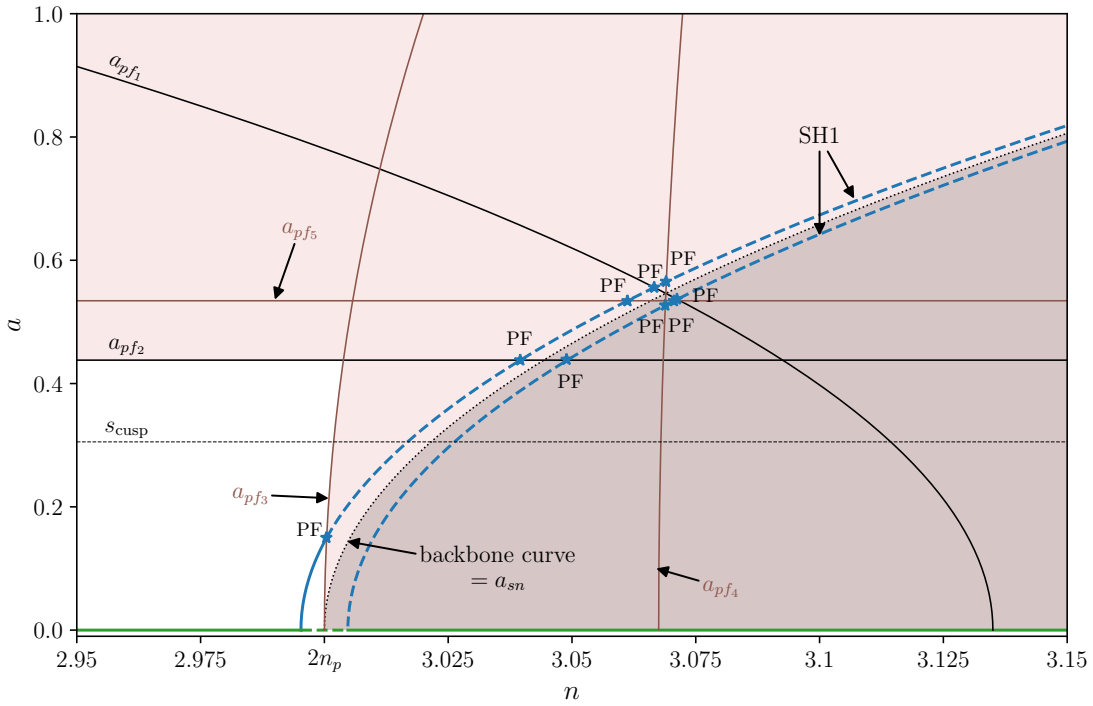

Figure 5: Order response of the pendulums and their stability. SH1 and TS are represented in blue and green, respectively. The bifurcation curves are represented in black and brown. Dashed lines indicate an unstable response. Blue stars with code name "PF" indicate a pitchfork bifurcation. Light and dark red areas correspond to instabilities due to pitchfork bifurcations only and to pitchfork and saddle-node bifurcations, respectively. $\bar{T}_1 = 0.01$, $n_p = 1.5$, $\eta = 1$, $\mu = 0.1$, $x_{[4]} = -0.25$, $\alpha_{[1]} = 0.5$, $\alpha_{[3]} = 0.1$, $\bar{b} = 0.002$.

not physically relevant as it exists only because of the approximation of the path function $z(s_i)$ [30]. The red areas correspond to unstable regions. Figure 5 shows that the bifurcation curve a_{pf_3} is the most dangerous one as it is very close to the operating point $n \approx 2n_p$.

5 Case study and design guidelines

The aim of this section is to compare the analytical results with numerical ones in order to validate the model and to provide design guidelines. Two different numerical resolutions are used in this paper:

- Equations (4a) and (4b) are integrated numerically using a Runge-Kutta algorithm until the steady state is reached. Then, the signals' amplitudes are obtained through a decomposition into Fourier series.
- Equations (4a) and (4b) are solved with MANLAB, which is a path-following and bifurcation analysis software [64, 65].

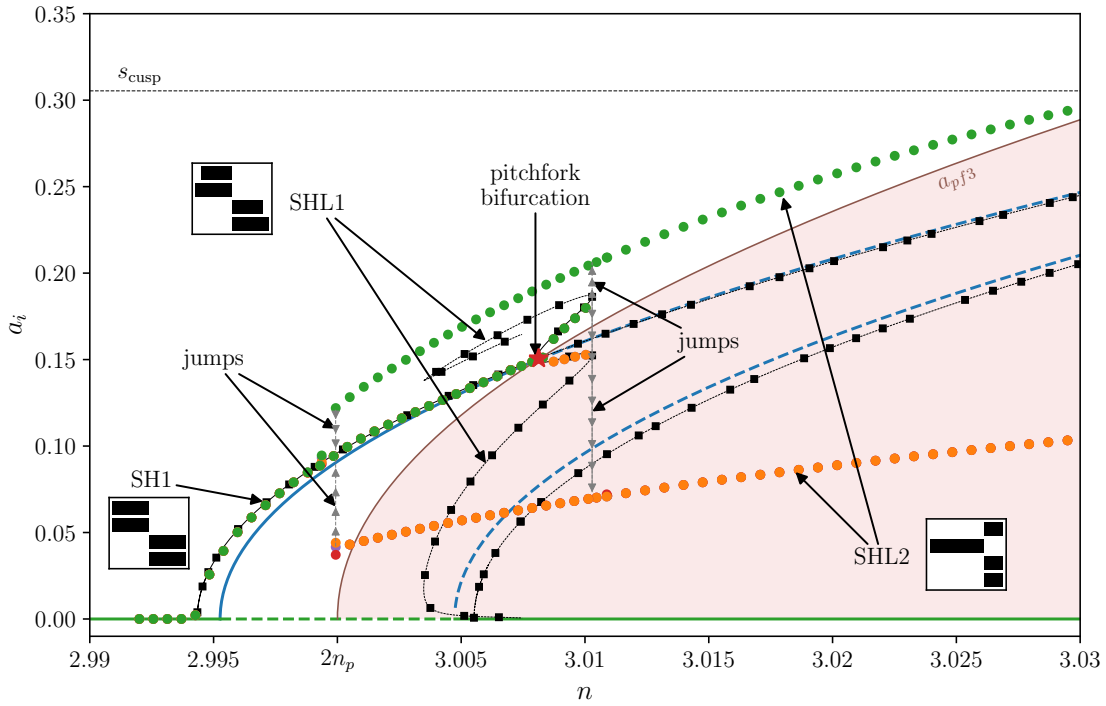

Figure 6: Order response of the pendulums. SH1 and TS are represented in blue and green, respectively. The bifurcation curve a_{pf_3} is represented in brown. Dashed lines indicate an unstable response and the red area corresponds to the instability zone delimited by a_{pf_3}. The solutions and the pitchfork bifurcation determined by MANLAB are represented by thin dark lines with square markers and by the red star, respectively. The coloured circles represent the pendulums' amplitudes obtained through time integration. SHL1 and SHL2 are localised solutions. The bar plots indicate the amplitude of the four pendulums at a given time and order on SH1, SHL1 and SHL2. $\bar{T}_1 = 0.01$ and other parameters are given in Tab. 1.

N	n_p	η	μ	$x_{[4]}$	$\alpha_{[1]}$	$\alpha_{[3]}$	b	b_r
4	1.5	1	0.1	0	0.5	-0.2	0.002	0.002

Table 1: Parameters of the CPVA studied in this section.

5.1 Order response for a CPVA made of 4 pendulums

Figure 6 shows the response of a CPVA made of $N = 4$ pendulums near the operating point, i.e. for $n \approx 2n_p$. Analytical results for SH1 and TS are shown in blue and green, respectively. The MANLAB results are shown as thin dark lines with square markers while time integration results are the coloured circles. The red star represents the pitchfork bifurcation determined using MANLAB. The area coloured in red corresponds to the instability zone delimited by a_{pf_3}.

The analytical model predicts well SH1 as the results obtained through MANLAB and time integration (when SH1 is stable) are close to the analytical ones. The bifurcation point is very accurately predicted by the model as

the intersection of a_{pf_3} and SH1 is superimposed with the red star, located at $n \approx 3.008$. This bifurcation point also fits very well with time integration results as the pendulums' amplitudes start to differ at $n \approx 3.008$. A reason for this accurate prediction could be that the analytical model is based on a perturbation method around $n = 2n_p$, which is very close to the order at the bifurcation. Another reason is that the parameters of the CPVA match well with the assumption of small parameters (*cf.* Eq. (21)).
After the pitchfork bifurcation, the pendulums respond on a 1st localised solution (SHL1[1]), where two pendulums oscillate at the same amplitude while the other two oscillate at a slightly lower one. Increasing further n, the system reaches a saddle-node bifurcation of SHL1, causing a jump (around $n = 3.01$) leading to a 2nd localised solution (SHL2). On this new solution, three pendulums oscillate at the same small amplitude while the fourth pendulum oscillates with an amplitude quite larger than SH1. Hence, this solution is highly undesired as it significantly reduces the torque range. If one performs a decreasing sweep starting from $n > 3.01$, the pendulums start responding on SHL2. Then, at $n \approx 3$, they jump on SH1. Finally, for $n < 2.994$, the pendulums stop oscillating as they reach the trivial solution.

In order to show that the analytical results remain valid for large numbers of pendulums, another comparison with numerical results is given in Appendix F for a CPVA made of 8 absorbers. Moreover, the case of a softened CPVA is presented in Appendix G. In addition, for readability reasons, only four different subharmonic solutions are shown in Fig. 6. More solutions are represented in Appendix H.

Figure 7 depicts the rotor's response associated to the pendulums' response shown in Fig. 6. The overall response is well predicted by the analytical model, though the amplitude is underestimated everywhere but at the antiresonance. The locus of the bifurcation point is very well predicted by the model. Figure 7 shows that the localised solutions decrease the efficiency of the filtration of $\theta^{(1)}$ around the operating point (i.e. near $n = 2n_p$), but they increase it at larger orders. Indeed, the response on SHL2 generates an antiresonance around $n = 3.02$. However, it also generates lower and higher harmonics, which are undesired. It is interesting to note that the bifurcation point seems to be on the antiresonance. To investigate this further, one can look for the order of the bifurcation point by equating the bifurcation curve a_{pf3} (*cf.* Eq. (47)) and the pendulums' amplitude on SH1 (*cf.* Eq. (29)) and solving for σ. This leads to

$$\sigma_{pf3} = -\chi \frac{c_p}{c_c} \sqrt{\frac{\tilde{T}_1^2}{4} - \frac{\tilde{b}^2}{\Lambda_m^2}}, \tag{49}$$

where $\chi = \pm 1$. Moreover, a_{pf3} bends to the right if $c_p < 0$ and to the left if $c_p > 0$, which implies $\chi = +1$. Hence, $\sigma_{pf3} = \sigma_{AR}$, where σ_{AR} is the position

[1] "SH" stands for "subharmonic", "L" for "localised" and "1" indicates that this is the first localised solution encountered for an increasing sweep.

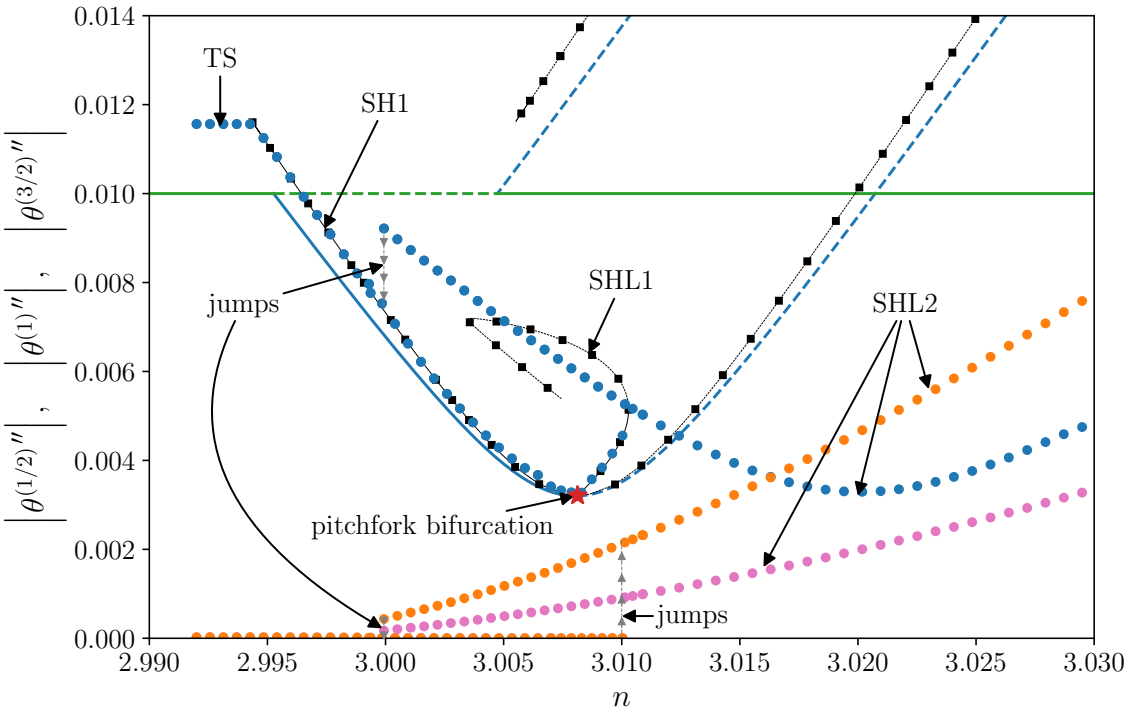

Figure 7: Order response of the rotor. SH1 and TS are represented in blue and green, respectively, and dashed lines indicate an unstable response. The solutions and the pitchfork bifurcation determined by MANLAB are represented by thin dark lines with square markers and by the red star, respectively. The pink, blue and orange circles represent the rotor's amplitude obtained through time integration for harmonics 1/2, 1 and 3/2, respectively. $\bar{T}_1 = 0.01$ and other parameters are given in Tab. 1.

of the antiresonance, derived in [30]. This means that the bifurcation point will always be located on the antiresonance.

Figs. 6 and 7 highlight the complexity of the response. Close from the operating point, SH1 is unstable and several localised solutions exist, some of them being simultaneously stable (more details on those localised solutions are given in Appendix H). Guidelines are given in the next section in order to avoid instabilities of SH1.

5.2 Avoidance of localisation

As explained in section 4.3 and observed in section 5.1, the bifurcation curve a_{pf_3} should be analysed carefully as it is very close to the operating point. As remarked previously, a_{pf_3} bends to the right (left, respectively) if $c_p < 0$ ($c_p > 0$, respectively), and the instability zone delimited by a_{pf_3} is located between this curve and $a = 0$. Hence, if a_{pf_3} bends to the left, it is the part of SH1 located to the left of a_{pf_3} that will be unstable (this situation is the opposite to that depicted in Fig. 6 and is represented in Fig. G4). Thus, to

avoid localisation, one should always have

$$2n_p > n \quad \text{and} \quad c_p < 0 \qquad \text{or} \qquad 2n_p < n \quad \text{and} \quad c_p > 0. \tag{50}$$

In other words, hardened pendulums should be over-tuned while softened pendulums should be under-tuned. The first configuration (with hardened over-tuned pendulums) should be favoured as it increases the torque range [30]. Note that if $n = 2n_p$, a_{pf_3} is undefined, but this situation is hazardous as SH1 might be unstable and it never occurs in practice due to manufacturing tolerances.

Though a_{pf_3} is the bifurcation curve to be treated with the most care, it is important to ensure that the other bifurcations are also avoided. Guidelines were given in [30] regarding the avoidance of intersections between SH1 and a_{pf_1} and a_{pf_2}, so that in the following we will focus only on a_{pf_4} and a_{pf_5}.
To find a condition allowing to avoid intersections between a_{pf_4} and SH1, we remind that in practice the excitation order n is fixed (equivalently, σ is fixed, *cf.* Eq. (24)). In addition, a_{pf_4} can be rearranged as

$$\sigma_{pf_4} = \tilde{\mu}\frac{\Lambda_c^2 n_p}{4\Lambda_m} - \frac{1}{4\Lambda_m n_p}\left(-c_c + 2c_p + \frac{c_t}{2}\right)a^2. \tag{51}$$

To avoid localisation, one should have $\sigma < \sigma_{pf_4}$ up to the cusp. This requirement is satisfied when

$$n_p > n\left(2 + \mu\frac{\Lambda_c^2}{4\Lambda_m}\right)^{-1} \quad \text{and} \tag{52a}$$

$$c_p < \left(\Lambda_c - \frac{1}{4}\right)c_t + \frac{c_c}{2} - 2\Lambda_m n_p n_t^2(1 + n_t^2)\sigma. \tag{52b}$$

As a_{pf_5} is constant, intersections between this curve and SH1 are avoided up to the cusp by choosing the CPVA's parameters such that a_{pf_5} does not exist or is located above s_{cusp}. Those two requirements are satisfied if

$$c_p < \frac{c_c}{2} + \left(\Lambda_c - \frac{3}{4}\right)c_t. \tag{53}$$

Satisfying Eqs. (50), (52) and (53) allows to avoid the localisation due to the presence of several pairs of pendulums. Hence, fulfilling those conditions maximises the torque capacity of the CPVA.

5.3 Representation of the stability in the design space

Figure 8 represents the stability of SH1 at a given excitation order and as a function of the linear and non-linear tunings, n_p and $\bar{c}_p$, where the later is

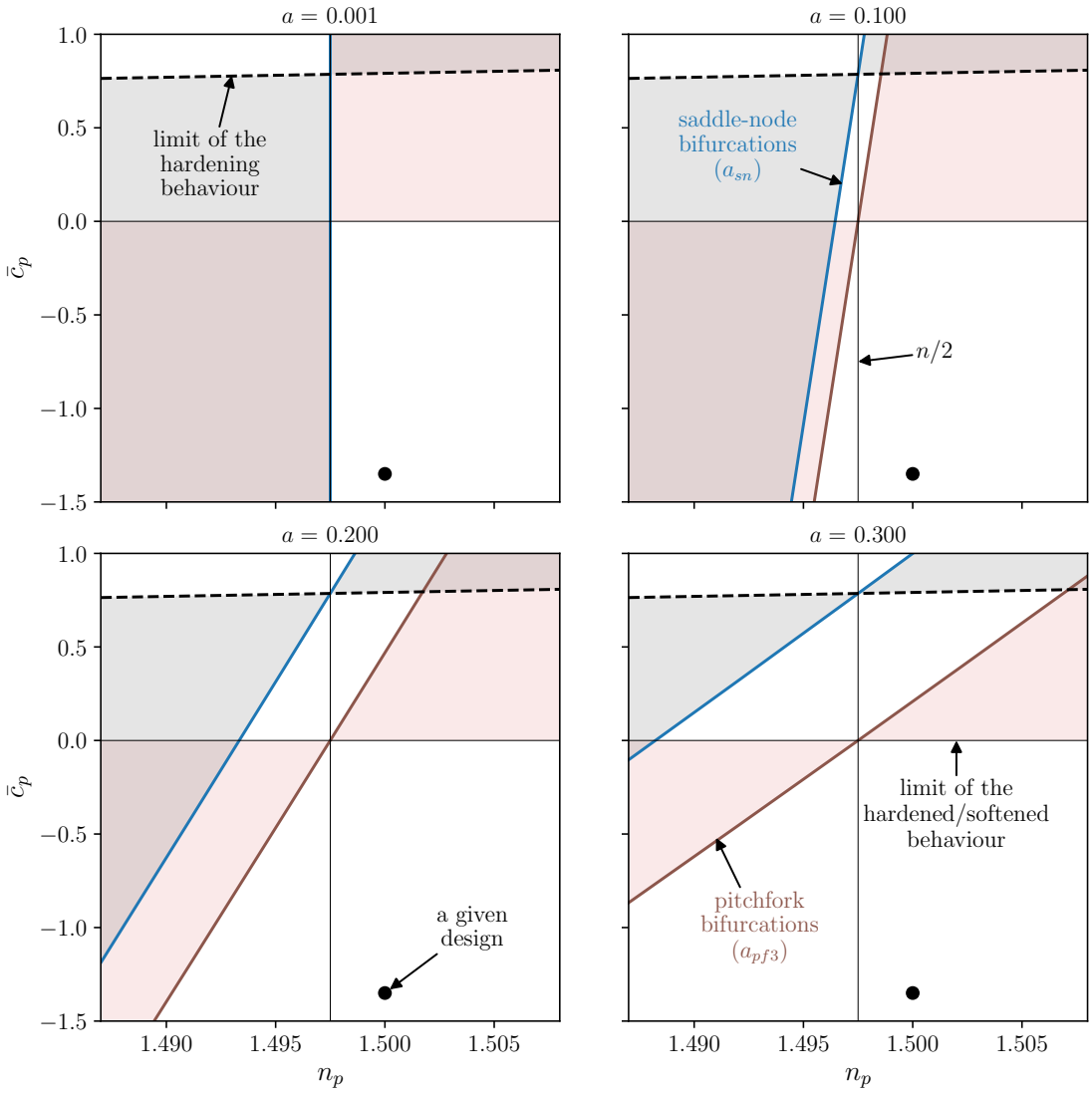

Figure 8: Representation of the stability in the design space for $n = 2.995$ and four different pendulums' amplitudes. The blue and brown curves are the bifurcation curves a_{sn} and a_{pf3}, respectively. Grey and red areas correspond to instabilities leading to a jump of SH1 and to a localised response, respectively. The dark red area includes those two type of instabilities. The black dot corresponds to the design represented in Fig. 6. The map with the smallest amplitude gives information on the stability of SH1 just after its appearance. The one with the largest amplitude gives information on the stability near the cusp. The parameters that are not varied in this figure are given in Tab. 1.

simply the unscaled version of c_p, i.e.

$$\bar{c}_p = 3(x_{[4]} + 2n_p^2 \eta \alpha_{[1]} \alpha_{[3]}). \tag{54}$$

Figure 8 contains four maps, all corresponding to a different pendulums' amplitude. The black dot corresponds to the design presented in Fig. 6. The

unstable zones represented in grey and red correspond to instabilities leading to a jump of SH1 and to a localised response, respectively. These zones are moving with the amplitude as a given design can be stable at a given amplitude but unstable at another one. Figure 8 illustrates the design rule (50). Indeed, over-tuned hardened and under-tuned softened CPVAs are not subject to localisation. Under-tuned softened CPVAs are subject to jumps of the response, but this is not an issue if the jump is small. However, large jumps should absolutely be avoided [30]. Regardless of this jump issue, over-tuned hardened CPVAs should be preferred as they have a larger torque range than under-tuned softened ones [30].

5.4 Basin of attraction of SH1

Several solutions emerge from TS at the period-doubling bifurcation points. An illustration of three of those solutions is given in Appendix H. It must be reminded that modes 1 are in 1:1:...:1 internal resonance (*cf.* section 2.2). Hence, any combination of modes 1 branches from the period-doubling bifurcation, and as there is an infinity of possible combinations of modes 1 (*cf.* Appendix A), there is an infinity of solutions emerging from the bifurcation. For this reason, it is crucial to ensure that the basin of attraction of SH1 is large enough so that bifurcations from TS lead to this particular combination of modes 1 rather than another one. The basin of attraction of SH1 is very difficult to assess as it depends on the initial positions and velocities of N pendulums and the rotor (the smallest number of pendulums for which there are several pairs is $N = 4$, which already implies 10 independent parameters in the initial conditions). Hence, an alternative method is proposed below to verify that TS bifurcates towards SH1.

Figure 9 represents the torque response of over-tuned hardened pendulums, for which SH1 is stable (*cf.* sections 5.2 and 5.3). Time integrations are performed for different torque amplitudes and the initial conditions used (black squares) correspond to the trivial solution. It is important to have in mind that in practice, bifurcations to SH1 take some time (*cf.* Fig. 10), so the CPVA will always go through TS before going to SH1. The coloured circles correspond to the time integration results after the steady-state is established. The full time-signals are given in Fig. 10. During the transient, the pendulums can reach a large amplitude, which is why no integrations were performed for $\bar{T}_1 > 0.04$ (in those cases, one of the pendulums reached its cusp during the transient). Figure 9 shows that for all the initial conditions tested, TS bifurcates to SH1, which implies that the basin of attraction of SH1 is larger than that of other solutions for the case considered here. The same results were observed for every over-tuned hardened CPVA investigated, from what we can reasonably assume that TS bifurcates to SH1 for such CPVAs. Time integrations with initial conditions slightly different from TS are proposed in Appendix I. Like for the TS initial conditions, the steady state solution obtained is SH1, which shows that

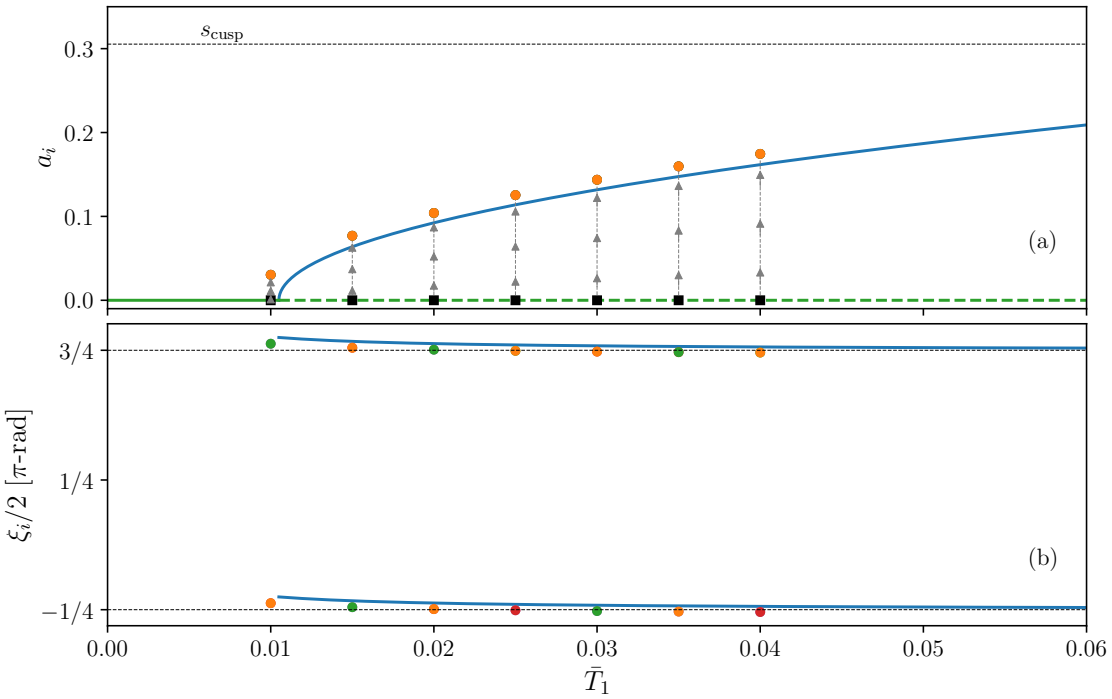

Figure 9: Torque response response of over-tuned hardened pendulums. The amplitude and phase are represented in (a) and (b), respectively. SH1 and TS are represented in blue and green, respectively. Dashed lines indicate an unstable response. The coloured circles represent the pendulums' amplitudes obtained through time integration. The black squares are the initial conditions for the time integrations. $n = 2.995$ and other parameters are given in Tab. 1.

the bifurcation from TS to SH1 is relatively robust to small perturbations of the trivial solution.

Looking in details at the time signals shown in Fig. 10, it is interesting to note that the smaller the torque amplitude, the longer it takes to reach the steady state.

6 Conclusion

This paper deals with the subharmonic response of CPVAs and its stability. Several pairs of pendulums are considered that admit a rotational motion relative to the rotor in addition to the traditional translational motion. First, a linear analysis showed that the system contains highly degenerated modes. Next, it was shown that the ideal subharmonic solution is associated with a specific motion of the system such that half of the pendulums move in unison and in phase opposition with the other half. Then, this subharmonic solution was computed using an analytical perturbation technique. Afterwards, a new method was used to assess the stability of this solution. It has the advantage of being valid for CPVAs made of any even number of pendulums. Moreover, it allowed to derive analytical expressions of the limit of instability zones. This led to new, accurate, design guidelines so that the system's parameters can

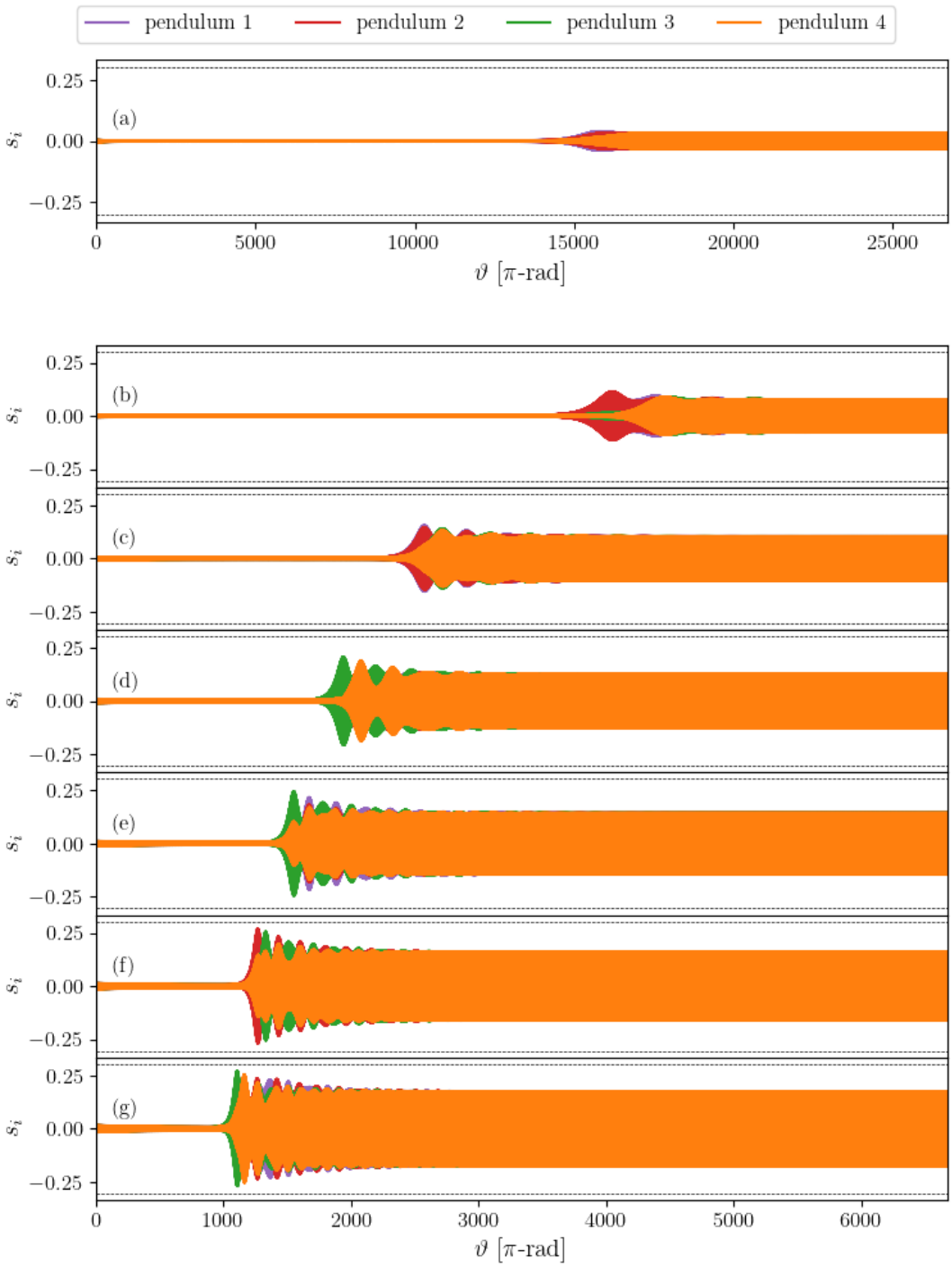

Figure 10: Temporal signals of the pendulums associated to the amplitudes and phases shown in Fig. 9. The torque amplitude for which the response is computed is increased as one goes from (a) to (g). The cusp is indicated by the horizontal black dashed lines.

be set to prevent the appearance of instabilities. Afterwards, the analytical developments were applied to case studies and compared to numerical resolutions of the system's dynamics. This validated the analytical model and highlighted the complexity of the problem. A representation of the stability in

the tuning parameters' space allowed to visualise the efficiency of the design guidelines proposed. Finally, it was verified that CPVA designs fulfilling the new guidelines do bifurcate to the desired subharmonic solution.

Statements and declarations

Funding. The authors declare that no funds, grants, or other support were received during the preparation of this manuscript.

Competing interests. The authors have no relevant financial or non-financial interests to disclose.

Author Contributions. All authors contributed to the study conception and design. Material preparation, data collection and analysis were performed by V. Mahé. The first draft of the manuscript was written by V. Mahé and all authors commented on previous versions of the manuscript. All authors read and approved the final manuscript.

Appendix A Details on the computation of the degenerated modes

A.1 Choice of the mode shapes

The eigenvalue problem to solve to find the modes of the system is

$$\left[-n^2\boldsymbol{M}+\boldsymbol{K}\right]\boldsymbol{\phi}=\boldsymbol{0}. \tag{A1}$$

The $N+1$ solutions $(n_{i0}, \boldsymbol{\phi_{i0}})$ are the linear modes. The computation of those modes leads to the eigenvalues and mode shapes given in Eq. (8). However, when searching for the $N-1$ mode shapes associated to eigenvalue $n_{10}=n_p$, one finds that they must only satisfy

$$\boldsymbol{\phi_{10_i}}[1]=0, \quad \sum_{i=1}^{N+1}\boldsymbol{\phi_{10_i}}[i]=0. \tag{A2}$$

These mode shapes must also be chosen such that modes 0, 1 and 2 span the whole space. Hence, instead of the simple form used in Eq. (8), the degenerated

mode shapes can for instance be written as

$$\boldsymbol{\phi_{10_1}} = \begin{bmatrix} 0 \\ 1 \\ -(1+p_1+p_2) \\ p_1 \\ p_2 \\ 0 \\ \vdots \\ 0 \end{bmatrix}, \quad \boldsymbol{\phi_{10_2}} = \begin{bmatrix} 0 \\ 0 \\ 1 \\ -(1+p_1+p_2) \\ p_1 \\ p_2 \\ 0 \\ \vdots \\ 0 \end{bmatrix}, \cdots$$

$$\boldsymbol{\phi_{10_{N-1}}} = \begin{bmatrix} 0 \\ p_2 \\ p_1 \\ 0 \\ \vdots \\ 0 \\ 1 \\ -(1+p_1+p_2) \end{bmatrix}, \quad p_1, p_2 \in \mathbb{R}. \tag{A3}$$

As $p_1, p_2 \in \mathbb{R}$, there is an infinite way of expressing the degenerated modes. The special case $p_1 = p_2 = 0$ corresponds to the mode shapes given in Eq. (8).

A.2 Response of a given degenerated mode

First of all, as the pendulums' equation can be uncoupled from the rotor's dynamics (*cf.* section 3.3), it is convenient to introduce the reduced mode shapes $\boldsymbol{\psi_{10_i}}$. They simply correspond to the mode shapes $\boldsymbol{\phi_{10_i}}$ in which the rotor's component is omitted (hence, they have size N). For a CPVA made of 4 pendulums, the reduced mode shapes of the degenerated modes are

$$\boldsymbol{\psi_{10_1}} = \begin{bmatrix} 1 \\ -(1+p_1+p_2) \\ p_1 \\ p_2 \end{bmatrix}, \quad \boldsymbol{\psi_{10_2}} = \begin{bmatrix} p_2 \\ 1 \\ -(1+p_1+p_2) \\ p_1 \end{bmatrix},$$

$$\boldsymbol{\psi_{10_3}} = \begin{bmatrix} p_2 \\ p_1 \\ 1 \\ -(1+p_1+p_2) \end{bmatrix}. \tag{A4}$$

Assume the pendulums respond on mode $\boldsymbol{\psi_{10_1}}$, whose amplitude and phase are u and $\beta/2$. Hence, the pendulums' amplitudes and phases are

$$\boldsymbol{a} = u \begin{bmatrix} 1 \\ |1+p_1+p_2| \\ |p_1| \\ |p_2| \end{bmatrix}, \quad \boldsymbol{\xi} = \begin{bmatrix} \beta \\ \begin{cases} \beta \text{ if } -(1+p_1+p_2) > 0 \\ \beta + 2\pi \text{ if } -(1+p_1+p_2) < 0 \end{cases} \\ \begin{cases} \beta \text{ if } p_1 > 0 \\ \beta + 2\pi \text{ if } p_1 < 0 \end{cases} \\ \begin{cases} \beta \text{ if } p_2 > 0 \\ \beta + 2\pi \text{ if } p_2 < 0 \end{cases} \end{bmatrix}. \tag{A5}$$

This can be inserted in Eqs. (C10a) and (C10b), resulting in 8 equations. These equations can be solved for u and β using the same procedure as in section 3.4. This yields four solutions for u but only one for β (see below). Two (three) solutions are the same if two (three) components of $\boldsymbol{\psi_{10_1}}$ are equal, and the i$^{\text{th}}$ solution should be ignored if the i$^{\text{th}}$ component of $\boldsymbol{\psi_{10_1}}$ is null. The i$^{\text{th}}$ pendulum's amplitude is simply obtained by multiplying the i$^{\text{th}}$ solution on u by the absolute value of the i^{th} component of $\boldsymbol{\psi_{10_1}}$. After introducing the notations

$$q_c = 1 + p_1 + p_2 + p_1p_2 + p_1^2 + p_2^2, \quad q_t = (1+p_1)(1+p_2)(p_1+p_2), \tag{A6}$$

the four solutions on u can be written as

$$u_1^2 = n_p \frac{2\Lambda_m\sigma \pm \sqrt{\tilde{T}_1^2\Lambda_m^2 - 4\tilde{b}^2}}{\frac{2}{N}c_cq_c - c_p + \frac{3}{2N}c_tq_t}, \tag{A7a}$$

$$u_2^2 = n_p \frac{2\Lambda_m\sigma \pm \sqrt{\tilde{T}_1^2\Lambda_m^2 - 4\tilde{b}^2}}{\frac{2}{N}c_cq_c - c_p(1+p_1+p_2)^2 - \frac{3}{2N}c_t\frac{q_t}{(1+p_1+p_2)}}, \tag{A7b}$$

$$u_3^2 = n_p \frac{2\Lambda_m\sigma \pm \sqrt{\tilde{T}_1^2\Lambda_m^2 - 4\tilde{b}^2}}{\frac{2}{N}c_cq_c - c_pp_1^2 + \frac{3}{2N}c_t\frac{q_t}{p_1}}, \tag{A7c}$$

$$u_4^2 = n_p \frac{2\Lambda_m\sigma \pm \sqrt{\tilde{T}_1^2\Lambda_m^2 - 4\tilde{b}^2}}{\frac{2}{N}c_cq_c - c_pp_2^2 + \frac{3}{2N}c_t\frac{q_t}{p_2}}. \tag{A7d}$$

There is only one solution for the phase, given by

$$\tan(\beta) = \mp\sqrt{\frac{\tilde{T}_1^2\Lambda_m^2}{4\tilde{b}^2} - 1}. \tag{A8}$$

Note that this is the same phase as SH1 (*cf.* Eq. (29b)). Thus, it seems that every combination of the degenerated modes responds with the same phase

(this is verified in Fig. H5(b) for three combinations). The free solutions can be deduced from the forced ones by setting $\tilde{b} = \tilde{T}_1 = 0$, leading to

$$u_1^2 = n_p \frac{2\Lambda_m \sigma}{\frac{2}{N} c_c q_c - c_p + \frac{3}{2N} c_t q_t}, \tag{A9a}$$

$$u_2^2 = n_p \frac{2\Lambda_m \sigma}{\frac{2}{N} c_c q_c - c_p (1 + p_1 + p_2)^2 - \frac{3}{2N} c_t \frac{q_t}{(1+p_1+p_2)}}, \tag{A9b}$$

$$u_3^2 = n_p \frac{2\Lambda_m \sigma}{\frac{2}{N} c_c q_c - c_p p_1^2 + \frac{3}{2N} c_t \frac{q_t}{p_1}}, \tag{A9c}$$

$$u_4^2 = n_p \frac{2\Lambda_m \sigma}{\frac{2}{N} c_c q_c - c_p p_2^2 + \frac{3}{2N} c_t \frac{q_t}{p_2}}. \tag{A9d}$$

Appendix B Shaking forces generated by the pendulums on the rotor

In section 3.1, we chose to split the pendulums in two groups $\mathcal{G}_1$ and $\mathcal{G}_2$, each one of size $N/2$, such that $\mathcal{G}_1 = \{1, 2, ..., N/2\}$ and $\mathcal{G}_2 = \{N/2 + 1, N/2 + 2, ..., N\}$. Then, we assumed that the pendulums all oscillate with the same amplitude and that those in $\mathcal{G}_1$ are in phase-opposition with those in $\mathcal{G}_2$ to obtain the optimal subharmonic solution SH1. However, we could have chosen to distribute the pendulums differently in these two groups to obtain other optimal solutions, as discussed in section 3.2 for instance. The choice for the definition of groups $\mathcal{G}_1$ and $\mathcal{G}_2$ does not affect the results derived in this paper, but it influences the resulting force generated by the pendulums on the rotor. This would have an importance if one were to consider a translational mobility of the rotor, as in [49–56]. This is illustrated in Fig. B1 for a CPVA made of $N = 6$ pendulums.

This figure represents the Coriolis forces generated by the pendulums on the rotor, which are responsible for the subharmonic filtering [30], and the resulting Coriolis force acting on the rotor. For the configuration on the left, the resulting force on the rotor is null. However, for the other two configurations, the resulting force exerted on the rotor is different from zero. This means that the Coriolis effect generates a shaking force which can lead to translational rotor vibrations. One could imagine introducing intentional mistuning among the absorbers to enforce a particular configuration (the one on the left for instance, for which there is no shaking force), but this investigation is out of the scope of this paper.

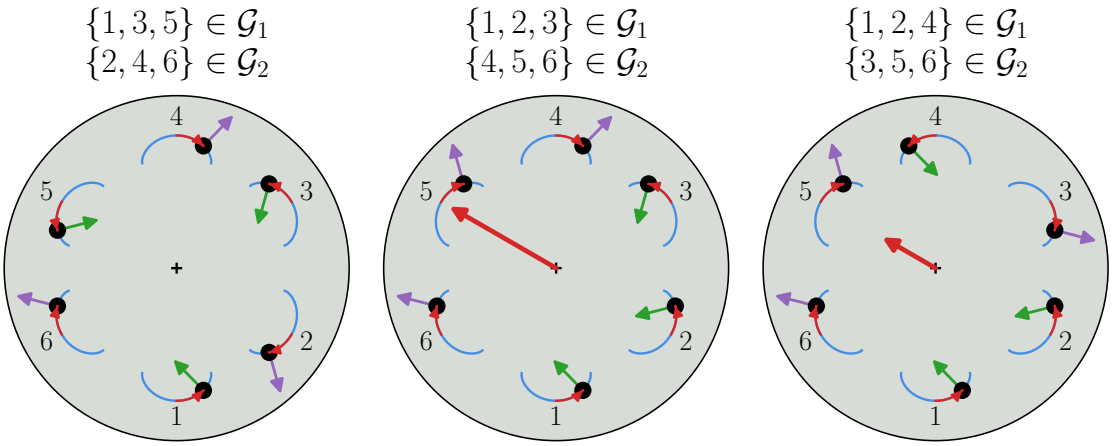

Figure B1: Three different subharmonic solution optimal for torsional vibration reduction but generating different shaking forces. The Coriolis forces generated on the rotor by the pendulums in $\mathcal{G}_1$ and $\mathcal{G}_2$ are shown in green and purple, respectively. The resulting force on the rotor in shown in red.

Appendix C System obtained through the method of multiple scales

The system of equations obtained through the application of the method of multiple scales is given by Eq. (26) where functions f_{a_i} and f_{ξ_i} are

$$\begin{aligned} f_{a_i}(\boldsymbol{a},\boldsymbol{\xi}) = &\left[\frac{2\Lambda_c^2 n_p^2 \tilde{\mu}}{N}\sum_{\substack{j=1\\ i\neq i}}^{N} a_j \sin(\Delta\xi_{ij})\right. \\ &+ \frac{1}{N}\sum_{\substack{j=1\\ i\neq i}}^{N}\left[c_c a_i a_j^2 \sin(2\Delta\xi_{ij}) - \frac{c_t}{2}(a_j^3 + a_j a_i^2)\sin(\Delta\xi_{ij})\right] \\ &\left. - 2n_p\tilde{b}a_i + \Lambda_m n_p a_i \tilde{T}_1 \cos(\xi_i)\right]\left[4\Lambda_m n_p\right]^{-1}, \end{aligned} \tag{C10a}$$

$$\begin{aligned} f_{\xi_i}(\boldsymbol{a},\boldsymbol{\xi}) = &\sigma a_i - 2\left[\frac{2\Lambda_c^2 n_p^2 \tilde{\mu}}{N}\left(a_i + \sum_{\substack{j=1\\ i\neq i}}^{N} a_j \cos(\Delta\xi_{ij})\right)\right. \\ &+ \frac{1}{N}\left((c_c - 2c_t)a_i^3\right. \\ &\left.+ \sum_{\substack{j=1\\ i\neq i}}^{N}\left[c_c a_i a_j^2 \cos(2\Delta\xi_{ij}) - \frac{c_t}{2}(a_j^3 + 3a_j a_i^2)\cos(\Delta\xi_{ij})\right]\right) \\ &\left. - c_p a_i^3 + \Lambda_m n_p a_i \tilde{T}_1 \sin(\xi_i)\right]\left[4\Lambda_m n_p\right]^{-1}. \end{aligned} \tag{C10b}$$

Constants c_p, c_c and c_t are defined in Eqs. (30) and (48) and $\Delta\xi_{ij}$ is defined as

$$\Delta\xi_{ij} = \frac{\xi_j - \xi_i}{2}. \tag{C11}$$

Appendix D Relations dealing with the roots of unity

Some useful relations about the roots of unity are given below. Consider the n^{th} root of unity

$$\nu = e^{\frac{2i\pi}{n}} \tag{D12}$$

and integers $q, k \in \mathbb{Z}$. Then one has

$$\nu^{qn+k} = \nu^k, \tag{D13}$$

$$\nu^{k^*} = \nu^{n-k}, \tag{D14}$$

$$\nu^{n-kq} = \nu^{k(n-q)}, \tag{D15}$$

$$\nu^{(n-k)(n-q)} = \nu^{kq}, \tag{D16}$$

$$\sum_{k=1}^{n-1} \nu^{qk} = \sum_{k=1}^{n-1} \nu^{q(n-k)} = \begin{cases} n-1 & \text{if } q = 0, \\ -1 & \text{if } q > 0. \end{cases} \tag{D17}$$

Superscript * indicate the complex conjugate.

Appendix E determinants of matrices $\boldsymbol{A_U}$, $\boldsymbol{A_G}$ and $\boldsymbol{B}$

The determinants of matrices $\boldsymbol{A_U}$, $\boldsymbol{A_G}$ and $\boldsymbol{B}$ are

$$\begin{aligned} \det(\boldsymbol{A_U}) = &\left(\Lambda_c^2 \tilde{\mu} n_p^2 + \left(c_c - 2c_p - \frac{3c_t}{2}\right) a^2\right) \\ &\left(\Lambda_c^2 \tilde{\mu} n_p^2 - 4\Lambda_m \sigma n_p + \left(c_c - 2c_p - \frac{c_t}{2}\right) a^2\right), \end{aligned} \tag{E18a}$$

$$\det(\boldsymbol{B}) = 4c_p a^2 \left(2\Lambda_m \sigma n_p + c_p a^2\right) \tag{E18b}$$

$$\begin{aligned} \det(\boldsymbol{A_G}) = &16(c_c - c_p) a^2 \left(-\Lambda_c^2 \tilde{\mu} n_p^2 + \left(c_p + \frac{3c_t}{2}\right) a^2\right), \\ &\left(-2\Lambda_m \sigma n_p + (c_c - c_p) a^2\right) \\ &\left(-\Lambda_c^2 \tilde{\mu} n_p^2 + 2\Lambda_m \sigma n_p + \left(c_p + \frac{c_t}{2}\right) a^2\right) / \det(\boldsymbol{A_U}). \end{aligned} \tag{E18c}$$

Appendix F Numerical validation of the model with a large number of pendulums

Figure F2 shows a zoom of Fig. 5 near the operating point (i.e. near $2n_p$) together with numerical solutions. A CPVA with $N = 8$ pendulums is considered. The MANLAB results are shown as thin dark lines with square markers while time integration results are the coloured circles. The red star represents the pitchfork bifurcation determined using MANLAB. The area coloured in red corresponds to the instability zone delimited by a_{pf_3}.

The analytical model predicts well SH1 as the MANLAB results are close to the analytical ones, especially on the upper branch. Moreover, the bifurcation point is very well predicted by the analytical model as the intersection of a_{pf_3} and SH1 is superimposed with the red star, located at $n \approx 3.0004$.

Results from time integration show the dynamics of the pendulums before

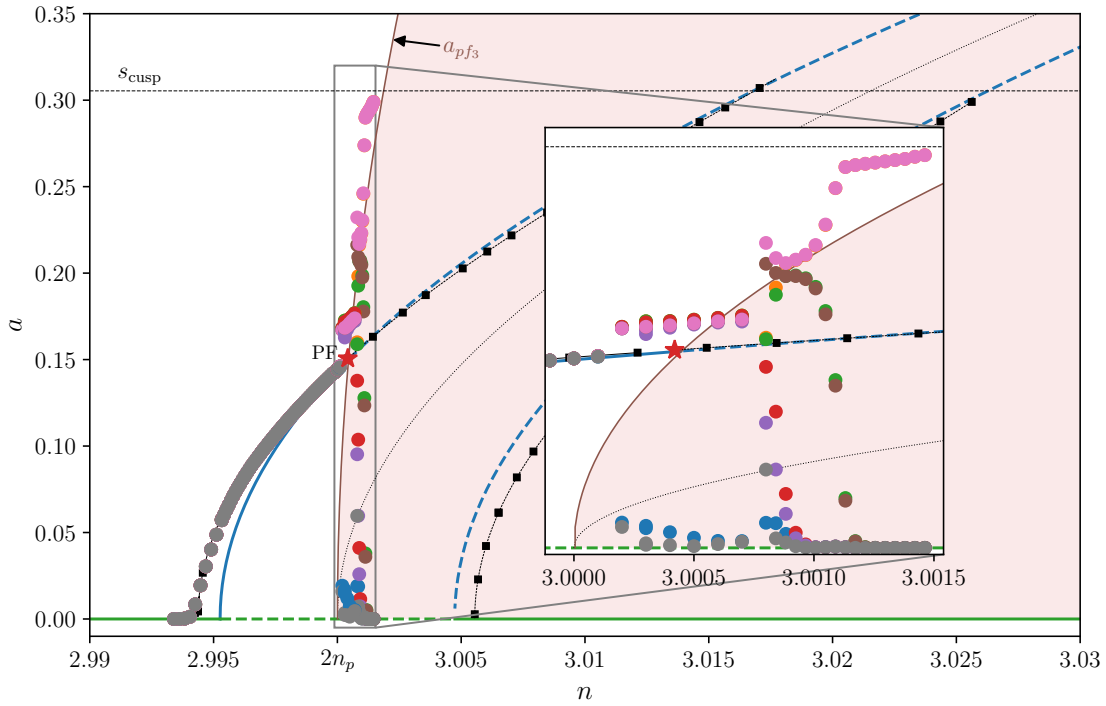

Figure F2: Order response of the pendulums. SH1 and TS are represented in blue and green, respectively. The bifurcation curve a_{pf_3} is represented in brown. Dashed lines indicate an unstable response and the red area corresponds to the instability zone delimited by a_{pf_3}. The solutions and the pitchfork bifurcation determined using MANLAB are represented by thin dark lines with square markers and by the red star, respectively. The coloured circles represent the pendulums' amplitudes obtained through time integration. $N = 8$, $\bar{T}_1 = 0.01$, $\bar{b}_r = 0.002$, and the other system parameters are the same as in Fig. 5.

and after the bifurcation. The small discrepancies between time integration and MANLAB results are probably due to the fact that the time integrations were stopped before the steady state was completely established. The zoom included in Fig. F2 offers a better view of the dynamics on the localised solution, which is quite complex. One can notice that around $n = 3.0012$, the solution is so localised that only two pendulums are moving. They oscillate with a much larger amplitude than SH1, which brings them to their cusp for $n \approx 3.0015$ instead of $n \approx 3.017$ if SH1 was stable.

Figure F3 shows two time signals of the pendulums: one before the localisation (a) and one after (b). Before the localisation, pendulums act as expected: they form two groups oscillating with the same amplitudes but in phase-opposition. After the bifurcation, the amplitudes among the groups are no more equal.

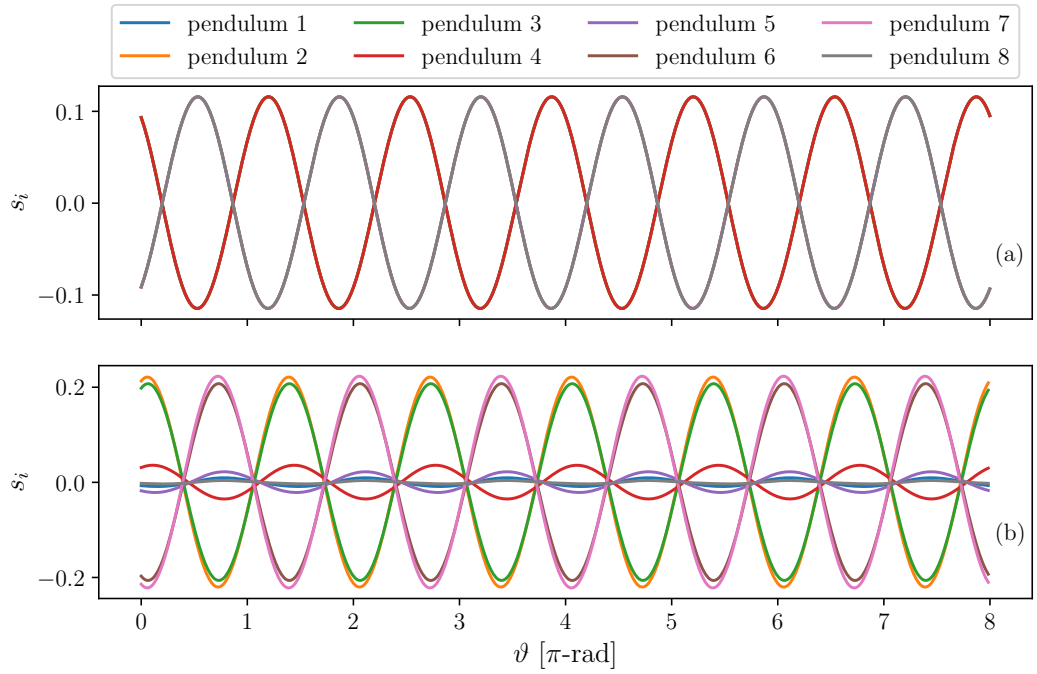

Figure F3: Temporal signals of the pendulums before (a) and after (b) the bifurcation. These signals correspond to the time integration results shown in Fig. F2 at $n = 2.998$ and $n = 3.001$, respectively.

Appendix G Numerical validation of the model with a softened CPVA

Figure G4 shows an order response of the pendulums of a softened CPVA. Starting on a stable part of SH1 and performing a decreasing sweep leads to a pitchfork bifurcation, located theoretically at the intersection between SH1 and a_{pf3}, around $n = 2.9990$. However, it is observed on the time integration results around $n = 2.9985$. This small difference might be due to a steady-state not reached when performing the time integrations. As the bifurcation is subcritical, the localised solution emerging from this point is unstable. This is why there is a jump. After performing several time integrations near the bifurcation point, we observed that SH1 can jump on two different localised solutions. The 1st localised solution (SHL1) corresponds to three pendulums oscillating in phase with the same small amplitude while the other pendulum oscillates in phase opposition and with a large amplitude. The 2nd localised solution (SHL2) corresponds to two pendulums oscillating in phase-opposition and with the same amplitude while the other two pendulums are immobile. SHL2 is stable down to $n \approx 2.9967$, at which points it jumps on SHL1. SHL1 is stable down to $n \approx 2.9940$. For lower orders, the pendulums respond on the trivial solution.

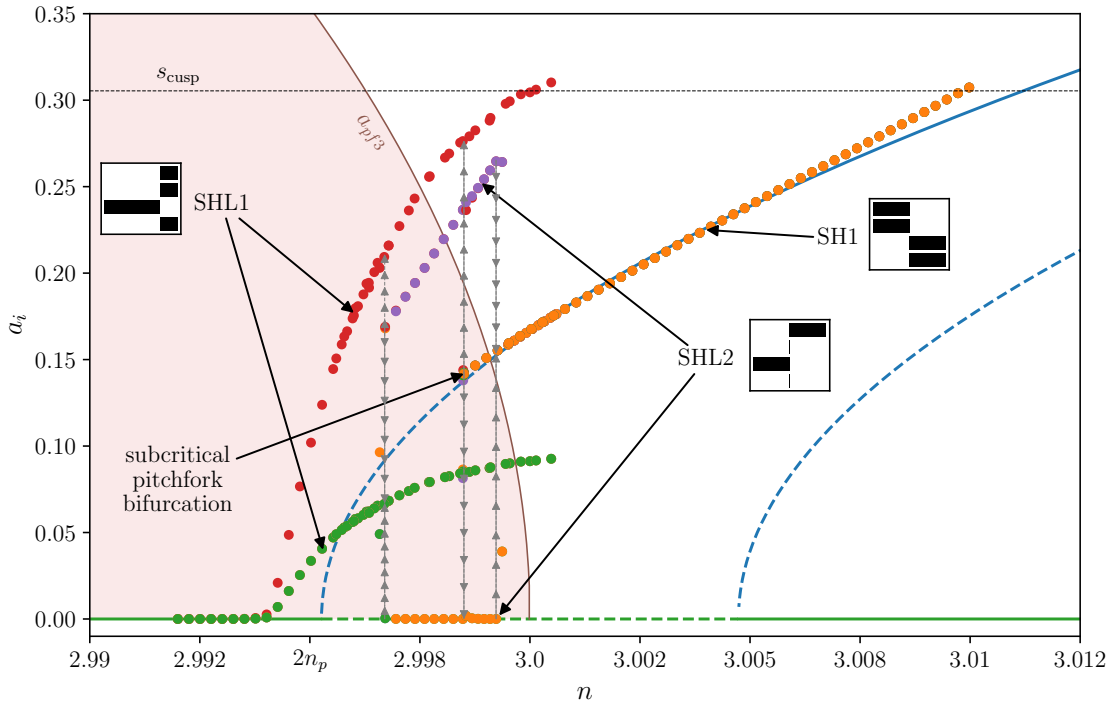

Figure G4: Order response of the pendulums. SH1 and TS are represented in blue and green, respectively. The bifurcation curve a_{pf_3} is represented in brown. Dashed lines indicate an unstable response and the red area corresponds to the instability zone delimited by a_{pf_3}. The coloured circles represent the pendulums' amplitudes obtained through time integration. The grey lines with up and down triangles indicate the jumps and their direction. SHL1 and SHL2 are localised solutions. The bar plots indicate the amplitude of the four pendulums at a given time and order on SH1, SHL1 and SHL2. $\bar{T}_1 = 0.01$ and other parameters are given in Tab. 1, excpet for $x_{[4]} = 0.5$.

Appendix H Details on the order response of a hardened-CPVA made of 4 pendulums

The complexity of the response depicted in Fig. 6 is furthered detailed in Fig. H5, which contains additional information. It includes

- A 3rd localised solution (SHL3) for which two amplitudes oscillate with the same amplitude and in phase-opposition while the other two are immobile.
- The pitchfork bifurcation of SHL1 leading to SHL3 (red star obtained with MANLAB).
- Analytical solutions for SHL2 (green and orange curves) and SHL3 (red curve). Like SH1, these two localised solutions are combinations of modes 1 but could have been introduced as degenerated modes of the system. The associated mode shapes would be

$$SHL2: \quad [0, 3, -1, -1, -1]^\intercal, \quad SHL3: \quad [0, 1, -1, 0, 0]^\intercal. \tag{H19}$$

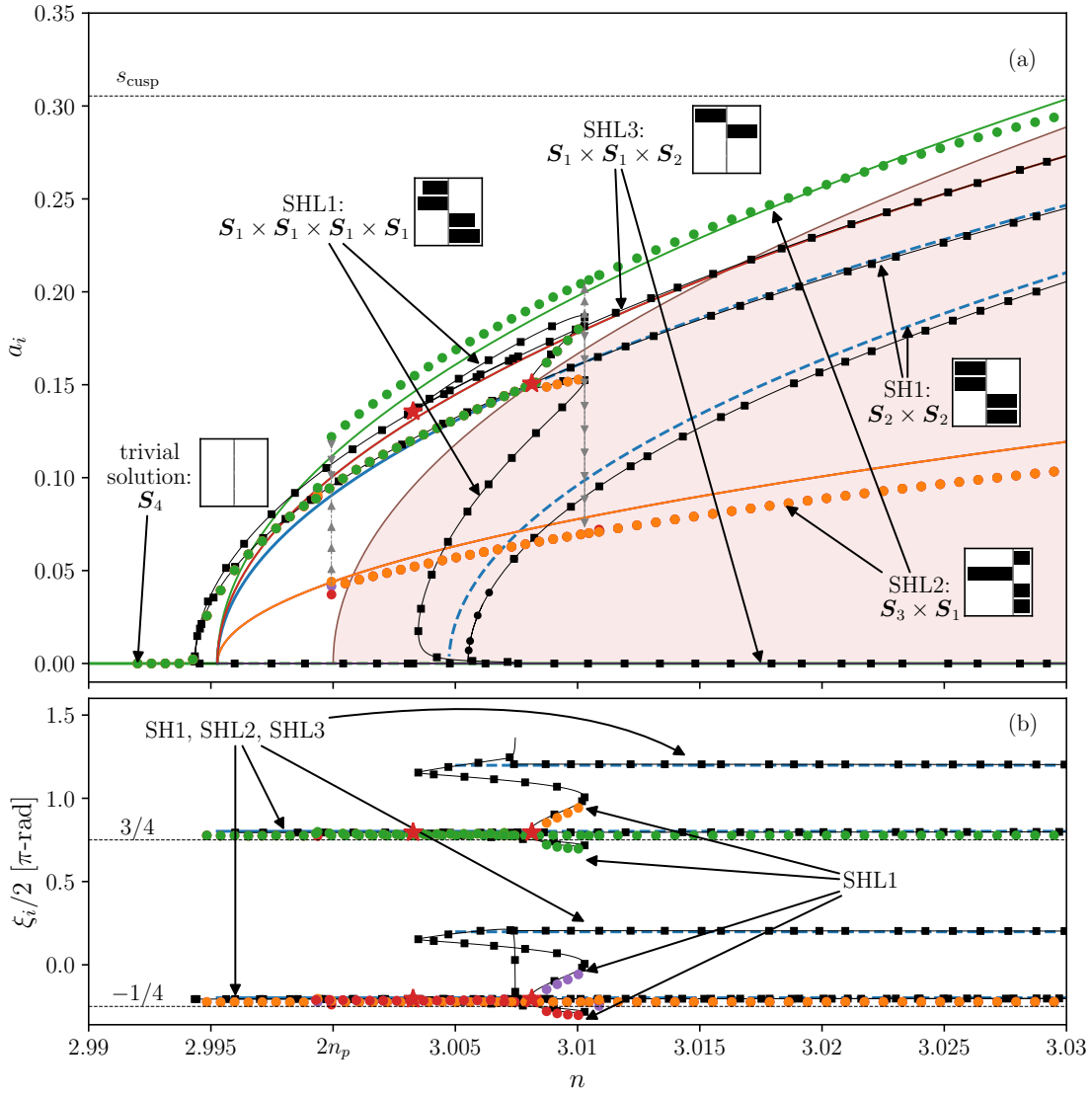

Figure H5: Order response of the pendulums. The amplitudes are given in (a) and the phases in (b). SH1 and TS are represented in blue and green, respectively. The bifurcation curve a_{pf_3} is represented in brown. Dashed lines indicate an unstable response and the red area corresponds to the instability zone delimited by a_{pf_3}. The solutions and the pitchfork bifurcations determined by MANLAB are represented by thin dark lines with square markers and by the red stars, respectively. The coloured circles represent the pendulums' amplitudes obtained through time integration. The analytical solutions corresponding to SHL2 are represented as green and orange curves while that of SHL3 is given by the red curve. $\bar{T}_1 = 0.01$ and other parameters are given in Tab. 1.

Only the upper branch of SHL2 and SHL3 are shown in Fig. H5(a) and the associated stability is not assessed analytically. The computation details of these two solutions are given in Appendix A.

- The phase on every solution.

- The symmetry groups composing the solutions.

Note that there might be other solutions that were not captured in Fig. H5, and that the number of possible solutions increases with the number of pendulums.

Appendix I Time integrations with initial conditions slightly different from the trivial solution

Figure I6 represents time integration results of the CPVA studied in section 5.4 with four different initial conditions but the same excitation parameters. The initial conditions correspond to perturbations of the trivial solution. The aim is to verify that despite these perturbations, the system bifurcates towards SH1 (or another combination of modes 1 similar to SH1, *cf.* section 3.2), like in section 5.4. Looking at Fig. I6, one can see that all four initial conditions tested lead to a desired solution, for which all pendulums oscillate with the same amplitude but half of them are in phase-opposition with the other half. This shows a robustness of the bifurcation towards SH1 or a similar configuration for the hardened CPVA investigated here.

References

[1] Carter, B.C.: Improvements in or Relating to Damping of Oscillation-Checking Devices. 337466, 1929. 337 466

[2] Sarazin, R.R.R.: Means Adapted to Reduce the Torsional Oscillations of Crankshafts. 2079226, 1931. 2 079 226

[3] Chilton, R.: Pendulum Counterweight. 2112984, 1935. 2 112 984

[4] Newland, D.E.: Nonlinear problems of centrifugal pendulum vibration absorbers. In: Mechanisms and Machines, vol. 1. Varna (Bulgaria), pp. 39–62 (1965)

[5] Chao, C.-P., Lee, C.-T., Shaw, S.W.: Non-unisson dynamics of multiple centrifugal pendulum vibration absorbers. Journal of Sound and Vibration **204**(5), 769–794 (1997). https://doi.org/10.1006/jsvi.1997.0960

[6] Chao, C.-P., Shaw, S.W., Lee, C.-T.: Stability of the Unison Response for a Rotating System With Multiple Tautochronic Pendulum Vibration Absorbers. Journal of Applied Mechanics **64**(1), 149–156 (1997). https://doi.org/10.1115/1.2787266

[7] Alsuwaiyan, A.S., Shaw, S.W.: Performance and dynamic stability of general-path centrifugal pendulum vibration absorbers. Journal of Sound and Vibration **252**(5), 791–815 (2002). https://doi.org/10.1006/jsvi.2000.3534

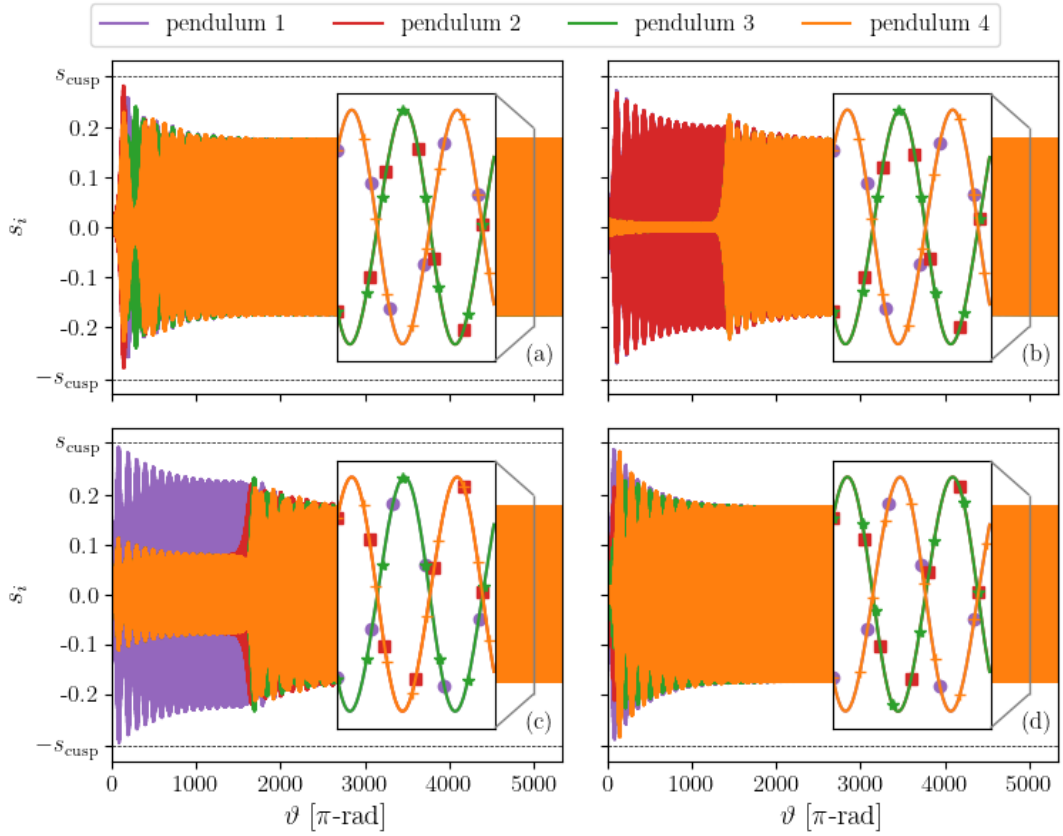

Figure I6: Temporal signals of the pendulums associated to time integrations of the CPVA whose parameters are given in Tab. 1. The excitation parameters are $n = 2.995$ and $\bar{T}_1 = 0.04$. The initial conditions correspond to a perturbation of the trivial solution (TS). In (a), a random noise between 0 and 0.01 is added. The upper bound of this noise corresponds to about 3.3% of the pendulums' cusp (in the present case, $s_{\text{cusp}} \approx 0.305$). In (b), the initial pendulums' position is $s_1 = -s_2 = 0.01$ and $s_3 = s_4 = 0$, which corresponds to a pendulums' response on mode 1_1. In (c) and (d), the initial pendulums' position is $s_1 = -0.03$, $s_2 = s_3 = s_4 = 0.01$ and $s_1 = -0.03$, $s_2 = 0.02$, $s_3 = 0.01$, $s_4 = 0$, respectively. These correspond to combinations of modes 1 different from SH1. The cusp is indicated by the horizontal black dashed lines.

[8] Shaw, S.W., Schmitz, P.M., Haddow, A.G.: Tautochronic Vibration Absorbers for Rotating Systems. Journal of Computational and Nonlinear Dynamics **1**(4), 283–293 (2006). https://doi.org/10.1115/1.2338652

[9] Shaw, S.W., Geist, B.: Tuning for Performance and Stability in Systems of Nearly Tautochronic Torsional Vibration Absorbers. Journal of Vibration and Acoustics **132**(4) (2010). https://doi.org/10.1115/1.4000840

[10] Alsuwaiyan, A.S., Shaw, S.W.: Non-synchronous and Localized Responses of Systems of Identical Centrifugal Pendulum Vibration Absorbers. Arabian Journal for Science and Engineering **39**(12), 9205–9217 (2014). https://doi.org/10.1007/s13369-014-1464-1

[11] Issa, J.S., Shaw, S.W.: Synchronous and non-synchronous responses of systems with multiple identical nonlinear vibration absorbers. Journal of Sound and Vibration **348**, 105–125 (2015). https://doi.org/10.1016/j.jsv.2015.03.021

[12] Nishimura, K., Ikeda, T., Harata, Y.: Localization phenomena in torsional rotating shaft systems with multiple centrifugal pendulum vibration absorbers. Nonlinear Dynamics **83**(3), 1705–1726 (2016). https://doi.org/10.1007/s11071-015-2441-2

[13] Grolet, A., Renault, A., Thomas, O.: Energy Localisation in Periodic Structures: Application to Centrifugal Pendulum Vibration Absorber. In: International Symposium on Transport Phenomena and Dynamics of Rotating Machinery, Maui (Hawaii) (2017)

[14] Cirelli, M., Cera, M., Pennestrì, E., Valentini, P.P.: Nonlinear design analysis of centrifugal pendulum vibration absorbers: An intrinsic geometry-based framework. Nonlinear Dynamics **102**(3), 1297–1318 (2020). https://doi.org/10.1007/s11071-020-06035-1

[15] Cera, M., Cirelli, M., Pennestrì, E., Valentini, P.P.: Design analysis of torsichrone centrifugal pendulum vibration absorbers. Nonlinear Dynamics **104**(2), 1023–1041 (2021). https://doi.org/10.1007/s11071-021-06345-y

[16] Mahe, V., Renault, A., Grolet, A., Thomas, O., Mahe, H.: Dynamic stability of centrifugal pendulum vibration absorbers allowing a rotational mobility. Journal of Sound and Vibration **517**, 116525 (2022). https://doi.org/10.1016/j.jsv.2021.116525

[17] Mahé, V., Renault, A., Grolet, A., Mahé, H., Thomas, O.: On the dynamic stability and efficiency of centrifugal pendulum vibration absorbers with rotating pendulums. Journal of Sound and Vibration **536**, 117157 (2022). https://doi.org/10.1016/j.jsv.2022.117157

[18] Renault, A., Thomas, O., Mahé, H.: Numerical antiresonance continuation of structural systems. Mechanical Systems and Signal Processing **116**, 963–984 (2019). https://doi.org/10.1016/j.ymssp.2018.07.005

[19] Lee, C.-T., Shaw, S.W.: On the counteraction of periodic torques for rotating systems using centrifugally driven vibration absorbers. Journal of Sound and Vibration **191**(5), 695–719 (1996). https://doi.org/10.1006/jsvi.1996.0151

[20] Shaw, S.W., Garg, V., Chao, C.-P.: Attenuation of Engine Torsional Vibrations Using Tuned Pendulum Absorbers. In: SAE Noise and Vibration Conference and Exposition, p. 971961 (1997). https://doi.org/10.4271/971961

[21] Ishida, Y., Inoue, T., Fukami, T., Ueda, M.: Torsional Vibration Suppression by Roller Type Centrifugal Vibration Absorbers. Journal of Vibration and Acoustics **131**(5), 051012 (2009). https://doi.org/10.1115/1.3147124

[22] Vidmar, B.J., Shaw, S.W., Feeny, B.F., Geist, B.K.: Nonlinear Interactions in Systems of Multiple Order Centrifugal Pendulum Vibration Absorbers. Journal of Vibration and Acoustics **135**(6) (2013). https://doi.org/10.1115/1.4024969

[23] Cirelli, M., Capuano, E., Valentini, P.P., Pennestrì, E.: The tuning conditions for circular, cycloidal and epicycloidal centrifugal pendula: A unified cartesian approach. Mechanism and Machine Theory **150**, 103859 (2020). https://doi.org/10.1016/j.mechmachtheory.2020.103859

[24] Cera, M., Cirelli, M., Pennestrì, E., Valentini, P.P.: Nonlinear dynamics of torsichrone CPVA with synchroringed form closure constraint. Nonlinear Dynamics (2021). https://doi.org/10.1007/s11071-021-06732-5

[25] Lee, C.-T., Shaw, S.W.: Torsional vibration reduction in internal combustion engines using centrifugal pendulums. Technical report (1995)

[26] Lee, C.-T., Shaw, S.W.: The non-linear dynamic response of paired centrifugal pendulum vibration absorbers. Journal of Sound and Vibration **203**(5), 731–743 (1997). https://doi.org/10.1006/jsvi.1996.0707

[27] Lee, C.-T., Shaw, S.W., Coppola, V.T.: A Subharmonic Vibration Absorber for Rotating Machinery. Journal of Vibration and Acoustics **119**(4), 590–595 (1997). https://doi.org/10.1115/1.2889766

[28] Chao, C.-P., Shaw, S.W.: The effects of imperfections on the performance of the subharmonic vibration absorber system. Journal of Sound and Vibration **215**(5), 1065–1099 (1998). https://doi.org/10.1006/jsvi.1998.1634

[29] Chao, C.-P., Shaw, S.W.: The dynamic response of multiple pairs of subharmonic torsional vibration absorbers. Journal of Sound and Vibration **231**(2), 411–431 (2000). https://doi.org/10.1006/jsvi.1999.2722

[30] Mahe, V., Renault, A., Grolet, A., Mahe, H., Thomas, O.: Subharmonic centrifugal pendulum vibration absorbers allowing a rotational mobility. Mechanical Systems and Signal Processing **177**, 109125 (2022). https://doi.org/10.1016/j.ymssp.2022.109125

[31] Nayfeh, A.H., Mook, D.T.: Nonlinear Oscillations. Wiley Classics Library. Wiley-VCH, New York (1995). https://doi.org/10.1002/9783527617586

[32] Shami, Z.A., Giraud-Audine, C., Thomas, O.: A nonlinear piezoelectric

shunt absorber with a 2:1 internal resonance: Theory. Mechanical Systems and Signal Processing **170**, 108768 (2022). https://doi.org/10.1016/j.ymssp.2021.108768

[33] Shami, Z.A., Giraud-Audine, C., Thomas, O.: A nonlinear piezoelectric shunt absorber with 2:1 internal resonance: Experimental proof of concept. Smart Materials and Structures **31**(3), 035006 (2022). https://doi.org/10.1088/1361-665X/ac4ab5

[34] Renault, A.: Calcul et optimisation d'absorbeurs pendulaires dans une chaîne de traction automobile [Simulation and optimisation of pendular absorbers for automotive powertrain]. PhD thesis, ENSAM, Lille, France (2018)

[35] Mahé, H., Renault, A., Thomas, O.: Dispositif D'amortissement Pendulaire [Pendular Damping Device]. 3055037, 2018. FR 3 055 037

[36] Mahé, H., Renault, A., Thomas, O.: Dispositif D'amortissement Pendulaire [Pendular Damping Device]. 3055038, 2018. FR 3 055 038

[37] Acar, M.A.: Design and tuning of centrifugal pendulum vibration absorbers. PhD thesis, Michigan State University, Michigan (2017)

[38] Mayet, J., Ulbrich, H.: Tautochronic centrifugal pendulum vibration absorbers: General design and analysis. Journal of Sound and Vibration **333**(3), 711–729 (2014). https://doi.org/10.1016/j.jsv.2013.09.042

[39] Cirelli, M., Gregori, J., Valentini, P.P., Pennestrí, E.: A design chart approach for the tuning of parallel and trapezoidal bifilar centrifugal pendulum. Mechanism and Machine Theory **140**, 711–729 (2019). https://doi.org/10.1016/j.mechmachtheory.2019.06.030

[40] Gomez, E.R., Arteaga, I.L., Kari, L.: Normal-force dependant friction in centrifugal pendulum vibration absorbers: Simulation and experimental investigations. Journal of Sound and Vibration **492**, 115815 (2021). https://doi.org/10.1016/j.jsv.2020.115815

[41] Tan, X., Yang, S., Yang, J., Li, J.: Study of dynamics of rotational centrifugal pendulum vibration absorbers based on tautochronic design. Meccanica (2021). https://doi.org/10.1007/s11012-021-01340-4

[42] Gomez, E.R., Sjöstrand, J., Kari, L., Arteaga, I.L.: Torsional vibrations in heavy-truck powertrains with flywheel attached centrifugal pendulum vibration absorbers. Mechanism and Machine Theory **167**, 104547 (2022). https://doi.org/10.1016/j.mechmachtheory.2021.104547

[43] Gomez, E.R., Kari, L., Arteaga, I.L.: Powertrain shuffle-mode resonance

suppression by means of flywheel mounted torsichrone centrifugal pendulum vibration absorbers. Journal of Sound and Vibration **534**, 117014 (2022). https://doi.org/10.1016/j.jsv.2022.117014

[44] Denman, H.H.: Tautochronic bifilar pendulum torsion absorbers for reciprocating engines. Journal of Sound and Vibration **159**(2), 251–277 (1992). https://doi.org/10.1016/0022-460X(92)90035-V

[45] Shaw, S.W., Wiggins, S.: Chaotic dynamics of a whirling pendulum. Physica D: Nonlinear Phenomena **31**(2), 190–211 (1988). https://doi.org/10.1016/0167-2789(88)90076-0

[46] Shen, L., Suter, B.W.: Bounds for Eigenvalues of Arrowhead Matrices and Their Applications to Hub Matrices and Wireless Communications. EURASIP Journal on Advances in Signal Processing **2009**(1), 379402 (2009). https://doi.org/10.1155/2009/379402

[47] Golubitsky, M., Stewart, I., Schaeffer, D.G.: Singularities and Groups in Bifurcation Theory. Applied Mathematical Sciences, vol. 2. Springer New York, New York, NY (1988). https://doi.org/10.1007/978-1-4612-4574-2

[48] Givois, A., Tan, J.-J., Touzé, C., Thomas, O.: Backbone curves of coupled cubic oscillators in one-to-one internal resonance: Bifurcation scenario, measurements and parameter identification. Meccanica **55**(3), 481–503 (2020). https://doi.org/10.1007/s11012-020-01132-2

[49] Cronin, D.L.: Shake reduction in an automobile engine by means of crankshaft-mounted pendulums. Mechanism and Machine Theory **27**(5), 517–533 (1992). https://doi.org/10.1016/0094-114X(92)90041-F

[50] Sarikaya, B., Inalpolat, M.: Response Sensitivity of Centrifugal Pendulum Vibration Absorbers to Symmetry-Breaking Absorber Imperfections. Journal of Sound and Vibration, 117037 (2022). https://doi.org/10.1016/j.jsv.2022.117037

[51] Bauchau, O.A., Rodriguez, J., Chen, S.-Y.: Modeling the Bifilar Pendulum Using Nonlinear, Flexible Multibody Dynamics. Journal of the American Helicopter Society **48**(1), 53–62 (2003). https://doi.org/10.4050/JAHS.48.53

[52] Shi, C., Parker, R.G.: Vibration Modes and Natural Frequency Veering in Three-Dimensional, Cyclically Symmetric Centrifugal Pendulum Vibration Absorber Systems. Journal of Vibration and Acoustics **136**(1), 011014 (2014). https://doi.org/10.1115/1.4025678

[53] Shi, C., Shaw, S.W., Parker, R.G.: Vibration reduction in a tilting rotor using centrifugal pendulum vibration absorbers. Journal of Sound and

Vibration **385**, 55–68 (2016). https://doi.org/10.1016/j.jsv.2016.08.035

[54] Shi, C., Parker, R.G.: Modal structure of centrifugal pendulum vibration absorber systems with multiple cyclically symmetric groups of absorbers. Journal of Sound and Vibration **332**(18), 4339–4353 (2013). https://doi.org/10.1016/j.jsv.2013.03.009

[55] Shi, C., Parker, R.G., Shaw, S.W.: Tuning of centrifugal pendulum vibration absorbers for translational and rotational vibration reduction. Mechanism and Machine Theory **66**, 56–65 (2013). https://doi.org/10.1016/j.mechmachtheory.2013.03.004

[56] Shi, C., Parker, R.G.: Modal properties and stability of centrifugal pendulum vibration absorber systems with equally spaced, identical absorbers. Journal of Sound and Vibration **331**(21), 4807–4824 (2012). https://doi.org/10.1016/j.jsv.2012.05.018

[57] Nayfeh, A.H.: Perturbation Methods. Wiley Classics Library. Wiley-VCH, Weinheim (1973). https://doi.org/10.1002/9783527617609

[58] Silvester, J.R.: Determinants of Block Matrices. The Mathematical Gazette **84**(501), 460 (2000). https://doi.org/10.2307/3620776

[59] Powell, P.D.: Calculating Determinants of Block Matrices. arXiv:1112.4379 [math] (2011) https://arxiv.org/abs/1112.4379 [math]

[60] Zhang, F. (ed.): The Schur Complement and Its Applications. Numerical Methods and Algorithms, vol. v. 4. Springer, New York (2005)

[61] De Mazancourt, T., Gerlic, D.: The inverse of a block-circulant matrix. IEEE Transactions on Antennas and Propagation **31**(5), 808–810 (1983). https://doi.org/10.1109/TAP.1983.1143132

[62] Eves, H.: Elementary Matrix Theory. Dover Books on Mathematics. Dover Publ, New York (1980)

[63] Miller, K.S.: On the Inverse of the Sum of Matrices. Mathematics Magazine **54**(2), 67–72 (1981)

[64] Guillot, L., Lazarus, A., Thomas, O., Vergez, C., Cochelin, B.: A purely frequency based Floquet-Hill formulation for the efficient stability computation of periodic solutions of ordinary differential systems. Journal of Computational Physics **416**, 109477 (2020). https://doi.org/10.1016/j.jcp.2020.109477

[65] Guillot, L., Cochelin, B., Vergez, C.: A Taylor series-based continuation method for solutions of dynamical systems. Nonlinear Dynamics **98**(4),

2827–2845 (2019). https://doi.org/10.1007/s11071-019-04989-5

Chapter 8

Proposition of an original centrifugal pendulum design and experimental investigation of its classical and subharmonic operations

Content

This chapter is divided in two parts. Section 8.1 is made of a paper about to be submitted to the *Journal of Sound and Vibration* [151]. It presents an original centrifugal pendulum vibration absorber (CPVA) design and provides experimental results on its classical and subharmonic operations. In section 8.2, we make use of the results presented in the paper to propose a CPVA tuned to filter order 20.

Regarding the paper, sections 1 to 3 repeat information from chapters 1, 2, 4, 6 and 7. They present the context of the study, the modelling of a CPVA (*cf.* section 2.1.1), a linear analysis (*cf.* section 2.2) and theoretical background related to the classic and subharmonic CPVA operations (*cf.*

chapters 4, 6 and 7). The reader might want to skip these sections of the article if he already read chapters 1, 2, 4, 6 and 7.

The novelty of the article starts in section 4, where an original CPVA architecture, made of spherical pendulums, is presented. Experimental results are provided in section 5 and validate several features of the analytical models developed in chapters 4, 6 and 7. The CPVA is seen to significantly reduce the vibrations both in classical and subharmonic operations, but its torque capacity is significantly limited by the slipping of the pendulums.

In section 8.2, the results from the paper are used to propose a CPVA tuned at order 10, hence filtering order 20 when in subharmonic operation. The slipping of the pendulums is found to be a significant issue that can hardly be overcome with the design proposed. Moreover, it is shown that a satisfying nonlinear tuning is not possible because of too demanding manufacturing tolerances.

8.1 Experimental investigation of the direct and subharmonic responses of a new design of centrifugal pendulum vibration absorber

Experimental investigation of the direct and subharmonic responses of a new design of centrifugal pendulum vibration absorber

V. Mahé[a,b], A. Renault[b], A. Grolet[a], H. Mahé[b], O. Thomas[a]

[a] *Arts et Metiers Institute of Technology, LISPEN, HESAM Université, F-59000 Lille, France*
[b] *Valeo Transmissions, Centre d'Étude des Produits Nouveaux, Espace Industriel Nord, Route de Poulainville, 80009 Amiens Cedex 1, France*

Abstract

The automotive industry uses centrifugal pendulum vibration absorbers (CPVAs) to reduce vibrations of the transmission system. These passive devices are made of several masses oscillating along a given trajectory relative to a rotor. This work addresses a recent design of CPVA, in which the pendulums rotate relatively to the rotor. Experimental measurements on a new CPVA architecture are compared with success to analytical models for both classical and subharmonic operations. The CPVA investigated is shown to have high performance but its pendulums are subjected to slipping. This slipping, which limits the operating range, is investigated analytically and experimentally.

Keywords: centrifugal pendulum vibration absorber, experimental investigation, subharmonic response, nonlinear dynamics

1. Introduction

In the frame of reducing polluting emissions and fuel consumption of vehicles using thermal engines, automotive manufacturers try to reduce the cylinder capacity and engine speed of rotation. These evolutions lead to a significant

Email addresses: vincent.mahe@ensam.eu (V. Mahé), alexandre.renault@valeo.com (A. Renault), aurelien.grolet@ensam.eu (A. Grolet), herve.mahe@valeo.com (H. Mahé), olivier.thomas@ensam.eu (O. Thomas)

increase of rotation irregularities called acyclisms, mainly due to higher combustion pressure. One of the main characteristics of these reciprocating engines is the linear dependence of the acyclism frequency to the engine speed of rotation. The coefficient of proportionality is the engine order and only depends on the architecture of the engine. During an acceleration phase, the engine sweeps a wide frequency range containing some driveline torsional modes. This situation may lead to significant noise and vibration levels into the passenger compartment and premature wear of the driveline components. Centrifugal pendulum vibration absorbers (CPVAs) have been used for many years to minimise acyclisms of automotive powertrains at the engine order [1–3]. These passive devices consist of oscillating masses (pendulums) moving along particular paths relative to a primary inertia (rotor) as shown in Fig. 1. In most CPVA designs, the pendulums' motion is a pure translation with respect to the rotor. However, many recent studies demonstrated that adding a rotational motion relative to the rotor can significantly improve the performance of a CPVA [4–14]. Because the pendulums are driven by the centrifugal acceleration field resulting from the rotation of the CPVA, their natural frequency is proportional to the engine speed of rotation. Hence, the CPVA acts like a classical dynamic vibration absorber [15] except that the antiresonance generated on the rotor is located at a fixed[1] order, so that the antiresonance frequency is changing linearly with the engine speed. This allows for a reduction of the vibrations over the whole engine speed range.

There are two ways of choosing the pendulums' tuning order. The "classical" way, used in industrial solutions, is to tune the pendulums on the engine order. This generates an antiresonance of the rotor at the engine order, allowing for significant vibration reduction. However, because of non-linearities inherent to CPVA systems, several dysfunctions occur at large excitation amplitudes, such

[1]It is fixed in the linear regime, but it is slightly changing at large pendulum amplitudes due to nonlinear effects. This is explained later in this section.

as jumps of the response [16], localisation of the pendulums' response [9, 17–28], a shift of the antiresonance [9, 29] and the generation of higher rotor harmonics [9, 30–35].

An alternative tuning, first studied by S. Shaw *et al.* [30, 36–40], is to set the pendulums' tuning order to half the engine order. In this case, the pendulums oscillate at half the engine order and generate a non-linear antiresonance of the rotor at the engine order. Moreover, in the case of perfect-tuning, the amplitude at the antiresonance is saturated, which allows for an efficient reduction of the rotor's vibrations [38]. This saturation effect is a known consequence of subharmonic solutions and proved useful in other fields of application (see e.g. [41, 42] and references therein). The investigations on the subharmonic operation were pursued by the authors of the current paper, who included the rotational motion of the pendulums [10] and proposed an original method to assess the stability of the response in the presence of $N/2$ pairs of pendulums [43].

Since the early studies on CPVAs, there has been several experimental investigations. M. A. Wachs [44] and M. Albright *et al.* [45] showed experimentally the reduction of vibrations due to the use of CPVAs in helicopters and racing cars, respectively. T. M. Nester [46] and A. G. Haddow *et al.* [47] were the first to compare a nonlinear analytical model of the unison motion (similar to the one presented in [19]) to experimental results. They both considered monofilar pendulums following circular paths. The first experiments dealing with purely translated pendulums following epicycloidal paths were performed by S. Shaw *et al.* [20]. Roller-type pendulums following a circular path were investigated by Y. Ishida *et al.* [32]. B. J. Vidmar performed several measurements on CPVAs made of pendulums tuned to several orders [48], leading to the validation of the associated analytical model [33]. He also looked at the response of the first three rotor harmonics and showed experimental time signals of the pendulums in classical-localised and subharmonic regimes. This allowed him to verify the apparition of instabilities predicted by his analytical model [48]. B. J Vidmar *et*

al. also investigated the effect of Coulomb friction on the response of a CPVA [49]. J. Mayet *et al.* proposed a new experimental set up and showed steady-state and transient time signals of both the rotor and pendulum [50]. R. Monroe and S. Shaw studied the large pendulums' amplitudes encountered in transient responses that mimic cylinder deactivation conditions [51]. E. R. Gomez *et al.* measured time-decays to identify the friction parameters of a CPVA [52]. E. R. Gomez *et al.* also investigated the performance of a CPVA mounted on a realistic powertrain [53]. Their results showed that the CPVA reduces the amplitude of the first harmonic on the driveline components but can increase the amplitude of higher harmonics. V. Mahé *et al.* compared the analytical prediction of localised responses with experimental measurements [28]. V. Manchi *et al.* showed that centrifugal double pendulum vibration absorbers can reduce the vibration of the driveline components at several orders [54].

The motivation of this paper is to provide new experimental results about the classical and subharmonic responses of a CPVA. Regarding the classical operation, a focus on the antiresonance allows to observe the antiresonance-shifting and to verify with a great accuracy the linear and nonlinear tuning parameters of the CPVA. In addition, like in [33], it is shown that the rotor's response contains higher harmonics whose amplitude is not negligible. These measurements validate the analytical model predicting the classical response of a CPVA with rotating pendulums [9]. Regarding the subharmonic operation, a forced response of the system confirms the saturation of the rotor's response. This validates the analytical predictions derived in [10]. Like in [33], time signals of the pendulums are also provided. In all the forced responses (in classical and subharmonic regimes), there is a torque level starting from which the measurements depart significantly from the analytical models. As these measurements are performed in stables regions, these discrepancies are not attributed to a nonlinear phenomenon but are assumed to be related to the slipping of the pendulums. This is investigated in depth both experimentally and analytically. These analysis lead to a method to assess the adherence coefficient of the pendulums on the

rotor's tracks. In turn, this can be used to estimate the effective torque capacity of the CPVA, which is reduced because of slipping. To the author's knowledge, this paper provides the first experimental study of the antiresonance-shifting and the saturation of the rotor's response. It is also the first assessment of system limitations due to the slipping of the pendulums. Moreover, this study deals with a new CPVA design in which the six pendulums have a spherical shape. This simple design allows to limit friction sources, thus maximising the performance.

This paper is organised as follows. Section 2 describes the modelling of the CPVA and presents a linear analysis. Theoretical background about the classical and subharmonic operations is provided in section 3. The CPVA investigated and the experimental set-up are described in section 4 and the experimental results are given in section 5. This paper ends with a conclusion in section 6.

2. Modelling and linear analysis

2.1. Modelling

The system studied is shown in Fig. 1. A rotor of inertia J_r rotates about its centre O. Its total angular position is $\vartheta(t) = \Omega t + \theta(t)$ where t is the time, Ω is the mean rotational velocity and $\theta(t)$ corresponds to the fluctuating part of the rotation. A torque $T(\vartheta) = T_0 + T_\theta(\vartheta)$ is applied to the rotor where T_0 is its constant part and $T_\theta(\vartheta)$ is periodic. At equilibrium, $T_0 = b_r\Omega$ where b_r is the linear viscous damping coefficient of the rotor, such that the constant torque balances with the damping to set the mean rotational speed Ω. N pendulums of mass m_i and inertia I_i (about their centre of mass) oscillate on their trajectory $\mathscr{C}_i$. Their position on these trajectories is given by the curvilinear abscissa $S_i(t)$ and their distance from O is $R_i(S_i)$. The characteristic dimension $R_{0i} = R_i(S_i = 0)$ is the distance between O and the vertex of the trajectory. In addition to the traditional translation motion, the present study considers that the pendulums rotate about their centre of mass according to the rotation func-

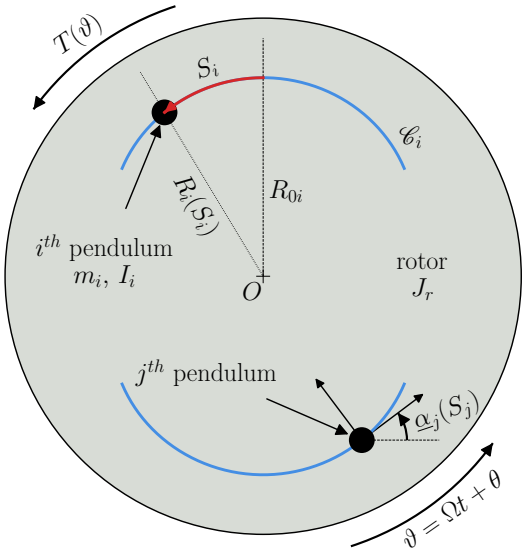

Figure 1: Representation of the system studied. It is made of $N = 2$ pendulums.

tion $\underline{\alpha}_i(S_i)$. As for the rotor, an equivalent linear viscous damping coefficient b_i is used to model the damping between the i^{th} pendulum and the rotor. In the later, pendulums and their associated trajectory and rotation functions will be considered identical so that subscript "i" will be dropped when addressing pendulums' parameters.

In order to write the equations of motion in a non-dimensional form, the following parameters and variables are introduced:

$$\begin{gathered}
s_i = \frac{S_i}{R_0}, \quad y = \frac{\dot{\vartheta}}{\Omega} = 1 + \frac{\dot{\theta}}{\Omega}, \quad \eta = \frac{I}{mR_0^2}, \quad \mu = \frac{NmR_0^2}{J_r + NI}, \\
\bar{b} = \frac{b}{m\Omega}, \quad \bar{b}_r = \frac{b_r}{(J_r + NI)\Omega}, \quad \bar{T}(\vartheta) = \bar{T}_0 + \bar{T}_\theta(\vartheta) = \frac{T(\vartheta)}{(J_r + NI)\Omega^2}, \\
x(s_i) = \frac{R(R_0 s_i)^2}{R_0^2}, \quad z(s_i) = \sqrt{x(s_i) - \frac{1}{4}\left(\frac{dx(s_i)}{ds_i}\right)^2}, \\
\alpha(s_i) = \underline{\alpha}(R_0 s_i), \quad \gamma(s_i) = \frac{d\alpha(s_i)}{ds_i},
\end{gathered} \tag{1}$$

where $(\dot{\bullet}) = \partial(\bullet)/\partial t$. The s_i and y are the $N+1$ degree-of-freedom of the system. They correspond to the dimensionless relative position of the pendulums and rotational velocity of the rotor, respectively. η and μ are inertia ratios, $\bar{b}$ and $\bar{b}_r$ are non-dimensional damping constants and $\bar{T}(\vartheta)$ is the non-dimensional torque applied on the rotor. $x(s_i)$ and $z(s_i)$ are trajectory functions while $\alpha(s_i)$ and $\gamma(s_i)$ are rotation functions. In this paper, $x(s_i)$ and $\alpha(s_i)$ are written as polynomials in the curvilinear abscissa s_i such that

$$x(s_i) = 1 - n_t^2 s_i^2 + \sum_{k=3}^{N_x} x_{[k]} s_i^k, \quad \alpha(s_i) = \sum_{k=0}^{N_\alpha} \alpha_{[k]} s_i^k, \tag{2}$$

where n_t is the order of the pendulums' trajectory and $x_{[k]}$, $\alpha_{[k]}$ are trajectory and rotation coefficients. In the special case $x_{[k]} = 0, \forall k$, the pendulums' trajectories are epicycloids of order n_t, which are the tautochronic trajectories when the rotor spins at a constant speed [55]. Note that trajectories defined as in Eq. (2) have a cusp point [55]. For small $x_{[k]}, \forall k$, the cusp point can be approximated by the cusp of the epicycloid, given by

$$s_{\text{cusp}} = \frac{1}{n_t \sqrt{1 + n_t^2}}. \tag{3}$$

In order to give $\bar{T}(\vartheta)$ the meaning of an external forcing term, we replace the independent variable t by the rotor's position ϑ [56], which can be seen as a non-dimensional time. Using the chain rule, one can show that

$$(\dot{\bullet}) = \Omega y (\bullet)', \quad (\ddot{\bullet}) = \Omega^2 y y' (\bullet)' + \Omega^2 y^2 (\bullet)'', \tag{4}$$

where $(\bullet)' = \partial(\bullet)/\partial\vartheta$ (the details can be found in [10]). Hence, the non-dimensional rotor's acceleration is now $\ddot{\vartheta}/\Omega^2 = \dot{y}/\Omega = y y'$. Using the non-dimensional quantities (1) and the chain rule (4), one can write the equations

of motion as

$$\frac{1}{N}\left[\sum_{i=1}^{N}(N+\mu x(s_i))yy' + \mu\left(z(s_i)+\eta\gamma(s_i)\right)\left(yy's_i' + y^2 s_i''\right)\right. \\ \left. + \mu y^2 s_i'\left(\frac{dx(s_i)}{ds_i} + \frac{dz(s_i)}{ds_i}s_i' + \eta\frac{d\gamma(s_i)}{ds_i}s_i'\right)\right] + \bar{b}_r y = \bar{T}(\vartheta), \tag{5a}$$

$$\left[z(s_i)+\eta\gamma(s_i)\right]y' + \left[1+\eta\gamma(s_i)^2\right]\left(y's_i' + ys_i''\right) + \eta\gamma(s_i)\frac{d\gamma(s_i)}{ds_i}y{s_i'}^2 \\ - \frac{1}{2}\frac{dx(s_i)}{ds_i}y + \bar{b}s_i' = 0, \qquad i = 1, ..., N. \tag{5b}$$

Computation details can be found in [10]. Equation (5a) governs the motion of the rotor while the N Eqs. (5b) govern the motion of the pendulums.

From now on, it is assumed that the fluctuating torque applied on the rotor contains only one harmonic whose non-dimensional form is $\bar{T}_1\cos(n\vartheta)$, where n is the excitation order. For a car engine, n corresponds to the number of strikes per revolution of the crankshaft.

2.2. Linear analysis

First of all, one can use Eq. (4) to show that, at first order, $1+\theta' \approx y$ and $\theta'' \approx yy' \approx y'$ (the demonstration can be found in [10]). Hence, it is possible to represent the motion of the rotor with position θ instead of velocity y. This way, all the degree-of-freedom of the system are positions, which facilitates the representation of the mode shapes. Using θ instead of y and the balance between the constant torque and the damping $\bar{b}_r = \bar{T}_0$ (*cf.* section 2.1), one can linearise Eqs. (5a) and (5b). This leads to the free, conservative, linear equations

$$(1+\mu)\theta'' + \frac{\mu\Lambda_c}{N}\sum_{i=1}^{N}s_i'' = 0, \tag{6a}$$

$$\Lambda_c\theta'' + \Lambda_m s_i'' + n_t^2 s_i = 0, \quad i = 1, ..., N. \tag{6b}$$

Λ_m and Λ_c are constants representing the equivalent mass of a pendulum due to the effect of the rotatory inertia and the linear coupling term between a pendulum and the rotor, respectively. They are given by

$$\Lambda_m = 1 + \eta\alpha_{[1]}^2, \quad \Lambda_c = 1 + \eta\alpha_{[1]}, \tag{7}$$

where $\alpha_{[1]}$ is the linear rotation coefficient (*cf.* Eq. (2)).

The linearised equations of motions (6) can be written as a matrix equation. Doing so, one can find that the eigenorders and mode shapes of the system are [9, 57]

$$\begin{aligned}
&n_{00} = 0, \quad n_{10} = n_p, \quad n_{20} = n_p \sqrt{\frac{1+\mu}{1+\mu\left(1-\frac{\Lambda_c^2}{\Lambda_m}\right)}} \\
&\boldsymbol{\phi_{00}} = [1, 0, ..., 0]^\intercal, \quad \boldsymbol{\phi_{20}} = \left[-\frac{\mu\Lambda_c}{1+\mu}, 1, ..., 1\right]^\intercal, \\
&\boldsymbol{\phi_{10_i}}[i+1] = -\boldsymbol{\phi_{10_i}}[i+2] = 1, \quad \boldsymbol{\phi_{10_i}}[j \neq \{i+1, i+2\}] = 0, \\
&i = 1, ..., N-1.
\end{aligned} \tag{8}$$

The eigenorders can be seen as non-dimensional eigenfrequencies, superscript $^\intercal$ indicates the transpose and $\boldsymbol{\phi_{10_i}}[j]$ refers to the j^{th} component of $\boldsymbol{\phi_{10_i}}$. n_p is the pendulums' tuning order, which is related to the trajectory order n_t such that

$$n_p = \frac{n_t}{\sqrt{\Lambda_m}}, \tag{9}$$

and it corresponds to the eingenorder of the pendulums when they are uncoupled from the rotor.

$(n_{00}, \boldsymbol{\phi_{00}})$ is a rigid body mode for which only the rotor is excited. $(n_{10}, \boldsymbol{\phi_{10_i}})$ are $N-1$ degenerated modes for which two pendulums are moving in phase-opposition. Their eigenvalue n_{10} has multiplicity $N-1$ and the rotor is a node of these modes. For a CPVA made of only two pendulums, $(n_{10}, \boldsymbol{\phi_{10}})$ is not degenerated and simply represents a phase-opposition motion of the pendulums. The group $\{(n_{10}, \boldsymbol{\phi_{10_i}}) \,|i \in \{1, ..., N-1\}\}$ will be referred-to as "modes 1". $(n_{20}, \boldsymbol{\phi_{20}})$ is a mode for which the pendulums move in unison but in phase-opposition with respect to the rotor (provided that $\Lambda_c > 0$, which is the case for reasonable parameters). It will be referred-to as the "unison mode" or "mode 2". To filter-out a fluctuating torque, one typically chooses $n_p \approx n$ to generate

an antiresonance on the rotor at $n_{AR} \approx n_p$ using the unison mode.

Note that in the case of a real automotive driveline (a simple model of which consists in successive rotors linked through torsional springs [58]), the CPVA should be placed as close as possible from the source of excitation (i.e. the engine). Doing so, the antiresonance generated by the pendulums exists on every driveline components located after the CPVA [59], which allows to isolate the whole driveline from the torque fluctuations.

3. Theoretical background

Many analytical investigations of CPVAs were carried out using a simplification of the initial equations of motion (5) accordingly to realistic assumptions [9, 10, 19, 21, 22, 28, 39, 43]. This requires to specify the trajectory and rotation functions, and in this paper we choose to express them as

$$x(s_i) = 1 - n_t^2 s_i^2 + x_{[4]} s_i^4, \quad \alpha(s_i) = \alpha_{[1]} s_i + \alpha_{[3]} s_i^3. \tag{10}$$

This way of expressing $x(s_i)$ and $\alpha(s_i)$ has the advantage to be easy to use in practice. Indeed, Eq. (9) shows that one can control the linear tuning through n_t and Λ_m, which is related to $\alpha_{[1]}$. In addition, we will show later in this section that the nonlinear tuning of the CPVA can be controlled through $x_{[4]}$ and $\alpha_{[3]}$. After the simplification procedure, the resulting simplified equations can be solved analytically using for instance the method of multiple scales [60].

Previous results [9] showed that the pendulums' response on mode 2 takes the form

$$s_i(\vartheta) = a\cos(n\vartheta - \xi), \quad \forall i, \tag{11}$$

where a and ξ are the amplitude and phase of the response, respectively. Their expression as a function of the system's parameters can be found in [9].
The other solution of interest is the subharmonic response of the pendulums

on a combination of modes 1 called SH1[1] such that, for an even number of pendulum, their response takes the form

$$\begin{aligned} s_i(\vartheta) &= a\cos\left(\frac{n}{2}\vartheta - \xi\right), \quad \forall i \in \{1, ..., N/2\}, \\ s_j(\vartheta) &= -a\cos\left(\frac{n}{2}\vartheta - \xi\right), \quad \forall j \in \{N/2+1, ..., N\}. \end{aligned} \tag{12}$$

Hence, half the pendulums are in phase opposition with the other half. Other subharmonic solutions involving only modes 1 exist [40, 43] but they are out of the scope of this paper. The expression of a and ξ as a function of the system's parameters can be found in [10, 43]. The rotor's acceleration can be written as

$$\theta'' = h_1\cos(n\vartheta - \psi_1) + h_2\cos(2n\vartheta - \psi_2) + h_3\cos(3n\vartheta - \psi_3), \tag{13}$$

where h_i and ψ_i, $i = \{1, 2, 3\}$, are the amplitudes and phases of the three first harmonics. Their expression as a function of the system's parameters can be found in [9, 10, 43]. Note that only the first three harmonics are retained as these are typically the dominant ones when the pendulums respond on mode 2 [21, 48]. In addition, a great advantage of the subharmonic response SH1 is that the rotor's response is harmonic, i.e. $h_i = 0$, $\forall i > 1$ [10, 30, 43].

A typical CPVA response is shown in Fig. 2. The classical (green) and subharmonic (blue) operations are described in details below.

3.1. The classical operation

In the case of the classical response, shown in details in Fig. 3, the pendulums respond on mode 2 and generate an antiresonance on the rotor' first harmonic around n_p. One of the main drawbacks of this operation principle is the generation of higher harmonics, shown in blue and orange in Fig. 3(b). The classical response is subjected to instabilities. Indeed, there are saddle-node (SN) bifurcations leading to jumps of the response and pitchfork (PF) bifurcations leading to coupled-mode solutions [61]. Details on the stability can be

[1] "SH" stands for "sumbharmonic" and "1" indicates that modes 1 are involved

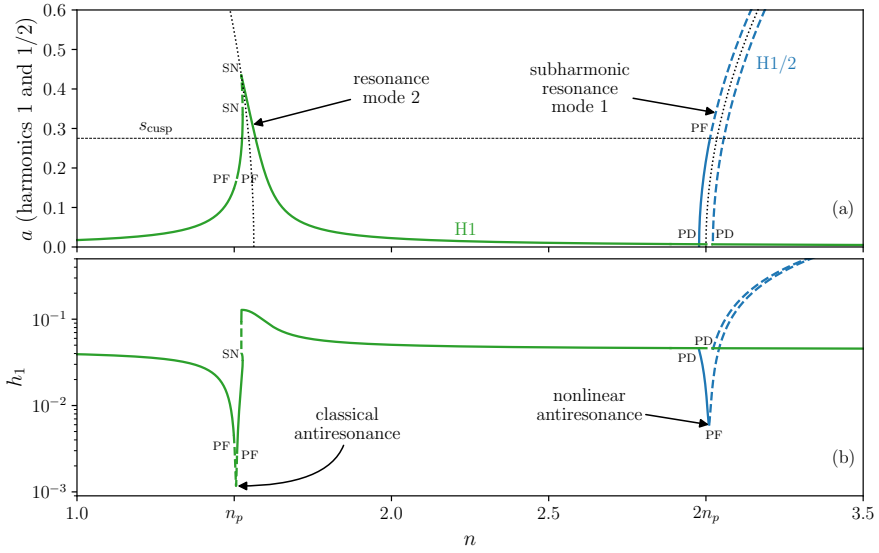

Figure 2: Amplitude response of the pendulums (a) and rotor (b) as a function of the excitation order. The classical response is shown in green while the subharmonic one is shown in blue. Dashed lines indicate unstable solutions and code names "SN", "PF" and "PD" refer to saddle-node, pitchfork and period-doubling bifurcations, respectively. The cusp of the pendulums' trajectory is shown as a black dashed line. The backbone curves of the response of mode 2 and the subharmonic response of SH1 are shown as black doted lines. No saddle-node bifurcation is shown for the upper branch of the rotor's response in classical operation as it is poorly represented by the analytical model (however this is of no importance as it is associated to a pendulums' amplitude larger than the cusp, which is not physical). $\bar{T}_1 = 0.0442$ and the parameters of the CPVA are given in Tab. 1 except for $\bar{b} = 0.0042$.

found in [9]. One can see that the classical response is softening as the resonance bends to the left. The expression of the backbone curve is given by [9]

$$n_2 = n_p + \frac{\Lambda_c^2 n_p^2 \mu}{2\Lambda_m n_p} - \frac{2c_t - c_c + c_p}{4\Lambda_m n_p} a^2, \tag{14}$$

where n_2 is the eigenorder of mode 2. c_c, c_t and c_p are nonlinear coefficients related to Coriolis effects, the large displacements along the trajectory, and the perturbation of the trajectory and rotation functions, respectively. They are given by

$$c_c = \mu n_t^4, \quad c_t = \frac{\Lambda_c}{2} \mu n_p^2 n_t^2 (1 + n_t^2), \quad c_p = 3(x_{[4]} + 2n_p^2 \eta \alpha_{[1]} \alpha_{[3]}). \tag{15}$$

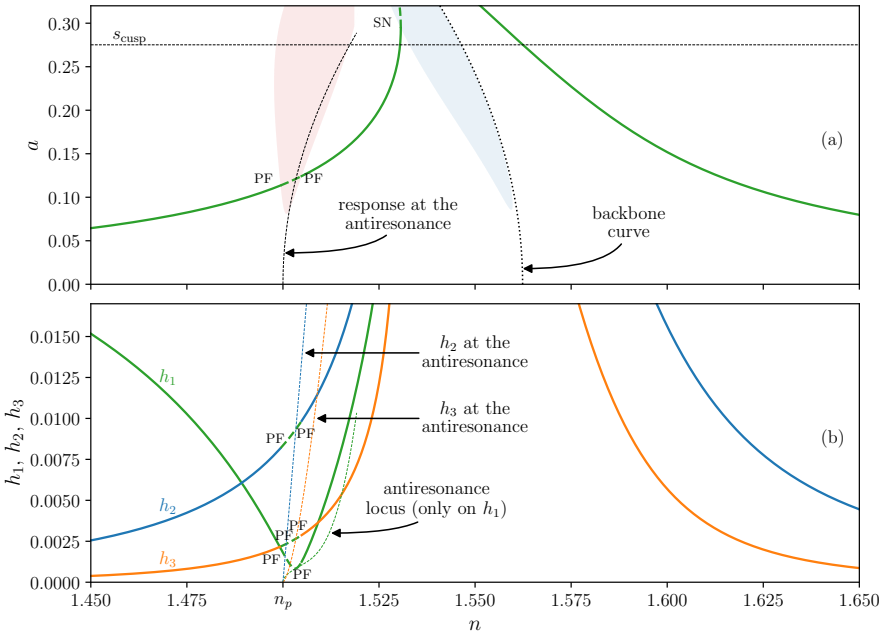

Figure 3: Amplitude response of the pendulums (a) and rotor (b) as a function of the excitation order. Dashed lines indicate unstable solutions and code names "SN" and "PF" refer to saddle-node and pitchfork bifurcations, respectively. The unstable zones leading to localisation and jumps are shown in red and blue, respectively. The bifurcations are located at the intersection between the border of these zones and the response. The cusp of the pendulums' trajectory and the backbone curve are shown as dashed and dotted lines in (a). Thin dashed lines indicate the response of a, h_1, h_2 and h_3 at the antiresonance order (note that the antiresonance exists only on h_1). $\bar{T}_1 = 0.0332$ and the parameters of the CPVA are given in Tab. 1 except for $\bar{b} = 0.0042$.

The value of c_p is easily controlled by choosing $x_{[4]}$ and $\alpha_{[3]}$, so it can be seen as a nonlinear tuning parameter. It is visible in Fig. 3 that because of nonlinear effects, the antiresonance order varies with the excitation amplitude. A good approximation of the antiresonance locus is given by [9]

$$n_{AR}^{(CL)} = n_p + \epsilon \frac{c_c - c_p}{4\Lambda_m n_p} a^2. \tag{16}$$

Superscript "(CL)" indicates that this is the antiresonance related to the classical operation. A limitation of the analytical model causes the rotor's response

180 to have a strange shape around the resonance in Fig. 2. However, this can simply be ignored as it corresponds to a situation where the pendulums oscillate beyond the cusp of their trajectory, which is non-physical.

3.2. The subharmonic operation

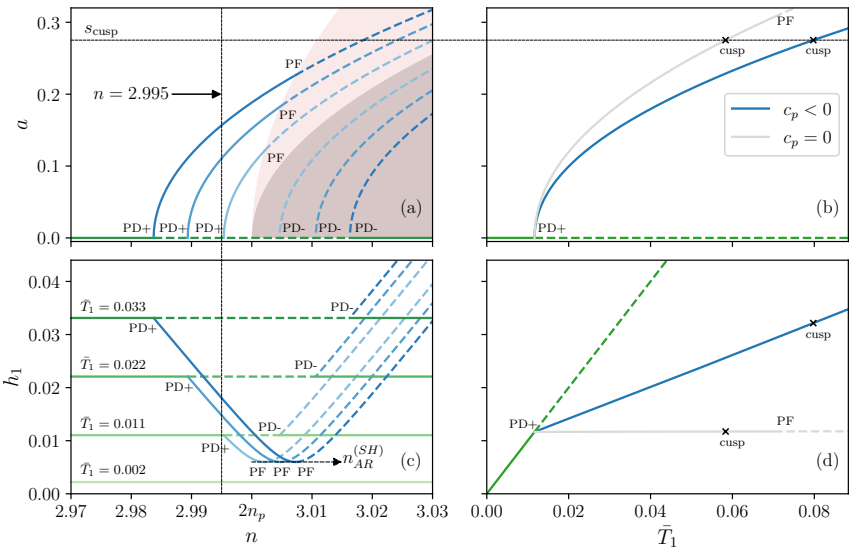

Figure 4: Order (left) and torque (right) responses of a CPVA. The order response is shown for four different torque amplitudes $\bar{T}_1 = \{0.002, 0.011, 0.022, 0.033\}$, and the torque response is shown for $n = 2.995$. The order associated to the torque response is shown as a vertical black line in (a) and (c). The pendulums' amplitude is given in (a), (b), and the rotor's amplitude is given in (c), (d). The response on SH1 is depicted in blue while a trivial solution with immobile pendulums is given in green. This trivial solution is an approximation of the response on mode 2 far from n_p [10]. Dashed lines indicate unstable solutions. The light and dark red areas indicate instabilities due to pitchfork bifurcations only and to both pitchfork and saddle-node bifurcations, respectively. "PF" indicates a pitchfork bifurcation while "PD+" and "PD-" indicate super- and sub-critial period doubling bifurcations, respectively. The cusp of the pendulums' trajectory is shown as a black dashed line. In addition, the cusp is indicated with black cross markers in the torque responses (b) and (d). The parameters of the CPVA are given in Tab. 1 except for $\bar{b} = 0.0042$.

The subharmonic response of the CPVA is displayed in blue in Figs. 2 and

4. Contrarily to the classical response, it is hardening as the resonance bends to the right. The backbone curve of SH1 is given by [10]

$$n_1^{(SH)} = 2n_p + \frac{c_c - c_p}{2n_p \Lambda_m} a^2. \tag{17}$$

The subharmonic response appears through period-doubling bifurcations (PD) from the classical response and generates a nonlinear antiresonance on the rotor around $2n_p$. The subharmonic response is also subjected to instabilities, as can be seen from the pitchfork bifurcation that leads to a response on a combination of modes 1 different from SH1 [43]. Details on the stability can be found in [10, 43]. As for the classical response, nonlinear effects cause the antiresonance order to shift as the excitation amplitude is increased. Its evolution is given by [10]

$$n_{AR}^{(SH)} = n_p - \frac{c_p}{c_c} \sqrt{\frac{\bar{T}_1^2}{4} - \frac{\bar{b}^2}{\Lambda_m^2}}. \tag{18}$$

Superscript "(SH)" indicates that this is the antiresonance related to the subharmonic operation. An interesting feature of the nonlinear antiresonance is that the rotor's amplitude at $n_{AR}^{(SH)}$ is independent from the excitation amplitude. Hence, if one chooses $c_p = 0$ such that $n_{AR}^{(SH)}$ is fixed (*cf.* Eq. (18)), the rotor's response saturates. This saturation phenomenon can lead to an efficient reduction of the rotor's vibrations. However, small negative c_p values should be preferred to avoid instabilities [43]. More details about the subharmonic response of a CPVA with $c_p < 0$ are given in Fig. 4. Fig. 4(a) indicates that with $c_p < 0$, there is an unstable zone located at $n > 2n_p$. In order to avoid these instabilities, the torque response shown in Fig. 4(b) and (d) is given for $n < 2n_p$. In Fig. 4(c), one can see that the antiresonance is shifting to the right and the rotor's amplitude at the antiresonance is fixed. There are no subharmonic responses for $\bar{T}_1 = 0.002$ as the torque is not large enough. The fact that there is a torque threshold to trigger the subharmonic response is a drawback compared to the classical response as there will be no filtration for small torques. The

torque threshold is given by [10]

$$\bar{T}_1^* = \sqrt{4(n-2n_p)^2 + \frac{4\bar{b}^2}{\Lambda_m^2}}. \tag{19}$$

To lower the threshold one can decrease $|n-2n_p|$, but care should be taken as $n > 2n_p$ is located in an unstable zone for $c_p < 0$. Another way of decreasing the threshold is to maximise the equivalent mass Λ_m by maximising the pendulums' rotatory inertia η and the magnitude of their linear rotation rate $\alpha_{[1]}$ (*cf.* Eq. (7)). Finally, as for the classical operation, one should aim for small damping. In Fig. 4(b), (d), the torque response of the CPVA with $c_p < 0$ is compared to that of a CPVA with $c_p = 0$. As $c_p = 0$ locks the antiresonance (*cf.* Eq. (17)), this configuration leads to the best filtration performances. However, choosing $c_p < 0$ still leads to significant filtration and increases the torque range as the pendulums hit their cusp for larger $\bar{T}_1$. Finally, it must be noted that it is not possible in practice to have $c_p = 0$ due to manufacturing tolerances. Further, if $c_p > 0$, the unstable zones would no longer be located at $n > 2n_p$ but at $n < 2n_p$ [43], so one must ensure that the sign of c_p will not change because of manufacturing tolerances.

4. Presentation of the experimental system

4.1. CPVA with spherical pendulums

The CPVA studied experimentally in this paper is shown in Fig. 5. It is made of a rotor and six spherical pendulums (balls) rolling on v-shaped tracks (*cf.* Fig. 7(a)). This simple design has several benefits. Contrarily to the usual bifilar pendulums [2] there are no rollers, so there are less sources of friction [52] and the system is easier to manufacture. In addition, an imperfect rollers' alignment in a bifilar CPVA could lead to contacts between the pendulums and the rotor, hence generating noise and additional friction, which are both undesirable. Indeed, each pendulum of a bifilar CPVA is usually made of two steel plates located on each side of the rotor and rigidly linked together [62, 63]. Each pendulum oscillates relatively to the rotor thanks to two rollers that roll on

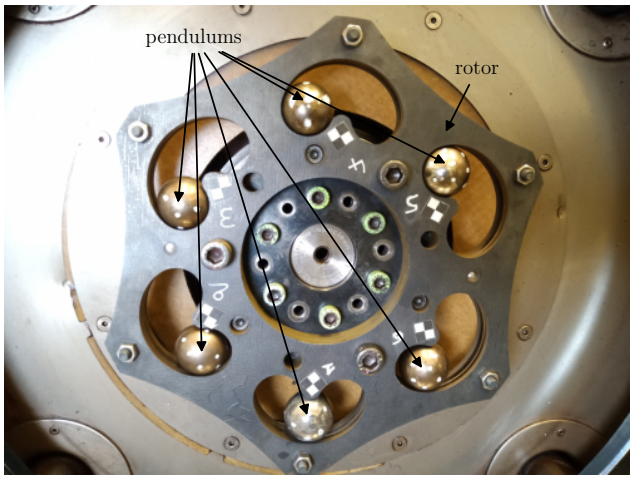

Figure 5: CPVA used for the experiments.

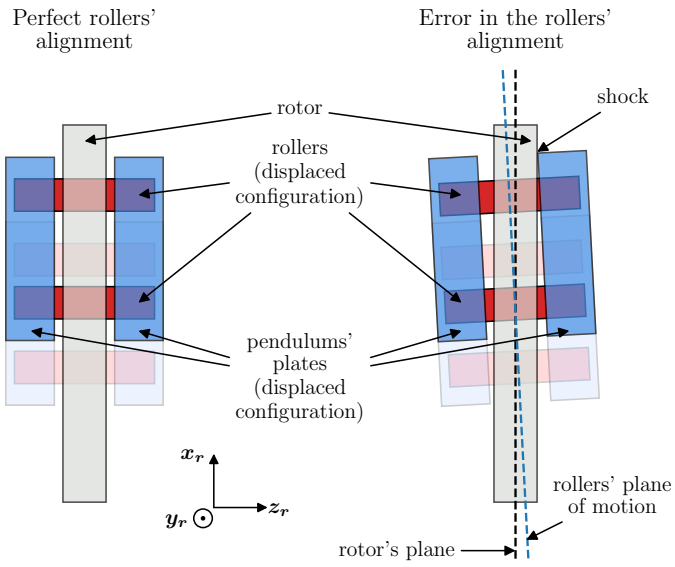

Figure 6: Top view of a bifilar CPVA with perfectly aligned (left) and misaligned (right) rollers to illustrate the shock problem. Light colors indicate the initial position of the pendulum while darker colors indicate a displaced configuration. $(\boldsymbol{x_r}, \boldsymbol{y_r}, \boldsymbol{z_r})$ is a frame attached to the rotor (see Fig. 7).

tracks designed on the rotor and on the pendulum's plates. If the rollers move slightly out of the rotor's plane, as illustrated in Fig. 6, they might drive the pendulums' plates into contact with the rotor, hence causing noise and friction. As spherical pendulums limit friction issues, they are likely to be less damped than bifilar CPVAs. It is for this reason and because of their simple architecture that it was chosen in this paper to investigate a CPVA with spherical pendulums.

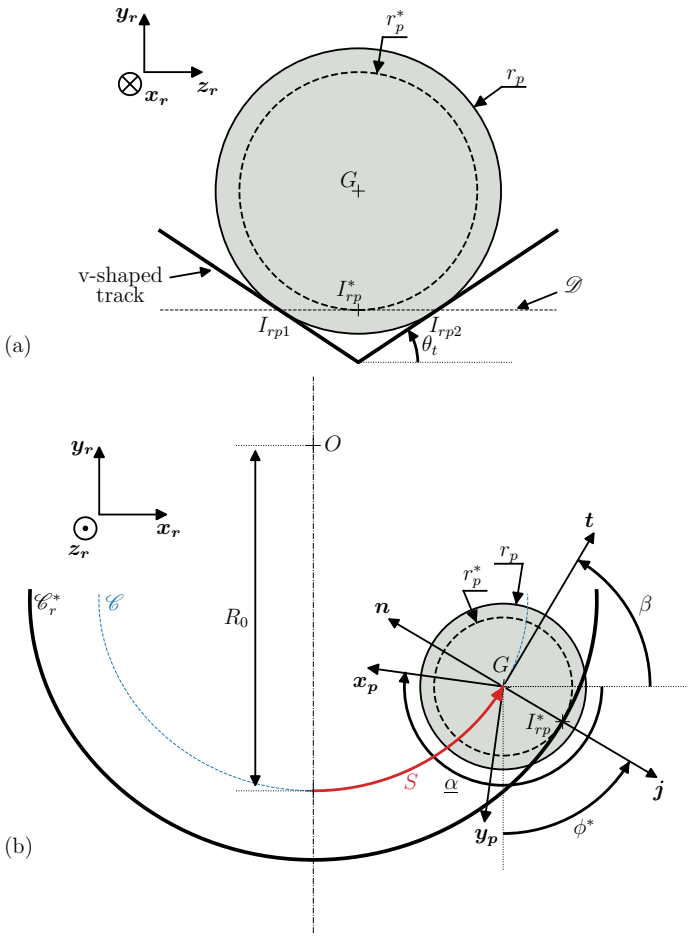

Figure 7: Side view (a) and front view (b) representation of a spherical pendulum.

A side-view representation of one of the pendulums is given in Fig. 7(a).

$\mathscr{R}_r(O, \boldsymbol{x_r}, \boldsymbol{y_r}, \boldsymbol{z_r})$ is a frame attached to the rotor at point O. θ_t is the angle of the v-shaped tracks with respect to $\boldsymbol{z_r}$. This track shape prevents the pendulums from moving along $\boldsymbol{z_r}$. A pendulum is a ball of center of mass G and radius r_p. It is in contact with the rotor's track at points I_{rp1} and I_{rp2}. It is convenient to introduce the virtual contact point I^*_{rp} lying on a line $\mathscr{D}$ passing through I_{rp1} and I_{rp2} such that $I_{rp1}I^*_{rp} = I_{rp2}I^*_{rp}$. Distance GI^*_{rp} defines the virtual radius of the ball, r^*_p, related to the real radius r_p such that

$$r^*_p = r_p \cos\theta_t. \tag{20}$$

Figure 7(b) gives a detailed front view representation of a pendulum. R_0, $\underline{\alpha}$, $\mathscr{C}$ and S were already described in Fig. 1. $\boldsymbol{n}$ and $\boldsymbol{t}$ are vectors normal and tangent to $\mathscr{C}$ at abscissa S, respectively. The angle between $\boldsymbol{t}$ and $\boldsymbol{x_r}$ is β. $\mathscr{R}_p(G, \boldsymbol{x_p}, \boldsymbol{y_p}, \boldsymbol{z_r})$ is a frame attached to the pendulum at point G. Its angular position with respect to $\mathscr{R}_r$ is $\underline{\alpha}$. $\mathscr{C}^*_r$ is the virtual rolling track of the rotor, defined as the successive positions of I^*_{rp}. $\boldsymbol{j}$ is a unitary vector whose direction is that of $\boldsymbol{GI^*_{rp}}$. The angle between $-\boldsymbol{y_r}$ and $\boldsymbol{j}$ is ϕ^*. Determining the form of $\underline{\alpha}$ is necessary to use the analytical model presented in section 3. This is done in Appendix A and leads to the linear rotation law

$$\underline{\alpha}(S) = -\frac{1}{r^*_p}S \Rightarrow \alpha_{[1]} = -\frac{R_0}{r^*_p}. \tag{21}$$

The shape of $\mathscr{C}^*_r$ that produces the desired trajectory $\mathscr{C}$ is computed in Appendix A. The dimensionless parameters of the CPVA investigated experimentally in this paper are given in Tab. 1.

N	n_p	η	μ	$x_{[4]}$	$\alpha_{[1]}$	$\alpha_{[3]}$
6	1.5	0.01	0.13	-0.2	-6.4	0

Table 1: Parameters of the CPVA attached on the bench.

4.2. Experimental set-up and protocol

The experimental setup is shown in Fig. 8. The rotor is fixed on a bench of inertia J_b using an adaptation system of inertia J_a, so that J_r has to be replaced

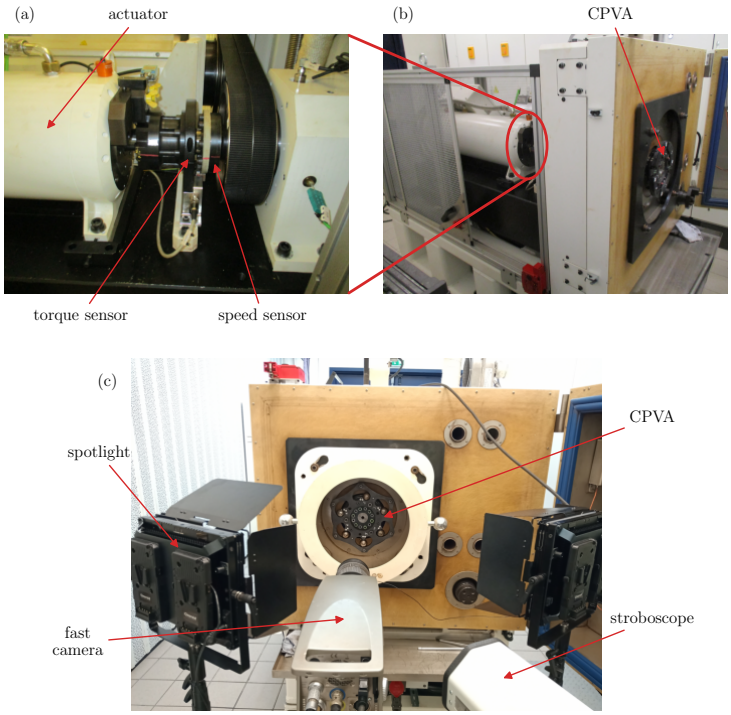

Figure 8: Experimental setup.

by the equivalent inertia $J_{eq} = J_r + J_b + J_a$ in the previous developments. The stroboscope was used to detect when the subharmonic response was activated. Indeed, even though the classical response is unstable around $n = 2n_p$, bifurcations towards the subharmonic regime can take some time [43]. In practice, it took from a few seconds to tens of seconds for the pendulums to start responding. As expected from [43], the bifurcation time was shorter for larger torque levels. This is why the torque sweeps performed in subharmonic regime were always started from large torque levels. All the sweeps were done slowly so that it is fair to assume the response is a succession of steady states. The amplitude of the rotor was retrieved using a sliding discrete Fourier transform. The fast camera was used to have access to the pendulums' motion. The full

procedure is detailed below:

1. The CPVA is centrifugated and an oscillating torque is applied through the actuator.
2. When the steady-state is reached, a movie of the rotating system is recorded using the fast camera.
3. A tracking algorithm is used on the movie to track the position of the six balls and a fixed point of the rotor. This leads to Cartesian coordinates in the Galilean frame $\mathscr{R}_0$.
4. The angular position of the rotor $\vartheta(t)$ is retrieved using the Cartesian coordinates of the rotor's fixed point chosen.
5. The Cartesian coordinates of the pendulums in $\mathscr{R}_r$ (i.e. with respect to the rotor) are computed from the Cartesian coordinates in $\mathscr{R}_0$ and ϑ.
6. The angular position of the pendulums' center of mass with respect to the rotor $\varphi_i(t)$ is computed using their Cartesian coordinates in $\mathscr{R}_r$.
7. The time signals of the curvilinear abscissa $S_i(t)$ are obtained using the relation between S and φ (*cf.* Appendix A.4).
8. The time signals $S_i(t)$ are decomposed into Fourier series to extract the pendulums' amplitudes and phases.
9. As the phase of the torque signal $T(\vartheta)$ is not known, the procedure described above does not allow to retrieve the relative phase ξ_i. Hence, a phase shift was applied to the measured pendulums' phases so that the phase of pendulum 3 matches the phase of the analytical model. Any pendulum could have been chosen as a reference. Nevertheless, it was preferable not to chose the first pendulum nor the fourth one as these sometimes oscillated differently from the others (*cf.* section 5).

5. Experimental results

5.1. Verification of the linear and nonlinear tunings

Figure 9 shows the rotor's amplitude for an order sweep going from $n = 1.4$ to $n = 1.6$ and back to $n = 1.4$. The experimental results fit very well with

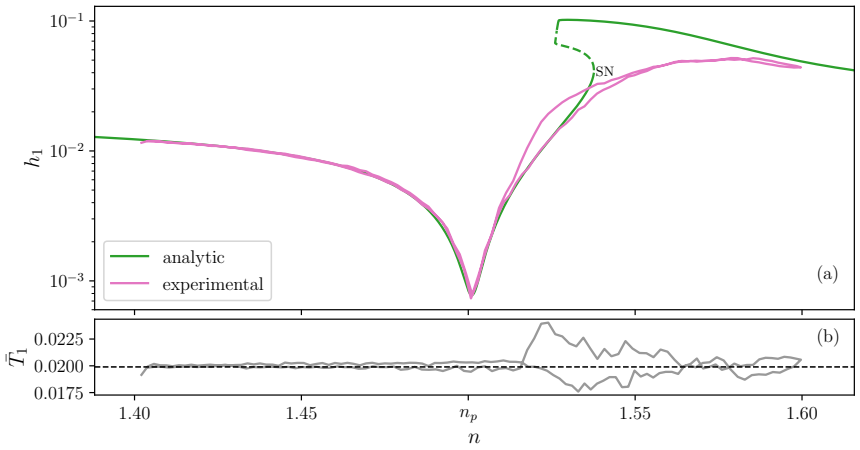

Figure 9: Amplitude response of the rotor (a) as a function of the excitation order. The torque instruction and actual torque are shown as black dashed and grey curves in (b), respectively. Dashed lines indicate unstable solutions and code name "SN" indicates a saddle-node bifurcation. For the same reason as in Fig. 2, no saddle-node bifurcation is represented on the upper branch of the rotor's response. $\bar{T}_1 = 0.020$ and the parameters of the CPVA are given in Tab. 1 except for $\bar{b} = 0.0067$.

the analytical ones, except around the resonance. The difference around the resonance is due to the torque instruction that cannot be enforced because the pendulums reached their cusp. The amplitude at the antiresonance is very low ($h_1 \approx 0.00076$), which highlights the high performance of this CPVA. This is largely due to the architecture that limits the sources of friction, thus leading to a low equivalent viscous damping coefficient. To quantify this performance, one can use the approximation $h_1 \approx \bar{T}_1$ for locked pendulums [9] and compute the gain. At the antiresonance, the gain is only 3.8%, meaning that the rotor's amplitude was divided by a factor 26. This corresponds to an attenuation of 28 [dB].

Figure 10 shows the rotor's amplitude for order sweeps close from the antiresonance at different torque levels. This allows to identify accurately the tuning order n_p and to assess the evolution of the antiresonance order $n_{AR}^{(CL)}$ as $\bar{T}_1$ is increased. For the lowest torque amplitude the antiresonance is located at

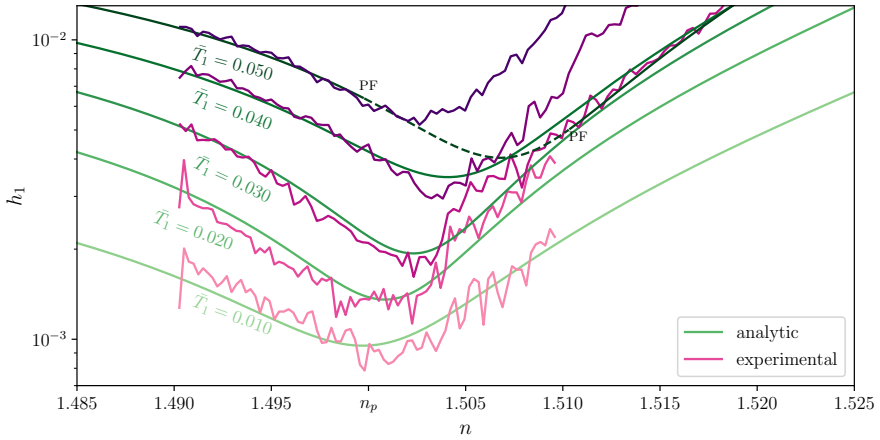

Figure 10: Amplitude response of the rotor as a function of the excitation order for five different torque amplitudes. Dashed lines indicate unstable solutions and code names "PF" refer to pitchfork bifurcations. The parameters of the CPVA are given in Tab. 1 except for $\bar{b} = \{0.017, 0.012, 0.011, 0.014, 0.013\}$ from the lowest to largest $\bar{T}_1$ values, respectively.

n_p, which indicates that the linear tuning of the CPVA is exactly the desired one. As predicted by the analytical model, $n_{AR}^{(CL)}$ shifts to the right as $\bar{T}_1$ is increased. This means that the actual $x_{[4]}$ value, which governs the nonlinear tuning, matches very well the prescribed one. The shifting of $n_{AR}^{(CL)}$ might seem like a problem that could have been using an appropriate design rule [9]. However, the prototype studied here was not design for classical operation but to investigate the subharminic response. Note that the analytical and experimental results for $\bar{T}_1 = 0.05$ do not match well starting from $n \approx 1.502$. This was to be expected as the analytical model predicts a pitchfork bifurcation at $n \approx 1.500$. Hence, the measured response after $n \approx 1.502$ probably corresponds to a non-unison motion of the pendulums. There are two explanations for the difference between the pitchfork bifurcation predicted and the order starting from which the measured response does not match the analytical one. Firstly, a localised pendulums' response can still lead to a rotor's response very close from that at unison [28]. Secondly, it takes time for the bifurcation to actually occur, so it is possible that the steady state was not yet reached between $n = 1.5$ and

$n = 1.502$. Finally, note that the damping coefficients used for each $\bar{T}_1$ value in Fig. 10 differ slightly. This changing value of $\bar{b}$ is likely due to different contact points between the rotor and pendulums. The parts in contact can have slightly different surface conditions, thus explaining why the equivalent viscous damping coefficient varies.

5.2. Torque response near the tuning order

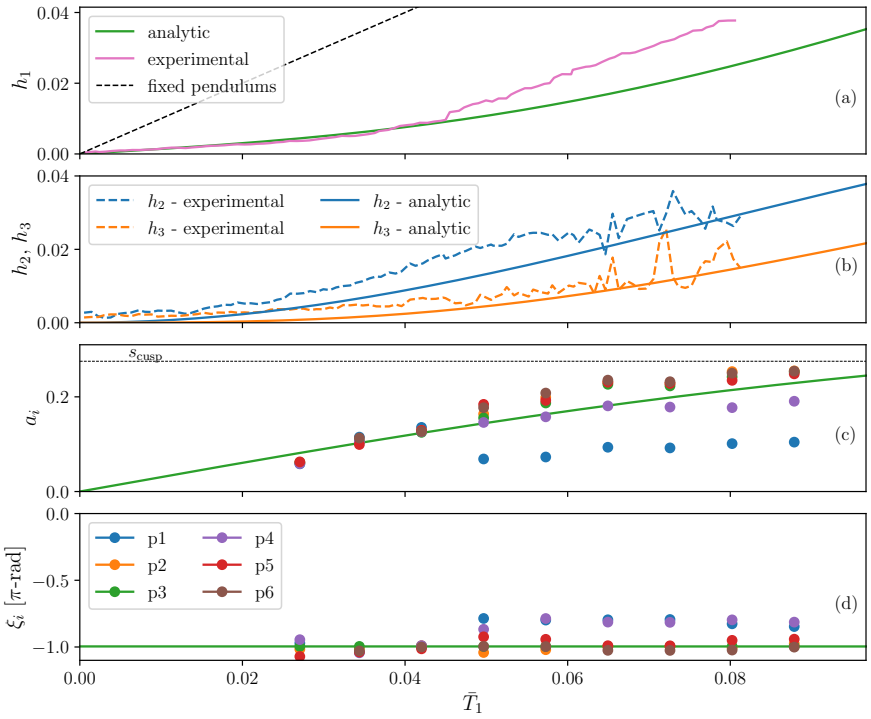

Figure 11: Amplitude of the rotor's first (a) and higher (b) harmonics and amplitude (c) and phase (d) of the pendulums as a function of the torque level $\bar{T}_1$. The response with fixed pendulums is shown in (a) instead of a response without pendulums in order to account for their rotational inertia. In the legend shown in (d), "pj" refers to "pendulum j". The pendulums are given an identification number in Fig. 5. $n = 1.49$ and the parameters of the CPVA are given in Tab. 1 except for $\bar{b} = 0.0027$.

A torque response of the system near the tuning order n_p is shown in Fig. 11.

The measured rotor and pendulums' responses fit well with the analytical model up to $\bar{T}_1 \approx 0.045$. Above this value, the rotor's amplitude is larger than expected, and the pendulums' responses differ from the analtical prediction. This undesired response is assumed to be due to a slipping of the pendulums. This is investigated in details in section 5.3. Note that the torque sweep was performed for $n = 1.49 < n_p$ in order to avoid the unstable zone leading to a localised solution (*cf.* Fig. 3). Fig. 11(a) shows that the pendulums achieve a significant filtration even though $n = 1.49$ is quite far from the antiresonance. This confirms the high performance of this CPVA, as discussed in section 5.1. The performance could have been further improved if the CPVA had been designed for the classical operation [9]. In Fig. 11(b), one can see that the amplitude of the 2^{nd} and 3^{rd} rotor harmonics is clearly not negligible. This confirms one of the major drawbacks of the classical CPVA operation, i.e. the generation of higher harmonics. These two harmonics are not as well predicted as the first one by the analytical model.

5.3. Evaluation of the slipping

The slipping of a pendulum is an undesired behaviour that occurs when $|f_t(\vartheta)| > \psi_a |f_n(\vartheta)|$ where f_t and f_n are the magnitude of the normal and tangential forces at the real contact points I_{rp1} and I_{rp2} (*cf.* Fig. 7(a)). The forces at those two points are identical as there are no out-of-plane motions of a pendulum. ψ_a is the adherence coefficient of a ball on the roller's track. To prevent slipping, one must preserve $|f_t(\vartheta)| < \psi_a |f_n(\vartheta)|$, which limits the maximum pendulums' amplitude and thus limits the torque range of the CPVA. In the following, ψ_a is determined experimentally and a method for approximating the torque at the adherence limit is proposed.

Applying Newton's second law on a CPVA of the form presented in Fig. 7 with a single pendulum and using the relations between the trajectories provided in Appendix A, one can find the dimensionless tangential and normal forces at

the virtual contact point I^*_{rp} to be

$$f^*_t = -\eta\gamma(s)\left(yy' + \gamma(s)(yy's' + y^2s'') + \frac{d\gamma(s)}{ds}y^2s'^2\right), \tag{22a}$$

$$f^*_n = \frac{1}{2}\frac{dx(s)}{ds}yy' + 2\frac{dz(s)}{ds}\left(\frac{dx(s)}{ds}\right)^{-1}y^2s'^2 + y^2z(s) + 2y^2s'. \tag{22b}$$

Neglecting terms of order ϵ in Eqs. (22) and linearising leads to

$$f^*_t = -\eta\alpha^2_{[1]}s'', \tag{23a}$$

$$f^*_n = 1 + 2s', \tag{23b}$$

and it is convenient to define the ratio

$$\psi^* = \left|\frac{f^*_t}{f^*_n}\right| = \left|\frac{\eta\alpha^2_{[1]}s''}{1+2s'}\right|. \tag{24}$$

Substituting the pendulums' classical response (11) in Eq. (24) leads to

$$\psi^{*(\mathrm{CL})} = \left|\frac{\eta\alpha^2_{[1]}n^2a^2\cos(n\vartheta - \xi)}{1 - 2na\sin(n\vartheta - \xi)}\right|. \tag{25}$$

Then, one can show that the maximum value of $\psi^{*(\mathrm{CL})}$ over a period is reached for a critical rotor angle ϑ_c such that

$$\sin(n\vartheta_c - \xi) = 2na \quad \Rightarrow \quad \cos(n\vartheta_c - \xi) = \pm\sqrt{1 - 4n^2a^2}, \tag{26}$$

and the associated maximum value is

$$\psi^{*(\mathrm{CL})}_{\max} = \frac{\eta\alpha^2_{[1]}n^2a}{\sqrt{1-4n^2a^2}}. \tag{27}$$

Because of the v-shaped rotor tracks (*cf.* Fig. 7(a)), the real forces are related to the virtual ones such that

$$f^*_t = 2f_t \quad \Rightarrow \quad f_t = f^*_t/2, \tag{28a}$$

$$f^*_n = 2f_n\cos(\theta_t) \quad \Rightarrow \quad f_n = \frac{f^*_n}{2\cos(\theta_t)}. \tag{28b}$$

Hence, the actual maximum of ratio $\psi = |f_t/f_n|$ over one period is

$$\psi^{(\mathrm{CL})}_{\max} = \cos\theta_t\frac{\eta\alpha^2_{[1]}n^2a}{\sqrt{1-4n^2a^2}}. \tag{29}$$

In the case of a subharmonic response, one would have substituted Eq. (12) instead of Eq. (11) in Eq. (24), leading to

$$\psi_{\max}^{(\mathrm{SH})} = \cos\theta_t \frac{\eta \alpha_{[1]}^2 n^2 a}{4\sqrt{1-n^2a^2}}. \tag{30}$$

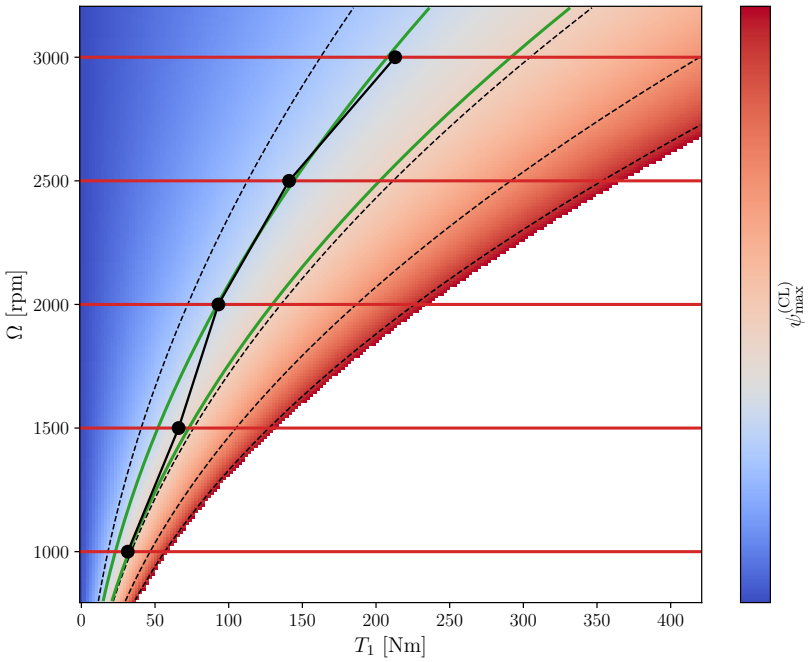

Figure 12: Map representing $\psi_{\max}^{(\mathrm{CL})}$ as a function of the dimensional torque amplitude and mean rotational velocity. This map is represented for $n = 1.49 < n_p$ such that the instabilities leading to a localised response are avoided. Black dashed lines are contour lines and horizontal red lines are constant Ω values. The black dots are experimental measurements of T_1 at the adherence limit. The two green curves indicate the range of ψ_a values obtained experimentally. The white part of the map corresponds to pendulums hitting their cusp. The parameters of the CPVA are given in Tab. 1. The dimensional damping b is kept constant and the nondimensional damping $\bar{b}$ varies with Ω (*cf.* Eq. (1)). For instance, for $\Omega = 1000$ [rpm], $\bar{b} = 0.0068$.

In Fig. 11(a), $\bar{T}_1 = 0.045$ can be interpreted as the torque at the limit of adherence, thus explaining the difference between the analytical and experimental results for $\bar{T}_1 > 0.045$. Similar torque responses were performed for several mean rotational speeds Ω in order to identify the torque at the adherence limit

as a function of Ω. The corresponding results are shown in Appendix B, and they are included in Fig. 12 which is a map representing $\psi_{\max}^{(\mathrm{CL})}$ as a function of Ω and T_1. With the help of this map one can identify the values of $\psi_{\max}^{(\mathrm{CL})}$ for which the system is at the limit of adherence. Those values, corresponding to ψ_a, lie between the two green curves. The five measurements lead to close but not equal values of ψ_a because, from one sweep to the other, the contact points on the pendulums are not the same. Because of wear and the white paint dots visible in Fig. 7, the surface of the balls is not perfectly uniform, thus explaining why a change in the contact points can change ψ_a (this is the same explanation as for the change in damping coefficient in Fig. 10). Despite this slightly changing ψ_a, its dependency on Ω and T_1 fits well with the evolution of $\psi_{\max}^{(\mathrm{CL})}$ represented by the analytical model.

Equating $\psi_{\max}^{(\mathrm{CL})}$ and $\psi_{\max}^{(\mathrm{SH})}$ to ψ_a leads to the amplitudes at the adherence limit

$$a_a^{(\mathrm{CL})} = \frac{\psi_a^2}{\eta^2 \alpha_{[1]}^2 n^4 \cos^2\theta_t + 4n^2\psi_a^2}, \tag{31a}$$

$$a_a^{(\mathrm{SH})} = \frac{16\psi_a^2}{\eta^2 \alpha_{[1]}^2 n^4 \cos^2\theta_t + 16n^2\psi_a^2}. \tag{31b}$$

Then, using the expression of the torque response in the classical [9] and subharmonic [10] operations, one obtains the torque at the adherence limit for both operations, written $T_{1a}^{(\mathrm{CL})}$ and $T_{1a}^{(\mathrm{SH})}$. Computing those torques is important for several reasons. First, the system wears out faster when the pendulums are slipping because of the friction at the contact points. Hence, when doing experiments, one should be careful not to exceed too much $T_{1a}^{(\mathrm{CL})}$ and $T_{1a}^{(\mathrm{SH})}$. Secondly, the desired operation of a system is that without slipping, so the effective torque range is actually limited by $T_{1a}^{(\mathrm{CL})}$ or $T_{1a}^{(\mathrm{SH})}$ (or the apparition of instabilities [10]) rather than pendulums hitting their cusp. To prevent slipping, one must try to enforce $a < a_a^{(\mathrm{CL})}$ (or $a < a_a^{(\mathrm{SH})}$) for as long as possible. This can be done by choosing materials that increase ψ_a. The other solutions are based on limiting the increase in a as $\bar{T}_1$ is increased, exactly as one would do to

avoid pendulums reaching their cusp. This can be done using linear and nonlinear detunings (this might decrease the performance) and using a larger inertia ratio μ (this is limited by the acceptable added mass and expanded shape of the pendulums) [10].

5.4. Subharmonic response

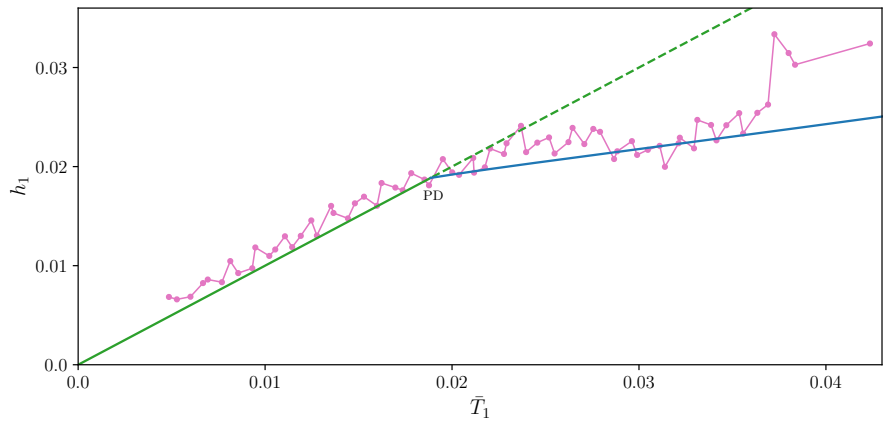

Figure 13: Torque response of the rotor's first harmonic for $n = 2.995$. The analytical subharmonic solution is shown in blue while the trivial response with immobile pendulums is represented in green. Measurements are shown in pink. Dashed lines indicate unstable solutions. PD indicates the period-doubling bifurcation. The parameters of the CPVA are given in Tab. 1 except for $\bar{b} = 0.011$.

A torque response of the rotor in subharmonic operation is shown in Fig. 13. As explained in section 4.2, it is preferable to start sweeps in subharmonic operation at large torques. In the case of Fig. 13, the sweep was started from $\bar{T}_1 \approx 0.042$ and then decreased. This initial torque value was chosen so as to trigger the subharmonic response quickly while minimising the slipping of the pendulums. Using the procedure described in section 5.3 with the values of ψ_a identified in Fig. 12, the torque at the limit of adherence is expected to be $\bar{T}_{1a}^{(\mathrm{SH})} \in [0.031, 0.042]$. Above $\bar{T}_1 = 0.037$, which is within the range of $\bar{T}_{1a}^{(\mathrm{SH})}$, the measurements do not fit with the analytical results because the pendulums are slipping. However, for $\bar{T}_1 \leq 0.037$, the experimental results are well predicted by

the analytical model. Particularly, from $\bar{T}_1 \approx 0.019$ to $\bar{T}_1 \approx 0.037$, one can see the saturation of the rotor's response due to the subharmonic filtration. Note that if the pendulums did not slip they would reach their cusp for $\bar{T}_1 \approx 0.081$, which is much larger than the actual limit due to slipping, $\bar{T}_1 = 0.037$. This highlights the importance of investigating the slipping as ignoring it would result in a large overestimation of the CPVA's torque range.

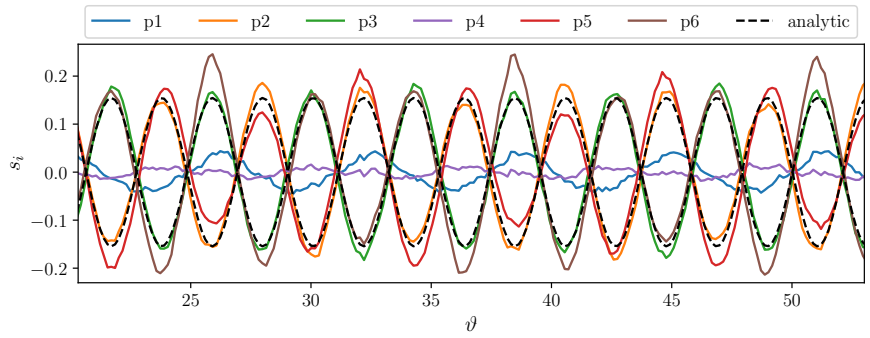

Figure 14: Time signals of the pendulums in subharmonic operation. The analytical results are represented using Eq. (12). "pj" refers to "pendulum j" and the pendulums are given an identification number in Fig. 5. The excitation parameters are $n = 2.995$, $\bar{T}_1 = 0.035$ and the CPVA parameters are given in Tab. 1 except for $\bar{b} = 0.010$.

Figure 14 represents a time record of the pendulums' signals. The experimental signals match well the analytical ones except for pendulums 1 and 4. The reason for this difference is explained hereafter. In order to investigate slipping in more details, markers were initially glued on some pendulums. This was done on every pendulum but the first one. The heat due to the oscillations caused these markers to melt on the tracks and pendulums after a few measurements. The CPVA was then cleaned to pursue the measurements, but still, this slightly modified the system. Pendulum 1 was not affected by these modifications and happened to slip more easily than the others, hence sometimes oscillating differently. This is illustrated in Appendix C for torque responses in classical operation. In the case of subharmonic operation, pendulums oscillate

by pairs [43]. This is why, in Fig. 14, another pendulum (the 4^{th} one) is also oscillating differently. Apart from the difference regarding pendulums 1 and 4 in Fig. 14, one can clearly see the phase-opposition oscillations of the pendulums at order $n/2$ due to the subharmonic response, as predicted by the analytical model.

6. Conclusion

This paper deals with the experimental investigation of a new CPVA design in both classical and subharmonic operations. Some theoretical background developed in former works was summarised. Then, experiments were conducted on a system consisting in a rotor on which roll six identical spherical pendulums distributed evenly. First, order responses around the pendulums' tuning order were performed. They validated the analytical model used in classical operation and evidenced the high performance of this new CPVA design, which was observed to provide an attenuation of 28 [dB]. These order sweeps were performed for several torque amplitudes, which allowed to visualise the shifting of the antiresonance and to verify with accuracy that the linear and nonlinear tunings were the expected ones. Secondly, torque sweeps were performed near the tuning order. They highlighted the main drawback of the classical operation, which is the generation of higher rotor harmonics. These measurements also evidenced a limitation of the CPVA design related to the slipping of the pendulums. This slipping was investigated in depth through experiments and analytical developments. A procedure to determine the adherence coefficient of the pendulums on the rotor's track was proposed. In turn, this allowed to estimate analytically the torque at the adherence limit, which sets the system's torque capacity. Finally, the subharmonic operation was investigated. As predicted by the analytical model, the saturation of the rotor's response was observed experimentally. The recorded time signals of the pendulums matched well with the responses expected from the analytical model, except for two of the pendulums. However, this difference was not attributed to a nonlinear phenomenon

but to small discrepancies amongst the pendulums, mainly due to wear caused by slipping, that sometimes led them to oscillate differently from the other ones. The present study only shows subharmonic responses were they are expected to be stable. It was not possible to investigate flawlessly instabilities leading to localised subharmonic solutions due to the discrepancies between pendulums caused by wear. However, preventing localisation is of utmost importance as it can decrease the filtration performances and reduce the torque capacity. For this reason, future work should aim at validating the unstable zones predicted by the analytical model.

References

[1] B. C. Carter, Improvements in or relating to damping of oscillation-checking devices, 337 466 (1929).

[2] R. R. R. Sarazin, Means adapted to reduce the torsional oscillations of crankshafts, 2 079 226 (1931).

[3] R. Chilton, Pendulum counterweight, 2 112 984 (1935).

[4] A. Renault, Calcul et optimisation d'absorbeurs pendulaires dans une chaîne de traction automobile [Simulation and optimisation of pendular absorbers for automotive powertrain], Ph.D. thesis, ENSAM, Lille, France (2018).

[5] H. Mahé, A. Renault, O. Thomas, Dispositif d'amortissement pendulaire [Pendular damping device], fR 3 055 037 (2018).

[6] H. Mahé, A. Renault, O. Thomas, Dispositif d'amortissement pendulaire [Pendular damping device], fR 3 055 038 (2018).

[7] M. A. Acar, Design and tuning of centrifugal pendulum vibration absorbers, Ph.D. thesis, Michigan State University, Michigan (2017).

[8] J. Mayet, H. Ulbrich, Tautochronic centrifugal pendulum vibration absorbers: General design and analysis, Journal of Sound and Vibration 333 (3) (2014) 711–729. doi:10.1016/j.jsv.2013.09.042.

[9] V. Mahé, A. Renault, A. Grolet, H. Mahé, O. Thomas, On the dynamic stability and efficiency of centrifugal pendulum vibration absorbers with rotating pendulums, Journal of Sound and Vibration 536 (2022) 117157. doi:10.1016/j.jsv.2022.117157.

[10] V. Mahe, A. Renault, A. Grolet, H. Mahe, O. Thomas, Subharmonic centrifugal pendulum vibration absorbers allowing a rotational mobility, Mechanical Systems and Signal Processing 177 (2022) 109125. doi:10.1016/j.ymssp.2022.109125.

[11] M. Cirelli, J. Gregori, P. Valentini, E. Pennestrí, A design chart approach for the tuning of parallel and trapezoidal bifilar centrifugal pendulum, Mechanism and Machine Theory 140 (2019) 711–729. doi:10.1016/j.mechmachtheory.2019.06.030.

[12] M. Cera, M. Cirelli, E. Pennestrì, P. Valentini, The kinematics of curved profiles mating with a caged idle roller - higher-path curvature analysis, Mechanism and Machine Theory 164 (2021) 104414. doi:10.1016/j.mechmachtheory.2021.104414.

[13] J. Mayet, M. A. Acar, S. W. Shaw, Effective and robust rocking centrifugal pendulum vibration absorbers, Journal of Sound and Vibration 527 (2022) 116821. doi:10.1016/j.jsv.2022.116821.

[14] X. Tan, S. Yang, J. Yang, J. Li, Study of dynamics of rotational centrifugal pendulum vibration absorbers based on tautochronic design, Meccanica (2021). doi:10.1007/s11012-021-01340-4.

[15] M. Auleley, O. Thomas, C. Giraud-Audine, H. Mahé, Enhancement of a dynamic vibration absorber by means of an electromagnetic shunt, Journal

of Intelligent Material Systems and Structures 32 (3) (2021) 331–354. doi:10.1177/1045389X20957097.

[16] D. E. Newland, Nonlinear problems of centrifugal pendulum vibration absorbers, in: Mechanisms and Machines, Vol. 1, Varna (Bulgaria), 1965, pp. 39–62.

[17] C.-P. Chao, C.-T. Lee, S. Shaw, Non-unisson dynamics of multiple centrifugal pendulum vibration absorbers, Journal of Sound and Vibration 204 (5) (1997) 769–794. doi:10.1006/jsvi.1997.0960.

[18] C.-P. Chao, S. W. Shaw, C.-T. Lee, Stability of the Unison Response for a Rotating System With Multiple Tautochronic Pendulum Vibration Absorbers, Journal of Applied Mechanics 64 (1) (1997) 149–156. doi:10.1115/1.2787266.

[19] A. Alsuwaiyan, S. W. Shaw, Performance and dynamic stability of general-path centrifugal pendulum vibration absorbers, Journal of Sound and Vibration 252 (5) (2002) 791–815. doi:10.1006/jsvi.2000.3534.

[20] S. W. Shaw, P. M. Schmitz, A. G. Haddow, Tautochronic Vibration Absorbers for Rotating Systems, Journal of Computational and Nonlinear Dynamics 1 (4) (2006) 283–293. doi:10.1115/1.2338652.

[21] S. W. Shaw, B. Geist, Tuning for Performance and Stability in Systems of Nearly Tautochronic Torsional Vibration Absorbers, Journal of Vibration and Acoustics 132 (4) (2010). doi:10.1115/1.4000840.

[22] A. S. Alsuwaiyan, S. W. Shaw, Non-synchronous and Localized Responses of Systems of Identical Centrifugal Pendulum Vibration Absorbers, Arabian Journal for Science and Engineering 39 (12) (2014) 9205–9217. doi:10.1007/s13369-014-1464-1.

[23] J. S. Issa, S. W. Shaw, Synchronous and non-synchronous responses of systems with multiple identical nonlinear vibration absorbers, Journal of

Sound and Vibration 348 (2015) 105–125. doi:10.1016/j.jsv.2015.03.021.

[24] K. Nishimura, T. Ikeda, Y. Harata, Localization phenomena in torsional rotating shaft systems with multiple centrifugal pendulum vibration absorbers, Nonlinear Dynamics 83 (3) (2016) 1705–1726. doi:10.1007/s11071-015-2441-2.

[25] A. Grolet, A. Renault, O. Thomas, Energy Localisation in Periodic Structures: Application to Centrifugal Pendulum Vibration Absorber, in: International Symposium on Transport Phenomena and Dynamics of Rotating Machinery, Maui (Hawaii), 2017.

[26] M. Cirelli, M. Cera, E. Pennestrì, P. P. Valentini, Nonlinear design analysis of centrifugal pendulum vibration absorbers: An intrinsic geometry-based framework, Nonlinear Dynamics 102 (3) (2020) 1297–1318. doi:10.1007/s11071-020-06035-1.

[27] M. Cera, M. Cirelli, E. Pennestrì, P. P. Valentini, Design analysis of torsichrone centrifugal pendulum vibration absorbers, Nonlinear Dynamics 104 (2) (2021) 1023–1041. doi:10.1007/s11071-021-06345-y.

[28] V. Mahe, A. Renault, A. Grolet, O. Thomas, H. Mahe, Dynamic stability of centrifugal pendulum vibration absorbers allowing a rotational mobility, Journal of Sound and Vibration 517 (2022) 116525. doi:10.1016/j.jsv.2021.116525.

[29] A. Renault, O. Thomas, H. Mahé, Numerical antiresonance continuation of structural systems, Mechanical Systems and Signal Processing 116 (2019) 963–984. doi:10.1016/j.ymssp.2018.07.005.

[30] C.-T. Lee, S. W. Shaw, On the counteraction of periodic torques for rotating systems using centrifugally driven vibration absorbers, Journal of Sound and Vibration 191 (5) (1996) 695–719. doi:10.1006/jsvi.1996.0151.

[31] S. W. Shaw, V. Garg, C.-P. Chao, Attenuation of Engine Torsional Vibrations Using Tuned Pendulum Absorbers, in: SAE Noise and Vibration Conference and Exposition, 1997, p. 971961. doi:10.4271/971961.

[32] Y. Ishida, T. Inoue, T. Fukami, M. Ueda, Torsional Vibration Suppression by Roller Type Centrifugal Vibration Absorbers, Journal of Vibration and Acoustics 131 (5) (2009) 051012. doi:10.1115/1.3147124.

[33] B. J. Vidmar, S. W. Shaw, B. F. Feeny, B. K. Geist, Nonlinear Interactions in Systems of Multiple Order Centrifugal Pendulum Vibration Absorbers, Journal of Vibration and Acoustics 135 (6) (Dec. 2013). doi:10.1115/1.4024969.

[34] M. Cirelli, E. Capuano, P. P. Valentini, E. Pennestrì, The tuning conditions for circular, cycloidal and epicycloidal centrifugal pendula: A unified cartesian approach, Mechanism and Machine Theory 150 (2020) 103859. doi:10.1016/j.mechmachtheory.2020.103859.

[35] M. Cera, M. Cirelli, E. Pennestrì, P. P. Valentini, Nonlinear dynamics of torsichrone CPVA with synchroringed form closure constraint, Nonlinear Dynamics (2021). doi:10.1007/s11071-021-06732-5.

[36] C.-T. Lee, S. W. Shaw, Torsional vibration reduction in internal combustion engines using centrifugal pendulums, Tech. rep. (1995).

[37] C.-T. Lee, S. W. Shaw, The non-linear dynamic response of paired centrifugal pendulum vibration absorbers, Journal of Sound and Vibration 203 (5) (1997) 731–743. doi:10.1006/jsvi.1996.0707.

[38] C.-T. Lee, S. W. Shaw, V. T. Coppola, A Subharmonic Vibration Absorber for Rotating Machinery, Journal of Vibration and Acoustics 119 (4) (1997) 590–595. doi:10.1115/1.2889766.

[39] C.-P. Chao, S. W. Shaw, The effects of imperfections on the performance of the subharmonic vibration absorber system, Journal of Sound and Vibration 215 (5) (1998) 1065–1099. doi:10.1006/jsvi.1998.1634.

[40] C.-P. Chao, S. W. Shaw, The dynamic response of multiple pairs of subharmonic torsional vibration absorbers, Journal of Sound and Vibration 231 (2) (2000) 411–431. doi:10.1006/jsvi.1999.2722.

[41] Z. A. Shami, C. Giraud-Audine, O. Thomas, A nonlinear piezoelectric shunt absorber with a 2:1 internal resonance: Theory, Mechanical Systems and Signal Processing 170 (2022) 108768. doi:10.1016/j.ymssp.2021.108768.

[42] Z. A. Shami, C. Giraud-Audine, O. Thomas, A nonlinear piezoelectric shunt absorber with 2:1 internal resonance: Experimental proof of concept, Smart Materials and Structures 31 (3) (2022) 035006. doi:10.1088/1361-665X/ac4ab5.

[43] V. Mahé, A. Renault, A. Grolet, H. Mahe, O. Thomas, On the stability of pairs of subharmonic centrifugal pendulum vibration absorbers allowing a rotational mobility, *Submitted to Nonlinear Dynamics*

.

[44] M. A. Wachs, The Main Rotor Bifilar Absorber and Its Effect on Helicopter Reliability/Maintainability, in: National Aerospace Engineering and Manufacturing Meeting, 1973, p. 730894. doi:10.4271/730894.

[45] M. Albright, T. Crawford, F. Speckhart, Dynamic Testing and Evaluation of the Torsional Vibration Absorber, in: SAE Technical Paper 942519, SAE International, 1994, p. 8. doi:10.4271/942519.

[46] T. M. Nester, Experimental investigation of circular path centrifugal pendulum vibration absorbers.pdf, Master's thesis, Michigan State University, Michigan (2002).

[47] A. G. Haddow, S. W. Shaw, Centrifugal Pendulum Vibration Absorbers: An Experimental and Theoretical Investigation, Nonlinear Dynamics 34 (3/4) (2003) 293–307. doi:10.1023/B:NODY.0000013509.51299.c0.

[48] B. J. Vidmar, Analysis and Design of Multiple Order Centrifugal Pendulum Vibration Absorbers, Ph.D. thesis, American Society of Mechanical Engineers, Chicago, Illinois, USA (Aug. 2012).

[49] B. J. Vidmar, B. F. Feeny, S. W. Shaw, A. G. Haddow, B. K. Geist, N. J. Verhanovitz, The effects of Coulomb friction on the performance of centrifugal pendulum vibration absorbers, Nonlinear Dynamics 69 (1-2) (2012) 589–600. doi:10.1007/s11071-011-0289-7.

[50] J. Mayet, D. Rixen, H. Ulbrich, Experimental Investigation of Centrifugal Pendulum Vibration Absorbers, in: International Conference on Vibration Problems, Lisbon (Portugal), 2013.

[51] R. J. Monroe, S. W. Shaw, Nonlinear Transient Dynamics of Pendulum Torsional Vibration Absorbers—Part II: Experimental Results, Journal of Vibration and Acoustics 135 (1) (Feb. 2013). doi:10.1115/1.4007560.

[52] E. R. Gomez, I. L. Arteaga, L. Kari, Normal-force dependant friction in centrifugal pendulum vibration absorbers: Simulation and experimental investigations, Journal of Sound and Vibration 492 (2021) 115815. doi:10.1016/j.jsv.2020.115815.

[53] E. R. Gomez, J. Sjöstrand, L. Kari, I. L. Arteaga, Torsional vibrations in heavy-truck powertrains with flywheel attached centrifugal pendulum vibration absorbers, Mechanism and Machine Theory 167 (2022) 104547. doi:10.1016/j.mechmachtheory.2021.104547.

[54] V. Manchi, C. Sujatha, Torsional vibration reduction of rotating shafts for multiple orders using centrifugal double pendulum vibration absorber, Applied Acoustics 174 (2021) 107768. doi:10.1016/j.apacoust.2020.107768.

[55] H. H. Denman, Tautochronic bifilar pendulum torsion absorbers for reciprocating engines, Journal of Sound and Vibration 159 (2) (1992) 251–277. doi:10.1016/0022-460X(92)90035-V.

[56] S. W. Shaw, S. Wiggins, Chaotic dynamics of a whirling pendulum, Physica D: Nonlinear Phenomena 31 (2) (1988) 190–211. doi:10.1016/0167-2789(88)90076-0.

[57] L. Shen, B. W. Suter, Bounds for Eigenvalues of Arrowhead Matrices and Their Applications to Hub Matrices and Wireless Communications, EURASIP Journal on Advances in Signal Processing 2009 (1) (2009) 379402. doi:10.1155/2009/379402.

[58] S. W. Shaw, M. A. Acar, B. F. Feeny, B. K. Geist, Modal Properties of Rotating Shafts with Order-Tuned Absorbers, in: J. De Clerck (Ed.), Topics in Modal Analysis I, Volume 7, Springer International Publishing, Cham, 2014, pp. 181–189. doi:10.1007/978-3-319-04753-9_18.

[59] M. Auleley, C. Giraud-Audine, H. Mahé, O. Thomas, Tunable electromagnetic resonant shunt using pulse-width modulation, Journal of Sound and Vibration 500 (2021) 116018. doi:10.1016/j.jsv.2021.116018.

[60] A. H. Nayfeh, Perturbation Methods, Wiley Classics Library, Wiley-VCH, Weinheim, 1973. doi:10.1002/9783527617609.

[61] V. Mahé, A. Renault, A. Grolet, H. Mahé, O. Thomas, Localised response of a centrifugal pendulum vibration absorber, *Submitted to Nonlinear Dynamics*.

[62] D. E. Newland, Developments in the Design of Centrifugal Pendulum Vibration Absorbers, The International Journal of Acoustics and Vibration 25 (2) (2020) 266–277. doi:10.20855/ijav.2020.25.21687.

[63] B. Geist, V. Ramakrishnan, P. Attibele, W. Resh, Precision requirements for the bifilar hinge slots of a centrifugal pendulum vibration absorber, Precision Engineering 52 (2018) 1–14. doi:10.1016/j.precisioneng.2017.08.001.

[64] A. Alsuwaiyan, S. Shaw, Localisation of free vibration modes in systems of nearly identical vibration absorbers, Journal of Sound and Vibration 228 (3) (1999) 703–711. doi:10.1006/jsvi.1999.2470.

[65] A. S. Alsuwaiyan, S. W. Shaw, Steady-State Responses in Systems of Nearly-Identical Torsional Vibration Absorbers, Journal of Vibration and Acoustics 125 (1) (2003) 80–87. doi:10.1115/1.1522420.

Appendix A. Kinematic features of spherical pendulums

Appendix A.1. Kinematic equations

To derive the kinematic equations, one first needs to express the velocity of the virtual contact point I^*_{rp} (*cf.* Fig. 7) as

$$\boldsymbol{v}_{I^*_{rp}\in(p)/(r)} = \boldsymbol{v}_{G\in(p)/(r)} + \dot{\underline{\alpha}}\boldsymbol{z_r} \times \boldsymbol{GI^*_{rp}}, \tag{A.1}$$

where (p) and (r) refer to the pendulum and the rotor, respectively. The model assumes rolling without slipping, so that $\boldsymbol{v}_{I^*_{rp}\in(p)/(r)} = 0$. Hence, Eq. (A.1) can be written as

$$\boldsymbol{v}_{I^*_{rp}\in(p)/(r)} = \left[\dot{S}\cos\beta + r^*_p\dot{\underline{\alpha}}\cos\phi^*\right]\boldsymbol{x_r} + \left[\dot{S}\sin\beta + r^*_p\dot{\underline{\alpha}}\sin\phi^*\right]\boldsymbol{y_r} = \boldsymbol{0}. \tag{A.2}$$

Using the chain rule $\partial(\bullet)/\partial t = \dot{S}\partial(\bullet)/\partial S$, defining $\Gamma(S) = d\underline{\alpha}(S)/dS$, noting that Eq. (A.2) holds $\forall\dot{S}$ and projecting it on $\boldsymbol{x_r}$ and $\boldsymbol{y_r}$ leads to the system of kinematic equations

$$\begin{cases} \cos\beta + r^*_p\Gamma\cos\phi^* = 0, & \text{(A.3a)} \\ \sin\beta + r^*_p\Gamma\sin\phi^* = 0. & \text{(A.3b)} \end{cases}$$

Appendix A.2. Rotation law

Computing the quadratic sum of Eqs. (A.3) leads to

$$r^{*2}_p\Gamma^2 = 1. \tag{A.4}$$

From Fig. 7(b) it is clear that $\underline{\alpha}(S)$ decreases as S increases. Hence, from Eq. (A.4), one can deduce

$$\underline{\alpha}(S) = -\frac{1}{r^*_p}S. \tag{A.5}$$

Appendix A.3. Rolling track of the rotor

The shape of the rolling track $\mathscr{C}_r^*$ is described by the successive positions of I_{rp}^*. As the pendulum is circular with a virtual radius r_p^*, $\mathscr{C}_r^*$ is simply a curve parallel to $\mathscr{C}$ and the distance between $\mathscr{C}_r^*$ and $\mathscr{C}$ is r_p^*. Still, it is useful to have an expression for the Cartesian coordinates of $\mathscr{C}_r^*$. The position of I_{rp}^* is given by

$$\boldsymbol{OI_{rp}^*} = \left[X_G + r_p^* \sin\phi^*\right] \boldsymbol{x_r} + \left[Y_G + r_p^* \cos\phi^*\right] \boldsymbol{y_r}, \tag{A.6}$$

where X_G and Y_G are the known Cartesian coordinates of G (*cf.* Appendix A.4). From the kinematic equations (A.3), one can find

$$\phi^* = \beta, \tag{A.7}$$

where β is a known trajectory function (*cf.* Appendix A.4). Hence, the Cartesian coordinates (X_r^*, Y_r^*) of $\mathscr{C}_r^*$ are

$$X_r^* = X_G + r_p^* \sin\beta, \quad Y_r^* = Y_G - r_p^* \cos\beta. \tag{A.8}$$

Appendix A.4. Trajectory functions

Figure A.15 illustrates the link between the trajectory functions. In this figure, $\mathscr{R}_{uv}(G, \boldsymbol{u}, \boldsymbol{v}, \boldsymbol{z_0})$ is an orthonormal frame such that $\boldsymbol{v}$ points from G to O and $\mathscr{R}_{uv}(G, \boldsymbol{u}, \boldsymbol{v}, \boldsymbol{z_0})$ is an orthonormal such that $\boldsymbol{t}$ and $\boldsymbol{n}$ are vectors tangent and normal to $\mathscr{C}$ at abscissa S, respectively. The shape of $\mathscr{C}$ can be parametrised relatively to the rotor through the path functions $R(S)$ and $\varphi(S)$ such that $\mathscr{C}$: $\{G, \boldsymbol{OG} = -R(S)[-\sin\varphi(S)\boldsymbol{x_r} + \cos\varphi(S)\boldsymbol{y_r}]\}$, where we have used $\boldsymbol{v} = -\sin\varphi(S)\boldsymbol{x_r} + \cos\varphi(S)\boldsymbol{y_r}$. However, in practice, it is convenient to describe a given trajectory using $X(S) = R^2(S)$. We show below how every trajectory function is related to X. For R this is trivial as $R(S) = \sqrt{X(S)}$. From Fig. A.15, as $\boldsymbol{u}$ is orthogonal to $\boldsymbol{v}$, one has

$$dS^2 = dR^2 + (Rd\varphi)^2, \tag{A.9}$$

from what we can write

$$\frac{d\varphi}{dS} = \pm\frac{1}{R}\sqrt{1 - \left(\frac{dR}{dS}\right)^2}. \tag{A.10}$$

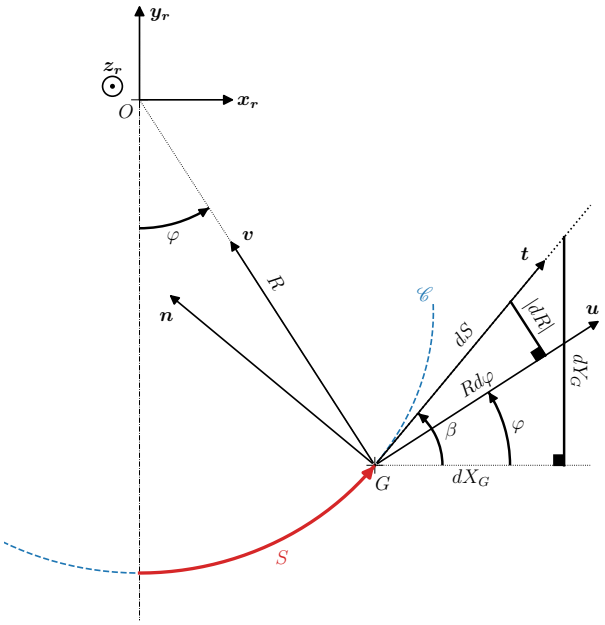

Figure A.15: Illustration of the relations between the trajectory functions.

The + solution is the most useful one as φ typically increases with S. However, for some trajectories (a circle for instance), $d\varphi/dS$ changes sign when $1-(dR/dS)^2$ passes through zero, in which case the $-$ solution should be used. $\varphi(S)$ is obtained by integrating Eq. (A.10), leading to

$$\varphi(S) = \int_0^S \pm\frac{1}{R}\sqrt{1-\left(\frac{dR}{dS'}\right)^2}\,ds', \tag{A.11}$$

where we have assumed $\varphi(S=0)=0$, which is the case in practice. Moreover, the Cartesian coordinates of G in $\mathscr{R}_r$ are simply given by

$$X_G(S) = R\sin\varphi, \quad Y_G(S) = -R\cos\varphi. \tag{A.12}$$

Finally, from Fig. A.15, one has

$$\beta(S) = \arctan\left(\frac{dY_G}{dX_G}\right) = \arctan\left(\frac{dY_G}{dS}\left(\frac{dX_G}{dS}\right)^{-1}\right). \tag{A.13}$$

Appendix A.5. Additional relations between the trajectory functions

If is convenient to introduce the dimensional function $Z(S)$, defined as

$$Z(S) = R(S)^2 \left| \frac{d\varphi(S)}{dS} \right| = \sqrt{X(S) - \frac{1}{4}\left(\frac{dX(S)}{dS}\right)^2}. \tag{A.14}$$

Note that the associated dimensionless function $z(s)$ was defined in Eq. (1). From Fig. A.15, one can deduce

$$\cos(\beta - \varphi) = R\frac{d\varphi}{dS}, \tag{A.15a}$$

$$\sin(\beta - \varphi) = -\frac{dR}{dS}, \tag{A.15b}$$

where the $-$ sign in the expression of $\sin(\beta - \varphi)$ comes from the fact that, in Fig. A.15, $dR < 0$. This way, it is possible to write $\boldsymbol{OG}$ as

$$\boldsymbol{OG} = -R\boldsymbol{v} = \frac{1}{2}\frac{dX(S)}{dS}\boldsymbol{t} - Z(S)\boldsymbol{n}. \tag{A.16}$$

The acceleration of the pendulum with respect to the rotor can be expressed

$$\left.\frac{d^2OG}{dt^2}\right|_{\mathscr{R}_r} = \frac{d}{dt}(\dot{S}\boldsymbol{t}), \quad \text{or} \quad \left.\frac{d^2OG}{dt^2}\right|_{\mathscr{R}_r} = \frac{d^2}{dt^2}(-R\boldsymbol{v}), \tag{A.17}$$

where $\mathscr{R}_r(0, \boldsymbol{x_r}, \boldsymbol{y_r}, \boldsymbol{z_0})$ is a frame attached to the rotor at point O. Then, by identification, one obtains

$$\frac{d\beta}{dS} = -R\frac{d^2R}{dS^2}\frac{d\varphi}{dS} - Z\left(\frac{d\varphi}{dS}\right)^2 + \frac{1}{2}\frac{dX}{dS}\frac{d^2\varphi}{dS^2} + 2\frac{d\varphi}{dS}. \tag{A.18}$$

Finally, using the definition of X (i.e. $X = R^2$) and Eqs. (A.14), (A.10) and (A.9), it is possible to show that

$$\frac{d\beta}{dS} = 2\frac{dZ}{dS}\left(\frac{dX}{dS}\right)^{-1}. \tag{A.19}$$

Appendix B. Measurement of the torque at the adherence limit

Figure B.16 represents torque responses of the rotor for five different mean rotational speeds Ω. Dimensional values T_1 are used as this is more convenient for the representation used in Fig. 12. The identified values of the torque at the adherence limit are given in Tab. B.2.

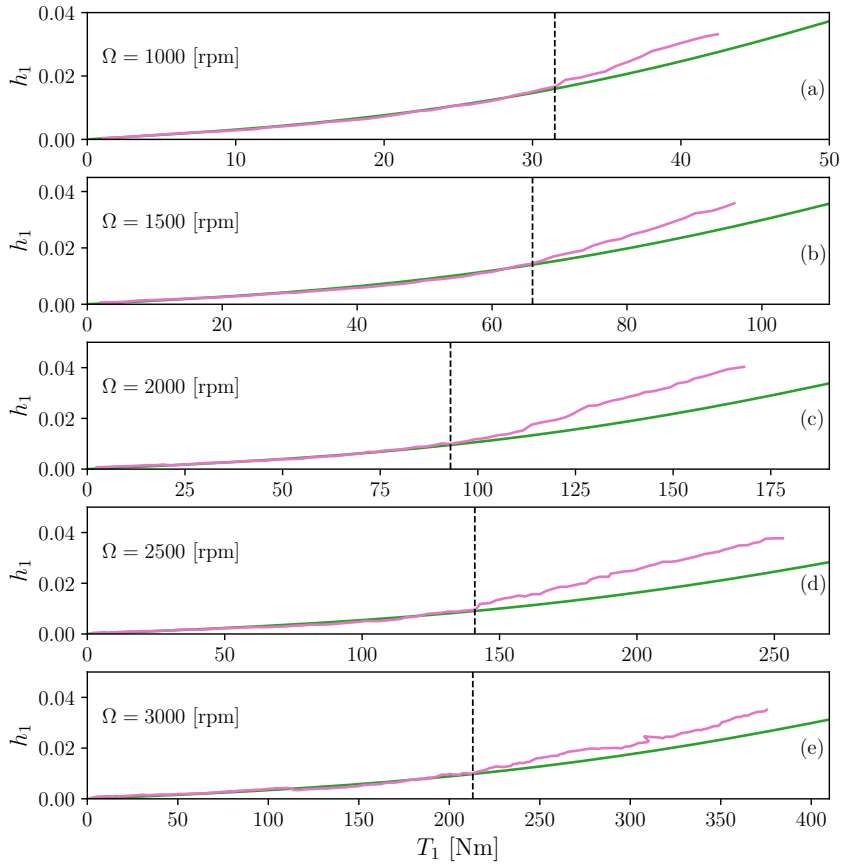

Figure B.16: Torque responses of the rotor's first harmonic for several mean rotational speeds. The green and pink lines correspond to the analytical and experimental results, respectively. The vertical dashed black lines identify the torque at the adherence limit. $n = 1.49$ and the parameters of the CPVA are given in Tab. 1 except for $\bar{b} = \{0.0068, 0.0045, 0.0034, 0.0027, 0.0023\}$ in (a), (b), (c), (d) and (e), respectively. It is normal that different values of $\bar{b}$ are used as they depend on Ω (*cf.* Eq. (1)).

Ω [rpm]	1000	1500	2000	2500	3000
T_1 [Nm]	31.5	66	93	141	213

Table B.2: Torque at the adherence limit as a function of Ω.

Appendix C. Details on the pendulums' responses in classical operation

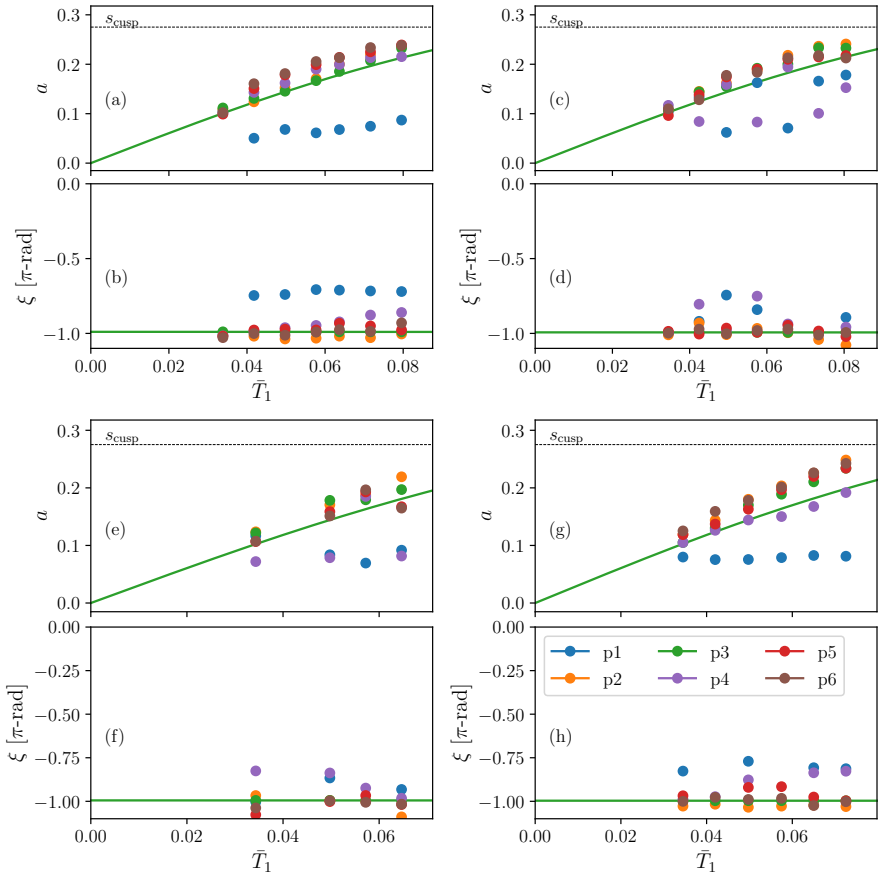

Figure C.17: Torque responses of the pendulums for several mean rotational speeds. The green lines correspond to the analytical results while the coloured circles are experimental data. "pj" refers to "pendulum j" and the pendulums are given an identification number in Fig. 5. $n = 1.49$ and the parameters of the CPVA are given in Tab. 1 except for $\bar{b} = \{0.0068, 0.0045, 0.0034, 0.0023\}$ in (a)-(b), (c)-(d), (e)-(f) and (g)-(h), respectively. It is normal that different values of $\bar{b}$ are used as they depend on Ω (*cf.* Eq. (1))

Figure C.17 represents analytical and experimental torque responses of the pendulums for four different mean rotational speeds Ω. As in section 5.2, the torque responses are measured for $n = 1.49 < n_p$ in order to avoid instabilities.

In Fig. C.17, one can see that pendulum 1, and sometimes also pendulum 4, oscillate differently from the others. However, this is not attributed to nonlinear energy localisation but to small differences amongst the pendulums, causing them to oscillate differently [64, 65]. Regarding pendulum 1, this is likely due to slipping causing premature wear, hence modifying slightly its rolling track and the pendulum itself, as explained in section 5.4. Regarding pendulum 4, no particular reason explaining a different oscillation was observed, so this should be investigated further in the future.

8.2 Subharmonic tuning of a centrifugal pendulum vibration absorber to filter-out order 20

8.2.1 Design proposition

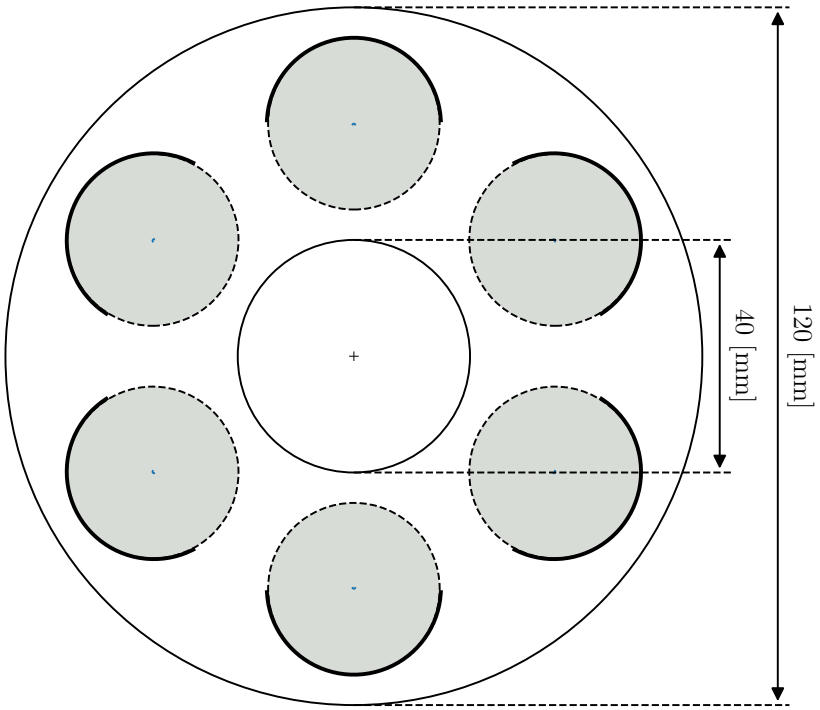

Figure 8.1: Global view of a CPVA tuned at order 10. Only the virtual radius of the pendulums is shown to better see the rolling tracks of the rotor. The parameters are given in Tab. 8.1.

A CPVA with spherical pendulums tuned at order 10 (hence filtering order 20 when in subharmonic operation) is shown in Fig. 8.1. It is made of six pendulums of radius $r_p = 15$ [mm] rolling on v-shaped tracks inclined by an angle of 10°, so the virtual radius of the pendulums is $r_p^* = 14.772$ [mm]. The CPVA occupies a diameter of 120 [mm], which is more reasonable than the prototype investigated previously in this chapter. The pendulums' path are shown in blue in Fig. 8.1. They almost look like dots as they are very small. Indeed, the cusp of these paths is only $S_{\text{cusp}} = 0.282$ [mm].

N	n_p	r_p [mm]	θ_t [°]	R_0
6	10	15	10	40

Table 8.1: Nominal parameters of the CPVA tuned at order 10.

8.2.2 The slipping issue

In this section, we address the slipping issue of the CPVA by evaluating its operating range. This range goes from the torque at the bifurcation, $\bar{T}_1^*$, to the torque at the limit of adherence $\bar{T}_{1a}$. Using the procedure described previously in this chapter, one can compute

$$\bar{T}_{1a}^2 = \left[\frac{c_c - c_p}{n_p \Lambda_m} \frac{100\psi_a^2 \cos^2\theta_t}{n^2(n^2 + 100\psi_a^2\cos^2\theta_t)} - 2(n - 2n_p)\right]^2 + \frac{(2\bar{b})^2}{\Lambda_m^2}. \tag{8.1}$$

Moreover, in the case of a spherical pendulum, one has

$$m = \frac{4\pi r_p^3 \rho}{3}, \quad I = \frac{8\pi r_p^5 \rho}{15}, \quad \alpha_{[1]} = -\frac{R_0}{r_p \cos\theta_t}, \quad \alpha_{[3]} = 0, \tag{8.2}$$

where ρ is the density of the material used. Hence, it is possible to express

$$\Lambda_m = 1 + \frac{2}{5\cos^2\theta_t}, \quad c_c = \mu n_p^4 \left(1 + \frac{2}{5\cos^2\theta_t}\right)^2, \quad c_p = 3x_{[4]}, \quad \bar{b} = \frac{3b}{4\pi r_p^3 \rho \Omega}. \tag{8.3}$$

This way, the torques at the bifurcation and at the adherence limit can be rewritten as

$$\bar{T}_1^{*2} = 4(n - 2n_p)^2 + \frac{9b^2}{\left(2\pi r_p^3 \rho \Omega\right)^2} \frac{1}{\left(1 + \frac{2}{5\cos^2\theta_t}\right)^2}, \tag{8.4a}$$

$$\begin{aligned}\bar{T}_{1a}^2 = &\left[\frac{\mu n_p^4 \left(1 + \frac{2}{5\cos^2\theta_t}\right)^2 - 3x_{[4]}}{\left(1 + \frac{2}{5\cos^2\theta_t}\right) n_p} \frac{100\psi_a^2\cos^2\theta_t}{n^2(n^2 + 100\psi_a^2\cos^2\theta_t)} - 2(n - 2n_p)\right]^2 \\ &+ \frac{9b^2}{\left(2\pi r_p^3 \rho \Omega\right)^2} \frac{1}{\left(1 + \frac{2}{5\cos^2\theta_t}\right)^2}.\end{aligned} \tag{8.4b}$$

The last terms of $\bar{T}_1^{*2}$ and $\bar{T}_{1a}^2$ are the same. Hence, one could increase r_p to lower the torque at the bifurcation, but this would also lower the torque at the adherence limit, leading to no gain on the final operating range. The only two parameters that appear in $\bar{T}_{1a}$ but not $\bar{T}_1^*$ are μ and $x_{[4]}$. $x_{[4]}$ cannot be chosen as desired as it is already constrained by the nonlinear tuning (*cf.* section 8.2.3). Hence, one can try to increase $\bar{T}_{1a}$ without changing $\bar{T}_1^*$ using μ. It is reminded that

$$\mu = \frac{NmR_0^2}{J_r + NI}. \tag{8.5}$$

However, the pendulums' inertia is negligible in front of the rotor's, so μ can only be increased by increasing N, R_0 or m. The best option is to choose the largest acceptable value for r_p (which would significantly increase m, *cf.* Eq. (8.2)) and then adjust N and R_0 to satisfy the design requirements. More details on this optimisation are shown in Appendix E. However, a radius $r_p = 15$ [mm] is already large. The remaining parameters that can be used to improve the torque range are θ_t and n_p. The

evolution of $\bar{T}_1^*$ and $\bar{T}_{1a}$ with these parameters is shown in Fig. 8.2. They both increase when n_p departs from $n/2$ but are not affected much by θ_t. Note that the maps particularly focus on $n_p > n/2$ as it is preferable to use overtuned hardened pendulums to avoid instabilities (*cf.* chapter 7). This is discussed in details in section 8.2.3. The black and dashed grey lines in Fig. 8.2 are contour lines indicating the limit of acceptable designs for $\bar{T}_1^*$ and $\bar{T}_{1a}$, respectively. The designs on the left of the black line in Fig. 8.2(a) allow for a relatively low torque at the bifurcation and those on the right of the grey line permit a satisfactory torque capacity. Unfortunately, the grey line is on the right of the black one, so there are no designs that lead to satisfying values of both $\bar{T}_1^*$ and $\bar{T}1a$. As $\mu = 0.263$ is already large in the case presented here, there are no possibilities to push the grey line further to the left to reach an acceptable design. Hence, it does not seem to be possible to filter-out order 20 torques using subharmonic CPVAs with spherical pendulums because the torque capacity is too limited by the slipping.

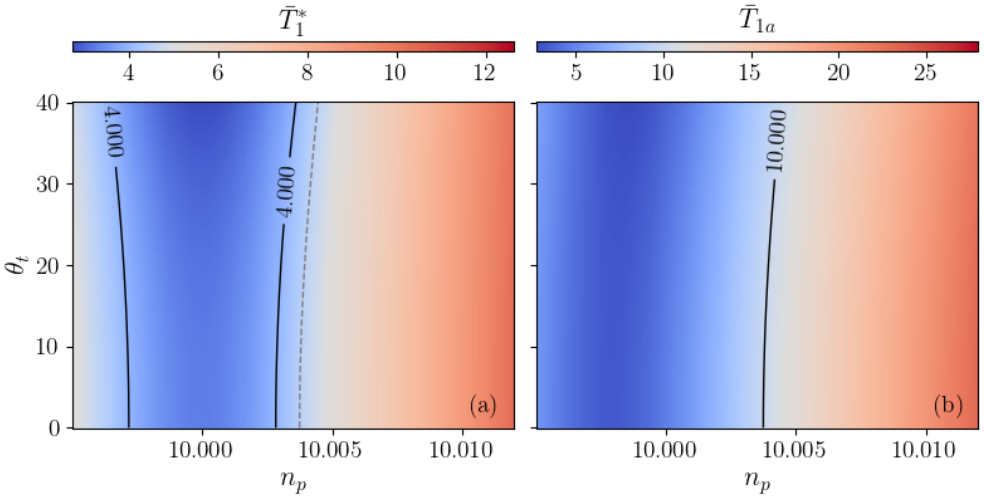

Figure 8.2: Representation of the torques at the bifurcation (a) and the adherence limit (b) as a function of the tuning order and the angle of the v-shaped tracks. The black lines are contour lines and the dashed grey lines in (a) represent the contour line of (b). The parameters are given in Tab. 8.1 except for $J_r = 4$ [g.m^2], $\Omega = 3000$ [rpm], $\rho = 8000$ [kg.m^3], $b = 0.2$ [N.m.s] and $\psi_a = 0.19$.

8.2.3 The nonlinear tuning issue

In chapter 7, it was advised to use overtuned hardened pendulums to avoid the instability leading to a localised response. However, as illustrated in Fig. 8.3(a), this nonlinear tuning requires a thin precision of the path, which can only be done with very small manufacturing tolerances. Indeed, in the case presented here, the difference near the cusp of the two paths is less than 1 [µm]. Nevertheless, the hardened path leads to a response quite different from the epicycloidal one, as shown in Fig. 8.3(b). Increasing $x_{[4]}$ further would reduce the manufacturing tolerance needed but it would also decrease

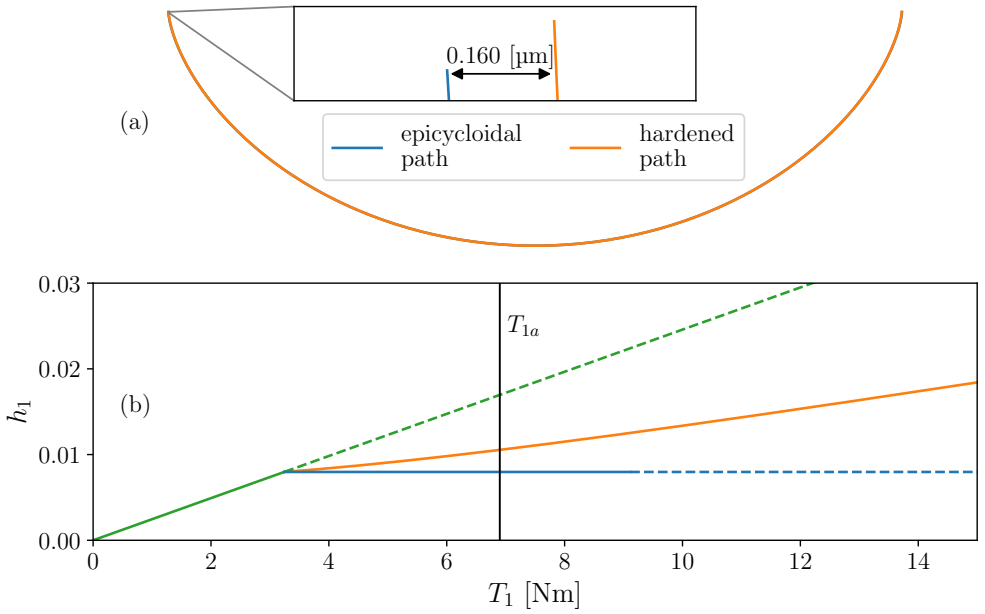

Figure 8.3: Comparison of an epicycloidal and hardened path (a). A torque response at $n = 20$ associated to the two paths is shown in (b). The vertical black line indicates the torque at the adherence limit for the hardened CPVA. The parameters are given in Tab. 8.1 except for $J_r = 4$ [g.m^2], $\Omega = 3000$ [rpm], $\rho = 8000$ [kg.m^3], $b = 0.2$ [N.m.s] and $\psi_a = 0.19$. In addition, $x_{[4]} = -1500$ for the hardened path.

too much the filtering efficiency. Hence, the manufacturing tolerances are too demanding to control the nonlinear tuning of a subharmonic CPVA tuned at order 10.

8.2.4 Discussion

In this section, a subharmonic CPVA was proposed based on the design presented in section 8.1, the subharmonic models developed in chapters 6 and 7, and using the damping and adherence coefficient identified in section 8.1. This resulted in pendulums having very short paths and subjected to slipping at torques lower than the desired torque capacity. It was also not possible to prescribe a nonlinear tuning due to the too demanding manufacturing tolerances. For these reasons, it does not seem possible to use subharmonic CPVAs to filter-out a torque at order 20.

Part IV
The centrifugal double pendulum

Summary of part IV

This summary presents the main results of part IV of this report, which deals with the use of centrifugal double pendulum vibration absorbers (CDPVAs). The automotive industry currently uses centrifugal pendulum vibration absorbers (CPVAs) to reduce the torsional vibrations of thermal powertrains. One of the main aims of this thesis is to adapt pendulum systems to electric vehicles, which are receiving more and more interest due to the increasingly stringent environmental standards. The torsional vibrations to be reduced in electric drivetrains occur at much larger orders than in thermal vehicles (*cf.* section 1.1). Unfortunately, high-order CPVA tuning is difficult to achieve because of demanding manufacturing tolerances (*cf.* section 2.2.3). This is why we are interested in the use of centrifugal double pendulums, whose tuning is more flexible, thus requiring less demanding manufacturing tolerances. In addition, double pendulums generate two rotor antiresonances. The use of the second antiresonance can help filtering high orders.

We list below the main topics dealt with in part IV of the thesis:

- Modelling of a CDPVA;
- Linear characteristics, tuning orders and optimisation of the linear tuning process;
- Nonlinear response of a CDPVA;
- The rotor's antiresonances, whose evolution is not trivial due to nonlinear effects;
- Instabilities of the unison response of a CDPVA.

The development of many of the results discussed in this summary requires elaborate algebraic manipulations, detailed in chapters 9, 10 and 11. Here, we report only the main results of part IV, described from a physical point of view.

Modelling [chap. 10]

The modelling of a CDPVA used in this thesis is presented in Fig. IV.1. It is made of a rotor whose angular position is $\vartheta(t) = \Omega t + \theta(t)$, where Ω is the mean rotational velocity and $\theta(t)$ captures the

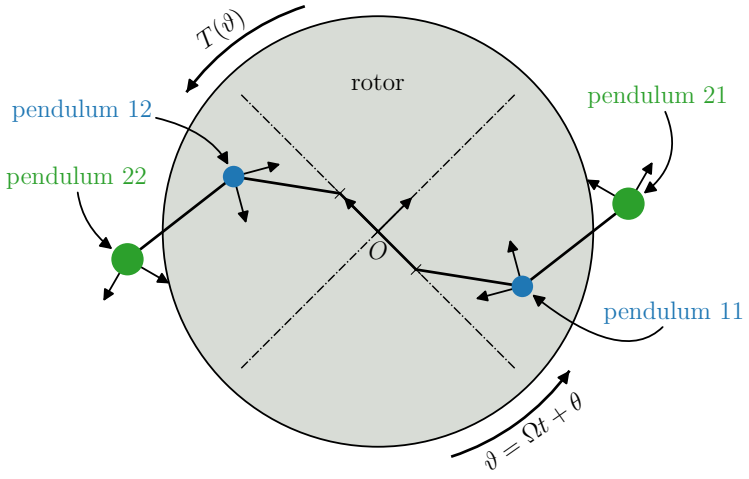

Figure IV.1: Representation of a CDPVA with $N = 2$ double pendulums.

fluctuations of the rotor's angular position. A periodic torque $T(\vartheta) = T_0 + T_1 \cos(n\vartheta)$ is applied on the rotor. T_0 is a constant torque component which balances with the rotor's damping to set its mean rotational velocity Ω. $T_1 \cos(n\vartheta)$ is a fluctuating torque of order n and is the source of the fluctuations $\theta(t)$. Note that in the following, we will write $\bar{T}_1 \cos(n\vartheta)$ the dimensionless fluctuating torque.

$N = 2$ identical double pendulums are attached to the rotor. Pendulums 1 (in blue) and 2 (in green) have different masses, inertias and lengths. The position of the centres of mass of pendulums 1 and 2 can be located relatively to the rotor and pendulums 1, respectively. In addition to their relative translation motion, the pendulums can rotate about their centre of mass. These rotations are indicated by the black frames attached to the pendulums in Fig. IV.1. They are not additional degree-of-freedom as they are functions of the pendulums' positions. Hence, the system has 5 degree-of-freedom: the rotor's position and the relative position of the four pendulums.

Linear features [chap. 10]

When the double pendulums are uncoupled from the rotor, the system has four modes (because the rotor is no longer a degree-of-freedom). They represent two phase-opposition and two unison motions of the double pendulums. The first phase-opposition and unison modes share the same eigenorder (analogous to an eigenfrequency) n_{p1}. Hence, these modes are degenerated. n_{p1} is the first tuning order of the double pendulums and depends on the system parameters. Similarly, the second phase-opposition and unison modes share the same eigenorder n_{p2} and they are degenerated.

When the double pendulums are coupled to the rotor, the CDPVA possesses five modes, rep-

resented in Fig. IV.2. Mode 0 is a rigid body mode for which the pendulums are immobile. The phase-opposition modes correspond to a phase-opposition motion of the two double pendulums and the rotor is a node of these modes. Their eigenorders are the tunings orders of the CDPVA. The unison modes represent a unison motion of the double pendulums, and (for reasonable parameters) at least one of the pendulums oscillates in phase-opposition with the rotor. Their eigenorders are slightly larger than the tuning orders.

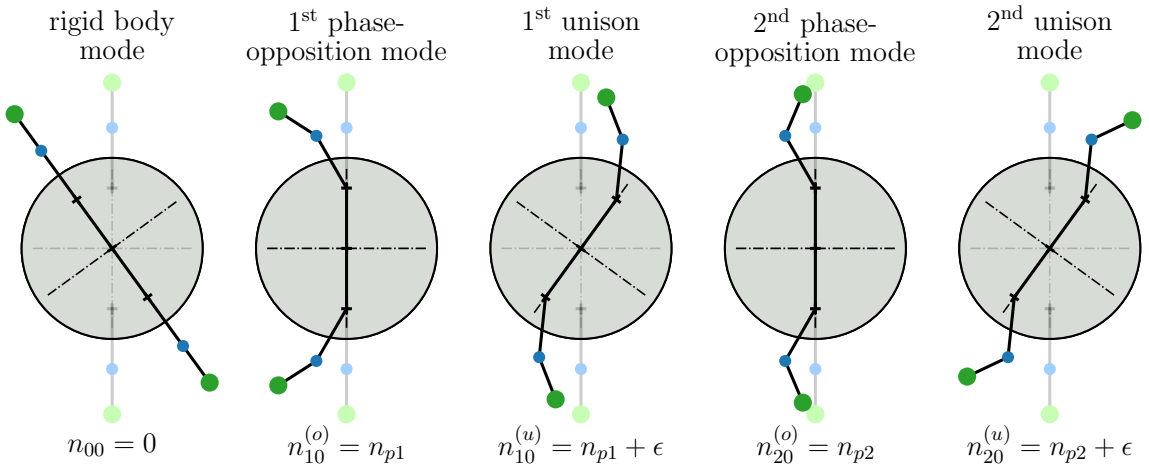

Figure IV.2: Modes of a CDPVA made of $N = 2$ double pendulums. ϵ is a small parameter indicating that the eigenorder of unison modes is slightly larger than the tuning orders. The rotation of the pendulums about their centre of mass is not represented in this figure.

The response of the CDPVA when a torque is applied on the rotor is shown in Fig. IV.3. One can see the two antiresonances generated by the double pendulums on the rotor in Fig. IV.3(a). They are located at the tuning orders n_{p1} and n_{p2}. Fig. IV.3(b) shows that the double pendulums respond only on the unison modes. This was expected because they are not affected by the rigid body mode, and the rotor is a node of the phase-opposition modes, so these are not excited by the external torque.

The choice of the tuning orders is crucial as it controls the locus of the rotor's antiresonances. However, it is not an easy task to find the CDPVA parameters that lead to the desired values of n_{p1} and n_{p2} while achieving satisfactory filtering efficiency. An original procedure is proposed in chapter 9 to facilitate this linear tuning process.

In this section we presented only the linear features of CDPVAs. However, these systems are subjected to nonlinearities of different sources: nonlinear coupling between the pendulums and the rotor, nonlinear coupling between the two pendulums of a double pendulum, pendulums' path and rotation nonlinearities. The nonlinear behaviour of CDPVAs is discussed thereafter.

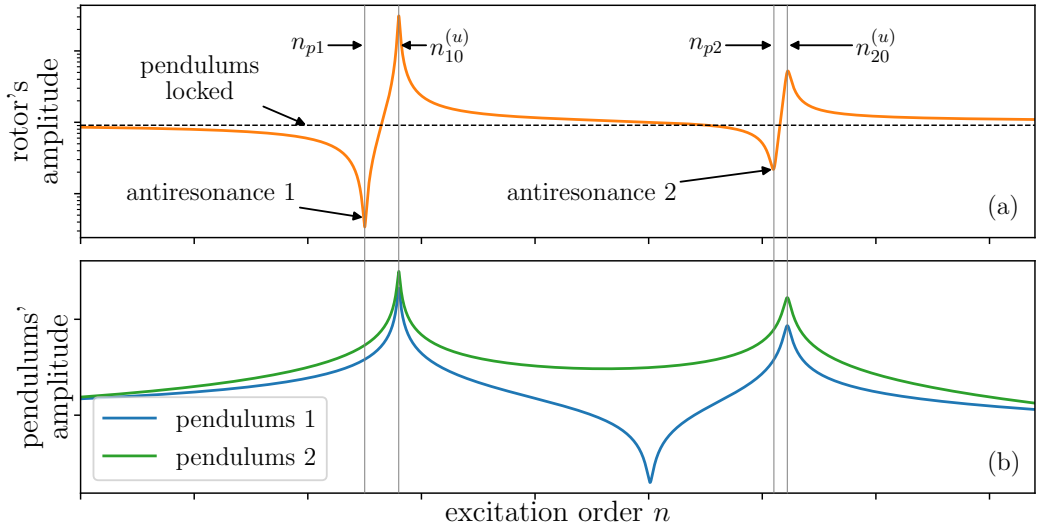

Figure IV.3: Linear response of a CDPVA showing the amplitude of the rotor's acceleration (a) and the pendulums' motion (b). The dashed black line in (a) corresponds to the rotor's response with fixed pendulums.

Stability of the unison response and performance [chap. 9, 10]

In practice, the CDPVA is to operate either at $n \approx n_{p1}$ or $n \approx n_{p2}$. In the first case, the resonance of the second unison mode is typically far (*cf.* Fig. IV.3), so its contribution can be neglected. Similarly, when $n \approx n_{p2}$, the contribution of the first unison mode is negligible. Note that these approximations hold only if there are no internal resonances between the two unison modes (i.e. n_{p2} is not close from an integer multiple of n_{p1}, *cf.* chapter 9). In addition, we explained previously that the rotor is a node of the phase-opposition modes, so they do not contribute to the linear response (*cf.* Fig. IV.3). Hence, it is fair to study the nonlinear response of a CDPVA assuming the pendulums respond only on one of the unison modes.

Figure IV.4 represents a typical CDPVA response around the first tuning order n_{p1}. The nonlinear response around n_{p2} is not discussed in this summary as it presents the same features as the one around n_{p1}. In Fig. IV.4(a)-(b), one can see the strong bending of the response to the left, showing the softening behaviour of the 1$^{\text{st}}$ unison mode. Because of this bending, there are saddle-node (SN) bifurcations at the intersections of the response with the blue instability zone. When sweeping in the order n, a jump occurs at the SN bifurcations (*cf.* section 2.5.1.1). This causes the pendulums to no longer act as absorbers but as amplifiers, which is very detrimental to the CDPVA efficiency. Hence, one should try to avoid these instabilities.

There is another instability zone (red area) represented in Fig. IV.4(a)-(b). This one is related to a perturbation of the unison solution by the 1$^{\text{st}}$ phase-opposition mode. This contribution of

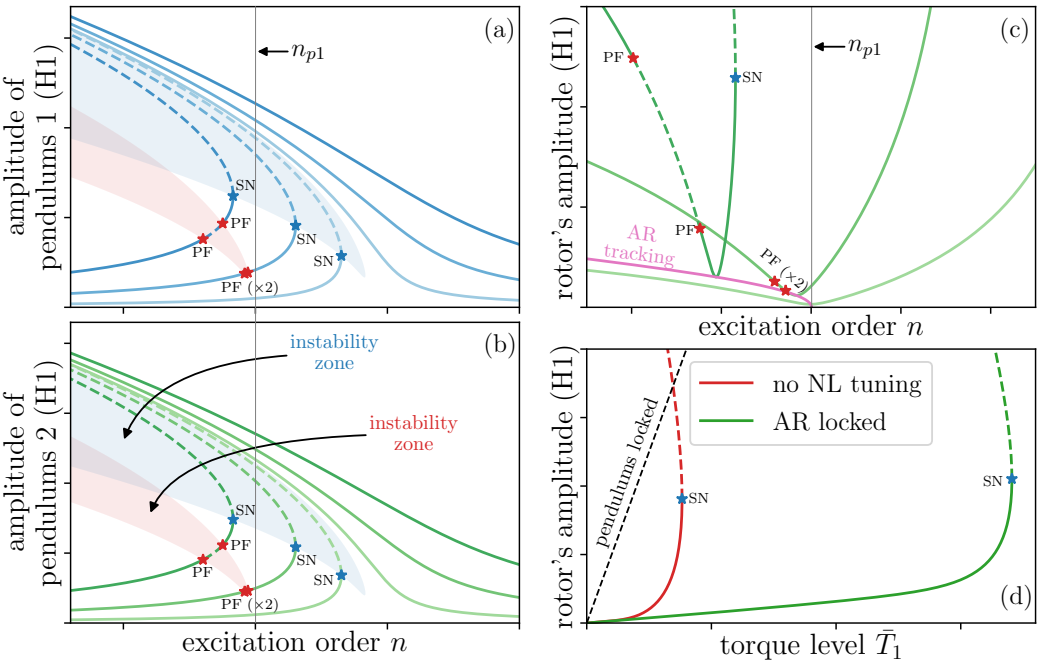

Figure IV.4: Response of the pendulums (a)-(b) and rotor (c) of a CDPVA around the first rotor antiresonance for three different forcing levels. Dashed lines indicate unstable solutions. The red and blue stars indicate pitchfork (PF) and saddle-node (SN) bifurcations, respectively. The red and blue areas are instability zones related to localisation and jumps of the response, respectively. The pink curve in (c) represents the locus of the antiresonance as the torque level is varied. (d) shows the amplitude of the rotor of two different CDPVAs as a function of the forcing and for the excitation order $n = n_{p1}$.

the phase-opposition mode is possible because it is in 1:1 internal resonance with the unison mode (*cf.* Fig. IV.2), so they can exchange energy. The contribution of the phase-opposition mode (not represented in Fig. IV.4) starts at the pitchfork (PF) bifurcations, located at the intersection of the response with the red instability zone. It leads to a coupled-mode solution, causing the response of the double pendulums to be localised, which means that they oscillate with different amplitudes (*cf.* chapter 10). Thus, because of localisation, some pendulums might oscillate with an amplitude much larger than expected. However, in real systems, the amplitude of motion is limited due to space requirements. This is why an original design guideline is proposed in chapter 10 to avoid these instabilities. Note that even though the CDPVA investigated contains only two double pendulums (*cf.* Fig. IV.1), the design guideline derived holds for any number of double pendulums (*cf.* chapter 10).

Figure IV.4(c) shows a zoom of the rotor's response around its first antiresonance. Because of the strong softening behaviour of the unison mode, the antiresonance shifts to the left as the forcing level is increased. This is detrimental for the filtering efficiency, because in practice the excitation order n

is fixed, and the designer chooses $n_{p1} = n$ for the rotor to be excited on its antiresonance. However, if this antiresonance shifts, the rotor is no longer excited on the minimum of its response, leading to a significant increase of its vibration level. The shifting of the antiresonance as the torque level is increased is represented by the pink curve, obtained through an original analytical antiresonance tracking procedure (*cf.* chapter 9). A design guideline preventing this shifting is proposed in chapter 9 and discussed thereafter.

The response of the rotor of two different CDPVAs is shown in Fig. IV.4(d) as a function of the forcing level and for an excitation order n equal to their first tuning order n_{p1}. The first rotor (red) corresponds to the CDPVA represented in Fig. IV.4(a)-(c), which exhibits a strong softening behaviour. The second rotor (green) is associated to a CDPVA tuned to lock the antiresonance at n_{p1} so that it does not shift as the forcing increases. The nonlinear CDPVA tuning proposed in chapters 9 and 10 is achieved through the appropriate choice of the pendulums' rotation law about heir centre of mass. The guideline to lock the antiresonance was obtained through the antiresonance tracking procedure illustrated in Fig. IV.4(c). It is extremely beneficial to vibration reduction as it lowers the rotor's amplitude and pushes the SN bifurcation to large torque levels. The rotor's amplitude increases significantly at large torque levels because the approximations used to derive the antiresonance locking guideline are less accurate at large pendulums' amplitudes.

Experimental investigation of a centrifugal double pendulum [chap. 11]

The theoretical results obtained in this thesis are based on very general CDPVA models. This way, these results can be used to design any CDPVA architecture. In chapter 11, we focus on a specific architecture, shown in Fig. IV.5. The double pendulums are made of a hollow cylinder (pendulum 1) in which rolls an h-shape cylinder (pendulum 2).

Figure IV.6 presents some of the main results of the tests conducted on the CDPVA prototype shown in Fig. IV.5. Order sweeps around the first rotor antiresonance are represented in this figure. The comparison of the linear model developed in chapter 9 with the experimental data in Fig. IV.6(a) allows to verify the proper linear tuning of the CDPVA. Note that the viscous damping coefficients identified are larger than expected. This causes the antiresonance order to be slightly lower than n_{p1} and is detrimental to an efficient vibration reduction. In Fig. IV.6(b), one can see that the nonlinear model developed in chapter 9 describes relatively well the shifting of the antiresonance as the torque level is increased. The significant discrepancies around the resonance might be due to the slipping of the pendulums, but this assumption remains to be verified. Unfortunately, it was not possible to observe the second rotor antiresonance due to limitations of the experimental set-up (*cf.* chapter 11).

A CDPVA prototype tuned at order 20 is proposed in chapter 11. The linear tuning appears feasible

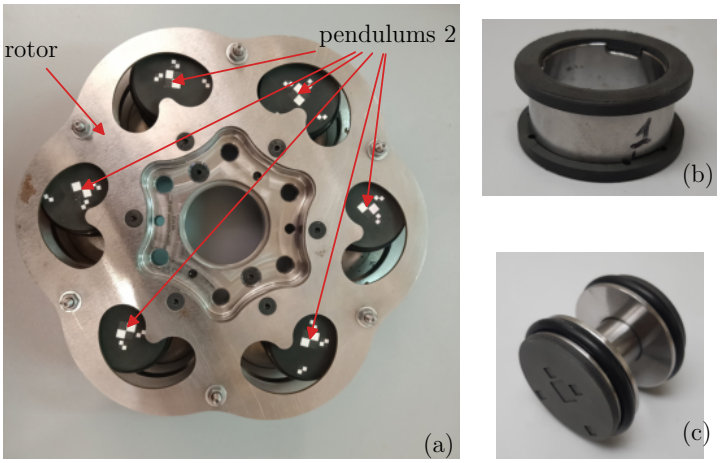

Figure IV.5: Prototype of a CDPVA with cylindrical double pendulums (a). Pendulums 1 (b) are hollow cylinders and pendulums 2 (c) are made of a small-radius cylinder linked to two larger cylinder, giving it an h-shape. In (a), pendulums 1 are hidden behind pendulums 2.

in practice, but the current design has other limitations. Indeed, with constant length pendulums, it is not possible to control the nonlinear tuning of this CDPVA. To remedy this, the pendulums should follow non-circular paths, as is the case for CPVAs (*cf.* section 2.1.3). This is left for future work, and one will have to ensure that the paths achieving the desired nonlinear tuning do not require too demanding manufacturing tolerances. The slipping of the pendulums was not investigated in chapter 11. It was seen to be a limitation of some CPVA designs (*cf.* chapter 8) and is also a concern for the CDPVA architecture shown in Fig. IV.5. Finally, the experimental identification of large damping coefficients questions the performance of this CDPVA architecture.

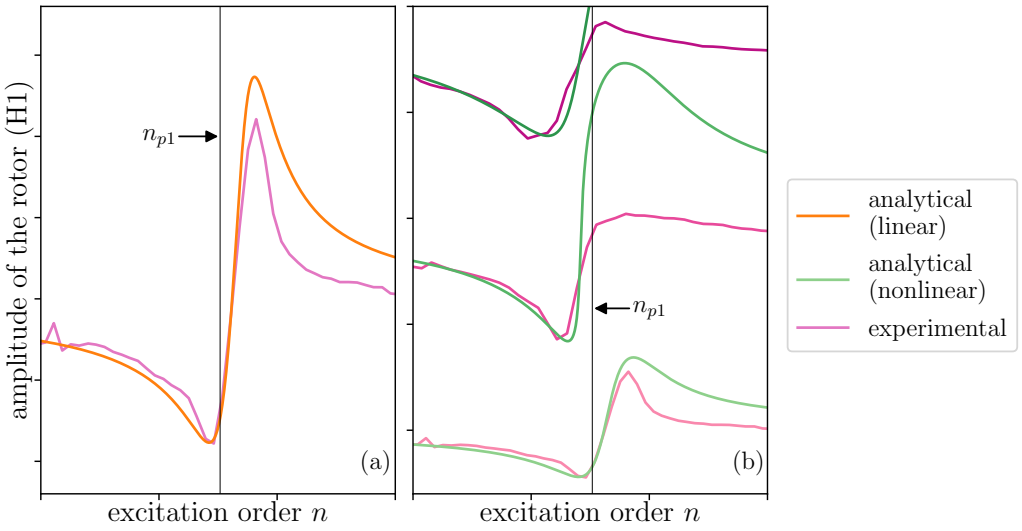

Figure IV.6: Response of the rotor around its first antiresonance in the linear (a) and nonlinear (b) regimes. Three different torque levels are represented in (b). The darker the line the larger the associated torque level.

Chapter 9

The unison response of centrifugal double pendulums

This chapter is made of a paper that is about to be submitted to the *Journal of Sound and Vibration* [155]. It focuses on the linear and nonlinear responses of a centrifugal double pendulum vibration absorber (CDPVA) with the aim to provide methods and guidelines to accelerate the tuning process and to improve the efficiency of the system.

The context of this study, described in section 1, repeats information from chapters 1 and 2. Hence, the reader might want to skip this section if he already read these chapters.

The novelty of the article starts in section 2, where the modelling of a CDPVA is detailed. Then, a linear analysis is led in section 3. The two tuning orders of the system are computed and the forced response is described. It has the particularity of presenting two rotor antiresonances. In addition, a method to efficiently design a CDPVA using performance indicators is proposed. The nonlinear response and stability of a CDPVA equipped with a single double pendulum is derived in section 4. It starts with a simplification of the equations of motion similar to the one presented in section 2.3.2 for a centrifugal pendulum, but in the present case it is adapted to double pendulums. Then, we assume a response on a single mode and we compute its response and stability using the method of multiple scales (*cf.* section 2.5.2.1). The results are applied to case studies in section 5 and verified through comparisons with numerical resolutions of the system's dynamics. A design guideline maximising the performance through the use of a nonlinear tuning locking one of the rotor's antiresonances is proposed.

Unison response of a centrifugal double pendulum vibration absorber

V. Mahé[a,b], A. Renault[b], A. Grolet[a], H. Mahé[b], O. Thomas[a]

[a] *Arts et Metiers Institute of Technology, LISPEN, HESAM Université, F-59000 Lille, France*
[b] *Valeo Transmissions, Centre d'Étude des Produits Nouveaux, Espace Industriel Nord, Route de Poulainville, 80009 Amiens Cedex 1, France*

Abstract

Centrifugal double pendulum vibration absorbers (CDPVAs) can be used to reduce torsional vibrations of rotating machines. These passive devices are made of several double pendulums oscillating relatively to a rotor. This study extends former works on CDPVAs by accounting for the relative rotation of the pendulums with respect to the rotor. First, the linear eigenmodes of the system are computed and an efficient design procedure based on the linear response is proposed. Then, the nonlinear behaviour is assessed through the construction of a dynamical model based on a perturbation method. Of particular interest is the shifting of the operating points, which are of primary importance for vibration reduction. The results obtained allow to propose new design guidelines that maximise the efficiency of the CDPVA. The validity of the model is confirmed through a comparison with a numerical resolution of the system's dynamics.

Keywords: centrifugal double pendulum vibration absorber, nonlinear dynamics, torsional vibration, antiresonance locking, secondary resonances

1. Introduction

In the frame of reducing polluting emissions and fuel consumption of vehicles using thermal engines, automotive manufacturers try to reduce the cylinder

Email addresses: vincent.mahe@ensam.eu (V. Mahé), alexandre.renault@valeo.com (A. Renault), aurelien.grolet@ensam.eu (A. Grolet), herve.mahe@valeo.com (H. Mahé), olivier.thomas@ensam.eu (O. Thomas)

capacity and engine speed of rotation. These evolutions lead to a significant increase of rotation irregularities called acyclisms, mainly due to higher combustion pressure. One of the main characteristics of these reciprocating engines is the linear dependence of the acyclism frequency to the engine speed of rotation. The coefficient of proportionality is the engine order and only depends on the architecture of the engine. During an acceleration phase, the engine sweeps a wide frequency range containing some driveline torsional modes. This situation may lead to significant noise and vibration levels in the passenger compartment and premature wear of the driveline components. This study deals with centrifugal double pendulum vibration absorbers (CDPVAs), which are a mean to reduce the vibrations of driveline components. The principle of operation of CDPVAs is very close from that of centrifugal pendulum vibration absorbers (CPVAs), which have been used for many years to minimise acyclisms of automotive powertrains at the engine order [1–3]. These passive devices consist of oscillating masses (pendulums) moving along paths relative to a primary inertia (rotor), as shown in Fig. 1 in the case of a CDPVA. Because the absorbers (single pendulums for a CPVA, double pendulums for a CDPVA) are driven by the centrifugal acceleration field resulting from the rotation of the system, their natural frequency is proportional to the engine speed of rotation. Hence, CPVAs and CDPVAs act as dynamic vibration absorbers tuned with respect to an order rather than a frequency. This allows the antiresonance frequency to shift linearly with the rotational velocity so that the vibrations are reduced over the whole engine speed range.

The first work dealing with a CDPVA was led by R. W. Zdanowich and T. S. Wilson [4], who focused on a particular architecture made of a pin (pendulum 1) rolling in a circular rotor cavity, and a ring (pendulum 2) whose inner radius rolls on the pin. They showed that these two-degree-of-freedom absorbers have two tuning orders and hence generate two rotor antiresonances. However, with their architecture, the system is to operate on a single mode and they gave design guidelines in the case where the pin's mass is negligible. Another inves-

tigation of a CDPVA was led by J.-G. Duh and M. Wenyong [5] whose aim was to reduce the vibrations caused by helicopter rotor blades, which requires the filtering of two distinct orders [6]. They focused on a design similar to the one proposed in [4] except for a more general shape of the ring, and they showed experimentally its filtering capacity. CDPVAs exhibit nonlinearities of different natures such as geometric nonlinearities due to the large amplitude of motion of the pendulums and their coupling, and inertial nonlinearities, for instance due to Coriolis effects. J.-G. Duh and M. Wenyong [5] performed a nonlinear analysis showing that overtuning their double pendulum design increases its efficiency at large excitation levels due to the softening behaviour. A more recent study of a CDPVA was led by V. Manchi and C. Sujatha [7]. They explained that one of the advantages of a CDPVA over a CPVA is the increased flexibility in the tuning process. Indeed, in the case of a CPVA tuned at high order, the pendulums' path is small so that the manufacturing tolerances are demanding [8]. Moreover, tuning a CPVA at low order requires long pendulums, which might be inconvenient due to space requirements. However, there are much more parameters for the tuning of a CDPVA than for a CPVA, so these issues can be avoided. In addition, the fact that CDPVAs can be used to filter-out several excitation orders can be useful in the case of cylinder deactivation for instance. V. Manchi and C. Sujatha [7] also showed that the modes of a CDPVA are not necessarily softening (in their case, the second mode is hardening), and they observed experimentally the vibration reduction effect with a CDPVA installed on the drive shaft of an automotive vehicle.

The work presented in [7] does not account for the rotational inertia of the pendulums, which contributes to the tuning orders [4, 5] and, for a CPVA, might significantly increase the performance [9–14]. The rotational motion of the pendulums with respect to the rotor is accounted for in many recent studies on CPVAs [15–26] but is yet to be investigated for CDPVAs. It is also known for a long time that the pendulums' path is of primary importance to control the behaviour of a CPVA [27–30]. It is often recommended to use epicycloids

as these are the tautochronic paths of the uncoupled pendulums [30]. However, many studies showed that slightly perturbed epicycloids can help avoiding instabilities [15, 17, 22, 24, 31–35] and increase the performance of the CPVA [14, 25]. Hence, studying the paths of the pendulums of a CDPVA could provide new possibilities to increase the efficiency of the system.

The motivation of this paper is to investigate the linear and nonlinear response of a CDPVA made of a single double pendulum using an analytical perturbation method. To achieve sufficient absorber inertia and to prevent rotor imbalance, one would typically use several double pendulums placed evenly around the axis of rotation of the rotor. However, in the same way as for CPVAs, the expected behaviour is a unison motion of the double pendulums. Hence, to facilitate the investigation of this unison motion, it is convenient to consider a single equivalent pendulum, as shown in Fig. 1. The rotational inertia of the pendulums is accounted for and these pendulums obey general rotation laws. This allows for a representation of double pendulums whose motion is not only a pure translation in the rotor's frame, but is also made of a rotational motion relative to the rotor. Hence, the framework used allows to represent a variety of CDPVAs, including the particular designs studied in [4, 5]. The influence of the pendulums' rotation laws on the linear tuning orders and the nonlinear behaviour is investigated. The pendulums considered in this paper have constant length, so the effect of their path on their response is left for future work. The efficiency of a CDPVA is closely related to the features of the antiresonances generated by the double pendulum on the rotor. If the rotor's amplitude at the antiresonance is low and the antiresonance order does not shift much as the torque amplitude is increased, the CDPVA will significantly reduce the vibrations over the whole torque range. The shifting of the antiresonance order was studied in [27, 36, 37] in the case of a CPVA whose pendulums oscillate along a circular path. In [12–14, 25], more general paths were investigated and guidelines were proposed to lock the antiresonance. A. Renault *et al.* presented a fully numerical antiresonance continuation method and applied it to Euler's

pendulum [38]. In the present paper, an analytical procedure similar to [25] is used to investigate the shifting of the antiresonances of a CDPVA.

This paper is organised as follows. Section 2 describes the modelling of the CDPVA. A linear analysis and a design procedure are presented in 3. The analytical model describing the nonlinear response of a CDPVA is derived in section 4. Case studies and design guidelines allowing to reduce the shifting of one of the antiresonances and to avoid jumps of the response are presented in section 5. This paper ends with a conclusion in section 6.

2. Modelling

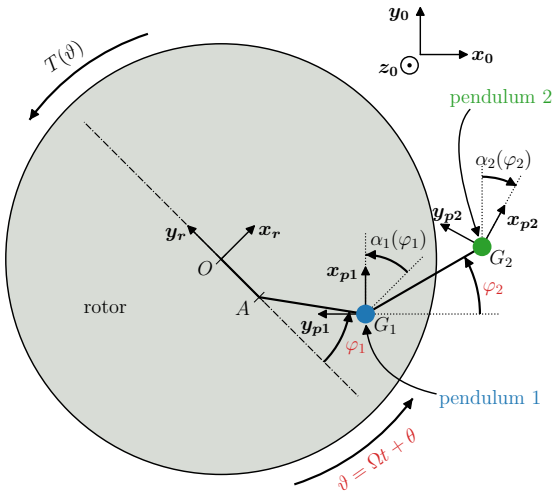

Figure 1: Representation of the system studied. Only one equivalent double pendulum is represented.

The system studied is shown in Fig. 1. A rotor of inertia J_r rotates about its centre O. The frame $\mathscr{R}_r(O, \boldsymbol{x_r}, \boldsymbol{y_r}, \boldsymbol{z_0})$ is attached to the rotor at point O. The rotation of this frame with respect to the Galilean frame $\mathscr{R}_0(O, \boldsymbol{x_0}, \boldsymbol{y_0}, \boldsymbol{z_0})$ is $\vartheta(t) = \Omega t + \theta(t)$ where t is the time, Ω is the mean rotational velocity and $\theta(t)$ corresponds to the fluctuating part of the rotation. A torque $T(\vartheta) = T_0 + T_\theta(\vartheta)$

is applied to the rotor where T_0 is its constant part and $T_\theta(\vartheta)$ is periodic. At equilibrium, $T_0 = b_r\Omega$ where b_r is the linear viscous damping coefficient of the rotor, such that the constant torque balances with the damping to set the mean rotational speed Ω.

A double pendulum is attached to the rotor at point A. The first pendulum is attached at a distance $OA = r$ from the rotor's center. It has length $AG_1 = \ell_1$, mass m_1 and inertia I_1 about its center of mass G_1. If in a real system there were N double pendulums, then m_1 and I_1 would represent the sum of the N masses and inertias of each first pendulums. The position of G_1 with respect to the rotor's frame $\mathscr{R}_r$ is located through angle $\varphi_1(t)$. The frame $\mathscr{R}_{p1}(G_1, \boldsymbol{x_{p1}}, \boldsymbol{y_{p1}}, \boldsymbol{z_0})$ is attached to pendulum 1 at point G_1. Its rotation with respect to the rotor's frame $\mathscr{R}_r$ is $\alpha_1(\varphi_1)$. The second pendulum is attached to the first one at point G_1. It has length $G_1G_2 = \ell_2$, mass m_2 and inertia I_2 about its center of mass G_2. As for pendulum 1, if a real system is made of N double pendulums, then m_2 and I_2 would represent the sum of the N masses and inertias of each second pendulums. The position of G_2 with respect to $\mathscr{R}_{p1}$ is located through angle $\varphi_2(t)$. The frame $\mathscr{R}_{p2}(G_2, \boldsymbol{x_{p2}}, \boldsymbol{y_{p2}}, \boldsymbol{z_0})$ is attached to pendulum 2 at point G_2. Its rotation with respect to $\mathscr{R}_{p1}$ is $\alpha_2(\varphi_2)$. As for the rotor, equivalent linear viscous damping coefficients b_1 and b_2 are used to model the damping between the rotor and pendulum 1 and between pendulum 1 and pendulum 2, respectively.

The dimensional equations of motion are derived in Appendix A.1, but it is more convenient to write them in a dimensionless form. To do so, the following

quantities are introduced:

$$
\begin{aligned}
y = \frac{\dot{\vartheta}}{\Omega} = 1 + \frac{\dot{\theta}}{\Omega}, \quad \mu = \frac{m_1(r+\ell_1)^2 + m_2(r+\ell_1+\ell_2)^2}{J_r + I_1 + I_2}, \\
\eta_1 = \frac{I_1}{m_1\ell_1^2}, \quad \eta_2 = \frac{I_2}{m_2\ell_2^2}, \quad \mu_2 = \frac{m_2}{m_1}, \quad \nu_r = \frac{r}{\ell_1}, \quad \nu_2 = \frac{\ell_2}{\ell_1}, \\
h = \frac{m_1\ell_1^2}{m_1(r+\ell_1^2) + m_2(r+\ell_1+\ell_2)^2} = \frac{1}{(\nu_r+1)^2 + \mu_2(\nu_r+1+\nu_2)^2}, \\
\bar{b}_r = \frac{b_r}{(J_r + I_1 + I_2)\Omega}, \quad \bar{b}_1 = h\frac{b_1}{m_1\ell_1^2\Omega}, \quad \bar{b}_2 = h\frac{b_2}{m_1\ell_1^2\Omega}, \\
\bar{T}(\vartheta) = \bar{T}_0 + \bar{T}_\theta(\vartheta) = \frac{T(\vartheta)}{(J_r + I_1 + I_1)\Omega^2}, \\
\Gamma_1(\varphi_1) = \frac{d\alpha_1(\varphi_1)}{d\varphi_1}, \quad \Gamma_2(\varphi_2) = \frac{d\alpha_2(\varphi_2)}{d\varphi_2},
\end{aligned}
\tag{1}
$$

where $(\dot{\bullet}) = \partial(\bullet)/\partial t$. $y(t)$, $\varphi_1(t)$ and $\varphi_2(t)$ are the 3 degree-of-freedom of the system. y corresponds to the dimensionless rotational velocity of the rotor. μ is the ratio of the pendulums' geometric inertias about O over the rotatory inertia of the whole system about O. η_1 and η_2 are the ratios of the rotational inertia of pendulums 1 and 2 about their center of mass over their geometric inertia about their attachment points, respectively. μ_2 is the mass ratio between pendulums 1 and 2. ν_r and ν_2 are dimensionless lengths associated to r and ℓ_2, respectively. h is the ratio of the geometric inertia of pendulum 1 about A over the geometric inertias of the pendulums about O. $\bar{b}_r$, $\bar{b}_1$ and $\bar{b}_2$ are non-dimensional damping constants and $\bar{T}(\vartheta)$ is the non-dimensional torque applied on the rotor. Γ_1 and Γ_2 are rotation functions. It is convenient to define these rotation functions as polynomials such that

$$
\alpha_1(\varphi_1) = \alpha_{11}\varphi_1 + \alpha_{13}\varphi_1^3 \quad \Rightarrow \quad \Gamma_1(\varphi_1) = \alpha_{11} + 3\alpha_{13}\varphi_1^2, \tag{2a}
$$

$$
\alpha_2(\varphi_2) = \alpha_{21}\varphi_2 + \alpha_{23}\varphi_2^3 \quad \Rightarrow \quad \Gamma_2(\varphi_2) = \alpha_{21} + 3\alpha_{23}\varphi_2^2. \tag{2b}
$$

$\alpha_1(\varphi_1)$ and $\alpha_2(\varphi_2)$ are chosen to be antisymmetric with respect to φ_1 and φ_2 based on the experience that, for practical reasons, rotation functions of CPVAs are antisymmetric. α_{11} and α_{21} are linear rotation coefficients involved in the linear response of the system, while α_{13} and α_{23} will contribute to the nonlinear behaviour of the CDPVA (*cf.* section 4.3).

In order to give $\bar{T}(\vartheta)$ the meaning of an external forcing term, we replace the independent variable t by the rotor's position ϑ [39], which can be seen as a non-dimensional time. Using the chain rule, one can show that

$$\dot{(\bullet)} = \Omega y (\bullet)', \quad \ddot{(\bullet)} = \Omega^2 y y' (\bullet)' + \Omega^2 y^2 (\bullet)'', \tag{3}$$

where $(\bullet)' = \partial(\bullet)/\partial\vartheta$ (the details can be found in [40]). Hence, the dimensionless rotor's acceleration is now $\ddot{\vartheta}/\Omega^2 = \dot{y}/\Omega = yy'$. Using the dimensionless quantities (1) and the chain rule (3), one can write the equations of motion as

$$\boldsymbol{M}(\boldsymbol{q})\boldsymbol{q}'' + \boldsymbol{C}\boldsymbol{q}' + \boldsymbol{K}(\boldsymbol{q})\boldsymbol{q} + \boldsymbol{f}_{\mathrm{nl}}(\boldsymbol{q}, \boldsymbol{q}', \boldsymbol{q}'') = \boldsymbol{f}(t). \tag{4}$$

$\boldsymbol{q} = [y, \varphi_1, \varphi_2]^\intercal$ is the vector containing the degree-of-freedom ($^\intercal$ indicates the transpose). $\boldsymbol{M}(\boldsymbol{q})$, $\boldsymbol{C}$, $\boldsymbol{K}(\boldsymbol{q})$ represent 3×3 mass, damping and stiffness matrices, respectively. $\boldsymbol{f}_{\mathrm{nl}}(\boldsymbol{q}, \boldsymbol{q}', \boldsymbol{q}'')$ and $\boldsymbol{f}(t)$ are vectors containing nonlinear inertial terms and forcing terms, respectively. In the system of three equations generated by Eq. (4), the first, second and third equations govern the motion of y, φ_1 and φ_2, respectively. These three dimensionless equations are given in Appendix A.2.

From now on, it is assumed that the fluctuating torque applied on the rotor contains only one harmonic whose non-dimensional form is $\bar{T}_\theta(\vartheta) = \bar{T}_1 \cos(n\vartheta)$, where n is the excitation order. For a car engine, n corresponds to the number of strikes per revolution of the crankshaft.

3. Linear analysis

This section presents a linear analysis of the CDPVA. First of all, one can use Eq. (3) to show that, at first order, $1 + \theta' \approx y$ and $\theta'' \approx yy' \approx y'$ (the demonstration can be found in [40]). Hence, it is possible to represent the motion of the rotor with position θ instead of velocity y. This way, all the degree-of-freedom of the system are positions, which facilitates the representation of the

mode shapes. Using θ instead of y and the balance between the constant torque and the damping $\bar{b}_r = \bar{T}_0$ (*cf.* section 2), one can linearise Eq. (4), leading to

$$(1+\mu)\theta'' + \mu\Lambda_{c1}\varphi_1'' + \mu\Lambda_{c2}\varphi_2'' + \bar{b}_r\theta' = \bar{T}_1\cos(n\vartheta), \tag{5a}$$

$$\Lambda_{c1}\theta'' + \Lambda_{m1}\varphi_1'' + \Lambda_{c12}\varphi_2'' + k_1\varphi_1 + k_{12}\varphi_2 + \bar{b}_1\varphi_1' = 0, \tag{5b}$$

$$\Lambda_{c2}\theta'' + \Lambda_{c12}\varphi_1'' + \Lambda_{m2}\varphi_2'' + k_{12}\varphi_1 + k_2\varphi_2 + \bar{b}_2\varphi_2' = 0. \tag{5c}$$

Λ_{m1} and Λ_{m2} are constants representing the equivalent mass of pendulums 1 and 2, respectively. Similarly, k_1 and k_2 represent their equivalent stiffness. Λ_{c1} and Λ_{c2} represent the inertial coupling between the pendulums and the rotor. Λ_{c12} and k_{12} represent the inertial and non-inertial couplings between the pendulums. The expression of these constants in terms of the system parameters is given in Appendix B.

3.1. Linear modal analysis

In order to determine the tuning orders of the double pendulum, one needs to compute the eigenorders of the uncoupled system, that is, the system where the rotor spins at a constant speed. In this case, the free, conservative equations associated to Eqs. (5) reduce to

$$\Lambda_{m1}\varphi_1'' + \Lambda_{c12}\varphi_2'' + k_1\varphi_1 + k_{12}\varphi_2 = 0, \tag{6a}$$

$$\Lambda_{c12}\varphi_1'' + \Lambda_{m2}\varphi_2'' + k_{12}\varphi_1 + k_2\varphi_2 = 0. \tag{6b}$$

Solving the eigenvalue problem associated to Eqs. (6) leads to the eigenmodes of the uncoupled system, $(n_{p1}, \boldsymbol{\psi}_{p1})$ and $(n_{p2}, \boldsymbol{\psi}_{p2})$. The two eigenorders[1] and associated eigenvectors are

$$\begin{aligned} n_{p1,2}^2 &= \frac{\Lambda_{m1}k_2 + \Lambda_{m2}k_1 - 2\Lambda_{c12}k_{12}}{2(\Lambda_{m1}\Lambda_{m2} - \Lambda_{c12}^2)} \\ &\mp \frac{\sqrt{4(\Lambda_{c12}k_1 - \Lambda_{m1}k_{12})(\Lambda_{c12}k_2 - \Lambda_{m2}k_{12}) + (\Lambda_{m1}k_2 - \Lambda_{m2}k_1)^2}}{2(\Lambda_{m1}\Lambda_{m2} - \Lambda_{c12}^2)} \end{aligned} \tag{7a}$$

$$\boldsymbol{\psi}_{pi} = [1, \chi_{pi}]^\intercal, \quad \chi_{pi} = \frac{n_{pi}^2\Lambda_{m1} - k_1}{k_{12} - n_{pi}^2\Lambda_{c12}}, \quad i = 1, 2. \tag{7b}$$

[1] Eigenorders can be seen as dimensionless eigenfrequencies.

160 n_{p1} and n_{p2} are the tuning orders of the CDPVA. For reasonable system parameters, one of the uncoupled modes represents an in-phase motion of the pendulums while the other mode represents a phase-opposition motion. Whether the in-phase mode is mode 1 or mode 2 depends on the system parameters.

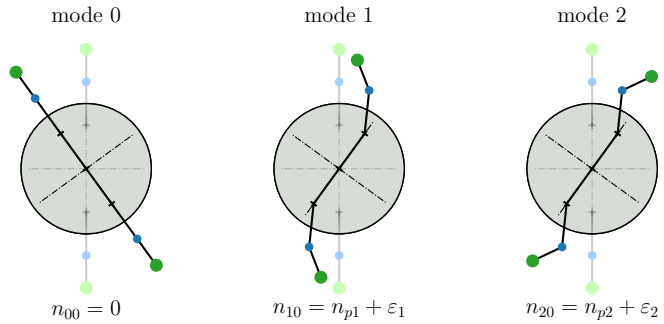

Figure 2: Modes of a CDPVA made of $N = 1$ double pendulum. The rotation of the pendulums about their centre of mass is not represented in this figure. ε_1 and ε_2 indicate that n_{10} and n_{20} are slightly larger than n_{p1} and n_{p2}, respectively.

To compute the eigenmodes of the coupled system, we can first rewrite the free, conservative equations associated to Eqs. (5) such that

$$\theta'' = -\frac{\mu}{1+\mu}\Lambda_{c1}\varphi_1'' - \frac{\mu}{1+\mu}\Lambda_{c2}\varphi_2'', \tag{8a}$$

$$\bar{\Lambda}_{m1}\varphi_1'' + \bar{\Lambda}_{c12}\varphi_2'' + k_1\varphi_1 + k_{12}\varphi_2 = 0, \tag{8b}$$

$$\bar{\Lambda}_{c12}\varphi_1'' + \bar{\Lambda}_{m2}\varphi_2'' + k_{12}\varphi_1 + k_2\varphi_2 = 0, \tag{8c}$$

where we have introduced the constants $\bar{\Lambda}_{m1}$, $\bar{\Lambda}_{m2}$, $\bar{\Lambda}_{c12}$, defined in Appendix B. First of all, it is obvious from Eqs. (8) that the system includes a rigid body mode $(n_{00}, \boldsymbol{\phi}_0)$ with

$$n_{00} = 0, \quad \boldsymbol{\phi}_0 = [1, 0, 0]^\intercal. \tag{9}$$

The pendulums are nodes of this mode. Two reduced eigenmodes $(n_{10}, \boldsymbol{\psi}_1)$ and $(n_{20}, \boldsymbol{\psi}_2)$ can be computed using Eqs. (8b) and (8c), just like for the uncoupled system. The two associated full modes $(n_{10}, \boldsymbol{\phi}_1)$ and $(n_{20}, \boldsymbol{\phi}_2)$, which include

the rotor's component, are obtained using Eq. (8a). This leads to

$$n_{10,20}^2 = \frac{\bar{\Lambda}_{m1}k_2 + \bar{\Lambda}_{m2}k_1 - 2\bar{\Lambda}_{c12}k_{12}}{2(\bar{\Lambda}_{m1}\bar{\Lambda}_{m2} - \bar{\Lambda}_{c12}^2)} \mp \frac{\sqrt{4(\bar{\Lambda}_{c12}k_1 - \bar{\Lambda}_{m1}k_{12})(\bar{\Lambda}_{c12}k_2 - \bar{\Lambda}_{m2}k_{12}) + (\bar{\Lambda}_{m1}k_2 - \bar{\Lambda}_{m2}k_1)^2}}{2(\bar{\Lambda}_{m1}\bar{\Lambda}_{m2} - \bar{\Lambda}_{c12}^2)} \tag{10a}$$

$$\boldsymbol{\phi}_i = [\varrho_i, 1, \chi_i]^\intercal, \quad \chi_i = \frac{n_{i0}^2\bar{\Lambda}_{m1} - k_1}{k_{12} - n_{i0}^2\bar{\Lambda}_{c12}}, \quad \varrho_i = -\frac{\mu(\Lambda_{c1} + \Lambda_{c2}\chi_i)}{1+\mu}, \quad i = 1, 2. \tag{10b}$$

Like for the uncoupled modes, modes 1 and 2 correspond to in-phase and phase-opposition motions of the pendulums. These modes are illustrated in Fig. 2 together with the rigid body mode. For reasonable system parameters, the pendulums are in phase-opposition with the rotor when they respond on the in-phase mode. When they respond on the phase-opposition mode, pendulum 1 or 2 can be in phase-opposition with the rotor, depending on system parameters. In practice, the inertia ratio μ is small. As it tends to zero, the reduced modes 1 and 2 (i.e. modes 1 and 2 without the rotor's component in the modal shapes) tend towards the uncoupled modes 1 and 2, respectively. In other words, the coupled and uncoupled modal shapes are close, and the n_{i0} are close from (but larger than) the n_{pi}.

As explained previously, there are much more parameters available for the tuning of a CDPVA than for a CPVA. Indeed, n_{p1} and n_{p2} depend on ν_r, ν_2, μ_2, η_1, η_2, α_{11}, α_{21}, that is, 7 parameters (this reduces to 4 parameters if the rotational inertia of the pendulums is neglected). For a CPVA, there are 3 tuning parameters if the pendulums' rotation is accounted for, and only 1 parameter otherwise [22]. The evolution of n_{p1} and n_{p2} as a function of ν_2 and μ_2 is displayed in Fig. 3. It is interesting to note that increasing μ_2 decreases n_{p1} but increases n_{p2}. V. Manchi *et al.* suggested to adjust the tuning through iterations on the system's parameters [7]. However, maps as those shown in Fig. 3 would be very useful in the design process as they show how the tuning orders evolve with some of the design parameters. This allows to converge towards a desired order much more efficiently than through manual iterations.

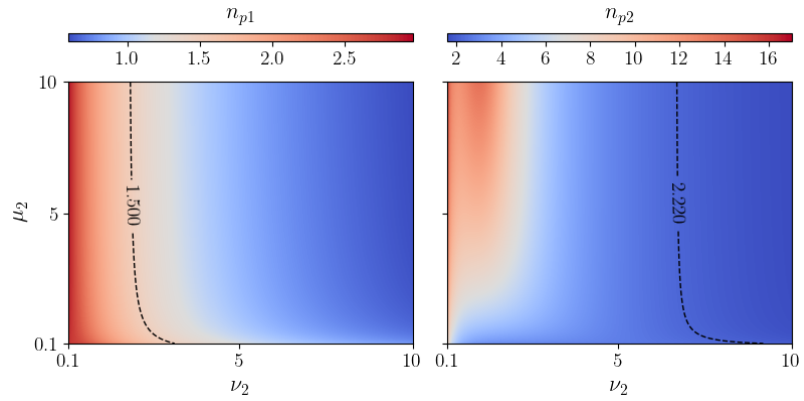

Figure 3: Evolution of the tuning orders as a function of ν_2 and μ_2. The contour lines correspond to the tuning orders of the design given in Tab. 1. The other designs represented have the same parameters except for ν_2 and μ_2, which are varied.

Finally, accounting for the pendulums' rotational inertia is mandatory for an accurate tuning. Indeed, if these inertias were neglected, the tuning orders of the CDPVA described in Tab. 1 would go from 1.500 and 2.220 to 1.732 and 2.576, which is quite different.

μ	η_1	η_2	μ_2	ν_r	ν_2	α_{11}	α_{21}	α_{13}	α_{23}	$\bar{b}_r$	$\bar{b}_1$, $\bar{b}_2$
0.1	2	4	0.1	3.745	1	0.4	0.3	0	0	0.0227	5×10^{-5}

Table 1: Parameters of the CDPVA studied in this section.

3.2. The linear forced response

The linear forced response of a CDPVA can be computed from Eqs. (5), which yields solutions of the form

$$\theta'' = h_1 \cos(n\vartheta - \psi_1), \quad \varphi_1 = a_1 \cos(n\vartheta - \xi_1), \quad \varphi_2 = a_2 \cos(n\vartheta - \xi_2). \quad (11)$$

Such a response is illustrated in Fig. 4. Because the CDPVA has two tuning orders, there are two antiresonances on the rotor's forced response, $n_{AR1} = n_{p1}$ and $n_{AR2} = n_{p2}$ (the demonstration is provided in Appendix C). Hence, if a torque of order n is applied to the rotor, one can choose $n_{p1} \approx n$ or $n_{p2} \approx n$

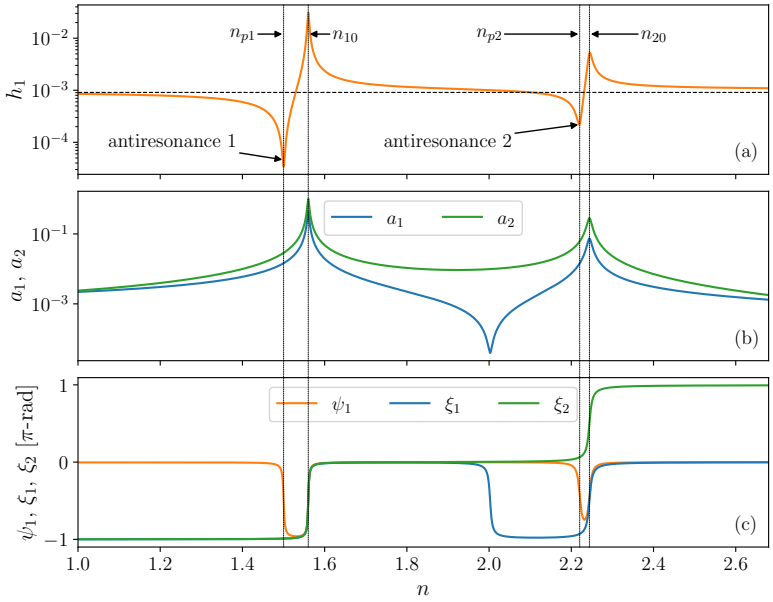

Figure 4: Linear response of a CDPVA showing the amplitude response of the rotor (a) and pendulums (b) and the phase response of the rotor and pendulums (c). The dashed black line in (a) corresponds to the rotor's response with fixed pendulums. $\bar{T}_1 = 0.001$ and the system parameters are given in Tab. 1.

to significantly reduce the vibration level. According to linear theory, CDPVAs can also be used to filter-out a torque containing order n and $2n$ harmonics by choosing a design such that $n_{p1} \approx n$ and $n_{p2} \approx 2n_{p1}$. This possibility is interesting but is limited by nonlinear effects (*cf.* section 5.1).

The CDPVA shown in Fig. 4 can operate efficiently at both n_{p1} and n_{p2} as both antiresonances are quite pronounced. Indeed, they reduce significantly the vibration level compared to the configuration with locked pendulums (black dashed line). Moreover, n_{p1} and n_{p2} are not too close from n_{10} and n_{20}, which is the sign of a robust design. Indeed, if an antiresonance is too close from a resonance, a very small undesired mistuning could lead to a dramatic vibration level of the rotor. This is discussed further in section 3.3.

Note that in practice, the excitation order is fixed such that n is a constant

and the CDPVA is tuned close to n. Mistuning can exist, either intentionally or because of material imperfections. Varying the excitation order, as in Fig. 4, is similar to introducing mistuning and is therefore relevant for studying the effect of mistuning on the system's response [35].

3.3. Linear performance indicators

As explained in the previous section, the linear performance of a CDPVA depends on whether its antiresonances are pronounced and far from the resonances. These two indicators can be quantified using the criteria Δn_i and G_i, $i = 1, 2$, defined as

$$\Delta n_i = n_i - n_{pi}, \tag{12a}$$

$$G_i = \left. \frac{h_1}{h_{1f}} \right|_{n=n_{pi}}, \tag{12b}$$

where h_{1f} is the amplitude of the rotor's acceleration with fixed pendulums. Δn_i directly measures the distance between the resonance and the antiresonance around mode i. G_i is a gain that quantifies the diminution of the rotor's vibrations thanks to the pendulums' motion. Its analytical expression is given in Appendix D. For high performance around mode i, the desired configuration is Δn_i large and G_i low.

The evolution of Δn_i and G_i, $i = 1, 2$, as a function of ν_2 and μ_2 is displayed in Fig. 5. The dashed black line indicates a fixed value of n_{pi}. To design a CDPVA with high-performance, one can follow this line and choose the point where Δn_i is the largest and G_i the smallest. Note that G_2 fluctuates a lot more than G_1 and even reaches values of 1, in which cases the antiresonance has no effect on the response. These designs, for which the second antiresonance is flat, are to be avoided absolutely if one wants to perform filtration using the second mode. Maps as those shown in Fig. 5 are extremely useful in the design process as they allow for a huge gain of time to converge towards a satisfactory design as compared to manual iterations on the parameters. The next step of improvement of the design process would be to use an optimisation

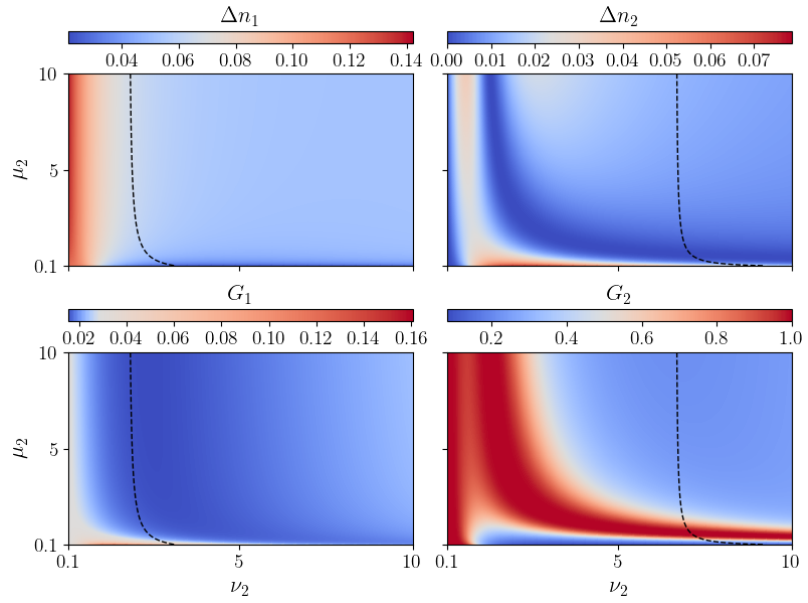

Figure 5: Evolution of the performance indicators Δn_i and G_i as a function of ν_2 and μ_2 for modes 1 left) and 2 (right). The dashed black lines correspond to the sets (ν_2, μ_2) that produce the same tuning orders as the design given in Tab. 1. The parameters used to create the maps are given in Tab. 1 except for ν_2 and μ_2, which are varied.

algorithm that yields the desired tuning order while achieving the best possible performance. However, such a procedure is out of the scope of this paper.

4. Nonlinear response of a CDPVA

The aim of this section is to present the construction of an analytical model describing the nonlinear response of a CDPVA. As for CPVAs [41], the construction starts with a scaling of the parameters. This allows for a simplification of the equations of motion such that the dynamics of the pendulums becomes uncoupled from that of the rotor. Then, as in [24], the pendulums' equations are written in matrix form and projected on the linear modes, leading to the simplified modal equations. The modal solutions are obtained by considering a response on a single mode and applying the method of multiple scales [42].

Finally, the modal responses are used to deduce the pendulums' motion, which in turn is used to obtain the rotor's response.

4.1. Scaling and simplified physical equations

The following hypothesis and remarks will govern the scaling:

- The optimum configuration is that with small rotor and pendulums' damping as it leads to the most pronounced antiresonances.
- The fluctuating torque is small compared to the rotor's kinetic energy ($J_r\Omega^2/2$ at equilibrium) so that $\bar{T}_1$ is small.
- The pendulums' geometric inertia about O is small compared to the rotatory inertia of the whole system, so that μ is small.
- As the rotor's kinetic energy is significant, the rotor's fluctuating speed is small compared to its mean rotational velocity, so y can be decomposed as

$$y(\vartheta) = 1 + y_\theta(\vartheta), \tag{13}$$

  where y_θ is small.
- The rotation laws considered in this paper are close from linear, so that α_{13} and α_{23} are small.

Hence, we can scale the parameters such that

$$\begin{gathered} \bar{b}_1 = \epsilon\tilde{b}_1, \quad \bar{b}_2 = \epsilon\tilde{b}_2, \quad \bar{b}_r = \epsilon\tilde{b}_r, \quad \bar{T}_1 = \epsilon\tilde{T}_1, \\ \mu = \epsilon\tilde{\mu}, \quad y_\theta = \epsilon\tilde{y}_\theta, \quad \theta' = \epsilon\tilde{\theta}', \quad \alpha_{13} = \epsilon\tilde{\alpha}_{13}, \quad \alpha_{23} = \epsilon\tilde{\alpha}_{23}, \end{gathered} \tag{14}$$

where ϵ is a small parameter that can for instance be chosen to be μ. In the following, only first-order terms will be retained in the rotor's equation. Hence, like in section 3, the approximation $\tilde{\theta}' \approx \tilde{y}_\theta$ can be used in order to represent the degree-of-freedom of the rotor through its position rather than its velocity [40].

Introducing the scaled parameters (14) in the rotor's equation (A.6), keeping only first-order terms and using Taylor series in φ_1 and φ_2, one obtains the rotor's simplified equation

$$\tilde{\theta}'' = f_\theta(\boldsymbol{\varphi}, \vartheta). \tag{15}$$

Equation (15) expresses the rotor's acceleration as a function of the pendulums' motion. $\boldsymbol{\varphi} = [\varphi_1, \varphi_2]^\intercal$ is the vector containing the pendulums' coordinates. Function $f_\theta(\boldsymbol{\varphi}, \vartheta)$, described in Appendix A.3, contains linear, quadratic and cubic terms in φ_1 and φ_2 and the external torque. Note that $f_\theta(\boldsymbol{\varphi}, \vartheta)$ involves the derivatives $\boldsymbol{\varphi}'$ and $\boldsymbol{\varphi}''$, but this is not indicated explicitly for the sake of readability. This remark holds for the rest of this paper.

The only nonlinearities that are currently scaled by ϵ are those involving μ, α_{13} or α_{23}. They represent the indirect coupling between the pendulums through the rotor and the nonlinear contribution of the rotation laws, respectively. However, the system exhibits additional nonlinearities coming from the circular path of pendulum 1 and from the direct coupling between the two pendulums. For those nonlinear terms to appear at order ϵ, further scaling is required. This is presented in Appendix A.3. With this additional scaling, the simplified equations of pendulums 1 and 2 can be written

$$\Lambda_{m1}\varphi_1'' + \Lambda_{c12}\varphi_2'' + k_1\varphi_1 + k_{12}\varphi_2 = -\epsilon f_{p1}(\boldsymbol{\varphi}, \vartheta), \tag{16a}$$

$$\Lambda_{c12}\varphi_1'' + \Lambda_{m2}\varphi_2'' + k_{12}\varphi_1 + k_2\varphi_2 = -\epsilon f_{p2}(\boldsymbol{\varphi}, \vartheta). \tag{16b}$$

Functions $f_{p1}(\boldsymbol{\varphi}, \vartheta)$ and $f_{p2}(\boldsymbol{\varphi}, \vartheta)$ are given in Appendix A.3. They contain linear, quadratic and cubic terms in φ_1 and φ_2. They also account for the external torque applied on the rotor and the pendulums' damping.

Equations (16a) and (16b) are linearly coupled, which complicates their solving. Hence, it is convenient to project them on the linear modes so as to obtain two linearly uncoupled modal equations which are more easily solvable. This is presented in the next section.

4.2. Simplified modal equations

The first step in deriving the modal equations is to rewrite Eqs. (16a) and (16b) in a matrix form using the vector of unknowns $\boldsymbol{\varphi}$. This matrix equation takes the form

$$\boldsymbol{M_p}\boldsymbol{\varphi}'' + \boldsymbol{K_p}\boldsymbol{\varphi} = -\epsilon \boldsymbol{f_p}(\boldsymbol{\varphi}, \vartheta) \tag{17}$$

and is to be projected on the reduced linear modes $(n_{10}, \boldsymbol{\psi}_1)$ and $(n_{20}, \boldsymbol{\psi}_2)$ (*cf.* section 3). As higher powers of ϵ are neglected in Eq. (17), one can use the Taylor series of the modal component χ_i (*cf.* section 3),

$$\chi_i = \chi_{pi} + \epsilon\tilde{\mu} w_i + \mathcal{O}(\epsilon^2), \quad i = 1, 2, \tag{18}$$

in order to write the reduced mode shapes $\boldsymbol{\psi}_1$ and $\boldsymbol{\psi}_2$ as

$$\boldsymbol{\psi}_i = \boldsymbol{\psi}_{pi} + \epsilon\tilde{\mu} \begin{bmatrix} 0 \\ w_i \end{bmatrix} + \mathcal{O}(\epsilon^2), \quad i = 1, 2. \tag{19}$$

w_i are constants that do not need to be defined as they will cancel later in the derivations (*cf.* Appendix A.4). Modes 1 and 2 are typically far from each other, so it makes sense to consider in a first approximation that the pendulums respond on a single mode. Hence, the pendulums' coordinates can be expressed as

$$\boldsymbol{\varphi} = \zeta_i \boldsymbol{\psi}_i = \zeta_i \boldsymbol{\psi}_{pi} + \zeta_i \epsilon\tilde{\mu} \begin{bmatrix} 0 \\ w_i \end{bmatrix} + \mathcal{O}(\epsilon^2), \quad i = 1 \text{ or } 2. \tag{20}$$

Introducing Eq. (20) in Eq. (17) and projecting on $\boldsymbol{\psi}_i$, one obtains the modal equation of mode i,

$$\zeta_i'' + n_{pi}^2 \zeta_i = -\frac{\epsilon}{\hat{\Lambda}_{mi}} \hat{f}_i(\zeta_i, \vartheta), \quad i = 1, 2. \tag{21}$$

Functions $\hat{f}_i$ are described in Appendix A.4. They involve the modal constants $\hat{\Lambda}_{mi}$, $\hat{k}_i$, $\hat{b}_i$, $\hat{\Lambda}_{ci}$, defined in Appendix B, which represent the modal mass, stiffness, damping and linear coupling with the rotor, respectively. Note that Eqs. (21) make use of $n_{pi}^2 = \hat{k}_i/\hat{\Lambda}_{mi}$. $\hat{f}_i(\zeta_i, \vartheta)$ contain linear, quadratic and cubic terms in ζ_i, and account for the damping and the external forcing.

4.3. Modal and physical solutions

The method of multiple scales [42] is used to find the solution of Eq. (21). Two rotation scales are introduced, $\vartheta_0 = \vartheta$ and $\vartheta_1 = \epsilon\vartheta$, and the modal coordinate is expanded such that

$$\zeta_i(\vartheta) = \zeta_{i0}(\vartheta_0, \vartheta_1) + \epsilon\zeta_{i1}(\vartheta_0, \vartheta_1). \tag{22}$$

As the excitation order n is close from n_{pi}, it is convenient to define the detuning term σ as

$$n = n_{pi} + \epsilon\sigma. \tag{23}$$

$\sigma > 0$ and $\sigma < 0$ correspond to under-tuned and over-tuned double pendulums, respectively. Applying the method of multiple scales yields a first-order solution of the form

$$\zeta_{i0}(\vartheta_0, \vartheta_1) = u_i(\vartheta_1)\cos\left(n\vartheta_0 - \beta_i(\vartheta_1)\right). \tag{24}$$

The modal amplitude u_i and phase β_i are governed by the system

$$\begin{cases} D_1 u_i = f_{u_i}(u_i, \beta_i), & \text{(25a)} \\ u_i D_1\beta_i = f_{\beta_i}(u_i, \beta_i), & \text{(25b)} \end{cases}$$

where $D_1(\bullet) = \partial(\bullet)/\partial\vartheta_1$. Functions f_{u_i} and f_{β_i} are given in Appendix F. They make use of the nonlinear coefficient

$$c_i = c_{pi} + c_{si} - c_{ci} + c_{ti}. \tag{26}$$

c_{pi} represents the nonlinearity coming from the rotation functions of pendulums 1 and 2, which can be seen as perturbations from linear rotation laws. It also accounts for the nonlinearity coming from the circular path of pendulum 1, which is seen as a perturbation of an epicycloidal path in the case of a CPVA [31]. c_{ci} and c_{si} are related to Coriolis effects and to the direct coupling between pendulums 1 and 2, respectively. c_{ti} accounts for nonlinear couplings through the rotor other than Coriolis effects. These definitions are chosen to identify the effect of the different sources of nonlinearity and to facilitate the comparison of

the results obtained in this paper with results dealing with CPVAs [25].

The solutions sought are those at steady-state, meaning that the amplitudes and phases are invariant with ϑ such that

$$D_1 u_i = D_1 \beta_i = 0. \tag{27}$$

The modal response is obtained by introducing the steady-state condition (27) in system (25) and solving for σ, $\tilde{T}_1$ and β_i. The solutions obtained are given in Appendix G. The stability of those solutions is obtained by evaluating the eigenvalues of the Jacobian of system

$$\begin{cases} D_1 u_i = f_{u_i}(u_i, \beta_i), & \text{(28a)} \\ D_1 \beta_i = f^*_{\beta_i}(u_i, \beta_i), & \text{(28b)} \end{cases}$$

where $f^*_{\beta_i} = f_{\beta_i}/u_i$. The instabilities encountered are related to a jump of the system's response, which is typical of Duffing oscillators [43].

The backbone curve of mode i is obtained by cancelling the damping and forcing in the forced order response (*cf.* Eq. (G.1a)), leading to

$$n_i = n_{pi} + \frac{\hat{\Lambda}^2_{ci} n_{pi} \mu}{2\hat{\Lambda}_{mi}} - \epsilon \frac{c_i}{4\hat{\Lambda}_{mi} n_{pi}} u_i^2. \tag{29}$$

n_i is the resonance order of mode i and c_i is seen to control the hardening/softening behaviour of this mode. It is of importance to note that the rotation coefficients α_{13} and α_{23} contribute only to c_{pi}, which appears in c_i (*cf.* Eq. (26)). Hence, one can choose these two rotation coefficients (or equivalently, choose c_{pi}) to modify the softening/hardening behaviour of the system. Thus, c_{pi} can be seen as the nonlinear tuning parameter of the CDPVA.

The pendulums' responses are directly deduced from Eq. (20), leading to

$$\varphi_1 = a_1 \cos(n\vartheta - \xi_1), \tag{30a}$$

$$\varphi_2 = a_2 \cos(n\vartheta - \xi_2), \tag{30b}$$

where the amplitudes a_1 and a_2 and phases ξ_1 and ξ_2 are given by

$$a_1 = u_i, \quad a_2 = |\chi_i| u_i, \quad \xi_1 = \beta_i, \quad \xi_2 = \begin{cases} \beta_i \text{ if } \chi_i > 0, \\ \beta + \pi \text{ if } \chi_i < 0. \end{cases} \tag{31}$$

The rotor's response is obtained by injecting the pendulums' responses (30) in the rotor's equation (15), leading to

$$\theta'' = h_1 \cos(n\vartheta - \psi_1) + h_2 \cos(2n\vartheta - \psi_2) + h_3 \cos(3n\vartheta - \psi_3). \tag{32}$$

Amplitudes h_i and phases ψ_i, $i = 1, 2, 3$, are given in Appendix G. θ'' contains only three harmonics due to the Taylor series up to cubic terms in φ_1 and φ_2 used in section 4.1, and because the pendulums' motion is harmonic at first order.

5. Case studies and design guidelines

The aim of this section is to compare the analytical results with numerical ones in order to validate the model and to provide design guidelines. The numerical solutions are obtained through a numerical integration of the equations of motion (4) using a Runge-Kutta algorithm. When the steady state is reached, the signals' amplitudes and phases are computed using a decomposition into Fourier series.

5.1. Typical nonlinear response of a CDPVA

The response of a CDPVA around modes 1 and 2 is given in Fig. 6. Both modes exhibit a softening behaviour, which causes jumps of the response. The response on mode 1 is quite well predicted, though discrepancies are visible on the upper branch, especially for the phases. The response on mode 2, shown on the right-hand side of Fig. 6, is also well predicted by the model, though discrepancies are visible. The difference between the analytical and numerical solutions on the lower branch before the antiresonance is due to the contribution of mode 1, which is neglected by the model. The upper branch goes down to

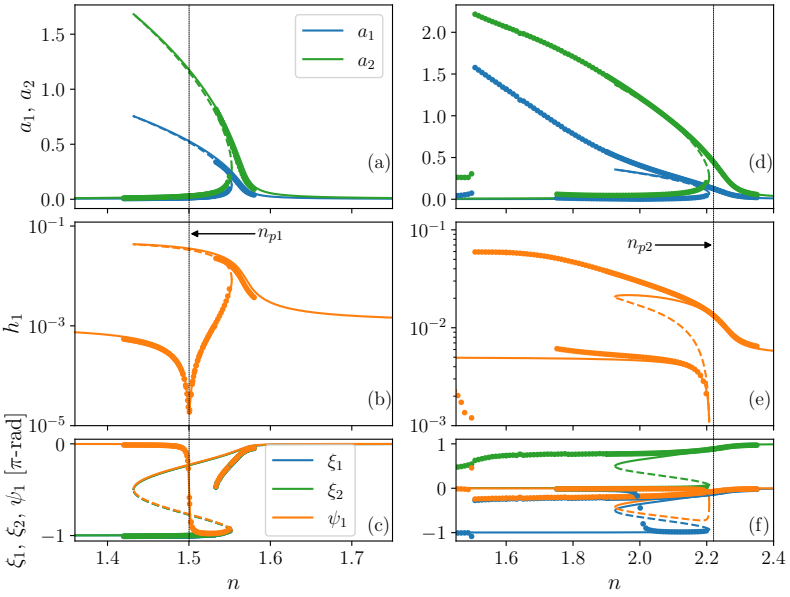

Figure 6: Amplitude response of the pendulums (a,d) and rotor (b,e) and their phases (c,f) as a function of the excitation order. The response on mode 1 is shown on the left and that on mode two on the right. The stable and unstable parts of the analytical solutions are shown as solid and dashed lines, respectively. The numerical solutions are the coloured circles. Note that both increasing and decreasing sweeps were performed to obtain these numerical results. $\bar{T}_1 = 0.01$ for the response on mode 1 and $\bar{T}_1 = 0.005$ for the response on mode 2. The system parameters are given in Tab. 1.

much lower orders than predicted analytically. Indeed, the saddle-node bifurcation was expected at $n \approx 1.923$, but it is seen to be around $n \approx 1.500$. Note that this saddle-node bifurcation makes the system jump from mode 2 to mode 1. This explains why the analytical results (which represent a motion on mode 2 only in the right-hand side of Fig. 6) and the numerical ones do not match for $n < 1.5$. The amplitude response of the rotor is given in Fig. 6(b) and (e). Again, it is well predicted by the analytical model. As shown in Fig. 6(c) and (f), the analytical model also allows to compute the phases of the pendulums and the rotor with a satisfying accuracy. Though the analytical model offer a useful overall prediction of the dynamics, its accuracy is obviously limited.

Several explanations for those limitations are provided below:

- To derive the simplified pendulums' equations (*cf.* section 4.1), Taylor series about 0 and up to cubic terms were used for φ_1 and φ_2. However, the amplitudes in Fig. 6(a) are quite large so more terms should be kept in the Taylor series.

- In section 4.1, several parameters were assumed small to appear at order ϵ. In the case of Fig. 6, some parameters are not that small. For instance, much smaller values of μ are often considered [7, 31, 34].

- In section 4.2, the pendulums are assumed to respond on a single mode. This assumption is relevant close from the resonances, but might be a source of errors as n departs from the resonance, especially if the two modes are close. This is visible in the right-hand side of Fig. 6 before the antiresonance, where the contribution of the two modes is significant.

- It is interesting to note that mode 2 is nonsimilar, meaning that the mode shape changes as the amplitude of motion increases [44]. This can be seen in Fig. 6(d) where the ratio a_2/a_1 is clearly not constant. The fact that mode 1 is nonsimilar generates several inaccuracies in the derivation of the modal equations (*cf.* section 4.2) and the reconstruction of the physical response (*cf.* section 4.3).

- There are also limitations related to the use of the method of multiple scales itself as it only provides approximate solutions.

Figure 7 shows the response of higher and lower harmonics of the rotor's acceleration as a function of the excitation order around modes 1 (left) and 2 (right). The model tends to strongly overestimate the amplitude of the higher harmonics h_2 and h_3. The same limitations as in Fig. 6 are visible. Indeed, around mode 1, the saddle node bifurcation occurs at much lower amplitudes than expected, and around mode 2 it occurs for much larger amplitudes. To

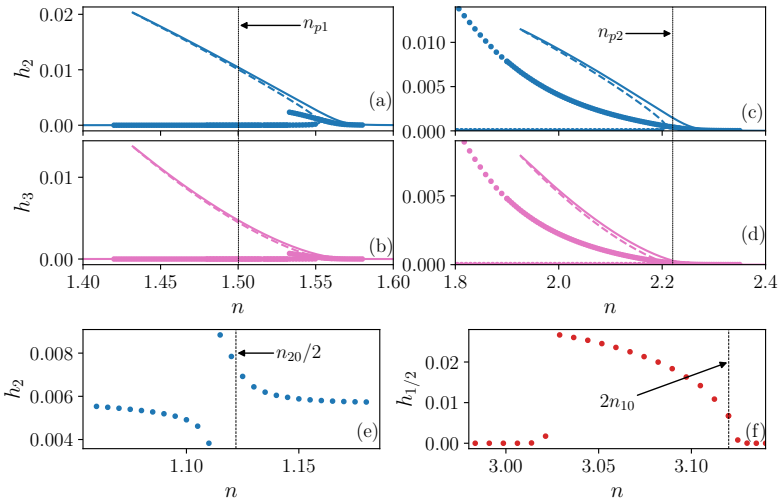

Figure 7: Amplitude of higher and lower rotor harmonics as a function of the excitation order. $h_{1/2}$ indicates the amplitude of harmonic 1/2 of the rotor's acceleration. The response around mode 1 is shown on the left and that around mode two on the right. The stable and unstable parts of the analytical solutions are shown as solid and dashed lines, respectively. The numerical solutions are the coloured circles. $\bar{T}_1 = 0.001$ for (a), (b), $\bar{T}_1 = 0.005$ for (c), (d), $\bar{T}_1 = 0.1$ for (e) and $\bar{T}_1 = 0.02$ for (f). The system parameters are given in Tab. 1.

represent more accurately those higher harmonics it is mandatory to keep more terms in the Taylor series used in section 4.1. It is interesting to remark the resonance peaks around $n_{20}/2$ in (e) and around $2n_{10}$ in (f). These peaks are due to a superharmonic resonance of mode 2 and a subharmonic resonance of mode 1, respectively. The order at the maximum amplitude is slightly lower than $n_{20}/2$ and $2n_{10}$ because of the softening behaviour. The existence of those secondary resonances questions the possibility to filter-out a torque containing harmonics n and $2n$ with a CDPVA. Indeed, using linear theory, one would assume that modes 1 and 2 behave independently and respond at distinct orders, hence allowing for the filtering of two-harmonic torques by setting $n_{p1} = n$ and $n_{p2} = 2n_{p1}$. However, Fig. 7 shows that modes 1 and 2 also respond at $2n_{10}$ and $n_{20}/2$, respectively. Thus, if $2n_{10} \approx n_{p2}$ and $n_{20}/2 \approx n_{p1}$, it is likely that antiresonances 1 and 2 be perturbed by modes 2 and 1, respectively. This is

particularly true for the subharmonic resonance of mode 1 which causes $h_{1/2}$ to have a large amplitude. To investigate this in details, one should consider a torque of the form $\bar{T}_\theta = \bar{T}_1 \cos(n\vartheta) + \bar{T}_2 \cos(2n\vartheta)$ (as done in [45–47] for a CPVA) and study secondary resonances (subharmonic resonances were investigated in [26, 40, 41, 45, 46, 48–50] for a CPVA), but this is out of the scope of this paper.

5.2. Tuning for performance

As explained in section 1, avoiding jumps of the response and controlling the shifting of the antiresonances is crucial to perform efficient vibration reduction. In this section, design guidelines allowing to avoid the jumps and to lock one of the antiresonances are derived.

To track the antiresonance order we apply the procedure described in [22] to the case of a CDPVA. Neglecting the damping and considering an excitation order small than the resonance of mode i, one has $\cos\beta_i = -1$ (the situation $\cos\beta_i = 1$ could also occur in theory but was not observed for reasonable parameters). Using this in the expression of the rotor's first harmonic (G.2a) leads to

$$h_1 = \left| \tilde{T}_1 - \tilde{\mu}\hat{\Lambda}_{ci} n^2 u_i + \frac{\tilde{\mu} n^2 c_{fi} u_i^3}{8} \right|. \tag{33}$$

Moreover, performing a Taylor series of $\tilde{T}_1$ in u_i using Eq. (G.1b) (and neglecting the damping again) leads to

$$\tilde{T}_1 = u_i \left| \tilde{\mu}\hat{\Lambda}_{ci} n_{pi}^2 - \frac{\hat{\Lambda}_{mi} n_{pi} (8\hat{\Lambda}_{ci} + 3c_{fi} u_i^2) u_i}{4\hat{\Lambda}_{ci}^2} \sigma + \frac{3c_{ti}/4 - c_i}{8\hat{\Lambda}_{ci}} u_i^2 \right| + \mathcal{O}(u_i^4). \tag{34}$$

For the three reasons listed thereafter, it is fair to assume that what is in the absolute value in Eq. (34) is positive until a jump of the response occurs. First, for small torques, u_i is small and the antiresonance is very close from n_{pi}. Hence, for small torques, the term $\tilde{\mu}\hat{\Lambda}_{ci} n_{pi}^2$ dominates. Secondly, this term is positive for reasonable system parameters. Thirdly, $\tilde{T}_1$ is monotonically increasing before a jump of the response is met. Hence, introducing Eq. (34) in Eq. (35) and

ignoring terms of order ϵ (such that $n \approx n_{pi}$) leads to

$$h_1 = \left| -\frac{\hat{\Lambda}_{mi} n_{pi} (8\hat{\Lambda}_{ci} + 3c_{fi} u_i^2) u_i}{4\hat{\Lambda}_{ci}^2} \sigma + \frac{c_{ti} - c_i}{8\hat{\Lambda}_{ci}} u_i^3 \right|. \tag{35}$$

It is not an issue that this expression be valid only up to a jump as jumps are to be avoided, otherwise they fix the maximum torque at which the system can operate. Because we neglected the damping, h_1 must be zero at the antiresonance. Hence, the antiresonance locus is obtained by solving $h_1 = 0$ for σ, leading to

$$n_{ARi} = n_{pi} + \epsilon \frac{c_{ci} - c_{pi} - c_{si}}{16\hat{\Lambda}_{mi} n_{pi}} u_i^2 + \mathcal{O}(u_i^4). \tag{36}$$

Thus, one can lock the antiresonance by setting the nonlinear tuning parameter c_{pi} such that

$$c_{pi} = c_{ci} - c_{si}. \tag{37}$$

Note that this is different from the condition leading to a straight backbone of the uncoupled double pendulum. Indeed, setting $\mu = 0$ in Eq. (29) leads to

$$n_{i(uc)} = n_{pi} - \epsilon \frac{c_{pi} + c_{si}}{4\hat{\Lambda}_{mi} n_{pi}} u_i^2, \tag{38}$$

so that the rule leading to a tautochronic uncoupled double pendulum around mode i is

$$c_{pi} = -c_{si}. \tag{39}$$

Rule (37) is also different from the condition yielding a tautochronic coupled double pendulum. Indeed, the behaviour is tautochronic if the backbone of the coupled system (29) is a straight line, that is,

$$c_{pi} = c_{ci} - c_{si} - c_{ti}. \tag{40}$$

The interesting feature of condition (40) is to avoid the jumps of the response. If $c_{pi} < c_{ci} - c_{si} - c_{ti}$, jumps occur at $n > n_{i0}$, which corresponds to orders larger than the operating point n_{pi}. If $c_{pi} > c_{ci} - c_{si} - c_{ti}$, a jump will eventually occur at the operating point. However, this is not an issue if the torque level at the

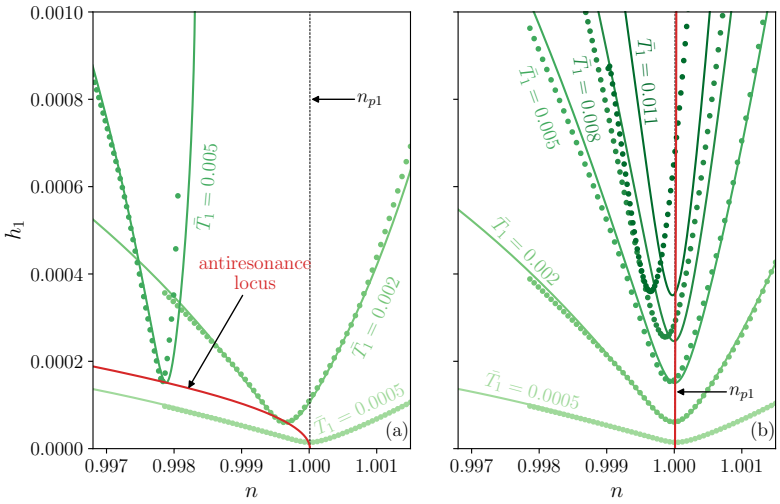

Figure 8: Rotor's response around antiresonance 1 for two different CDPVAs. The CDPVA in (a) is not nonlinearly tuned whereas that in (b) is tuned accordingly to rule (37) to lock its first antiresonance. The stable and unstable parts of the analytical responses are shown as solid and dashed green lines, respectively. The darker the line the larger the associated torque level. The analytical antiresonance tracking, performed using Eq. (36), is shown as a solid red line. The numerical solutions are the green circles. The system parameters for the CDPVA in (a) are given in Tab. 2. For the CDPVA in (b), the parameters are the same except for $\alpha_{13} = 0.0357$.

jump is larger than the maximum torque to be filtered.

Figure 8 shows the order response of the rotor of two CDPVAs, one is tuned accordingly to the design rule (37) to lock n_{AR1} and the other one is not. This figure zooms around the first antiresonance and responses at several torque levels are represented so we can observe how n_{AR1} evolves with the forcing. As expected, the use of the design rule almost locks the antiresonance, hence allowing for an improved vibration reduction over the whole torque range. Indeed, for the CDPVA in Fig. 8(b), the antiresonance has only slightly shifted for $\bar{T}_1 = 0.008$, whereas n_{AR1} is already significantly lower than n_{p1} at $\bar{T}_1 = 0.002$ for the CDPVA in Fig. 8(a). Moreover, rule (37) hardens the behaviour of the response in the case presented here. This has the nice property of pushing the

jump point to higher torque levels.

It is interesting to remark that at large amplitudes the rotor's response can loop around the antiresonance. Such a situation is presented in Appendix H. This looping feature is highly detrimental as it renders the antiresonance unstable, hence preventing the CDPVA to achieve large vibration reduction.

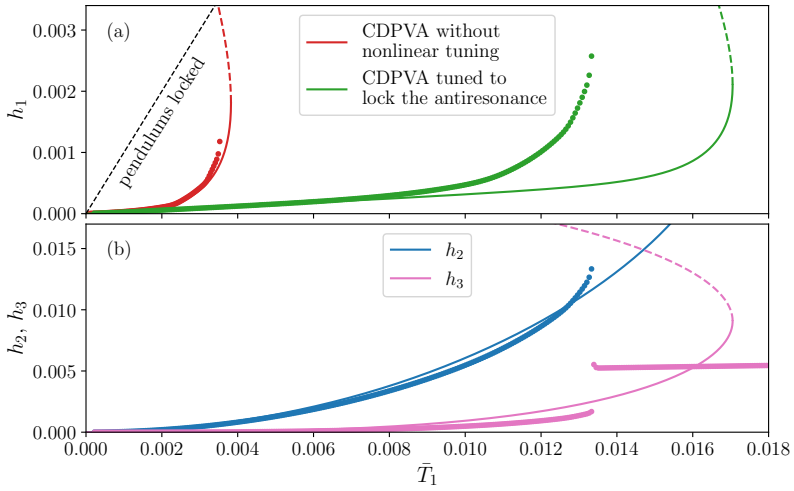

Figure 9: Rotor's response at $n = 1 = n_{p1}$ for two different CDPVAs as a function of the torque level. One of the CDPVAs is not nonlinearly tuned (it is the same as that studied in section 5.1) whereas the other one is tuned accordingly to rule (37). The first harmonic is shown in (a) for both CDPVAs while the higher harmonics are shown in (b) for the nonlinearly tuned CDPVA only. The stable and unstable parts of the analytical responses are shown as solid and dashed lines, respectively. The numerical solutions are the coloured circles. The system parameters for the CDPVA that is not nonlinearly tuned are given in Tab. 2. For the other CDPVA, the parameters are the same except for $\alpha_{13} = 0.0357$.

To visualise the improvement in vibration reduction due to the antiresonance locking, Fig. 9(a) presents a torque response at $n = n_{p1}$ of h_1 for the two CDPVAs discussed above. The response for these two CDPVAs is approximately the same up to $\bar{T}_1 \approx 0.001$. Above this value, the softening behaviour of the untuned CDPVA becomes significant, causing a shift of the antiresonance that is captured in Fig. 9(a) through the quick increase in the rotor's first harmonic

amplitude. The amplitude increases up to $\bar{T}_1 \approx 0.0038$, at which point a jump of the response occurs, causing a dramatic increase of the vibrations. For the tuned CDPVA, h_1 increases almost linearly up to $\bar{T}_1 \approx 0.008$. It is only after this value that the softening effect becomes visible, with a quicker increase in amplitude and the occurrence of a jump at $\bar{T}_1 \approx 0.0134$. Hence, rule (37) allows for a large increase of the filtering efficiency and torque capacity of the CDPVA. Note that the jump is predicted at $\bar{T}_1 \approx 0.017$ by the analytical model. This inaccuracy can be understood from Fig. 8, where one sees that the antiresonance gets narrower as the torque level increases. Hence, a high accuracy is required to predict the response near the antiresonance for large torque levels. However, the accuracy of the model is limited for the reasons explained in section 5.1. Fig. 9(b) shows the higher harmonics of the rotor's response for the CDPVA tuned accordingly to rule (37). The amplitude of harmonics 2 and 3 is well predicted by the analytical model before the jump. Clearly, the amplitude of these higher harmonics is not negligible in front of h_1. This means that the CDPVA is efficient at reducing the vibrations at order n but causes issues at orders $2n$ and $3n$. This is a known problem with CPVAs [21, 25, 51].

μ	η_1	η_2	μ_2	ν_r	ν_2	α_{11}	α_{21}	α_{13}	α_{23}	$\bar{b}_r$	$\bar{b}_1$, $\bar{b}_2$
0.15	6	4	0.2	1.551	0.3	-0.32	0.3	0	0	0.022	5×10^{-5}

Table 2: Parameters of the CDPVA studied in this section.

6. Conclusion

This paper deals with the use of CDPVAs to reduce the torsional vibrations of a rotating machine. In order to increase the accuracy of former CDPVA models, we took into account the rotation of the pendulums about their centre of mass. A linear analysis was carried out to compute the eigenmodes of the system. This allowed to derive the expression of the two tuning orders of the double pendulum, which correspond to the orders of the two antiresonances generated on the rotor. In addition, an efficient design procedure based on

the linear response was proposed. This allows to quickly converge towards a CDPVA tuned at the desired order(s) and with a satisfactory performance. Then, the dynamic response of the system and its stability were computed using a perturbation method, and the validity of this analytical model was verified through a comparison with numerical solutions. Because of nonlinearities, the resonance and antiresonance orders can increase/decrease with the amplitude of motion. In this paper, we derived new design guidelines that prevent the shifting of one of the antiresonances and limit jumps of the response, thus maximising the filtering over the whole torque range. These guidelines are based on a choice of nonlinear rotation laws that balances the other sources of nonlinearities in order to lock one of the antiresonances or to render the double pendulum tautochronic. The efficiency of the design rule locking the antiresonance was confirmed with a torque sweep. We also showed that the nonlinearities lead to the generation of higher and lower harmonics, partly due to secondary resonances of the modes of the system. This should be investigated in the future as it might prevent the use of a CDPVA to filter out a torque made of two harmonics. Also of interest for future works is the pendulums' path. In the present study, both pendulums have constant length so they follow circular paths, but considering more general paths could prove useful in the tuning process. Finally, the present paper considers a CDPVA made of a single equivalent double pendulum. However, it is known from studies on CPVAs that systems made of several absorbers can be subjected to energy localisation. This should be investigated in the future.

References

[1] B. C. Carter, Improvements in or relating to damping of oscillation-checking devices, 337 466 (1929).

[2] R. R. R. Sarazin, Means adapted to reduce the torsional oscillations of crankshafts, 2 079 226 (1931).

[3] R. Chilton, Pendulum counterweight, 2 112 984 (1935).

[4] R. W. Zdanowich, T. S. Wilson, The elements of pendulum dampers, Proceedings of the Institution of Mechanical Engineers 143 (1) (1940) 182–210. doi:10.1243/PIME_PROC_1940_143_028_02.

[5] J.-G. Duh, M. Wenyong, Development of monofilar rotor hub vibration absorber, Tech. rep. (1983).

[6] C. Shi, R. G. Parker, S. W. Shaw, Tuning of centrifugal pendulum vibration absorbers for translational and rotational vibration reduction, Mechanism and Machine Theory 66 (2013) 56–65. doi:10.1016/j.mechmachtheory.2013.03.004.

[7] V. Manchi, C. Sujatha, Torsional vibration reduction of rotating shafts for multiple orders using centrifugal double pendulum vibration absorber, Applied Acoustics 174 (2021) 107768. doi:10.1016/j.apacoust.2020.107768.

[8] B. Geist, V. Ramakrishnan, P. Attibele, W. Resh, Precision requirements for the bifilar hinge slots of a centrifugal pendulum vibration absorber, Precision Engineering 52 (2018) 1–14. doi:10.1016/j.precisioneng.2017.08.001.

[9] J. Mayet, H. Ulbrich, Tautochronic centrifugal pendulum vibration absorbers: General design and analysis, Journal of Sound and Vibration 333 (3) (2014) 711–729. doi:10.1016/j.jsv.2013.09.042.

[10] J. Mayet, H. Ulbrich, First-order optimal linear and nonlinear detuning of centrifugal pendulum vibration absorbers, Journal of Sound and Vibration 335 (2015) 34–54. doi:10.1016/j.jsv.2014.09.017.

[11] M. A. Acar, Design and tuning of centrifugal pendulum vibration absorbers, Ph.D. thesis, Michigan State University, Michigan (2017).

[12] H. Mahé, A. Renault, O. Thomas, Dispositif d'amortissement pendulaire [Pendular damping device], fR 3 055 038 (2018).

[13] H. Mahé, A. Renault, O. Thomas, Dispositif d'amortissement pendulaire [Pendular damping device], fR 3 055 037 (2018).

[14] A. Renault, Calcul et optimisation d'absorbeurs pendulaires dans une chaîne de traction automobile [Simulation and optimisation of pendular absorbers for automotive powertrain], Ph.D. thesis, ENSAM, Lille, France (2018).

[15] M. Cirelli, M. Cera, E. Pennestrì, P. P. Valentini, Nonlinear design analysis of centrifugal pendulum vibration absorbers: An intrinsic geometry-based framework, Nonlinear Dynamics 102 (3) (2020) 1297–1318. doi:10.1007/s11071-020-06035-1.

[16] M. Cera, M. Cirelli, E. Pennestrì, P. Valentini, The kinematics of curved profiles mating with a caged idle roller - higher-path curvature analysis, Mechanism and Machine Theory 164 (2021) 104414. doi:10.1016/j.mechmachtheory.2021.104414.

[17] M. Cera, M. Cirelli, E. Pennestrì, P. P. Valentini, Design analysis of torsichrone centrifugal pendulum vibration absorbers, Nonlinear Dynamics 104 (2) (2021) 1023–1041. doi:10.1007/s11071-021-06345-y.

[18] M. Cera, M. Cirelli, E. Pennestrì, P. P. Valentini, Nonlinear dynamics of torsichrone CPVA with synchroringed form closure constraint, Nonlinear Dynamics (2021). doi:10.1007/s11071-021-06732-5.

[19] E. R. Gomez, I. L. Arteaga, L. Kari, Normal-force dependant friction in centrifugal pendulum vibration absorbers: Simulation and experimental investigations, Journal of Sound and Vibration 492 (2021) 115815. doi:10.1016/j.jsv.2020.115815.

[20] X. Tan, S. Yang, J. Yang, J. Li, Study of dynamics of rotational centrifugal pendulum vibration absorbers based on tautochronic design, Meccanica (2021). doi:10.1007/s11012-021-01340-4.

[21] E. R. Gomez, J. Sjöstrand, L. Kari, I. L. Arteaga, Torsional vibrations in heavy-truck powertrains with flywheel attached centrifugal pendulum vibration absorbers, Mechanism and Machine Theory 167 (2022) 104547. doi:10.1016/j.mechmachtheory.2021.104547.

[22] V. Mahe, A. Renault, A. Grolet, O. Thomas, H. Mahe, Dynamic stability of centrifugal pendulum vibration absorbers allowing a rotational mobility, Journal of Sound and Vibration 517 (2022) 116525. doi:10.1016/j.jsv.2021.116525.

[23] J. Mayet, M. A. Acar, S. W. Shaw, Effective and robust rocking centrifugal pendulum vibration absorbers, Journal of Sound and Vibration 527 (2022) 116821. doi:10.1016/j.jsv.2022.116821.

[24] V. Mahé, A. Renault, A. Grolet, H. Mahé, O. Thomas, Localised response of a centrifugal pendulum vibration absorber, *Submitted to Nonlinear Dynamics*.

[25] V. Mahé, A. Renault, A. Grolet, H. Mahé, O. Thomas, On the dynamic stability and efficiency of centrifugal pendulum vibration absorbers with rotating pendulums, Journal of Sound and Vibration 536 (2022) 117157. doi:10.1016/j.jsv.2022.117157.

[26] V. Mahé, A. Renault, A. Grolet, H. Mahe, O. Thomas, On the stability of pairs of subharmonic centrifugal pendulum vibration absorbers allowing a rotational mobility, *Submitted to Nonlinear Dynamics*

.

[27] D. E. Newland, Nonlinear Aspects of the Performance of Centrifugal Pendulum Vibration Absorbers, Journal of Engineering for Industry 86 (3) (1964) 257–263. doi:10.1115/1.3670529.

[28] D. E. Newland, Nonlinear problems of centrifugal pendulum vibration absorbers, in: Mechanisms and Machines, Vol. 1, Varna (Bulgaria), 1965, pp. 39–62.

[29] J. F. Madden, Constant frequency bifilar vibration absorber, 4 218 187 (1980).

[30] H. H. Denman, Tautochronic bifilar pendulum torsion absorbers for reciprocating engines, Journal of Sound and Vibration 159 (2) (1992) 251–277. doi:10.1016/0022-460X(92)90035-V.

[31] A. Alsuwaiyan, S. W. Shaw, Performance and dynamic stability of general-path centrifugal pendulum vibration absorbers, Journal of Sound and Vibration 252 (5) (2002) 791–815. doi:10.1006/jsvi.2000.3534.

[32] S. W. Shaw, B. Geist, Tuning for Performance and Stability in Systems of Nearly Tautochronic Torsional Vibration Absorbers, Journal of Vibration and Acoustics 132 (4) (2010). doi:10.1115/1.4000840.

[33] A. S. Alsuwaiyan, S. W. Shaw, Non-synchronous and Localized Responses of Systems of Identical Centrifugal Pendulum Vibration Absorbers, Arabian Journal for Science and Engineering 39 (12) (2014) 9205–9217. doi:10.1007/s13369-014-1464-1.

[34] J. S. Issa, S. W. Shaw, Synchronous and non-synchronous responses of systems with multiple identical nonlinear vibration absorbers, Journal of Sound and Vibration 348 (2015) 105–125. doi:10.1016/j.jsv.2015.03.021.

[35] A. Grolet, A. Renault, O. Thomas, Energy Localisation in Periodic Structures: Application to Centrifugal Pendulum Vibration Absorber, in: International Symposium on Transport Phenomena and Dynamics of Rotating Machinery, Maui (Hawaii), 2017.

[36] M. Sharif-Bakhtiar, S. W. Shaw, Effects of Nonlinearities and Damping on the Dynamic Response of a Centrifugal Pendulum Vibration Absorber, Journal of Vibration and Acoustics 114 (3) (1992) 305–311. doi:10.1115/1.2930262.

[37] A. G. Haddow, S. W. Shaw, Centrifugal Pendulum Vibration Absorbers: An Experimental and Theoretical Investigation, Nonlinear Dynamics 34 (3/4) (2003) 293–307. doi:10.1023/B:NODY.0000013509.51299.c0.

[38] A. Renault, O. Thomas, H. Mahé, Numerical antiresonance continuation of structural systems, Mechanical Systems and Signal Processing 116 (2019) 963–984. doi:10.1016/j.ymssp.2018.07.005.

[39] S. W. Shaw, S. Wiggins, Chaotic dynamics of a whirling pendulum, Physica D: Nonlinear Phenomena 31 (2) (1988) 190–211. doi:10.1016/0167-2789(88)90076-0.

[40] V. Mahe, A. Renault, A. Grolet, H. Mahe, O. Thomas, Subharmonic centrifugal pendulum vibration absorbers allowing a rotational mobility, Mechanical Systems and Signal Processing 177 (2022) 109125. doi:10.1016/j.ymssp.2022.109125.

[41] C.-P. Chao, S. W. Shaw, The effects of imperfections on the performance of the subharmonic vibration absorber system, Journal of Sound and Vibration 215 (5) (1998) 1065–1099. doi:10.1006/jsvi.1998.1634.

[42] A. H. Nayfeh, Perturbation Methods, Wiley Classics Library, Wiley-VCH, Weinheim, 1973. doi:10.1002/9783527617609.

[43] I. Kovacic, M. J. Brennan, The Duffing Equation: Nonlinear Oscillators and Their Behaviour, John Wiley & Sons, 2011. doi:10.1002/9780470977859.

[44] R. M. Rosenberg, J. K. Kuo, Nonsimilar Normal Mode Vibrations of Nonlinear Systems Having Two Degrees of Freedom, Journal of Applied Mechanics 31 (2) (1964) 283–290. doi:10.1115/1.3629599.

[45] C.-T. Lee, S. W. Shaw, The non-linear dynamic response of paired centrifugal pendulum vibration absorbers, Journal of Sound and Vibration 203 (5) (1997) 731–743. doi:10.1006/jsvi.1996.0707.

[46] B. J. Vidmar, Analysis and Design of Multiple Order Centrifugal Pendulum Vibration Absorbers, Ph.D. thesis, American Society of Mechanical Engineers, Chicago, Illinois, USA (Aug. 2012).

[47] B. J. Vidmar, S. W. Shaw, B. F. Feeny, B. K. Geist, Nonlinear Interactions in Systems of Multiple Order Centrifugal Pendulum Vibration Absorbers, Journal of Vibration and Acoustics 135 (6) (Dec. 2013). doi:10.1115/1.4024969.

[48] C.-T. Lee, S. W. Shaw, Torsional vibration reduction in internal combustion engines using centrifugal pendulums, Tech. rep. (1995).

[49] C.-T. Lee, S. W. Shaw, V. T. Coppola, A Subharmonic Vibration Absorber for Rotating Machinery, Journal of Vibration and Acoustics 119 (4) (1997) 590–595. doi:10.1115/1.2889766.

[50] C.-P. Chao, S. W. Shaw, The dynamic response of multiple pairs of subharmonic torsional vibration absorbers, Journal of Sound and Vibration 231 (2) (2000) 411–431. doi:10.1006/jsvi.1999.2722.

[51] C.-T. Lee, S. W. Shaw, On the counteraction of periodic torques for rotating systems using centrifugally driven vibration absorbers, Journal of Sound and Vibration 191 (5) (1996) 695–719. doi:10.1006/jsvi.1996.0151.

Appendix A. Details on the computation of the equations of motion

Appendix A.1. Dimensional equations

The kinetic energy of the system represented in Fig. 1 is

$$\mathcal{T} = \frac{1}{2} J_r \boldsymbol{\Omega}^2_{\mathscr{R}_r/\mathscr{R}_0} + \frac{1}{2} m_1 \boldsymbol{v}^2_{G_1} + \frac{1}{2} I_1 \boldsymbol{\Omega}^2_{\mathscr{R}_{p1}/\mathscr{R}_0} + \frac{1}{2} m_2 \boldsymbol{v}^2_{G_2} + \frac{1}{2} I_2 \boldsymbol{\Omega}^2_{\mathscr{R}_{p2}/\mathscr{R}_0}, \quad \text{(A.1)}$$

where $\boldsymbol{v}_{G_1}$ and $\boldsymbol{v}_{G_2}$ are the velocities of points G_1 and G_2 in the Galilean frame, respectively, and $\boldsymbol{\Omega}_{\mathscr{R}_r/\mathscr{R}_0}$, $\boldsymbol{\Omega}_{\mathscr{R}_{p1}/\mathscr{R}_0}$ and $\boldsymbol{\Omega}_{\mathscr{R}_{p2}/\mathscr{R}_0}$ are the rotational velocities

of the rotor, pendulum 1 and pendulum 2 with respect to the Galilean frame, respectively. These three rotational velocities are given by

$$\boldsymbol{\Omega}_{\mathscr{R}_r/\mathscr{R}_0} = \dot{\vartheta}\boldsymbol{z_0}, \tag{A.2a}$$

$$\boldsymbol{\Omega}_{\mathscr{R}_{p1}/\mathscr{R}_0} = [\dot{\vartheta} + \dot{\alpha}_1(\varphi_1)]\boldsymbol{z_0}, \tag{A.2b}$$

$$\boldsymbol{\Omega}_{\mathscr{R}_{p2}/\mathscr{R}_0} = [\dot{\vartheta} + \dot{\alpha}_1(\varphi_1) + \dot{\alpha}_2(\varphi_2)]\boldsymbol{z_0} \tag{A.2c}$$

The potential energy $\mathcal{U}$ is neglected as the gravitational acceleration is assumed negligible in front of the centrifugal acceleration. Hence, the Lagrangian is $\mathcal{L} = \mathcal{T}$. There are four external loads applied on the system:

- A torque $T(\vartheta)\boldsymbol{z_0}$ is applied on the rotor, where $\boldsymbol{z_0}$ is the out-of-plane unit vector (*cf.* Fig. 1). It is the external forcing.
- A resistive torque $-b_r\dot{\vartheta}\boldsymbol{z_0}$ is applied on the rotor. It represents the damping between the rotor and the ground.
- A resistive torque $-b_1\dot{\varphi}_1\boldsymbol{z_0}$ is applied on pendulum 1. It represents the damping between the rotor and pendulum 1.
- A resistive torque $-b_2\dot{\varphi}_2\boldsymbol{z_0}$ is applied on pendulum 2. It represents the damping between pendulum 2 and pendulum 1.

Using the Euler-Lagrange equations together with the principle of virtual powers, one obtains the equations of motion

$$
\begin{aligned}
&\Big[J_r + I_1 + I_2 + (m_1+m_2)\left(r^2 + \ell_1^2 + 2r\ell_1\cos\varphi_1\right) \\
&+ m_2\ell_2\left(2r\cos\left(\alpha_1+\varphi_2\right) + 2\ell_1\cos\left(\alpha_1-\varphi_1+\varphi_2\right) + \ell_2\right)\Big]\ddot{\vartheta} \\
&+ \Big[(I_1 + I_2 + m_2\ell_2^2)\Gamma_1 + (m_1+m_2)\left(\ell_1^2 + r\ell_1\cos\varphi_1\right) \\
&+ m_2 r\ell_2\Gamma_1\cos\left(\alpha_1+\varphi_2\right) \\
&+ m_2\ell_1\ell_2\left(1+\Gamma_1\right)\cos\left(\alpha_1-\varphi_1+\varphi_2\right)\Big]\ddot{\varphi}_1 \\
&+ \Big[I_2\Gamma_2 + m_2\ell_2^2 + m_2 r\ell_2\cos\left(\alpha_1+\varphi_2\right) \\
&+ m_2\ell_1\ell_2\cos\left(\alpha_1-\varphi_1+\varphi_2\right)\Big]\ddot{\varphi}_2 \\
&+ m_2\ell_1\ell_2\frac{d\Gamma_1}{d\varphi_1}\dot{\varphi}_1^2\cos\left(\alpha_1-\varphi_1+\varphi_2\right) \\
&- m_2\ell_1\ell_2\left(\left(\Gamma_1-1\right)\dot{\varphi}_1 + \dot{\varphi}_2\right)\left(\left(\Gamma_1+1\right)\dot{\varphi}_1 + \dot{\varphi}_2 + 2\dot{\vartheta}\right) \\
&\sin\left(\alpha_1-\varphi_1+\varphi_2\right) \\
&+ m_2 r\ell_2\frac{d\Gamma_1}{d\varphi_1}\dot{\varphi}_1^2\cos\left(\alpha_1+\varphi_2\right) \\
&- m_2 r\ell_2\left(\Gamma_1\dot{\varphi}_1 + \dot{\varphi}_2\right)\left(\Gamma_1\dot{\varphi}_1 + \dot{\varphi}_2 + 2\dot{\vartheta}\right)\sin\left(\alpha_1+\varphi_2\right) \\
&+ \left(I_1 + I_2 + m_2\ell_2^2\right)\frac{d\Gamma_1}{d\varphi_1}\dot{\varphi}_1^2 \\
&+ I_2\frac{d\Gamma_2}{d\varphi_2}\dot{\varphi}_2^2 - \left(m_1+m_2\right)r\ell_1\left(\dot{\varphi}_1 + 2\dot{\vartheta}\right)\dot{\varphi}_1\sin\varphi_1 + b_r\dot{\vartheta} = T(\vartheta),
\end{aligned}
\tag{A.3}
$$

$$
\begin{aligned}
&[((I_1+I_2)\Gamma_1+(m_1+m_2)\left(\ell_1^2+r\ell_1\cos\varphi_1\right)+m_2\ell_2^2\Gamma_1\\
&+m_2r\ell_2\Gamma_1\cos\left(\alpha_1+\varphi_2\right)+m_2\ell_1\ell_2\left(\Gamma_1+1\right)\cos\left(\alpha_1-\varphi_1+\varphi_2\right)]\ddot{\vartheta}\\
&+\Big[\left(I_1+I_2+m_2\ell_2^2\right)\Gamma_1^2+\left(m_1+m_2\right)\ell_1^2\\
&+2m_2\ell_1\ell_2\Gamma_1\cos\left(\alpha_1-\varphi_1+\varphi_2\right)\Big]\ddot{\varphi}_1\\
&+\left[I_2\Gamma_1\Gamma_2+m_2\ell_2^2\Gamma_1+m_2\ell_1\ell_2\cos\left(\alpha_1-\varphi_1+\varphi_2\right)\right]\ddot{\varphi}_2\\
&+\left(m_1+m_2\right)r\ell_1\dot{\vartheta}^2\sin\varphi_1+m_2r\ell_2\Gamma_1\dot{\vartheta}^2\sin\left(\alpha_1+\varphi_2\right)\\
&-m_2\ell_1\ell_2\left[\Gamma_1\left(\Gamma_1-1\right)\dot{\varphi}_1^2+2\Gamma_1\dot{\varphi}_1\dot{\varphi}_2-\Gamma_1\dot{\vartheta}^2+\left(\dot{\varphi}_2+\dot{\vartheta}\right)^2\right]\\
&\sin\left(\alpha_1-\varphi_1+\varphi_2\right)\\
&+m_2\ell_1\ell_2\frac{d\Gamma_1}{d\varphi_1}\dot{\varphi}_1^2\cos\left(\alpha_1-\varphi_1+\varphi_2\right)\\
&+\left(I_1+I_2+m_2\ell_2^2\right)\Gamma_1\frac{d\Gamma_1}{d\varphi_1}\dot{\varphi}_1^2+I_2\Gamma_1\frac{d\Gamma_2}{d\varphi_2}\dot{\varphi}_2^2\\
&+b_1\dot{\varphi}_1=0,
\end{aligned}
\tag{A.4}
$$

$$
\begin{aligned}
&\Big[I_2\Gamma_2+m_2\ell_2^2+m_2r\ell_2\cos\left(\alpha_1+\varphi_2\right)+m_2\ell_1\ell_2\cos\left(\alpha_1-\varphi_1+\varphi_2\right)\Big]\ddot{\vartheta}\\
&+\left[I_2\Gamma_1\Gamma_2+m_2\ell_2^2\Gamma_1+m_2\ell_1\ell_2\cos\left(\alpha_1-\varphi_1+\varphi_2\right)\right]\ddot{\varphi}_1\\
&+\left[I_2\Gamma_2^2+m_2\ell_2^2\right]\ddot{\varphi}_2+m_2r\ell_2\dot{\vartheta}^2\sin\left(\alpha_1+\varphi_2\right)\\
&+m_2\ell_1\ell_2\left(\dot{\varphi}_1+\dot{\vartheta}\right)^2\sin\left(\alpha_1-\varphi_1+\varphi_2\right)\\
&+\left(I_2\Gamma_2+m_2\ell_2^2\right)\frac{d\Gamma_1}{d\varphi_1}\dot{\varphi}_1^2+I_2\Gamma_2\frac{d\Gamma_2}{d\varphi_2}\dot{\varphi}_2^2+b_2\dot{\varphi}_2=0,
\end{aligned}
\tag{A.5}
$$

where $\Gamma_1(\varphi_1)$ and $\Gamma_2(\varphi_2)$ are rotation functions defined in Eq. (2). Equations (A.3), (A.4) and (A.5) govern the motion of the rotor, pendulum 1 and pendulum 2, respectively. Neglecting I_1 and I_2 in Eqs. (A.3), (A.4) and (A.5) and considering a simple pendulum such that $\alpha_1(\varphi_1)=\varphi_1$, one obtains the equations of motion given in [7][1].

[1] It is not exactly the same equations as the CDPVA considered in [7] is equipped with torsional springs while it is not the case in the present paper.

Appendix A.2. Dimensionless equations

One can use the procedure described in section 2 to derive the dimensionless equations of the system. These equations are

$$
\begin{aligned}
&\Big[1+\mu+2\mu h[v_r\left(1+\mu_2\right)\left(\cos\varphi_1-1\right)+\mu_2 v_2 v_r\left(\cos\left(\alpha_1+\varphi_2\right)-1\right)\\
&+\mu_2 v_2\left(\cos\left(\alpha_1-\varphi_1+\varphi_2\right)-1\right)]\Big]yy'\\
&+\mu h\Big\{\Big[\left(\eta_1+\mu_2 v_2^2\eta_2+\mu_2 v_2^2\right)\Gamma_1+\left(1+\mu_2\right)\left(1+v_r\cos\varphi_1\right)\\
&+\mu_2 v_r v_2\Gamma_1\cos\left(\alpha_1+\varphi_2\right)+\mu_2 v_2\left(1+\Gamma_1\right)\cos\left(\alpha_1-\varphi_1+\varphi_2\right)\Big]\\
&\left(yy'\varphi_1'+y^2\varphi_1''\right)\\
&+\mu_2 v_2\Big[v_2\eta_2\Gamma_2+v_2+v_r\cos\left(\alpha_1+\varphi_2\right)+\cos\left(\alpha_1-\varphi_1+\varphi_2\right)\Big]\\
&\left(yy'\varphi_2'+y^2\varphi_2''\right)\\
&+\mu_2 v_2\frac{d\Gamma_1}{d\varphi_1}y^2\varphi_1'^2\cos\left(\alpha_1-\varphi_1+\varphi_2\right)\\
&-\mu_2 v_2 y^2\left(\left(\Gamma_1-1\right)\varphi_1'+\varphi_2'\right)\left(\left(\Gamma_1+1\right)\varphi_1'+\varphi_2'+2\right)\sin\left(\alpha_1-\varphi_1+\varphi_2\right)\\
&+\mu_2 v_r v_2\frac{d\Gamma_1}{d\varphi_1}y^2\varphi_1'^2\cos\left(\alpha_1+\varphi_2\right)\\
&-\mu_2 v_r v_2 y^2\left(\Gamma_1\varphi_1'+\varphi_2'\right)\left(\Gamma_1\varphi_1'+\varphi_2'+2\right)\sin\left(\alpha_1+\varphi_2\right)\\
&+\left(\eta_1+\mu_2 v_2^2\eta_2+\mu_2 v_2^2\right)\frac{d\Gamma_1}{d\varphi_1}y^2\varphi_1'^2+\mu_2 v_2^2\eta_2\frac{d\Gamma_2}{d\varphi_2}y^2\varphi_2'^2\\
&-\left(1+\mu_2\right)v_r y^2\left(\varphi_1'+2\right)\varphi_1'\sin\varphi_1\Big\}+\bar{b}_r y=\bar{T}(\vartheta),
\end{aligned}
\tag{A.6}
$$

$$
\begin{aligned}
&\Big[\left(\eta_1+\mu_2v_2^2\eta_2+\mu_2v_2^2\right)\Gamma_1+(1+\mu_2)\left(1+v_r\cos\varphi_1\right)\\
&+\mu_2v_rv_2\Gamma_1\cos\left(\alpha_1+\varphi_2\right)+\mu_2v_2\left(1+\Gamma_1\right)\cos\left(\alpha_1-\varphi_1+\varphi_2\right)\Big]y'\\
&+\Big[\left(\eta_1+\mu_2v_2^2\eta_2+\mu_2v_2^2\right)\Gamma_1^2+1+\mu_2+2\mu_2v_2\Gamma_1\cos\left(\alpha_1-\varphi_1+\varphi_2\right)\Big]\\
&\left(y'\varphi_1'+y\varphi_1''\right)\\
&+\mu_2v_2\Big[v_2\eta_2\Gamma_1\Gamma_2+v_2\Gamma_1+\cos\left(\alpha_1-\varphi_1+\varphi_2\right)\Big]\\
&\left(y'\varphi_2'+y\varphi_2''\right)+\left(1+\mu_2\right)v_ry\sin\varphi_1\\
&+\mu_2v_rv_2\Gamma_1y\sin\left(\alpha_1+\varphi_2\right)\\
&-\mu_2v_2y\left[\Gamma_1\left(\Gamma_1-1\right)\varphi_1'^2+2\Gamma_1\varphi_1'\varphi_2'-\Gamma_1+\left(\varphi_2'+1\right)^2\right]\\
&\sin\left(\alpha_1-\varphi_1+\varphi_2\right)+\mu_2v_2\frac{d\Gamma_1}{d\varphi_1}y\varphi_1'^2\cos\left(\alpha_1-\varphi_1+\varphi_2\right)\\
&+\left(\eta_1+\mu_2v_2^2\eta_2+\mu_2v_2^2\right)\Gamma_1\frac{d\Gamma_1}{d\varphi_1}y\varphi_1'^2\\
&+\mu_2v_2^2\eta_2\Gamma_1\frac{d\Gamma_2}{d\varphi_2}y\varphi_2'^2+\bar{b}_1\varphi_1'/h=0,
\end{aligned}
\tag{A.7}
$$

$$
\begin{aligned}
&\mu_2v_2\Big[v_2\eta_2\Gamma_2+v_2+v_r\cos\left(\alpha_1+\varphi_2\right)+\cos\left(\alpha_1-\varphi_1+\varphi_2\right)\Big]y'\\
&+\mu_2v_2\Big[v_2\eta_2\Gamma_1\Gamma_2+v_2\Gamma_1+\cos\left(\alpha_1-\varphi_1+\varphi_2\right)\Big]\left(y'\varphi_1'+y\varphi_1''\right)\\
&+\mu_2v_2^2\Big[1+\eta_2\Gamma_2^2\Big]\left(y'\varphi_2'+y\varphi_2''\right)+\mu_2v_rv_2y\sin\left(\alpha_1+\varphi_2\right)\\
&+\mu_2v_2y\left(\varphi_1'+1\right)^2\sin\left(\alpha_1-\varphi_1+\varphi_2\right)+\mu_2v_2^2\left(1+\eta_2\Gamma_2\right)\frac{d\Gamma_1}{d\varphi_1}y\varphi_1'^2\\
&+\mu_2v_2^2\eta_2\Gamma_2\frac{d\Gamma_2}{d\varphi_2}y\varphi_2'^2+\bar{b}_2\varphi_2'/h=0.
\end{aligned}
\tag{A.8}
$$

Appendix A.3. Simplified equations

The simplified rotor equation is

$$
\begin{aligned}
\tilde{\theta}''=\tilde{\mu}\Big\{&-\Lambda_{c1}\varphi_1''-\Lambda_{c2}\varphi_2''+\frac{1}{2}\left[g_dX_1^2+g_1\varphi_1^2+g_fX_2^2\right]\varphi_1''\\
&+\frac{1}{2}\left[g_aX_1^2+g_bX_2^2\right]\varphi_2''+2\left[k_1\varphi_1\varphi_1'+k_{12}\left(\varphi_2\varphi_1'+\varphi_1\varphi_2'\right)+k_2\varphi_2\varphi_2'\right]\\
&+g_aX_1'\left(X_2'+\varphi_1'\right)X_1+g_1\varphi_1\varphi_1'^2+g_bX_2'^2X_2\Big\}+\tilde{T}_1\cos(n\vartheta),
\end{aligned}
\tag{A.9}
$$

where constants g_1, g_a, g_b and g_f are defined in Appendix B and notations X_1 and X_2 are defined as

$$
X_1=\alpha_{11}\varphi_1-\varphi_1+\varphi_2,\quad X_2=\alpha_{11}\varphi_1+\varphi_2. \tag{A.10}
$$

To derive the simplified pendulums' equations, further scaling is necessary. For the nonlinear terms to appear at least at order ϵ in the equation of pendulum 1, it is required that the term

$$\begin{aligned} &- g_a X_1^2 \left(\alpha_{11} \varphi_1'' + \frac{\varphi_2''}{2} \right) - \frac{g_c}{6} X_1^3 - \frac{g_1}{6} \varphi_1^3 - \frac{g_f}{6} X_2^3 \\ &- g_a X_1 \left(X_2'^2 - \alpha_{11} \varphi_1'^2 + 2\varphi_2' \right) \end{aligned} \tag{A.11}$$

be of order ϵ. g_c is a nonlinear constant defined in Appendix B. This scaling is justified for $g_1\varphi_1^3/6$ as this term represents the nonlinearity due to the path of pendulum 1 (*cf.* Appendix E), which is usually considered to be small [40]. However, for the other terms of expression (A.11), the scaling by ϵ is not easily justified but is a choice that might be a source of inaccuracies in the final results. The same scaling requirement arises for the equation of pendulum 2. In that case, it is the term

$$-\frac{g_a}{6} \left[3X_1^2 \varphi_1'' + X_1^3 - 6X_1 \varphi_1' (\varphi_1' + 2) \right] - \frac{g_b}{6} X_2^3 \tag{A.12}$$

that is required to be of order ϵ. To scale terms (A.11) and (A.12), it is convenient to introduce the additional scaled parameters

$$g_1 = \epsilon \tilde{g}_1, \quad g_a = \epsilon \tilde{g}_a, \quad g_b = \epsilon \tilde{g}_b, \quad g_c = \epsilon \tilde{g}_c, \quad g_f = \epsilon \tilde{g}_f. \tag{A.13}$$

With this additional scaling, the simplified pendulums' equations are given by Eqs (16), where f_{p1} and f_{p2} can be split such that

$$f_{p1}(\boldsymbol{\varphi}, \vartheta) = f_{L1}(\boldsymbol{\varphi}) + f_{Q1}(\boldsymbol{\varphi}) + f_{C1}(\boldsymbol{\varphi}) + f_{f1}(\boldsymbol{\varphi}, \vartheta), \tag{A.14a}$$

$$f_{p2}(\boldsymbol{\varphi}, \vartheta) = f_{L2}(\boldsymbol{\varphi}) + f_{Q2}(\boldsymbol{\varphi}) + f_{C2}(\boldsymbol{\varphi}) + f_{f2}(\boldsymbol{\varphi}, \vartheta). \tag{A.14b}$$

f_{Li}, f_{Qi}, f_{Ci} and f_{fi}, $i = 1, 2$, contain exclusively linear, quadratic, cubic and

forcing terms. These functions are

$$f_{L1}(\boldsymbol{\varphi}) = -\tilde{\mu}\Lambda_{c1}\left(\Lambda_{c1}\varphi_1'' + \Lambda_{c2}\varphi_2''\right) + \tilde{b}_1\varphi_1', \tag{A.15a}$$

$$\begin{aligned} f_{Q1}(\boldsymbol{\varphi}) = &-2\tilde{g}_a X_1\varphi_2' - \tilde{\mu}\left(\Lambda_{m1}\varphi_1' + \Lambda_{c12}\varphi_2'\right)\left(\Lambda_{c1}\varphi_1'' + \Lambda_{c2}\varphi_2''\right) \\ &+ 2\tilde{\mu}\Lambda_{c1}\left(k_1\varphi_1\varphi_1' + k_{12}\left(\varphi_1'\varphi_2 + \varphi_2'\varphi_1\right) + k_2\varphi_2'\varphi_2\right), \end{aligned} \tag{A.15b}$$

$$\begin{aligned} f_{C1}(\boldsymbol{\varphi}) = &-\tilde{g}_a X_1^2\left(\alpha_{11}\varphi_1'' + \frac{\varphi_2''}{2}\right) - \frac{\tilde{g}_c X_1^3}{6} - \frac{\tilde{g}_1}{6}\varphi_1^3 - \frac{\tilde{g}_f}{6}X_2^3 \\ &- \tilde{g}_a X_1\left[X_2'^2 - \alpha_{11}\varphi_1'^2\right] + r_1\left(\varphi_1''\varphi_1^2 + \varphi_1\varphi_1'^2\right) \\ &+ r_{12a}\left(\varphi_2''\varphi_2^2 + 2\varphi_2\varphi_2'^2\right) + r_{12b}\varphi_1^2\varphi_2'' + r_{g12}\varphi_1^2\varphi_2 + r_{g1a}\varphi_1^3 \\ &+ \tilde{\mu}\Bigg\{2\left(\Lambda_{m1}\varphi_1' + \Lambda_{c12}\varphi_2'\right) \\ &\left(k_1\varphi_1\varphi_1' + k_{12}\left(\varphi_1'\varphi_2 + \varphi_2'\varphi_1\right) + k_2\varphi_2'\varphi_2\right) \\ &+ \frac{1}{2}\left(g_d X_1^2 + g_f X_2^2 + g_1\varphi_1^2\right)\left(\Lambda_{c2}\varphi_2'' + 2\Lambda_{c1}\varphi_1''\right) \\ &+ \frac{\Lambda_{c1}}{2}\Big(\left(g_a X_1^2 + g_b X_2^2\right)\varphi_2'' \\ &+ 2\left[g_a X_1 X_1'\left(X_2' + \varphi_1'\right) + g_b X_2 X_2'^2 + g_1\varphi_1\varphi_1'^2\right]\Big)\Bigg\}, \end{aligned} \tag{A.15c}$$

$$\begin{aligned} f_{f1}(\boldsymbol{\varphi}, \vartheta) = &\Big[\Lambda_{c1} + \left(\Lambda_{m1} - g_e X_1^2\right)\varphi_1' + \left(\Lambda_{c12} - \frac{g_a}{2}X_1^2\right)\varphi_2' \\ &- \frac{g_d}{2}X_1^2 - \frac{g_f}{2}X_2^2 - \frac{g_1}{2}\varphi_1^2\Big]\tilde{T}_1\cos(n\vartheta) \end{aligned} \tag{A.15d}$$

for pendulum 1 and

$$f_{L2}(\boldsymbol{\varphi}) = -\tilde{\mu}\Lambda_{c2}\left(\Lambda_{c1}\varphi_1'' + \Lambda_{c2}\varphi_2''\right) + \tilde{b}_2\varphi_2', \tag{A.16a}$$

$$\begin{aligned} f_{Q2}(\boldsymbol{\varphi}) = {} & 2\tilde{g}_a X_1\varphi_1' - \tilde{\mu}\left(\Lambda_{c12}\varphi_1' + \Lambda_{m2}\varphi_2'\right)\left(\Lambda_{c1}\varphi_1'' + \Lambda_{c2}\varphi_2''\right) \\ & + 2\Lambda_{c2}\tilde{\mu}\left(k_1\varphi_1\varphi_1' + k_{12}\left(\varphi_1'\varphi_2 + \varphi_2'\varphi_1\right) + k_2\varphi_2'\varphi_2\right) \end{aligned} \tag{A.16b}$$

$$\begin{aligned} f_{C2}(\boldsymbol{\varphi}) = {} & -\frac{\tilde{g}_a}{6}\left[3X_1^2\varphi_1'' + X_1^3 - 6X_1\varphi_1'^2\right] - \frac{\tilde{g}_f}{6}X_2^3 + r_{12a}\varphi_1''\varphi_2^2 \\ & + r_{12b}\left(\varphi_1''\varphi_1^2 + 2\varphi_1\varphi_1'^2\right) + r_2\left(\varphi_2''\varphi_2^2 + \varphi_2\varphi_2'^2\right) + r_{g1b}\varphi_1^3 \\ & + \tilde{\mu}\Big\{2\left(\Lambda_{c12}\varphi_1' + \Lambda_{m2}\varphi_2'\right) \\ & \left(k_1\varphi_1\varphi_1' + k_{12}\left(\varphi_1'\varphi_2 + \varphi_2'\varphi_1\right) + k_2\varphi_2'\varphi_2\right) \\ & + \frac{1}{2}\left(g_a X_1^2 + g_b X_2^2\right)\left(\Lambda_{c1}\varphi_1'' + 2\Lambda_{c2}\varphi_2''\right) \\ & + \frac{\Lambda_{c2}}{2}\Big(\left[g_d X_1^2 + g_f X_2^2 + g_1\varphi_1^2\right]\varphi_1'' \\ & + 2\left[g_a X_1 X_1'\left(X_2' + \varphi_1'\right) + g_b X_2 X_2'^2 + g_1\varphi_1\varphi_1'^2\right]\Big)\Big\} \end{aligned} \tag{A.16c}$$

$$\begin{aligned} f_{f2}(\boldsymbol{\varphi}, \vartheta) = {} & \left[\Lambda_{c2} + \left(\Lambda_{c12} - \frac{g_a}{2}X_1^2\right)\varphi_1' + \Lambda_{m2}\varphi_2' - \frac{g_a}{2}X_1^2 - \frac{g_b}{2}X_2^2\right] \\ & \tilde{T}_1\cos(n\vartheta) \end{aligned} \tag{A.16d}$$

for pendulum 2. g_d and g_e are nonlinear constants defined in Appendix B.

Appendix A.4. Modal simplified equations

Following the procedure described in section 4.2, one obtains the modal equations (21), where functions $\hat{f}_i$ can be decomposed as

$$\hat{f}_i(\zeta_i, \vartheta) = \hat{f}_{Li}(\zeta_i) + \hat{f}_{Qi}(\zeta_i) + \hat{f}_{Ci}(\zeta_i) + \hat{f}_{fi}(\zeta_i, \vartheta). \tag{A.17}$$

$\hat{f}_{Li}$, $\hat{f}_{Qi}$, $\hat{f}_{Ci}$ and $\hat{f}_{fi}$ contain exclusively linear, quadratic, cubic and forcing terms. These functions are

$$\hat{f}_{Li}(\zeta_i) = -\tilde{\mu}\hat{\Lambda}_{ci}^2\zeta_i'' + \hat{b}_i\zeta_i', \tag{A.18a}$$

$$\hat{f}_{Qi}(\zeta_i) = 2\tilde{\mu}\hat{\Lambda}_{ci}\hat{k}_i\zeta_i\zeta_i' - \tilde{\mu}\hat{\Lambda}_{ci}\hat{\Lambda}_{mi}\zeta_i'\zeta_i'', \tag{A.18b}$$

$$\begin{aligned}\hat{f}_{Ci}(\zeta_i) = &-\frac{1}{6}\left[\tilde{g}_1 + \tilde{g}_a\left(\alpha_{11} - 1 + \chi_{pi}\right)^4 + \tilde{g}_b\left(\alpha_{11} + \chi_{pi}\right)^4\right]\zeta_i^3 \\ &+ \left(\hat{r}_i + 2\hat{r}_{12i}\right)\left(\zeta_i^2\zeta_i'' + \zeta_i\zeta_i'^2\right) + \hat{r}_{gi}\zeta_i^3 + 2\tilde{\mu}\hat{\Lambda}_{mi}\hat{k}_i\zeta_i\zeta_i'^2 \\ &- \tilde{g}_a\left(\alpha_{11} + \chi_{pi}\right)\left(\alpha_{11} - 1 + \chi_{pi}\right)^2\left(\zeta_i^2\zeta_i'' + \zeta_i\zeta_i'^2\right) \\ &+ \tilde{\mu}\hat{\Lambda}_{ci}c_{fi}\left(\zeta_i^2\zeta_i'' + \zeta_i\zeta_i'^2\right)\end{aligned} \tag{A.18c}$$

$$\hat{f}_{fi}(\zeta_i, \vartheta) = \Big[\hat{\Lambda}_{ci} + \hat{\Lambda}_{mi}\zeta_i' - \frac{c_{fi}}{2}\zeta_i^2 - g_a\chi_{pi}^2\left(\alpha_{11} + \chi_{pi}\right) \tag{A.18d}$$

$$\left(\alpha_{11} - 1 + \chi_{pi}\right)^2\zeta_i^2\zeta_i'\Big]\tilde{T}_1\cos(n\vartheta). \tag{A.18e}$$

c_{fi} is a modal parameter contributing to the forcing and described in Appendix B. Note that the modal projection generates a linear term

$$2\tilde{\mu}w_i[(\Lambda_{c12} + \Lambda_{m2}\chi_{pi})\zeta_i'' + (k_{12} + k_2\chi_{pi})\zeta_i], \tag{A.19}$$

which could be included in $\hat{f}_{Li}(\zeta_i)$. However, using the first order solution of the modal equation, $\zeta_i'' = -n_{pi}^2\zeta_i$, this additional term reduces to

$$2\tilde{\mu}w_i[k_{12} + k_2\chi_{pi} - n_{pi}^2(\Lambda_{c12} + \Lambda_{m2}\chi_{pi})]\zeta_i, \tag{A.20}$$

and from the definition of χ_{pi} (*cf.* section 3.1), we have $k_{12} + k_2\chi_{pi} - n_{pi}^2(\Lambda_{c12} + \Lambda_{m2}\chi_{pi}) = 0$. Hence, w_i does not contribute to the response at the order retained.

Appendix B. Notations

The expression of the notations introduced in section 3 is

$$
\begin{aligned}
\Lambda_{m1} &= h[1+(\eta_1+\eta_2\mu_2\nu_2^2)\alpha_{11}^2+\mu_2(1+\nu_2\alpha_{11})^2],\\
\Lambda_{m2} &= h\mu_2\nu_2^2(1+\eta_2\alpha_{21}^2),\\
\Lambda_{c1} &= h[1+\nu_r+(\eta_1+\eta_2\mu_2\nu_2^2+\mu_2\nu_2^2)\alpha_{11}+\mu_2(1+\nu_r+\nu_2)],\\
\Lambda_{c2} &= h\mu_2\nu_2[\nu_2(1+\eta_2\alpha_{21})+1+\nu_r],\\
\Lambda_{c12} &= h\mu_2\nu_2[1+\nu_2\alpha_{11}(1+\eta_2\alpha_{21})],\\
k_1 &= h[(1+\mu_2)\nu_r+\mu_2\nu_2\left((\alpha_{11}-1)^2+\nu_r\alpha_{11}^2\right)],\\
k_2 &= h\mu_2\nu_2(1+\nu_r),\\
k_{12} &= h\mu_2\nu_2[(1+\nu_r)\alpha_{11}-1],\\
\bar{\Lambda}_{m1} &= \Lambda_{m1}-\frac{\mu}{1+\mu}\Lambda_{c1}^2,\\
\bar{\Lambda}_{m2} &= \Lambda_{m2}-\frac{\mu}{1+\mu}\Lambda_{c2}^2,\\
\bar{\Lambda}_{c12} &= \Lambda_{c12}-\frac{\mu}{1+\mu}\Lambda_{c1}\Lambda_{c2}.
\end{aligned}
\tag{B.1}
$$

The expression of the nonlinear coefficients introduced in section 4 is

$$
\begin{aligned}
g_1 &= h\nu_r(1+\mu_2),\\
g_a &= h\mu_2\nu_2,\\
g_b &= \nu_r g_a,\\
g_c &= (\alpha_{11}-1)g_a,\\
g_d &= (\alpha_{11}+1)g_a,\\
g_e &= \alpha_{11}g_a,\\
g_f &= \nu_r\alpha_{11}g_a,\\
r_1 &= 6h[(\eta_1+\mu_2\nu_2^2\eta_2+\mu_2\nu_2^2)\alpha_{11}+\mu_2\nu_2]\tilde{\alpha}_{13}\\
r_{12a} &= 3h\mu_2\nu_2^2\eta_2\alpha_{11}\tilde{\alpha}_{23},\\
r_{12b} &= 3h\mu_2\nu_2^2\eta_2(1+\eta_2\alpha_{21})\tilde{\alpha}_{13},\\
r_2 &= 6h\mu_2\nu_2^2\eta_2\alpha_{21}\tilde{\alpha}_{23},\\
r_{g1a} &= 4(k_1\alpha_{11}-g_a)\tilde{\alpha}_{13},\\
r_{g1b} &= k_2\tilde{\alpha}_{13},\\
r_{g12} &= 3k_2\tilde{\alpha}_{13},
\end{aligned}
\tag{B.2}
$$

and the expression of the modal parameters is

$$
\begin{aligned}
\hat{\Lambda}_{mi} &= \Lambda_{m1} + 2\chi_{pi}\Lambda_{c12} + \chi_{pi}^2\Lambda_{m2},\\
\hat{k}_i &= k_1 + 2\chi_{pi}k_{12} + \chi_{pi}^2 k_2,\\
\hat{\Lambda}_{ci} &= \Lambda_{c1} + \chi_{pi}\Lambda_{c2},\\
\hat{b}_i &= \tilde{b}_1 + \chi_{pi}^2\tilde{b}_2,\\
\hat{r}_i &= r_1 + \chi_{pi}^4 r_2,\\
\hat{r}_{12i} &= r_{12a}\chi_{pi}^3 + r_{12b}\chi_{pi},\\
\hat{r}_{gi} &= r_{g1a} + (r_{g1b} + r_{g12})\chi_{pi},\\
c_{fi} &= g_1 + g_a(\alpha_{11} - 1 + \chi_{pi})^2(\alpha_{11} + 1 + \chi_{pi}) + g_b(\alpha_{11} + \chi_{pi})^3,\\
c_{pi} &= \tilde{g}_1 + 4n_{pi}^2(\hat{r}_i + 2\hat{r}_{12i}) - 6\hat{r}_{gi}\\
c_{si} &= \tilde{g}_a(\alpha_{11} - 1 + \chi_{pi})^2[(\alpha_{11} - 1 + \chi_{pi})^2 - 4n_{pi}^2(\alpha_{11} + \chi_{pi})]\\
&\quad + \tilde{g}_b(\alpha_{11} + \chi_{pi})^4,\\
c_{ti} &= 4\tilde{\mu}\hat{\Lambda}_{ci}n_{pi}^2 c_{fi},\\
c_{ci} &= 4\tilde{\mu}\hat{\Lambda}_{mi}\hat{k}_i n_{pi}^2,\\
\delta_{ni} &= \frac{\hat{\Lambda}_{ci}^2 n_{pi}}{2\hat{\Lambda}_{mi}}.
\end{aligned}
\tag{B.3}
$$

Appendix C. Antiresonances of the rotor's response

The antiresonances of the rotor are computed from the conservative equations associated to system (5). These antiresonances are the solutions of

$$
\det\begin{pmatrix}
\bar{T}_1 & -n^2\Lambda_{c1} & -n^2\Lambda_{c2}\\
0 & k_1 - n^2\Lambda_{m1} & k_{12} - n^2\Lambda_{c12}\\
0 & k_{12} - n^2\Lambda_{c12} & k_2 - n^2\Lambda_{m2}
\end{pmatrix} = 0, \tag{C.1}
$$

which we can develop as

$$
\bar{T}_1 \det\begin{pmatrix}
k_1 - n^2\Lambda_{m1} & k_{12} - n^2\Lambda_{c12}\\
k_{12} - n^2\Lambda_{c12} & k_2 - n^2\Lambda_{m2}
\end{pmatrix} = 0. \tag{C.2}
$$

The determinant to be computed is the same as that associated to the eigenvalue problem of the uncoupled system (6). Hence, the solutions of Eq. (C.2) are

$$n_{AR1} = n_{p1}, \quad n_{AR2} = n_{p2}. \tag{C.3}$$

It is fair to assume that the antiresonances of the non-conservative system are also given by Eq. (C.3) as damping in a CDPVA is typically desired to be as small as possible.

Appendix D. Performance indicator G_i

To compute G_i, one first needs to project the equations of motion (5) on the linear modes (*cf.* section 3.1) and to neglect the modal coupling through the damping (this is relevant as damping is small) in order to obtain an uncoupled problem in terms of the modal coordinates. This can be solved to obtain the complex amplitudes of the modal coordinates, given by

$$\hat{R}_0 = \frac{\tilde{f}_0}{\tilde{m}_0} \frac{1}{-n^2 + jn\tilde{b}_0/\tilde{m}_0}, \tag{D.1a}$$

$$\hat{R}_i = \frac{\tilde{f}_i}{\tilde{m}_i} \frac{1}{n_{i0}^2 - n^2 + jn\tilde{b}_i/\tilde{m}_i}, \quad i = 1, 2. \tag{D.1b}$$

$\hat{R}_i$, $\tilde{m}_i$, $\tilde{b}_i$ and $\tilde{f}_i$ are the complex amplitude, mass, damping coefficient and forcing associated to mode i, $i = 0, 1, 2$. n_{i0} are the natural orders given in section 3.1. We give

$$\tilde{m}_0 = \frac{1+\mu}{\mu}, \tag{D.2a}$$

$$\begin{aligned} \tilde{m}_i = {} & \Lambda_{c12}\chi_i + \Lambda_{c1}\varrho_i + \Lambda_{m1} + \chi_i(\Lambda_{c12} + \Lambda_{c2}\varrho_i + \Lambda_{m2}\chi_i) \\ & + \varrho_i \left(\Lambda_{c1} + \Lambda_{c2}\chi_i + \frac{\varrho_i(1+\mu)}{\mu} \right) \end{aligned} \tag{D.2b}$$

$$\tilde{b}_0 = \frac{\bar{b}_r}{\mu}, \quad \tilde{b}_i = \bar{b}_1 + \bar{b}_2 + \frac{\bar{b}_r}{\mu}\varrho_i^2, \quad \tilde{f}_0 = \frac{\bar{T}_1}{\mu}, \quad \tilde{f}_i = \frac{\bar{T}_1\varrho_i}{\mu}. \tag{D.2c}$$

As we look for the response at $n = n_{pi}$, several approximations can be done. First, the contribution of mode $j \neq \{0, i\}$ is negligible so the rotor's amplitude

reduces to

$$|\theta| = \hat{R}_0 + \varrho_i \hat{R}_i. \tag{D.3}$$

Moreover, it is fair to neglect the contribution of $\tilde{b}_0$ as it has a very small influence on the response. Finally, we obtain

$$|h_1^2|_{n=n_{pi}} = \left| \frac{(\tilde{f}_0 \tilde{m}_0 (n_{pi}^2 - n_i^2) + \varrho_i \tilde{f}_i \tilde{m}_0 n_{pi}^2)^2 + \tilde{f}_0^2 n_{pi}^2 \tilde{b}_i^2}{\tilde{m}_0^2 \tilde{m}_i^2 (n_i - n_{pi})^2 (n_i + n_{pi})^2 + \tilde{m}_0^2 n_{pi}^2 \tilde{b}_i^2} \right|. \tag{D.4}$$

The rotor's amplitude with fixed pendulums is directly obtained from Eq. (5a) in which we set $\varphi_1 = \varphi_2 = 0$, leading to

$$h_{1f} = \frac{\bar{T}_1}{1 + \mu}. \tag{D.5}$$

G_i can be deduced directly from Eqs. (D.4) and (D.5).

Appendix E. Relation between coefficient g_1 and the path nonlinearity of a CPVA

In the special case where pendulum 2 is massless, i.e. $\mu_2 = \eta_2 = 0$, g_1 reduces to

$$g_1 = \frac{\nu_r}{(1 + \nu_r)^2}. \tag{E.1}$$

When studying a CPVA, the path is often controlled through the path function [22]

$$x(s) = 1 - \nu_r s^2 + x_{[4]} s^4, \tag{E.2}$$

where s is the dimensionless curvilinear abscissa of the pendulum along its path and $x_{[4]}$ is the first-order nonlinear coefficient of the path. s is usually defined as [22]

$$s = \frac{S}{r + \ell_1}. \tag{E.3}$$

Moreover, in the case of a circular path, one has [14, 31]

$$\begin{aligned} S = \ell_1 \varphi_1 \quad \Rightarrow \quad \frac{\varphi_1}{s} = \frac{r + \ell_1}{\ell_1} = (1 + \nu_r), \\ x_{[4]} = \frac{\nu_r (1 + \nu_r)^2}{12}. \end{aligned} \tag{E.4}$$

Hence, one has the relation

$$g_1 = \frac{x_{[4]}}{12(1+\nu_r)^4}, \tag{E.5}$$

where the factor $(1+\nu_r)^4$ comes from the fact that the pendulum's motion is written in terms of s or φ_1 and the factor 12 simply depends on the way g_1 and $x_{[4]}$ are defined. Thus, g_1 can be thought of as the equivalent of $x_{[4]}$.

Appendix F. Application of the method of multiple scales

The system obtained through the method of multiple scales is given by Eq. (25) where functions f_{u_i} and f_{β_i} are

$$f_{u_i}(u_i,\beta_i) = \frac{-8\hat{b}_i n_{pi} u_i - (8\hat{\Lambda}_{ci} - c_{fi}u_i^2)\tilde{T}_1 \sin\beta_i}{16\hat{\Lambda}_{mi} n_{pi}} \tag{F.1a}$$

$$f_{\beta_i}(u_i,\beta_i) = \sigma u_i - \tilde{\mu}\delta_{ni}u_i + \frac{c_i u_i^3 - (8\hat{\Lambda}_{ci} - 3c_{fi}u_i^2)\tilde{T}_1 \cos\beta_i}{16\hat{\Lambda}_{mi} n_{pi}}. \tag{F.1b}$$

Constants c_i, c_{fi} and δ_{ni} are defined in Eq. (26) and Appendix B, respectively.

Appendix G. Steady state solutions

The amplitude and phase response of mode i are given by

$$\sigma = \tilde{\mu}\delta_{ni} - \frac{c_i u_i^2}{16\hat{\Lambda}_{mi} n_{pi}} \pm \frac{8\hat{\Lambda}_{ci} - 3c_{fi}u_i^2}{16\hat{\Lambda}_{mi} n_{pi}} \sqrt{\frac{\tilde{T}_1^2}{u_i^2} - \frac{64\hat{b}_i^2 n_{pi}^2}{(8\hat{\Lambda}_{ci} - c_{fi}u_i^2)^2}}, \tag{G.1a}$$

$$\tilde{T}_1^2 = u_i^2 \left[\frac{\left(16\hat{\Lambda}_{mi} n_{pi}(\sigma - \tilde{\mu}\delta_{ni}) + c_i u_i^2\right)^2}{(8\hat{\Lambda}_{ci} - 3c_{fi}u_i^2)^2} + \frac{64\hat{b}_i^2 n_{pi}^2}{(8\hat{\Lambda}_{ci} - c_{fi}u_i^2)^2} \right], \tag{G.1b}$$

$$\tan\beta_i = \frac{-8\hat{b}_i n_{pi}}{16\hat{\Lambda}_{mi} n_{pi}(\sigma - \tilde{\mu}\delta_{ni}) + c_i u_i^2} \frac{8\hat{\Lambda}_{ci} - 3c_{fi}u_i^2}{8\hat{\Lambda}_{ci} - c_{fi}u_i^2}. \tag{G.1c}$$

When the pendulums respond on mode i, the amplitudes and phases of the three first harmonics of the rotor's acceleration are given by

$$h_1^2 = \bar{T}_1^2 + \mu \bar{T}_1 n^2 u_i \cos\beta_i \left(2\hat{\Lambda}_{ci} - \frac{c_{fi}}{4}u_i^2\right) + \frac{\mu^2}{4} n^4 u_i^2 \left(2\hat{\Lambda}_{ci} - \frac{c_{fi}}{4}u_i^2\right)^2 \tag{G.2a}$$

$$\tan\psi_1 = \frac{\mu n^2 u_i \sin\beta_i (8\hat{\Lambda}_{ci} - c_{fi}u_i^2)}{\mu n^2 u_i \cos\beta_i (8\hat{\Lambda}_{ci} - c_{fi}u_i^2) + 8\bar{T}_1}, \tag{G.2b}$$

$$h_2 = \mu n_{pi} \hat{k}_i u_i^2, \tag{G.2c}$$

$$\tan\psi_2 = \frac{-\cos(2\beta_i)}{\sin(2\beta_i)}, \tag{G.2d}$$

$$h_3 = \frac{3\epsilon|c_{ti}|}{32\hat{\Lambda}_{ci}} u_i^3, \tag{G.2e}$$

$$\tan\psi_3 = \frac{-\sin(3\beta_i)}{-\cos(3\beta_i)}. \tag{G.2f}$$

Appendix H. Looping of the rotor's response around the antiresonance

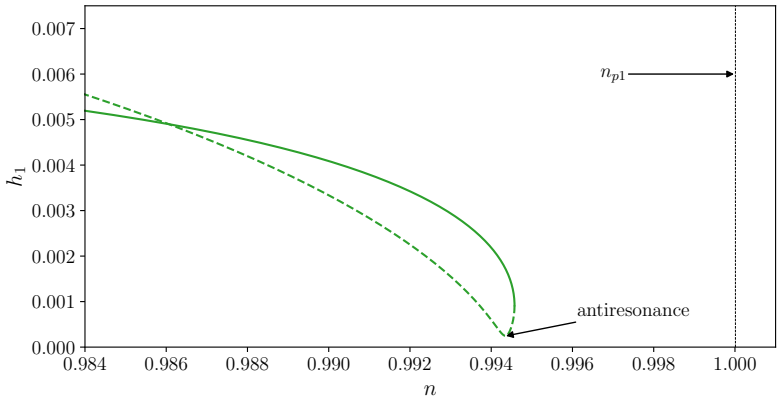

Figure H.10: Rotor's response around the first antiresonance as a function of the excitation order. The stable and unstable parts of the analytical solutions are shown as solid and dashed lines, respectively. $\bar{T}_1 = 0.008$ and the system parameters are given in Tab. 2.

Figure H.10 shows the rotor's response around the first antiresonance at a large torque level. One can see the looping of the rotor's response around n_{AR1}, which causes the antiresonance to be unstable.

Chapter 10

Stability of the unison response of centrifugal double pendulums

This chapter is made of a paper about to be submitted to the *Journal of Theoretical, Computational and Applied Mechanics* [153]. It focuses on the stability of the response of a CDPVA made of several double pendulums. We particularly discuss the instability of the unison response that causes a localised solution to appear. Hence, it is the logical continuity of chapter 9 where the nonlinear response of a CDPVA was derived but the instabilities related to the presence of multiple double pendulums were ignored.

The context of this study, described in section 1, repeats information from chapters 1 and 2. Hence, the reader might want to skip this section if he already read these chapters. Moreover, sections 2 to 4.1 are very similar to information provided in chapter 9. They present the modelling, a linear analysis and the derivation of physical simplified equations for a CDPVA made of two double pendulums, whereas a single double pendulum was considered in chapter 9. Hence, the reader might want to go quickly over these sections if he already read chapter 9.

The novelty of the article starts in section 4.2, where we consider that the system might respond on two modes, whereas only a single-mode response was investigated in chapter 9. The modal and physical solutions are computed in section 4.3 and their stability is assessed in section 4.4 using the method of multiple scales (*cf.* section 2.5.2.1). The results are applied to case studies in section 5 and verified through comparisons with numerical resolutions of the system's dynamics. Numerical investigations showed the existence of quasi-periodic and even chaotic solutions. Moreover, it is verified that the analytical model, though derived considering only two double pendulums, allows to predict bifurcations towards localised solutions no matter the number of pendulums considered. A design guideline allowing to avoid instabilities is proposed and represented in the parameter space with other guidelines from chapter 9. This allows to identify the ideal tuning of a CDPVA.

On the dynamic stability of centrifugal double pendulum vibration absorbers

V. Mahé[a,b], A. Renault[b], A. Grolet[a], H. Mahé[b], O. Thomas[a]

[a] *Arts et Metiers Institute of Technology, LISPEN, HESAM Université, F-59000 Lille, France*
[b] *Valeo Transmissions, Centre d'Étude des Produits Nouveaux, Espace Industriel Nord, Route de Poulainville, 80009 Amiens Cedex 1, France*

Abstract

Centrifugal double pendulum vibration absorbers (CDPVAs) can be used to reduce torsional vibrations of rotating machines. These passive devices are made of several double pendulums oscillating relatively to a rotor. The expected behaviour of such devices is a unison motion of the double pendulums. However, these systems are subjected to nonlinear energy localisation phenomena, causing the pendulums to oscillate differently and decreasing their efficiency. This issue is investigated in details using an analytical model based on a perturbation method, allowing to predict the unison response and its stability. These analytical results are validated through numerical resolutions of the system's dynamics and original design guidelines are provided. These guidelines and the stability information are then visualised in the design space to help identify the optimal CDPVA designs.

Keywords: centrifugal pendulum vibration absorber, nonlinear dynamics, torsional vibration, energy localisation

1. Introduction

In the frame of reducing polluting emissions and fuel consumption of vehicles using thermal engines, automotive manufacturers try to reduce the cylinder

Email addresses: vincent.mahe@ensam.eu (V. Mahé), alexandre.renault@valeo.com (A. Renault), aurelien.grolet@ensam.eu (A. Grolet), herve.mahe@valeo.com (H. Mahé), olivier.thomas@ensam.eu (O. Thomas)

capacity and engine speed of rotation. These evolutions lead to a significant increase of rotation irregularities called acyclisms, mainly due to higher combustion pressure. One of the main characteristics of these reciprocating engines is the linear dependency of the acyclism frequency to the engine speed of rotation. The coefficient of proportionality is the engine order and only depends on the architecture of the engine. During an acceleration phase, the engine sweeps a wide frequency range containing some driveline torsional modes. This situation may lead to significant noise and vibration levels into the passenger compartment and premature wear of the driveline components. This study deals with centrifugal double pendulum vibration absorbers (CDPVAs), which are a mean to reduce the vibrations of driveline components. The principle of operation of CDPVAs is very close from that of centrifugal pendulum vibration absorbers (CPVAs), which have been used for many years to minimise acyclisms of automotive powertrains at the engine order [1–3]. These passive devices consist of oscillating masses (pendulums) moving along paths relative to a primary inertia (rotor) as shown in Fig. 1 in the case of a CDPVA. Because the absorbers (single pendulums for a CPVA, double pendulums for a CDPVA) are driven by the centrifugal acceleration field resulting from the rotation of the system, their natural frequency is proportional to the engine speed of rotation. Hence, CPVAs and CDPVAs act as dynamic vibration absorbers tuned with respect to an order rather than a frequency. This allows the antiresonance frequency to shift linearly with the rotational velocity so that the vibrations are reduced over the whole engine speed range.

CDPVAs were first investigated by R. W. Zdanowich and T. S. Wilson [4], who showed that they generate two rotor antiresonances. Later, J.-G. Duh and M. Wenyong [5] presented experimental evidence of the filtering effect of CDPVAs at two distinct orders. It is important to be aware that CDPVAs exhibit nonlinearities of different natures: geometric nonlinearities due to the large amplitude of motion of the pendulums and their coupling, and inertial nonlinearities, for instance due to Coriolis effects. J.-G. Duh and M. Weny-

ong [5] showed that overtuning the double pendulums increases the efficiency at large excitation levels due to the softening behaviour of their CDPVA design. Recently, V. Manchi and C. Sujatha [6] exposed the advantages of CDPVAs over CPVAs, proposed an analytical approach to approximate the system's response, and showed experimentally the vibration reduction effect of CDPVAs. V. Mahe *et al.* extended these investigations by accounting for the rotational inertia of the pendulums about their center of mass, allowing the model to better represent real systems [7]. An original analytical approach was presented and design guidelines allowing to maximise the efficiency of the CDPVA were derived. To the author's knowledge, these are the only four studies dealing with CDPVAs. However, many studies were carried out on CPVAs, whose challenging design issues are close from those of CDPVAs. One of the first research topics on CPVAs was the shape of the pendulums' path [8–11], as circular paths were known to cause nonlinear jumps of the system's response. Among the other main issues investigated are the localisation of the pendulums' response [12–25], the shift of the antiresonance [8, 24, 26–29] and the generation of higher rotor harmonics [24, 30–35]. Though most studies on CPVAs consider purely translated pendulums, some works, mostly recent ones, also account for their rotation about their center of mass [4, 21–25, 28, 36–53]. This increased interest for rocking absorbers is probably due to pioneer results from by J. Mayet *et al.* showing that the rotational motion can significantly improve the efficiency of a CPVA [41].

The motivation of this paper is to increase the knowledge on CDPVAs by investigating the instabilities of the unison response related to symmetry-breaking bifurcations. To the authors' knowledge, it is the first study of the localisation phenomenon in CDPVAs. An original method to study efficiently this phenomenon is presented, and the analytical results are compared with numerical resolutions of the system's dynamics. The analytical approach is close from that used in [7] except that $N > 1$ double pendulums are considered, so that localised solutions can exist. The procedure to assess the stability of the unison

solution is similar to that used in [25] and [52], which focused on the stability of the localised and subharmonic responses of two-pendulums CPVAs, respectively.

This paper is organised as follows. Section 2 describes the modelling of the CDPVA and a linear analysis is detailed in 3. The analytical model describing the nonlinear response of a CDPVA and its stability is derived in section 4. Case studies and guidelines to avoid localisation and achieve maximum performance are presented in section 5. This paper ends with a conclusion in section 6.

2. Modelling

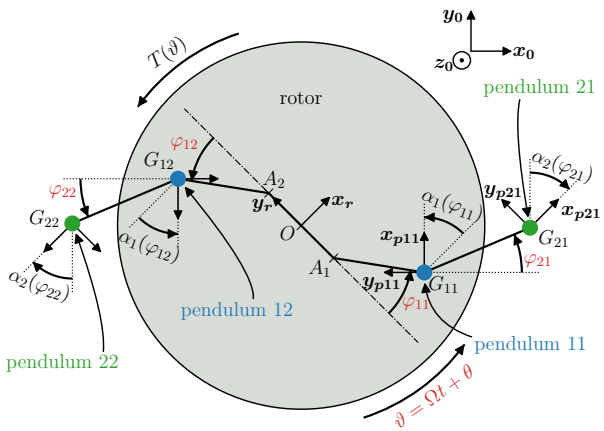

Figure 1: Representation of the system studied. Only two double pendulums are represented here.

The system studied is shown in Fig. 1. A rotor of inertia J_r rotates about its centre O. The frame $\mathscr{R}_r(O, \boldsymbol{x_r}, \boldsymbol{y_r}, \boldsymbol{z_0})$ is attached to the rotor at point O. The rotation of this frame with respect to the Galilean frame $\mathscr{R}_0(O, \boldsymbol{x_0}, \boldsymbol{y_0}, \boldsymbol{z_0})$ is $\vartheta(t) = \Omega t + \theta(t)$ where t is the time, Ω is the mean rotational velocity and $\theta(t)$ corresponds to the fluctuating part of the rotation. A torque $T(\vartheta) = T_0 + T_\theta(\vartheta)$ is applied to the rotor where T_0 is its constant part and $T_\theta(\vartheta)$ is periodic. At

equilibrium, $T_0 = b_r\Omega$ where b_r is the linear viscous damping coefficient of the rotor, such that the constant torque balances with the damping to set the mean rotational speed Ω.

N double pendulums are attached to the rotor, one at point at point A_1 the other at A_2. For the i$^{\text{th}}$ double pendulum, the first pendulum is attached at a distance $OA_i = r$ from the rotor's center. It has length $A_iG_{1i} = \ell_1$, mass m_1 and inertia I_1 about its center of mass G_{1i}. The position of G_{1i} with respect to $\mathscr{R}_r$ is located through angle $\varphi_{1i}(t)$. The frame $\mathscr{R}_{p1i}(G_{1i}, \boldsymbol{x_{p1i}}, \boldsymbol{y_{p1i}}, \boldsymbol{z_0})$ is attached to pendulum 1i at point G_{1i}. Its rotation with respect to $\mathscr{R}_r$ is $\alpha_1(\varphi_{1i})$. The second pendulum is attached to the first one at point G_{1i}. It has length $G_{1i}G_{2i} = \ell_2$, mass m_2 and inertia I_2 about its center of mass G_{2i}. The position of G_{2i} with respect to $\mathscr{R}_{p1i}$ is located through angle $\varphi_{2i}(t)$. The frame $\mathscr{R}_{p2i}(G_{2i}, \boldsymbol{x_{p2i}}, \boldsymbol{y_{p2i}}, \boldsymbol{z_0})$ is attached to pendulum 2 at point G_{2i}. Its rotation with respect to $\mathscr{R}_{p1i}$ is $\alpha_2(\varphi_{2i})$. As for the rotor, equivalent linear viscous damping coefficients b_1 and b_2 are used to model the damping between the rotor and pendulums 1i and between pendulums 1i and pendulums 2i, respectively.

The dimensional equations of motion are derived in [7] in the case of a single double pendulum. To write these equations in a dimensionless form, the following quantities are introduced:

$$
\begin{aligned}
y = \frac{\dot\vartheta}{\Omega} = 1 + \frac{\dot\theta}{\Omega}, \quad \mu &= \frac{N\left(m_1(r+\ell_1)^2 + m_2(r+\ell_1+\ell_2)^2\right)}{J_r + N(I_1+I_2)},\\
\eta_1 = \frac{I_1}{m_1\ell_1^2}, \quad \eta_2 = \frac{I_2}{m_2\ell_2^2}, \quad \mu_2 &= \frac{m_2}{m_1}, \quad \nu_r = \frac{r}{\ell_1}, \quad \nu_2 = \frac{\ell_2}{\ell_1},\\
h = \frac{m_1\ell_1^2}{m_1(r+\ell_1^2) + m_2(r+\ell_1+\ell_2)^2} &= \frac{1}{(\nu_r+1)^2 + \mu_2(\nu_r+1+\nu_2)^2},\\
\bar b_r = \frac{b_r}{(J_r + N(I_1+I_2))\Omega}, \quad \bar b_1 = h\frac{b_1}{m_1\ell_1^2\Omega}, \quad \bar b_2 &= h\frac{b_2}{m_1\ell_1^2\Omega},\\
\bar T(\vartheta) = \bar T_0 + \bar T_\theta(\vartheta) &= \frac{T(\vartheta)}{(J_r + N(I_1+I_2))\Omega^2},\\
\Gamma_1(\varphi_{1i}) = \frac{d\alpha_1(\varphi_{1i})}{d\varphi_{1i}}, \quad \Gamma_2(\varphi_{2i}) &= \frac{d\alpha_2(\varphi_{2i})}{d\varphi_{2i}},
\end{aligned}
\tag{1}
$$

where $(\dot\bullet) = \partial(\bullet)/\partial t$. $y(t)$, $\varphi_{1i}(t)$ and $\varphi_{2i}(t)$ are the $2N+1$ degree-of-freedom of

the system. y corresponds to the dimensionless rotational velocity of the rotor. μ, η_1, η_2 and h are inertia ratios. μ_2 is the mass ratio between pendulums 1i and 2i. ν_r and ν_2 are dimensionless lengths associated to r and ℓ_2, respectively. $\bar{b}_r$, $\bar{b}_1$ and $\bar{b}_2$ are non-dimensional damping constants and $\bar{T}(\vartheta)$ is the non-dimensional torque applied on the rotor. Γ_1 and Γ_2 are rotation functions. It is convenient to define these rotation functions as polynomials such that

$$\alpha_1(\varphi_{1i}) = \alpha_{11}\varphi_{1i} + \alpha_{13}\varphi_{1i}^3 \quad \Rightarrow \quad \Gamma_1(\varphi_{1i}) = \alpha_{11} + 3\alpha_{13}\varphi_{1i}^2, \tag{2a}$$

$$\alpha_2(\varphi_{2i}) = \alpha_{21}\varphi_{2i} + \alpha_{23}\varphi_{2i}^3 \quad \Rightarrow \quad \Gamma_2(\varphi_{2i}) = \alpha_{21} + 3\alpha_{23}\varphi_{2i}^2. \tag{2b}$$

$\alpha_1(\varphi_{1i})$ and $\alpha_2(\varphi_{2i})$ are chosen to be antisymmetric with respect to φ_{1i} and φ_{2i} based on the experience that, for practical reasons, rotation functions of CPVAs are antisymmetric. α_{11} and α_{21} are linear rotation coefficients involved in the linear response of the system, while α_{13} and α_{23} will contribute to the nonlinear behaviour of the CDPVA (*cf.* section 4.3).

In order to give $\bar{T}(\vartheta)$ the meaning of an external forcing term, we replace the independent variable t by the rotor's position ϑ [54], which can be seen as a non-dimensional time. Using the chain rule, one can show that

$$(\dot{\bullet}) = \Omega y(\bullet)', \quad (\ddot{\bullet}) = \Omega^2 yy'(\bullet)' + \Omega^2 y^2(\bullet)'', \tag{3}$$

where $(\bullet)' = \partial(\bullet)/\partial\vartheta$ (the details can be found in [52]). Hence, the dimensionless rotor's acceleration is now $\ddot{\vartheta}/\Omega^2 = \dot{y}/\Omega = yy'$. Using the dimensionless quantities (1) and the chain rule (3), one can write the equations of motion as

$$\boldsymbol{M}(\boldsymbol{q})\boldsymbol{q}'' + \boldsymbol{C}\boldsymbol{q}' + \boldsymbol{K}(\boldsymbol{q})\boldsymbol{q} + \boldsymbol{f}_{\text{nl}}(\boldsymbol{q}, \boldsymbol{q}', \boldsymbol{q}'') = \boldsymbol{f}(t). \tag{4}$$

$\boldsymbol{q} = [y, \varphi_{11}, \ldots, \varphi_{1N}, \varphi_{21}, \ldots, \varphi_{2N}]^\intercal$ is the vector containing the degree-of-freedom ($^\intercal$ indicates the transpose). $\boldsymbol{M}(\boldsymbol{q})$, $\boldsymbol{C}$, $\boldsymbol{K}(\boldsymbol{q})$ represent the mass, damping and stiffness matrices, respectively. $\boldsymbol{f}_{\text{nl}}(\boldsymbol{q}, \boldsymbol{q}', \boldsymbol{q}'')$ and $\boldsymbol{f}(t)$ are vectors containing nonlinear inertial terms and forcing terms, respectively. In the system of three equations generated by Eq. (4), the first governs the motion of y, the next N

ones govern the φ_{1i} and the last N equations govern the φ_{2i}. These $2N+1$ dimensionless equations are given in Appendix A.

From now on, it is assumed that the fluctuating torque applied on the rotor contains only one harmonic whose non-dimensional form is $\bar{T}_\theta(\vartheta) = \bar{T}_1 \cos(n\vartheta)$, where n is the excitation order. For a car engine, n corresponds to the number of strikes per revolution of the crankshaft.

3. Linear analysis

This section presents a linear analysis of the CDPVA. First of all, one can use Eq. (3) to show that, at first order, $1 + \theta' \approx y$ and $\theta'' \approx yy' \approx y'$ (the demonstration can be found in [52]). Hence, it is possible to represent the motion of the rotor with position θ instead of velocity y. This way, all the degree-of-freedom of the system are positions, which facilitates the representation of the mode shapes. Using θ instead of y and the balance between the constant torque and the damping $\bar{b}_r = \bar{T}_0$ (*cf.* section 2), one can linearise the free, conservative equations associated to Eq. (4), leading to

$$(1+\mu)\theta'' + \frac{\mu}{N}\sum_{i=1}^{N}[\Lambda_{c1}\varphi''_{1i} + \Lambda_{c2}\varphi''_{2i}] = 0, \tag{5a}$$

$$\Lambda_{c1}\theta'' + \Lambda_{m1}\varphi''_{1i} + \Lambda_{c12}\varphi''_{2i} + k_1\varphi_{1i} + k_{12}\varphi_{2i} = 0, \quad i = 1, ..., N, \tag{5b}$$

$$\Lambda_{c2}\theta'' + \Lambda_{c12}\varphi''_{1i} + \Lambda_{m2}\varphi''_{2i} + k_{12}\varphi_{1i} + k_2\varphi_{2i} = 0, \quad i = 1, ..., N. \tag{5c}$$

Λ_{m1} and Λ_{m2} are constants representing the equivalent mass of pendulums 1i and 2i, respectively. Similarly, k_1 and k_2 represent their equivalent stiffness. Λ_{c1} and Λ_{c2} represent the inertial coupling between a double pendulum and the rotor. Λ_{c12} and k_{12} represent the inertial and non-inertial couplings between pendulums 1i and 2i. The expression of these constants in terms of the system parameters is given in Appendix B.

In order to compute the eigenmodes of the system, it is convenient to rewrite

system (5) as

$$\theta'' = -\frac{\mu}{N(1+\mu)} \sum_{i=1}^{N} \left[\Lambda_{c1}\varphi''_{1i} + \Lambda_{c2}\varphi''_{2i}\right], \tag{6a}$$

$$\begin{aligned} &-\frac{\mu}{N(1+\mu)} \sum_{j=1}^{N} \left[\Lambda_{c1}^2\varphi''_{1j} + \Lambda_{c1}\Lambda_{c2}\varphi''_{2j}\right] \\ &+\Lambda_{m1}\varphi''_{1i} + \Lambda_{c12}\varphi''_{2i} + k_1\varphi_{1i} + k_{12}\varphi_{2i} = 0, \quad i = 1, ..., N, \end{aligned} \tag{6b}$$

$$\begin{aligned} &-\frac{\mu}{N(1+\mu)} \sum_{j=1}^{N} \left[\Lambda_{c1}\Lambda_{c2}\varphi''_{1j} + \Lambda_{c2}^2\varphi''_{2j}\right] \\ &+\Lambda_{c12}\varphi''_{1i} + \Lambda_{m2}\varphi''_{2i} + k_{12}\varphi_{1i} + k_2\varphi_{2i} = 0, \quad i = 1, ..., N. \end{aligned} \tag{6c}$$

This way, one can use Eqs. (6b) and (6c), which are independent from θ, to compute "reduced" eigenmodes, i.e. eigenmodes where the mode shape contains only the pendulums' components. In a second step, Eq. (6a) can be used to compute the "full" eigenmodes, including the mode shape's component on θ. Eqs. (6b) and (6c) can also be used to compute the uncoupled modes by simply setting $\mu = 0$.

These computations are done in Appendix C for $N = 2$ double pendulums, leading to the four uncoupled modes

$$\boldsymbol{\psi}^{(o)}_{\boldsymbol{pi}} = [1, -1, \chi_{pi}, -\chi_{pi}]^\intercal, \quad \boldsymbol{\psi}^{(u)}_{\boldsymbol{pi}} = [1, 1, \chi_{pi}, \chi_{pi}]^\intercal, \quad n_{pi}, \quad i = 1, 2. \tag{7}$$

Superscripts (o) and (u) indicate phase-opposition and unison motions of the two double pendulums, respectively. Note that modes $(n_{pi}, \boldsymbol{\psi}^{(o)}_{\boldsymbol{pi}})$ and $(n_{pi}, \boldsymbol{\psi}^{(u)}_{\boldsymbol{pi}})$ are degenerated as they have the same eigenorder[1] n_{pi}. The expression of n_{pi} and the modal components χ_{pi} are given in Appendix C.

The five modes of the coupled system are given by

$$\begin{aligned} \boldsymbol{\phi_0} &= [1, 0, 0, 0, 0]^\intercal, \quad n_{00} = 0, \\ \boldsymbol{\phi}^{(o)}_{\boldsymbol{i}} &= [0, 1, -1, \chi_{pi}, -\chi_{pi}]^\intercal, \quad n^{(o)}_{i0} = n_{pi}, \\ \boldsymbol{\phi}^{(u)}_{\boldsymbol{i}} &= [\varrho_i, 1, 1, \chi_i, \chi_i]^\intercal, \quad n^{(u)}_{i0} > n_{pi}, \quad i = 1, 2, \end{aligned} \tag{8}$$

[1] An eigenorder can be seen as a dimensionless eigenfrequency.

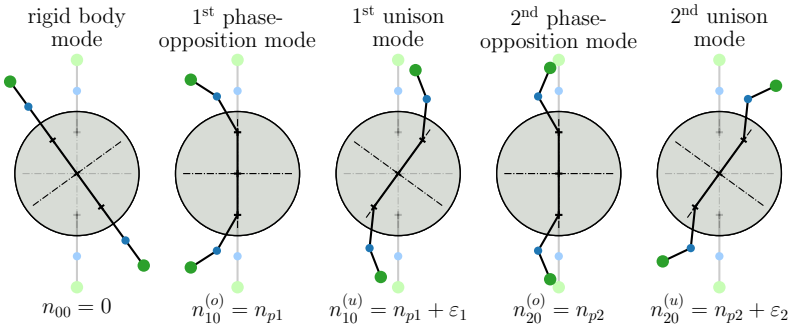

Figure 2: Modes of a CDPVA made of $N = 2$ double pendulums. The rotation of the pendulums about their centre of mass is not represented in this figure. ε_1 and ε_2 indicate that $n_{10}^{(u)}$ and $n_{20}^{(u)}$ are slightly larger than n_{p1} and n_{p2}, respectively.

where the ϱ_i are given in Appendix C. These modes are illustrated in Fig. 2. As for the uncoupled modes, superscripts (o) and (u) indicate phase-opposition and unison motions of the two double pendulums, respectively. $(n_{00}, \boldsymbol{\phi_0})$ is a rigid body mode for which only the rotor responds. The rotor is a node of the phase-opposition modes $(n_{i0}^{(o)}, \boldsymbol{\phi_i}^{(o)})$, and these modes are the same as the uncoupled phase-opposition modes, except for the presence of a null rotor's component. As for CPVAs, one could expect these phase-opposition modes to become degenerated if a CDPVA with more than two double pendulums is considered [23]. $(n_{i0}^{(u)}, \boldsymbol{\phi_i}^{(u)})$ are modes for which the two double pendulums move in unison. To filter-out a fluctuating torque, one can set $n_{pi} \approx n$ to generate and antiresonance on the rotor at $n_{ARi} \approx n$ using the unison mode i.

The linear forced response of a CDPVA can be computed from the linear equations associated to Eq. (4), which yields solutions of the form

$$\begin{aligned} \theta'' = h_1 \cos(n\vartheta - \psi_1), \quad \varphi_{1i} = a_1 \cos(n\vartheta - \xi_1), \\ \varphi_{2i} = a_2 \cos(n\vartheta - \xi_2), \quad i = 1, ..., N. \end{aligned} \tag{9}$$

Such a response is illustrated in Fig. 3. Because the CDPVA has two tuning orders, there are two antiresonances on the rotor's forced response, $n_{AR1} = n_{p1}$ and $n_{AR2} = n_{p2}$.

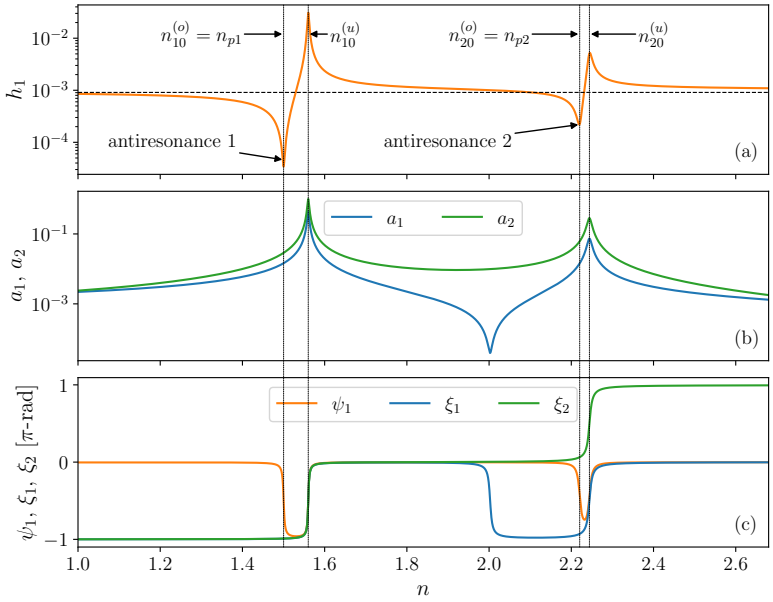

Figure 3: Linear response of a CDPVA showing the amplitude response of the rotor (a) and pendulums (b) and the phase response of the rotor and pendulums (c). The dashed black line in (a) corresponds to the rotor's response with fixed pendulums. $\bar{T}_1 = 0.001$ and the system parameters are given in Tab. 1.

Note that in practice, the excitation order is fixed such that n is a constant and the CDPVA is tuned close to n. Mistuning can exist, either intentionally or because of material imperfections. Varying the excitation order, as in Fig. 3, is similar to introducing mistuning and is therefore relevant for studying the effect of mistuning on the system's response [20].

μ	η_1	η_2	μ_2	ν_r	ν_2	α_{11}	α_{21}	α_{13}	α_{23}	$\bar{b}_r$	$\bar{b}_1$, $\bar{b}_2$
0.1	2	4	0.1	3.745	1	0.4	0.3	0	0	0.0227	5×10^{-5}

Table 1: Parameters of the CDPVA studied in this section.

4. Nonlinear response of a CDPVA

The aim of this section is to present the construction of an analytical model describing the nonlinear response of a CDPVA and its stability. As for CPVAs [55], the construction starts with a scaling of the parameters. This allows a simplification of the equations of motion such that the dynamics of the pendulums becomes uncoupled from that of the rotor. Then, as in [25], the pendulums' equations are written in matrix form and projected on the linear modes, leading to the simplified modal equations. The modal solutions are obtained by considering a response on a single mode and applying the method of multiple scales [56]. Finally, the modal responses are used to deduce the pendulums' motion, which in turn is used to obtain the rotor's response.

4.1. Scaling and simplified physical equations

In order to derive analytical solutions of Eq. (4), it is necessary to simply these equations. The procedure is the same as in [7], so only the main steps are reminded here. The rotor's rotational velocity is decomposed as

$$y(\vartheta) = 1 + y_\theta(\vartheta). \tag{10}$$

As for CPVAs [52], it is relevant to assume small damping, small fluctuations of the rotor's rotational velocity, small torque amplitudes, small ratio of the pendulums' geometric inertia over the CDPVA's rotational inertia. Moreover, the rotation laws considered are close from linear. Hence, we can scale the parameters such that [7]

$$\begin{gathered} \bar{b}_1 = \epsilon\tilde{b}_1, \quad \bar{b}_2 = \epsilon\tilde{b}_2, \quad \bar{b}_r = \epsilon\tilde{b}_r, \quad \bar{T}_1 = \epsilon\tilde{T}_1, \\ \mu = \epsilon\tilde{\mu}, \quad y_\theta = \epsilon\tilde{y}_\theta, \quad \theta' = \epsilon\tilde{\theta}', \quad \alpha_{13} = \epsilon\tilde{\alpha}_{13}, \quad \alpha_{23} = \epsilon\tilde{\alpha}_{23}, \end{gathered} \tag{11}$$

where ϵ is a small parameter that can for instance be chosen to be μ. In the following, only first-order terms will be retained in the rotor's equation. Hence, like in section 3, the approximations $\tilde{\theta}' \approx \tilde{y}_\theta$ and $\tilde{\theta}'' \approx \tilde{y}'_\theta$ can be used in order to represent the degree-of-freedom of the rotor through its position rather than its

velocity [52]. Introducing the scaled parameters (11) in Eq. (4) and retaining only terms of order ϵ^0 and ϵ, one can express the rotor's acceleration in terms of the pendulums' motion and uncouple the pendulums' equations from the rotor's dynamics, similarly as for CPVAs [15]. Moreover, to solve the pendulums' equations, it is necessary that nonlinear terms appear at least at order ϵ. However, with the current scaling, only two sources of nonlinearities appear at order ϵ. The first ones are those related to the indirect coupling between the pendulums through the rotor appear at order ϵ (because they involve $\tilde{\mu}$). The second ones are those related to the nonlinear part of the rotation laws (because they involve $\epsilon\tilde{\alpha}_{13}$ and $\epsilon\tilde{\alpha}_{23}$). In order that the nonlinearities related to the direct coupling between the pendulums and to the circular shape of their path appear at order ϵ, further scaling is required. This is presented in Appendix A. Now that all the nonlinear terms appear at order ϵ, on can use Taylor series in φ_{1i} and φ_{2i} to obtain the simplified equations

$$\tilde{\theta}'' = f_\theta(\boldsymbol{\varphi}, \vartheta), \tag{12a}$$

$$\Lambda_{m1}\varphi_{1i}'' + \Lambda_{c12}\varphi_{2i}'' + k_1\varphi_{1i} + k_{12}\varphi_{2i} = -\epsilon f_{p1}(\boldsymbol{\varphi}, \vartheta), \quad i = 1, ..., N, \tag{12b}$$

$$\Lambda_{c12}\varphi_{1i}'' + \Lambda_{m2}\varphi_{2i}'' + k_{12}\varphi_{1i} + k_2\varphi_{2i} = -\epsilon f_{p2}(\boldsymbol{\varphi}, \vartheta), \quad i = 1, ..., N. \tag{12c}$$

The simplified Eqs. (12a), (12b) and (12c) govern the motion of the rotor, pendulums 1 and pendulums 2, respectively. $\boldsymbol{\varphi} = [\varphi_{11}, ..., \varphi_{1N}, \varphi_{21}, ..., \varphi_{2N}]^\intercal$ is the vector containing the pendulums' coordinates. Functions $f_\theta(\boldsymbol{\varphi}, \vartheta)$, $f_{p1i}(\boldsymbol{\varphi}, \vartheta)$ and $f_{p2i}(\boldsymbol{\varphi}, \vartheta)$, described in Appendix A, contain linear, quadratic and cubic terms in φ_{1j} and φ_{2j}, $j = 1, ..., N$, and the external torque. Note that these functions involve the derivatives $\boldsymbol{\varphi}'$ and $\boldsymbol{\varphi}''$, but this is not indicated explicitly for the sake of readability. As Eqs. (12b) and (12c) do not involve θ, one can solve them to obtain the φ_{1i} and φ_{2i}, and inject the results in Eq. (12a) to retrieve the rotor's acceleration. However, Eqs. (12b) and (12c) are linearly coupled, which complicates their solving. Hence, it is convenient to project them on the linear modes so as to obtain linearly uncoupled modal equations which are more easily solvable. This is presented in the next section.

4.2. Simplified modal equations

In order to derive the simplified modal equations, Eqs. (12b) and (12c) must first be written in matrix form using the vector of unknowns $\boldsymbol{\varphi}$. This matrix equation takes the form

$$\boldsymbol{M_p}\boldsymbol{\varphi}'' + \boldsymbol{K_p}\boldsymbol{\varphi} = -\epsilon \boldsymbol{f_p}(\boldsymbol{\varphi}, \vartheta). \tag{13}$$

Then, we can use a modal expansion of $\boldsymbol{\varphi}$ and project the matrix equation on the linear modes to obtain the modal equations. In this paper, we will look for the response near the tuning order n_{pi}, $i = 1$ or 2, and n_{p1} is relatively far from n_{p2}. Thus, it is relevant to keep only the i$^{\text{th}}$ phase-opposition and unison modes in the modal expansion as the contribution of the other modes to the system's response is negligible. Hence, we can use the truncated modal expansion

$$\boldsymbol{\varphi} = \rho_i \boldsymbol{\psi_i^{(o)}} + \zeta_i \boldsymbol{\psi_i^{(u)}} \tag{14}$$

where $\boldsymbol{\psi_i^{(o)}}$ and $\boldsymbol{\psi_i^{(u)}}$ are the reduced mode shapes (i.e. without the rotor's component) associated to $\boldsymbol{\phi_i^{(o)}}$ and $\boldsymbol{\phi_i^{(u)}}$ (*cf.* section 3). ρ_i and ζ_i are the modal coordinates of the i$^{\text{th}}$ phase-opposition and unison modes, respectively. The localisation phenomenon investigated in this paper is due to a 1:1 internal resonance [57] between the i$^{\text{th}}$ phase-opposition and unison modes [25], which is another reason making the modal expansion (14) relevant. Nevertheless, it must be noted that if $n_{p2} \approx 2n_{p1}$, secondary resonances of the modes can lead to complex responses that are not captured with the truncated modal expansion (14) [7, 52, 53].

As higher powers of ϵ will be neglected in the modal equations, one can use the Taylor series of the modal component χ_i (*cf.* section 3),

$$\chi_i = \chi_{pi} + \epsilon\tilde{\mu} w_i + \mathcal{O}(\epsilon^2), \quad i = 1, 2, \tag{15}$$

in order to write the reduced mode shapes $\boldsymbol{\psi_i^{(u)}}$ as

$$\boldsymbol{\psi_i^{(u)}} \approx \boldsymbol{\psi_{pi}^{(u)}} + \epsilon\tilde{\mu}[0, 0, w_i, w_i]^\intercal, \quad i = 1, 2. \tag{16}$$

190 w_i are constants that do not need to be defined as they will cancel later in the derivations (*cf.* Appendix A.3).

Introducing the modal expansion (14) in the matrix equation (13), projecting on the i$^{\text{th}}$ phase-opposition and unison modes and using the approximation (16), one obtains the modal equations,

$$\rho_i'' + n_{pi}^2 \rho_i = -\frac{\epsilon}{\hat{\Lambda}_{mi}} \hat{f}_i^{(o)}(\rho_i, \zeta_i, \vartheta), \quad i = 1, 2, \tag{17a}$$

$$\zeta_i'' + n_{pi}^2 \zeta_i = -\frac{\epsilon}{\hat{\Lambda}_{mi}} \hat{f}_i^{(u)}(\rho_i, \zeta_i, \vartheta), \quad i = 1, 2, \tag{17b}$$

Functions $\hat{f}_i^{(o)}$ and $\hat{f}_i^{(u)}$ are described in Appendix A. They involve the modal constants $\hat{\Lambda}_{mi}$, $\hat{k}_i$, $\hat{b}_i$, $\hat{\Lambda}_{ci}$, defined in Appendix B, which represent the modal
195 mass, stiffness, damping and linear coupling with the rotor, respectively. Note that Eqs. (17a) and (17b) make use of $n_{pi}^2 = \hat{k}_i / \hat{\Lambda}_{mi}$. Functions $\hat{f}_i^{(o)}(\rho_i, \zeta_i, \vartheta)$ and $\hat{f}_i^{(u)}(\rho_i, \zeta_i, \vartheta)$ contain linear, quadratic and cubic terms in ρ_i and ζ_i, and account for the damping and the external forcing.

4.3. Modal and physical solutions

The method of multiple scales [56] is used to find the solution of Eqs. (17a) and (17b). Two rotation scales are introduced, $\vartheta_0 = \vartheta$ and $\vartheta_1 = \epsilon\vartheta$, and the modal coordinates are expanded such that

$$\rho_i(\vartheta) = \rho_{i0}(\vartheta_0, \vartheta_1) + \epsilon \rho_{i1}(\vartheta_0, \vartheta_1), \tag{18a}$$

$$\zeta_i(\vartheta) = \zeta_{i0}(\vartheta_0, \vartheta_1) + \epsilon \zeta_{i1}(\vartheta_0, \vartheta_1). \tag{18b}$$

As the excitation order n is close from n_{pi}, it is convenient to define the detuning term σ as

$$n = n_{pi} + \epsilon\sigma. \tag{19}$$

$\sigma > 0$ and $\sigma < 0$ correspond to under-tuned and over-tuned double pendulums, respectively. Applying the method of multiple scales yields first-order solutions

of the form

$$\rho_{i0}(\vartheta_0, \vartheta_1) = v_i(\vartheta_1)\cos\left(n\vartheta_0 - \phi_i(\vartheta_1)\right), \tag{20a}$$

$$\zeta_{i0}(\vartheta_0, \vartheta_1) = u_i(\vartheta_1)\cos\left(n\vartheta_0 - \beta_i(\vartheta_1)\right). \tag{20b}$$

The modal amplitudes v_i, u_i and phases ϕ_i, β_i are governed by the system

$$\begin{cases} D_1 v_i = f_{v_i}(\boldsymbol{u}_i, \boldsymbol{\beta}_i), & \text{(21a)} \\ v_i D_1 \phi_i = f_{\phi_i}(\boldsymbol{u}_i, \boldsymbol{\beta}_i), & \text{(21b)} \\ D_1 u_i = f_{u_i}(\boldsymbol{u}_i, \boldsymbol{\beta}_i), & \text{(21c)} \\ u_i D_1 \beta_i = f_{\beta_i}(\boldsymbol{u}_i, \boldsymbol{\beta}_i), & \text{(21d)} \end{cases}$$

where $D_1(\bullet) = \partial(\bullet)/\partial\vartheta_1$ and $\boldsymbol{u}_i = [v_i, u_i]^\intercal$ and $\boldsymbol{\beta}_i = [\phi_i, \beta_i]^\intercal$ are vectors containing the modal amplitudes and phases, respectively. Functions f_{v_i}, f_{u_i}, f_{ϕ_i} and f_{β_i} are given in Appendix D. They make use of the nonlinear coefficient

$$c_i = c_{pi} + c_{si} - c_{ci} + c_{ti}. \tag{22}$$

c_{pi} represents the nonlinearity coming from the rotation functions of pendulums 1 and 2, which can be seen as perturbations from linear rotation laws. It also accounts for the nonlinearity coming from the circular path of pendulums 1, which is seen as a perturbation of an epicycloidal path in the case of a CPVA [14]. c_{ci} and c_{si} are related to Coriolis effects and to the direct coupling between pendulums 1 and 2, respectively. c_{ti} accounts for nonlinear couplings through the rotor other than Coriolis effects. These definitions are chosen to identify the effect of the different sources of nonlinearity and to facilitate the comparison of the results obtained in this paper with results dealing with CPVAs [24]. Moreover, it is of importance to note that the rotation coefficients α_{13} and α_{23} contribute only to c_{pi}, which appears in c_i (*cf.* Eq. (22)). Hence, one can choose these two rotation coefficients (or equivalently, choose c_{pi}) to modify the softening/hardening behaviour of the system. Thus, c_{pi} can be seen as the nonlinear tuning parameter of the CDPVA. The functions involved in system (21) also make use of the nonlinear coefficient c_{mi}, which is exclusively related to the nonlinear modal coupling.

The steady-state solution for the i$^{\text{th}}$ unison mode was derived in [7] and can also be computed from Eqs. (21c) and (21d) by setting $v_i = 0$ and enforcing the steady-state condition $D_1 u_i = D_1 \beta_i = 0$. These solutions are given in Appendix E. The pendulums' responses at unison are directly deduced from Eq. (14), leading to

$$\varphi_{11} = \varphi_{12} = a_1 \cos(n\vartheta - \xi_1), \tag{23a}$$

$$\varphi_{21} = \varphi_{22} = a_2 \cos(n\vartheta - \xi_2), \tag{23b}$$

where the amplitudes a_1 and a_2 and phases ξ_1 and ξ_2 are given by

$$a_1 = u_i, \quad a_2 = |\chi_i| u_i, \quad \xi_1 = \beta_i, \quad \xi_2 = \begin{cases} \beta_i \text{ if } \chi_i > 0, \\ \beta + \pi \text{ if } \chi_i < 0. \end{cases} \tag{24}$$

The rotor's response is obtained by injecting the pendulums' responses (23) in the rotor's equation (12a), leading to

$$\theta'' = h_1 \cos(n\vartheta - \psi_1) + h_2 \cos(2n\vartheta - \psi_2) + h_3 \cos(3n\vartheta - \psi_3). \tag{25}$$

Amplitudes h_i and phases ψ_i, $i = 1, 2, 3$, are given in Appendix E.

4.4. Stability of the response on the unison mode

It is not possible to assess the stability of the i$^{\text{th}}$ unison mode using directly the system of polar coordinates (21) as this would lead to a singularity because of $v_i = 0$. Hence, as in [52, 55], we use a change from polar to Cartesian coordinates. To this aim, the new variables

$$\begin{aligned} p_{1i} &= v_i \cos\phi_i, \quad q_{1i} = v_i \sin\phi_i, \\ p_{2i} &= u_i \cos\beta_i, \quad q_{2i} = u_i \sin\beta_i \end{aligned} \tag{26}$$

are defined. (p_{1i}, q_{1i}) and (p_{2i}, q_{2i}) are the Cartesian coordinates of the i$^{\text{th}}$ phase-opposition and unison modes, respectively. Using these new coordinates,

system (21) can be rewritten under the form

$$\begin{cases} D_1 p_{1i} = f_{p_{1i}}(\boldsymbol{p}_i, \boldsymbol{q}_i), & \text{(27a)} \\ D_1 q_{1i} = f_{q_{1i}}(\boldsymbol{p}_i, \boldsymbol{q}_i), & \text{(27b)} \\ D_1 p_{2i} = f_{p_{2i}}(\boldsymbol{p}_i, \boldsymbol{q}_i), & \text{(27c)} \\ D_1 q_{2i} = f_{q_{2i}}(\boldsymbol{p}_i, \boldsymbol{q}_i). & \text{(27d)} \end{cases}$$

$\boldsymbol{p}_i = [p_{1i}, p_{2i}]^\intercal$ and $\boldsymbol{q}_i = [q_{1i}, q_{2i}]^\intercal$ are vectors containing the Cartesian coordinates. $f_{p_{1i}}$, $f_{q_{1i}}$, $f_{p_{2i}}$ and $f_{q_{2i}}$ are functions given in Appendix D. The Jacobian of system (27) evaluated on the i$^{\text{th}}$ unison solution has the special form

$$\boldsymbol{J}_i = \begin{bmatrix} \boldsymbol{A}_i & \boldsymbol{0} \\ \boldsymbol{0} & \boldsymbol{B}_i \end{bmatrix}, \quad \boldsymbol{A}_i = \begin{bmatrix} \frac{\partial f_{p_{1i}}}{\partial p_{1i}} & \frac{\partial f_{p_{1i}}}{\partial q_{1i}} \\ \frac{\partial f_{q_{1i}}}{\partial p_{1i}} & \frac{\partial f_{q_{1i}}}{\partial q_{1i}} \end{bmatrix}, \quad \boldsymbol{B}_i = \begin{bmatrix} \frac{\partial f_{p_{2i}}}{\partial p_{2i}} & \frac{\partial f_{p_{2i}}}{\partial q_{2i}} \\ \frac{\partial f_{q_{2i}}}{\partial p_{2i}} & \frac{\partial f_{q_{2i}}}{\partial q_{2i}} \end{bmatrix}, \tag{28}$$

so that the eigenvalues of $\boldsymbol{J}_i$ are the eigenvalues of $\boldsymbol{A}_i$ and $\boldsymbol{B}_i$. Instabilities occur when the real part of one of the eigenvalues becomes positive. As $\boldsymbol{J}_i$ is evaluated on the i$^{\text{th}}$ unison mode, $\boldsymbol{A}_i$ represents the effect of a perturbation of the phase-opposition mode one the unison one while $\boldsymbol{B}_i$ represents the effect of a perturbation of the unison mode on itself. Hence, instabilities related to $\boldsymbol{B}_i$ indicate saddle-node bifurcations that cause jumps of the response. This instability is typical of Duffing oscillators [58]. On the other hand, instabilities related to $\boldsymbol{A}_i$ indicate pitchfork bifurcations leading to a coupled-mode solution, which causes localisation [25]. The trace of $\boldsymbol{A}_i$ and $\boldsymbol{B}_i$ is

$$\text{trace}(\boldsymbol{A}_i) = \text{trace}(\boldsymbol{B}_i) = -\frac{\hat{b}_i}{\Lambda_{mi}} < 0. \tag{29}$$

As it is negative, the sign of the real part of the eigenvalues is given by the sign of the determinants of $\boldsymbol{A}_i$ and $\boldsymbol{B}_i$. More specifically, the unison response is subjected to localisation if $\det(\boldsymbol{A}_i) < 0$ and to jumps if $\det(\boldsymbol{B}_i) < 0$. The expression of these determinants is given in Appendix F.1. The limits of the unstable zones describe bifurcation curves, that is, curves describing all the possible bifurcation points. By computing $\det(\boldsymbol{A}_i) = 0$, one obtains the bifurcation curve n_{pf_i}, which describes the pitchfork bifurcations. Similarly, computing $\det(\boldsymbol{B}_i) = 0$ leads to the bifurcation curve n_{sn_i}, describing the saddle-node bifurcations. The expression of these curves is given in Appendix F.2.

5. Case studies and design guidelines

The aim of this section is to compare the analytical results with numerical ones in order to validate the model and to provide design guidelines. The numerical solutions are obtained through a numerical integration of the equations of motion (4) using a Runge-Kutta algorithm. When the steady state is reached, the signals' amplitudes and phases are computed using a decomposition into Fourier series.

5.1. Typical localised response

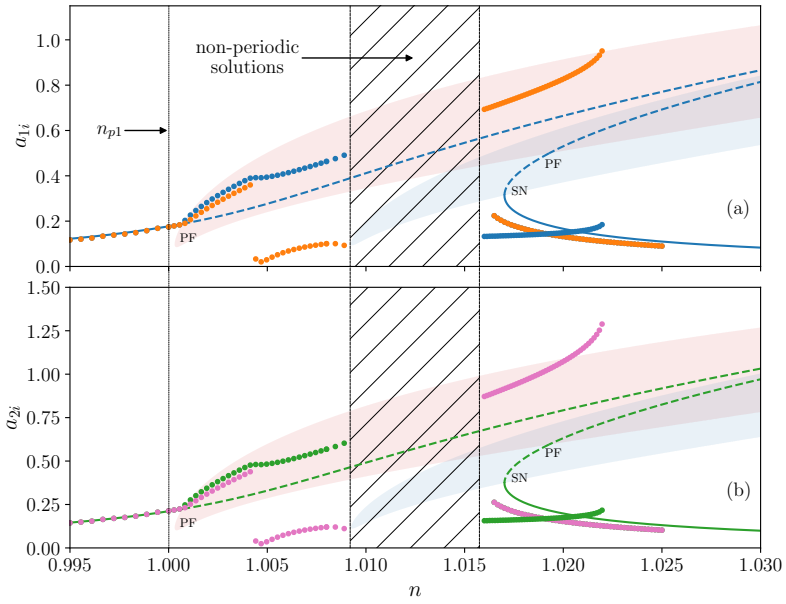

Figure 4: Pendulums' amplitude around mode 1 as a function of the excitation order. The stable and unstable parts of the analytical solutions are shown as solid and dashed lines, respectively. The red and blue areas are the instability regions related to localisation and jumps, respectively. The numerical solutions for pendulums 11 and 12 are the blue and orange circles, respectively. The numerical solutions for pendulums 21 and 22 are the green and pink circles, respectively. $\bar{T}_1 = 0.005$ and the system parameters are given in Tab. 2.

Figure 4 represents the amplitude response of the two double pendulums of a CDPVA around mode 1 as a function of the excitation order. The fact that the

response bends to the right exhibits the hardening behaviour of the response. The pitchfork bifurcation at $n \approx 1.0007$, which leads to a localised solution, is very well predicted by the model. On the first part of the localised solution, the pendulums oscillate with approximately the same amplitude but this amplitude is larger than that of the unison solution. Then, at $n \approx 1.0043$, there is a jump of the response of pendulums 12 and 22. This jump is probably due to a looping of the response, as observed in [25] for a CPVA. This could be investigated in more details using continuation methods such as MANLAB [59] instead of time integrations. However, a detailed investigation of the localised response is out of the scope of this paper. After the jump, the amplitudes of pendulums 12 and 22 are much lower than those of pendulums 11 and 21, respectively. They even approach zero at $n \approx 1.0047$. The localised solution continues up to $n \approx 1.0090$ at which point an instability gives rise to non-periodic solutions. The time signals of pendulums 11 and 12 at $n = 1.0092$ and the associated Poincaré maps are shown in Fig. 5(a) and (c), respectively. This allows to see that the response on the left-hand side of the non-periodic band is quasi-periodic. The time signals of pendulums 11 and 12 at $n = 1.0155$ and the associated Poincaré maps are shown in Fig. 5(b) and (d). The shape of the Poincaré maps seems to indicate that the response on the right-hand side of the non-periodic band is chaotic [60]. There is another bifurcation at $n \approx 1.0157$ after which the non-periodic solutions are unstable. This bifurcation leads to another part of the localised solution. It is stable up to $n \approx 1.0220$ after which a jump occurs, leading back to the unison motion.

Figure 6 represent the amplitude of the rotor's harmonics as a function of the excitation order. It is interesting to see that the localised response does not worsen the vibration reduction as compared to the unison response. It even seems to improve the filtration as the response of every harmonic is lower on the localised solution than for the unison pendulums' motion. The improvement of the filtration with the localised solution was a feature observed previously for CPVAs [19, 25, 61]. In practice the pendulums' path are not infinite, so the pendulums' amplitudes are physically limited, usually by means of stoppers.

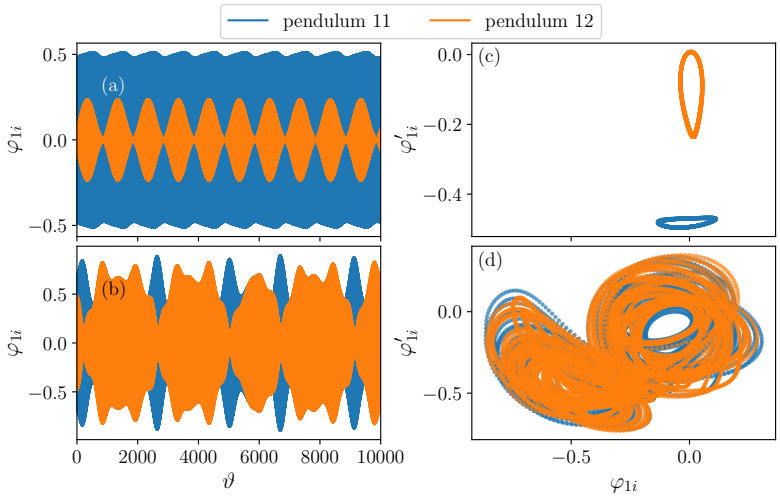

Figure 5: The time signals of pendulums 11 and 12 at the limits of the non-periodic part of the response are shown in (a) and (b). The parameters are the same as those of Fig. 4 and $n = \{1.0092, 1.0155\}$ in (a) and (b), respectively. The Poincaré maps associated to the time signals in (a) and (b) are given in (c) and (d), respectively. Note that in (d) the signal used to compute the Poincaré map is longer than that shown in (b).

This is the true drawback of localisation: the amplitude of one or more pendulums is larger than that predicted by the unison response, so it will reach its maximum amplitude for smaller torque levels. This limits the torque capacity of the system, just like for CPVAs [24].

N	μ	η_1	η_2	μ_2	ν_r	ν_2	α_{11}	α_{21}	α_{13}	α_{23}	$\bar{b}_r$	$\bar{b}_1$, $\bar{b}_2$
2	0.15	6	4	0.2	1.551	0.3	-0.32	0.3	0.06	0	0.0227	5×10^{-5}

Table 2: Parameters of the CDPVA studied in this section.

In this section, only responses around unison mode 1 are presented. There are several reasons for this. Firstly, with the case study considered here but around unison mode 2, the unstable zone leading to localisation was contained within the unstable zone causing jumps. In other words, around the 2$^{\text{nd}}$ unison mode, the red area shown in Fig. 4 is contained within the blue area. Hence,

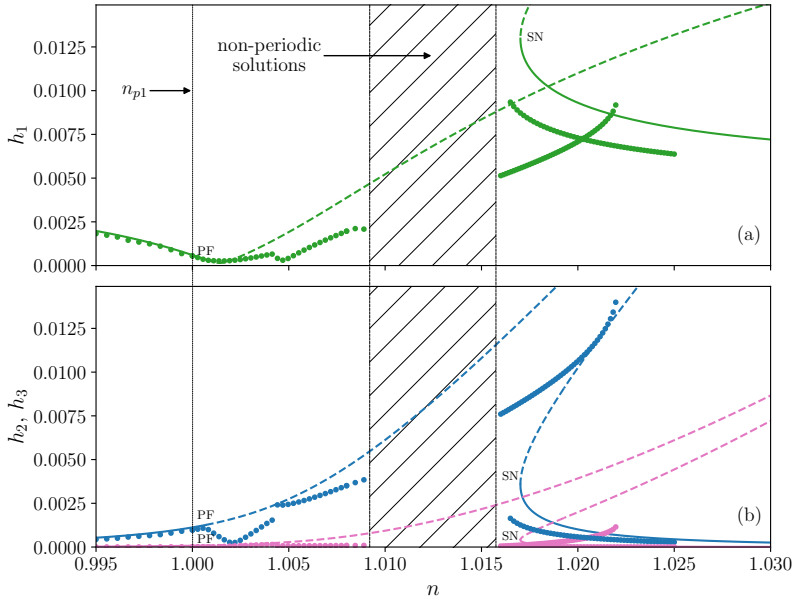

Figure 6: Amplitude of the rotor's first harmonic (a) and higher harmonics (b) around mode 1 as a function of the excitation order. The stable and unstable parts of the analytical solutions are shown as solid and dashed lines, respectively. The numerical solutions are the coloured circles. $\bar{T}_1 = 0.005$ and the system parameters are given in Tab. 2.

localisation can not be captured with time integrations around unison mode 2. Secondly, the construction of the model is exactly the same for responses around unison modes 1 and 2. Hence, if the analytical approach is validated for one mode it means that it is also correct for the other one. This being said, the accuracy of the model is unlikely to be the same for the two modes, as already seen with CDPVAs containing a single double pendulum [7].

5.2. Extension of the model to CDPVAs with $N > 2$ double pendulums

The analytical model is constructed with the assumption that the CDPVA contains $N = 2$ double pendulums. In the case where it contains $N > 2$ double pendulums, the phase-opposition modes become $N-1$-degenerated, just like for CPVAs containing $N > 2$ pendulums [53]. Hence, to assess the stability of the i^{th} unison mode, one should look for its interaction with the $N-1$ degenerated

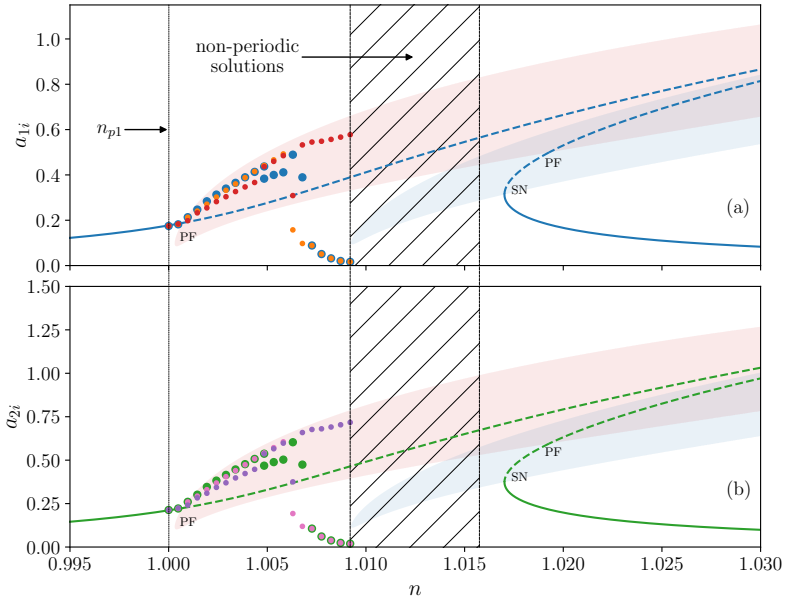

Figure 7: Pendulums' amplitude around mode 1 as a function of the excitation order. The stable and unstable parts of the analytical solutions are shown as solid and dashed lines, respectively. The red and blue areas are the instability regions related to localisation and jumps, respectively. The numerical solutions for the pendulums are the coloured circles. The blue and green circles are larger so they can be seen even when behind another marker. $\bar{T}_1 = 0.005$ and the system parameters are given in Tab. 2, except for $N = 3$.

phase-opposition modes whose eigenorder is n_{pi}. However, as these $N-1$ modes are all in 1:1:...:1 internal resonance, the unison mode could interact with any of those modes or combinations of them. Thus, it is likely that the pitchfork bifurcation leading to a localised solution is the same for any $N > 2$. This is verified below for $N = 3$.

Figure 7 shows the response of the three double pendulums of a CDPVA around mode 1. Numerical solutions are shown only between the tuning order and the zone where non-periodic solutions exist. As in the case of $N = 2$ double pendulums, the pitchfork bifurcation at $n \approx 1.0007$ is very well predicted by the model. Hence, the analytical model appears to be valid for CDPVAs made

of any number of double pendulums.

5.3. Avoiding localisation

Now that the localisation was observed and its drawbacks exposed, it could be interesting to know how to avoid it. This is done in this section.
One can obtain an approximate expression of the bifurcation curve related to localisation by ignoring damping and using Taylor series of n_{pf_i} in u_i. This leads to

$$n_{pf_i} \approx n_{pi} + \epsilon \frac{-2(c_{pi} + c_{si} + 2c_{mi}) \pm |c_{pi} + c_{si} + 6c_{mi} - c_{ci}|}{16\hat{\Lambda}_{mi} n_{pi}} u_i^2. \qquad (30)$$

Depending whether n_{pi} increases or decreases with u_i, one can know whether the unstable zone leading to localisation is located at $n < n_{pi}$, $n > n_{pi}$ or both. There are three different cases to consider:

1. If $\text{sign}\left[-2(c_{pi} + c_{si} + 2c_{mi}) + |c_{pi} + c_{si} + 6c_{mi} - c_{ci}|\right] < 0$, then localisation occurs for orders smaller than the tuning order. Hence, localisation is avoided if $n \geq n_{pi}$. It is relevant to include n_{pi} is the range avoiding localisation as damping pushes the unstable zone away from n_{pi}. This can be seen in Fig. 4 where the localisation zone starts at an order slightly larger than n_{pi}.
2. If $\text{sign}\left[-2(c_{pi} + c_{si} + 2c_{mi}) - |c_{pi} + c_{si} + 6c_{mi} - c_{ci}|\right] < 0$ and $\text{sign}\left[-2(c_{pi} + c_{si} + 2c_{mi}) + |c_{pi} + c_{si} + 6c_{mi} - c_{ci}|\right] > 0$, then localisation occurs at the tuning order. This situation is to be avoided as it would require a large linear detuning to avoid localisation. This would be at the expense of filtering efficiency as the system would have to operate far from the antiresonance.
3. If $\text{sign}\left[-2(c_{pi} + c_{si} + 2c_{mi}) - |c_{pi} + c_{si} + 6c_{mi} - c_{ci}|\right] > 0$, then localisation occurs for orders larger than the tuning order. Hence, localisation is avoided if $n \leq n_{pi}$.

The three cases described above are represented in Fig. 8. First of all, the approximated version of n_{pf_1} allows for a satisfactory description of the unstable

zones. In (a) and (c), the localisation can be avoided even for $n = n_{p1}$. Small linear mistuning can be used to increase the robustness of the system in front of undesired mistuning, coming for instance from manufacturing imperfections. However, in case (b), localisation occurs at $n = n_{p1}$, so mistuning has to be used. The nonlinear tuning chosen in this case ($\alpha_{13} = 0.0417$) is the tuning for tautochronic uncoupled pendulums (i.e. tautochronic pendulums when the rotor spins at a constant speed). Case (c) seems to depict the best situation as it allows to avoid both kinds of instabilities. However, it might not be the preferred one in practice due to the shifting of the antiresonance limiting the efficiency of the vibration reduction. This shifting was studied in [7] and its relation with the avoidance of the instabilities is discussed in section 5.4.

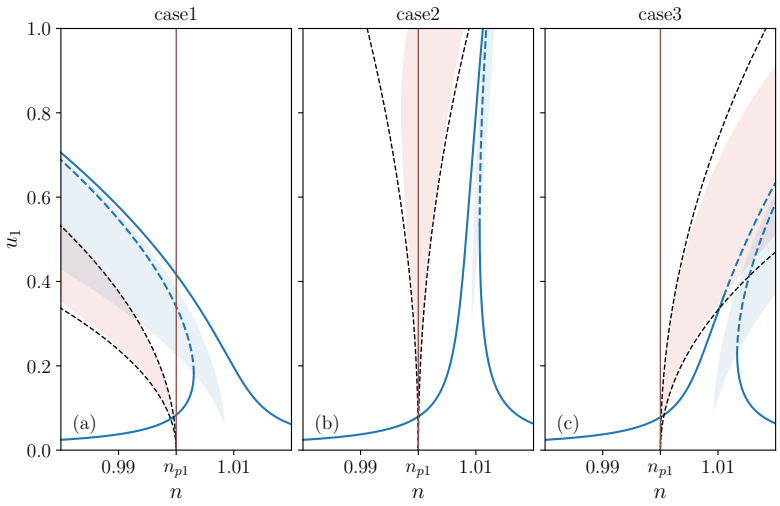

Figure 8: Amplitude of mode 1 as a function of the excitation order. (a), (b) and (c) represent systems tuned accordingly to the cases 1, 2 and 3 described in section 5.3, respectively. The stable and unstable parts of the analytical solutions are shown as solid and dashed lines, respectively. The red and blue areas are the instability regions related to localisation and jumps, respectively. The dashed black lines correspond to the approximated contours of the unstable zone leading to localisation. They are obtained using Eq. (30). $\bar{T}_1 = 0.002$ and the system parameters are given in Tab. 2 except for $\alpha_{13} = \{0, 0.0417, 0.06\}$ in (a), (b) and (c), respectively.

5.4. Representation in the design space

In order to determine which CDPVA designs are the best to filter-out a harmonic torque of order n, it is convenient to represent the maximum amount of information in a design space. Among the most important information are the stability of the response and the efficiency of the vibration reduction. The later one can be assessed indirectly by analysing the shifting of the antiresonance as the pendulums' amplitudes increase. This was done in [7], and it was found that the shifting of the i$^{\text{th}}$ antiresonance is limited by setting

$$c_{pi} = c_{ci} - c_{si}. \tag{31}$$

It can also be interesting to represent other particular designs, as for instance those yielding tautochronic coupled and tautochronic uncoupled double pendulums. These designs satisfy the relations [7]

$$c_{pi} = c_{ci} - c_{si} - c_{ti} \quad \text{and} \quad c_{pi} = -c_{si}, \tag{32}$$

respectively.

Figure 9 shows two maps representing the stability information and the design rules as a function of the tuning order and the nonlinear tuning parameter. Note the we introduced the unscaled nonlinear tuning parameter $\bar{c}_{pi} = \epsilon c_{pi}$. The design rules represented are Eqs. (31) and (32) together with cases 1 and 3 from section 5.3, which aim at preventing the apparition of instabilities. Note that the tuning order n_{p1} is not a parameter of the system. Hence, it was chosen to vary it indirectly by varying α_{11}. In the maps, α_{11} takes values from -0.35 to -0.29 so that n_{p1} varies around $n = 1$ (note that in this range of values, $n_{p1}(\alpha_1 1)$ is almost linear). As it is n_{p1} which is close from n, Fig. 9 is associated to the response around mode 1. Each map is represented for a different range of amplitudes. In Fig. 9(a), the modal amplitude is varied from 0 to 0.75 while in Fig. 9(b) it is varied from 0 to 1. The colors indicate the stability. The designs subjected to localisation (jump) in the amplitude range of a map are shown

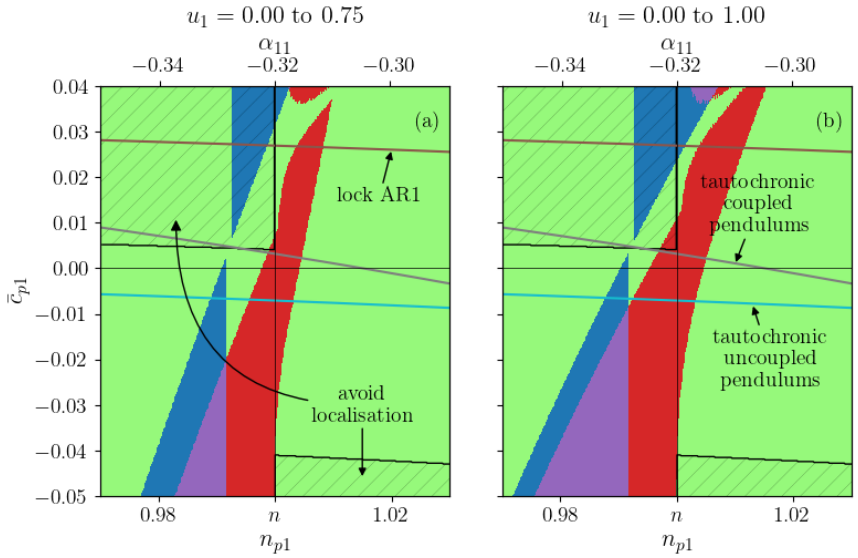

Figure 9: Maps representing the stability of the response around mode 1 as a function of the tuning order n_{p1} and the nonlinear tuning parameter $\bar{c}_{pi}$. Hence, each point on the map represents a given CDPVA design. Each map is shown for a given order n and a given range of modal amplitude u_i. Stable designs are depicted in green while designs subjected to localisation or jumps are shown in red or blue, respectively. The designs subjected to both localisation and jumps are represented in purple. The hatched areas represent the design that should prevent localisation according to the observations of section 5.3. The brown line corresponds to recommendation (31), locking the antiresonance 1. The designs along the grey line yield tautochronic coupled pendulums. Larger and lower values of c_{p1} yield softening and hardening behaviours of the response, respectively. The designs along the cyan line yield tautochronic uncoupled pendulums. $n = 1$ and the parameters are given in Tab. 2. n_{p1} is varied indirectly by varying α_{11}, which takes values from from -0.35 to -0.29.

in red (blue). The designs that are subjected to both kinds of instabilities are shown in purple and those that remain stable over the whole amplitude range are shown in green.

355 One can see in the maps that cases 1 and 3 presented in section 5.3 limit the apparition of localised responses, but case 1 does not completely prevent it. This is particularly visible in Fig. 9(b), where there are designs that are unstable

in the lower right-hand corner of the top hatched area. This small inaccuracy of the design rule is due to a complex shape of the unstable region, as shown in Appendix G. The maps also show that tautochronic uncoupled pendulums (cyan curve) are subjected to localisation for tuning orders close from n. This was already observed in Fig. 8 and confirms that these designs should not be used. To a lesser extent, the same situation occurs for tautochronic coupled pendulums (grey curve). Indeed, one can see in Fig. 9(a) that tautochronic coupled pendulums with tuning orders close from n are subjected to instabilities. However, at moderate amplitudes, small undertuning can help avoiding localisation. The most interesting case is that of pendulums tuned to lock the antiresonance (brown curve), as it corresponds to the CDPVA achieving the best performance [7]. One can see that a CDPVA tuned accordingly to Eq. (31) and with $n_{p1} = n$ is still stable at an amplitude $u_1 = 0.75$. This is the best situation as the rotor is excited exactly on the linear antiresonance, the antiresonance order is almost locked thanks to the nonlinear design rule, and the system is stable. The only drawback of this configuration is that it is still subjected to jumps at large amplitudes, as can be seen in Fig. 9(b). To deal with this issue and increase the torque range, one can decide to overtune slightly the double pendulums by choosing $n_{p1} > n$ and/or harden the response by decreasing c_{p1}. This will push the jump towards higher pendulums' amplitudes at the expense of performance.

6. Conclusion

This paper deals with the stability of the response of CDPVAs. A linear analysis was carried out to compute the eigenmodes of a system with $N = 2$ double pendulums. This allowed to understand what additional modes appear with the presence of several double pendulums. Then, the dynamic response of the system and its stability were computed using a perturbation method, and the validity of this analytical model was verified through a comparison with numerical solutions. Though the model is based on a CDPVA with $N = 2$

pendulums, the prediction of the pitchfork bifurcations leading to a localised solution was observed to be the same for any $N > 2$ double pendulums. Design guidelines to avoid localisation were derived from the model. A representation of these guidelines and the stability in the design space allowed to see that they indeed help preventing the apparition of localised responses. Additional guidelines from former works were also included in these representations in the design space. One of them, allowing for a maximised performance, was seen to be compatible with the avoidance of localisation and jumps out to large amplitudes.

References

[1] B. C. Carter, Improvements in or relating to damping of oscillation-checking devices, 337 466 (1929).

[2] R. R. R. Sarazin, Means adapted to reduce the torsional oscillations of crankshafts, 2 079 226 (1931).

[3] R. Chilton, Pendulum counterweight, 2 112 984 (1935).

[4] R. W. Zdanowich, T. S. Wilson, The elements of pendulum dampers, Proceedings of the Institution of Mechanical Engineers 143 (1) (1940) 182–210. doi:10.1243/PIME_PROC_1940_143_028_02.

[5] J.-G. Duh, M. Wenyong, Development of monofilar rotor hub vibration absorber, Tech. rep. (1983).

[6] V. Manchi, C. Sujatha, Torsional vibration reduction of rotating shafts for multiple orders using centrifugal double pendulum vibration absorber, Applied Acoustics 174 (2021) 107768. doi:10.1016/j.apacoust.2020.107768.

[7] V. Mahé, A. Renault, A. Grolet, H. Mahé, O. Thomas, Unison response of a centrifugal double pendulum vibration absorber, *Submitted to the Journal of Sound and Vibration.*

[8] D. E. Newland, Nonlinear Aspects of the Performance of Centrifugal Pendulum Vibration Absorbers, Journal of Engineering for Industry 86 (3) (1964) 257–263. doi:10.1115/1.3670529.

[9] D. E. Newland, Nonlinear problems of centrifugal pendulum vibration absorbers, in: Mechanisms and Machines, Vol. 1, Varna (Bulgaria), 1965, pp. 39–62.

[10] J. F. Madden, Constant frequency bifilar vibration absorber, 4 218 187 (1980).

[11] H. H. Denman, Tautochronic bifilar pendulum torsion absorbers for reciprocating engines, Journal of Sound and Vibration 159 (2) (1992) 251–277. doi:10.1016/0022-460X(92)90035-V.

[12] C.-P. Chao, C.-T. Lee, S. Shaw, Non-unisson dynamics of multiple centrifugal pendulum vibration absorbers, Journal of Sound and Vibration 204 (5) (1997) 769–794. doi:10.1006/jsvi.1997.0960.

[13] C.-P. Chao, S. W. Shaw, C.-T. Lee, Stability of the Unison Response for a Rotating System With Multiple Tautochronic Pendulum Vibration Absorbers, Journal of Applied Mechanics 64 (1) (1997) 149–156. doi:10.1115/1.2787266.

[14] A. Alsuwaiyan, S. W. Shaw, Performance and dynamic stability of general-path centrifugal pendulum vibration absorbers, Journal of Sound and Vibration 252 (5) (2002) 791–815. doi:10.1006/jsvi.2000.3534.

[15] S. W. Shaw, P. M. Schmitz, A. G. Haddow, Tautochronic Vibration Absorbers for Rotating Systems, Journal of Computational and Nonlinear Dynamics 1 (4) (2006) 283–293. doi:10.1115/1.2338652.

[16] S. W. Shaw, B. Geist, Tuning for Performance and Stability in Systems of Nearly Tautochronic Torsional Vibration Absorbers, Journal of Vibration and Acoustics 132 (4) (2010). doi:10.1115/1.4000840.

[17] A. S. Alsuwaiyan, S. W. Shaw, Non-synchronous and Localized Responses of Systems of Identical Centrifugal Pendulum Vibration Absorbers, Arabian Journal for Science and Engineering 39 (12) (2014) 9205–9217. doi:10.1007/s13369-014-1464-1.

[18] J. S. Issa, S. W. Shaw, Synchronous and non-synchronous responses of systems with multiple identical nonlinear vibration absorbers, Journal of Sound and Vibration 348 (2015) 105–125. doi:10.1016/j.jsv.2015.03.021.

[19] K. Nishimura, T. Ikeda, Y. Harata, Localization phenomena in torsional rotating shaft systems with multiple centrifugal pendulum vibration absorbers, Nonlinear Dynamics 83 (3) (2016) 1705–1726. doi:10.1007/s11071-015-2441-2.

[20] A. Grolet, A. Renault, O. Thomas, Energy Localisation in Periodic Structures: Application to Centrifugal Pendulum Vibration Absorber, in: International Symposium on Transport Phenomena and Dynamics of Rotating Machinery, Maui (Hawaii), 2017.

[21] M. Cirelli, M. Cera, E. Pennestrì, P. P. Valentini, Nonlinear design analysis of centrifugal pendulum vibration absorbers: An intrinsic geometry-based framework, Nonlinear Dynamics 102 (3) (2020) 1297–1318. doi:10.1007/s11071-020-06035-1.

[22] M. Cera, M. Cirelli, E. Pennestrì, P. P. Valentini, Design analysis of torsichrone centrifugal pendulum vibration absorbers, Nonlinear Dynamics 104 (2) (2021) 1023–1041. doi:10.1007/s11071-021-06345-y.

[23] V. Mahe, A. Renault, A. Grolet, O. Thomas, H. Mahe, Dynamic stability of centrifugal pendulum vibration absorbers allowing a rotational mobility, Journal of Sound and Vibration 517 (2022) 116525. doi:10.1016/j.jsv.2021.116525.

[24] V. Mahé, A. Renault, A. Grolet, H. Mahé, O. Thomas, On the dynamic stability and efficiency of centrifugal pendulum vibration absorbers with rotating pendulums, Journal of Sound and Vibration 536 (2022) 117157. doi:10.1016/j.jsv.2022.117157.

[25] V. Mahé, A. Renault, A. Grolet, H. Mahé, O. Thomas, Localised response of a centrifugal pendulum vibration absorber, *Submitted to Nonlinear Dynamics*.

[26] M. Sharif-Bakhtiar, S. W. Shaw, Effects of Nonlinearities and Damping on the Dynamic Response of a Centrifugal Pendulum Vibration Absorber, Journal of Vibration and Acoustics 114 (3) (1992) 305–311. doi:10.1115/1.2930262.

[27] A. G. Haddow, S. W. Shaw, Centrifugal Pendulum Vibration Absorbers: An Experimental and Theoretical Investigation, Nonlinear Dynamics 34 (3/4) (2003) 293–307. doi:10.1023/B:NODY.0000013509.51299.c0.

[28] A. Renault, Calcul et optimisation d'absorbeurs pendulaires dans une chaîne de traction automobile [Simulation and optimisation of pendular absorbers for automotive powertrain], Ph.D. thesis, ENSAM, Lille, France (2018).

[29] A. Renault, O. Thomas, H. Mahé, Numerical antiresonance continuation of structural systems, Mechanical Systems and Signal Processing 116 (2019) 963–984. doi:10.1016/j.ymssp.2018.07.005.

[30] C.-T. Lee, S. W. Shaw, On the counteraction of periodic torques for rotating systems using centrifugally driven vibration absorbers, Journal of Sound and Vibration 191 (5) (1996) 695–719. doi:10.1006/jsvi.1996.0151.

[31] S. W. Shaw, V. Garg, C.-P. Chao, Attenuation of Engine Torsional Vibrations Using Tuned Pendulum Absorbers, in: SAE Noise and Vibration Conference and Exposition, 1997, p. 971961. doi:10.4271/971961.

[32] Y. Ishida, T. Inoue, T. Fukami, M. Ueda, Torsional Vibration Suppression by Roller Type Centrifugal Vibration Absorbers, Journal of Vibration and Acoustics 131 (5) (2009) 051012. doi:10.1115/1.3147124.

[33] B. J. Vidmar, S. W. Shaw, B. F. Feeny, B. K. Geist, Nonlinear Interactions in Systems of Multiple Order Centrifugal Pendulum Vibration Absorbers, Journal of Vibration and Acoustics 135 (6) (Dec. 2013). doi:10.1115/1.4024969.

[34] M. Cirelli, E. Capuano, P. P. Valentini, E. Pennestrì, The tuning conditions for circular, cycloidal and epicycloidal centrifugal pendula: A unified cartesian approach, Mechanism and Machine Theory 150 (2020) 103859. doi:10.1016/j.mechmachtheory.2020.103859.

[35] M. Cera, M. Cirelli, E. Pennestrì, P. P. Valentini, Nonlinear dynamics of torsichrone CPVA with synchroringed form closure constraint, Nonlinear Dynamics (2021). doi:10.1007/s11071-021-06732-5.

[36] R. Chilton, Rocking dynamic damper, 2184734 (1939).

[37] L. J. Stone, Improvements in or relating to vibration-damping devices, 598 811 (1945).

[38] R. G. Mitchiner, R. G. Leonard, Centrifugal Pendulum Vibration Absorbers—Theory and Practice, Journal of Vibration and Acoustics 113 (4) (1991) 503–507. doi:10.1115/1.2930214.

[39] A. Wedin, Reduction of Vibrations in Engines using Centrifugal Pendulum Vibration Absorbers, Ph.D. thesis (2011).

[40] B. J. Vidmar, B. F. Feeny, S. W. Shaw, A. G. Haddow, B. K. Geist, N. J. Verhanovitz, The effects of Coulomb friction on the performance of centrifugal pendulum vibration absorbers, Nonlinear Dynamics 69 (1-2) (2012) 589–600. doi:10.1007/s11071-011-0289-7.

[41] J. Mayet, H. Ulbrich, Tautochronic centrifugal pendulum vibration absorbers: General design and analysis, Journal of Sound and Vibration 333 (3) (2014) 711–729. doi:10.1016/j.jsv.2013.09.042.

[42] J. Mayet, H. Ulbrich, First-order optimal linear and nonlinear detuning of centrifugal pendulum vibration absorbers, Journal of Sound and Vibration 335 (2015) 34–54. doi:10.1016/j.jsv.2014.09.017.

[43] M. A. Acar, Design and tuning of centrifugal pendulum vibration absorbers, Ph.D. thesis, Michigan State University, Michigan (2017).

[44] H. Mahé, A. Renault, O. Thomas, Dispositif d'amortissement pendulaire [Pendular damping device], fR 3 055 038 (2018).

[45] H. Mahé, A. Renault, O. Thomas, Dispositif d'amortissement pendulaire [Pendular damping device], fR 3 055 037 (2018).

[46] M. Cirelli, J. Gregori, P. Valentini, E. Pennestrí, A design chart approach for the tuning of parallel and trapezoidal bifilar centrifugal pendulum, Mechanism and Machine Theory 140 (2019) 711–729. doi:10.1016/j.mechmachtheory.2019.06.030.

[47] E. R. Gomez, I. L. Arteaga, L. Kari, Normal-force dependant friction in centrifugal pendulum vibration absorbers: Simulation and experimental investigations, Journal of Sound and Vibration 492 (2021) 115815. doi:10.1016/j.jsv.2020.115815.

[48] X. Tan, S. Yang, J. Yang, J. Li, Study of dynamics of rotational centrifugal pendulum vibration absorbers based on tautochronic design, Meccanica (2021). doi:10.1007/s11012-021-01340-4.

[49] E. R. Gomez, J. Sjöstrand, L. Kari, I. L. Arteaga, Torsional vibrations in heavy-truck powertrains with flywheel attached centrifugal pendulum vibration absorbers, Mechanism and Machine Theory 167 (2022) 104547. doi:10.1016/j.mechmachtheory.2021.104547.

[50] E. R. Gomez, L. Kari, I. L. Arteaga, Powertrain shuffle-mode resonance suppression by means of flywheel mounted torsichrone centrifugal pendulum vibration absorbers, Journal of Sound and Vibration 534 (2022) 117014. doi:10.1016/j.jsv.2022.117014.

[51] J. Mayet, M. A. Acar, S. W. Shaw, Effective and robust rocking centrifugal pendulum vibration absorbers, Journal of Sound and Vibration 527 (2022) 116821. doi:10.1016/j.jsv.2022.116821.

[52] V. Mahe, A. Renault, A. Grolet, H. Mahe, O. Thomas, Subharmonic centrifugal pendulum vibration absorbers allowing a rotational mobility, Mechanical Systems and Signal Processing 177 (2022) 109125. doi:10.1016/j.ymssp.2022.109125.

[53] V. Mahé, A. Renault, A. Grolet, H. Mahe, O. Thomas, On the stability of pairs of subharmonic centrifugal pendulum vibration absorbers allowing a rotational mobility, *Submitted to Nonlinear Dynamics*

.

[54] S. W. Shaw, S. Wiggins, Chaotic dynamics of a whirling pendulum, Physica D: Nonlinear Phenomena 31 (2) (1988) 190–211. doi:10.1016/0167-2789(88)90076-0.

[55] C.-P. Chao, S. W. Shaw, The effects of imperfections on the performance of the subharmonic vibration absorber system, Journal of Sound and Vibration 215 (5) (1998) 1065–1099. doi:10.1006/jsvi.1998.1634.

[56] A. H. Nayfeh, Perturbation Methods, Wiley Classics Library, Wiley-VCH, Weinheim, 1973. doi:10.1002/9783527617609.

[57] A. Givois, J.-J. Tan, C. Touzé, O. Thomas, Backbone curves of coupled cubic oscillators in one-to-one internal resonance: Bifurcation scenario, measurements and parameter identification, Meccanica 55 (3) (2020) 481–503. doi:10.1007/s11012-020-01132-2.

[58] I. Kovacic, M. J. Brennan, The Duffing Equation: Nonlinear Oscillators and Their Behaviour, John Wiley & Sons, 2011. doi:10.1002/9780470977859.

[59] L. Guillot, A. Lazarus, O. Thomas, C. Vergez, B. Cochelin, A purely frequency based Floquet-Hill formulation for the efficient stability computation of periodic solutions of ordinary differential systems, Journal of Computational Physics 416 (2020) 109477. doi:10.1016/j.jcp.2020.109477.

[60] A. H. Nayfeh, B. Balachandran, Applied Nonlinear Dynamics: Analytical, Computational and Experimental Methods, Wiley Series in Nonlinear Science, Wiley-VCH, Weinheim, 2004.

[61] M. A. Acar, S. W. Shaw, Application of the Harmonic Balance Method to Centrifugal Pendulum Vibration Absorbers, in: D. Di Miao, P. Tarazaga, P. Castellini (Eds.), Special Topics in Structural Dynamics, Volume 6, Springer International Publishing, Cham, 2016, pp. 243–252. doi:10.1007/978-3-319-29910-5_25.

Appendix A. Details on the equations of motion

590 *Appendix A.1. Dimensionless equations*

One can use the procedure described in section 2 to derive the dimensionless equations of the system. These equations are

$$
\begin{aligned}
&\Big[1+\mu+\frac{2\mu h}{N}\sum_{i=1}^{N}\left[v_r\left(1+\mu_2\right)\left(\cos\varphi_{1i}-1\right)\right.\\
&+\mu_2 v_2 v_r\left(\cos\left(\alpha_1(\varphi_{1i})+\varphi_{2i}\right)-1\right)\\
&\left.+\mu_2 v_2\left(\cos\left(\alpha_1(\varphi_{1i})-\varphi_{1i}+\varphi_{2i}\right)-1\right)\right]\Big]yy'\\
&+\frac{\mu h}{N}\sum_{i=1}^{N}\Big\{\Big[\left(\eta_1+\mu_2 v_2^2\eta_2+\mu_2 v_2^2\right)\Gamma_1(\varphi_{1i})+\left(1+\mu_2\right)\left(1+v_r\cos\varphi_{1i}\right)\\
&+\mu_2 v_r v_2\Gamma_1(\varphi_{1i})\cos\left(\alpha_1(\varphi_{1i})+\varphi_{2i}\right)\\
&+\mu_2 v_2\left(1+\Gamma_1(\varphi_{1i})\right)\cos\left(\alpha_1(\varphi_{1i})-\varphi_{1i}+\varphi_{2i}\right)\Big]\\
&\left(yy'\varphi'_{1i}+y^2\varphi''_{1i}\right)\\
&+\mu_2 v_2\Big[v_2\eta_2\Gamma_2(\varphi_{2i})+v_2+v_r\cos\left(\alpha_1(\varphi_{1i})+\varphi_{2i}\right)+\\
&\cos\left(\alpha_1(\varphi_{1i})-\varphi_{1i}+\varphi_{2i}\right)\Big]\left(yy'\varphi'_{2i}+y^2\varphi''_{2i}\right)\\
&+\mu_2 v_2\frac{d\Gamma_1(\varphi_{1i})}{d\varphi_{1i}}y^2\varphi'^2_{1i}\cos\left(\alpha_1(\varphi_{1i})-\varphi_{1i}+\varphi_{2i}\right)\\
&-\mu_2 v_2 y^2\left(\left(\Gamma_1(\varphi_{1i})-1\right)\varphi'_{1i}+\varphi'_{2i}\right)\left(\left(\Gamma_1(\varphi_{1i})+1\right)\varphi'_{1i}+\varphi'_{2i}+2\right)\\
&\sin\left(\alpha_1(\varphi_{1i})-\varphi_{1i}+\varphi_{2i}\right)+\mu_2 v_r v_2\frac{d\Gamma_1(\varphi_{1i})}{d\varphi_{1i}}y^2\varphi'^2_{1i}\cos\left(\alpha_1(\varphi_{1i})+\varphi_{2i}\right)\\
&-\mu_2 v_r v_2 y^2\left(\Gamma_1(\varphi_{1i})\varphi'_{1i}+\varphi'_{2i}\right)\left(\Gamma_1(\varphi_{1i})\varphi'_{1i}+\varphi'_{2i}+2\right)\\
&\sin\left(\alpha_1(\varphi_{1i})+\varphi_{2i}\right)\\
&+\left(\eta_1+\mu_2 v_2^2\eta_2+\mu_2 v_2^2\right)\frac{d\Gamma_1(\varphi_{1i})}{d\varphi_{1i}}y^2\varphi'^2_{1i}+\mu_2 v_2^2\eta_2\frac{d\Gamma_2(\varphi_{2i})}{d\varphi_{2i}}y^2\varphi'^2_{2i}\\
&-\left(1+\mu_2\right)v_r y^2\left(\varphi'_{1i}+2\right)\varphi'_{1i}\sin\varphi_{1i}\Big\}+\bar{b}_r y=\bar{T}(\vartheta),
\end{aligned}
\tag{A.1}
$$

$$
\begin{aligned}
&\Big[\left(\eta_1 + \mu_2 v_2^2 \eta_2 + \mu_2 v_2^2\right) \Gamma_1(\varphi_{1i}) + (1+\mu_2)\,(1 + v_r \cos\varphi_{1i}) \\
&+ \mu_2 v_r v_2 \Gamma_1(\varphi_{1i}) \cos\left(\alpha_1(\varphi_{1i}) + \varphi_{2i}\right) \\
&+ \mu_2 v_2 \left(1 + \Gamma_1(\varphi_{1i})\right) \cos\left(\alpha_1(\varphi_{1i}) - \varphi_{1i} + \varphi_{2i}\right) \Big] y' \\
&+ \Big[\left(\eta_1 + \mu_2 v_2^2 \eta_2 + \mu_2 v_2^2\right) \Gamma_1(\varphi_{1i})^2 + 1 + \mu_2 \\
&+ 2\mu_2 v_2 \Gamma_1(\varphi_{1i}) \cos\left(\alpha_1(\varphi_{1i}) - \varphi_{1i} + \varphi_{2i}\right) \Big] \\
&(y'\varphi'_{1i} + y\varphi''_{1i}) \\
&+ \mu_2 v_2 \Big[v_2 \eta_2 \Gamma_1(\varphi_{1i}) \Gamma_2(\varphi_{2i}) + v_2 \Gamma_1(\varphi_{1i}) + \cos\left(\alpha_1(\varphi_{1i}) - \varphi_{1i} + \varphi_{2i}\right) \Big] \\
&(y'\varphi'_{2i} + y\varphi''_{2i}) + (1+\mu_2)\, v_r y \sin\varphi_{1i} \\
&+ \mu_2 v_r v_2 \Gamma_1(\varphi_{1i}) y \sin\left(\alpha_1(\varphi_{1i}) + \varphi_{2i}\right) \\
&- \mu_2 v_2 y \Big[\Gamma_1(\varphi_{1i}) \left(\Gamma_1(\varphi_{1i}) - 1\right) \varphi'^2_{1i} + 2\Gamma_1(\varphi_{1i}) \varphi'_{1i} \varphi'_{2i} \\
&- \Gamma_1(\varphi_{1i}) + \left(\varphi'_{2i} + 1\right)^2 \Big] \sin\left(\alpha_1(\varphi_{1i}) - \varphi_{1i} + \varphi_{2i}\right) \\
&+ \mu_2 v_2 \frac{d\Gamma_1(\varphi_{1i})}{d\varphi_{1i}} y \varphi'^2_{1i} \cos\left(\alpha_1(\varphi_{1i}) - \varphi_{1i} + \varphi_{2i}\right) \\
&+ \left(\eta_1 + \mu_2 v_2^2 \eta_2 + \mu_2 v_2^2\right) \Gamma_1(\varphi_{1i}) \frac{d\Gamma_1(\varphi_{1i})}{d\varphi_{1i}} y \varphi'^2_{1i} \\
&+ \mu_2 v_2^2 \eta_2 \Gamma_1(\varphi_{1i}) \frac{d\Gamma_2(\varphi_{2i})}{d\varphi_{2i}} y \varphi'^2_{2i} + \bar{b}_1 \varphi'_{1i}/h = 0,
\end{aligned}
\tag{A.2}
$$

$$
\begin{aligned}
&\mu_2 v_2 \Big[v_2 \eta_2 \Gamma_2(\varphi_{2i}) + v_2 + v_r \cos\left(\alpha_1(\varphi_{1i}) + \varphi_{2i}\right) \\
&+ \cos\left(\alpha_1(\varphi_{1i}) - \varphi_{1i} + \varphi_{2i}\right) \Big] y' \\
&+ \mu_2 v_2 \Big[v_2 \eta_2 \Gamma_1(\varphi_{1i}) \Gamma_2(\varphi_{2i}) + v_2 \Gamma_1(\varphi_{1i}) + \cos\left(\alpha_1(\varphi_{1i}) - \varphi_{1i} + \varphi_{2i}\right) \Big] \\
&(y'\varphi'_{1i} + y\varphi''_{1i}) \\
&+ \mu_2 v_2^2 \Big[1 + \eta_2 \Gamma_2(\varphi_{2i})^2 \Big] (y'\varphi'_{2i} + y\varphi''_{2i}) + \mu_2 v_r v_2 y \sin\left(\alpha_1(\varphi_{1i}) + \varphi_{2i}\right) \\
&+ \mu_2 v_2 y \left(\varphi'_{1i} + 1\right)^2 \sin\left(\alpha_1(\varphi_{1i}) - \varphi_{1i} + \varphi_{2i}\right) \\
&+ \mu_2 v_2^2 \left(1 + \eta_2 \Gamma_2(\varphi_{2i})\right) \frac{d\Gamma_1(\varphi_{1i})}{d\varphi_{1i}} y \varphi'^2_{1i} \\
&+ \mu_2 v_2^2 \eta_2 \Gamma_2(\varphi_{2i}) \frac{d\Gamma_2(\varphi_{2i})}{d\varphi_{2i}} y \varphi'^2_{2i} + \bar{b}_2 \varphi'_{2i}/h = 0.
\end{aligned}
\tag{A.3}
$$

Appendix A.2. Simplified equations

One can use the procedure described in section 4.1 to derive the simplified equations. The simplified rotor equation is

$$\begin{aligned}\tilde{\theta}'' = \tilde{\mu}\sum_{i=1}^{N}\Big\{ &-\Lambda_{c1}\varphi_{1i}'' - \Lambda_{c2}\varphi_{2i}'' + \frac{1}{2}\left[g_d X_{1i}^2 + g_1\varphi_{1i}^2 + g_f X_{2i}^2\right]\varphi_{1i}'' \\ &+ \frac{1}{2}\left[g_a X_{1i}^2 + g_b X_{2i}^2\right]\varphi_{2i}'' \\ &+ 2\left[k_1\varphi_{1i}\varphi_{1i}' + k_{12}\left(\varphi_{2i}\varphi_{1i}' + \varphi_{1i}\varphi_{2i}'\right) + k_2\varphi_{2i}\varphi_{2i}'\right] \\ &+ g_a X_{1i}'\left(X_{2i}' + \varphi_{1i}'\right)X_{1i} + g_1\varphi_{1i}\varphi_{1i}'^2 + g_b X_{2i}'^2 X_{2i}\Big\} + \tilde{T}_1\cos(n\vartheta),\end{aligned} \tag{A.4}$$

where constants g_1, g_a, g_b and g_f are defined in Appendix B and notations X_{1i} and X_{2i} are defined as

$$X_{1i} = \alpha_{11}\varphi_{1i} - \varphi_{1i} + \varphi_{2i}, \quad X_{2i} = \alpha_{11}\varphi_{1i} + \varphi_{2i}. \tag{A.5}$$

To derive the simplified pendulums' equations, additional scaling is required so that the nonlinearities coming from the circular path of pendulums 1i and the direct coupling between the pendulums appear at order ϵ. This is done by introducing the additional scaled parameters

$$g_1 = \epsilon\tilde{g}_1, \quad g_a = \epsilon\tilde{g}_a, \quad g_b = \epsilon\tilde{g}_b, \quad g_c = \epsilon\tilde{g}_c, \quad g_f = \epsilon\tilde{g}_f. \tag{A.6}$$

Details can be found in [7]. This way, one can split the functions f_{p1i} and f_{p2i} which appear in the simplified pendulums' equations (12b) and (12c) such that

$$f_{pji}(\boldsymbol{\varphi}, \vartheta) = f_{Lji}(\boldsymbol{\varphi}) + f_{Qji}(\boldsymbol{\varphi}) + f_{Cji}(\boldsymbol{\varphi}) + f_{fji}(\boldsymbol{\varphi}, \vartheta), \tag{A.7a}$$

$$j = 1, 2, \quad i = 1, ..., N. \tag{A.7b}$$

f_{Lji}, f_{Qji}, f_{Cji} and f_{fji} contain exclusively linear, quadratic, cubic and forcing

terms. These functions are

$$f_{L1i}(\boldsymbol{\varphi}) = -\frac{\tilde{\mu}\Lambda_{c1}}{N}\sum_{j=1}^{N}\left(\Lambda_{c1}\varphi''_{1j} + \Lambda_{c2}\varphi''_{2j}\right) + \tilde{b}_1\varphi'_{1i}, \tag{A.8a}$$

$$\begin{aligned} f_{Q1i}(\boldsymbol{\varphi}) = &-2\tilde{g}_a X_{1i}\varphi'_{2i} \\ &- \frac{\tilde{\mu}}{N}\sum_{j=1}^{N}\left(\Lambda_{m1}\varphi'_{1i} + \Lambda_{c12}\varphi'_{2i}\right)\left(\Lambda_{c1}\varphi''_{1j} + \Lambda_{c2}\varphi''_{2j}\right) \\ &+ \frac{2\tilde{\mu}\Lambda_{c1}}{N}\sum_{j=1}^{N}\left(k_1\varphi_{1j}\varphi'_{1j} + k_{12}\left(\varphi'_{1j}\varphi_{2j} + \varphi'_{2j}\varphi_{1j}\right)\right. \\ &\left. + k_2\varphi'_{2j}\varphi_{2j}\right) \end{aligned} \tag{A.8b}$$

$$\begin{aligned} f_{C1i}(\boldsymbol{\varphi}) = &-\tilde{g}_a X_{1i}^2\left(\alpha_{11}\varphi''_{1i} + \frac{\varphi''_{2i}}{2}\right) - \frac{\tilde{g}_c X_{1i}^3}{6} - \frac{\tilde{g}_1}{6}\varphi_{1i}^3 - \frac{\tilde{g}_f}{6}X_{2i}^3 \\ &- \tilde{g}_a X_{1i}\left[X_{2i}'^2 - \alpha_{11}\varphi_{1i}'^2\right] + r_1\left(\varphi''_{1i}\varphi_{1i}^2 + \varphi_{1i}\varphi_{1i}'^2\right) \\ &+ r_{12a}\left(\varphi''_{2i}\varphi_{2i}^2 + 2\varphi_{2i}\varphi_{2i}'^2\right) + r_{12b}\varphi_{1i}^2\varphi''_{2i} + r_{g12}\varphi_{1i}^2\varphi_{2i} \\ &+ r_{g1a}\varphi_{1i}^3 + \frac{\tilde{\mu}}{N}\sum_{j=1}^{N}\Bigg\{2\left(\Lambda_{m1}\varphi'_{1i} + \Lambda_{c12}\varphi'_{2i}\right) \\ &\left(k_1\varphi_{1j}\varphi'_{1j} + k_{12}\left(\varphi'_{1j}\varphi_{2j} + \varphi'_{2j}\varphi_{1j}\right) + k_2\varphi'_{2j}\varphi_{2j}\right) \\ &+ \frac{1}{2}\left(g_d X_{1i}^2 + g_f X_{2i}^2 + g_1\varphi_{1i}^2\right)\left(\Lambda_{c2}\varphi''_{2j} + \Lambda_{c1}\varphi''_{1j}\right) \\ &+ \frac{\Lambda_{c1}}{2}\Big(\left[g_d X_{1j}^2 + g_f X_{2j}^2 + g_1\varphi_{1j}^2\right]\varphi''_{1j} \\ &+ \left(g_a X_{1j}^2 + g_b X_{2j}^2\right)\varphi''_{2j} \\ &+ 2\left[g_a X_{1j}X'_{1j}\left(X'_{2j} + \varphi'_{1j}\right) + g_b X_{2j}X_{2j}'^2 + g_1\varphi_{1j}\varphi_{1j}'^2\right]\Big)\Bigg\} \end{aligned} \tag{A.8c}$$

$$\begin{aligned} f_{f1}(\boldsymbol{\varphi},\vartheta) = &\Big[\Lambda_{c1} + \left(\Lambda_{m1} - g_e X_{1i}^2\right)\varphi'_{1i} + \left(\Lambda_{c12} - \frac{g_a}{2}X_{1i}^2\right)\varphi'_{2i} \\ &- \frac{g_d}{2}X_{1i}^2 - \frac{g_f}{2}X_{2i}^2 - \frac{g_1}{2}\varphi_{1i}^2\Big]\tilde{T}_1\cos(n\vartheta), \end{aligned} \tag{A.8d}$$

for pendulums 1 and

$$f_{L2i}(\boldsymbol{\varphi}) = -\frac{\tilde{\mu}\Lambda_{c2}}{N}\sum_{j=1}^{N}\left(\Lambda_{c1}\varphi''_{1j} + \Lambda_{c2}\varphi''_{2j}\right) + \tilde{b}_2\varphi'_{2i}, \tag{A.9a}$$

$$\begin{aligned} f_{Q2i}(\boldsymbol{\varphi}) &= 2\tilde{g}_a X_{1i}\varphi'_{1i} \\ &- \frac{\tilde{\mu}}{N}\sum_{j=1}^{N}\left(\Lambda_{c12}\varphi'_{1i} + \Lambda_{m2}\varphi'_{2i}\right)\left(\Lambda_{c1}\varphi''_{1j} + \Lambda_{c2}\varphi''_{2j}\right) \\ &+ \frac{2\Lambda_{c2}\tilde{\mu}}{N}\sum_{j=1}^{N}\Big(k_1\varphi_{1j}\varphi'_{1j} + k_{12}\Big(\varphi'_{1j}\varphi_{2j} + \varphi'_{2j}\varphi_{1j}\Big) \\ &+ k_2\varphi'_{2j}\varphi_{2j}\Big), \end{aligned} \tag{A.9b}$$

$$\begin{aligned} f_{C2i}(\boldsymbol{\varphi}) &= -\frac{\tilde{g}_a}{6}\left[3X_{1i}^2\varphi''_{1i} + X_{1i}^3 - 6X_{1i}'^2\varphi'_{1i}\right] - \frac{\tilde{g}_f}{6}X_{2i}^3 + r_{12a}\varphi''_{1i}\varphi_{2i}^2 \\ &+ r_{12b}\left(\varphi''_{1i}\varphi_{1i}^2 + 2\varphi_{1i}\varphi_{1i}'^2\right) + r_2\left(\varphi''_{2i}\varphi_{2i}^2 + \varphi_{2i}\varphi_{2i}'^2\right) + r_{g1b}\varphi_{1i}^3 \\ &+ \frac{\tilde{\mu}}{N}\sum_{j=1}^{N}\Big\{2\left(\Lambda_{c12}\varphi'_{1i} + \Lambda_{m2}\varphi'_{2i}\right) \\ &\left(k_1\varphi_{1j}\varphi'_{1j} + k_{12}\left(\varphi'_{1j}\varphi_{2j} + \varphi'_{2j}\varphi_{1j}\right) + k_2\varphi'_{2j}\varphi_{2j}\right) \\ &+ \frac{1}{2}\left(g_a X_{1i}^2 + g_b X_{2i}^2\right)\left(\Lambda_{c1}\varphi''_{1j} + \Lambda_{c2}\varphi''_{2j}\right) \\ &+ \frac{\Lambda_{c2}}{2}\Big(\left[g_d X_{1j}^2 + g_f X_{2j}^2 + g_1\varphi_{1j}^2\right]\varphi''_{1j} \\ &+ \left[g_a X_{1j}^2 + g_b X_{2j}^2\right]\varphi''_{2j} \\ &+ 2\left[g_a X_{1j}X'_{1j}\left(X'_{2j} + \varphi'_{1j}\right) + g_b X_{2j}X'_{2j} + g_1\varphi_{1j}\varphi_{1j}'^2\right]\Big)\Big\}, \end{aligned} \tag{A.9c}$$

$$\begin{aligned} f_{f2}(\boldsymbol{\varphi},\vartheta) &= \Big[\Lambda_{c2} + \Lambda_{c12}\varphi'_{1i} + \Lambda_{m2}\varphi'_{2i} - g_{12}\frac{\varphi_{2i}^2}{2} \\ &- k_{12}\frac{(\varphi_{1i}+\varphi_{2i})^2}{2} - g_{12}\frac{\varphi_{2i}^2}{2}\varphi'_{1i}\Big]\tilde{T}_1\cos(n\vartheta) \end{aligned} \tag{A.9d}$$

for pendulums 2. g_d and g_e are nonlinear constants defined in Appendix B.

Appendix A.3. Simplified modal equations

Following the procedure described in section 4.2, one obtains the modal equations (17a) and (17b). Functions $\hat{f}_i^{(o)}$ and $\hat{f}_i^{(u)}$ can be decomposed as

$$\hat{f}_i^{(o)}(\rho_i,\zeta_i,\vartheta) = \hat{f}_{Li}^{(o)}(\zeta_i) + \hat{f}_{Qi}^{(o)}(\rho_i,\zeta_i) + \hat{f}_{Ci}^{(o)}(\rho_i,\zeta_i) + \hat{f}_{fi}^{(o)}(\rho_i,\zeta_i,\vartheta), \tag{A.10a}$$

$$\hat{f}_i^{(u)}(\rho_i,\zeta_i,\vartheta) = \hat{f}_{Li}^{(u)}(\zeta_i) + \hat{f}_{Qi}^{(u)}(\rho_i,\zeta_i) + \hat{f}_{Ci}^{(u)}(\rho_i,\zeta_i) + \hat{f}_{fi}^{(u)}(\rho_i,\zeta_i,\vartheta). \tag{A.10b}$$

$\hat{f}_{Li}^{(\mathrm{x})}$, $\hat{f}_{Qi}^{(\mathrm{x})}$, $\hat{f}_{Ci}^{(\mathrm{x})}$ and $\hat{f}_{fi}^{(\mathrm{x})}$, $\mathrm{x} = \{o, u\}$, $i = \{1, 2\}$, contain exclusively linear, quadratic, cubic and forcing terms. These functions are

$$\hat{f}_{Li}^{(o)}(\rho_i) = \hat{b}_i\rho_i', \tag{A.11a}$$

$$\hat{f}_{Qi}^{(o)}(\rho_i,\zeta_i) = -\tilde{\mu}\hat{\Lambda}_{ci}\hat{\Lambda}_{c1i}\rho_i'\zeta_i'', \tag{A.11b}$$

$$\begin{aligned}\hat{f}_{Ci}^{(o)}(\rho_i,\zeta_i) = &-\frac{1}{6}\left[\tilde{g}_1 + \tilde{g}_a\left(\alpha_{11}-1+\chi_{pi}\right)^4 + \tilde{g}_b\left(\alpha_{11}+\chi_{pi}\right)^4\right]\\ &\left(\rho_i^2+3\zeta_i^2\right)\rho_i + \left(\hat{r}_i+2\hat{r}_{12i}\right)\left[\left(\rho_i^2+\zeta_i^2\right)\rho_i'' + \rho_i\left(\rho_i'^2+\zeta_i'^2\right)\right.\\ &\left.+2\zeta_i\left(\rho_i\zeta_i''+\rho_i'\zeta_i'\right)\right] + \hat{r}_{gi}\left(\rho_i^2+3\zeta_i^2\right)\rho_i\\ &+2\tilde{\mu}\hat{\Lambda}_{mi}\hat{k}_i\left(\rho_i\rho_i'+\zeta_i\zeta_i'\right)\rho_i' - \tilde{g}_a\left(\alpha_{11}+\chi_{pi}\right)\\ &\left(\alpha_{11}-1+\chi_{pi}\right)^2\left(\rho_i+\zeta_i\right)\left[\left(\rho_i+\zeta_i\right)\rho_i'' + 2\rho_i'\zeta_i'\right]\\ &+\tilde{\mu}\hat{\Lambda}_{ci}c_{fi}\rho_i\zeta_i\zeta_i'',\end{aligned} \tag{A.11c}$$

$$\begin{aligned}\hat{f}_{fi}^{(o)}(\rho_i,\zeta_i,\vartheta) = &\left[\hat{\Lambda}_{mi}\rho_i' - c_{fi}\rho_i\zeta_i - g_a\chi_{pi}^2\left(\alpha_{11}+\chi_{pi}\right)\left(\alpha_{11}-1+\chi_{pi}\right)^2\right.\\ &\left.\left(\left(\rho_i^2+\zeta_i^2\right)\rho_i' + 2\rho_i\zeta_i\zeta_i'\right)\right]\tilde{T}_1\cos(n\vartheta)\end{aligned} \tag{A.11d}$$

for the phase-opposition modes and

$$\hat{f}_{Li}^{(u)}(\zeta_i) = -\tilde{\mu}\hat{\Lambda}_{ci}^2\zeta_i'' + \hat{b}_i\zeta_i', \tag{A.12a}$$

$$\hat{f}_{Qi}^{(u)}(\rho_i,\zeta_i) = 2\tilde{\mu}\hat{\Lambda}_{ci}\hat{k}_i\left(\zeta_i\zeta_i' + \rho_i\rho_i'\right) - \tilde{\mu}\hat{\Lambda}_{ci}\left(\hat{\Lambda}_{mi}\zeta_i' + \hat{\Lambda}_{c2i}\rho_i'\right)\zeta_i'', \tag{A.12b}$$

$$\begin{aligned}\hat{f}_{Ci}^{(u)}(\rho_i,\zeta_i) = &-\frac{1}{6}\left[\tilde{g}_1 + \tilde{g}_a\left(\alpha_{11}-1+\chi_{pi}\right)^4 + \tilde{g}_b\left(\alpha_{11}+\chi_{pi}\right)^4\right]\\ &\left(3\rho_i^2+\zeta_i^2\right)\zeta_i + \left(\hat{r}_i + 2\hat{r}_{12i}\right)\left[\left(\rho_i^2+\zeta_i^2\right)\zeta_i'' + \zeta_i\left(\rho_i'^2+\zeta_i'^2\right)\right.\\ &\left.+ 2\rho_i\left(\zeta_i\rho_i'' + \rho_i'\zeta_i'\right)\right] + \hat{r}_{gi}\left(3\rho_i^2+\zeta_i^2\right)\zeta_i\\ &+ 2\tilde{\mu}\hat{\Lambda}_{mi}\hat{k}_i\left(\rho_i\rho_i' + \zeta_i\zeta_i'\right)\zeta_i' - \tilde{g}_a\left(\alpha_{11}+\chi_{pi}\right)\\ &\left(\alpha_{11}-1+\chi_{pi}\right)^2\left(\rho_i+\zeta_i\right)\left[\left(\rho_i+\zeta_i\right)\zeta_i'' + \rho_i'^2 + \zeta_i'^2\right]\\ &+ \tilde{\mu}\hat{\Lambda}_{ci}c_{fi}\Big[\zeta_i\left(\zeta_i'^2+\rho_i'^2\right) + 2\rho_i\rho_i'\zeta_i' + \left(\zeta_i^2+\rho_i^2\right)\zeta_i''\\ &+ \rho_i\zeta_i\rho_i''\Big],\end{aligned} \tag{A.12c}$$

$$\begin{aligned}\hat{f}_{fi}^{(u)}(\rho_i,\zeta_i,\vartheta) = &\Big[\hat{\Lambda}_{ci} + \hat{\Lambda}_{mi}\zeta_i' - \frac{1}{2}c_{fi}\left(\rho_i^2+\zeta_i^2\right) - g_a\chi_{pi}^2\left(\alpha_{11}+\chi_{pi}\right)\\ &\left(\alpha_{11}-1+\chi_{pi}\right)^2\left(\left(\rho_i^2+\zeta_i^2\right)\zeta_i' + 2\rho_i\zeta_i\rho_i'\right)\Big]\tilde{T}_1\cos(n\vartheta)\end{aligned} \tag{A.12d}$$

for the unison modes. c_{fi} is a modal parameter contributing to the forcing and described in Appendix B. Note that the modal projection generates a linear term

$$2\tilde{\mu}w_i[(\Lambda_{c12}+\Lambda_{m2}\chi_{pi})\zeta_i'' + (k_{12}+k_2\chi_{pi})\zeta_i], \tag{A.13}$$

which could be included in $\hat{f}_{Li}^{(u)}(\zeta_i)$. However, using the first order solution $\zeta_i'' = -n_{pi}^2\zeta_i$, this additional term reduces to

$$2\tilde{\mu}w_i[k_{12}+k_2\chi_{pi} - n_{pi}^2(\Lambda_{c12}+\Lambda_{m2}\chi_{pi})]\zeta_i, \tag{A.14}$$

and from the definition of χ_{pi} (*cf.* section 3), $k_{12}+k_2\chi_{pi}-n_{pi}^2(\Lambda_{c12}+\Lambda_{m2}\chi_{pi}) =$ 0. Hence, the term (A.13) does not contribute to the response at the order retained.

Appendix B. Notations

The expression of the notations introduced in section 3 is

$$
\begin{aligned}
\Lambda_{m1} &= h[1+(\eta_1+\eta_2\mu_2\nu_2^2)\alpha_{11}^2+\mu_2(1+\nu_2\alpha_{11})^2],\\
\Lambda_{m2} &= h\mu_2\nu_2^2(1+\eta_2\alpha_{21}^2),\\
\Lambda_{c1} &= h[1+\nu_r+(\eta_1+\eta_2\mu_2\nu_2^2+\mu_2\nu_2^2)\alpha_{11}+\mu_2(1+\nu_r+\nu_2)],\\
\Lambda_{c2} &= h\mu_2\nu_2[\nu_2(1+\eta_2\alpha_{21})+1+\nu_r],\\
\Lambda_{c12} &= h\mu_2\nu_2[1+\nu_2\alpha_{11}(1+\eta_2\alpha_{21})],\\
k_1 &= h[(1+\mu_2)\nu_r+\mu_2\nu_2\left((\alpha_{11}-1)^2+\nu_r\alpha_{11}^2\right)],\\
k_2 &= h\mu_2\nu_2(1+\nu_r),\\
k_{12} &= h\mu_2\nu_2[(1+\nu_r)\alpha_{11}-1],\\
\bar{\Lambda}_{m1} &= \Lambda_{m1}-\frac{\mu}{1+\mu}\Lambda_{c1}^2,\\
\bar{\Lambda}_{m2} &= \Lambda_{m2}-\frac{\mu}{1+\mu}\Lambda_{c2}^2,\\
\bar{\Lambda}_{c12} &= \Lambda_{c12}-\frac{\mu}{1+\mu}\Lambda_{c1}\Lambda_{c2}.
\end{aligned}
\tag{B.1}
$$

The expression of the nonlinear coefficients introduced in section 4 is

$$
\begin{aligned}
g_1 &= h\nu_r(1+\mu_2),\\
g_a &= h\mu_2\nu_2,\\
g_b &= \nu_r g_a,\\
g_c &= (\alpha_{11}-1)g_a,\\
g_d &= (\alpha_{11}+1)g_a,\\
g_e &= \alpha_{11}g_a,\\
g_f &= \nu_r\alpha_{11}g_a,\\
r_1 &= 6h[(\eta_1+\mu_2\nu_2^2\eta_2+\mu_2\nu_2^2)\alpha_{11}+\mu_2\nu_2]\tilde{\alpha}_{13}\\
r_{12a} &= 3h\mu_2\nu_2^2\eta_2\alpha_{11}\tilde{\alpha}_{23},\\
r_{12b} &= 3h\mu_2\nu_2^2\eta_2(1+\eta_2\alpha_{21})\tilde{\alpha}_{13},\\
r_2 &= 6h\mu_2\nu_2^2\eta_2\alpha_{21}\tilde{\alpha}_{23},\\
r_{g1a} &= 4(k_1\alpha_{11}-g_a)\tilde{\alpha}_{13},\\
r_{g1b} &= k_2\tilde{\alpha}_{13},\\
r_{g12} &= 3k_2\tilde{\alpha}_{13},
\end{aligned}
\tag{B.2}
$$

and the expression of the modal parameters is

$$
\begin{aligned}
\hat{\Lambda}_{mi} &= \Lambda_{m1} + 2\chi_{pi}\Lambda_{c12} + \chi_{pi}^2\Lambda_{m2},\\
\hat{k}_i &= k_1 + 2\chi_{pi}k_{12} + \chi_{pi}^2 k_2,\\
\hat{\Lambda}_{ci} &= \Lambda_{c1} + \chi_{pi}\Lambda_{c2},\\
\hat{b}_i &= \tilde{b}_1 + \chi_{pi}^2\tilde{b}_2,\\
\hat{r}_i &= r_1 + \chi_{pi}^4 r_2,\\
\hat{r}_{12i} &= r_{12a}\chi_{pi}^3 + r_{12b}\chi_{pi},\\
\hat{r}_{gi} &= r_{g1a} + (r_{g1b} + r_{g12})\chi_{pi},\\
c_{fi} &= g_1 + g_a(\alpha_{11} - 1 + \chi_{pi})^2(\alpha_{11} + 1 + \chi_{pi}) + g_b(\alpha_{11} + \chi_{pi})^3,\\
c_{pi} &= \tilde{g}_1 + 4n_{pi}^2(\hat{r}_i + 2\hat{r}_{12i}) - 6\hat{r}_{gi}\\
c_{si} &= \tilde{g}_a(\alpha_{11} - 1 + \chi_{pi})^2[(\alpha_{11} - 1 + \chi_{pi})^2 - 4n_{pi}^2(\alpha_{11} + \chi_{pi})]\\
&\quad + \tilde{g}_b(\alpha_{11} + \chi_{pi})^4,\\
c_{ti} &= 4\tilde{\mu}\hat{\Lambda}_{ci}n_{pi}^2 c_{fi},\\
c_{ci} &= 4\tilde{\mu}\hat{\Lambda}_{mi}\hat{k}_i n_{pi}^2,\\
c_{mi} &= \tilde{g}_a n_{pi}^2(\alpha_{11} + \chi_{pi})(\alpha_{11} - 1 + \chi_{pi})^2,\\
\delta_{ni} &= \frac{\hat{\Lambda}_{ci}^2 n_{pi}}{2\hat{\Lambda}_{mi}}.
\end{aligned}
\tag{B.3}
$$

Appendix C. Linear modal analysis with $N = 2$ double pendulums

With $N = 2$ double pendulums, the reduced eigenvalue problem formed by Eqs. (6b) and (6c) is

$$
\boldsymbol{A}_r\boldsymbol{\psi}_r = \boldsymbol{0}, \quad \boldsymbol{A}_r = \boldsymbol{K}_r - n^2\boldsymbol{M}_r \tag{C.1}
$$

with

$$\boldsymbol{M}_r = \begin{bmatrix} \bar{\Lambda}_{m1} + \frac{\mu\Lambda_{c1}^2}{2(1+\mu)} & -\frac{\mu\Lambda_{c1}^2}{2(1+\mu)} & \bar{\Lambda}_{c12} + \frac{\mu\Lambda_{c1}\Lambda_{c2}}{2(1+\mu)} & -\frac{\mu\Lambda_{c1}\Lambda_{c2}}{2(1+\mu)} \\ -\frac{\mu\Lambda_{c1}^2}{2(1+\mu)} & \bar{\Lambda}_{m1} + \frac{\mu\Lambda_{c1}^2}{2(1+\mu)} & -\frac{\mu\Lambda_{c1}\Lambda_{c2}}{2(1+\mu)} & \bar{\Lambda}_{c12} + \frac{\mu\Lambda_{c1}\Lambda_{c2}}{2(1+\mu)} \\ \bar{\Lambda}_{c12} + \frac{\mu\Lambda_{c1}\Lambda_{c2}}{2(1+\mu)} & -\frac{\mu\Lambda_{c1}\Lambda_{c2}}{2(1+\mu)} & \bar{\Lambda}_{m2} + \frac{\mu\Lambda_{c2}^2}{2(1+\mu)} & -\frac{\mu\Lambda_{c2}^2}{2(1+\mu)} \\ -\frac{\mu\Lambda_{c1}\Lambda_{c2}}{2(1+\mu)} & \bar{\Lambda}_{c12} + \frac{\mu\Lambda_{c1}\Lambda_{c2}}{2(1+\mu)} & -\frac{\mu\Lambda_{c2}^2}{2(1+\mu)} & \bar{\Lambda}_{m2} + \frac{\mu\Lambda_{c2}^2}{2(1+\mu)} \end{bmatrix}, \tag{C.2a}$$

$$\boldsymbol{K}_r = \begin{bmatrix} k_1 & 0 & k_{12} & 0 \\ 0 & k_1 & 0 & k_{12} \\ k_{12} & 0 & k_2 & 0 \\ 0 & k_{12} & 0 & k_2 \end{bmatrix}. \tag{C.2b}$$

The four solutions of $\det(\boldsymbol{A}_r) = 0$ are n_{p1}, n_{10}, n_{p2} and n_{20} with

$$\begin{aligned} n_{p1,2}^2 &= \frac{\Lambda_{m1}k_2 + \Lambda_{m2}k_1 - 2\Lambda_{c12}k_{12}}{2(\Lambda_{m1}\Lambda_{m2} - \Lambda_{c12}^2)} \\ &\mp \frac{\sqrt{4(\Lambda_{c12}k_1 - \Lambda_{m1}k_{12})(\Lambda_{c12}k_2 - \Lambda_{m2}k_{12}) + (\Lambda_{m1}k_2 - \Lambda_{m2}k_1)^2}}{2(\Lambda_{m1}\Lambda_{m2} - \Lambda_{c12}^2)}, \end{aligned} \tag{C.3a}$$

$$\begin{aligned} n_{10,20}^2 &= \frac{\bar{\Lambda}_{m1}k_2 + \bar{\Lambda}_{m2}k_1 - 2\bar{\Lambda}_{c12}k_{12}}{2(\bar{\Lambda}_{m1}\bar{\Lambda}_{m2} - \bar{\Lambda}_{c12}^2)} \\ &\mp \frac{\sqrt{4(\bar{\Lambda}_{c12}k_1 - \bar{\Lambda}_{m1}k_{12})(\bar{\Lambda}_{c12}k_2 - \bar{\Lambda}_{m2}k_{12}) + (\bar{\Lambda}_{m1}k_2 - \bar{\Lambda}_{m2}k_1)^2}}{2(\bar{\Lambda}_{m1}\bar{\Lambda}_{m2} - \bar{\Lambda}_{c12}^2)}. \end{aligned} \tag{C.3b}$$

To compute the mode shapes associated to n_{p1} and n_{p2}, it is convenient to use row operations on $\boldsymbol{A}_r$ and substitute n for n_{pi}, $i = 1, 2$ in order to form matrix $\boldsymbol{A}_r^{(1i)}$. This matrix is such that

$$\begin{aligned} \mathcal{R}_1^{(1i)} &= [\mathcal{R}_1]_{n=n_{pi}}, \quad \mathcal{R}_2^{(1i)} = [\mathcal{R}_1 + \mathcal{R}_2]_{n=n_{pi}}, \\ \mathcal{R}_3^{(1i)} &= [\mathcal{R}_3]_{n=n_{pi}}, \quad \mathcal{R}_4^{(1i)} = [\mathcal{R}_3 + \mathcal{R}_4]_{n=n_{pi}}, \end{aligned} \tag{C.4}$$

where $\mathcal{R}_j^{(1i)}$ and $\mathcal{R}_j$ refer to the j^{th} row of $\boldsymbol{A}_r^{(1i)}$ and $\boldsymbol{A}_r$, respectively. Then, one can compute the reduced mode shape $\boldsymbol{\psi}_{ri}^{(o)}$ associated to the eigenvalue n_{pi}. It must satisfy $\boldsymbol{A}_r^{(1i)}\boldsymbol{\psi}_{ri}^{(o)} = \boldsymbol{0}$. Using either the 2^{nd} of 4^{th} line of $\boldsymbol{A}_r^{(1i)}\boldsymbol{\psi}_{ri}^{(o)} = \boldsymbol{0}$ and normalising the first component to one, one finds that $\boldsymbol{\psi}_{ri}^{(o)}$ has the shape

$$\boldsymbol{\psi}_{ri}^{(o)} = [1, -1, \chi_{pi}, -\chi_{pi}]^{\intercal}, \tag{C.5}$$

where χ_{pi} is a constant. Using the 1^{st} line of $\boldsymbol{A}_r^{(1i)}\boldsymbol{\psi}_{ri}^{(o)} = \boldsymbol{0}$, one finds that

$$\chi_{pi} = \frac{n_{pi}^2\Lambda_{m1} - k_1}{k_{12} - n_{pi}^2\Lambda_{c12}}. \tag{C.6}$$

Finally, to retrieve the rotor's component, we rewrite Eq. (6a) as

$$\theta = -\frac{\mu}{N(1+\mu)} \sum_{i=1}^{N} \left[\Lambda_{c1} \varphi_{1i} + \Lambda_{c2} \varphi_{2i} \right], \tag{C.7}$$

and we substitute φ_{1i} and φ_{2i} for their components in $\boldsymbol{\psi}_{ri}^{(o)}$. This way, we obtain the full mode shape $\boldsymbol{\phi}_i^{(o)}$, which contains the rotor's component ϱ_i. For the two modes considered here, we have $\varrho_i = 0$ such that

$$\boldsymbol{\phi}_i^{(o)} = [0, 1, -1, \chi_{pi}, -\chi_{pi}]^\intercal. \tag{C.8}$$

The two mode shapes associated to n_{10} and n_{20} are computed using the exact same procedure but another matrix $\boldsymbol{A}_r^{(2i)}$ defined such that

$$\begin{aligned} \mathcal{R}_1^{(2i)} &= [\mathcal{R}_1]_{n=n_{i0}}, \quad \mathcal{R}_2^{(2i)} = [\mathcal{R}_1 - \mathcal{R}_2]_{n=n_{i0}}, \\ \mathcal{R}_3^{(2i)} &= [\mathcal{R}_3]_{n=n_{i0}}, \quad \mathcal{R}_4^{(2i)} = [\mathcal{R}_3 - \mathcal{R}_4]_{n=n_{i0}}, \end{aligned} \tag{C.9}$$

where $\mathcal{R}_j^{(2i)}$ refers to the j$^{\text{th}}$ row of $\boldsymbol{A}_r^{(2i)}$. This way, we obtain the mode shape associated to n_{i0},

$$\boldsymbol{\phi}_i^{(u)} = [\varrho_i, 1, 1, \chi_i, \chi_i]^\intercal. \tag{C.10}$$

with

$$\chi_i = \frac{n_{i0}^2 \bar{\Lambda}_{m1} - k_1}{k_{12} - n_{i0}^2 \bar{\Lambda}_{c12}}, \quad \varrho_i = -\frac{\mu(\Lambda_{c1} + \Lambda_{c2}\chi_i)}{1+\mu}. \tag{C.11}$$

The last mode of the CDPVA with $N = 2$ double pendulums is the rigid-body mode $(n_0, \boldsymbol{\phi}_0)$ with

$$n_0 = 0, \quad \boldsymbol{\phi}_0 = [1, 0, 0, 0, 0]^\intercal. \tag{C.12}$$

Indeed, one can easily see that this rigid-body mode satisfies the eigenvalue problem associated to system (6).

Appendix D. Application of the method of multiple scales

Appendix D.1. Polar coordinates

The system obtained through the method of multiple scales is given by Eq. (21) where functions f_{v_i}, f_{u_i}, f_{ϕ_i} and f_{β_i} are

$$\begin{aligned}
f_{v_i}(\boldsymbol{u}_i,\boldsymbol{\beta}_i) = &\Big[\Big(c_i - \frac{c_{ti}}{2}\Big) v_i u_i^2 \sin\left(2\phi_i - 2\beta_i\right) \\
&- 2c_{mi} v_i u_i \left(4v_i \sin\left(\phi_i - \beta_i\right) - 3u_i \sin\left(2\phi_i - 2\beta_i\right)\right) \\
&- 8\hat{b}_i n_{pi} v_i + 2c_{fi}\tilde{T}_1 v_i u_i \sin\left(2\phi_i - \beta_i\right)\Big] \Big[16\hat{\Lambda}_{mi} n_{pi}\Big]^{-1}
\end{aligned} \tag{D.1a}$$

$$\begin{aligned}
f_{\phi_i}(\boldsymbol{u}_i,\boldsymbol{\beta}_i) = &\sigma v_i + \Big[\Big(c_i - \frac{c_{ti}}{2}\Big) v_i \left[u_i^2 \cos\left(2\phi_i - 2\beta_i\right) + v_i^2 + 2u_i^2\right] \\
&+ \Big(2c_{ci} u_i^2 - \frac{c_{ti}}{2} v_i^2\Big) v_i - 2c_{mi} v_i \\
&\left[v_i^2 - 2u_i^2 + 4v_i u_i \cos\left(\phi_i - \beta_i\right) - 3u_i^2 \cos\left(2\phi_i - 2\beta_i\right)\right] \\
&+ 2c_{fi}\tilde{T}_1 v_i u_i \left(2\cos\beta_i + \cos\left(2\phi_i - \beta_i\right)\right)\Big] \Big[16\hat{\Lambda}_{mi} n_{pi}\Big]^{-1},
\end{aligned} \tag{D.1b}$$

$$\begin{aligned}
f_{u_i}(\boldsymbol{u}_i,\boldsymbol{\beta}_i) = &-\Big[\Big(c_i - \frac{c_{ti}}{2}\Big) v_i^2 u_i \sin\left(2\phi_i - 2\beta_i\right) \\
&+ 2c_{mi} v_i \left(v_i^2 + u_i^2\right) \sin\left(\phi_i - \beta_i\right) \\
&+ 8\hat{b}_i n_{pi} u_i + \tilde{T}_1 \Big(c_{fi} v_i^2 \sin\left(2\phi_i - \beta_i\right) \\
&+ \Big(8\hat{\Lambda}_{ci} - c_{fi}\left(2v_i^2 + u_i^2\right)\Big) \sin\beta_i\Big)\Big] \Big[16\hat{\Lambda}_{mi} n_{pi}\Big]^{-1},
\end{aligned} \tag{D.1c}$$

$$\begin{aligned}
f_{\beta_i}(\boldsymbol{u}_i,\boldsymbol{\beta}_i) = &\sigma u_i - \tilde{\mu}\delta_{ni} u_i \\
&+ \Big[\Big(c_i - \frac{c_{ti}}{2}\Big) u_i \left(v_i^2 \cos\left(2\phi_i - 2\beta_i\right) + 2v_i^2 + u_i^2\right) \\
&+ \Big(2c_{ci} v_i^2 + \frac{c_{ti}}{2} u_i^2\Big) u_i \\
&+ 2c_{mi} v_i \left[\left(v_i^2 - 5u_i^2\right) \cos\left(\phi_i - \beta_i\right) + 4v_i u_i\right] \\
&- \tilde{T}_1 \Big(- c_{fi} v_i^2 \cos\left(2\phi_i - \beta_i\right) \\
&+ \Big(8\hat{\Lambda}_{ci} - c_{fi}\left(2v_i^2 + 3u_i^2\right)\Big) \cos\beta_i\Big)\Big] \Big[16\hat{\Lambda}_{mi} n_{pi}\Big]^{-1}.
\end{aligned} \tag{D.1d}$$

Constants c_{fi}, c_{ti}, c_{ci}, c_{pi}, c_{mi}, c_i and δ_{ni} are defined in Appendix B.

Appendix D.2. Cartesian coordinates

The functions involved in the system obtained through the method of multiple scales written in Cartesian coordinates are

$$
\begin{aligned}
f_{p_{1i}}(\boldsymbol{p}_i,\boldsymbol{q}_i) = &-\sigma q_{1i} - \Big[8\hat{b}_i n_{pi} p_{1i} + 2c_{fi}\tilde{T}_1\left(p_{1i}q_{2i} + p_{2i}q_{1i}\right)\\
&+ \left(c_i - \frac{c_{ti}}{2}\right)\left(p_{1i}^2 q_{1i} + 2p_{1i}p_{2i}q_{2i} + p_{2i}^2 q_{1i} + q_{1i}^3 + 3q_{1i}q_{2i}^2\right)\\
&- \frac{c_{ti}}{2}\left(p_{1i}^2 q_{1i} + q_{1i}^3\right) + 2c_{ci}\left(q_{1i}p_{2i}^2 + q_{1i}q_{2i}^2\right)\\
&- 2c_{mi}\Big(\left(p_{1i}^2 + p_{2i}^2\right)q_{1i} + 4q_{2i}\left(p_{1i}^2 + q_{1i}^2\right) + q_{1i}^3 - 6p_{1i}p_{2i}q_{2i}\\
&- 5q_{1i}q_{2i}^2\Big)\Big]\left[16\hat{\Lambda}_{mi}n_{pi}\right]^{-1}
\end{aligned}
\tag{D.2a}
$$

$$
\begin{aligned}
f_{q_{1i}}(\boldsymbol{p}_i,\boldsymbol{q}_i) = &\sigma p_{1i} + \Big[-8\hat{b}_i n_{pi} q_{1i} + 2c_{fi}\tilde{T}_1\left(3p_{1i}p_{2i} + q_{1i}q_{2i}\right)\\
&+ \left(c_i - \frac{c_{ti}}{2}\right)\left(p_{1i}^3 + 3p_{1i}p_{2i}^2 + p_{1i}q_{1i}^2 + p_{1i}q_{2i}^2 + 2p_{2i}q_{1i}q_{2i}\right)\\
&- \frac{c_{ti}}{2}\left(p_{1i}^3 + p_{1i}q_{1i}^2\right) + 2c_{ci}\left(p_{1i}p_{2i}^2 + p_{1i}q_{2i}^2\right)\\
&- 2c_{mi}\Big(\left(q_{1i}^2 + q_{2i}^2\right)p_{1i} + 4p_{2i}\left(p_{1i}^2 + q_{1i}^2\right) + p_{1i}^3 - 6p_{2i}q_{1i}q_{2i}\\
&- 5p_{1i}p_{2i}^2\Big)\Big]\left[16\hat{\Lambda}_{mi}n_{pi}\right]^{-1}
\end{aligned}
\tag{D.2b}
$$

$$
\begin{aligned}
f_{p_{2i}}(\boldsymbol{p}_i,\boldsymbol{q}_i) = &-\left(\sigma - \tilde{\mu}\delta_{ni}\right)q_{2i} - \Big[8\hat{b}_i n_{pi} p_{2i} + 2c_{fi}\tilde{T}_1\left(p_{1i}q_{1i} + p_{2i}q_{2i}\right)\\
&+ \left(c_i - \frac{c_{ti}}{2}\right)\left(p_{1i}^2 q_{2i} + 2p_{1i}p_{2i}q_{1i} + p_{2i}^2 q_{2i} + 3q_{1i}^2 q_{2i} + q_{2i}^3\right)\\
&+ \frac{c_{ti}}{2}\left(p_{2i}^2 q_{2i} + q_{2i}^3\right) + 2c_{ci}\left(p_{1i}^2 q_{2i} + q_{1i}^2 q_{2i}\right)\\
&+ 2c_{mi}\Big(\left(p_{1i}^2 + p_{2i}^2\right)q_{1i} + 4q_{2i}\left(p_{1i}^2 + q_{1i}^2\right) + q_{1i}^3 - 6p_{1i}p_{2i}q_{2i}\\
&- 5q_{1i}q_{2i}^2\Big)\Big]\left[16\hat{\Lambda}_{mi}n_{pi}\right]^{-1}
\end{aligned}
\tag{D.2c}
$$

$$
\begin{aligned}
f_{q_{2i}}(\boldsymbol{p}_i,\boldsymbol{q}_i) = &\left(\sigma - \tilde{\mu}\delta_{ni}\right)p_{2i} - \Big[8\hat{b}_i n_{pi} q_{2i}\\
&+ \tilde{T}_1\left(8\hat{\Lambda}_{ci} - c_{fi}\left(3p_{1i}^2 + 3p_{2i}^2 + q_{1i}^2 + q_{2i}^2\right)\right)\\
&- \left(c_i - \frac{c_{ti}}{2}\right)\left(3p_{1i}^2 p_{2i} + 2p_{1i}q_{1i}q_{2i} + p_{2i}^3 + p_{2i}q_{1i}^2 + p_{2i}q_{2i}^2\right)\\
&- \frac{c_{ti}}{2}\left(p_{2i}^3 + p_{2i}q_{2i}^2\right) - 2c_{ci}\left(p_{1i}^2 p_{2i} + q_{1i}^2 p_{2i}\right)\\
&- 2c_{mi}\Big(\left(q_{1i}^2 + q_{2i}^2\right)p_{1i} + 4p_{2i}\left(p_{1i}^2 + q_{1i}^2\right) + p_{1i}^3 - 6p_{2i}q_{1i}q_{2i}\\
&- 5p_{1i}p_{2i}^2\Big)\Big]\left[16\hat{\Lambda}_{mi}n_{pi}\right]^{-1}
\end{aligned}
\tag{D.2d}
$$

Appendix E. Steady state solutions

The amplitude and phase response of mode i are given by

$$\sigma = \tilde{\mu}\delta_{ni} - \frac{c_i u_i^2}{16\hat{\Lambda}_{mi} n_{pi}} \pm \frac{8\hat{\Lambda}_{ci} - 3c_{fi}u_i^2}{16\hat{\Lambda}_{mi} n_{pi}} \sqrt{\frac{\tilde{T}_1^2}{u_i^2} - \frac{64\hat{b}_i^2 n_{pi}^2}{(8\hat{\Lambda}_{ci} - c_{fi}u_i^2)^2}}, \tag{E.1a}$$

$$\tilde{T}_1^2 = u_i^2 \left[\frac{\left(16\hat{\Lambda}_{mi} n_{pi}(\sigma - \tilde{\mu}\delta_{ni}) + c_i u_i^2\right)^2}{(8\hat{\Lambda}_{ci} - 3c_{fi}u_i^2)^2} + \frac{64\hat{b}_i^2 n_{pi}^2}{(8\hat{\Lambda}_{ci} - c_{fi}u_i^2)^2} \right], \tag{E.1b}$$

$$\tan\beta_i = \frac{-8\hat{b}_i n_{pi}}{16\hat{\Lambda}_{mi} n_{pi}(\sigma - \tilde{\mu}\delta_{ni}) + c_i u_i^2} \frac{8\hat{\Lambda}_{ci} - 3c_{fi}u_i^2}{8\hat{\Lambda}_{ci} - c_{fi}u_i^2}. \tag{E.1c}$$

When the pendulums respond on mode i, the amplitudes and phases of the three first harmonics of the rotor's acceleration are given by

$$\begin{aligned} h_1^2 = {} & \tilde{T}_1^2 + \tilde{\mu}\tilde{T}_1 n^2 u_i \cos\beta_i \left(2\hat{\Lambda}_{ci} - \frac{c_{fi}}{4}u_i^2\right) \\ & + \frac{\tilde{\mu}^2}{4} n^4 u_i^2 \left(2\hat{\Lambda}_{ci} - \frac{c_{fi}}{4}u_i^2\right)^2 \end{aligned} \tag{E.2a}$$

$$\tan\psi_1 = \frac{\tilde{\mu} n^2 u_i \sin\beta_i (8\hat{\Lambda}_{ci} - c_{fi}u_i^2)}{\tilde{\mu} n^2 u_i \cos\beta_i (8\hat{\Lambda}_{ci} - c_{fi}u_i^2) + 8\tilde{T}_1}, \tag{E.2b}$$

$$h_2 = \frac{c_{ci}}{4\hat{\Lambda}_{ci} n_{pi}} u_i^2, \tag{E.2c}$$

$$\tan\psi_2 = \frac{-\cos(2\beta_i)}{\sin(2\beta_i)}, \tag{E.2d}$$

$$h_3 = \frac{3c_{ti}}{32\hat{\Lambda}_{ci}} u_i^3, \tag{E.2e}$$

$$\tan\psi_3 = \frac{-\sin(3\beta_i)}{-\cos(3\beta_i)}. \tag{E.2f}$$

Appendix F. Results from the stability analysis

Appendix F.1. Determinants of $\boldsymbol{A}_i$ and $\boldsymbol{B}_i$

Th determinants of $\boldsymbol{A}_i$ and $\boldsymbol{B}_i$ are

$$\begin{aligned}
\det(\boldsymbol{A}_i) = \Big[& -256\hat{\Lambda}_{ci}\hat{\Lambda}_{mi}n_{pi}\sigma + 8\Big(4\hat{\Lambda}_{mi}c_{fi}n_{pi}\left(2\tilde{\mu}\delta_{ni}+\sigma\right) \\
& - \hat{\Lambda}_{ci}\left(2c_i - c_{ti} + 4c_{ci} - 4c_{mi}\right)\Big)u_i^2 \\
& + c_{fi}\left(2c_i - 3c_{ti} + 12c_{ci} - 12c_{mi}\right)u_i^4\Big] \\
& \Big[-256\hat{\Lambda}_{ci}\hat{\Lambda}_{mi}n_{pi}\sigma + 8\Big(12\hat{\Lambda}_{mi}c_{fi}n_{pi}\left(2\tilde{\mu}\delta_{ni}-\sigma\right) \\
& - \hat{\Lambda}_{ci}\left(6c_i - 3c_{ti} + 4c_{ci} + 20c_{mi}\right)\Big)u_i^2 \\
& + 3c_{fi}\left(2c_i - 3c_{ti} + 4c_{ci} + 20c_{mi}\right)u_i^4\Big] \\
& \left[1024\hat{\Lambda}_{mi}^2 n_{pi}^2\left(8\hat{\Lambda}_{ci} - 3c_{fi}u_i^2\right)^2\right]^{-1} \\
& + \hat{b}_i^2\left[64\hat{\Lambda}_{ci}^2 - 16\hat{\Lambda}_{ci}c_{fi}u_i^2 + 3c_{fi}^2\left(32\hat{\Lambda}_{ci}-5\right)u_i^4 - 12c_{fi}^3u_i^6\right] \\
& \left[4\hat{\Lambda}_{mi}^2\left(8\hat{\Lambda}_{ci} - c_{fi}u_i^2\right)^2\right]^{-1}
\end{aligned} \tag{F.1}$$

and

$$\begin{aligned}
\det(\boldsymbol{B}_i) = & \left(8\hat{\Lambda}_{ci} - c_{fi}u_i^2\right)\left[16\hat{\Lambda}_{mi}n_{pi}\left(\tilde{\mu}\delta_{ni}-\sigma\right) - c_iu_i^2\right] \\
& \Big[128\hat{\Lambda}_{ci}\hat{\Lambda}_{mi}n_{pi}\left(\tilde{\mu}\delta_{ni}-\sigma\right) \\
& + 8\left(6\hat{\Lambda}_{mi}c_{fi}n_{pi}\left(\tilde{\mu}\delta_{ni}-\sigma\right) - 3\hat{\Lambda}_{ci}c_i\right)u_i^2 + 3c_{fi}c_iu_i^4\Big] \\
& \left[256\hat{\Lambda}_{mi}^2 n_{pi}^2\left(8\hat{\Lambda}_{ci} - 3c_{fi}u_i^2\right)^2\right]^{-1} \\
& + \hat{b}_i^2\Big[64\hat{\Lambda}_{ci}^2 - 16\hat{\Lambda}_{ci}c_{fi}u_i^2 + 3c_{fi}^2\left(32\hat{\Lambda}_{ci}-5\right)u_i^4 - 12c_{fi}^3u_i^6\Big] \\
& \left[4\hat{\Lambda}_{mi}^2\left(8\hat{\Lambda}_{ci} - c_{fi}u_i^2\right)^2\right]^{-1}
\end{aligned} \tag{F.2}$$

Appendix F.2. Bifurcation curves

The bifurcation curves are

$$n_{pf_i} = n_{pi} + \epsilon\frac{A_{pf_i} \pm \sqrt{B_{pf_i}}}{C_{pf_i}}, \tag{F.3a}$$

$$n_{sn_i} = n_{pi} + \epsilon\frac{A_{sn_i} \pm \sqrt{B_{sn_i}}}{C_{sn_i}}, \tag{F.3b}$$

with

$$
\begin{aligned}
A_{pf_i} &= 256\hat{\Lambda}_{mi}\hat{\Lambda}_{ci}\tilde{\mu}\delta_{ni}c_{fi}n_{pi}u_i^2 + 4\hat{\Lambda}_{ci}c_{fi}\left(2c_i - 3c_{ti} + 4c_{ci}\right)u_i^4 \\
&\quad - 32\hat{\Lambda}_{ci}^2\left(2c_i - c_{ti} + 2c_{ci}\right)u_i^2 + 3c_{ci}c_{fi}^2u_i^6 \\
&\quad - 4c_{mi}u_i^2\left(4\hat{\Lambda}_{ci} - c_{fi}u_i^2\right)\left(8\hat{\Lambda}_{ci} - 3c_{fi}u_i^2\right),
\end{aligned}
\tag{F.4a}
$$

$$
\begin{aligned}
B_{pf_i} &= \frac{\left(8\hat{\Lambda}_{ci} - 3c_{fi}u_i^2\right)^2}{16}\Bigg[- 256\hat{b}_i^2n_{pi}^2\frac{8\hat{\Lambda}_{ci} + 3c_{fi}u_i^2}{8\hat{\Lambda}_{ci} - c_{fi}u_i^2} \\
&\quad \left(64\hat{\Lambda}_{ci}^2 - 16\hat{\Lambda}_{ci}c_{fi}u_i^2 + 3c_{fi}^2(32\hat{\Lambda}_{ci} - 5)u_i^4 - 12c_{fi}^3u_i^6\right) \\
&\quad + \Big(64\hat{\Lambda}_{mi}\tilde{\mu}\delta_{ni}n_{pi}c_{fi} - 8\hat{\Lambda}_{ci}\left(2c_i + 12c_{mi} - c_{ti}\right) \\
&\quad + c_{fi}\left(2c_i - 3c_{ti} + 8c_{ci} + 4c_{mi}\right)u_i^2\Big)^2u_i^4\Bigg],
\end{aligned}
\tag{F.4b}
$$

$$
C_{pf_i} = 8\hat{\Lambda}_{mi}n_{pi}\left(8\hat{\Lambda}_{ci} - c_{fi}u_i^2\right)\left(8\hat{\Lambda}_{ci} + 3c_{fi}u_i^2\right) \tag{F.4c}
$$

and

$$
A_{sn_i} = 2\left[\left(8\hat{\Lambda}_{ci} + 3c_{fi}u_i^2\right)\hat{\Lambda}_{mi}n_{pi}\tilde{\mu}\delta_{ni} - \hat{\Lambda}_{ci}c_iu_i^2\right], \tag{F.5a}
$$

$$
\begin{aligned}
B_{sn_i} &= -\frac{\left(8\hat{\Lambda}_{ci} - 3c_{fi}u_i^2\right)^2}{64\left(8\hat{\Lambda}_{ci} - c_{fi}u_i^2\right)^3}\Big[64\hat{b}_i^2n_{pi}^2(8\hat{\Lambda}_{ci} + 3c_{fi}u_i^2) \\
&\quad \left(64\hat{\Lambda}_{ci}^2 - 16\hat{\Lambda}_{ci}c_{fi}u_i^2 + 3c_{fi}^2\left(32\hat{\Lambda}_{ci} - 5\right)u_i^4 - 12c_{fi}^3u_i^6\right) \\
&\quad - c_i^2\left(8\hat{\Lambda}_{ci} - c_{fi}u_i^2\right)^3u_i^4\Big],
\end{aligned}
\tag{F.5b}
$$

$$
C_{sn_i} = 2\hat{\Lambda}_{mi}n_{pi}\left(8\hat{\Lambda}_{ci} + 3c_{fi}u_i^2\right) \tag{F.5c}
$$

Appendix G. Illustration of a localisation zone with a complex shape

Figure G.10 illustrates a situation where the unstable zone related to localisation has a complicated shape. In that case, the Taylor series up to u_1^2 used in section 5.3 are not sufficient to guarantee that the unstable zone will not cross the operating point at large amplitudes. Indeed, though at small amplitudes the red zone tends to shift to the left, it shifts back to the right at larger amplitudes and crosses the vertical line $n = n_{p1}$ at an amplitude $u_1 \approx 0.72$.

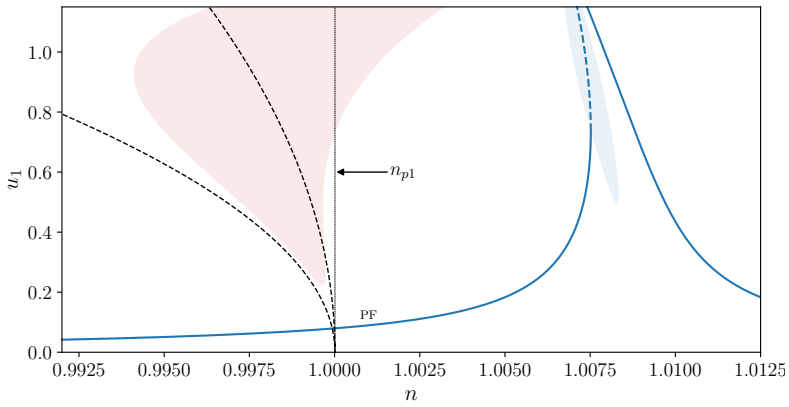

Figure G.10: Amplitude of mode 1 as a function of the excitation order. The stable and unstable parts of the analytical solutions are shown as solid and dashed lines, respectively. The red and blue areas are the instability regions related to localisation and jumps, respectively. The dashed black lines correspond to the approximated contours of the unstable zone leading to localisation. They are obtained using Eq. (30). $\bar{T}_1 = 0.002$ and the system parameters are given in Tab. 2 except for $\alpha_{13} = 0.0391$.

Chapter 11

Experimental investigation of the response of centrifugal double pendulums

Content

The aim of this chapter is to propose a realistic centrifugal double pendulum vibration absorber (CDPVA) design and to verify experimentally that the analytical and numerical models derived in chapters 9 and 10 are correct. Section 11.1 presents an original CDPVA architecture, a prototype build accordingly and the experimental set-up used for the tests. The experimental results are described in section 11.2. They validate several features of the models and expose the difficulties encountered during the measurements. Because of bench limitations, it was not possible to test a CDPVA tuned

at high order. Still, section 11.3 proposes a CDPVA design with a secondary antiresonance at order 20.

11.1 Presentation of the experimental system

11.1.1 Architecture of the centrifugal double pendulum vibration absorber

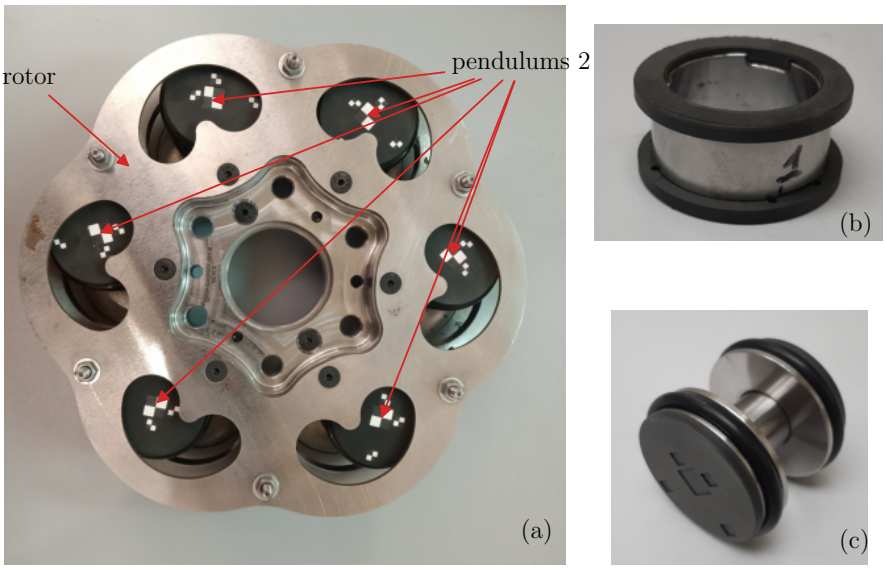

Figure 11.1: CDPVA used for the experiments (a). Pendulums 1 (b) are hollow cylinders and pendulums 2 (c) are made of a small-radius cylinder linked to two larger cylinder, whose aim is to increase the mass and inertia. In (a), pendulums 1 are hidden behind pendulums 2.

The CDPVA studied experimentally in this chapter is shown in Fig. 11.1(a). It is made of a rotor of inertia J_r and six double pendulums. A detailed view of this architecture with a single pendulum is presented in Fig. 11.2(a) (the dimensions of the system are different for readability purposes). Pendulum 1 (blue) is a hollow cylinder of centre of mass G_1, external radius r_{p1}, thickness e and width w_1. It rolls on the rotor's rolling track, which is a circular hole of centre A and radius r_0. The position of A is such that $OA = r$. Note that in practice the rotor's rolling track is not a full circle, which limits the amplitude of pendulum 1. Pendulum 2, whose centre of mass is G_2, is made of three parts, as can be seen in Fig. 11.2(c). There is a cylinder of radius r_{p2} and width w_2 which rolls on the inner part of pendulum 1. On each side of this small-radius cylinder are two additional cylinders of radius r_{p2a} and width w_{2a}, giving pendulum 2 an h-shape. Their purpose is to provide an easier control on the mass and inertia of pendulum 2. The parametrisation of the double pendulum is exactly the same as that used in chapters 9 and 10. Indeed, the position of G_1 and the rotation of pendulum 1 with respect to the rotor are measured through the angles φ_1 and $\alpha_1(\varphi_1)$, respectively. Similarly, the position of G_2 and the rotation of pendulum 2 with respect to pendulum 1 are measured through the angles φ_2 and $\alpha_2(\varphi_2)$, respectively.

In order to use the models presented in chapters 9 and 10, it is necessary to express the lengths

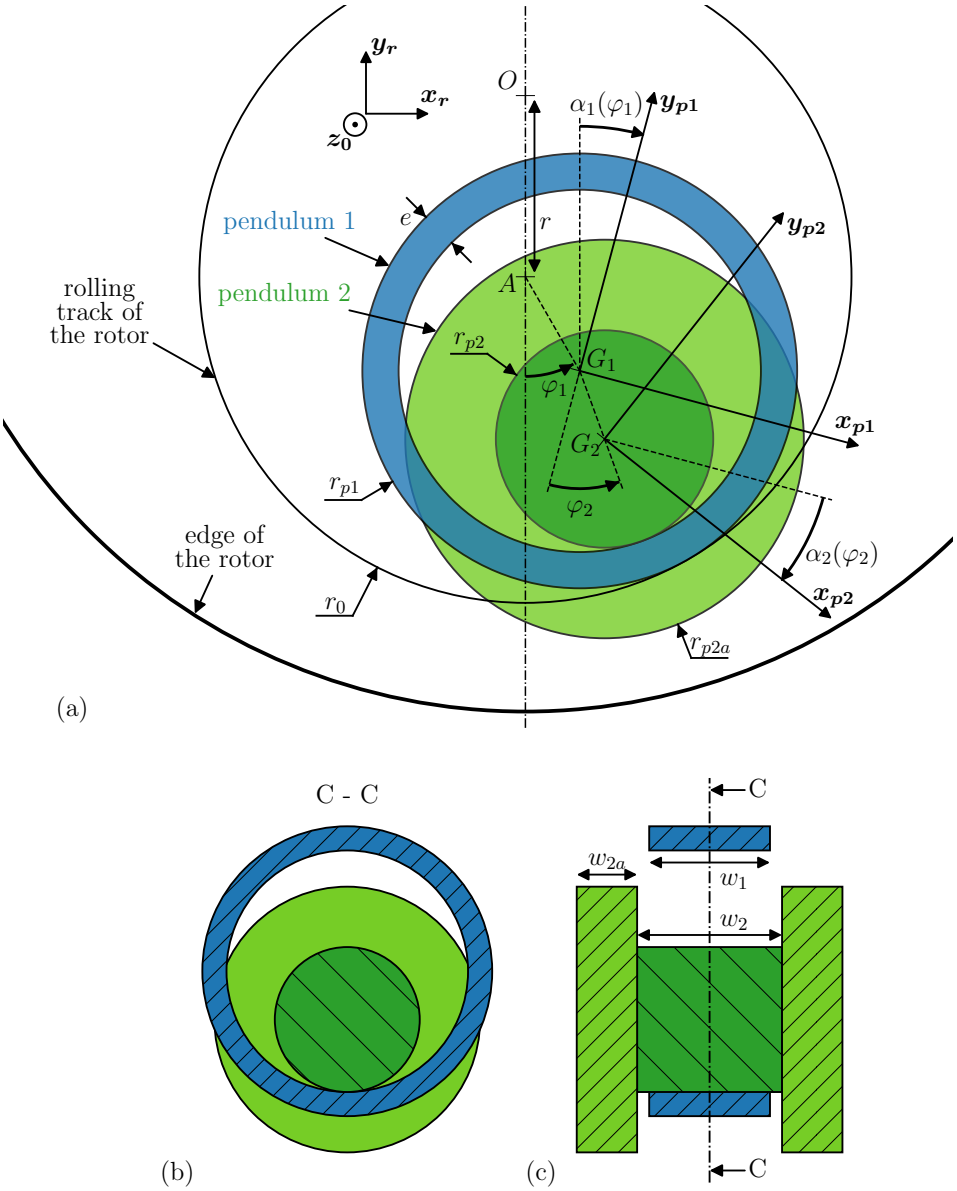

Figure 11.2: Front view (a) and side view (b) of a double pendulum rolling on the rotor.

$\ell_1 = AG_1$, $\ell_2 = G_1G_2$ as a function of the dimensions of the system. It is easy to find

$$\ell_1 = r_0 - r_{p1}, \quad \ell_2 = r_{p1} - e - r_{p2}. \tag{11.1}$$

Moreover, the rolling without slipping conditions between pendulum 1 and the rotor and between

r	r_0	r_{p1}	w_1	e	r_{p2}	w_2	r_{p2a}	w_{2a}
60	25.5	15.49	15	3	8.45	18	19	8

Table 11.1: Dimensions of the prototype (all in [mm]).

N	r [mm]	ℓ_1 [mm]	ℓ_2 [mm]	m_1 [g]	m_2 [g]	I_1 [g.m^2]	I_2 [g.m^2]	J_r [g.m^2]
6	60	10.01	4.04	30.85	169.55	0.006147	0.02684	11.373

Table 11.2: Parameters of the CDPVA used for the models.

pendulum 2 and pendulum 1 imply

$$\alpha_1(\varphi_1) = \left(1 - \frac{r_0}{r_{p1}}\right)\varphi_1 \quad \Rightarrow \quad \alpha_{11} = 1 - \frac{r_0}{r_{p1}}, \quad \alpha_{13} = 0 \tag{11.2a}$$

$$\alpha_2(\varphi_2) = \left(1 - \frac{r_{p1} - e}{r_{p2}}\right)\varphi_2 \quad \Rightarrow \quad \alpha_{21} = 1 - \frac{r_{p1} - e}{r_{p2}}, \quad \alpha_{23} = 0. \tag{11.2b}$$

α_{i1} and α_{i3}, $i = 1, 2$, are the linear and nonlinear rotation coefficients introduced in chapters 9 and 10. Finally, the masses an inertias of pendulums 1 and 2, written m_1, m_2, I_1 and I_2, respectively, can be expressed as

$$\begin{aligned} m_1 &= \rho_1 w_1 \pi (r_{p1}^2 - (r_{p1} - e)^2), \quad I_1 = \frac{1}{2} m_1 (r_{p1}^2 + (r_{p1} + e)^2), \\ m_2 &= \rho_2 w_2 \pi r_{p1}^2 + 2\rho_2 w_{2a} \pi r_{p2a}^2, \quad I_2 = \frac{1}{2}\rho_2 w_2 \pi r_{p1}^4 + \rho_2 w_{2a} \pi r_{p2a}^4, \end{aligned} \tag{11.3}$$

where ρ_1 and ρ_2 are the density of the materials used for pendulums 1 and 2, respectively. In practice, the pendulums are slightly more complicated than perfect cylinders made of a single material (*cf.* Fig. 11.1). For instance, the real pendulums are equipped with plastic stoppers whose role it to prevent steel/steel friction and chocks. Friction and chocks are not desired but they are likely to occur when the system starts (the pendulums go from rest to their centrifugated position) and stops (the pendulums go back to their rest position). Chocks might also occur when the pendulums hit the end of their path. Even though the pendulums are not perfect cylinders made of a single material, using Eq. (11.3) with $\rho_1 = \rho_2 = \rho = 7800$ [kg/m^3] (this is the density of the steel used) provides values of masses and inertias close from the real ones. The parameters of the prototype are given in Tabs. 11.1, 11.2 and 11.3. Note that m_1 and m_2 were not computed from Eq. (11.3) (which yields values of 31.051 [g] and 174.141 [g], respectively), but were measured on the real system. However, the values used for I_1 and I_2 are those computed from Eq. (11.3) as they could not be measured and lead to good fittings between the model and the experiments (*cf.* section 11.2). With such parameters, the tuning orders of the CDPVA are $n_{p1} = 1.303$ and $n_{p2} = 8.101$.

μ	η_1	η_2	μ_2	ν_r	ν_2	α_{11}	α_{21}	α_{13}	α_{23}
0.323	1.988	9.700	5.496	5.994	0.403	-0.646	-0.478	0	0

Table 11.3: Dimensionless parameters of the CDPVA.

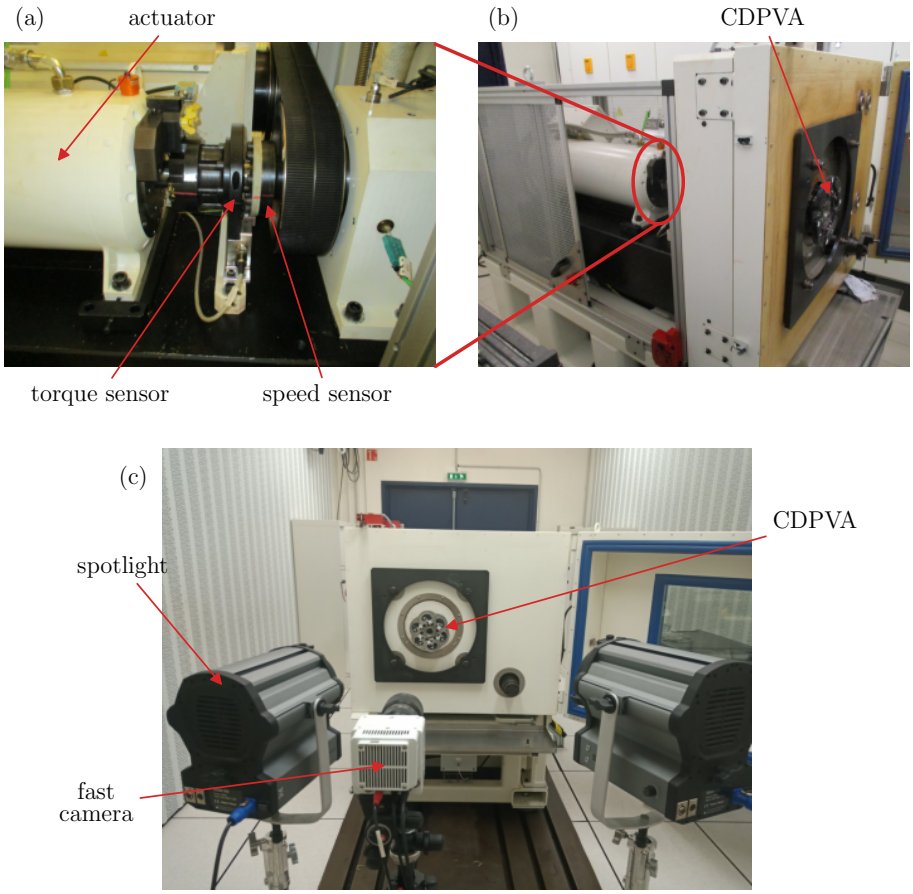

Figure 11.3: Experimental set-up. Note that the bench shown in (a) and (b) is not exactly the same as the one shown in (c). Still, both benches are designed in the same way.

11.1.2 Experimental set-up

The experimental set-up is shown in Fig. 11.3. The rotor is fixed on a bench of inertia $J_b = 8.5$ [g.m^2]. This value is deduced from the response of the bench in Fig. 11.6, using the fact that its angular acceleration $\ddot{\theta}_b$ must be $|\ddot{\theta}_b| = T_1/J_b$. As the rotor is fixed on the bench, J_r has to be replaced by the equivalent inertia $J_{eq} = J_r + J_b = 19.873$ [g.m^2] in the models developed in chapters 9 and 10. The experimental results include order sweeps, torque sweeps and fast camera videos. All the sweeps were done slowly for the response to be close from a succession of steady states. The amplitude of the

rotor was retrieved using a sliding discrete Fourier transform.

11.2 Experimental analysis

11.2.1 Expected results

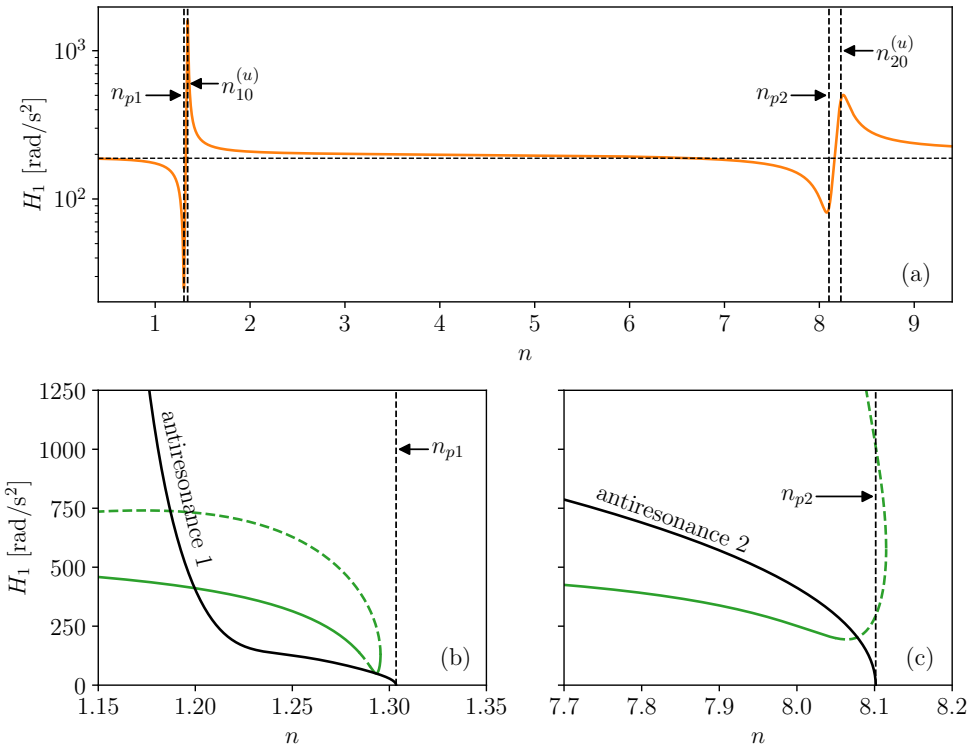

Figure 11.4: Linear response of the CDPVA (a) and nonlinear responses around the first (b) and second (c) antiresonances. In (b) and (c), the black line represents the evolution of the antiresonance with the torque and the dashed lines indicate unstable solutions. $\Omega = 1000$ [rpm] and the forcing level is $T_1 = 5$ [Nm] in (a) and $T_1 = 15$ [Nm] in (b) and (c). The damping is set to $b_1 = b_2 = 10$ [Nm.s].

Figure 11.4 shows the expected response of the rotor of the CDPVA investigated in this chapter. These results are obtained using the models developed in chapters 9 and 10. H_1 is the dimensional amplitude of the rotor's acceleration. Note that there is a small modification to take into account the large value of μ in the rotor's response computed from the nonlinear model. In chapter 9, μ was assumed to be small and the rotor's acceleration too, so the term $(1+\mu)\theta''$ in the rotor's equation was approximated by simply θ'' ($(\bullet)' = \partial(\bullet)/\partial\vartheta$ where ϑ is the rotor's angular position). However, in the present case, $\mu = 0.323$ so it is quite inaccurate to use $(1+\mu)\theta'' \approx \theta''$. To account for this, we simply redefine the amplitude of the first harmonic of the rotor's acceleration obtained in chapter 9 as $h_1 \leftarrow h_1/(1+\mu)$. With this new definition of h_1, we can define the dimensional amplitude $H_1 = h_1\Omega^2$.

As expected from section 11.1.1, the linear antiresonances shown in Fig. 11.4 are located at 1.3 and 8.1. One can see on the linear response that the first antiresonance is very close from the resonance. In addition, Fig. 11.4(b) shows that the first antiresonance and resonance bend to the left as the torque increases, so the resonance will actually pass through n_{p1}. This makes the first antiresonance poorly robust, but this issue was not considered during the tuning process. Indeed, the aim of this PhD is to design pendulums able to operate at high orders, so the second antiresonance is much more meaningful than the first one. This second antiresonance is more robust than the first one as it is further from the linear resonance and the response does not bend much to the left as the torque is increased (it does, but at larger amplitudes than that represented in (c)). However, this second antiresonance is less pronounced than the first one. The performance could have been increased using the linear performance indicators presented in chapter 9, but at the time of the specification of the prototype, there was an error in the model of the CDPVA, so the predictions were misleading.

The error was that the second pendulum was parametrised differently such that φ_2 was defined as $\boldsymbol{AG_1}.\boldsymbol{G_1G_2} = \cos\varphi_2$ (*cf.* Fig. 11.2), as in [125], instead of $-\boldsymbol{y_{p1}}.\boldsymbol{G_1G_2} = \cos\varphi_2$. These two parametrisations happen to be the same in the case of a first pendulum with the simple rotation law $\alpha_1(\varphi_1) = \varphi_1$, but not with more complex rotations, as is the case here. Note also that the parametrisation used in [125] can be used in the general case but then α_2 would be a function of both φ_1 and φ_2, which is not convenient. With the model containing the error, the CDPVA was expected to have antiresonances at 1.750 and 4.001. It might seem beneficial that the second antiresonance appears to be at approximately twice the expected one (it is at 8.101 instead of 4.001), as we aim at designing CDPVAs for high orders. However, this will come to be a difficulty as the experimental set-ups available at Valeo do not currently allow to investigate the response of pendulum devices at high orders. This is discussed further in the next section.

11.2.2 Overview of the response and bench-related issues

An overview of the measurements is presented in Fig. 11.5. This figure shows the amplitude of the first harmonic of the rotor's acceleration as a function of the order (on the left) and frequency (on the right). The response associated to several mean rotational velocities and torques is displayed. First, looking at Fig. 11.5(a), (c) and (d), one can see an antiresonance around $n = 1.3$, as expected from the model. A focus on this antiresonance is presented in section 11.2.3. Then, one can see an antiresonance in (a), (b), (c) and (d) at orders 5.6, 4.5, 3.7 and 3.1, respectively. Looking at (e)-(h), one can see that these antiresonances actually correspond to a single antiresonance fixed at 92 [Hz]. This was unexpected and is discussed further later in this section. From the model, it is expected to observe an antiresonance at $n = 8.1$ in (a)-(d). However, no such antiresonance is visible. Instead, there is an increase of the rotor's response around $n = 8$ in (a). One could think this is due to

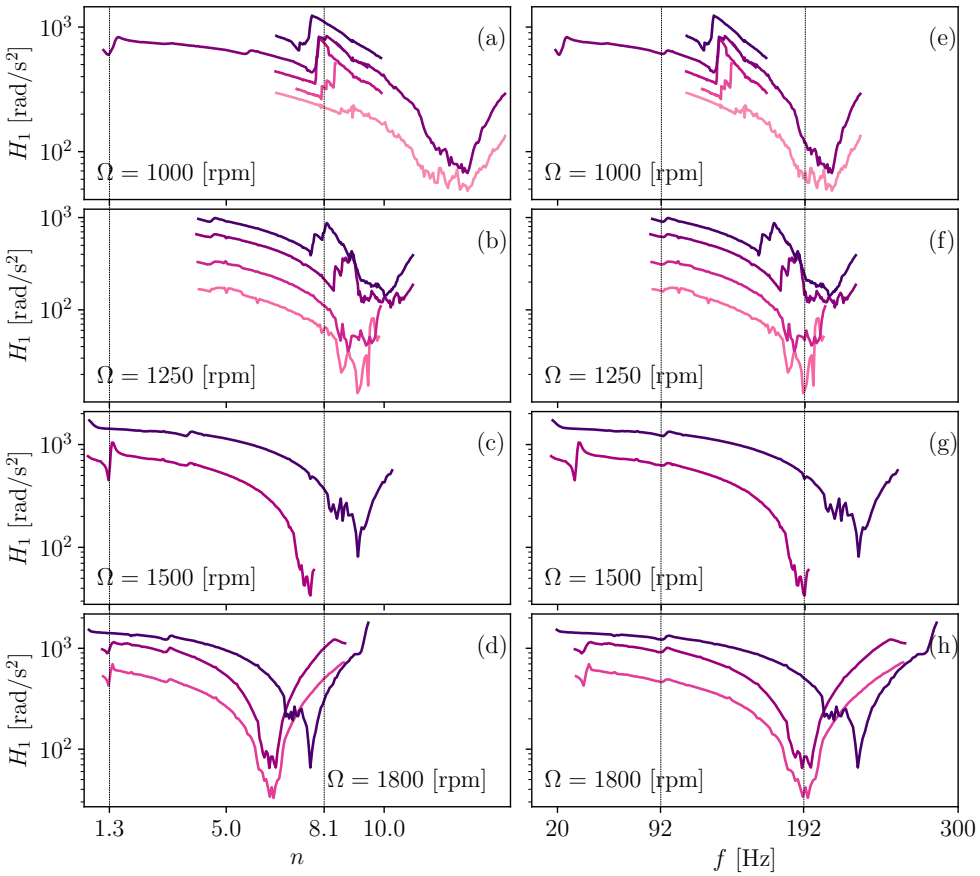

Figure 11.5: Overview of the measurements. The amplitude of the first harmonic of the rotor's acceleration is represented as a function of the order (a)-(d) and frequency (e)-(h), for different mean rotational velocities and for several torque levels. The darker the line the larger the associated torque level. $T_1 = \{10, 12, 15, 20, 30\}$ [Nm] in (a) and (e), $T_1 = \{5, 10, 20, 30\}$ [Nm] in (b) and (f), $T_1 = \{20, 30\}$ [Nm] in (c) and (g) and $T_1 = \{15, 30\}$ [Nm] in (d) and (h). The vertical lines in (a)-(d) indicate the expected location of the two antiresonances. The vertical lines in (e)-(h) indicate the location of two unexpected antiresonances fixed in frequency.

the pendulums responding on the resonance of mode 2 and thus amplifying the rotor's vibrations. However, fast camera videos showed that there was no swinging of the pendulums but an unexpected radial motion with a magnitude of about 1 [mm]. Finally, there is an extremely large antiresonance around orders 12, 9.2, 8 and 6.7 in (a), (b), (c) and (d), respectively. (e)-(h) indicate that this is again a single antiresonance located at 192 [Hz] and which appears to shift to the right as the amplitude increases. It seems that because of this antiresonance, the overall response of the rotor's acceleration is absolutely not flat. This very troublesome feature is discussed further below.

Figure 11.6 shows the response of the bench alone and the rotor without the pendulums as a

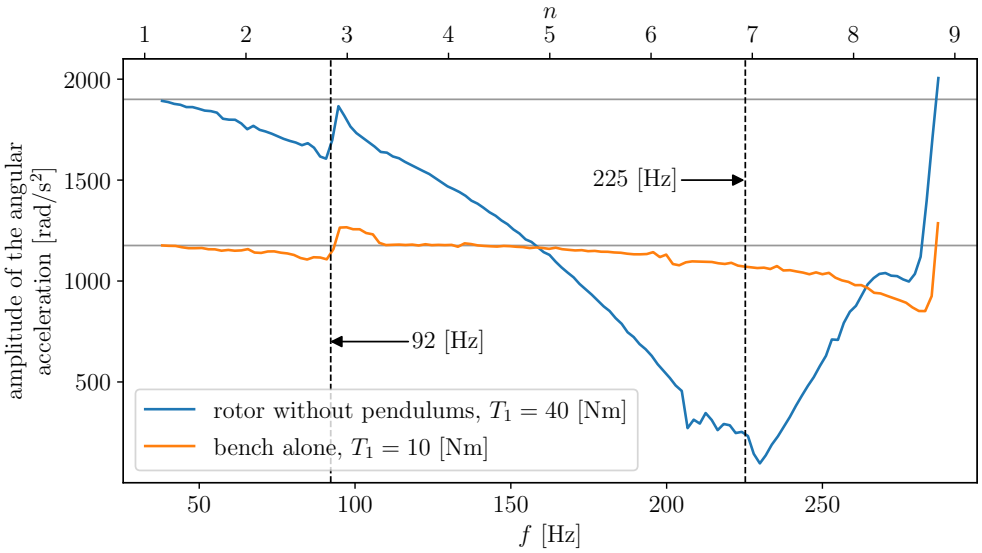

Figure 11.6: Amplitude of the angular acceleration of the bench alone (orange) and the rotor without the pendulums as a function of the frequency (bottom) and order (top). The rotational velocity is $\Omega = 1950$ [rpm]. The vertical dashed lines indicate the position of two antiresonances. The horizontal grey lines help assessing the flatness of the responses.

function of the frequency and order. There is an antiresonance at 92 [Hz], like in Fig. 11.5(e)-(h), even for the response of the bench alone. This means that this antiresonance is not related to the rotor nor the pendulums. Moreover, the fact that it does no shift with the addition of inertia (it remains at 92 [Hz] after adding the rotor and the pendulums) might indicate that it is related to the acquisition system of the bench. Apart from this antiresonance, the response of the bench is almost flat up to 200 [Hz], after which it starts decreasing. The addition of the rotor creates a large diminution in the response centred at 225 [Hz] but affecting all the frequency band. One can compute where this antiresonance would be centred after adding the pendulums' masses using

$$\sqrt{\frac{J_r + J_b}{J_r + J_b + N\left(I_1 + I_2 + m_1(r+\ell_1)^2 + m_2(r+\ell_1+\ell_2)^2\right)}} \times 225 = 192 \text{ [Hz]}. \tag{11.4}$$

This corresponds to what was observed in Fig. 11.5. Hence, this issue is not related to the pendulums but to the installation of the rotor on the bench. Note that because of this large antiresonance, there is no flat part in the rotor's response, even at low orders. This issue unfortunately prevented the visualisation of the second antiresonance. However, the response near the first antiresonance is discussed in the next section.

11.2.3 Focus on the first antiresonance

Figure 11.7 shows the rotor's response around the first antiresonance. A comparison with the linear model described in chapter 9 is proposed in (a) and shows a good fitting. Damping causes the

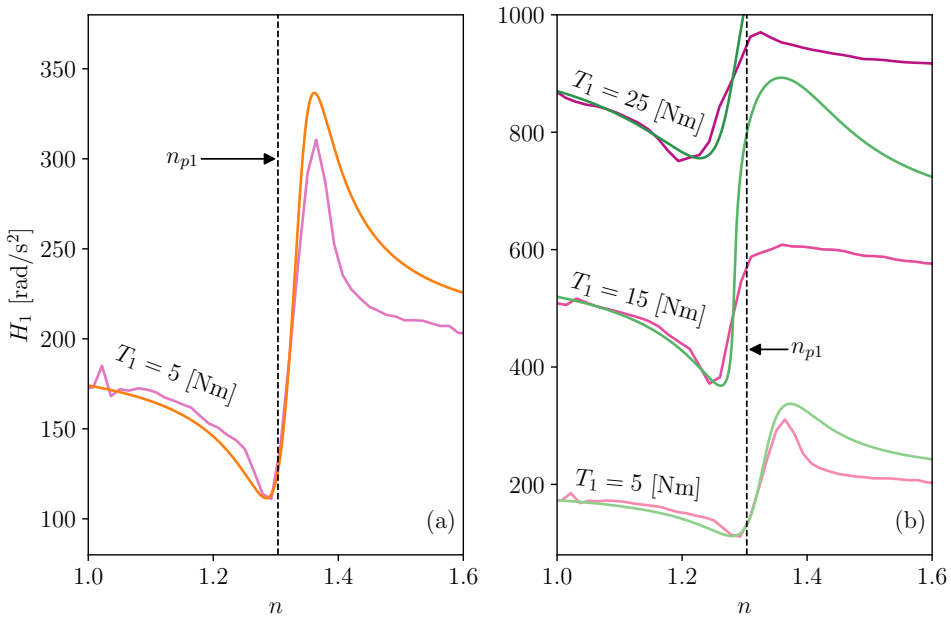

Figure 11.7: Rotor's response around the first antiresonance in the linear regime (a) and the nonlinear regime (b). The rotational velocity is $\Omega = 1000$ [rpm]. The dampings used in (a) are $b_1 = b_2 = 50$ [Nm.s] and the ones used in (b) are $b_1 = b_2 = \{70, 80, 150\}$ [Nm.s] for the responses at $T_1 = \{5, 15, 25\}$ [Nm], respectively.

antiresonance order to be slightly lower than n_{p1}. There is a small difference at the resonance. This is probably due to the fact that the order sweep was going slightly too fast so there are not enough points after using the sliding Fourier transforms to describe accurately the resonance. Another reason, which might also explain the difference after the resonance, is that the large antiresonance discussed in section 11.2.2 decreases the rotor's vibrations over the whole frequency band, even the part represented in Fig. 11.7. This decrease is more pronounced as the order increases, explaining why it has an effect after the antiresonance but not before.

The evolution of the antiresonance with larger torque levels is compared in (b) with the nonlinear analytical model proposed in chapter 9 (and using the small modification explained in section 11.2.1). The analytical model allows for a rather accurate description of the locus of the antiresonance. However, like in (a), the response after the antiresonance is strongly overestimated by the model. This difference gets larger as the torque amplitude is increased. The damping values necessary to fit the model with the experiments are significantly larger than expected and even increase as the torque amplitude increases. This large damping might be due to an imperfect rolling-without-slipping motion of the pendulums, causing friction. The slipping duration over one period increases as the pendulums amplitude increases, which could explain the increase of the damping with the forcing. A detailed

study of the occurrence of slipping was proposed in chapter 8 for a CPVA but is not carried out in the current chapter for a CDPVA.

11.2.4 Discussion on the experimental study

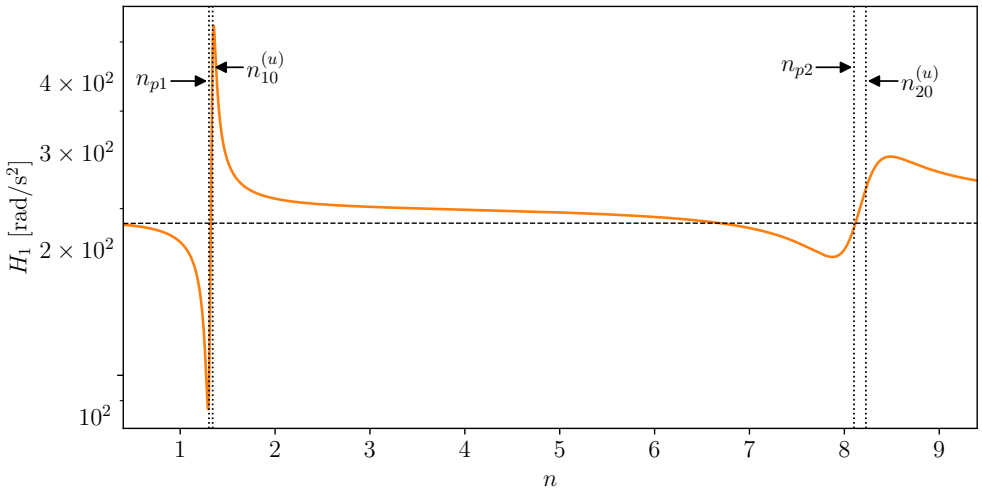

Figure 11.8: Rotor's linear response with the damping level identified from the measurements. The horizontal dashed black line represents the amplitude when the pendulums are fixed. $T_1 = 5$ [Nm], $\Omega = 1500$ [rpm] and $b_1 = b_2 = 50$ [Nm.s].

The linear response of the rotor is shown again in Fig. 11.8, but this time using the smallest damping values identified from section 11.2.3, that is, $b_1 = b_2 = 50$ [Nm.s]. With this large damping value, the performance at the second antiresonance is poor, and the actual antiresonance is significantly shifted compared to the conservative one. Though the damping values identified around mode 1 might not be exactly the same of those for mode 2, this seems to indicate that it is quite difficult to observe the second antiresonance with the current prototype. However, as explained in 11.2.2, this is not the only difficulty. Indeed, the bench used was not initially designed to investigate the dynamics of heavy pendulums systems at high order but to to test light CPVAs (i.e. with a rotor of inertia $J_r \approx 2$ [g.m^2]) at low orders (typically, $n = 1$ or $n = 2$). There is another bench available at Valeo which might be more suited for the current heavy prototype, but this is a work in progress. It could also be possible to design another CDPVA with a second antiresonance at lower orders (for instance $n_{p2} = 4$), which would facilitate the tests on the benches available. Moreover, the performance of this new prototype around its second antiresonance could be improved using the linear design tool introduced in chapter 9 and applied in the next section.

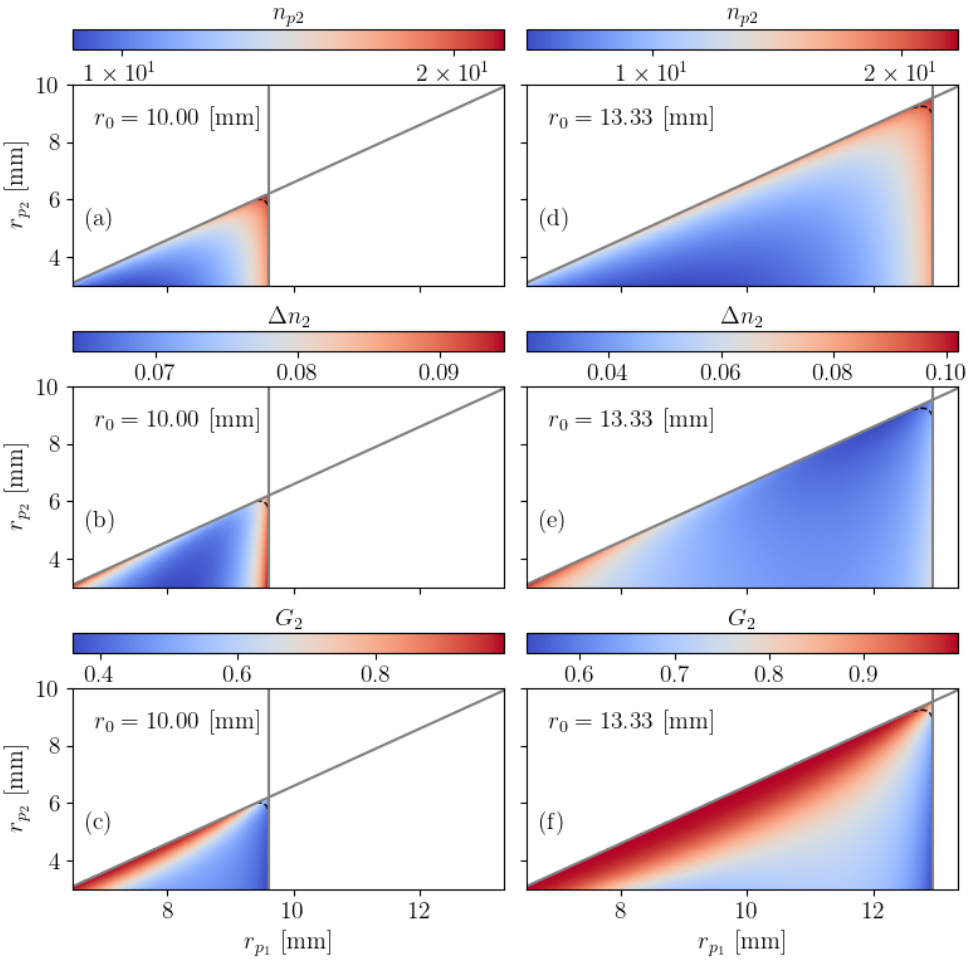

Figure 11.9: Evolution of the second antiresonance and the performance indicators Δn_2 and G_2 as a function of r_{p1} and r_{p2} for a small value of r_0 (left) and a larger one (right). The black dashed line in the maps indicate the designs for which $n_{p2} = 20$. The parameters used to create the maps are given in Tab. 11.4, except for r_{p1}, r_{p2} and r_0, which are varied. Moreover, the tolerance is set to $\delta = 0.4$ [mm].

11.3 High order tuning of centrifugal double pendulums

11.3.1 A design tool for centrifugal double pendulums with cylindrical pendulums

In order to facilitate the design process, design maps similar to those presented in chapter 9 are introduced. These maps are shown in Fig. 11.9 and indicate the value of the second antiresonance and the performance indicators Δn_2 and G_2 as a function of the pendulums' radii r_{p1} and r_{p2}. Δn_2 and G_2, described in details in chapter 9, represent the distance between the antiresonance and the resonance (a large distance is a sign of robustness to design imperfections) and the gain due to the use of the pendulums (a low gain indicates a large decrease of the rotor's vibrations), respectively.

N	r	r_0	r_{p1}	w_1	e	r_{p2}	w_2	r_{p2a}	w_{2a}
6	40	12.06	11.533	15	3	7.99	18	15	8

Table 11.4: Parameters of a CDPVA tuned to order 20 (all in [mm] except for N which is dimensionless).

The maps are represented for two values of r_0 (a low one on the left-hand side, a larger one on the right-hand side). First, notice the triangular shape of the maps. This is due to both r_{p1} and r_{p2} begin upper-bounded. Indeed, r_{p1} cannot exceed $r_0 - \delta$, where δ is a chosen tolerance. This sets the vertical grey lines in Fig. 11.9. Moreover, r_{p2} cannot exceed $r_{p1} - e - \delta$, which sets the oblique grey lines in the maps. Furthermore, notice that it is relevant to use r_{p1}, r_{p2} and r_0 as the main design parameters. Indeed, r can be quite limited due to design constraints. In the present case, it is set to $r = 40$ [mm] in order to obtain a CDPVA significantly smaller than the prototype presented previously in this chapter. w_1, w_2, w_{2a} and r_{p2a} only play a role in the masses and inertias of the pendulums, but not in their lengths. Hence, their effect is expected to be limited compared to r_{p1}, r_{p2} and r_0. The parameter left is e, which plays and important role as it contributes to the length of the second pendulum, but its variations are quite limited. Indeed, it cannot be decreased too much otherwise the physical resistance of pendulums 1 would be too small.

11.3.2 Presentation of a centrifugal double pendulum vibration absorber tuned to order 20

Now, let us focus on the most interesting designs visible in Fig. 11.9. The black dashed line visible in the top corner of the triangles indicates the designs with a tuning order $n_{p2} = 20$. This drastically limits the design options and imposes that both r_{p1} and r_{p2} be close from their limits. Looking at Δn_2 and G_2, it seems that performance is better for smaller r_0, which is beneficial as it advantages compact designs. The best performance is achieved along the vertical grey line. Those maps allowed to quickly converge towards the design presented in Fig. 11.10. It occupies a diameter of 114 [mm], which is relevant given the space requirement in the gearbox of an electric vehicle. Note that the room occupied is set by the rotor's radius, whose edge was chosen to be at a minimal distance of 5 [mm] from the rolling track for physical resistance purposes. Hence, the CDPVA's diameter is given by $2(r + r_0 + 5)$ [mm]. The inner diameter of the CDPVA might also be an important parameter. Like for the outer diameter, it can be estimated imposing a maximal internal radius $r - r_0 - 5$ [mm], which, in the present case, leads to an internal diameter of about 46 [mm].

The linear response of the CDPVA is shown in Fig. 11.11. Though the damping is significant (it is the one identified from Fig. 11.7(a)), the vibration reduction effect due to the second antiresonance

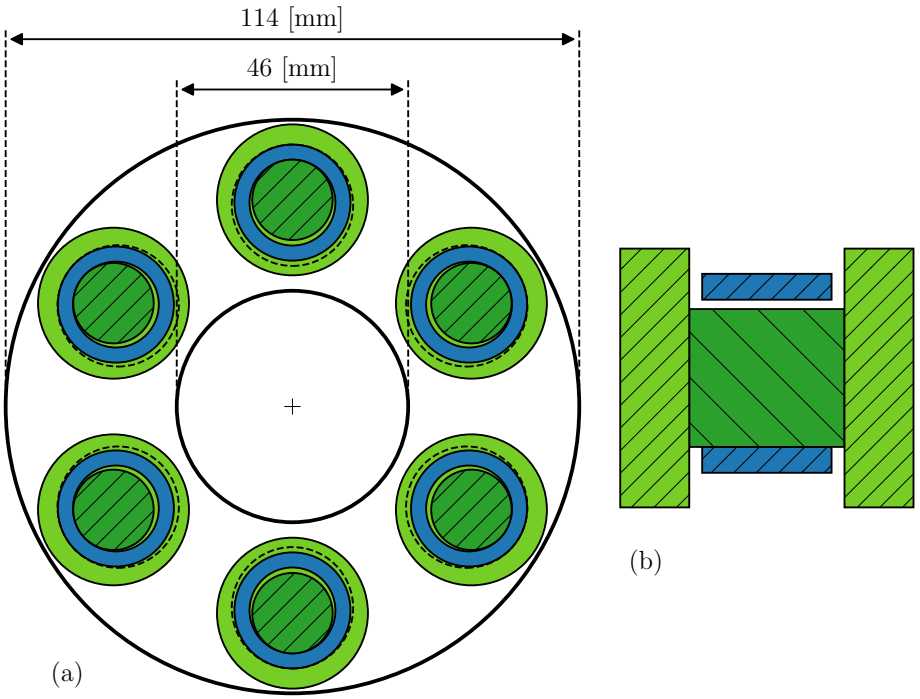

Figure 11.10: Global view of the CDPVA tuned to order 20 (a). Side view of a double pendulum (b). The parameters are given in Tab. 11.4.

is satisfying. However, one should be be careful about manufacturing tolerances. For instance, if e is 30 [µm] thinner than expected, the antiresonance and resonance go from 20.001 and 20.268 to 19.884 and 20.250. In that case, the rotor is no longer excited on his antiresonance but closer to its resonance, hence decreasing the filtering efficiency (there is still vibration reduction though). In practice, 30 [µm] would not correspond to the manufacturing tolerances (they are smaller than that), but rather to the order of magnitude of the summation of all the manufacturing errors. The effect of the manufacturing tolerances becomes even more important when considering the nonlinear behaviour of the system. Indeed, the CDPVA is a nonlinear system that requires nonlinear tuning in order to prevent the shifting of its antiresonance and the apparition of a localised response, as detailed in chapters 9 and 10. In those two chapters, it was proposed to control the nonlinear tuning through the nonlinear coefficients of the rotation laws, α_{13} and α_{23}. However, the design proposed in the current chapter necessarily leads to $\alpha_{13} = \alpha_{23} = 0$ (*cf.* section 11.1.1). Hence, one needs to find another way to deal with the nonlinear tuning. This could be done using a non-circular rolling-tracks in order to control the path of pendulums 1, like what is proposed in chapters 3 to 8 for CPVAs. However, this requires lower manufacturing tolerances, which might becomes too demanding. Another concern that was quickly addressed previously is the slipping of the pendulums. It was observed in chapter 8 that

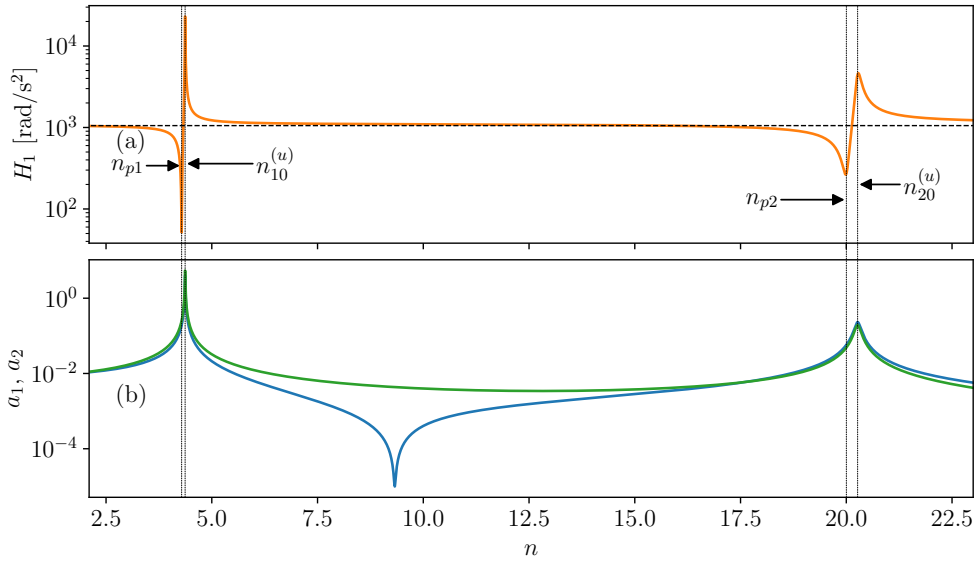

Figure 11.11: Rotor's and pendulums' linear responses for the CDPVA tuned to order 20 and with the damping level identified from the measurements. The horizontal dashed black line represents the amplitude when the pendulums are fixed. $T_1 = 5$ [Nm], $\Omega = 1500$ [rpm] and $b_1 = b_2 = 50$ [Nm.s]. The other parameters can be retrieved from Tab. 11.4 and Eq. (11.3) appart from $J_r = 8$ [g.m^2].

this reduces the torque capacity of a CPVA, and it is likely that the same issue exists for a CDPVA.

11.4 Conclusion

An original CDPVA architecture made of two cylinder-pendulums was introduced in this chapter. A prototype was build and tested on a measurement bench. The first antiresonance was well identified and matched well with both the linear and nonlinear models developed in the previous chapters. However, the comparison between the models and the experimental data was incomplete as it was not possible to observe the second antiresonance due to difficulties related to the bench. The identification of the first antiresonance allowed to estimate the damping to use in the models. This damping happened to be larger than expected, which lowers the performance of the CDPVA. Then, a design tool was presented and helped computing the dimensions of a compact CDPVA tuned on order 20. Though this CDPVA achieves satisfying linear performances, its robustness and the control of its nonlinear behaviour are a concern due to manufacturing tolerances. Further work is necessary to determine whether these limitations are acceptable or not. If so, the performance of other CDPVA designs, such as the one proposed by J.-G. Duh and M. Wenyong [123] (*cf.* Fig. 1.18), could be investigated.

Conclusion

Conclusion

With the aim of providing the best possible service to the car driver, the problems of noise, comfort, fuel consumption and vehicle reliability are currently the major concerns of the automotive industry. In thermal vehicles, the internal combustion engine is a major contributor to these problems because of the generation of torsional vibrations that are transmitted to the drivetrain components. This issue has been investigated for a long time but improvements and a better comprehension are still needed. In addition, due to increasingly stringent environmental standards concerning polluting emissions and fuel consumption of thermal vehicles, car manufacturers are more and more attracted towards electric vehicles. These are known to be more quiet than thermal vehicles, but sources of noise previously hidden by the engine's noise are a new disturbance that car manufacturers want to reduce to meet the demands of their customers. The most disturbing of these low-volume sources are the transmission errors that occur in the gearbox. They lead to fluctuations of the torque transmitted which generates vibrations of the drivetrain and causes the housing of the gearbox to radiate an irritating whining noise (*cf.* chapter 1). Several types of absorbers are available to reduce the torsional vibrations and the problems they generate. However, the most appropriate passive absorption mean seems to be the centrifugal pendulum vibration absorber (CPVA), which has been used in thermal powertrains for almost a century. The special feature of these pendulum absorbers is the linear dependence of their natural frequency to the engine speed, which allows them to reduce the vibrations over the whole speed range. However, the characteristics of the excitation signals in electric powertrains are significantly different from those of thermal ones, which requires an adaptation of the CPVAs currently used in the industry. To meet this objective and to improve the CPVAs currently used in thermal engines, two major axes of research were favoured:

- Increase the general knowledge on CPVAs with a particular focus on its current limitations and on original operation principles;

- Adapt pendulum absorbers to operate in electric powertrains through the proposition of original architectures.

The results from these two axes are summarised thereafter.

General knowledge on CPVAs

One of the objectives of the thesis was to increase the general knowledge on CPVAs in order to improve the ones currently used in thermal powertrains and to have a better understanding of some special operations and concepts that could prove useful in the adaptation of pendulum absorbers to electric powertrains.

Most studies on CPVAs consider only purely translated pendulums, but it was shown a few years ago that allowing a rotational mobility in addition to the traditional translation motion increases the performance. Hence, every study presented in this report took into account a rotation of the pendulums with respect to the rotor. It was shown in chapter 2 that this rotation acts like an added mass and modifies the linear coupling between the pendulums and the rotor of a CPVA. Moreover, it contributes to the nonlinear response in a way similar to the pendulums' path.

Chapters 3, 5 and 4 focused on the localisation phenomenon, which causes one or more pendulums to oscillate with a phase and/or amplitude different from the others. It is a known issue with CPVAs, not necessarily because it lowers the filtering efficiency but because it reduces the torque capacity. Two different models predicting the apparition of such instabilities of the unison response were proposed in chapters 3 and 4. The first model, validated experimentally, is accurate at low tuning orders so it useful in the case of CPVAs used in the frame of cylinder deactivation. The second model, more complex, is valid no matter the tuning order, so it is more general. In both cases, new design guidelines allowing to avoid instabilities were proposed. The localised response itself was analysed in chapter 5, where its dynamics were detailed. Interestingly, it was shown that in some cases localisation does not lower the torque capacity and enhances the filtering, so it can be beneficial to vibration reduction.

Epicycloidal paths are often used in the industry because they are the tautochronic paths of a pendulum in a uniform centrifugal acceleration field. However, in practice, the acceleration field varies because the rotor's angular speed fluctuates, so the epicycloid is no longer a tautochronic path (*cf.* chapter 4). In addition, assessing the shifting of the antiresonance as the torque level is increased is more relevant to performance evaluation than the tautochronic property. Indeed, if the antiresonance is locked, the rotor is always excited where its response is minimum, which maximises the vibration reduction. This shifting was investigated in details in chapter 4 where it was shown that the pendulums locking the antiresonance are those whose path and rotation nonlinearities balance with the nonlinearities related to the Coriolis effect. In such a configuration, the rotor's response is dominated

by higher harmonics because the amplitude of the first harmonic is very low. The accuracy of the antiresonance tracking developed in chapter 4 was verified experimentally in chapter 8. Furthermore, chapter 4 introduced a representation in the design space of the stability of CPVA designs and of the guidelines to avoid localisation and to lock the antiresonance. This design tool allowed to identify easily the designs that remain stable while achieving the best vibration reduction.

The CPVAs used in the industry are tuned close from the fundamental frequency of the engine torque. However, they could also be tuned at half the engine order, in which case the CPVA operation is subharmonic. This was investigated in details in chapters 6 and 7, where it was shown that the filtering of the rotor's vibrations is done through the torque generated by the Coriolis effect. The main advantages of the subharmonic operation are that the pendulums do not generate higher rotor harmonics and cause a saturation of the rotor's response. As in classical operation, the antiresonance can shift as the torque level increases, hence perturbing the saturation effect. Guidelines on the CPVA tuning were proposed to increase the torque capacity while limiting the drawbacks of the antiresonance shifting (*cf.* chapter 6). This was observed to achieve satisfying vibration reduction but the torque capacity is lower than that of CPVAs in classical operation. In addition, these guidelines are not compatible with a stable response if the CPVA is made of several pairs of pendulums (*cf.* chapter 7). In that case, other guidelines were provided to prevent the apparition of subharmonic localised solutions. The analytical models used in chapters 6 and 7 were validated experimentally in chapter 8.

Another major contribution of the thesis is the investigation of centrifugal double pendulum vibration absorbers (CDPVA), which make use of double pendulums instead of the simple pendulums used in CPVAs (*cf.* chapters 9 and 10). As the absorbers are now two degree-of-freedom systems, the rotor possesses two antiresonances. The tuning of a CDPVA depends on a lot more parameters than that of a CPVA, which is both an advantage and a drawback as it allows for more flexibility in the tuning but increases the complexity. This is why an efficient tuning process was proposed in chapter 9. It is based on the computation of the two tuning orders and the assessment of linear performance indicators. A nonlinear analytical model representing the unison response and its stability was developed in chapters 9 and 10. The experimental investigation of a CDPVA led in chapter 11 allowed to validate several features of this analytical model. This model allowed to derive design guidelines to lock one of the antiresonances (which maximises the performance around the associated tuning order) while avoiding the appearance of localised solutions. As for CPVAs, the guidelines and stability state were represented in the design space to identify easily the optimum CDPVA designs. The construction of the nonlinear analytical model was rendered possible thanks to the python code presented in Appendix F, which automatises the method of multiple scales.

Adaptation of pendulum absorbers to electric powertrains

The other objective of the thesis was to design pendulum absorber systems able to operate at high orders to reduce the vibrations of electric powertrains. The main difficulties to tackle are the demanding manufacturing tolerances necessary for an accurate high-order tuning and the small space available for a CPVA.

The subharmonic operation is particularly relevant for high-order tuning as it allows to divide by two the tuning order required. An original CPVA design made of spherical pendulums was presented in chapter 8. This simple design overcomes limitations of bifilar CPVAs that would be too detrimental at high frequencies. A prototype tuned at low order was build and experimental investigations showed its large attenuation capacity in classical operation and the saturation of the rotor's response in subharmonic operation. However, the performance was significantly limited by the shifting of the pendulums which reduces the torque capacity by about 50%. A CPVA tuned on order 10, hence filtering order 20 when in subharmonic operation, was presented in chapter 8. Unfortunately, the slipping of the pendulums and the too demanding manufacturing tolerances for the nonlinear tuning currently prevent the use of such a CPVA.

The use of a CDPVA can also help filtering high orders thanks to the flexibility of the tuning process. An original CDPVA design made of an h-shape cylinder rolling inside a hollow cylinder was presented in chapter 11. A prototype tuned at relatively low orders was build and experimental investigations showed the rotor's first antiresonance. Unfortunately, it was not possible to observe the second antiresonance, which is the most useful one, due to limitations of the experimental set-up. The damping values used to match the analytical model from chapters 9 and 10 with the measurements were larger than expected, which is detrimental to the efficiency of the CDPVA. A CDPVA with a second antiresonance at order 20 was proposed in chapter 11. The linear tuning appears feasible and sufficiently robust, but the current design still has limitations. Indeed, in order to control the nonlinear tuning of the CDPVA, the rolling tracks of the rotor should not be circular but have a more complex shape, which would require smaller manufacturing tolerances. These small tolerances and the possible slipping of the pendulums are a concern to the use of CDPVAs at high orders.

Perspectives

Though the thesis led to many interesting results, there is still work to be done. The main perspectives are listed below.

- In the analytical model developed in chapter 4, only quadratic and cubic nonlinear terms are

retained. However, the approach allows to consider higher-order nonlinear terms. Accounting for nonlinear terms of order 5 would prove useful to derive more accurate design guidelines.

- In chapter 7, it was observed that the period-doubling bifurcation leading to the subharmonic pendulums' response can take some time to occur. This is an issue as it delays the subharmonic filtering of the rotor's vibrations. Studies of the bifurcation time would be useful as they might provide guidelines to minimise this delay.
- It was suggested in previous studies that a two-harmonic torque could be filtered using a CPVA with pendulums tuned on two different orders. The few studies on the subject could be pursued by adapting the models developed in this thesis to a CPVA with pendulums tuned on two orders.
- In this thesis, several design rules optimising the intrinsic efficiency of a CPVA were derived. However, the optimal CPVA design might differ slightly when it is coupled to the driveline. The benefit of using the design rules on a CPVA installed in a driveline should be investigated in the future.
- The CDPVAs studied in this report have pendulums following circular paths so that their nonlinear tuning is controlled only through the pendulums' rotation. However, considering non-circular paths would provide another mean for nonlinear tuning, which could be more practical than using the nonlinear contribution of the rotation law. For instance, the use of non-circular paths is the only way to control the nonlinear tuning of the CDPVA design presented in chapter 11.
- A procedure based on linear considerations was presented in chapter 9 to quickly converge towards satisfying CDPVA parameters. Though this approach saves a lot of time in the designing process, it remains limited. The use of an optimisation algorithm would prove more efficient.
- The fast camera videos obtained from the experiments presented in chapter 11 have not yet been post-treated. Once this is done, the analysis of the pendulums' motion might provide a better understanding of the measurements and could help validating more features of the analytical model developed in chapters 9 and 10.
- The tests on the CDPVA prototype presented in chapter 11 were limited because of the set-up used. Using another test bench might provide more interesting results, in particular the observation of the rotor's second antiresonance.
- Several studies suggested that CDPVAs could be used to filter the fundamental and second harmonics of an exciting torque. However, results from chapter 9 showed that internal resonances might be problematic when trying to filter two orders simultaneously. The analysis of a CDPVA subjected to a torque made of two harmonics would indicate whether filtering orders n and $2n$ is possible or not.

- The slipping of the pendulums was seen to be a major limitation of the CPVA investigated in chapter 8, but was not analysed for the CDPVA presented in chapter 11. The slipping of these double pendulums must be studied to see whether it is problematic or not.
- The only CDPVA design investigated is the one presented in chapter 11. However, other designs should also be analysed as they might be more efficient. To begin with, one could study the CDPVA design shown in Fig. 1.18.
- It was shown in this report that subharmonic CPVAs and classical CDPVAs both allow to filter higher orders than classical CPVAs. It would be interesting the assess the subharmonic response of a CDPVA as it should rather easily allow for a high-order filtering. However, the performance of such a system is a concern as it would combine the drawbacks of both the subharmonic operation and the CDPVAs.
- It was explained in chapter 1 that centrifugated beams could be order-tuned. The limitations of these devices are not yet well understood and deserve more investigations.
- In this thesis, we focused only on passive absorbers, among which pendulum systems appeared to be the optimum devices. However, the semi-passive absorption means discussed in section 1.2.2 might be the best solution for reducing the torsional vibrations of an electric powertrain. These devices should receive more attention in the future.
- The python code presented in Appendix F proved extremely useful to solve the equations met during the thesis. Nevertheless, it deserves several improvements. First, it could be modified to be usable with nonlinear systems presenting internal resonances other than 1:1:...:1. Secondly, additional functions allowing for a stability analysis through the computation of the Jacobian could be included. The computation of the Jacobian is sometimes required to be done using Cartesian coordinates (*cf.* chapters 7 and 10). An automatic change from polar to Cartesian coordinates could be implemented in the code.

Bibliography

[1] U. Tietge, J. Dornoff, P. Mock, and S. Díaz, "CO2 emissions from new passenger cars in Europe: Car manufacturers' performance in 2021," p. 11, 2021.

[2] A. Renault, *Calcul et optimisation d'absorbeurs pendulaires dans une chaîne de traction automobile [Simulation and optimisation of pendular absorbers for automotive powertrain]*. PhD thesis, ENSAM, Lille, France, 2018.

[3] J. Ligier and E. Baron, *Acyclismes et Vibrations*. Editions Technip, 2002.

[4] E. Rigaud, *Interactions dynamiques entre denture, lignes d'arbres, roulements et carter dans les transmissions par engrenages*. PhD thesis, Ecole Centrale de Lyon, Lyon, 1998.

[5] E. Abboud, *Simulation, Mastering and Reduction of Vibration Noises in Electric Car Gearbox Transmission Systems*. PhD thesis, ENSAM, Lille, 2022.

[6] E. Abboud, A. Grolet, H. Mahé, and O. Thomas, "Computation of dynamic transmission error for gear transmission systems using modal decomposition and Fourier series," *Forschung im Ingenieurwesen*, Nov. 2021.

[7] E. Abboud, A. Grolet, H. Mahé, and O. Thomas, "On the combination of multiple harmonics in direct and parametric forcing of an oscillator: New results on parametric amplification," *Meccanica*.

[8] D. Mohanraj, J. Gopalakrishnan, B. Chokkalingam, and L. Mihet-Popa, "Critical Aspects of Electric Motor Drive Controllers and Mitigation of Torque Ripple—Review," *IEEE Access*, vol. 10, pp. 73635–73674, 2022.

[9] M. O. Hamiti, *Réduction des ondulations de couple d'une machine synchrone à réluctance variable*. PhD thesis, Université de Lorraine, Nancy, 2009.

[10] H. Wu, D. Depernet, and V. Lanfranchi, "Comparison of Torque Ripple Reductions and Copper Losses of Three Synchronous Reluctance Machines," in *2017 IEEE Vehicle Power and Propulsion Conference (VPPC)*, (Belfort), pp. 1–6, IEEE, Dec. 2017.

[11] M. A. H. RASID, *Contribution to Multi-Physical Studies of Small Synchronous-Reluctance Machine for Automotive Equipment*. PhD thesis, Université Technologique de Compiègne, Compiègne, 2016.

[12] N. Bianchi, E. Fornasiero, M. Ferrari, and M. Castiello, "Experimental Comparison of PM Assisted Synchronous Reluctance Motors," in *Energy Conversion Congress and Exposition (ECCE)*, (Pittsburgh, USA), p. 8, 2014.

[13] M. Özsoy, O. Kaplan, and M. Akar, "The effect of stator slot number and pole number on motor performance in double-sided axial flux induction motors for electric vehicles," *Electrical Engineering*, Aug. 2022.

[14] H. Wu, D. Depernet, V. Lanfranchi, K. E. K. Benkara, and M. A. H. Rasid, "A Novel and Simple Torque Ripple Minimization Method of Synchronous Reluctance Machine Based on Torque Function Method," *IEEE Transactions on Industrial Electronics*, vol. 68, pp. 92–102, Jan. 2021.

[15] S.-M. Nina, *A Transmission-Error-Based Gear Dynamic Model – Applications to Single- and Multi-Mesh Transmissions*. PhD thesis, INSA, Lyon, 2016.

[16] H. Frahm, "Device for damping vibrations of bodies," 1911.

[17] M. Auleley, O. Thomas, C. Giraud-Audine, and H. Mahé, "Enhancement of a dynamic vibration absorber by means of an electromagnetic shunt," *Journal of Intelligent Material Systems and Structures*, vol. 32, pp. 331–354, Feb. 2021.

[18] K. Jaboviste, E. Sadoulet-Reboul, O. Sauvage, and G. Chevallier, "A Framework for the Design of Rotating Multiple Tuned Mass Damper," in *Conference and Exposition on Structural Dynamics*, (Houston (USA)), pp. 393–397, 2020.

[19] E. Gourdon, N. Alexander, C. Taylor, C. Lamarque, and S. Pernot, "Nonlinear energy pumping under transient forcing with strongly nonlinear coupling: Theoretical and experimental results," *Journal of Sound and Vibration*, vol. 300, pp. 522–551, Mar. 2007.

[20] T. M. Silva, M. A. Clementino, C. De Marqui, and A. Erturk, "An experimentally validated piezoelectric nonlinear energy sink for wideband vibration attenuation," *Journal of Sound and Vibration*, vol. 437, pp. 68–78, Dec. 2018.

[21] E. Matta, "Seismic effectiveness and robustness of tuned mass dampers versus nonlinear energy sinks in a lifecycle cost perspective," *Bulletin of Earthquake Engineering*, vol. 19, pp. 513–551, Jan. 2021.

[22] K.-C. Chuang, Z.-W. Yuan, Y. Guo, and X.-F. Lv, "Extracting torsional band gaps and transient waves in phononic crystal beams: Method and validation," *Journal of Sound and Vibration*, vol. 467, p. 115004, Feb. 2020.

[23] S. S. Rao, *Vibration of Continuous Systems*. Hoboken, N.J: Wiley, 2007.

[24] O. Thomas, A. Sénéchal, and J.-F. Deü, "Hardening/softening behavior and reduced order modeling of nonlinear vibrations of rotating cantilever beams," *Nonlinear Dynamics*, vol. 86, pp. 1293–1318, Oct. 2016.

[25] P. P. Valentini, M. Cirelli, and S. Di Donato, "The compliant centrifugal pendulum as the vibration absorber with second-order elasto-kinematic approximation," *Journal of Vibration and Control*, vol. 27, pp. 1370–1381, June 2021.

[26] L. H. Jones, "The transverse vibration of a rotating beam with tip mass: The method of integral equations," *Quarterly of Applied Mathematics*, vol. 33, pp. 193–203, Oct. 1975.

[27] S. Hoa, "Vibration of a rotating beam with tip mass," *Journal of Sound and Vibration*, vol. 67, pp. 369–381, Dec. 1979.

[28] H. H. Yoo, S. Seo, and K. Huh, "The effect of a concentrated mass on the modal characteristics of a rotating cantilever beam," *Proceedings of the Institution of Mechanical Engineers, Part C: Journal of Mechanical Engineering Science*, vol. 216, pp. 151–163, Feb. 2002.

[29] M. Auleley, C. Giraud-Audine, H. Mahé, and O. Thomas, "Tunable electromagnetic resonant shunt using pulse-width modulation," *Journal of Sound and Vibration*, vol. 500, p. 116018, May 2021.

[30] M. Auleley, *Conception et calcul d'amortisseurs vibratoires semi-actifs pour groupe moto-propulseur automobile*. PhD thesis, ENSAM, Lille, 2020.

[31] G. Paillot, *Amortisseur Hybride Embarqué Pour La Réduction Des Vibrations de Torsion et de l'acyclisme Des Vilebrequins [Hybrid Embedded Damper for the Mitigation of Torsional Vibrations and Rotational Irregularities]*. PhD thesis, INSA, Lyon, 2022.

[32] G. Paillot, E. Besnier, S. Chesné, and D. Rémond, "Experimental validation of a new hybrid self-supplied crankshaft torsional vibrations damper," *Mechanical Systems and Signal Processing*, vol. 182, p. 109560, Jan. 2023.

[33] G. Paillot, S. Chesné, and D. Rémond, "Hybrid coupled damper for the mitigation of torsional vibrations and rotational irregularities in an automotive crankshaft: Concept and design subtleties," *Mechanics Based Design of Structures and Machines*, pp. 1–18, May 2021.

[34] B. J. Vidmar, S. W. Shaw, B. F. Feeny, and B. K. Geist, "Nonlinear Interactions in Systems of Multiple Order Centrifugal Pendulum Vibration Absorbers," *Journal of Vibration and Acoustics*, vol. 135, Dec. 2013.

[35] B. J. Vidmar, *Analysis and Design of Multiple Order Centrifugal Pendulum Vibration Absorbers*. PhD thesis, American Society of Mechanical Engineers, Chicago, Illinois, USA, Aug. 2012.

[36] B. Gunston, *World Encyclopedia of Aero Engines - From the Pioneers to the Present Day*. Sutton publishing, fifth ed., 2006.

[37] B. C. Carter, "Improvements in or relating to damping of oscillation-checking devices," 1929. 337 466.

[38] R. R. R. Sarazin, "Means adapted to reduce the torsional oscillations of crankshafts," 1931. 2 079 226.

[39] R. Chilton, "Pendulum counterweight," 1935. 2 112 984.

[40] M. A. Wachs, "The Main Rotor Bifilar Absorber and Its Effect on Helicopter Reliability/Maintainability," in *National Aerospace Engineering and Manufacturing Meeting*, p. 730894, Feb. 1973.

[41] M.-N. H. Hamouda and G. A. Pierce, "Helicopter Vibration Suppression Using Simple Pendulum Absorbers on the Rotor Blade," *Journal of the American Helicopter Society*, vol. 29, pp. 19–29, July 1984.

[42] H. H. Denman, "Tautochronic bifilar pendulum torsion absorbers for reciprocating engines," *Journal of Sound and Vibration*, vol. 159, no. 2, pp. 251–277, 1992.

[43] R. Chilton, "Rocking dynamic damper," 1939. 2184734.

[44] R. W. Zdanowich and T. S. Wilson, "The elements of pendulum dampers," *Proceedings of the Institution of Mechanical Engineers*, vol. 143, pp. 182–210, June 1940.

[45] L. J. Stone, "Improvements in or relating to vibration-damping devices," 1945. 598 811.

[46] "Les amortisseurs dynamiques de vibrations [Dynamic vibration dampers]," *Revue technique Hispano Suiza*, no. 3, 1939.

[47] J. Mayet and H. Ulbrich, "Tautochronic centrifugal pendulum vibration absorbers: General design and analysis," *Journal of Sound and Vibration*, vol. 333, pp. 711–729, Feb. 2014.

[48] J. A. C. Mayet, *Centrifugal Vibration Absorbers: Theory and Application*. PhD thesis, Technische Universität München, München, 2015.

[49] H. Mahé, A. Renault, and O. Thomas, "Dispositif d'amortissement pendulaire [Pendular damping device]," 2018. FR 3 055 038.

[50] H. Mahé, A. Renault, and O. Thomas, "Dispositif d'amortissement pendulaire [Pendular damping device]," 2018. FR 3 055 037.

[51] T. Krause, E. Kremer, and P. Movlazada, "Theory and simulation of centrifugal pendulum absorber with trapezoidal suspension," in *10th International Conference on Vibration Problems*, (Liberec), 2011.

[52] M. Cirelli, J. Gregori, P. Valentini, and E. Pennestrí, "A design chart approach for the tuning of parallel and trapezoidal bifilar centrifugal pendulum," *Mechanism and Machine Theory*, vol. 140, pp. 711–729, Oct. 2019.

[53] E. S. Taylor, "Crankshaft torsional vibration in radial aircraft engines," *S.A.E. JOURNAL*, vol. 38, no. 3, p. 9, 1936.

[54] R. R. Stephenson and E. W. Gaylord, "Natural frequency of the compound centrifugal pendulum," *Applied Scientific Research*, vol. 10, pp. 180–184, Jan. 1961.

[55] W. F. Paul, "Vibration damped helicopter rotor," 1970. 3 540 809.

[56] J. F. Madden, "Constant frequency bifilar vibration absorber," 1980. 4 218 187.

[57] A. R. S. Bramwell, G. Done, and D. Balmford, *Helicopter Dynamics*. Butterworth Heinemann, second ed., 2001.

[58] D. L. Cronin, "Shake reduction in an automobile engine by means of crankshaft-mounted pendulums," *Mechanism and Machine Theory*, vol. 27, pp. 517–533, Sept. 1992.

[59] M. Albright, T. Crawford, and F. Speckhart, "Dynamic Testing and Evaluation of the Torsional Vibration Absorber," in *SAE Technical Paper 942519*, p. 8, SAE International, 1994.

[60] Y. Ishida, T. Inoue, T. Fukami, and M. Ueda, "Torsional Vibration Suppression by Roller Type Centrifugal Vibration Absorbers," *Journal of Vibration and Acoustics*, vol. 131, p. 051012, Oct. 2009.

[61] K. Kadoi, T. Inoue, J. Kawano, and M. Kondo, "Nonlinear analysis of a torsional vibration of a multidegrees-of-freedom system with centrifugal pendulum vibration absorbers and its suppression," *Journal of Vibration and Acoustics*, vol. 140, p. 061008, Dec. 2018.

[62] D. E. Newland, "Nonlinear Aspects of the Performance of Centrifugal Pendulum Vibration Absorbers," *Journal of Engineering for Industry*, vol. 86, pp. 257–263, Aug. 1964.

[63] D. E. Newland, "Nonlinear problems of centrifugal pendulum vibration absorbers," in *Mechanisms and Machines*, vol. 1, (Varna (Bulgaria)), pp. 39–62, 1965.

[64] C. Huygens, *Horologium Oscillatorium Sive de Motu Pendulorum Ad Horologia Aptato. Demostrationes Geometricae.* 1673.

[65] A. Alsuwaiyan and S. W. Shaw, "Performance and dynamic stability of general-path centrifugal pendulum vibration absorbers," *Journal of Sound and Vibration*, vol. 252, pp. 791–815, May 2002.

[66] S. W. Shaw and B. Geist, "Tuning for Performance and Stability in Systems of Nearly Tautochronic Torsional Vibration Absorbers," *Journal of Vibration and Acoustics*, vol. 132, no. 4, 2010.

[67] V. Mahé, A. Renault, A. Grolet, H. Mahé, and O. Thomas, "On the dynamic stability and efficiency of centrifugal pendulum vibration absorbers with rotating pendulums," *Journal of Sound and Vibration*, vol. 536, p. 117157, Oct. 2022.

[68] J. Mayet and H. Ulbrich, "First-order optimal linear and nonlinear detuning of centrifugal pendulum vibration absorbers," *Journal of Sound and Vibration*, vol. 335, pp. 34–54, Jan. 2015.

[69] M. Cirelli, M. Cera, E. Pennestrì, and P. P. Valentini, "Nonlinear design analysis of centrifugal pendulum vibration absorbers: An intrinsic geometry-based framework," *Nonlinear Dynamics*, vol. 102, pp. 1297–1318, Nov. 2020.

[70] R. G. Mitchiner and R. G. Leonard, "Centrifugal Pendulum Vibration Absorbers—Theory and Practice," *Journal of Vibration and Acoustics*, vol. 113, pp. 503–507, Oct. 1991.

[71] M. A. Acar, *Design and Tuning of Centrifugal Pendulum Vibration Absorbers.* PhD thesis, Michigan State University, Michigan, 2017.

[72] M. Cera, M. Cirelli, E. Pennestrì, and P. P. Valentini, "Design analysis of torsichrone centrifugal pendulum vibration absorbers," *Nonlinear Dynamics*, vol. 104, pp. 1023–1041, Apr. 2021.

[73] X. Tan, S. Yang, J. Yang, and J. Li, "Study of dynamics of rotational centrifugal pendulum vibration absorbers based on tautochronic design," *Meccanica*, 2021.

[74] J. Mayet, M. A. Acar, and S. W. Shaw, "Effective and robust rocking centrifugal pendulum vibration absorbers," *Journal of Sound and Vibration*, vol. 527, p. 116821, June 2022.

[75] V. Mahe, A. Renault, A. Grolet, H. Mahe, and O. Thomas, "Subharmonic centrifugal pendulum vibration absorbers allowing a rotational mobility," *Mechanical Systems and Signal Processing*, vol. 177, p. 109125, Sept. 2022.

[76] V. Mahe, A. Renault, A. Grolet, O. Thomas, and H. Mahe, "Dynamic stability of centrifugal pendulum vibration absorbers allowing a rotational mobility," *Journal of Sound and Vibration*, vol. 517, p. 116525, Jan. 2022.

[77] E. Sarrouy, A. Grolet, and F. Thouverez, "Global and bifurcation analysis of a structure with cyclic symmetry," *International Journal of Non-Linear Mechanics*, vol. 46, pp. 727–737, June 2011.

[78] A. Grolet and F. Thouverez, "Free and forced vibration analysis of a nonlinear system with cyclic symmetry: Application to a simplified model," *Journal of Sound and Vibration*, vol. 331, pp. 2911–2928, June 2012.

[79] F. Fontanela, A. Grolet, L. Salles, and N. Hoffmann, "Computation of quasi-periodic localised vibrations in nonlinear cyclic and symmetric structures using harmonic balance methods," *Journal of Sound and Vibration*, vol. 438, pp. 54–65, Jan. 2019.

[80] A. Alsuwaiyan and S. Shaw, "Localisation of free vibration modes in systems of nearly identical vibration absorbers," *Journal of Sound and Vibration*, vol. 228, no. 3, pp. 703–711, 1999.

[81] A. S. Alsuwaiyan and S. W. Shaw, "Steady-State Responses in Systems of Nearly-Identical Torsional Vibration Absorbers," *Journal of Vibration and Acoustics*, vol. 125, pp. 80–87, Jan. 2003.

[82] B. Sarikaya and M. Inalpolat, "Response Sensitivity of Centrifugal Pendulum Vibration Absorbers to Symmetry-Breaking Absorber Imperfections," *Journal of Sound and Vibration*, p. 117037, May 2022.

[83] C.-P. Chao, C.-T. Lee, and S. Shaw, "Non-unisson dynamics of multiple centrifugal pendulum vibration absorbers," *Journal of Sound and Vibration*, vol. 204, pp. 769–794, July 1997.

[84] C.-P. Chao, S. W. Shaw, and C.-T. Lee, "Stability of the Unison Response for a Rotating System With Multiple Tautochronic Pendulum Vibration Absorbers," *Journal of Applied Mechanics*, vol. 64, pp. 149–156, Mar. 1997.

[85] A. S. Alsuwaiyan and S. W. Shaw, "Non-synchronous and Localized Responses of Systems of Identical Centrifugal Pendulum Vibration Absorbers," *Arabian Journal for Science and Engineering*, vol. 39, no. 12, pp. 9205–9217, 2014.

[86] J. S. Issa and S. W. Shaw, "Synchronous and non-synchronous responses of systems with multiple identical nonlinear vibration absorbers," *Journal of Sound and Vibration*, vol. 348, pp. 105–125, July 2015.

[87] A. Grolet, A. Renault, and O. Thomas, "Energy Localisation in Periodic Structures: Application to Centrifugal Pendulum Vibration Absorber," in *International Symposium on Transport Phenomena and Dynamics of Rotating Machinery*, (Maui (Hawaii)), 2017.

[88] K. Nishimura, T. Ikeda, and Y. Harata, "Localization phenomena in torsional rotating shaft systems with multiple centrifugal pendulum vibration absorbers," *Nonlinear Dynamics*, vol. 83, pp. 1705–1726, Feb. 2016.

[89] T. M. Nester, A. G. Haddow, and S. W. Shaw, "Experimental Investigation of a System With Multiple Nearly Identical Centrifugal Pendulum Vibration Absorbers," in *Volume 5: 19th Biennial Conference on Mechanical Vibration and Noise, Parts A, B, and C*, (Chicago, Illinois, USA), pp. 913–921, ASMEDC, Jan. 2003.

[90] T. M. Nester, P. M. Schmitz, A. G. Haddow, and S. W. Shaw, "Experimental observations of centrifugal pendulum vibration absorbers," in *International Symposium on Transport Phenomena and Dynamics of Rotating Machinery*, (Honolulu (Hawaii)), 2004.

[91] S. W. Shaw, P. M. Schmitz, and A. G. Haddow, "Tautochronic Vibration Absorbers for Rotating Systems," *Journal of Computational and Nonlinear Dynamics*, vol. 1, pp. 283–293, Oct. 2006.

[92] C.-T. Lee and S. W. Shaw, "Torsional vibration reduction in internal combustion engines using centrifugal pendulums," tech. rep., 1995.

[93] C.-T. Lee and S. W. Shaw, "On the counteraction of periodic torques for rotating systems using centrifugally driven vibration absorbers," *Journal of Sound and Vibration*, vol. 191, no. 5, pp. 695–719, 1996.

[94] S. W. Shaw and C.-T. Lee, "Half-order centrifugal pendulum vibration absorber system," 1996. 5 495 924.

[95] C.-T. Lee and S. W. Shaw, "The non-linear dynamic response of paired centrifugal pendulum vibration absorbers," *Journal of Sound and Vibration*, vol. 203, pp. 731–743, June 1997.

[96] C.-T. Lee, S. W. Shaw, and V. T. Coppola, "A Subharmonic Vibration Absorber for Rotating Machinery," *Journal of Vibration and Acoustics*, vol. 119, no. 4, pp. 590–595, 1997.

[97] C.-P. Chao and S. W. Shaw, "The effects of imperfections on the performance of the subharmonic vibration absorber system," *Journal of Sound and Vibration*, vol. 215, pp. 1065–1099, Sept. 1998.

[98] C.-P. Chao and S. W. Shaw, "The dynamic response of multiple pairs of subharmonic torsional vibration absorbers," *Journal of Sound and Vibration*, vol. 231, pp. 411–431, Mar. 2000.

[99] A. Wedin, *Reduction of Vibrations in Engines Using Centrifugal Pendulum Vibration Absorbers*. PhD thesis, 2011.

[100] O. A. Bauchau, J. Rodriguez, and S.-Y. Chen, "Modeling the Bifilar Pendulum Using Nonlinear, Flexible Multibody Dynamics," *Journal of the American Helicopter Society*, vol. 48, pp. 53–62, Jan. 2003.

[101] R. J. Monroe, S. W. Shaw, A. H. Haddow, and B. K. Geist, "Accounting for Roller Dynamics in the Design of Bifilar Torsional Vibration Absorbers," *Journal of Vibration and Acoustics*, vol. 133, Dec. 2011.

[102] B. Geist, V. Ramakrishnan, P. Attibele, and W. Resh, "Precision requirements for the bifilar hinge slots of a centrifugal pendulum vibration absorber," *Precision Engineering*, vol. 52, pp. 1–14, Apr. 2018.

[103] M. Cera, M. Cirelli, E. Pennestrì, and P. Valentini, "The kinematics of curved profiles mating with a caged idle roller - higher-path curvature analysis," *Mechanism and Machine Theory*, vol. 164, p. 104414, Oct. 2021.

[104] E. R. Gomez, I. L. Arteaga, and L. Kari, "Normal-force dependant friction in centrifugal pendulum vibration absorbers: Simulation and experimental investigations," *Journal of Sound and Vibration*, vol. 492, p. 115815, Feb. 2021.

[105] L. Chen, J. Yuan, H. Cai, and J. Hu, "Dynamic Model and Dynamic Response of Automobile Dual-Mass Flywheel with Bifilar-Type Centrifugal Pendulum Vibration Absorber," *Shock and Vibration*, vol. 2021, pp. 1–26, May 2021.

[106] M. Cera, M. Cirelli, E. Pennestrì, and P. Valentini, "Design and comparison of centrifugal dampers modern architectures: The influence of roller kinematics on tuning conditions and absorbers nonlinear dynamics," *Mechanism and Machine Theory*, vol. 174, p. 104876, Aug. 2022.

[107] E. R. Gomez, J. Sjöstrand, L. Kari, and I. L. Arteaga, "Torsional vibrations in heavy-truck powertrains with flywheel attached centrifugal pendulum vibration absorbers," *Mechanism and Machine Theory*, vol. 167, p. 104547, Jan. 2022.

[108] E. R. Gomez, L. Kari, and I. L. Arteaga, "Powertrain shuffle-mode resonance suppression by means of flywheel mounted torsichrone centrifugal pendulum vibration absorbers," *Journal of Sound and Vibration*, vol. 534, p. 117014, Sept. 2022.

[109] M. Pfabe and C. Woernle, "Reduction of Periodic Torsional Vibration using Centrifugal Pendulum Vibration Absorbers," *PAMM*, vol. 9, pp. 285–286, Dec. 2009.

[110] M. Sharif-Bakhtiar and S. Shaw, "The dynamic response of a centrifugal pendulum vibration absorber with motion-limiting stops," *Journal of Sound and Vibration*, vol. 126, pp. 221–235, Oct. 1988.

[111] S. W. Shaw and S. Wiggins, "Chaotic Motions of a Torsional Vibration Absorber," *Journal of Applied Mechanics*, vol. 55, pp. 952–958, Dec. 1988.

[112] M. Sharif-Bakhtiar and S. W. Shaw, "Effects of Nonlinearities and Damping on the Dynamic Response of a Centrifugal Pendulum Vibration Absorber," *Journal of Vibration and Acoustics*, vol. 114, no. 3, pp. 305–311, 1992.

[113] C. Shi and R. G. Parker, "Vibration Modes and Natural Frequency Veering in Three-Dimensional, Cyclically Symmetric Centrifugal Pendulum Vibration Absorber Systems," *Journal of Vibration and Acoustics*, vol. 136, p. 011014, Feb. 2014.

[114] C. Shi, S. W. Shaw, and R. G. Parker, "Vibration reduction in a tilting rotor using centrifugal pendulum vibration absorbers," *Journal of Sound and Vibration*, vol. 385, pp. 55–68, Dec. 2016.

[115] D. E. Newland, "Developments in the design of centrifugal pendulum vibration absorbers," in *International Congress on Sound and Vibration*, (London), 2017.

[116] Y. Ishida, T. Inoue, T. Kagawa, and M. Ueda, "Nonlinear Analysis and Experiments on Torsional Vibration of a Rotor with a Centrifugal Pendulum Vibration Absorber," *Journal of System Design and Dynamics*, vol. 2, no. 3, pp. 715–726, 2008.

[117] C. Shi and R. G. Parker, "Modal structure of centrifugal pendulum vibration absorber systems with multiple cyclically symmetric groups of absorbers," *Journal of Sound and Vibration*, vol. 332, pp. 4339–4353, Sept. 2013.

[118] S. W. Shaw, M. A. Acar, B. F. Feeny, and B. K. Geist, "Modal Properties of Rotating Shafts with Order-Tuned Absorbers," in *Topics in Modal Analysis I, Volume 7* (J. De Clerck, ed.), pp. 181–189, Cham: Springer International Publishing, 2014.

[119] M. Cera, M. Cirelli, E. Pennestrì, and P. P. Valentini, "Nonlinear dynamics of torsichrone CPVA with synchroringed form closure constraint," *Nonlinear Dynamics*, 2021.

[120] W. Li, T. Gao, Y. Cui, W. Guo, and W. Shi, "Study and Simulation of Isolation Performance of Torsional Vibration of DMF-CS with Centrifugal Pendulum-Type Absorber," in *Proceedings of the FISITA 2012 World Automotive Congress* (SAE-China and FISITA, eds.), vol. 198, (Berlin, Heidelberg), pp. 121–133, Springer Berlin Heidelberg, 2013.

[121] A. Kooy, "The evolution of the centrifugal pendulum-type absorber not only for DMF," in *Schaeffler Kolloquium*, 2014.

[122] S. Lee, S. K. Jayachandran, Y. Jang, and D. Lee, "Torsional Filtration Improvement with Centrifugal Pendulum DMF in Rear Wheel Drive System," *International Journal of Automotive Technology*, vol. 20, pp. 917–922, Oct. 2019.

[123] J.-G. Duh and M. Wenyong, "Development of monofilar rotor hub vibration absorber," tech. rep., 1983.

[124] C. Shi, R. G. Parker, and S. W. Shaw, "Tuning of centrifugal pendulum vibration absorbers for translational and rotational vibration reduction," *Mechanism and Machine Theory*, vol. 66, pp. 56–65, Aug. 2013.

[125] V. Manchi and C. Sujatha, "Torsional vibration reduction of rotating shafts for multiple orders using centrifugal double pendulum vibration absorber," *Applied Acoustics*, vol. 174, p. 107768, Mar. 2021.

[126] M. A. Acar, S. W. Shaw, and B. F. Feeny, "Nonlinear Dynamics of Flexible Rotating Shafts With Centrifugal Pendulum Vibration Absorbers," in *Volume 8: 27th Conference on Mechanical Vibration and Noise*, (Boston, Massachusetts, USA), p. V008T13A077, American Society of Mechanical Engineers, Aug. 2015.

[127] S. Gozen, B. J. Olson, S. W. Shaw, and C. Pierre, "Resonance Suppression in Multi-Degree-of-Freedom Rotating Flexible Structures Using Order-Tuned Absorbers," *Journal of Vibration and Acoustics*, vol. 134, Dec. 2012.

[128] T. Inoue, R. Okumura, S. Yabui, and X. Jiang, "Evaluation of Relationship Between Shape of a Rigid Body Unifilar Centrifugal Pendulum Vibration Absorber and Vibration Suppression Performance," *Journal of Vibration and Acoustics*, vol. 143, p. 031014, June 2021.

[129] E. Smith, "Analysis and simulation of centrifugal pendulum vibration absorbers," Master's thesis, Royal Institute of Technology, Stackholm, 2015.

[130] T. M. Theisen, "Gravity's effect on centrifugal pendulum vibration absorbers," Master's thesis, Michigan State University, Michigan, 2011.

[131] M. Mu, "Gravitation effects on centrifugal pendulum vibration absorbers linear analysis," Master's thesis, Michigan State University, Michigan, 2015.

[132] D. Tchokogoué, M. Mu, B. F. Feeny, B. K. Geist, and S. W. Shaw, "The Effects of Gravity on the Response of Centrifugal Pendulum Vibration Absorbers," *Journal of Vibration and Acoustics*, vol. 143, p. 061011, Dec. 2021.

[133] R. Dragani and M. Sarra, "The centrifugal pendulum as a non linear torsional vibration absorber," *Meccanica*, vol. 18, pp. 67–70, June 1983.

[134] B. J. Vidmar, B. F. Feeny, S. W. Shaw, A. G. Haddow, B. K. Geist, and N. J. Verhanovitz, "The effects of Coulomb friction on the performance of centrifugal pendulum vibration absorbers," *Nonlinear Dynamics*, vol. 69, pp. 589–600, July 2012.

[135] R. J. Monroe and S. W. Shaw, "Nonlinear Transient Dynamics of Pendulum Torsional Vibration Absorbers—Part I: Theory," *Journal of Vibration and Acoustics*, vol. 135, Feb. 2013.

[136] R. J. Monroe and S. W. Shaw, "Nonlinear Transient Dynamics of Pendulum Torsional Vibration Absorbers—Part II: Experimental Results," *Journal of Vibration and Acoustics*, vol. 135, Feb. 2013.

[137] J. Mayet, D. Rixen, and H. Ulbrich, "Experimental Investigation of Centrifugal Pendulum Vibration Absorbers," in *International Conference on Vibration Problems*, (Lisbon (Portugal)), 2013.

[138] C. Shi and R. G. Parker, "Modal properties and stability of centrifugal pendulum vibration absorber systems with equally spaced, identical absorbers," *Journal of Sound and Vibration*, vol. 331, pp. 4807–4824, Oct. 2012.

[139] M. Hosek, H. Elmali, and N. Olgac, "A tunable torsional vibration absorber: The centrifugal delayed resonator," *Journal of Sound and Vibration*, vol. 205, pp. 151–165, Aug. 1997.

[140] L. Ineichen, "Controllable centrifugal pendulum," *PAMM*, vol. 10, pp. 611–612, Dec. 2010.

[141] A. H. Nayfeh, *Perturbation Methods*. Wiley Classics Library, Weinheim: Wiley-VCH, 1973.

[142] M. A. Acar and S. W. Shaw, "Application of the Harmonic Balance Method to Centrifugal Pendulum Vibration Absorbers," in *Special Topics in Structural Dynamics, Volume 6* (D. Di Miao, P. Tarazaga, and P. Castellini, eds.), pp. 243–252, Cham: Springer International Publishing, 2016.

[143] L. Guillot, B. Cochelin, and C. Vergez, "A Taylor series-based continuation method for solutions of dynamical systems," *Nonlinear Dynamics*, vol. 98, pp. 2827–2845, Dec. 2019.

[144] L. Guillot, A. Lazarus, O. Thomas, C. Vergez, and B. Cochelin, "A purely frequency based Floquet-Hill formulation for the efficient stability computation of periodic solutions of ordinary differential systems," *Journal of Computational Physics*, vol. 416, p. 109477, Sept. 2020.

[145] A. G. Haddow and S. W. Shaw, "Torsional Vibration Absorbers: A Testing and Evaluation Apparatus," in *SAE 2001 Noise & Vibration Conference & Exposition*, pp. 2001–01–1577, Apr. 2001.

[146] T. M. Nester, "Experimental investigation of circular path centrifugal pendulum vibration absorbers.pdf," Master's thesis, Michigan State University, Michigan, 2002.

[147] A. G. Haddow and S. W. Shaw, "Centrifugal Pendulum Vibration Absorbers: An Experimental and Theoretical Investigation," *Nonlinear Dynamics*, vol. 34, pp. 293–307, Dec. 2003.

[148] V. Mahé, A. Renault, A. Grolet, O. Thomas, and H. Mahé, "Réducteur pour véhicule électrique ou hybride avec au moins un dispositif d'amortissement pendulaire." *FR3 119 873*.

[149] V. Mahé, A. Renault, A. Grolet, O. Thomas, and H. Mahé, "Stabilité dynamique des amortisseurs de vibrations à pendule centrifuge permettant une mobilité rotationelle." *FR 2 200 339*.

[150] A. Renault, O. Thomas, and H. Mahé, "Numerical antiresonance continuation of structural systems," *Mechanical Systems and Signal Processing*, vol. 116, pp. 963–984, Feb. 2019.

[151] V. Mahé, A. Renault, A. Grolet, H. Mahé, and O. Thomas, "Experimental investigation of the direct and subharmonic responses of a new design of centrifugal pendulum vibration absorber," , *Submitted to the Journal of Sound and Vibration*.

[152] V. Mahé, A. Renault, A. Grolet, H. Mahé, and O. Thomas, "Localised response of a centrifugal pendulum vibration absorber," , *Submitted to Nonlinear Dynamics*.

[153] V. Mahé, A. Renault, A. Grolet, H. Mahé, and O. Thomas, "On the dynamic stability of centrifugal double pendulum vibration absorbers," , *Submitted to Nonlinear Dynamics*.

[154] V. Mahé, A. Renault, A. Grolet, H. Mahe, and O. Thomas, "On the stability of pairs of subharmonic centrifugal pendulum vibration absorbers allowing a rotational mobility," , *Submitted to Nonlinear Dynamics*.

[155] V. Mahé, A. Renault, A. Grolet, H. Mahé, and O. Thomas, "Unison response of a centrifugal double pendulum vibration absorber," , *Submitted to the Journal of Sound and Vibration*.

[156] V. Mahé, A. Renault, A. Grolet, H. Mahé, and O. Thomas, "Réponse et stabilité d'absorbeurs pendulaires centrifuges sous-harmoniques," in *15ème Colloque National En Calcul Des Structures (CSMA)*, (Presqu'île de Giens (France)), 2022.

[157] V. Mahé, A. Renault, A. Grolet, H. Mahé, and O. Thomas, "Stabilité et performance d'absorbeurs pendulaires centrifuges admettant une mobilité de rotation," in *25ème Congrès Français de Mécanique (CFM)*, (Nantes (France)), 2022.

[158] V. Mahé, A. Renault, A. Grolet, H. Mahé, and O. Thomas, "Subharmonic filtration in rotating machines using centrifugal pendulum vibration absorbers," in *Congrès Français d'Acoustique (CFA)*, (Marseille (France)), 2022.

[159] V. Mahé, A. Renault, A. Grolet, H. Mahé, and O. Thomas, "Dynamic stability of tuned vibration absorbers allowing a rotational mobility," in *European Nonlinear Dynamics Conference (ENOC)*, (Lyon (France)), 2022.

[160] S. W. Shaw and S. Wiggins, "Chaotic dynamics of a whirling pendulum," *Physica D: Nonlinear Phenomena*, vol. 31, pp. 190–211, June 1988.

[161] I. Kovacic and M. J. Brennan, *The Duffing Equation: Nonlinear Oscillators and Their Behaviour*. John Wiley & Sons, 2011.

[162] S. H. Strogatz, *Nonlinear Dynamics and Chaos: With Applications to Physics, Biology, Chemistry, and Engineering*. Boulder, Colo: Westview Press, second ed., 2018.

[163] G. L. Baker and J. A. Blackburn, *The Pendulum: A Case Study in Physics*. Oxford ; New York: Oxford University Press, 2005.

[164] L. Shen and B. W. Suter, "Bounds for Eigenvalues of Arrowhead Matrices and Their Applications to Hub Matrices and Wireless Communications," *EURASIP Journal on Advances in Signal Processing*, vol. 2009, p. 379402, Dec. 2009.

[165] A. H. Nayfeh and B. Balachandran, *Applied Nonlinear Dynamics: Analytical, Computational and Experimental Methods*. Wiley Series in Nonlinear Science, Weinheim: Wiley-VCH, 2004.

[166] G. Floquet, "Sur les équations différentielles linéaires à coefficients périodiques," *Annales scientifiques de l'École normale supérieure*, vol. 12, pp. 47–88, 1883.

[167] A. Lazarus and O. Thomas, "A harmonic-based method for computing the stability of periodic solutions of dynamical systems," *Comptes Rendus Mécanique*, vol. 338, pp. 510–517, Sept. 2010.

[168] O. Thomas, *Dynamique linéaire et non linéaire de structures élastiques et piézoélectriques*. HDR, Ecole normale supérieure de Cachan, Paris, 2011.

[169] Y. A. Kuznetsov, *Elements of Applied Bifurcation Theory, Second Edition*, vol. 112. Springer-Verlag, 1998.

[170] S. K. Lele, "Compact finite difference schemes with spectral-like resolution," *Journal of Computational Physics*, vol. 103, pp. 16–42, Nov. 1992.

[171] W. H. Press, S. A. Teukolsky, W. T. Vetterling, and B. P. Flannery, *Numerical Recipes in C: The Art of Scientific Computing*, vol. 17. 1992.

[172] E. J. Doedel, A. R. Champneys, T. Fairgrieve, Y. A. Kuznetsov, B. Sandstede, and X. Wang, "AUTO 97: Continuation And Bifurcation Software For Ordinary Differential Equations (with HomCont)," 1999.

[173] A. Dhooge, W. Govaerts, and Y. A. Kuznetsov, "MATCONT: A MATLAB package for numerical bifurcation analysis of ODEs," *ACM Transactions on Mathematical Software*, vol. 29, pp. 141–164, June 2003.

[174] R. Seydel, *Practical Bifurcation and Stability Analysis*, vol. 5 of *Interdisciplinary Applied Mathematics*. New York, NY: Springer New York, 2010.

[175] L. Guillot, *De l'intérêt d'un Formalisme Quadratique Pour La Continuation Des Solutions d'un Système Dynamique et de Leurs Bifurcations - Application Aux Instruments à Anche*. PhD thesis, Aix-Marseille Université, Marseille (France), 2020.

[176] M. Abramowitz and I. A. Stegun, *Handbook of Mathematical Functions*. Department of Commerce - United States of America, tenth ed., 1972.

List of appendixes

Appendix A

Study of a centrifugated beam

A.1 Modelling of the problem

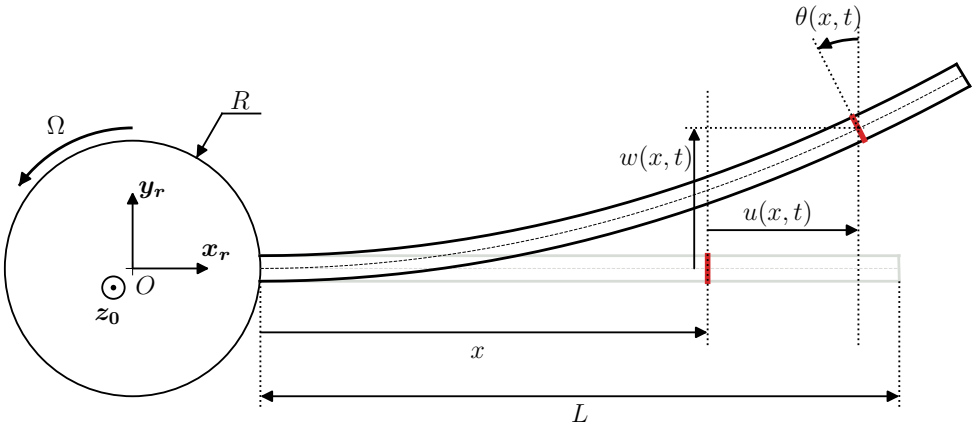

Figure A.1: Illustration of a beam of length L clamped on a rotor of radius R and spinning at a constant angular velocity Ω.

The problem investigated here is illustrated in Fig. A.1. We are interested in the free vibrations of a beam of length L clamped on a rotor of radius R spinning with an angular velocity Ω about axis $\boldsymbol{z}_0$. The frame $\mathscr{R}_r(O, \boldsymbol{x_r}, \boldsymbol{y_r}, \boldsymbol{z_0})$ is attached to the rotor at point O. The displacements of the cross-section of the beam located at x in its rest configuration along axes $\boldsymbol{x_r}$ and $\boldsymbol{y_r}$ are $u(x)$ and $w(x)$, respectively. In addition, the rotation of the cross-section is $\theta(x)$. The area of a cross section is A and the mass per unit length of the beam is ρ. In the following, the rotational inertia of the beam is neglected. The equations of motion on u and w, derived in [24], are

$$\rho A\ddot{u} = N' + \rho A\Omega^2(R + x + u), \tag{A.1a}$$

$$\rho A\ddot{w} = (Nw')' - M'', \tag{A.1b}$$

where N is the axial load, M is the bending moment and $(\bullet)' = \partial(\bullet)/\partial x$. N and M are related to u

and w such that

$$N = EAu', \quad M = EIw'', \tag{A.2}$$

where E and I are the Young's modulus of the beam and its second moment of area about axis $\boldsymbol{z_0}$, respectively. It is convenient to decompose some quantities into a static and a dynamic component in order to write

$$u(x,t) = u_s(x) + u_d(x,t), \tag{A.3a}$$
$$w(x,t) = w_s(x) + w_d(x,t), \tag{A.3b}$$
$$N(x,t) = N_s(x) + N_d(x,t), \tag{A.3c}$$

where indices "s" and "d" refer to "static" and "dynamic", respectively. It must be noted that

- The transverse displacement of the beam oscillates about 0, meaning that $w_s(x) = 0 \forall x$.
- There is no external axial load applied on the beam, meaning that u and N only contain a static component.

From these observations, we can write

$$u(x,t) = u_s(x), \tag{A.4}$$
$$w(x,t) = w_d(x,t), \tag{A.5}$$
$$N(x,t) = N_s(x). \tag{A.6}$$

In the following, indices s and d are omitted. As u does not depend on t, Eq. (A.1a) can be rewritten

$$0 = N' + \rho A \Omega^2 (R + x + u). \tag{A.7}$$

The boundary conditions (BCs) are detailed below. As the beam is clamped at $x = 0$, we have

$$w(0,t) = 0 \ \forall t, \tag{A.8a}$$
$$w'(0,t) = 0 \ \forall t, \tag{A.8b}$$
$$u(0) = 0 \quad \Rightarrow \quad N'(0) = -\rho A \Omega^2 R. \tag{A.8c}$$

At $x = L$, we have

$$M(L,t) = 0 \ \forall t \quad \Rightarrow \quad w''(L,t) = 0 \ \forall t, \tag{A.9a}$$
$$M'(L,t) = 0 \ \forall t \quad \Rightarrow \quad w'''(L,t) = 0 \ \forall t, \tag{A.9b}$$
$$N(L) = 0. \tag{A.9c}$$

A.2 Derivation of a simplified equation

In order to simplify Eq. (A.7), we can assume

$$u \ll R + x, \quad \forall x. \tag{A.10}$$

There are two justifications for this:

- $u \ll L$, so the assumption is verified for sufficiently large values of x.
- From the BC at $x = 0$, we have $u(0) = 0$, so the assumption is also valid for small values of x.

Using assumption (A.10) in Eq. (A.7), we obtain

$$N' = -\rho A \Omega^2 (R + x). \tag{A.11}$$

It is more convenient to write the equations in a dimensionless form. To do so, we introduce the dimensionless quantities

$$\bar{x} = \frac{x}{L}, \quad \bar{t} = \frac{t}{T_0}, \quad \bar{w} = \frac{w}{w_0}, \quad \bar{N} = \frac{N}{N_0}, \quad \bar{\Omega} = \frac{\Omega}{\Omega_0}, \quad \bar{R} = \frac{R}{L}, \tag{A.12}$$

where T_0, w_0, N_0 and Ω_0 are characteristic time, displacement, load and angular frequencies, respectively. It is convenient to set them as

$$T_0 = L^2 \sqrt{\frac{\rho A}{EI}}, \quad \Omega_0 = \frac{1}{T_0}, \quad N_0 = \frac{EI}{L^2} \Omega^2, \tag{A.13}$$

and the choice of w_0 is arbitrary as it will cancel in the equations. Introducing the dimensionless quantities in the equations, using the chain rules

$$\frac{\partial(\bullet)}{\partial x} = \frac{1}{L} \frac{\partial(\bullet)}{\partial \bar{x}}, \quad \frac{\partial(\bullet)}{\partial t} = \frac{1}{T_0} \frac{\partial(\bullet)}{\partial \bar{t}} \tag{A.14}$$

and redefining $\bar{(\bullet)} \leftarrow (\bullet)$, $(\bullet)' = \partial(\bullet)/\partial x$, $\dot{(\bullet)} = \partial(\bullet)/\partial t$, we obtain the dimensionless equations of motion

$$N' + \Omega^2 (R + x) = 0, \tag{A.15a}$$

$$\ddot{w} + w'''' - \Omega^2 (N w')' = 0, \tag{A.15b}$$

with the BCs

$$w(0, t) = 0 \ \forall t, \tag{A.16a}$$

$$w'(0, t) = 0 \ \forall t, \tag{A.16b}$$

$$N'(0) = -\Omega^2 R \tag{A.16c}$$

and

$$w''(1, t) = 0 \ \forall t, \tag{A.17a}$$

$$w'''(1, t) = 0 \ \forall t, \tag{A.17b}$$

$$N(1) = 0. \tag{A.17c}$$

Integrating Eq. (A.15a) and using the BC on N at $x = 1$, we can obtain

$$N = \Omega^2 \left[R(1 - x) + \frac{1}{2} - \frac{x^2}{2} \right]. \tag{A.18}$$

This can be introduced in Eq. (A.15b) so that the dynamics are governed only by this equation and the BCs on w.

There are no general solutions for Eq. (A.15b), so additional assumptions are required. In a first step, we can assume that Ω is small so that the term $\Omega^2(Nw')'$ can be neglected. In this case, Eq. (A.15b) reduces to

$$\ddot{w} + w'''' = 0, \tag{A.19}$$

which corresponds to the well-known problem of a the bending of a clamped-free beam [23]. Of interest here is the case where Ω is large so that the bending stiffness w'''' can be neglected. In such a situation, Eq. (A.15b) reduces to

$$\ddot{w} - \Omega^2(Nw')' = 0. \tag{A.20}$$

This equation is solved thereafter in a special case.

A.3 Modes of the centrifugated beam

We can use the separation of variables

$$w(x,t) = q(t)\phi(x) \tag{A.21}$$

in Eq. (A.20), rearrange it and use Eq. (A.18) in order to obtain the two equations

$$\ddot{q} + \omega^2 q = 0, \tag{A.22a}$$

$$\Omega^2 \left[R(1-x) + \frac{1}{2} - \frac{x^2}{2} \right] \phi'' - \Omega^2(R+x)\phi' + \omega^2\phi = 0, \tag{A.22b}$$

where ω is a constant. The solutions for q are simply

$$q(t) = A_q \cos(\omega t) + B_d \sin(\omega t), \tag{A.23}$$

where A_q and B_q are constants depending on the initial conditions. However, there are no analytical solutions for Eq. (A.22b). To derive an analytical solution, we can assume $R = 0$, in which case Eq. (A.22b) reduces to

$$\left[(1-x^2)\phi'\right]' + \lambda(\lambda+1)\phi = 0, \tag{A.24}$$

where we have introduced

$$\lambda(\lambda+1) = 2n^2, \quad n = \frac{\omega}{\Omega}. \tag{A.25}$$

Eq. (A.24) is a Legendre equation of degree λ and order 0 [176]. Its general solution is

$$\phi(x) = AP_\lambda(x) + BQ_\lambda(x), \tag{A.26}$$

where A and B are constants to be determined and P_λ and Q_λ are Legendre functions of the first and second kind and of degree λ. These functions are defined as [176]

$$P_\lambda(x) = {}_2F_1\left(-\lambda, \lambda+1; 1; \frac{1-x}{2}\right) \quad \text{for } |1-x|<2, \tag{A.27a}$$

$$Q_\lambda(x) = \frac{\sqrt{\pi}\Gamma(\lambda+1)}{2^{\lambda+1}\Gamma(\lambda+3/2)}\frac{1}{x^{\lambda+1}}{}_2F_1\left(\frac{\lambda+1}{2}, \frac{\lambda+2}{2}; \lambda+\frac{3}{2}; \frac{1}{x^2}\right) \quad \text{for } |x|>1, \tag{A.27b}$$

where Γ and ${}_2F_1$ are the Gamma and the hypergeometric functions, respectively. In the present case, $|x| \leq 1$ so that $Q_\lambda(x)$ is undefined, from what we deduce $B = 0$. Hence, the general form of the solution reduces to

$$\phi(x) = P_\lambda(x), \tag{A.28}$$

where we have chosen $A = 1$. The BCs derived previously do not apply to the present case as they were derived for Eq. (A.15b), which is a fourth order equation in x, hence requiring four BCs, whereas Eq. (A.20) is only a second order equation in x, hence requiring only two BCs. Actually, neglecting the bending stiffness of the beam is equivalent to considering it is a string, so it makes sense that only two BCs are required. For a string fixed at $x = 0$ and free at $x = 1$, the BCs on the transverse displacement are [23]

$$w(0,t) = 0 \quad \forall t, \tag{A.29a}$$

$$N(1)w'(1,t) = 0 \quad \forall t. \tag{A.29b}$$

The second BC is already satisfied because $N(1) = 0$ (*cf.* Eq. (A.18)). Hence, the only BC to be satisfied by ϕ is

$$\phi(0) = 0 \quad \Rightarrow {}_2F_1\left(-\lambda, \lambda+1; 1; \frac{1}{2}\right) = 0. \tag{A.30}$$

Moreover, we can use the relation [176]

$${}_2F_1\left(a, b; \frac{1}{2}(a+b+1); \frac{1}{2}\right) = \pi^{1/2}\frac{\Gamma((a+b+1)/2)}{\Gamma((a+1)/2)\Gamma((b+1)/2)}, \quad (a+b+1)/2 \neq 0, -1, -2, \ldots \tag{A.31}$$

with $a = -\lambda$ and $b = \lambda + 1$ in order to rewrite the BC as

$$\pi^{1/2}\frac{\Gamma(1)}{\Gamma((-\lambda+1)/2)\Gamma((\lambda+2)/2)} = 0. \tag{A.32}$$

In addition, we can use [176]

$$\Gamma(1) = 1, \quad \frac{1}{\Gamma(z)} = 0 \quad \text{for } z = -m,\ m \in \{0 \cup \mathbb{N}\} \tag{A.33}$$

with $z = (-\lambda+1)/2$ and $z = (\lambda+2)/2$ to rewrite the BC as

$$\frac{1}{\Gamma((-\lambda+1)/2)\Gamma((\lambda+2)/2)} = 0 \quad \Rightarrow \quad \lambda = 2m+1 \quad \text{or} \quad \lambda = -2m-2. \tag{A.34}$$

Hence, the general solution $\phi(x) = P_\lambda(x)$ must satisfy one of the two conditions on λ described above. However, because of the relation [176]

$$P_\lambda(x) = P_{-\lambda-1}(x), \tag{A.35}$$

both conditions are equivalent. Thus, the solutions of Eq. (A.24) are (to a multiplicative constant)

$$\phi_m(x) = P_{\lambda_m}(x), \quad \lambda_m = 2m + 1. \tag{A.36}$$

As λ_m is an integer, the mode shapes P_{λ_m} are not Legendre functions of the first kind but Legendre polynomials of odd degree. The eigenorders are directly deduced from Eqs. (A.25) and (A.36). Finally, the modes of the centrifugated beam are $(n_m, \phi_m(x))$ with

$$n_m = \sqrt{(2m+1)(m+1)}, \quad \phi_m(x) = P_{2m+1}(x), \quad m \in \{0 \cup \mathbb{N}\}. \tag{A.37}$$

The five first values of n_m are given in Tab. A.1 and the associated mode shapes are represented in Fig. A.2. It can reasonably be assumed that the first mode would be the one providing the best filtering efficiency if the rotor was subjected to a fluctuating torque. However, for a rotor of zero radius, the first eigenorder is low ($n_0 = 1$). Ongoing works investigate the possibility to increase this eigenorder by considering the case $R \neq 0$ and by adding a mass on the beam. Nevertheless, the first results tend to show that reaching a high order is difficult and that the rotational velocity above which the bending stiffness can be neglected is large. The study presented here has no practical application but shows that beams can be order-tuned (when their bending stiffness is negligible). In addition, the results obtained can be used to validate numerical simulations of centrifugated beams.

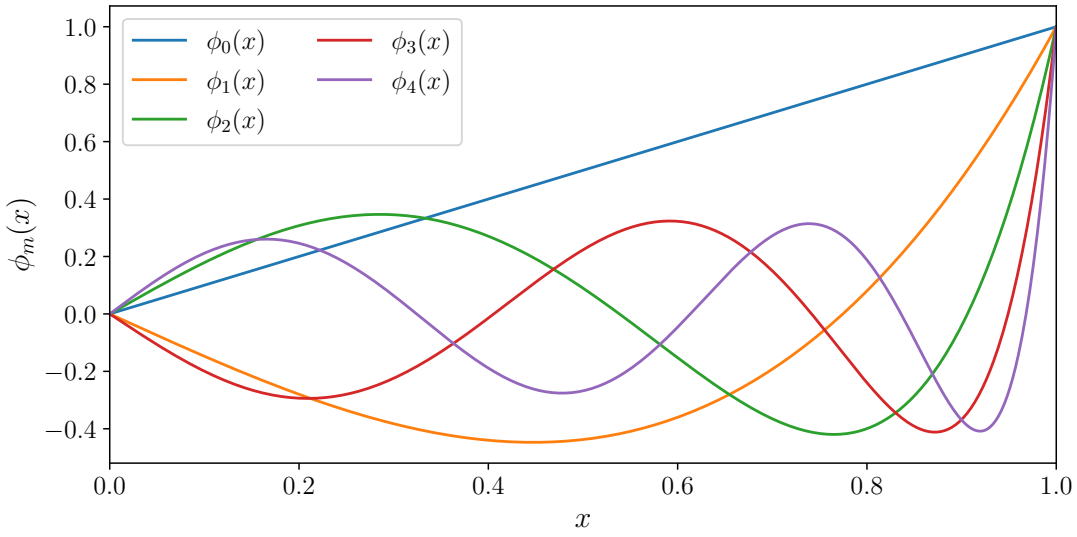

Figure A.2: Five first mode shapes of a centrifugated beam clamped on a rotor with zero radius.

m	0	1	2	3	4
n_m	1	2.449	3.873	5.292	6.708

Table A.1: Five first eigenorders of a centrifugated beam clamped on a rotor with zero radius.

Appendix B

Details on the linear response of a centrifugal pendulum vibration absorber

B.1 Computation of the linear response

It is convenient to compute the forced response using the truncated modal basis $\mathbf{\Phi} = [\boldsymbol{\phi}_{\mathbf{00}}, \boldsymbol{\phi}_{\mathbf{20}}]$. Indeed, the rotor is a node of modes $\boldsymbol{\phi}_{\mathbf{10}_i}$, so they do not contribute to the linear forced response. Hence, we can use the truncated expansion

$$\boldsymbol{q} = \begin{bmatrix} \theta \\ s_1 \\ \vdots \\ s_N \end{bmatrix} = \zeta_0 \boldsymbol{\phi}_{\mathbf{00}} + \zeta_2 \boldsymbol{\phi}_{\mathbf{20}}, \tag{B.1}$$

where ζ_0 and ζ_2 are the modal coordinates of the rigid body and unison modes, respectively. Projecting the linear equations (2.24) on the truncated modal basis and neglecting the coupling through the damping leads to the two equations

$$(1+\mu)\zeta_0'' + \bar{b}_r \zeta_0' = \bar{T}_1, \tag{B.2a}$$

$$\zeta_2'' + \frac{\tilde{b}_2}{\tilde{m}_2}\zeta_2' + n_2^2 \zeta_2 = -\frac{\Lambda_c \bar{T}_1}{(1+\mu)\Lambda_m - \mu\Lambda_c^2}, \tag{B.2b}$$

where the modal mass and damping of mode 2 are given by

$$\tilde{m}_2 = \Lambda_m - \frac{\mu\Lambda_c^2}{1+\mu}, \quad \tilde{b}_2 = \bar{b} + \frac{\mu\Lambda_c^2}{(1+\mu)^2}\bar{b}_r. \tag{B.3}$$

Looking for periodic solutions of the form $\zeta_0 = \Re[\hat{\mathrm{Z}}_0 e^{jn\tau}]$ and $\zeta_2 = \Re[\hat{\mathrm{Z}}_2 e^{jn\tau}]$ where $j = \sqrt{-1}$, we obtain the expression of the complex modal amplitudes

$$\hat{\mathrm{Z}}_0 = \frac{\bar{T}_1}{(1+\mu)} \frac{1}{-n^2 + jn\bar{b}_r}, \tag{B.4a}$$

$$\hat{\mathrm{Z}}_2 = -\frac{\bar{T}_1 \Lambda_c}{[(1+\mu)\Lambda_m - \mu\Lambda_c^2]\left[n_{20}^2 - n^2 + jn\tilde{b}_2/\tilde{m}_2\right]}. \tag{B.4b}$$

Finally, the physical solutions are $\boldsymbol{q} = \Re[\hat{\boldsymbol{Q}} e^{jn\tau}]$ where the complex amplitudes $\hat{\boldsymbol{Q}}$ are obtained through $\hat{\boldsymbol{Q}} = \boldsymbol{\Phi}\hat{\boldsymbol{Z}}$ with $\hat{\boldsymbol{Z}} = [\hat{\mathrm{Z}}_0, \hat{\mathrm{Z}}_2]^\intercal$.

To derive the locus of the rotor's antiresonances, we can use Cramer's rule on the matrix equation associated to Eqs. (2.24). These antiresonances are the solutions of

$$\begin{vmatrix} \bar{T}_1 & \Lambda_c & \cdots & \cdots & \Lambda_c \\ 0 & n_t - n^2\Lambda_m & 0 & \cdots & 0 \\ \vdots & 0 & \ddots & \ddots & \vdots \\ \vdots & \vdots & \ddots & \ddots & 0 \\ 0 & 0 & \cdots & 0 & n_t - n^2\Lambda_m \end{vmatrix} = 0. \tag{B.5}$$

Developing with respect to the first column, this reduces to

$$\begin{vmatrix} n_t - n^2\Lambda_m & 0 & \cdots & 0 \\ 0 & \ddots & \ddots & \vdots \\ \vdots & \ddots & \ddots & 0 \\ 0 & \cdots & 0 & n_t - n^2\Lambda_m \end{vmatrix} = 0, \tag{B.6}$$

whose N solutions are all

$$n_{AR} = n_p. \tag{B.7}$$

Hence, we see that in the absence of damping, the rotor possesses a single antiresonance at order $n_{AR} = n_p$.

B.2 Evaluation of the linear performance

This Appendix presents the details of the linear performance analysis summarised in section 2.2.4. To do this, we analyse the variations of the performance indicators G_θ, Δn and G_s (*cf.* Eq. (2.34))

as a function of the system parameters. The expressions of the performance indicators are

$$G_\theta = \sqrt{\frac{\left[(1+\mu)^2\bar{b} + \mu\Lambda_c^2\bar{b}_r\right]^2}{(1+\mu)^4\bar{b}^2 + n_p^2\mu^2(1+\mu)^2\Lambda_c^4}}, \tag{B.8a}$$

$$\Delta n = \left(\sqrt{\frac{1+\mu}{1+\mu\left(1-\frac{\Lambda_c^2}{\Lambda_m}\right)}} - 1\right) n_p, \tag{B.8b}$$

$$G_s = \sqrt{\frac{\Lambda_m\Lambda_c^2(1+\mu)^3}{n_p^2\left[\Lambda_m\Lambda_c^4 n_p^2\mu^2(1+\mu)^3 + ((1+\mu)\Lambda_m - \mu\Lambda_c^2)\left(\Lambda_c\mu\bar{b}_r + (1+\mu)^2\bar{b}\right)^2\right]}}. \tag{B.8c}$$

Influence of the damping

When the damping increases, the term $\left[(1+\mu)^2\bar{b} + \mu\Lambda_c^2\bar{b}_r\right]^2$ increases faster than $\left[(1+\mu)^2\bar{b}\right]^2$. Hence, as expected, increasing whether $\bar{b}$ or $\bar{b}_r$ deteriorates G_θ.

The damping has no influence on Δn.

Increasing the damping lowers G_s assuming $(1+\mu)\Lambda_m - \mu\Lambda_c^2 > 0$, which is the case for realistic parameters.

Influence of the tuning order

n_p appears only at the denominator of G_θ, so that high tuning orders should provide a better performance.

Δn increases linearly with n_p.

G_s decreases with n_p.

Influence of the inertia ratio

To simplify the study of the variations of G_θ with μ, we propose to use a Taylor series of G_θ in μ (we recall that μ is a small parameter), which leads to

$$G_\theta = 1 + \mu\frac{\bar{b}_r\Lambda_c^2}{\bar{b}} - \mu^2\Lambda_c^2\frac{\Lambda_c^2 n_p^2 + 4\bar{b}_r\bar{b}}{2\bar{b}^2} + \mathcal{O}(\mu^3). \tag{B.9}$$

The term multiplying μ is positive, which means that for μ very small, G_θ increases with μ. However, the damping is very small which implies that the term $-\Lambda_c^4 n_p^2/2\bar{b}^2$, which multiplies μ^2, becomes dominant above a critical value of μ_{crit} given by

$$\mu_{\text{crit}} = \frac{\bar{b}\bar{b}_r}{\Lambda_c^2 n_p^2 + 4\bar{b}\bar{b}_r}. \tag{B.10}$$

As the damping coefficients are intended to be small, we have $\mu_{\text{crit}} \approx 0$, and we can estimate that increasing μ only improves the performance of the system.

As $1 - \Lambda_c^2/\Lambda_m < 1$, Δn increases with μ.

As we did previously for G_θ, it is insightful to compute a Taylor series of G_s in μ to assess its evolution. Doing so, we obtain

$$G_s \approx \frac{\Lambda_c}{n_p \bar{b}} - \mu \Lambda_c \frac{(2\Lambda_m - \Lambda_c^2)\bar{b} + 2\Lambda_c \Lambda_m \bar{b}_r}{2\Lambda_m n_p \bar{b}^2} - \mu^2 \Lambda_c \frac{4\Lambda_c^4 \Lambda_m^2 n_p^2}{8\Lambda_m^2 \bar{b}^3 n_p}, \tag{B.11}$$

where we neglected terms of order μ^3 and the contributions of $\bar{b}$ and $\bar{b}_r$ to the numerator of the coefficient of μ^2 (we recall that in practice, damping is small). From Eq. (B.11), we see that when μ is very small, G_s typically decreases with μ as $(2\Lambda_m - \Lambda_c^2)\bar{b} + 2\Lambda_c \Lambda_m \bar{b}_r \geq 0$ for reasonable values of Λ_c. For larger values of μ, G_s quickly decreases as the coefficient of μ^2 is negative and its magnitude is much larger than that of the coefficient of μ.

The evolution of the performance indicators with μ is represented in Fig. B.1.

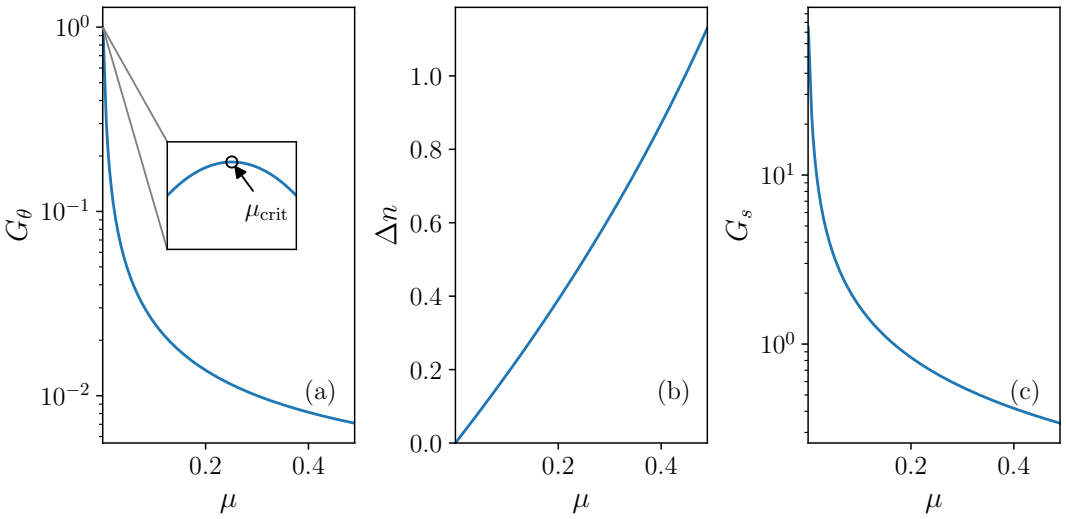

Figure B.1: Evolution of G_θ (a), Δn (b) and G_s (c) as a function of the inertia ratio μ. $n_p = 2$, $\eta = 1$, $\alpha_{[1]} = 0.5$, $\bar{b} = 0.01$, $\bar{b}_r = 0.001$.

Influence of the equivalent pendulums' mass

Λ_m does not appear in G_θ, so it has no effect on this performance indicator.

The smaller $1 - \Lambda_c^2/\Lambda_m$, the larger Δn. Hence, increasing Λ_m decreases Δn (we remind that $\Lambda_m \geq 1$, *cf.* Eq. (2.25a)).

G_s is not affected much by Λ_m. Indeed, dividing Eq. (B.8c) by $\sqrt{\Lambda_m}$, we obtain

$$G_s = \sqrt{\frac{\Lambda_c^2(1+\mu)^3}{n_p^2\left[\Lambda_c^4 n_p^2\mu^2(1+\mu)^3 + ((1+\mu)\Lambda_m - \mu\Lambda_c^2/\Lambda_m)\left(\Lambda_c\mu\bar{b}_r + (1+\mu)^2\bar{b}\right)^2\right]}}, \tag{B.12}$$

which shows that Λ_m only affects the damping terms in G_s, which are small. In addition, $-\mu\Lambda_c^2/\Lambda_m < 0$, so increasing Λ_m very slightly decreases G_s.

Influence of the linear coupling term between a pendulum and the rotor

The parameter that has the most interesting effect on linear performance is Λ_c. Both G_θ and Δn are even functions of Λ_c. We can compute the zeros of $\partial G_\theta/\partial\Lambda_c$ and $\partial\Delta n/\partial\Lambda_c$, leading to

$$\frac{\partial G_\theta}{\partial\Lambda_c} = 0 \quad \Rightarrow \quad \Lambda_c \in \left\{-\sqrt{\frac{\bar{b}\bar{b}_r}{\mu n_p^2}},\ 0,\ \sqrt{\frac{\bar{b}\bar{b}_r}{\mu n_p^2}}\right\}, \tag{B.13a}$$

$$\frac{\partial\Delta n}{\partial\Lambda_c} = 0 \quad \Rightarrow \quad \Lambda_c = 0. \tag{B.13b}$$

The evolution of the performance indicators with Λ_c is represented in Fig. B.2. We remind that in the case of purely translated pendulums, $\Lambda_c = 1$ (*cf.* Eq. (2.25b)), and it increases (decreases) for positive (negative) values of $\alpha_{[1]}$.

Increasing Λ_c above 1 improves all performance indicators, meaning that in the frame of a linear study, positive values of $\alpha_{[1]}$ should be preferred. On the contrary, decreasing Λ_c decreases the performance indicators G_θ and Δn until $\Lambda_c = 0$. For this special value, $G_\theta = 1$, $\Delta n = 0$ and $G_s = 0$, so the system acts as if there were no pendulums. This should not be a surprise as $\Lambda_c = 0$, which occurs for $\alpha_{[1]} = -1/\eta$, corresponds to a situation where there is no coupling between the pendulums and the rotor (*cf.* Eq. (2.24)). Decreasing Λ_c below $-\sqrt{\bar{b}\bar{b}_r/\mu n_p^2} \approx 0$ improves the performance indicators G_θ and Δn, but it requires large negative values of $\alpha_{[1]}$, which is difficult to achieve in practice.

The evolution of G_s is not presented in details here as its variations with Λ_c are difficult to analyse analytically. Nevertheless, it is clear from Fig. B.2 that increasing Λ_c above 1 improves this indicator. Decreasing Λ_c below 1 first deteriorates G_s until it reaches a maximum, for $\Lambda_c \approx 0.2$. Then, decreasing Λ_c from 0.2 to 0, G_s decreases until it reaches 0. This is the optimal value of this indicator, but it corresponds to inactive pendulums, so it is absolutely not compatible with the performance indicators G_θ and Δn. The evolution of G_s with negative values of Λ_c is not discussed in details as G_s is almost symmetric with respect to $\Lambda_c = 0$.

Influence of the linear rotation coefficient

The evolution of the performance indicators as a function of the linear rotation coefficient $\alpha_{[1]}$ is discussed in section 2.2.4. Here, we only detail the computation of particular values of $\alpha_{[1]}$. First, one

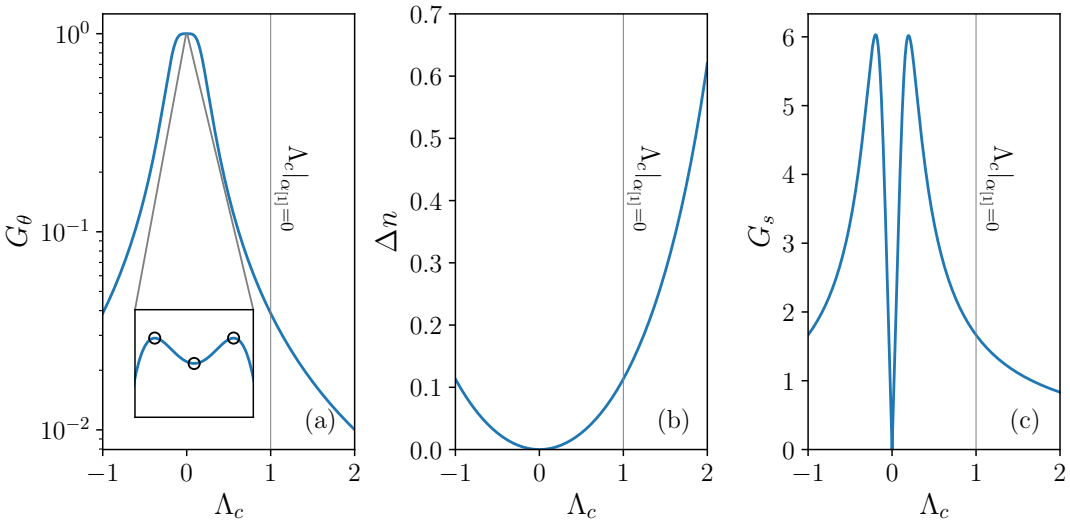

Figure B.2: Evolution of G_θ (a), Δn (b) and G_s (c) as a function of the coupling term Λ_c. The three black circles in the zoom of (a) indicate the solutions of $\partial G_\theta/\partial\Lambda_c = 0$. $n_p = 2$, $\mu = 0.15$, $\Lambda_m = 1.25$, $\bar{b} = 0.01$, $\bar{b}_r = 0.001$.

can compute the zeros of $\partial\Delta n/\partial\alpha_{[1]}$, leading to

$$\frac{\partial\Delta n}{\partial\alpha_{[1]}} = 0 \quad \Rightarrow \quad \alpha_{[1]} = \begin{cases} -\dfrac{1}{\eta} \;\Rightarrow\; \Delta n = 0, \\ \\ 1 \;\Rightarrow\; \Delta n = n_p\left(\sqrt{\dfrac{1+\mu}{1-\eta\mu}} - 1\right). \end{cases} \tag{B.14}$$

Moreover, if there is no rotation, the value of Δn reduces to

$$\Delta n = n_p\left(\sqrt{1+\mu} - 1\right). \tag{B.15}$$

To find a value of $\alpha_{[1]} \neq 0$ that yields the same value of Δn, it is convenient to look for the solutions of

$$n_{20}^2 - n_{20}^2\Big|_{\alpha_{[1]}=0} = n_{20}^2 - n_p^2(1+\mu) = 0. \tag{B.16}$$

This way, we find that

$$\alpha_{[1]} = \frac{2}{1-\eta} \tag{B.17}$$

leads to the same value of Δn as $\alpha_{[1]} = 0$.

Appendix C

Equivalent inertia of a driveline

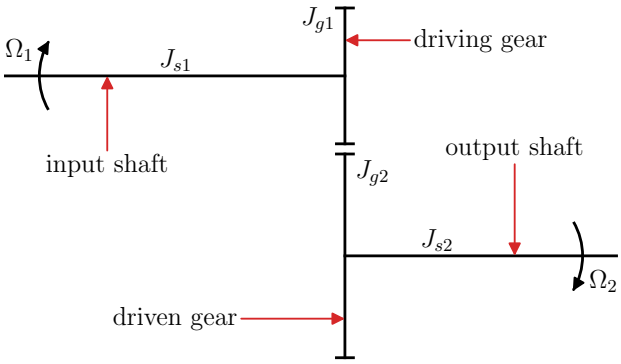

Figure C.1: Illustration of a gear train.

A simplified representation of an electric car gearbox is illustrated in Fig. C.1. It is made of a single gear train where the input and output shafts have inertias J_{s1} and J_{s2} and the driving and driven gears have inertias J_{g1} and J_{g2}, respectively. Hence, the total inertias at the input and output are $J_1 = J_{s1} + J_{g1}$ and $J_2 = J_{s2} + J_{g2}$. The input shaft spins at an angular velocity Ω_1 and the output one at a velocity Ω_2, so that the gear ratio is $\rho = \Omega_2/\Omega_1$. The kinetic energy of the system is

$$\begin{aligned} \mathcal{T} &= \frac{1}{2} J_1 \Omega_1^2 + \frac{1}{2} J_2 \Omega_2^2 \\ &= \frac{1}{2}(J_1 + J_2 \rho^2)\Omega_1^2 \\ &= \frac{1}{2}(J_1/\rho^2 + J_2)\Omega_2^2. \end{aligned} \tag{C.1}$$

Hence, the equivalent inertia of the gear train expressed on the shaft that spins at Ω_1 (i.e. the input shaft) is $J_{1\text{eq}} = (J_1 + J_2\rho^2)$. Similarly, the equivalent inertia of the whole system evaluated at the output is $J_{2\text{eq}} = (J_1/\rho^2 + J_2)$. For gear ratios less than 1, which is the case in electric car gearboxes,

we have $J_{1\text{eq}} < J_{2\text{eq}}$. From this analysis, we can deduce that the equivalent inertia of a driveline is smaller when evaluated at the input.

Appendix D

Application of the method of multiple scales to a Duffing oscillator

The MMS is applied to the Duffing oscillator presented in section 2.5.1.1. We only consider terms up to order ϵ, so that we only need to introduce $t_0 = t$ (fast scale) and $t_1 = \epsilon t$ (slow scale) and to look for a solution of the from $x(t) = x_0(t_0, t_1) + \epsilon x_1(t_0, t_1)$. We give

$$\frac{\partial(\bullet)}{\partial t} = \frac{\partial(\bullet)}{\partial t_0} + \epsilon \frac{\partial(\bullet)}{\partial t_1}, \tag{D.1a}$$

$$\frac{\partial^2(\bullet)}{\partial t^2} = \frac{\partial^2(\bullet)}{\partial t_0^2} + 2\epsilon \frac{\partial^2(\bullet)}{\partial t_0 \partial t_1} + \mathcal{O}(\epsilon^2). \tag{D.1b}$$

In addition, we consider the the Duffing oscillator is weakly damped, weakly forced and weakly nonlinear, meaning that c, F and γ are of order ϵ. To make this explicit, it is convenient to introduce

$$c = \epsilon \tilde{c}, \quad F = \epsilon \tilde{F}, \quad \gamma = \epsilon \tilde{\gamma}. \tag{D.2}$$

Introducing the above in Eq. (2.44), grouping the terms by powers of ϵ and defining $D_0(\bullet) = \partial(\bullet)/\partial t_0$, $D_1(\bullet) = \partial(\bullet)/\partial t_1$, we obtain the system of two equations

$$D_0^2(x_0) + \omega_0^2 x_0 = 0, \tag{D.3a}$$

$$D_0^2(x_1) + \omega_0^2 x_1 = -2D_0 D_1(x_0) - \tilde{c} D_0(x_0) - \tilde{\gamma} x_0^3 + \tilde{F} \cos(\omega t_0). \tag{D.3b}$$

The general solution of Eq. (D.3b) is

$$x_0(t_0, t_1) = A(t_1) e^{i\omega_0 t_0} + [cc], \tag{D.4}$$

where A is a complex quantity, i is the imaginary number and $[cc]$ refers to the complex conjugate. We choose to look for solutions around the resonance ω_0 so that it is convenient to introduce the detuning σ as

$$\omega = \omega_0 + \epsilon \sigma. \tag{D.5}$$

Introducing Eq. (D.4) in Eq. (D.3b) and using $\cos(\omega t_0) = e^{i\sigma t_1}e^{i\omega_0 t_0}/2 + [cc]$, we obtain

$$D_0^2(x_1) + \omega_0^2 x_1 = \underbrace{\left[-2i\omega_0 D_1(A) - i\tilde{c}\omega_0 A - 3\tilde{\gamma}A^2\bar{A} + \frac{\tilde{F}e^{i\sigma t_1}}{2}\right]}_{\text{secular term}} e^{i\omega_0 t_0} - \tilde{\gamma}A^3 e^{3i\omega_0 t_0} + [cc], \tag{D.6}$$

where $(\bar{\bullet})$ denotes the conjugate of $(\bullet)$. In Eq. (D.6), it is interesting to see that x_0 acts as a forcing term in the equation on x_1. More specifically, x_1 is forced at frequencies ω_0 and $3\omega_0$. However, its resonance frequency is ω_0, so the forcing at frequency ω_0 makes x_1 explode. For the solution to be bounded, one needs the secular term to be null. Hence, the equation to be satisfied is

$$-2i\omega_0 D_1(A) - i\tilde{c}\omega_0 A - 3\tilde{\gamma}A^2\bar{A} + \frac{\tilde{F}e^{i\sigma t_1}}{2} = 0. \tag{D.7}$$

It is convenient to define the amplitude a and phase φ such that

$$A(t_1) = \frac{1}{2}a(t_1)e^{i\varphi(t_1)} \tag{D.8}$$

in order to describe the oscillator's motion through polar coordinates. Introducing Eq. (D.8) in Eq. (D.7) and grouping the real and imaginary terms, we obtain the two equations

$$\begin{cases} 4\omega_0 D_1(a) + 2\omega_0\tilde{c}a - 2\tilde{F}\sin(\sigma t_1 - \varphi) = 0, & \text{(D.9a)} \\ 4\omega_0 a D_1(\varphi) - \frac{3}{2}\tilde{\gamma}a^3 + 2\tilde{F}\cos(\sigma t_1 - \varphi) = 0. & \text{(D.9b)} \end{cases}$$

Phase φ does not have a physical meaning, so it is more convenient to use $\xi(t_1) = \sigma t_1 - \varphi(t_1)$, which corresponds to the relative phase between the response and the excitation, in order to write the solution as

$$x_0(t_0, t_1) = a(t_1)\cos(\omega_0 t_0 + \varphi(t_1)) = a(t_1)\cos(\omega t_0 - \xi(t_1)). \tag{D.10}$$

The equations governing $a(t_1)$ and $\xi(t_1)$ are

$$\begin{cases} D_1(a) = f_a(a, \xi), & \text{(D.11a)} \\ aD_1(\xi) = f_\xi(a, \xi), & \text{(D.11b)} \end{cases}$$

where functions $f_a(a, \xi)$ and $f_\xi(a, \xi)$ are defined as

$$f_a(a, \xi) = \frac{2\tilde{F}\sin(\xi) - 2\omega_0\tilde{c}a}{4\omega_0}, \tag{D.12a}$$

$$f_\xi(a, \xi) = \frac{2\tilde{F}\cos(\xi) - \frac{3}{2}\tilde{\gamma}a^3 + 4\omega_0\sigma a}{4\omega_0}. \tag{D.12b}$$

From the chain rule described in Eq. (D.1a), we have

$$\begin{cases} \frac{da}{dt} = \epsilon f_a(a, \xi), & \text{(D.13a)} \\ a\frac{d\xi}{dt} = \epsilon f_\xi(a, \xi). & \text{(D.13b)} \end{cases}$$

Now, we can use the procedure described in section 2.5.1.2 to compute the fixed points and their stability. The fixed points are

$$x(t) = a\cos(\omega t - \xi) \tag{D.14}$$

where a and ξ are such that

$$\sigma(a) = \frac{3\tilde{\gamma}a^2 \pm 4\sqrt{\tilde{F}^2/a^2 - \tilde{c}a^2}}{8\omega_0}, \tag{D.15a}$$

$$\tilde{F}(a) = a\sqrt{\frac{9}{16}\tilde{\gamma}^2 a^4 - 3\tilde{\gamma}\omega_0\sigma a^2 + 4\omega_0^2 + \tilde{c}^2\omega_0^2}, \tag{D.15b}$$

$$\sin(\xi) = \frac{\omega_0\tilde{c}a}{\tilde{F}}, \tag{D.15c}$$

$$\cos(\xi) = \frac{\frac{3}{4}\tilde{\gamma}a^3 - 2\omega_0\sigma a}{\tilde{F}}. \tag{D.15d}$$

The stability of these periodic solutions are assessed by evaluating the eigenvalues of the Jacobian associated to system (D.13). These eigenvalues are given by

$$\lambda_{1,2} = -\frac{\tilde{c}}{2} \pm \frac{\sqrt{-(3\tilde{\gamma}a^2 - 8\omega_0\sigma)(9\tilde{\gamma}a^2 - 8\omega_0\sigma)}}{8\omega_0}. \tag{D.16}$$

Appendix E

Maximising the inertia ratio of a centrifugal pendulum vibration absorber with spherical pendulums

E.1 Maximum number of pendulums for a given configuration

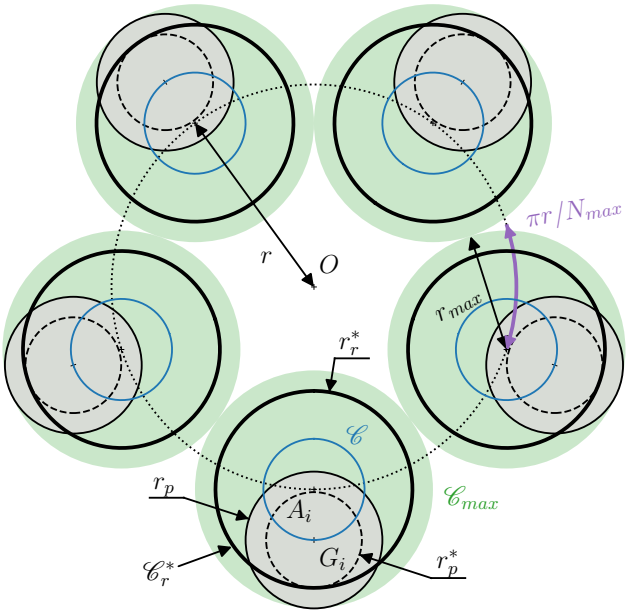

Figure E.1: Illustration of the procedure to compute the maximum number of pendulums that can be used for a given configuration.

Here, we are interested in the maximum number of pendulums N_{max} that can be used in a fixed configuration, i.e. without changing the dimensions and tracks of the system. The approach to

calculating N_{max} is illustrated in Fig. E.1 and detailed below. First of all, the path of the pendulums is considered circular. The path of the i^{th} pendulum $\mathscr{C}$ (in blue) is therefore a circle centred on A_i, of radius $r_r - r_p^*$, and the rotor's virtual track $\mathscr{C}_r^*$ (in black) is also a circle centred on A_i, of radius r_r^*. This choice of circular path makes it possible to simply introduce the surface swept by the i^{th} pendulum as being a circle of radius $r_r^* - r_p^* + r_p$ centred on A_i (green areas). The criterion chosen to restrict the maximum number of pendulums is to prevent shocks between these pendulums when they are in phase opposition (as is the case in subharmonic operation), which amounts to preventing the overlap of the green surfaces. Figure E.1 represents precisely the critical case where the $\mathscr{C}_{max}$ circles delimiting the scanned surfaces are tangent. A good approximation of the maximum radius of these circles is $r_{max} \leq \pi r/N_{max}$, which can be written as

$$r_r^* - r_p^* + r_p \leq \pi r/N_{max}. \tag{E.1}$$

We can then define the maximum number of pendulums such that

$$N_{max} \leq \frac{\pi r}{r_r^* - r_p^* + r_p}. \tag{E.2}$$

It should be noted that this approximation of the maximum number of pendulums is more accurate when the radius of the pendulums is small in front of r. Indeed, in such configurations, the maximum number of pendulums is high, and the circle of centre O and radius r intersects $\mathscr{C}_{max}$ closer to the tangency point. The criterion $r_{max} \leq \pi r/N_{max}$ is then more precise.

E.2 Evolution of the inertia ratio with the pendulums' radius

The aim here is to analyse the evolution of different characteristics of the system as a function of the radius of the pendulums r_p. To do this, the procedure is as follows:

- A circle of radius R_{max} centred on O is introduced, inside which all the pendulums must be contained (R_{max} thus defines the available space). They are placed as far as possible from O in order to increase their moment of inertia with respect to O, which results in $R_0 = R_{max} - r_p$.
- All parameters independent of r_p are fixed. This includes the inclination of the v-shaped tracks θ_t, the tuning order n_p and the rotor's inertia J_r.
- The chosen path is the epicycloid $X(S) = R_0^2 - n_t^2 S^2$ whose distance R_0 evolves as explained above.
- The number of pendulums used by the system is maximal, i.e. $N = N_{max}$ is chosen using Eq. (E.2). In this equation, r_r^* is the radius of curvature of $\mathscr{C}_r^*$ associated with $S = 0$, i.e. $r_r^* = r_p^* + \ell$, and r and ℓ are obtained using the definition $n_t = \sqrt{r/\ell}$ and $R_0 = r + \ell$.

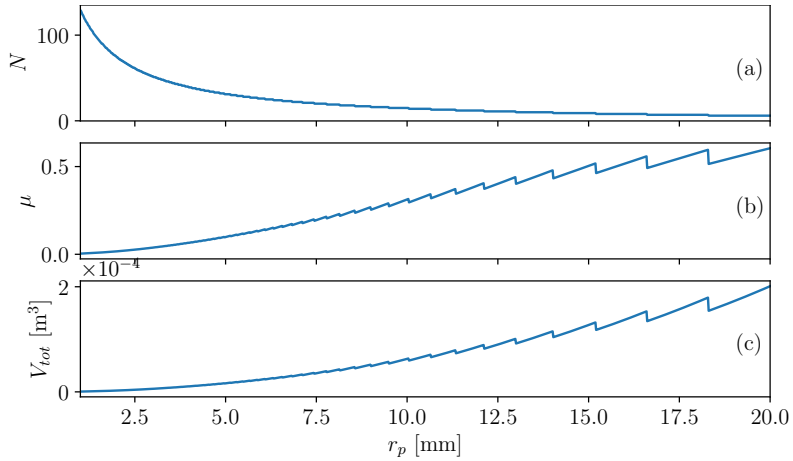

Figure E.2: Evolution of (a) N, (b) μ and (c) V_{tot} (volume occupied by the pendulums) as a function of r_p. $n_p = 10$, $R_{max} = 60$ [mm], $J_r = 4$ [g.m^2], $\rho = 8000$ [kg/m^3], $\cos\theta_t = 0.7$.

Figure E.2 shows the evolution of N, μ and the volume occupied by the pendulums as a function of r_p. Each of the curves evolves discontinuously because the number of pendulums N is an integer. Logically, Fig. E.2(a) shows that the maximum number of pendulums decreases with r_p because the pendulums get bigger and bigger while the space in which they must fit remains fixed.
Figure E.2(b) shows the inertia ratio μ increases with the radius of the pendulums, even though the total number of pendulums decreases. This is because the mass of the pendulums is proportional to r_p^3, so a small increase in the radius of the pendulums causes a large increase in their mass. It is also interesting to note that the calculation of N_{max} is based solely on the space requirement in the rotor's plane whereas increasing r_p also increases the space requirement out of this plane. The use of large-radius pendulums therefore increases the total mass of the pendulums, but not the space required in the rotor's plane. This is clearly visible in Fig. E.2(c) which shows that the volume occupied by the pendulums increases with r_p.

Appendix F

A python code for the automatised implementation of the method of multiple scales

F.1 Minimal working example: the Duffing oscillator

We propose to present briefly the python code that automatises the method of multiple scales (MMS) through a minimal working example: the resolution of the Duffing equation [161]

$$\ddot{x} + c\dot{x} + \omega_0^2 x + \gamma x^3 = F\cos\omega t, \tag{F.1}$$

where x is the displacement of the oscillator, c, ω_0 and γ are its damping, natural frequency and nonlinear coefficient, respectively, and F and ω are the amplitude and the frequency of the forcing, respectively. A script to solve this equation is given below:

```
from sympy import (symbols, Function)
from sympy.physics.vector.printing import init_vprinting
import Func_MMS_Nddl

init_vprinting(use_latex=True)

#%% Description of the problem

# Definition of quantities
omega0, eps = symbols(r'\omega_0, \epsilon',real=True,positive=True)
gamma       = symbols(r'\gamma',real=True)
t           = symbols('t')
x           = Function('x')(t)
ddx         = x.diff(t,2)

```

```
16 # Duffing equation
17 Eq_Duff = ddx + omega0**2*x + eps*gamma*x**3
18
19 #%% Application of the MMS
20 Ne = 4 # order of the expansions
21 Eqs = [Eq_Duff]
22 var = [x]
23 kwargs = dict(forcing='forced', damping='damped', sol_SS=True)
24
25 MMS, SS = Func_MMS_Nddl.apply_MMS(Eqs, eps, Ne, t, var, omega0, **kwargs)
26
27 # Extract the results
28 c, F, sigma = list(map(MMS.get,['c','F','sigma']))
29 keys        = ['a','beta','fa','fbeta','sol_sigma_bbc',
30                'sol_sigma','sin_beta','cos_beta']
31 values      = list(map(SS.get,keys))
32 a, beta, fa, fbeta, sig_bbc, sig_a, sin_beta, cos_beta = values
```

The script is described below:

- In lines 1 to 3, the modules necessary to the script are imported. `sympy` is Python's symbolic mathematics module, from which we import the functions `symbols` and `Function`, which allow to define parameters and variables. `init_vprinting` is only used to control the display. Indeed, at line 5, one can see that it takes as argument `use_latex=True`, meaning that `sympy` expressions will be printed like math expressions in latex. `Func_MMS_Nddl` contains all the necessary functions to apply the MMS to N degree-of-freedom systems and is described in details in section F.2. With the current version, these systems cannot exhibit internal resonances other than 1:1:...1.

- Parameters and variables are defined in lines 10 to 14. Note that `eps` is the small parameter ϵ to be used in the MMS (*cf.* Appendix D) and `ddx` is $\ddot{x}$.

- The duffing equation is written in line 17. ϵ is used in this equation to indicate that the nonlinearity is small. The forcing and damping are not included in this equation, they will be added later.

- Lines 20 to 23 prepare the call of function `apply_MMS`, which applies the MMS. `Ne` is the order of the expansions used in the MMS. That is, every term that appears at orders larger than ϵ^{N_e} are neglected. `Eqs` is a list containing the equations of the system. In the present case, there is a single equation as the Duffing oscillator is a 1 degree-of-freedom system. In the same way, `var` is a list containing the unknowns of the system. `kwargs` is a dictionary containing the keyword arguments to be passed to `apply_MMS`. `forcing='forced'` means that we want to

include forcing in the equation. The default forcing is $f(t) = F\cos(\omega t)$, but more complex forms, such as parametric forcing, can be included using other keyword arguments. `damping='damped'` means that we want to account for damping. This adds a viscous damping term $c\dot{x}$ in the equation. `sol_SS=True` means that we will look for a steady-state solution of the equation.

- Function `apply_MMS` is called in line 25. In the arguments, passing `omega0` means that the MMS is applied around ω_0, that is to say, $\omega = \omega_0 + \epsilon\sigma$ where σ is a detuning term. This function returns the dictionaries `MMS` and `SS`, which contain the results of the application of the MMS and their evaluation at steady state, respectively.
- Several items are extracted from the dictionaries in lines 28 to 32. a and β are the amplitude and phase of the response such that

$$x = a\cos(\omega t - \beta). \tag{F.2}$$

`fa` and `fbeta` contain the expression of functions f_a and f_β, which govern a and β such that

$$\begin{cases} 0 = f_a(a,\beta), & \text{(F.3a)} \\ 0 = f_\beta(a,\beta). & \text{(F.3b)} \end{cases}$$

Note that if steady state was not assumed, these functions would govern the evolution of a and β with time such that

$$\begin{cases} \dfrac{da}{dt} = f_a(a,\beta), & \text{(F.4a)} \\ a\dfrac{d\beta}{dt} = f_\beta(a,\beta). & \text{(F.4b)} \end{cases}$$

`sig_bbc` contains the expression of the backbone curve of the oscillator. `sig_a` contains the expression of the forced response of the oscillator under the form $\sigma(a)$. The forced response is complete with `sin_beta` and `cos_beta`, which contain the expression of $\sin\beta$ and $\cos\beta$, respectively. Note that dictionaries `MMS` and `SS` contain a lot more items than those extracted here.

One of the results of the script described above is the backbone curve

$$\omega_{\text{bbc}} = \omega_0 + \epsilon\sigma_{\text{bbc}} = \omega_0 + \frac{3\epsilon\gamma a^2}{8\omega_0} - \frac{15\epsilon^2\gamma^2 a^4}{256\omega_0^3} + \frac{123\epsilon^3\gamma^3 a^6}{8192\omega_0^5} - \frac{921\epsilon^4\gamma^4 a^8}{262144\omega_0^7}. \tag{F.5}$$

It took 204 seconds to run the code on a regular laptop whereas it would definitively have taken much longer to do the computations by hand. This would be even more true when solving complicated nonlinear equations, such as the ones derived in chapter 10. The scripts `Duffing.py` and `Func_MMS_Nddl.py`, which allow to test the example, are provided in the supplementary materials.

F.2 Description of the module `Func_MMS_Nddl`

`Func_MMS_Nddl` contains 10 functions described briefly below (more informations are provided in the script `Func_MMS_Nddl.py` via comments).

- `apply_MMS` is the main function of the module. It calls calls successively the different functions necessary to the application of the MMS and returns the result.
- `init_MMS` initialises the equations to apply the MMS. It is this function that creates the time scales and expands the unknowns.
- `Equations_MMS` computes the equations at each order of ϵ. It is also in this function that the damping and forcing can be added.
- `sol_EqOi` computes the secular terms and solves the equations at each order. This is where most of the computations are done.
- `modulation_equations` computes the modulation equations from the secular terms. It is here that variables $a(t)$ and $\beta(t)$ are introduced and that functions f_a and f_β are computed.
- `eval_SS` evaluates the modulation equations at steady state and solves them if desired.
- `Chain_rule_dfdt` applies the chain rule to transform first-order time derivatives into derivatives in terms of the time scales. This function is used in `init_MMS`.
- `Chain_rule_ddfdt2` applies the chain rule to transform second-order time derivatives into derivatives in terms of the time scales. This function is used in `init_MMS`.
- `collect_PDE` is a workaround to the the `sympy` function `collect`, which does not work when applied to an expression containing partial derivatives in different variables. This function is used in `sol_EqOi`.
- `solve_poly_2` is a workaround to the `sympy` function `solve`, which can take a very long time to compute the solution of a second-order polynomial if the coefficients of this polynomial have long expressions. This function is used in `eval_SS`.

Résumé Français

Contenu

1 Introduction et généralités

1.1 Sources de vibrations

Dans le contexte de normes environnementales de plus en plus strictes, les constructeurs automobiles doivent s'adapter pour développer des véhicules moins polluants. Dans ce but, une première solution est de réduire la taille des moteurs thermiques. Cependant, la réduction de la taille du moteur augmente son acyclisme, provoquant des vibrations de torsion plus importantes de la chaîne cinématique [3]. L'acyclisme d'un moteur thermique est illustré en Fig. 1, où l'on voit que le couple $T(\vartheta)$ fournit par le moteur varie énormément en fonction de la position angulaire ϑ du vilebrequin. Le couple total peut se décomposer en une partie constante T_0, utile au mouvement du véhicule, et une partie fluctuante $T_\theta(\vartheta)$, indésirable car source de vibrations de torsion de la chaîne cinématique, tel que

$$T(\vartheta) = T_0 + T_\theta(\vartheta). \tag{1}$$

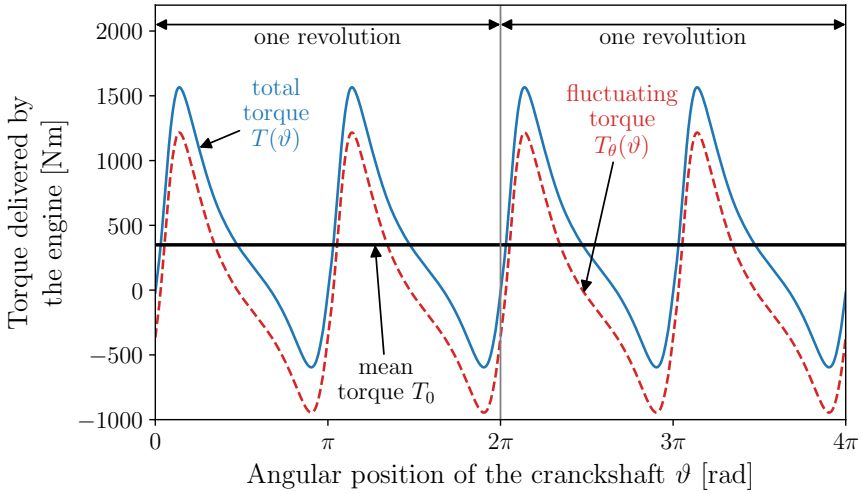

Figure 1: Couple caractéristique délivré par un moteur à quatre temps, quatre cylindres, pour une vitesse de 1000 [tr/min].

Une autre solution pour réduire les émissions polluantes de véhicules est de s'orienter vers des motorisations électriques. Les moteurs électriques fournissent généralement un couple presque constant, de telle manière que les vibrations qu'ils génèrent sont souvent négligeables. Cependant, les erreurs de transmission dues à la flexibilité des engrenages constituant la boîte de transmission causent des fluctuations du couple transmit par ces engrenages, générant des vibrations de torsion non négligeables [5]. Il est à noter que cette source de vibration existait déjà dans la boîte de vitesse de motorisations thermiques, mais elle était masquée par le moteur qui génère des fluctuations de couple bien plus importantes. Le couple transmit par un train d'engrenages prend la même forme que le couple acyclique généré par un moteur thermique, donné par l'Eq. (1) et représenté en Fig. 1. Dans le cas d'un train

d'engrenage, ϑ représente la position angulaire de l'un des deux engrenages.

Que ce soit dans une motorisation thermique ou électrique, le couple $T(\vartheta)$ est périodique en ϑ et sa fréquence fondamentale s'exprime

$$\omega_e = n_e \dot{\vartheta} \approx n_e \Omega \tag{2}$$

où n_e est l'ordre d'excitation, $\dot{\vartheta}$ est la vitesse de rotation instantanée ($\dot{(\bullet)} = \partial(\bullet)/\partial t$ où t est le temps), et Ω est la vitesse de rotation moyenne. La période de $T(\vartheta)$ est $2\pi/n_e$. L'ordre d'excitation n_e dépend du système considéré. Pour un moteur thermique, n_e correspond au nombre d'explosions par révolution et son ordre de grandeur est $n_e \sim 2$. Dans un train d'engrenage, n_e correspond au nombre de dents de l'engrenage dont la position est notée ϑ, et on a typiquement $n_e \sim 20$. $T(\vartheta)$ peut être décomposé en une série de Fourier d'ordre fondamental n_e tel que

$$T(\vartheta) = T_0 + \sum_{k=1}^{\infty} T_{ck} \cos(k n_e \vartheta) + T_{sk} \sin(k n_e \vartheta), \tag{3}$$

où T_{ck} et T_{sk} sont les coefficients de Fourier. L'équation (4) met en évidence que la partie fluctuante du couple, $T_\theta(\vartheta)$, contient plusieurs harmoniques. Il est intéressant de noter que l'on peut également décomposer $T(t)$ en une série de Fourier en utilisant l'approximation $\omega_e \approx n_e \Omega$ afin d'écrire

$$T(t) \approx T_0 + \sum_{k=1}^{\infty} T_{ck} \cos(k \omega_e t) + T_{sk} \sin(k \omega_e t). \tag{4}$$

On voit via l'Eq. (2) que la fréquence d'excitation dépend (quasiment) linéairement de la vitesse de rotation moyenne. De plus, la chaîne cinématique est un ensemble complexe contenant de nombreux modes de vibration à des fréquences fixes. Ainsi, lorsque l'automobiliste accélère ou décélère, il fait varier ω_e, ce qui peut générer des résonances de la chaîne cinématique. Ces situations de résonance, générant des niveaux de vibration inacceptables, sont illustrées en Fig. 2 pour un groupe motopropulseur thermique avec deux configurations de rapport de vitesse engagé (l'un en bleu, l'autre en rouge). Cette figure prend en compte les résonances rencontrées à cause des quatre premiers harmoniques du couple $T_\theta(\vartheta)$. Toutefois, en pratique, l'harmonique 1 est de loin la plus gênante car elle possède la plus grande amplitude. Par la suite, on s'intéressera à réduire les vibrations générées par cette harmonique fondamentale.

1.2 L'absorbeur pendulaire centrifuge

Les absorbeurs pendulaires centrifuges (APCs) sont utilisés depuis près d'un siècle pour contrebalancer l'acyclisme de moteurs thermiques. Ils sont constitués de N masses (pendules) oscillant par rapport à un rotor, comme illustré en Fig. 3. Les pendules sont tous identiques, de masse m et d'inertie I, et suivent une trajectoire notée $\mathscr{C}$ (en bleu). Leur position le long de cette trajectoire est

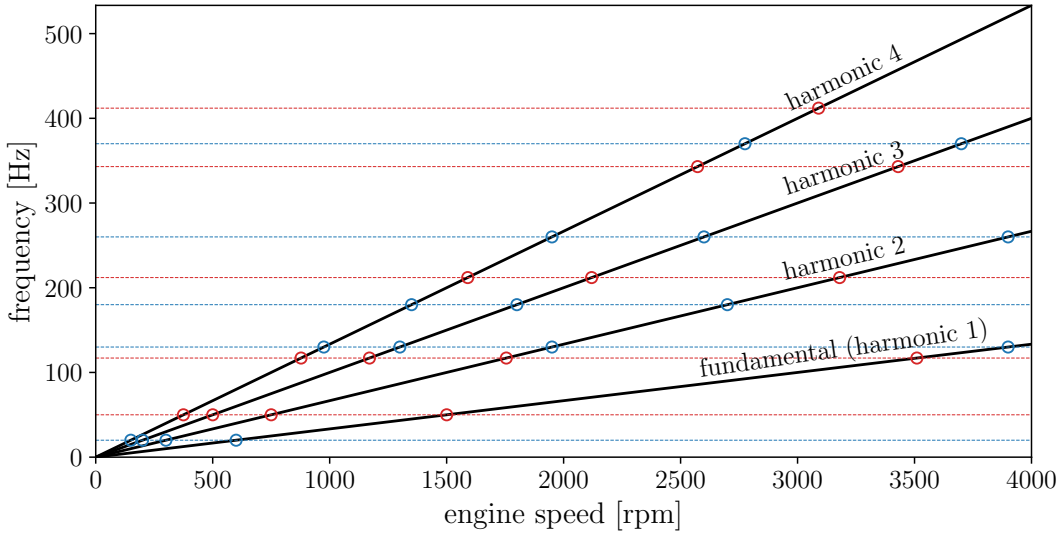

Figure 2: Illustration des nombreux points critiques (cercles) correspondants à une résonance de la chaîne cinématique via l'intersection des harmoniques de l'excitation (en noir) avec les modes de la chaîne cinématique (lignes pointillées). Deux configurations de la chaîne cinématique sont représentées, l'une en bleu et l'autre en rouge, correspondant à des rapports de transmission différents.

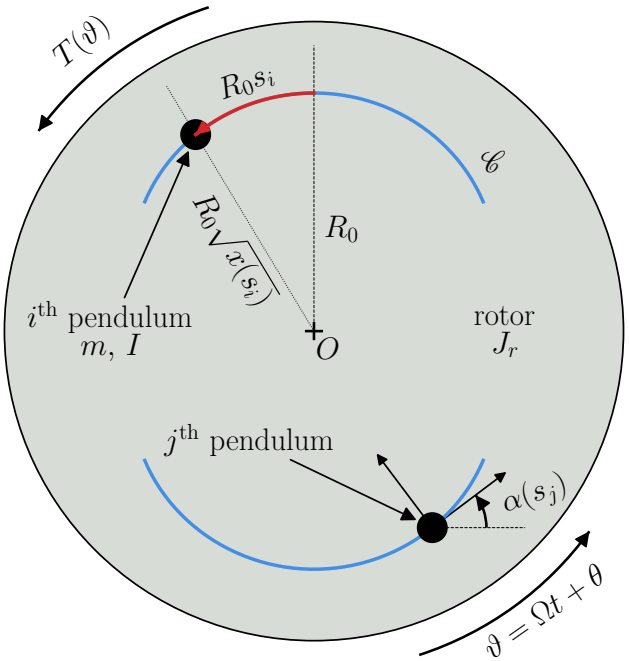

Figure 3: Représentation d'un APC constitué de deux pendules. Les courbes bleues représentent la trajectoire des pendules.

repérée via l'abscisse curviligne sans dimension s_i. Dans leur position de repos (i.e. pour $s_i = 0$), les pendules sont à une distance R_0 du centre du rotor. La forme de la trajectoire est contrôlée via la fonction $x(s_i)$. L'un des apports importants de cette thèse est de prendre en compte la rotation des pendules par rapport au rotor, notée $\alpha(s_i)$. Le rotor possède une inertie J_r et sa position angulaire est $\vartheta(t) = \Omega t + \theta(t)$, où $\theta(t)$ capture les vibrations de torsion. Ces vibrations sont dues au couple $T(\vartheta) = T_0 + T_\theta(\vartheta)$ appliqué sur le rotor.

L'intérêt de l'utilisation d'absorbeurs pendulaires est que leur fréquence propre ω_p est proportionnelle à la vitesse de rotation moyenne Ω du système, tout comme la fréquence fondamentale de l'excitation ω_e. Ceci est dû au fait que les pendules évoluent dans un champ d'accélération centrifuge plutôt que dans le champ de la gravité (cette hypothèse est valide à partir de $\Omega = 800$ [tr/min] environ). Ainsi, en accordant les pendules tel que $\omega_p = \omega_e$, ils réduisent très fortement les vibrations du rotor sur toute la plage de régime de fonctionnement de la machine. Cette réduction de vibration se fait par la génération d'une antirésonance (i.e. d'un minimum de vibration) du rotor à ω_p. Le coefficient de proportionnalité entre ω_p et Ω est l'ordre d'accord des pendules n_p, tel que l'on peut écrire

$$\omega_p = n_p \Omega. \tag{5}$$

C'est donc en choisissant n_p tel que $n_p = n_e$ que l'on assure $\omega_p = \omega_e$ (*cf.* Eq. (2)).

Le choix de n_p s'effectue via un contrôle précis des fonctions de trajectoire $x(s_i)$ et de rotation $\alpha(s_i)$ des pendules. Dans cette thèse, on choisit d'exprimer ces fonctions sous la forme

$$x(s_i) = 1 - n_t^2 s_i^2 + x_{[4]} s_i^4, \tag{6a}$$

$$\alpha(s_i) = \alpha_{[1]} s_i + \alpha_{[3]} s_i^3, \tag{6b}$$

où n_t et $x_{[4]}$ sont des coefficients de trajectoire et $\alpha_{[1]}$ et $\alpha_{[3]}$ sont des coefficients de rotation. Le cas $x_{[4]} = \alpha_{[3]} = 0$ est particulièrement intéressant car il correspond au cas d'une trajectoire épicycloïdale et d'une loi de rotation linéaire. La trajectoire épicycloïdale a longtemps été préférée car, pour des pendules purement translatés et découplés du rotor, elle mène à un comportement tautochrone des pendules. C'est-à-dire que leur période d'oscillation ne dépend pas de l'amplitude de leur mouvement, ce qui en fait des oscillateurs linéaires. L'ajout d'une mobilité de rotation suivant une loi linéaire ne vient pas perturber le comportement linéaire des pendules. L'ajout des coefficients $x_{[4]}$ et $\alpha_{[3]}$ correspond à l'introduction intentionnelle de non-linéarités. Cela permet de compenser les non-linéarités issues du couplage non-linéaire entre les pendules et le rotor. Les paramètres d'accord d'un APC sont l'ordre d'accord n_p, qui joue le rôle d'un paramètre d'accord linéaire, et un paramètre d'accord non-linéaire c_p, permettant d'améliorer les performances du système à de grandes amplitudes de mouvement. L'expression de ces paramètres est

$$n_p = \frac{n_t}{\sqrt{1 + \eta \alpha_{[1]}^2}}, \quad c_p = 3(x_{[4]} + 2 n_p^2 \eta \alpha_{[1]} \alpha_{[3]}), \tag{7a}$$

où $\eta = I/mR_0^2$ est l'inertie sans dimension d'un pendule. Il est intéressant de noter que n_p ne dépend que des coefficients n_t et $\alpha_{[1]}$, qui gouvernent le comportement linéaire, alors que c_p dépend en plus de $x_{[4]}$ et $\alpha_{[3]}$, qui contrôlent le comportement non-linéaire. Le designer peut donc utiliser n_t et $\alpha_{[1]}$ pour choisir n_p, puis, dans un second temps, utiliser $x_{[4]}$ et $\alpha_{[3]}$ pour choisir c_p.

1.3 Analyse linéaire d'un absorbeur pendulaire centrifuge

Un APC possède $N+1$ degrés de liberté (le rotor et les N pendules). Les équations du mouvement sans dimension conservatives linéarisées gouvernant ce système sont données par

$$(1+\mu)\theta'' + \frac{\mu\Lambda_c}{N}\sum_{i=1}^{N} s_i'' = \bar{T}_\theta(\tau), \tag{8a}$$

$$\Lambda_c\theta'' + \Lambda_m s_i'' + n_t^2 s_i = 0, \quad i = 1, ..., N, \tag{8b}$$

où μ est un ratio d'inertie (typiquement $\mu \ll 1$), Λ_c est un terme de couplage linéaire entre un pendule et le rotor, Λ_m représente une masse équivalente de pendule, $\bar{T}_\theta$ est le couple fluctuant sans dimension, τ est le temps sans dimension et $(\bullet)' = \partial(\bullet)/\partial\tau$. Ces paramètres sans dimension sont définis tel que

$$\mu = \frac{NmR_0^2}{J_r + NI}, \quad \Lambda_c = 1 + \eta\alpha_{[1]}, \quad \Lambda_m = 1 + \eta\alpha_{[1]}^2, \quad \bar{T}_\theta(\tau) \approx \bar{T}_\theta(\vartheta) = \frac{T_\theta(\vartheta)}{(J_r + NI)\Omega^2}, \quad \tau = \Omega t. \tag{9}$$

Il est à noter que la rotation des pendules (visible ici via $\alpha_{[1]}$) influe le couplage linéaire pendule/rotor et la masse équivalente d'un pendule, ce qui peut être utilisé pour améliorer les performances de l'APC (*cf.* section 2.2.4).

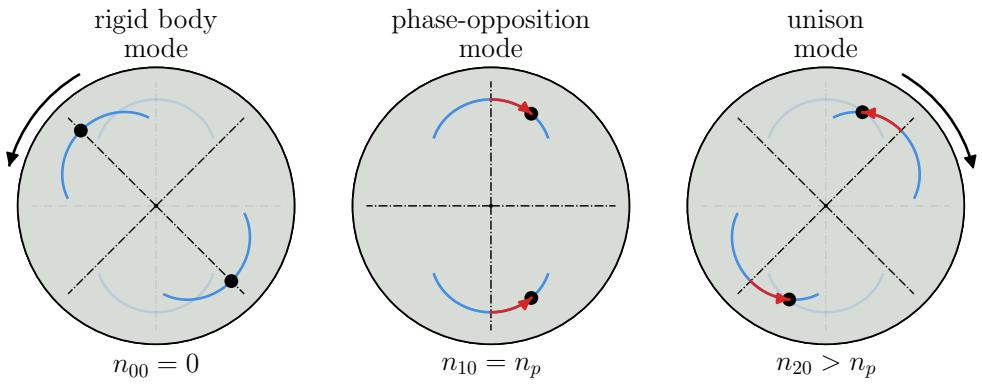

Figure 4: Modes d'un APC composé de $N = 2$ pendules. La rotation des pendules autour de leur centre de masse n'est pas représentée sur cette figure.

Le problème aux valeurs propres associé aux système (8) est

$$[\boldsymbol{K} - n^2\boldsymbol{M}]\boldsymbol{\phi} = \boldsymbol{0}, \tag{10}$$

où $\boldsymbol{M}$ et $\boldsymbol{K}$ sont les matrices de masse et de raideur du système. Les solutions, composées d'un ordre propre n et d'une forme propre $\boldsymbol{\phi}$, sont les modes du système. Il est à noter que les solutions n peuvent être vues comme une fréquence propre sans dimension. En résolvant le problème aux valeurs propres, on obtient les $N+1$ modes linéaires $(n_{00}, \boldsymbol{\phi_{00}})$, $(n_{10}, \boldsymbol{\phi_{10_1}})$, ..., $\left(n_{10}, \boldsymbol{\phi_{10_{N-1}}}\right)$, $(n_{20}, \boldsymbol{\phi_{20}})$, dont les ordres propres et les déformées modales sont

$$\begin{aligned} n_{00} = 0, \quad \boldsymbol{\phi_{00}} = [1, 0, ..., 0]^\intercal, \\ n_{10} = n_p, \quad \boldsymbol{\phi_{10_1}} = [0, 1, -1, 0..., 0]^\intercal, \ ..., \ \boldsymbol{\phi_{10_{N-1}}} = [0, 0, ...0, 1, -1]^\intercal, \\ n_{20} = n_p \sqrt{\frac{1+\mu}{1+\mu\left(1-\frac{\Lambda_c^2}{\Lambda_m}\right)}}, \quad \boldsymbol{\phi_{20}} = \left[-\frac{\mu\Lambda_c}{1+\mu}, 1, ..., 1\right]^\intercal, \end{aligned} \tag{11}$$

où l'exposant $^\intercal$ indique la transposée. Ces modes sont illustrés en Fig. 4 pour un APC composé de $N = 2$ pendules. $(n_{00}, \boldsymbol{\phi_{00}})$ est un mode de corps rigide pour lequel seul le rotor est excité. Les $(n_{10}, \boldsymbol{\phi_{10_i}})$ sont $N-1$ modes dégénérés pour lesquels seuls deux pendules se déplacent en opposition de phase, les autres restant immobiles. Leur valeur propre $n_{10} = n_p$ est de multiplicité $N-1$ et le rotor est un nœud de ces modes. Pour un APC composé de seulement deux pendules, $(n_{10}, \boldsymbol{\phi_{10}})$ n'est pas dégénéré et représente simplement un mouvement d'opposition de phase des pendules. Le mode $(n_{20}, \boldsymbol{\phi_{20}})$ est un mode pour lequel les pendules se déplacent à l'unisson mais en opposition de phase par rapport au rotor (à condition que $\Lambda_c > 0$, ce qui est le cas pour des paramètres raisonnables). On l'appellera le "mode unisson" ou le "mode 2".

Dans cette section, nous supposons que le couple appliqué sur le rotor ne contient que l'harmonique fondamentale tel que $\bar{T}_\theta(\tau) = \bar{T}_1 \cos(n\tau)$ et nous analysons la réponse forcée linéaire du système. Notons qu'en pratique, $n = n_e$ est fixe, mais il est pratique de faire varier n afin de mieux comprendre la dynamique d'un APC en obtenant une courbe qui peut être interprétée comme une fonction de réponse en fréquence. Le calcul de la réponse forcée de l'APC conduit à des solutions de la forme

$$\theta'' = h_1 \cos(n\tau - \psi_1), \quad s_i = s = a\cos(n\tau - \xi), \quad i = 1, ..., N, \tag{12}$$

où h_1, ψ_1, a et ξ sont les amplitudes et les phases de l'accélération du rotor et du mouvement des pendules, respectivement.

Les pendules génèrent une antirésonance sur le rotor à l'ordre $n_{AR} = n_p$. Cette antirésonance est visible en Fig. 5(a), qui représente l'amplitude du rotor en fonction de l'ordre d'excitation. Comme l'objectif est de réduire au maximum l'amplitude des fluctuations θ au point de fonctionnement $n = n_e$ (on rappelle que dans un système réel, l'excitation se fait à un ordre fixe n_e, *cf.* section 1.1), il est judicieux de choisir de régler les pendules de telle sorte que $n_p = n_e$, d'où le nom "ordre d'accord" attribué à n_p. De plus, si $n_p = n_e$ tel que le rotor est excité sur son antirésonance pour toutes les vitesses de rotation, il est recommandé de minimiser au maximum l'amortissement du système pour

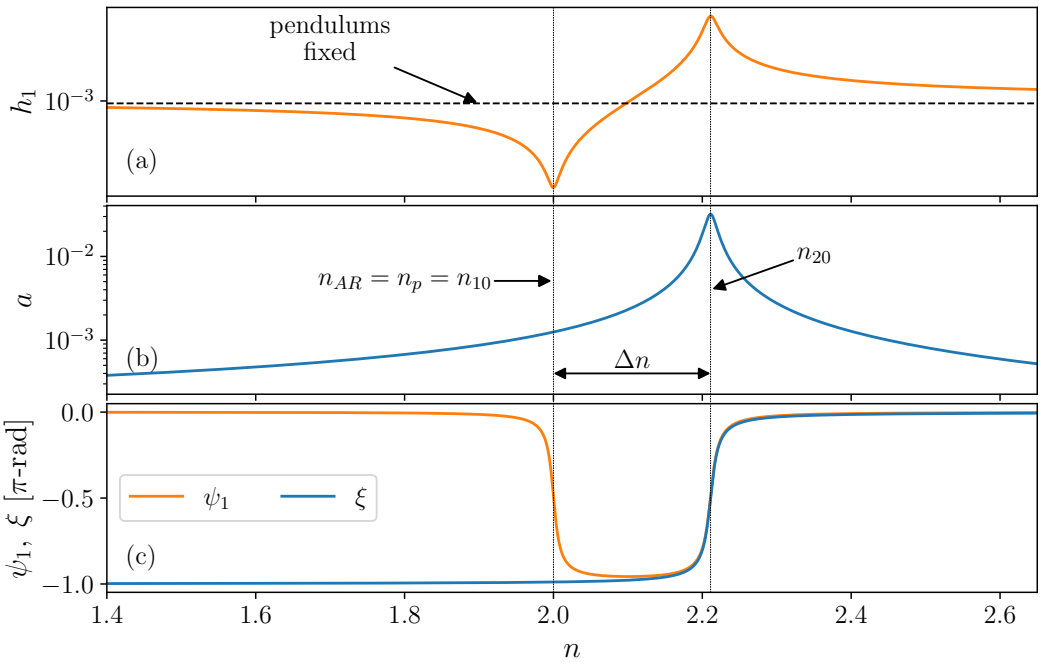

Figure 5: Réponse linéaire d'un APC constitué de deux pendules accordés à l'ordre 2. Les amplitudes du rotor et des pendules sont représentées respectivement en (a) et (b), tandis que leurs phases sont indiquées en (c). Dans (a), la ligne pointillée noire horizontale correspond à la réponse du rotor lorsque les pendules sont fixes. *Deltan* est un indicateur de performance utilisé dans la section 2.2.4. $n_p = 2$, $\mu = 0,1$, $\eta = 1$, $\alpha_{[1]} = 1$, $\bar{T}_1 = 0,001$. Les coefficients d'amortissement des pendules et du rotor sont fixés à $\bar{b} = 0,025$ et $\bar{b}_r = 0,002$, respectivement

avoir des vibrations du rotor presque nulles. En Fig. 5(a), la réponse du rotor est comparée au cas avec des pendules fixes. La comparaison avec des pendules fixes permet de tenir compte de l'inertie qu'ils ajoutent au système, elle est donc plus pertinente que la comparaison avec le cas sans pendule.

En Fig. 5(b), on peut voir que les pendules répondent uniquement sur le mode unisson (en effet, il n'y a pas de pic de résonance proche de l'ordre propre $n = n_{10}$). Ceci est dû au fait que le rotor est un nœud des modes 1, de sorte que ces modes ne sont pas excités par le couple externe (*cf.* Eq. (11)). En observant les Figs. 5(a) et (c), on peut voir que les pendules réduisent les vibrations du rotor lorsqu'ils sont en opposition de phase par rapport au couple externe (c'est-à-dire avant la résonance), mais qu'ils agissent comme des amplificateurs lorsqu'ils sont en phase avec lui (c'est-à-dire après la résonance).

1.4 Objectifs et contributions

Cette thèse comporte deux objectifs principaux :

- Augmenter l'efficacité des absorbeurs pendulaires actuellement utilisés dans l'industrie en se con-

centrant particulièrement sur leurs limitations actuelles et sur des principes de fonctionnement originaux ;

- Adapter les absorbeurs pendulaires actuellement utilisés dans des véhicules thermiques à des véhicules électriques via la proposition d'architectures originales.

Pour mener à bien ces objectifs, plusieurs axes de recherche ont été étudiés. Le premier axe est l'étude de l'accord classique d'un APC, qui correspond à un accord tel que $n_p \approx n_e$. C'est cette configuration qui est actuellement utilisée dans l'industrie, et elle nécessite d'être améliorée pour satisfaire les besoins des moteurs thermiques les plus récents. Le second axe est l'accord sous-harmonique de l'APC, qui correspond à $n_p \approx n_e/2$. Cette configuration, beaucoup moins étudiée dans la littérature que la précédente, permet également de filtrer un couple via la création d'une antirésonance purement non-linéaire. Le facteur deux entre n_p et n_e permet de filtrer des ordres élevés et peut donc s'avérer utile à l'adaptation d'APCs à des motorisations électriques. Le dernier axe de recherche est l'utilisation d'absorbeurs à double pendules centrifuges (ADPCs) à la place d'APCs. Ces systèmes, encore très peu étudiés, permettent plus de flexibilité d'accord et pourraient donc s'avérer utiles dans l'adaptation d'absorbeurs pendulaires à des véhicules électriques.

Les principales contributions de cette thèse sont listées ci-dessous :

- Prise en compte et optimisation de la mobilité de rotation des pendules ;
- Étude approfondie de l'accord sous-harmonique, menant à une réponse purement non-linéaire ;
- Étude du phénomène non-linéaire de localisation d'énergie, qui mène des pendules identiques à osciller différemment (accord classique et sous-harmonique) ;
- Étude du désaccord non-linéaire de l'antirésonance générée par les pendules sur le rotor (accord classique et non-linéaire) ;
- Proposition de règles de design analytiques pour profiter au maximum de la rotation des pendules et pour éviter la localisation et le désaccord de l'antirésonance, améliorant ainsi les performances de l'APC ;
- Étude linéaire et non-linéaire d'un ADPC ;
- Proposition de règles de design analytiques pour éviter la localisation et le désaccord des antirésonances d'un ADPC, améliorant ainsi grandement ses performances ;
- Proposition de prototypes originaux d'APC et d'ADPC ;
- Études expérimentales d'APC et d'ADPC validant en partie les résultats théoriques.

Ces contributions sont détaillées dans les sections suivantes.

2 Accord classique d'un absorbeur pendulaire centrifuge

On présente ici une synthèse des principaux résultats des chapitres 3, 4 et 5, constituant la partie II de ce rapport. Dans cette partie, le système considéré est l'absorbeur pendulaire centrifuge (APC, ou "CPVA" en anglais pour "centrifugal pendulum vibration absorber") décrit dans les chapitres 1 et 2. Dans un souci d'exhaustivité, une brève description du système est rappelée ici. Il est constitué d'un rotor sur lequel sont fixés N pendules oscillant le long de leur trajectoire et tournant autour de leur centre de masse, comme illustré en Fig. 6. Le système est excité par un couple contenant une partie constante et une partie périodique. Pour simplifier l'analyse, nous considérons que le couple fluctuant contient une seule harmonique d'amplitude $\bar{T}_1$ et d'ordre n. Bien que dans ce résumé nous considérons un système composé de $N = 2$ pendules pour des raisons de simplicité, la plupart des résultats dérivés dans la partie II sont valables quel que soit le nombre de pendules.

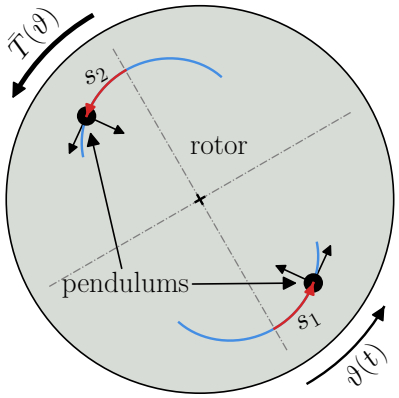

Figure 6: Illustration d'un APC composé de $N = 2$ pendules. Les repères noirs attachés aux pendules représentent leur rotation par rapport au rotor.

La trajectoire et la loi de rotation des pendules sont gouvernés par les fonctions

$$x(s_i) = 1 - n_t^2 s_i^2 + x_{[4]} s_i^4, \tag{13a}$$

$$\alpha(s_i) = \alpha_{[1]} s_i + \alpha_{[3]} s_i^3, \tag{13b}$$

où s_i représente l'abscisse curviligne du i$^{\text{ème}}$ pendule (*cf.* Fig. 6), n_t, $x_{[4]}$ sont des paramètres de trajectoire et $\alpha_{[1]}$, $\alpha_{[3]}$ sont des paramètres de rotation. Il s'avère que le comportement du système peut être contrôlé en utilisant seulement deux paramètres : l'ordre d'accord des pendules n_p et le paramètre d'accord non-linéaire c_p (*cf.* chapitres 4). Ces deux paramètres d'accord dépendent des paramètres de trajectoire et de rotation ainsi que de l'inertie sans dimension des pendules η, de sorte que

$$n_p = \frac{n_t}{\sqrt{1 + \eta \alpha_{[1]}^2}}, \quad c_p = 3(x_{[4]} + 2 n_p^2 \eta \alpha_{[1]} \alpha_{[3]}). \tag{14}$$

Dans la suite, nous présenterons la réponse d'APCs accordés de différentes manières afin de mettre en évidence la richesse de leur dynamique.

La partie II du manuscrit se concentre sur l'accord classique d'un APC, qui fait référence aux cas où l'ordre d'excitation est proche de l'ordre d'accord, c'est-à-dire $n \approx n_p$. L'accord classique est celui qui est actuellement utilisé dans les véhicules automobiles, mais il doit encore être amélioré (*cf.* chapitre 1).

Rappelons que le système possède trois modes, illustrés en Fig. 7. Le mode 0 est un mode de corps rigide pour lequel les pendules sont immobiles. Le mode d'opposition de phase correspond à un mouvement d'opposition de phase des pendules et le rotor est un nœud de ce mode. L'ordre propre associé (analogue à une fréquence propre) est l'ordre d'accord n_p de l'APC. Le mode d'unisson représente un mouvement à l'unisson des pendules, qui sont en opposition de phase avec le rotor. L'ordre propre associé est légèrement supérieur à n_p.

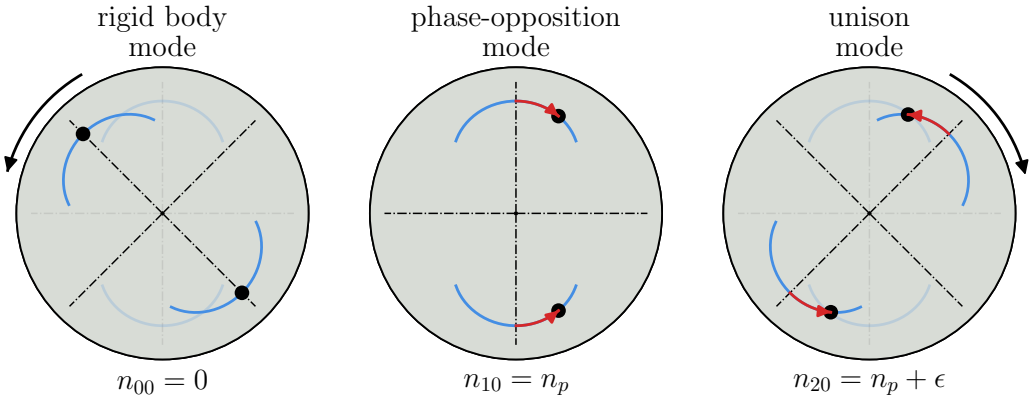

Figure 7: Modes d'un APC constitué de $N = 2$ pendules. ϵ est un petit paramètre indiquant que l'ordre propre du mode d'unisson est légèrement plus grand que l'ordre d'accord. La rotation des pendules autour de leur centre de masse n'est pas représentée sur cette figure.

Nous avons proposé dans le chapitre 2 de simplifier les équations du mouvement complètes d'un APC afin d'étudier analytiquement son comportement non-linéaire. Deux processus de simplification différents ont été suggérés, conduisant à deux modèles simplifiés différents : un modèle dit "simple" (utilisé dans les chapitres 3 et 5), et l'autre dit "précis" (utilisé dans le chapitre 4). Il existe trois différences principales entre ces modèles :

- Les non-linéarités affectant les pendules dans le modèle simple sont uniquement liées à leur trajectoire et à leur loi de rotation. En revanche, le modèle précis prend également en compte le couplage non-linéaire entre les pendules, lié aux effets d'inertie.
- Dans le modèle simple, les pendules sont excités directement (ici, directement signifie "non

paramétriquement") par le couple externe. Le modèle précis tient compte à la fois du forçage direct et paramétrique des pendules par le couple externe.

- Le modèle simple permet de calculer analytiquement les deux premières harmoniques du rotor alors que le modèle précis permet de dériver ses trois premières harmoniques.

Les deux modèles sont utilisés dans la littérature (sans la contribution de la rotation, voir [65, 66, 86] par exemple), mais ils ne sont pas comparés. Une comparaison est proposée dans le chapitre 4 et montre que le modèle précis devrait être utilisé dans la plupart des cas. Néanmoins, il existe encore des cas où le modèle simple est utile :

- Bien que le modèle simple ait un domaine de validité beaucoup plus petit que le modèle précis, il est moins complexe et fournit une estimation correcte du comportement de l'APC pour de faibles valeurs de l'ordre d'accord n_p. Ceci est vérifié dans le chapitre 3.
- Le modèle simple permet d'étudier la solution en modes couplés du système (c'est-à-dire que les pendules répondent simultanément sur les modes d'unisson et d'opposition de phase) alors que le modèle précis ne le permet pas. En effet, sa plus grande complexité ne permet pas de dériver une solution analytique pour la solution en modes couplés cohérente avec la solution sur le mode d'unisson. Le modèle simple est utilisé dans le chapitre 5 pour étudier la solution en modes couplés.

La figure 8 représente une réponse non-linéaire typique du système lorsqu'il est soumis à un couple harmonique avec un ordre d'excitation variable n (similaire à une fonction de réponse en fréquence avec une fréquence d'excitation variable). L'amplitude des pendules est représentée en (a) et l'amplitude de l'accélération du rotor en (b). La partie droite de la Fig. 8 traite de l'accord sous-harmonique d'un APC, qui fait l'objet de la partie III et n'est donc pas détaillée ici.

Le contenu des chapitres constituant la partie II est illustré sur le côté gauche de la Fig. 8. Les courbes vertes représentent la réponse de l'APC pour des pendules oscillant à l'unisson. Les amplitudes des pendules sont physiquement limitées en raison de la finitude de leur trajectoire, et cette limite est indiquée par s_{cusp} dans la Fig. 8(a). Lorsque les pendules oscillent sur le mode d'unisson et avant sa résonance, ils exercent un couple sur le rotor qui s'oppose au couple extérieur. Ceci génère l'antirésonance classique visible dans la Fig. 8(b) au voisinage de n_p (elle est exactement à n_p dans le cas linéaire et conservatif).

En pratique, l'ordre d'excitation n étant fixe, on accordera typiquement les pendules de telle sorte que $n_p = n$ pour que le rotor soit excité sur son antirésonance, réduisant ainsi ses vibrations au maximum. Cependant, ce comportement idéal est perturbé par des effets non-linéaires qui détériorent l'efficacité des APC. Ces effets non désirés sont énumérés ci-dessous et discutés en détail par la suite :

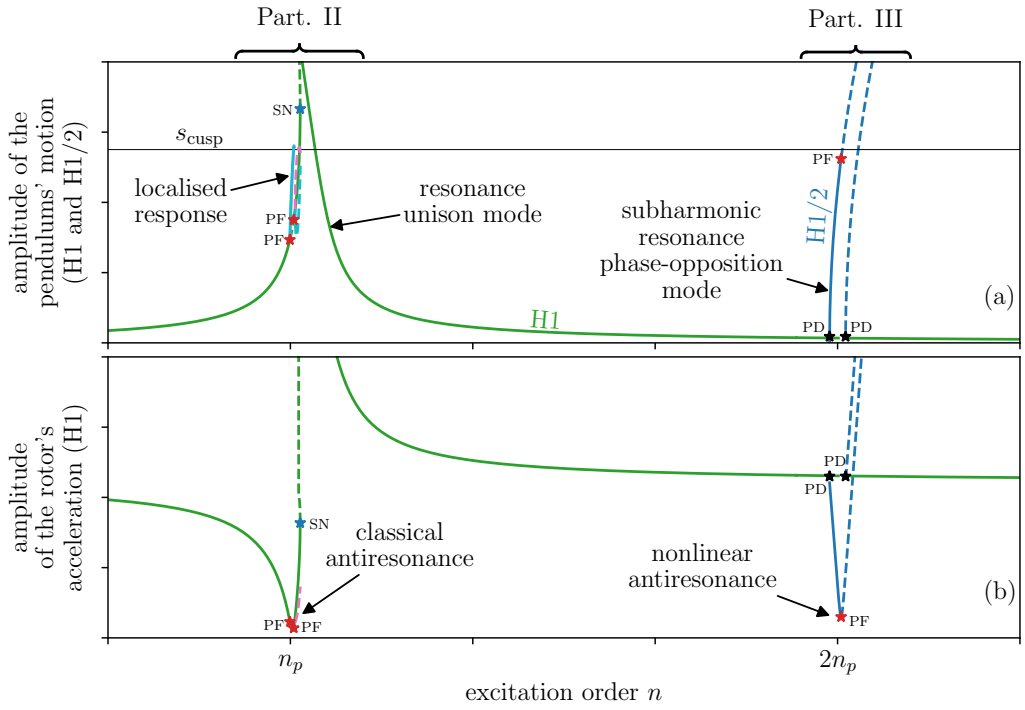

Figure 8: Réponse typique en amplitude des pendules (a) et du rotor (b) d'un APC en fonction de l'ordre d'excitation. La partie gauche de cette figure correspond au champ d'intérêt de la partie II tandis que la partie droite correspond au champ d'intérêt de la partie III. Les courbes vertes et bleues correspondent aux pendules répondant sur les modes d'unisson et d'opposition de phase, respectivement, et les lignes pointillées indiquent les solutions instables. Les harmoniques 1 et 1/2 de la réponse des pendules sont représentées en (a) alors que seule la première harmonique du rotor est représentée en (b). La ligne noire horizontale en (a) indique le point de rebroussement de la trajectoire des pendules. Les étoiles rouges, bleues et noires indiquent respectivement les bifurcations fourche (PF pour "pitchfork"), nœud-col (SN pour "saddle-node") et de doublement de période (PD pour "period doubling").

- La réponse à l'unisson est soumise à plusieurs instabilités. Cela est visible en Fig. 8 par la présence de bifurcations fourche (PF, étoiles rouges) et de bifurcations nœud-col (SN, étoiles bleues). Les bifurcations PF entraînent des mouvements de pendules désynchronisés (cela correspond à la réponse localisée en rose et en cyan dans la Fig. 8) et les bifurcations SN mènent les pendules à ne plus agir comme des absorbeurs mais comme des amplificateurs.

- En raison des effets non-linéaires, une augmentation de l'amplitude du couple externe entraîne un décalage de l'ordre classique d'antirésonance, qui s'écarte alors de n_p. Nous appelons cela le désaccordage non-linéaire de l'antirésonance. Dans ce cas, et parce qu'en pratique l'ordre d'excitation n est fixé, le rotor n'est pas excité sur le minimum de sa réponse sur toute la plage de couple. Ainsi, le désaccordage non-linéaire de l'antirésonance empêche une réduction optimale

des vibrations du rotor.

Dans la partie II, nous étudions les réponses à l'unisson et localisées en utilisant principalement des méthodes analytiques. L'analyse de la réponse à l'unisson a conduit à l'élaboration de règles de conception originales permettant de prévenir l'apparition d'instabilités et de limiter le déplacement de l'antirésonance classique. L'étude de la réponse localisée a permis de mieux comprendre ce phénomène et de montrer que, dans certains cas, il n'est pas préjudiciable à l'efficacité du filtrage de l'APC. Ces points sont détaillés par la suite.

Le développement de nombreux résultats discutés dans ce résumé nécessite des manipulations algébriques élaborées, détaillées dans les chapitres 3, 4 et 5. Nous ne rapportons ici que les principaux résultats de la partie II, décrits d'un point de vue physique.

2.1 Stabilité de la solution à l'unisson et réponse localisée [chap. 3, 4, 5]

Si l'on considère maintenant que l'ordre d'excitation n est fixe et que le paramètre de contrôle est l'amplitude du couple $\bar{T}_1$, les résultats typiques des chapitres 3, 4 et 5 peuvent être résumés dans la Fig. 9. Cette figure représente la réponse forcée de deux APCs différents excités sur leur ordre d'accord, c'est-à-dire $n = n_p$. La différence entre les deux APCs est leur accord non-linéaire c_p, qui est contrôlé par la trajectoire et la rotation des pendules (*cf.* Eq. (14)).

Nous examinons d'abord la réponse de l'APC représenté en Fig. 9(a)-(b). Lors de la réalisation d'un balayage en couple croissant (ce qui se produit souvent dans la pratique, lorsque le conducteur de la voiture accélère par exemple), l'amplitude des pendules et du rotor augmente jusqu'à atteindre la bifurcation SN inférieure. Á ce moment, un saut soudain de la réponse se produit. Après ce saut, les oscillations du rotor sont beaucoup plus importantes que si les pendules étaient bloqués. Ceci est dû au fait que la phase des oscillations des pendules a changé de π de sorte que le couple qu'ils génèrent sur le rotor s'ajoute maintenant au couple externe au lieu de s'y opposer. Cette situation doit absolument être évitée dans la pratique pour éviter la défaillance de certains composants de la chaîne cinématique.

La Fig. 9(c)-(d) montre la réponse d'un autre APC en fonction de l'amplitude de forçage et excité à son ordre d'accord. Pendant un balayage croissant de $\bar{T}_1$, l'amplitude des pendules et du rotor augmente jusqu'à atteindre la bifurcation PF. À des niveaux de couple plus importants, la réponse à l'unisson est instable et les pendules oscillent avec des amplitudes différentes. L'énergie est localisée sur le pendule oscillant avec la plus grande amplitude, d'où le nom de "solution localisée". En augmentant encore l'amplitude du couple, on constate que la localisation fait que les pendules atteignent leur point de rebroussement à un niveau de couple beaucoup plus faible que s'ils oscillaient à l'unisson. Le niveau de couple associé définit la capacité en couple de l'APC, et sa réduction est le principal inconvénient de la localisation. On pourrait penser que la localisation diminue également l'efficacité

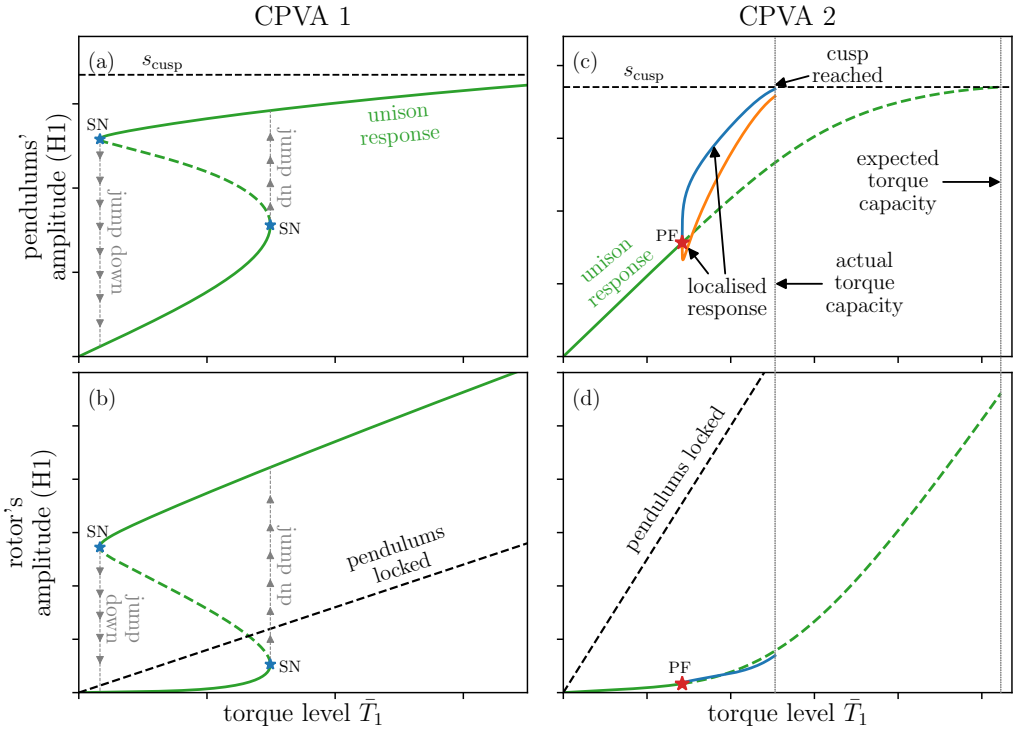

Figure 9: Réponse en couple d'un premier APC (à gauche) et d'un second (à droite) en fonction de l'amplitude du couple. (a), (c) et (b), (d) représentent les amplitudes des pendules et du rotor, respectivement. La courbe verte correspond au mouvement des pendules à l'unisson, tandis que les courbes bleue et orange dans (c) et (d) correspondent à la réponse localisée. Les lignes pointillées indiquent les solutions instables. Les étoiles rouges et bleues indiquent les bifurcations fourche (PF) et nœud-col (SN), respectivement. Dans tous les graphiques, $n = n_p$ de sorte que les APCs sont excités sur leur ordre d'accord.

de filtration de l'APC, mais ce n'est pas nécessairement le cas. On peut le voir dans la figure 9(d), où l'amplitude de la première harmonique du rotor est légèrement inférieure avec des pendules localisés (courbe bleue) qu'avec un mouvement à l'unisson (courbe verte). Dans le chapitre 5, nous montrons même que dans certains cas particuliers la localisation ne réduit pas la capacité de couple et diminue les vibrations du rotor, de sorte qu'elle améliore l'efficacité de l'APC. Néanmoins, il s'agit de scénarios inhabituels et il est bien plus souvent préférable d'éviter la localisation.

La cause de l'existence de solutions localisées, discutée en détail dans le chapitre 5, peut être comprise à partir de l'expansion modale suivante (nous considérons un APC composé de $N = 2$

pendules pour simplifier le raisonnement)

$$\begin{bmatrix} s_1 \\ s_2 \end{bmatrix} = \underbrace{\zeta_1 \begin{bmatrix} 1 \\ -1 \end{bmatrix}}_{\substack{\text{mode d'opposition} \\ \text{de phase}}} + \underbrace{\zeta_2 \begin{bmatrix} 1 \\ 1 \end{bmatrix}}_{\substack{\text{mode} \\ \text{d'unisson}}} . \tag{15}$$

s_1 et s_2 sont les coordonnées des pendules tandis que ζ_1 et ζ_2 sont les coordonnées modales. Lorsque seul le mode d'unisson répond (c'est-à-dire $\zeta_1 = 0$, $\zeta_2 \neq 0$), les pendules se déplacent à l'unisson. C'est le scénario le plus attendu car le mode d'opposition de phase n'est pas directement excité par le couple externe (*cf.* section 2.2). Cependant, comme les ordres propres des modes d'unisson et d'opposition de phase sont proches, ces modes sont en résonance interne 1:1 (*cf.* chapitre 5). Il peut donc y avoir des échanges d'énergie entre eux, et par conséquent le mode d'opposition de phase peut contribuer à la réponse des pendules (i.e. $\zeta_1 \neq 0$, $\zeta_2 \neq 0$). Ce phénomène non-linéaire entraîne une oscillation différente des pendules tel que $s_1 = \zeta_1 + \zeta_2 \neq s_2 = -\zeta_1 + \zeta_2$ (*cf.* Eq. (15)), ce qui conduit à une localisation de l'énergie.
L'étude analytique de la solution localisée et de sa stabilité dans le chapitre 5 a grandement facilité l'observation numérique de réponses quasi-périodiques et chaotiques d'APCs. De plus, l'analyse expérimentale présentée au chapitre 3 a permis d'observer la localisation là où le modèle analytique l'avait prédit.

La figure 10 représente la réponse des pendules de trois APCs différents en fonction de l'ordre d'excitation. Ces APCs ont les mêmes paramètres, à l'exception de leur accord non-linéaire.

Les zones rouges et bleues sont des zones d'instabilité. Les bifurcations PF et SN, qui provoquent respectivement la localisation et les sauts de la réponse, sont situées aux intersections de ces zones avec la réponse à l'unisson. Par conséquent, pour obtenir un mouvement d'unisson stable, il faut éviter ces intersections. Cela peut être fait par un réglage linéaire et non-linéaire spécifique de l'APC, qui affecte à la fois le comportement raidissant/assouplissant de la réponse (visible par la courbure de la réponse dans la Fig. 10) et le lieu des zones d'instabilité. Par exemple, l'accord des APCs 1 et 3 (*cf.* Fig. 10(a) et (c)) permet d'éviter les instabilités à $n = n_p$, ce qui est pratique puisque l'antirésonance du rotor est située près de n_p. Au contraire, l'APC 2 (*cf.* Fig. 10(b)) ne parvient pas à éviter l'apparition d'instabilités à $n = n_p$, et le réglage non-linéaire associé n'est donc pas recommandé.

Les chapitres 3 et 4 contiennent des règles d'accord simples permettant d'éviter systématiquement les instabilités de la réponse à l'unisson. Ces directives constituent une contribution majeure de la thèse.

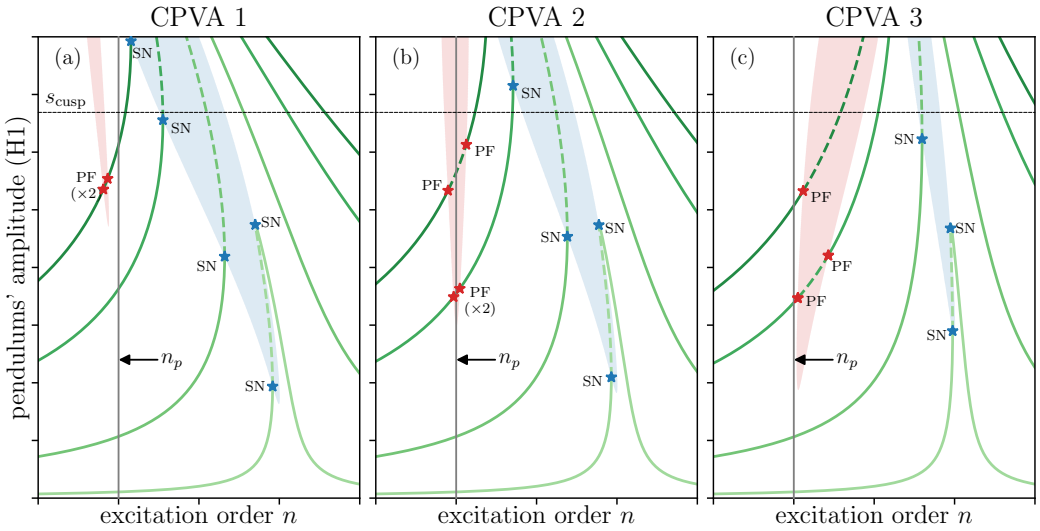

Figure 10: Réponse en amplitude des pendules de trois APCs avec différents paramètres d'accord non-linéaires et pour plusieurs niveaux de forçage. Les courbes vertes représentent le mouvement d'unisson et les lignes pointillées indiquent les solutions instables. Plus la courbe est sombre, plus le niveau de couple associé est important. Les étoiles rouges et bleues indiquent respectivement les bifurcations fourche (PF) et nœud-col (SN). Les zones rouges et bleues sont des zones d'instabilité liées à la localisation et aux sauts de la réponse, respectivement. Pour plus de lisibilité, les réponses localisées prenant naissance au niveau des bifurcations PF ne sont pas représentées.

2.2 Décalage de l'antirésonance et performance [chap. 4]

En raison de la nature non-linéaire du système, l'ordre de l'antirésonance classique du rotor dépend de l'amplitude des variables, qui dépend à son tour de l'amplitude du couple de forçage. La Fig. 11(a) illustre l'évolution de la réponse du rotor autour de son antirésonance (courbes vertes) lorsque le niveau de couple augmente. La courbe rose, qui passe par chaque antirésonance, est le résultat d'une procédure analytique de suivi d'antirésonance proposée au chapitre 4. Pour que l'antirésonance soit verrouillée à $n = n_p$, il faut que cette courbe rose soit une ligne parfaitement verticale. Ceci est utilisé pour obtenir des directives de conception et est discuté par la suite.

Les figures 11(b) et (c) comparent la réponse de deux APCs en fonction du niveau de forçage et pour un ordre d'excitation $n = n_p$. L'APC représenté en rouge est réglé pour avoir des pendules découplés tautochrones. Cette configuration, souvent abordée dans la littérature, signifie que la période d'oscillation des pendules ne dépend pas de leur amplitude de mouvement lorsque le rotor tourne à vitesse constante. C'est l'évolution de l'antirésonance de cet APC qui est représentée en Fig. 11(a). L'autre APC, représenté en vert dans (b)-(c), est accordé pour verrouiller l'antirésonance à $n = n_p$.

La figure 11(c) montre que le verrouillage de l'antirésonance réduit l'amplitude de la première harmonique du rotor par rapport au cas tautochrone. Cela souligne l'avantage de verrouiller l'antirésonance pour réduire les vibrations du rotor. Dans la Fig. 11(b), nous pouvons voir que le verrouillage de

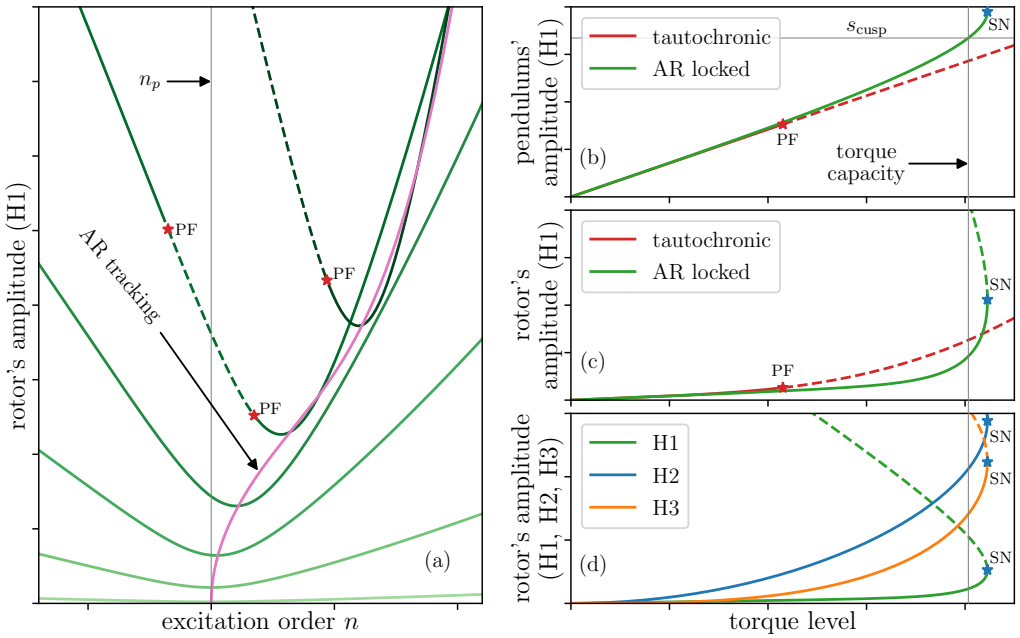

Figure 11: La réponse de deux APCs différents est représentée dans cette figure. (a) montre l'amplitude de la première harmonique d'un rotor autour de son antirésonance et pour plusieurs niveaux de forçage. Ce rotor fait partie d'un APC avec des pendules tautochrones. Plus la ligne est foncée, plus le niveau de forçage associé est grand. Les lignes pointillées indiquent des solutions instables. La courbe rose représente le lieu d'antirésonance lorsque l'amplitude du couple augmente. Les réponses des pendules et du rotor de deux APCs sont présentées en (b) et (c) en fonction du niveau de forçage et pour $n = n_p$. L'un des APCs est celui représenté en (a). L'autre est accordé pour verrouiller l'antirésonance à $n = n_p$. (d) représente les trois premières harmoniques du rotor de l'APC accordé pour verrouiller l'antirésonance en fonction du niveau de forçage. Les étoiles rouges et bleues indiquent les bifurcations fourche (PF) et nœud-col (SN), respectivement.

l'antirésonance augmente légèrement l'amplitude des pendules à l'unisson par rapport au cas tautochrone. Cependant, les pendules tautochrones sont soumis à une localisation (due à la présence de la bifurcation PF) bien avant leur point de rebroussement, ce qui pourrait diminuer significativement leur capacité de couple. Au contraire, les pendules bloquant l'antirésonance ne sont pas soumis à des instabilités avant d'atteindre leur point de rebroussement. Par conséquent, la règle de conception limitant le décalage de l'antirésonance est compatible avec l'évitement des instabilités discuté précédemment.

En Fig. 11(d), nous pouvons voir l'amplitude des trois premières harmoniques du rotor de l'APC accordé pour verrouiller l'antirésonance. La réduction de la première harmonique ramène au premier plan la contribution des harmoniques supérieures du rotor générées à cause des non-linéarités introduites par les pendules. En effet, près du point de rebroussement, les amplitudes des harmoniques 2 (en bleu) et 3 (en orange) du rotor sont environ 9 et 6 fois plus grandes que l'amplitude de l'harmonique

fondamentale (en vert), respectivement. Ceci pourrait être problématique mais peut être évité en utilisant par exemple un APC en fonctionnement sous-harmonique, ce qui est le sujet de la partie III de ce rapport.

2.3 Représentation dans l'espace de design et optimisation [chap. 3, 4]

Afin d'effectuer une optimisation de la conception du système, il est proposé dans les chapitres 3 et 4 de représenter les règles de conception et l'état de stabilité de la réponse à l'unisson dans l'espace de conception. Les coordonnées de cet espace sont les paramètres de l'APC. Cette représentation fournit une vue d'ensemble de la stabilité d'une plage de designs d'APCs et indique ceux qui satisfont certaines caractéristiques données. Ainsi, il est possible d'évaluer simultanément l'efficacité de ces différents designs.

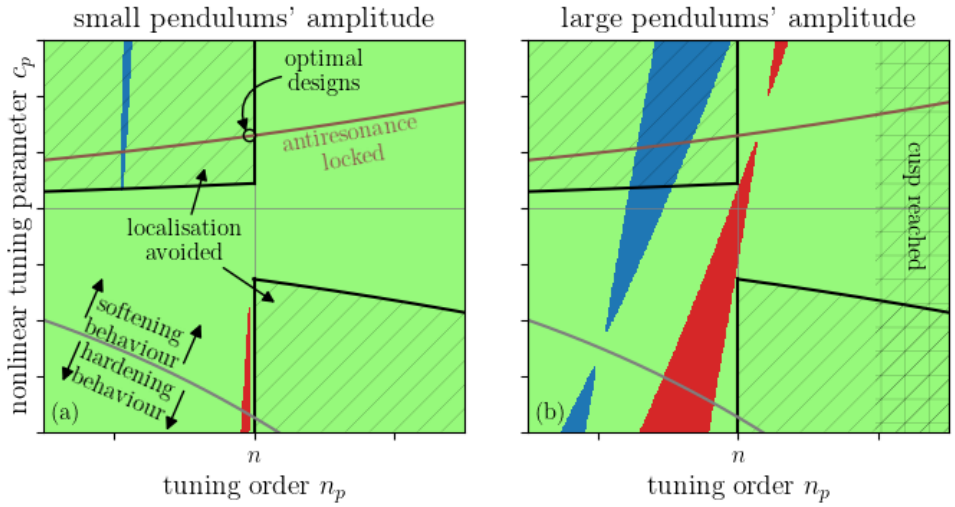

Figure 12: Cartes représentant l'état de stabilité et certaines règles de design dans l'espace de conception. Chaque carte est représentée pour un ordre d'excitation n donné et une amplitude de pendule donnée. Les zones vertes, bleues et rouges correspondent aux conceptions qui sont stables, soumises à des sauts et soumises à la localisation, respectivement.

La Fig. 12 représente les informations de stabilité (vert-stable, rouge-instable et bleu-instable) dans un espace de conception avec les paramètres d'accord linéaire n_p et non-linéaire c_p comme coordonnées (qui sont liées à la trajectoire des pendules et à la fonction de rotation, *cf.* Eq. (14)). Elle représente également la règle de design verrouillant l'antirésonance (courbe brune) et une autre règle imposant une réponse linéaire du mode d'unisson de manière à éviter les sauts de réponse (ligne grise). En outre, l'indication des designs d'APCs pour lesquels les pendules ont atteint leur point de rebroussement (zone hachurée en Fig. 12(b)) fournit une information liée à la capacité de couple. Chaque carte est présentée pour un ordre d'excitation donné et une amplitude de pendule donnée. Les configurations optimales sont celles qui sont stables sur la plus grande plage de couple tout en ayant leur antirésonance fixe et

aussi proche que possible de n. Dans la Fig. 12, ces conditions correspondent aux designs situés près de l'intersection de la ligne marron avec la zone hachurée supérieure.

3 Accord sous-harmonique d'un absorbeur pendulaire centrifuge

On présente ici une synthèse des principaux résultats des chapitres 6, 7 et 8, constituant la partie III de ce rapport. Dans cette partie, le système considéré est l'absorbeur pendulaire centrifuge (APC, ou "CPVA" en anglais pour "centrifugal pendulum vibration absorber") décrit dans les chapitres 1 et 2. Dans un souci d'exhaustivité, une brève description du système est rappelée ici. Il est constitué d'un rotor sur lequel sont fixés N pendules oscillant le long de leur trajectoire et tournant autour de leur centre de masse, comme illustré en Fig. 13. Le système est excité par un couple contenant une partie constante et une partie périodique. Pour simplifier l'analyse, nous considérons que le couple fluctuant contient une seule harmonique d'amplitude $\bar{T}_1$ et d'ordre n.

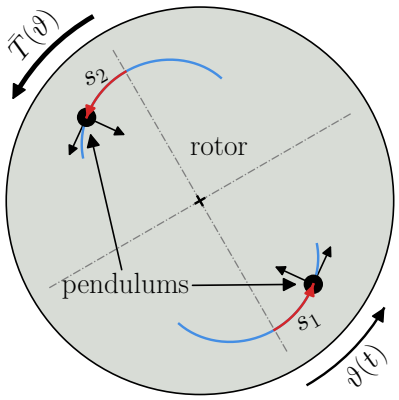

Figure 13: Illustration d'un APC composé de $N = 2$ pendules. Les repères noirs attachés aux pendules représentent leur rotation par rapport au rotor.

La trajectoire et la loi de rotation des pendules sont régies par des fonctions

$$x(s_i) = 1 - n_t^2 s_i^2 + x_{[4]} s_i^4, \tag{16a}$$
$$\alpha(s_i) = \alpha_{[1]} s_i + \alpha_{[3]} s_i^3, \tag{16b}$$

où s_i représente l'abscisse curviligne du i$^{\text{ème}}$ pendule (*cf.* Fig. 13), n_t, $x_{[4]}$ sont des paramètres de trajectoire et $\alpha_{[1]}$, $\alpha_{[3]}$ des paramètres de rotation. Il s'avère que le comportement du système peut être contrôlé par l'ordre d'accord des pendules n_p et le paramètre d'accord non-linéaire c_p (*cf.* chapitre 7). Ces deux paramètres d'accord dépendent des paramètres de trajectoire et de rotation et de l'inertie

sans dimension des pendules η, de sorte que

$$n_p = \frac{n_t}{\sqrt{1+\eta\alpha_{[1]}^2}}, \quad c_p = 3(x_{[4]} + 2n_p^2\eta\alpha_{[1]}\alpha_{[3]}). \tag{17}$$

Dans la suite, nous allons présenter le comportement d'APCs accordés de différentes manières afin de mettre en évidence la richesse de leur dynamique.

Rappelons que pour $N = 2$ pendules, le système possède trois modes, illustrés en Fig. 14. Le mode 0 est un mode de corps rigide pour lequel les pendules sont immobiles. Le mode d'opposition de phase correspond à un mouvement d'opposition de phase des pendules et le rotor est un nœud de ce mode. L'ordre propre associé (analogue à une fréquence propre) est l'ordre d'accord n_p de l'APC. Le mode d'unisson représente un mouvement à l'unisson des pendules, qui sont en opposition de phase avec le rotor. L'ordre propre associé est légèrement supérieur à n_p.

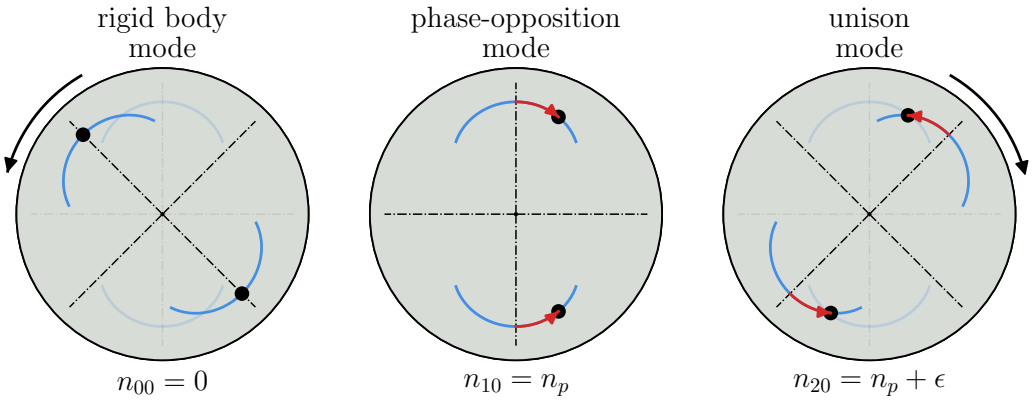

Figure 14: Modes d'un APC composé de $N = 2$ pendules. ϵ est un petit paramètre indiquant que l'ordre propre du mode d'unisson est légèrement plus grand que l'ordre d'accord. La rotation des pendules autour de leur centre de masse n'est pas représentée sur cette figure.

Dans cette partie, nous nous concentrons sur l'accord sous-harmonique d'un APC, qui fait référence aux cas où l'ordre d'excitation est proche de deux fois l'ordre d'accord, c'est-à-dire $n \approx 2n_p$. Cette condition d'accord ne peut être réalisée que grâce à la nature non-linéaire du système. En effet, on montrera que la solution avec des pendules oscillant à l'unisson présente une bifurcation de doublement de période, qui permet aux pendules d'osciller à la moitié de l'ordre d'excitation.

Ce facteur deux entre l'accord et l'excitation permet de filtrer les couples d'ordre élevé rencontrés dans les véhicules électriques (*cf.* section 1.1.1.3) sans accorder les pendules à des ordres aussi élevés. Ceci est pratique car l'accord à ordre élevé est difficile à réaliser en pratique en raison des tolérances de fabrication (*cf.* section 2.2.3).

Le chapitre 6 traite du calcul de la réponse sous-harmonique et de sa stabilité pour un APC composé de $N = 2$ pendules. Dans le cas N pair mais supérieur à 2, le mode d'opposition de phase

illustré en Fig. 14 devient dégénéré. Cela complique considérablement l'analyse de la réponse sous-harmonique et est abordé dans le chapitre 7. Le chapitre 8 présente une étude expérimentale sur un prototype conçu pour fonctionner en régime sous-harmonique suivant les recommandations exposées dans les chapitres 6 et 7.

La figure 15 représente une réponse non-linéaire typique du système lorsqu'il est soumis à un couple harmonique avec un ordre d'excitation variable n (similaire à une fonction de réponse en fréquence avec une fréquence d'excitation variable). L'amplitude des pendules est représentée en (a) et l'amplitude de l'accélération du rotor en (b). La partie gauche de la Fig. 15 traite de l'accord classique d'un APC, qui fait l'objet de la partie II et n'est donc pas détaillée ici.

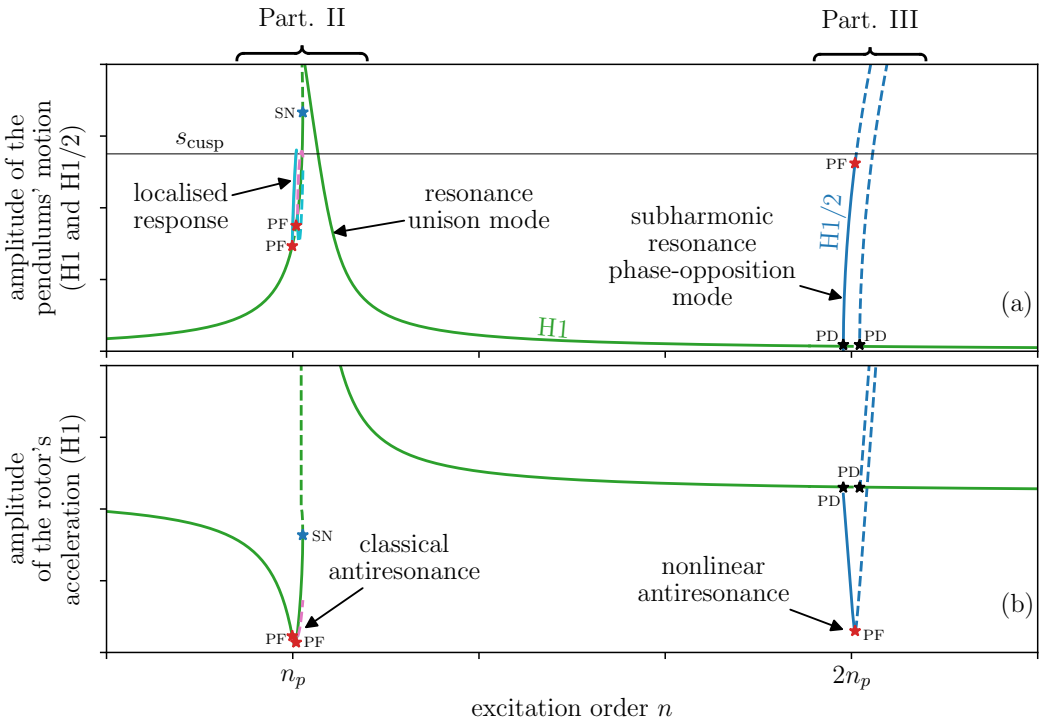

Figure 15: Réponse typique en amplitude des pendules (a) et du rotor (b) d'un APC en fonction de l'ordre d'excitation. La partie gauche de cette figure est le champ d'intérêt de la partie II tandis que la partie droite est celui de la partie III. Les courbes vertes et bleues correspondent aux pendules répondant sur les modes d'unisson et d'opposition de phase, respectivement, et les lignes pointillées indiquent les solutions instables. Les harmoniques 1 et 1/2 de la réponse des pendules sont montrées en (a) alors que seule la première harmonique du rotor est montrée en (b). La ligne noire horizontale en (a) indique le point de rebroussement de la trajectoire des pendules. Les étoiles rouges, bleues et noires indiquent respectivement les bifurcations fourche (PF pour "pitchfork"), nœud-col (SN pour "saddle-node") et de doublement de période (PD pour "period doubling").

Le champ des chapitres constituant la partie III est illustré sur le côté droit de la Fig. 15. Les amplitudes des pendules sont physiquement limitées en raison de la finitude de leur trajectoire, et cette

limite est indiquée par s_{cusp} dans la Fig. 15(a). Les courbes vertes représentent la réponse de l'APC pour des pendules oscillant à l'unisson. Cette réponse est soumise à des instabilités à $n \approx 2n_p$. En effet, on peut voir deux bifurcations de doublement de période (PD, étoiles noires) donnant naissance à une réponse sous-harmonique des pendules sur le mode d'opposition de phase. Ce mouvement sous-harmonique (d'ordre 2) signifie que les pendules oscillent à la moitié de l'ordre du couple. C'est pourquoi les courbes bleues en (a) représentent l'harmonique 1/2 du mouvement des pendules. Le mouvement sous-harmonique des pendules exerce un couple sur le rotor qui s'oppose au couple externe, ce qui conduit à la génération de l'antirésonance non-linéaire du rotor visible en (b) autour de $2n_p$.

En pratique, l'ordre d'excitation n est fixe, on pourrait donc accorder les pendules de telle sorte que $n_p = n/2$ pour que le rotor soit excité sur son antirésonance non-linéaire, réduisant ainsi au maximum ses vibrations. Cependant, ce comportement idéal est perturbé par des effets non-linéaires qui détériorent l'efficacité du fonctionnement sous-harmonique de l'APC. Ces effets non désirés sont énumérés ci-dessous et discutés en détail par la suite :

- En raison des effets non-linéaires, une augmentation de l'amplitude du couple externe entraîne un décalage de l'ordre d'antirésonance non-linéaire qui s'écarte de $2n_p$. Dans ce cas, et parce qu'en pratique l'ordre d'excitation n est fixe, le rotor n'est pas excité sur le minimum de sa réponse sur toute la plage de couple. Ainsi, le désaccord non-linéaire de l'antirésonance empêche une réduction optimale des vibrations du rotor.

- La réponse sous-harmonique est soumise à plusieurs sources d'instabilités. La plus préoccupante est liée à la bifurcation fourche (PF, étoile rouge) qui est située exactement sur l'antirésonance non-linéaire (*cf.* Fig. 15(b)). Cette bifurcation PF conduit à une réponse différente du mouvement d'opposition de phase souhaité des pendules. D'autres instabilités, non visibles sur la Fig. 15, sont dues à une réponse sous-harmonique du mode unisson qui perturbe également le mouvement d'opposition de phase.

Dans la partie III, la réponse sous-harmonique est étudiée en utilisant principalement des méthodes analytiques. Ceci a permis d'acquérir une meilleure compréhension de cette solution particulière et a également conduit à l'élaboration de règles de conception originales permettant de prévenir l'apparition d'instabilités et de limiter le déplacement de l'antirésonance non-linéaire. Ces différents aspects, qui maximisent l'efficacité de l'APC, sont détaillés par la suite.

Le développement de nombreux résultats discutés dans ce résumé nécessite des manipulations algébriques élaborées, détaillées dans les chapitres 6, 7 et 8. Nous ne rapportons ici que les principaux résultats de la partie III, décrits d'un point de vue physique.

3.1 Bases de la réponse sous-harmonique [chap. 6]

Pour un APC constitué de deux absorbeurs, le fonctionnement sous-harmonique souhaité est une réponse des pendules sur la sous-harmonique du mode d'opposition de phase tel qu'ils oscillent à la moitié de l'ordre du couple et avec des phases opposées. En tenant compte de ce mouvement d'opposition de phase, l'accélération du rotor peut être exprimée au premier ordre (*cf.* chapitre 6)

$$\underbrace{\theta''}_{\substack{\text{accélération}\\ \text{du rotor}}} = \underbrace{\bar{T}_1 \cos(n\vartheta)}_{\substack{\text{couple}\\ \text{extérieur}}} + \underbrace{\mu n_t^2 \left(s_1 s_1' + s_2 s_2'\right)}_{\text{effet de Coriolis}} = \bar{T}_1 \cos(n\vartheta) + 2\mu n_t^2 s s', \quad s = s_1 = -s_2, \tag{18}$$

où s_1 et s_2 sont les coordonnées des pendules 1 et 2, respectivement, et μ et n_t sont un rapport d'inertie et l'ordre de la trajectoire des pendules (*cf.* sections 2.1.2.2 et 2.1.3). Le seul terme équilibrant le couple externe dans l'équation (18) est dû à l'effet de Coriolis et présente une non-linéarité quadratique. Une conséquence de cette non-linéarité est que le terme ss' oscille à deux fois la fréquence de s. Ceci explique comment les oscillations des pendules sous-harmoniques à $n_p = n/2$ génèrent un couple d'ordre n qui peut réduire les vibrations du rotor. De plus, aucune harmonique supérieure du rotor n'est générée par le fonctionnement sous-harmonique car chaque terme de l'accélération du rotor (18) oscille à l'ordre n. Il s'agit d'un avantage significatif par rapport au fonctionnement classique.

Une réponse sous-harmonique typique pour un APC composé de $N = 2$ pendules est représentée dans la Fig. 16. Cet APC est dit "parfaitement accordé" car les fonctions de trajectoire et de rotation des pendules sont une épicycloïde et une rotation linéaire, elles ne génèrent donc pas de non-linéarités supplémentaires dans le système (*cf.* section 2.1.3).

Regardons d'abord les Fig. 16(c)-(d), qui représentent une réponse forcée de l'APC à deux fois son ordre d'accord (i.e. $n = 2n_p$). La réponse sous-harmonique (courbes bleues) apparaît par une bifurcation PD à partir d'une solution triviale (courbes vertes). Cette solution triviale est en fait une approximation de la réponse sur le mode unisson loin de sa résonance (*cf.* Fig. 15 et chapitre 6). La bifurcation PD n'est pas située à couple nul, ce qui signifie qu'il existe un seuil de couple pour déclencher la réponse sous-harmonique. C'est l'un des inconvénients du fonctionnement sous-harmonique car il le rend inefficace à des niveaux de couple faibles. Ce seuil existe parce que le mode d'opposition de phase est excité de manière paramétrique par le couple externe (*cf.* chapitre 6). Le niveau de couple amenant les pendules au point de rebroussement de leur trajectoire est représentée en Fig. 16(c) et est définit comme la capacité en couple de l'APC.

Une autre particularité du fonctionnement sous-harmonique est le phénomène de saturation. Celui-ci est visible dans la Fig. 16(d), où l'amplitude du rotor est indépendante du niveau de forçage. Le fait que les vibrations n'augmentent pas avec le forçage est une particularité extrêmement intéressante à utiliser pour la réduction des vibrations.
Le phénomène de saturation est également visible sur la figure 16(b), qui représente la réponse du

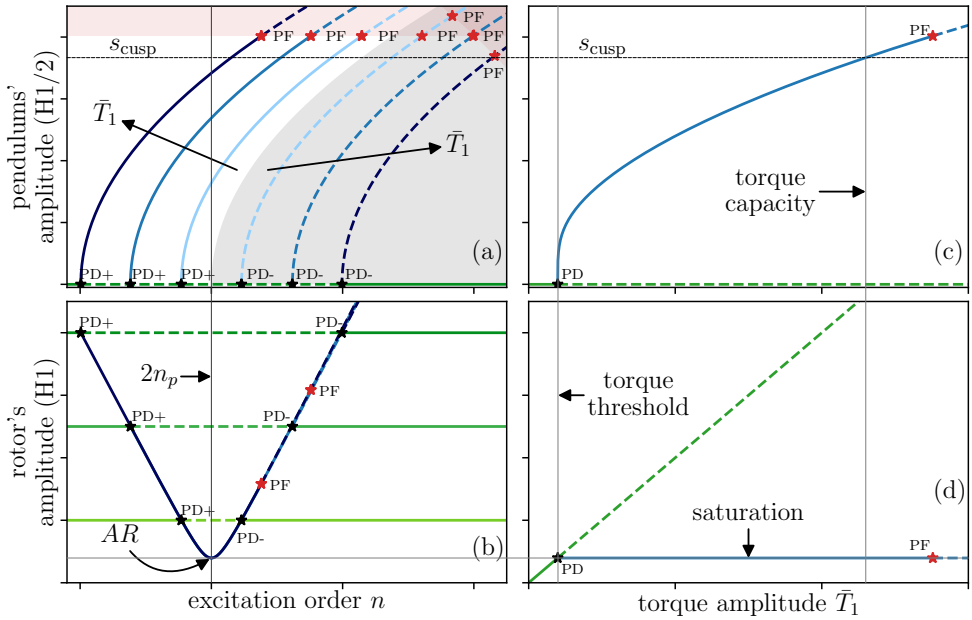

Figure 16: À gauche, on représente l'amplitude des pendules (a) et du rotor (b) en fonction de l'ordre d'excitation et pour trois niveaux de couple. Plus la ligne est foncée, plus le niveau de couple associé est important. A droite, nous représentons également l'amplitude des pendules (c) et du rotor (d), mais en fonction du niveau de forçage et à l'ordre $n = 2n_p$. Les courbes verte et bleue correspondent respectivement à la solution avec pendules immobiles et au fonctionnement sous-harmonique. Les lignes pointillées indiquent les solutions instables. Les étoiles rouges et noires correspondent respectivement aux bifurcations fourche (PF) et de doublement de période (PD+ pour supercritique, PD- pour sous-critique). Les zones rouges et grises indiquent les zones d'instabilité liées à la localisation de la solution sous-harmonique et aux sauts, respectivement.

rotor autour de son antirésonance pour trois niveaux de couple différents. Sur cette figure, les branches instables et stables de la réponse se chevauchent, de sorte qu'elles ne peuvent pas être distinguées. De plus, les réponses associées aux trois niveaux de couple représentés (chacun prenant naissance à deux bifurcations PD) se chevauchent de sorte que seule celle correspondant au forçage le plus important, représentée en bleu foncé, est visible. Le fait que les réponses se chevauchent signifie que l'antirésonance (AR) ne se déplace pas avec le forçage, ce qui illustre le phénomène de saturation.

En outre, la réponse sous-harmonique est soumise à plusieurs instabilités. Les bifurcations PD peuvent être sous-critiques (PD-) (*cf.* section 2.5.1.3), dans ce cas elles donnent naissance à des solutions sous-harmoniques instables. Ces solutions instables sont situées dans la zone grise dans la Fig. 16(a). Il est à noter qu'elles correspondent aux branches inférieures de la réponse sous-harmonique, qui se courbe vers la droite, présentant ainsi un comportement raidissant.
La zone rouge dans la Fig. 16(a) indique une autre zone d'instabilité de la solution sous-harmonique.

Les bifurcations PF se produisent aux croisements de la réponse avec cette zone. Elles donnent lieu à des solutions à modes couplés pour lesquelles le mode d'unisson contribue à la réponse sous-harmonique (*cf.* chapitre 6). C'est l'inverse de la situation rencontrée en fonctionnement classique, où la réponse à l'unisson est perturbée par la contribution du mode d'opposition de phase (*cf.* partie II). Ces solutions à modes couplés font osciller les pendules différemment et diminuent l'efficacité de filtration de l'APC. Il est à noter que chaque bifurcation PF dans la Fig. 16 se produit au-dessus du point de rebroussement. Elles ne sont donc pas un problème car les pendules ne peuvent pas osciller à de telles amplitudes. Néanmoins, il peut y avoir des cas autres que celui décrit dans la Fig. 16 pour lesquels ces instabilités sont problématiques. Par conséquent, des règles de design sont fournies dans le chapitre 6 pour s'assurer que la solution sous-harmonique reste stable jusqu'à ce que les pendules atteignent leur point de rebroussement.

3.2 Stabilité de la solution sous-harmonique en présence de plusieurs paires de pendules et désaccord non-linéaire [chap. 6, 7]

Dans un APC constitué de plusieurs paires de pendules, le mode d'opposition de phase est dégénéré, et la solution sous-harmonique désirée, notée "SH1", correspond à des combinaisons particulières de ces modes dégénérés (*cf.* chapitre 7). Ces combinaisons doivent être telles que les N pendules oscillent avec la même amplitude, mais $N/2$ pendules sont en opposition de phase avec les autres $N/2$. L'une de ces configurations est illustrée dans la Fig. 17. SH1 est la solution sous-harmonique idéale car elle empêche un ou plusieurs pendules d'osciller avec une plus grande amplitude que les autres (c'est-à-dire qu'elle évite la localisation), ce qui maximise la capacité en couple de l'APC.

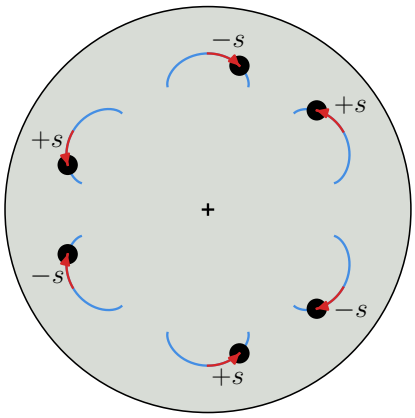

Figure 17: Illustration du mouvement souhaité en régime sous-harmonique pour un APC composé de six pendules. Ce mouvement désiré correspond à la solution appelée “SH1”. Il est à noter que nous ne représentons ici qu'une seule configuration satisfaisant SH1, mais il en existe d'autres (trois pendules successifs à l'unisson et en opposition de phase avec les trois suivants par exemple).

La réponse d'un APC non-linéairement désaccordé (c'est-à-dire que les fonctions de trajectoire

et/ou de rotation des pendules sont différentes d'une épicycloïde et d'une loi de rotation linéaire) composé de plusieurs paires de pendules est illustrée dans la Fig. 18.

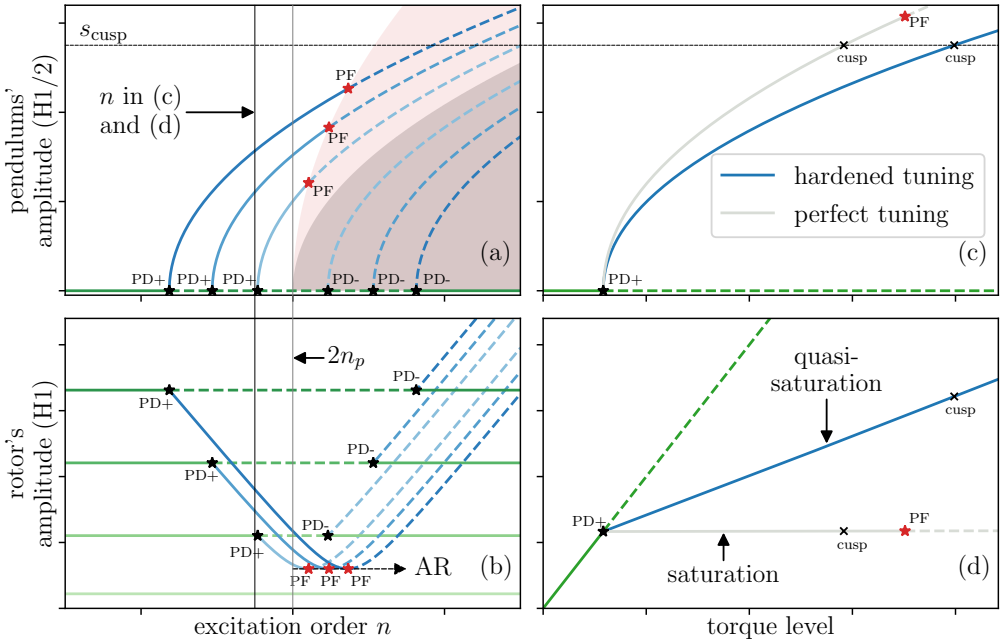

Figure 18: Amplitude des pendules (harmonique 1/2) et du rotor (harmonique 1) en fonction de l'ordre d'excitation ((a), (b), respectivement) et en fonction du niveau de couple ((c), (d), respectivement). Quatre niveaux de couple sont représentés dans (a) et (b), et plus les courbes sont foncées, plus le niveau de couple est élevé. Les courbes vertes et bleues correspondent respectivement à la solution avec pendules immobiles et au fonctionnement sous-harmonique. Il est à noter que l'APC dont la réponse sous-harmonique est représentée en bleu est intentionnellement non-linéairement désaccordé. Les lignes pointillées indiquent des solutions instables. Les étoiles rouges et noires correspondent à des bifurcations fourche (PF) et de doublement de période (PD), respectivement. Les zones rouges et grises indiquent les zones d'instabilité liées à la localisation de la solution sous-harmonique et aux sauts, respectivement. Dans (a) et (b), la ligne grise verticale indique l'ordre d'excitation correspondant à la réponse en couple illustrée dans (c) et (d).

Tout d'abord, on peut remarquer la présence d'une zone rouge à partir de $n = 2n_p$ dans la Fig. 18(a), qui n'existait pas en présence de seulement deux pendules (*cf.* Fig. 16(a)). Elle correspond à une zone d'instabilité supplémentaire qui n'existe que lorsque plusieurs paires de pendules sont utilisées. En effet, dans ce cas, les modes dégénérés en opposition de phase sont tous en résonance interne 1:1, ils peuvent donc échanger de l'énergie et ainsi provoquer des instabilités de la solution désirée SH1.

Les bifurcations PF, situées aux intersections de SH1 et de la zone d'instabilité, donnent naissance à des solutions sous-harmoniques localisées. Dans ce cas, les pendules ont des mouvements différents et au moins l'un d'entre eux oscille avec une amplitude supérieure à SH1. Ainsi, lorsque le couple

augmente, il atteint son point de rebroussement à un niveau de forçage plus faible que prévu, ce qui réduit la capacité en couple de l'APC. De plus, cette solution sous-harmonique localisée conduit généralement à une augmentation des vibrations du rotor (*cf.* chapitre 7). Pour ces raisons, ces instabilités ne sont pas souhaitées. De plus, elles sont particulièrement gênantes car les bifurcations PF donnant naissance à la solution localisée sont situées exactement à l'antirésonance du rotor, comme cela est visible dans la Fig. 18(b).
Une règle de conception permettant d'éviter ces instabilités est proposée dans le chapitre 7. Il s'agit d'une contribution majeure à l'étude des pendules centrifuges en fonctionnement sous-harmonique.

Dans la Fig. 18(a), la zone d'instabilité rouge est située à $n \geq 2n_p$ car le désaccord non-linéaire de l'APC est choisi pour raidir SH1 (c'est-à-dire pour rendre la réponse plus raide qu'avec un accord parfait). Si le désaccord non-linéaire était choisi pour assouplir SH1, la zone d'instabilité serait située à $n \leq 2n_p$. L'accord parfait n'existe jamais en pratique, en raison des tolérances de fabrication par exemple. Par conséquent, pour savoir où se trouve la zone d'instabilité et pouvoir l'éviter, il faut utiliser un niveau minimum de désaccord non-linéaire. Cependant, cela entraîne un décalage de l'antirésonance lorsque le niveau de couple augmente, comme le montre la Fig. 18(b). En raison de ce décalage, la saturation de la réponse du rotor, visible en Fig. 18(d), n'est plus parfaite.

Il y a un équilibre à trouver entre éviter les instabilités et limiter le décalage de l'antirésonance. La configuration la plus recommandée est un APC raidit avec des pendules sur-accordés (c'est-à-dire $2n_p > n$), ce qui correspond à la configuration présentée dans la Fig. 18. Cela présente l'avantage d'augmenter légèrement la capacité en couple par rapport au cas parfaitement accordé (*cf.* Fig. 18(c)-(d)). Néanmoins, pour une application donnée, l'utilisation d'un accord d'APC sous-harmonique conduit à une capacité de couple beaucoup plus faible qu'un accord classique (*cf.* chapitre 6). C'est l'un des principaux inconvénients du fonctionnement sous-harmonique.

Enfin, il est important de noter qu'il existe une infinité de combinaisons possibles des modes dégénérés en opposition de phase qui prennent naissance aux bifurcations PD. Cependant, nous voulons que les pendules répondent sur une combinaison SH1 (on rappelle qu'il y a plusieurs configurations possibles, *cf.* chapitre 7, comme par exemple celle illustrée dans la Fig. 17). C'est pourquoi nous avons vérifié numériquement dans le chapitre 7 que le bassin d'attraction de SH1 est suffisamment grand pour que les bifurcations PD conduisent les pendules à répondre sur SH1. Ceci a été vérifié pour un APC sur-accordé et raidit, ce qui correspond à la configuration recommandée précédemment pour rendre SH1 stable tout en maximisant la capacité de couple.

3.3 Étude expérimentale d'un design original d'absorbeur pendulaire centrifuge [chap. 8]

Les résultats théoriques obtenus dans cette thèse sont basés sur des modèles d'APC très généraux. Ainsi, ces résultats peuvent être utilisés pour concevoir n'importe quelle architecture d'APC. Néan-

moins, il faut garder à l'esprit que l'objectif principal de la thèse est de proposer des solutions pour adapter les systèmes d'absorbeurs pendulaires aux véhicules électriques, ce qui nécessite le filtrage d'ordres élevés (*cf.* section 1.1.1.3). C'est pourquoi un design original d'APC, dédié à l'accord à ordre élevé, est proposé et étudié dans cette thèse. Ce design, étudié dans le chapitre 8 et présenté dans la Fig. 19, est constitué de pendules de forme sphérique. Sa simplicité permet de surmonter les problèmes rencontrés avec les APCs bifilaires à des ordres élevés (*cf.* chapitre 8).

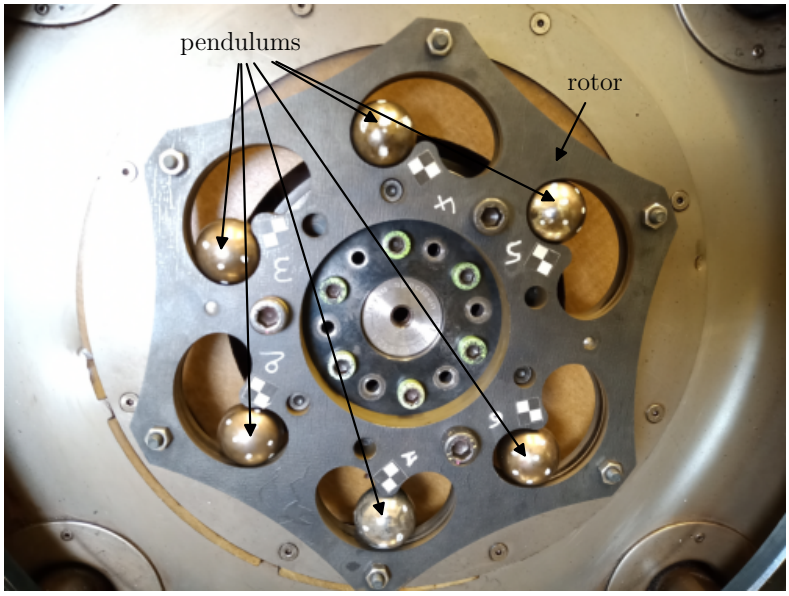

Figure 19: Prototype d'un APC à pendules sphériques

Le prototype a été testé en fonctionnement sous-harmonique, mais aussi en fonctionnement classique. Un des objectifs des tests en fonctionnement classique était de valider la conception de l'APC (identification des paramètres d'accord linéaires et non-linéaires, des coefficients d'amortissement, ...) en utilisant une configuration d'accord bien connue, et donc plus facile à étudier.

Les principaux résultats sont présentés dans la Fig. 20. La Fig. 20(a) montre un balayage en ordre proche de l'ordre d'accord des pendules. La bonne concordance du modèle avec les données expérimentales a permis de valider l'accord des pendules et d'identifier leur coefficient d'amortissement (il est à noter que la divergence autour de la résonance est due à une défaillance dans le contrôle du couple d'entrée, *cf.* Fig. 20(b)). L'atténuation particulièrement importante de 28 [dB] met en évidence les hautes performances de filtration du prototype. Cependant, il s'est avéré que le glissement des pendules, étudié dans le chapitre 8, réduit de manière significative la capacité en couple de l'APC. Ce problème de glissement est un inconvénient majeur de cette architecture.

La filtration sous-harmonique peut être observée dans la Fig. 20(c), où une réponse en couple du

rotor est représentée pour n légèrement inférieur à $2n_p$. Comme expliqué précédemment, ce sur-accord est choisi pour éviter les instabilités. Les résultats analytiques correspondent bien aux données expérimentales jusqu'à un niveau de couple donné, au-delà duquel les pendules commencent à glisser. Malheureusement, le glissement des pendules réduit considérablement la capacité en couple de l'APC (le couple à la limite d'adhérence est environ égal à 50% du couple au point de rebroussement). À notre connaissance, la Fig. 20(c) montre la première preuve de filtration sous-harmonique avec un APC.

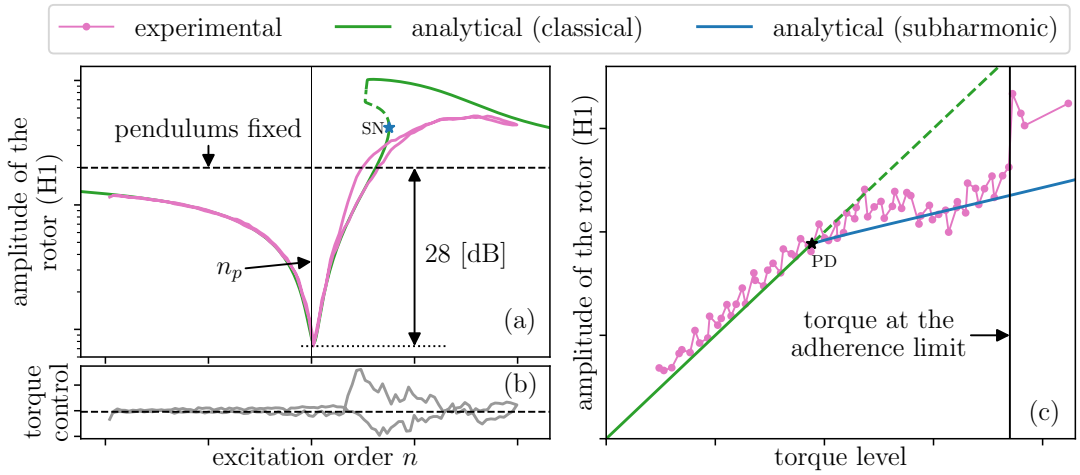

Figure 20: Réponses expérimentales (rose) et analytiques (vert et bleu) du prototype d'APC en fonctionnement classique (a) et sous-harmonique (c). La réponse en couple en (c) est représentée pour un ordre d'excitation n légèrement inférieur à $2n_p$. Les étoiles bleues et noires indiquent les bifurcations nœud-col (SN) et de doublement de période (PD), respectivement. (b) indique le contrôle du niveau de couple pendant le balayage en ordre en fonctionnement classique. La ligne noire pointillée indique le couple cible tandis que la ligne grise indique le couple réel.

Un prototype d'APC à pendules sphériques accordé à l'ordre 10 est proposé dans le chapitre 8 pour filtrer l'ordre 20 en fonctionnement sous-harmonique. Cependant, l'accord non-linéaire d'un APC d'ordre aussi élevé nécessite des tolérances de fabrication trop exigeantes. De plus, la réduction de la capacité en couple due au glissement des pendules est trop préjudiciable pour une performance satisfaisante. Pour ces raisons, l'accord sous-harmonique ne semble pas suffisant pour adapter les pendules centrifuges aux groupes motopropulseurs électriques.

4 Absorbeurs à doubles pendules centrifuges

On présente ici les principaux résultats de la partie IV de ce rapport, qui traite de l'utilisation d'absorbeurs à double pendules centrifuges (ADPC, ou "CDPVA" en anglais pour "centrifugal double pendulum vibration absorber"). L'industrie automobile utilise actuellement des absorbeurs pendulaires centrifuges (APC) pour réduire les vibrations de torsion des groupes motopropulseurs de véhicules

thermiques. L'un des principaux objectifs de cette thèse est d'adapter les systèmes pendulaires aux véhicules électriques, qui suscitent de plus en plus d'intérêt en raison des normes environnementales de plus en plus strictes. Les vibrations de torsion à réduire dans les chaînes de transmission électriques se produisent à des ordres beaucoup plus élevés que dans les véhicules thermiques (*cf.* section 1.1). Malheureusement, l'accord d'un APC à ordre élevé est difficile à réaliser en raison de tolérances de fabrication exigeantes (*cf.* section 2.2.3). C'est pourquoi nous nous intéressons à l'utilisation de doubles pendules centrifuges, dont l'accord est plus flexible et nécessite donc des tolérances de fabrication moins exigeantes. De plus, les doubles pendules génèrent deux antirésonances du rotor. L'utilisation de la deuxième antirésonance peut aider à filtrer des ordres élevés.

Les principaux sujets traités dans la partie IV de la thèse sont listé ci-dessous :

- Modélisation d'un ADPC ;
- Caractéristiques linéaires, ordres d'accord et optimisation du processus d'accord linéaire ;
- Réponse non-linéaire d'un ADPC ;
- Les antirésonances du rotor, dont l'évolution n'est pas triviale en raison des effets non-linéaires ;
- Instabilités de la réponse à l'unisson d'un ADPC.

Le développement de plusieurs des résultats discutés dans ce résumé nécessite des manipulations algébriques élaborées, détaillées dans les chapitres 9, 10 et 11. Nous ne rapportons ici que les principaux résultats de la partie IV, décrits d'un point de vue physique.

4.1 Modélisation [chap. 10]

La modélisation d'un ADPC utilisée dans cette thèse est présentée en Fig. 21. Il est constitué d'un rotor dont la position angulaire est $\vartheta(t) = \Omega t + \theta(t)$, où Ω est la vitesse de rotation moyenne et $\theta(t)$ capte les fluctuations de la position angulaire du rotor. Un couple périodique $T(\vartheta) = T_0 + T_1 \cos(n\vartheta)$ est appliqué sur le rotor. T_0 est une composante constante du couple qui s'équilibre avec l'amortissement du rotor pour fixer sa vitesse de rotation moyenne Ω. $T_1 \cos(n\vartheta)$ est un couple fluctuant d'ordre n et est la source des fluctuations $\theta(t)$. Il est à noter que dans la suite, nous écrirons $\bar{T}_1 \cos(n\vartheta)$ le couple fluctuant sans dimension.

$N = 2$ double pendules identiques sont attachés au rotor. Les pendules 1 (en bleu) et 2 (en vert) ont des masses, des inerties et des longueurs différentes. La position des centres de masse des pendules 1 et 2 peut être repérée par rapport au rotor et aux pendules 1, respectivement. En plus de leur mouvement de translation relative, les pendules peuvent tourner autour de leur centre de masse.

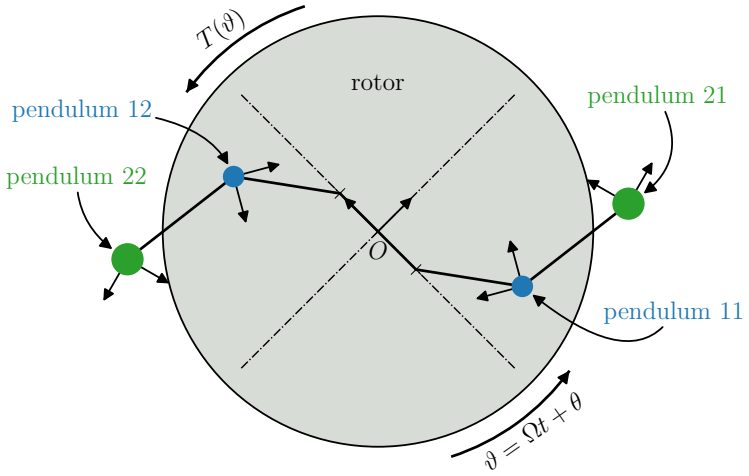

Figure 21: Représentation d'un ADPC constitué de $N = 2$ double pendules.

Ces rotations sont indiquées par les repères noirs attachés aux pendules dans la Fig. 21. Elles ne correspondent pas à des degrés de liberté supplémentaires car elles sont des fonctions des positions des pendules. Par conséquent, le système possède 5 degrés de liberté : la position du rotor et la position relative des quatre pendules.

4.2 Caractéristiques linéaires [chap. 10]

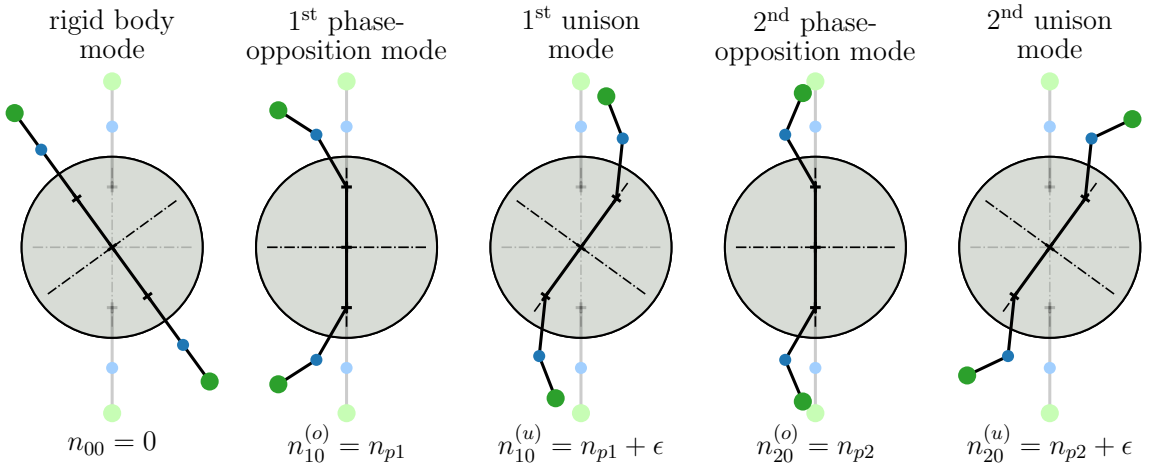

Figure 22: Modes d'un ADPC composé de $N = 2$ doubles pendules. ϵ est un petit paramètre indiquant que l'ordre propre des modes d'unisson est légèrement plus grand que les ordres d'accord. La rotation des pendules autour de leur centre de masse n'est pas représentée sur cette figure.

Lorsque les double pendules sont découplés du rotor, le système présente quatre modes (car le rotor n'est plus un degré de liberté). Ces modes représentent deux mouvements en opposition de phase et

deux mouvements à l'unisson des doubles pendules. Les premiers modes d'opposition de phase et d'unisson partagent le même ordre propre (analogue à une fréquence propre) n_{p1}. Par conséquent, ces modes sont dégénérés. n_{p1} est le premier ordre d'accord des pendules doubles et dépend des paramètres du système. De même, les seconds modes d'opposition de phase et d'unisson partagent le même ordre propre n_{p2} et ils sont dégénérés.

Lorsque les doubles pendules sont couplés au rotor, l'ADPC possède cinq modes, représentés en Fig. 22. Le mode 0 est un mode de corps rigide pour lequel les pendules sont immobiles. Les modes d'opposition de phase correspondent à un mouvement d'opposition de phase des deux pendules doubles et le rotor est un nœud de ces modes. Leurs ordres propres sont les ordres d'accord de l'ADPC. Les modes d'unisson représentent un mouvement d'unisson des doubles pendules, et (pour des paramètres raisonnables) au moins un des pendules oscille en opposition de phase avec le rotor. Leurs ordres propres sont légèrement plus grands que les ordres d'accord.

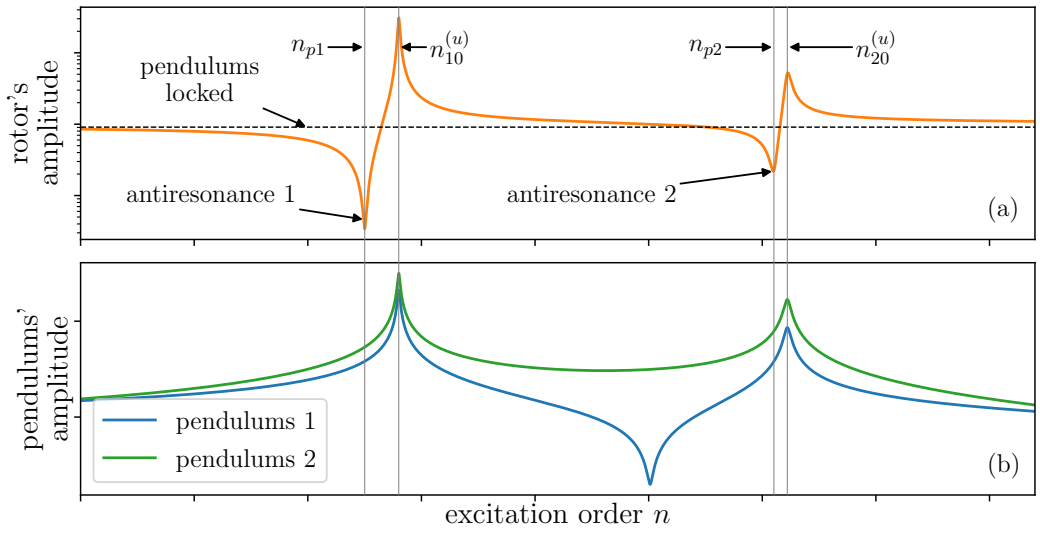

Figure 23: Réponse linéaire d'un ADPC montrant l'amplitude de l'accélération du rotor (a) et du mouvement des pendules (b). La ligne noire pointillée en (a) correspond à la réponse du rotor avec des pendules fixes.

La réponse d'un ADPC lorsqu'un couple est appliqué sur le rotor est représentée en Fig. 23. On peut voir les deux antirésonances générées par les double pendules sur le rotor en Fig. 23(a). Elles sont situées aux ordres d'accord n_{p1} et n_{p2}. La Fig. 23(b) montre que les double pendules ne répondent que sur les modes d'unisson. Ceci était attendu car ils ne sont pas affectés par le mode de corps rigide, et le rotor est un nœud des modes d'opposition de phase, donc ceux-ci ne sont pas excités par le couple externe.

Le choix des ordres d'accord est crucial car il contrôle le lieu des antirésonances du rotor. Cepen-

dant, il n'est pas facile de trouver les paramètres de l'ADPC qui conduisent aux valeurs souhaitées de n_{p1} et n_{p2} tout en obtenant une efficacité de filtration satisfaisante. Une procédure originale est proposée dans le chapitre 9 pour faciliter ce processus d'accord linéaire.

Dans cette section, nous avons présenté uniquement les caractéristiques linéaires des ADPCs. Cependant, ces systèmes sont soumis à des non-linéarités de différentes sources : couplage non-linéaire entre les pendules et le rotor, couplage non-linéaire entre les deux pendules d'un double pendule, non-linéarités de trajectoire et de rotation des pendules. Le comportement non-linéaire des ADPCs est discuté par la suite.

4.3 Stabilité de la réponse à l'unisson et performance [chap. 9, 10]

En pratique, l'ADPC fonctionne soit à $n \approx n_{p1}$ soit à $n \approx n_{p2}$. Dans le premier cas, la résonance du second mode d'unisson est généralement éloignée (*cf.* Fig. 23), sa contribution peut donc être négligée. De même, lorsque $n \approx n_{p2}$, la contribution du premier mode d'unisson est négligeable. Notez que ces approximations ne sont valables que s'il n'y a pas de résonances internes entre les deux modes d'unisson (c'est-à-dire que n_{p2} n'est pas proche d'un multiple entier de n_{p1}, *cf.* chapitre 9). De plus, nous avons expliqué précédemment que le rotor est un nœud des modes d'opposition de phase, ils ne contribuent donc pas à la réponse linéaire (*cf.* Fig. 23). Il est donc pertinent d'étudier la réponse non-linéaire d'un ADPC en supposant que les pendules ne répondent que sur l'un des modes d'unisson.

La Fig. 24 représente une réponse typique d'un ADPC autour du premier ordre d'accord n_{p1}. La réponse non-linéaire autour de n_{p2} n'est pas détaillée dans ce résumé car elle présente les mêmes caractéristiques que celle autour de n_{p1}. Dans la Fig. 24(a)-(b), on peut voir la forte courbure de la réponse vers la gauche, montrant le comportement assouplissant du 1$^{\text{er}}$ mode d'unisson. À cause de cette courbure, il y a des bifurcations nœuds-col (SN pour "saddle-node") aux intersections de la réponse avec la zone d'instabilité bleue. Lors du balayage en ordre n, un saut se produit au niveau des bifurcations SN (*cf.* section 2.5.1.1). Les pendules n'agissent alors plus comme des absorbeurs mais comme des amplificateurs, ce qui est très préjudiciable à l'efficacité de l'ADPC. Il faut donc éviter ces instabilités.

Il existe une autre zone d'instabilité (zone rouge) représentée dans la Fig. 24(a)-(b). Celle-ci est liée à une perturbation de la solution à l'unisson par le 1$^{\text{er}}$ mode d'opposition de phase. Cette contribution du mode d'opposition de phase est possible car il est en résonance interne 1:1 avec le mode d'unisson (*cf.* Fig. 22), ils peuvent donc échanger de l'énergie. La contribution du mode d'opposition de phase (non représentée dans la Fig. 24) commence aux bifurcations fourches (PF pour "pitchfork") situées aux intersections de la réponse avec la zone d'instabilité rouge. Ces bifurcations conduisent à une solution à modes couplés, entraînant la localisation de la réponse des doubles pendules, ce qui signifie

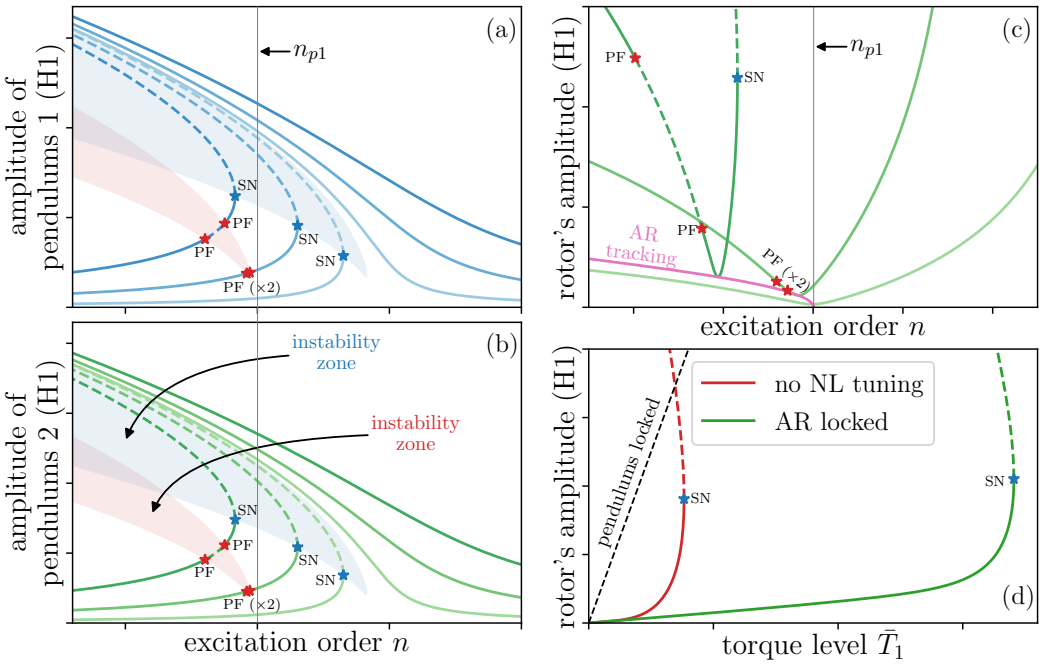

Figure 24: Réponse des pendules (a)-(b) et du rotor (c) d'un ADPC autour de la première antirésonance du rotor pour trois niveaux de forçage différents. Les lignes pointillées indiquent les solutions instables. Les étoiles rouges et bleues indiquent respectivement les bifurcations fourche (PF) et nœud-col (SN). Les zones rouges et bleues sont des zones d'instabilité liées à la localisation et aux sauts de la réponse, respectivement. La courbe rose dans (c) représente le lieu de l'antirésonance lorsque le niveau de couple varie. (d) montre l'amplitude du rotor de deux ADPCs différents en fonction du forçage et pour l'ordre d'excitation $n = n_{p1}$.

qu'ils oscillent avec des amplitudes différentes (*cf.* chapitre 10). Ainsi, en raison de la localisation, certains pendules peuvent osciller avec une amplitude beaucoup plus grande que prévu. Cependant, dans les systèmes réels, l'amplitude du mouvement est limitée pour des raisons d'espace disponible. C'est pourquoi une règle de conception originale est proposée au chapitre 10 pour éviter ces instabilités. Il est à noter que même si l'ADPC étudié ne contient que deux double pendules (*cf.* Fig. 21), la règle de conception obtenue est valable pour un nombre quelconque de double pendules (*cf.* chapitre 10).

La figure 24(c) montre un zoom de la réponse du rotor autour de sa première antirésonance. En raison du fort comportement assouplissant du mode d'unisson, l'antirésonance se déplace vers la gauche lorsque le niveau de forçage augmente. Ceci est préjudiciable à l'efficacité de la filtration, car en pratique l'ordre d'excitation n est fixé, et le concepteur choisit $n_{p1} = n$ pour que le rotor soit excité sur son antirésonance. Cependant, si cette antirésonance se déplace, le rotor n'est plus excité sur le minimum de sa réponse, ce qui conduit à une augmentation significative de son niveau de vibration. Le décalage de l'antirésonance lorsque le niveau de couple est augmenté est représenté par la courbe rose, obtenue via une procédure analytique originale de suivi d'antirésonance (*cf.* chapitre 9). Une

règle de conception prévenant ce décalage est proposée au chapitre 9 et discutée par la suite.

La réponse du rotor de deux ADPCs différents est représentée en Fig. 24(d) en fonction du niveau de forçage et pour un ordre d'excitation n égal à leur premier ordre d'accord n_{p1}. Le premier rotor (rouge) correspond à l'ADPC représenté en Fig. 24(a)-(c), qui présente un fort comportement assouplissant. Le second rotor (vert) est associé à un ADPC accordé pour verrouiller l'antirésonance à n_{p1} afin qu'elle ne se décale pas lorsque le forçage augmente. L'accord non-linéaire de l'ADPC proposé dans les chapitres 9 et 10 est réalisé par le choix de la loi de rotation des pendules autour de leur centre de masse. La règle de design pour verrouiller l'antirésonance a été obtenue via la procédure de suivi d'antirésonance illustrée en Fig. 24(c). Elle est extrêmement bénéfique pour la réduction des vibrations car elle diminue l'amplitude du rotor et repousse la bifurcation SN à des niveaux de couple élevés. L'amplitude du rotor augmente de manière significative pour de grands niveaux de couple car les approximations utilisées pour obtenir la règle de verrouillage d'antirésonance sont moins précises à de fortes amplitudes de pendule.

4.4 Étude expérimentale d'un double pendule centrifuge [chap. 11]

Les résultats théoriques obtenus dans cette thèse sont basés sur des modèles d'ADPC très généraux. Ainsi, ces résultats peuvent être utilisés pour concevoir n'importe quelle architecture d'ADPC. Dans le chapitre 11, nous nous concentrons sur une architecture spécifique, représentée en Fig. 25. Les doubles pendules sont constitués d'un cylindre creux (pendule 1) dans lequel roule un cylindre en forme de h (pendule 2).

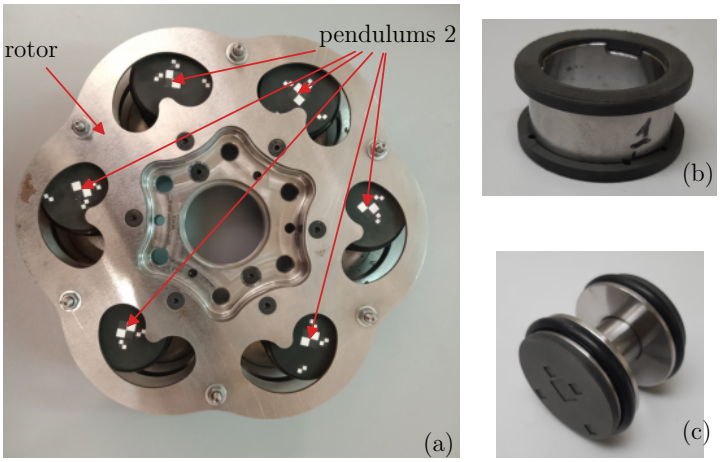

Figure 25: Prototype d'un ADPC à double pendules cylindriques (a). Les pendules 1 (b) sont des cylindres creux et les pendules 2 (c) sont constitués d'un cylindre de petit rayon rigidement lié à deux cylindres de plus grand diamètre, ce qui leur donne une forme en h. En (a), les pendules 1 sont cachés derrière les pendules 2.

La Fig. 26 représente certains des principaux résultats des tests effectués sur le prototype d'ADPC

visible en Fig. 25. Les balayages en ordre autour de la première antirésonance du rotor sont représentés sur cette figure. La comparaison du modèle linéaire développé dans le chapitre 9 avec les données expérimentales en Fig. 26(a) permet de vérifier le bon accord linéaire de l'ADPC. Il est à noter que les coefficients d'amortissement visqueux identifiés sont plus grands que prévu. Ceci entraîne un ordre d'antirésonance légèrement inférieur à n_{p1} et est préjudiciable à une réduction efficace des vibrations. En Fig. 26(b), on peut voir que le modèle non-linéaire développé dans le chapitre 9 décrit relativement bien le décalage de l'antirésonance lorsque le niveau de couple augmente. Les écarts importants autour de la résonance pourraient être dus au glissement des pendules, mais cette hypothèse reste à vérifier. Malheureusement, il n'a pas été possible d'observer la seconde antirésonance du rotor en raison des limitations du dispositif expérimental (*cf.* chapitre 11).

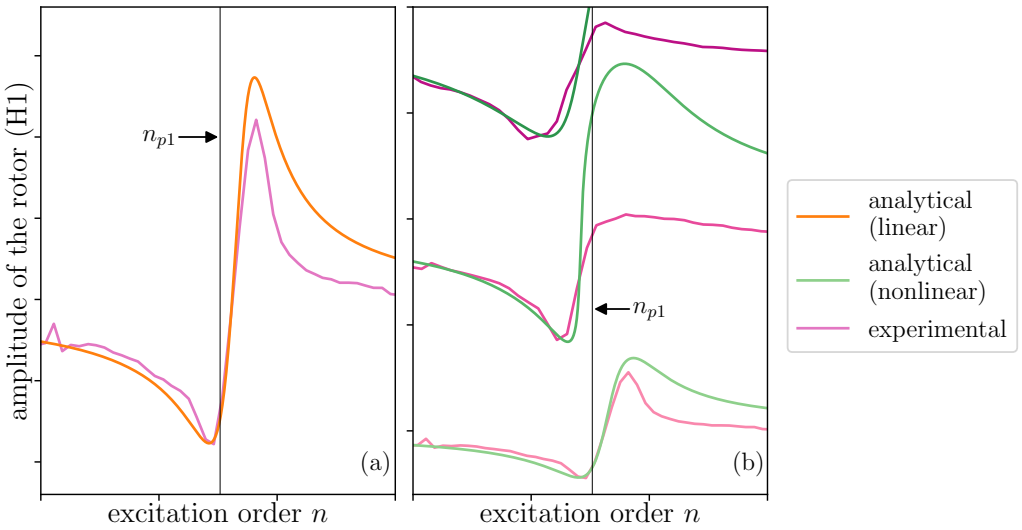

Figure 26: Réponse du rotor autour de sa première antirésonance en régime linéaire (a) et non-linéaire (b). Trois niveaux de couple différents sont représentés en (b). Plus la ligne est foncée, plus le niveau de couple associé est important.

Un prototype d'ADPC accordé à l'ordre 20 est proposé dans le chapitre 11. L'accord linéaire semble réalisable en pratique, mais la conception actuelle présente d'autres limitations. En effet, avec des pendules de longueur constante, il n'est pas possible de contrôler l'accord non-linéaire de cet ADPC. Pour remédier à cela, les pendules devraient suivre des trajectoires non circulaires, comme c'est le cas pour les APC (*cf.* section 2.1.3). Ceci est une piste importante pour un travail futur, et il faudra s'assurer que les trajectoires permettant d'obtenir l'accord non-linéaire souhaité ne nécessitent pas des tolérances de fabrication trop exigeantes. De plus, le glissement des pendules n'a pas été étudié dans le chapitre 11, quand bien même il est apparu comme une limitation de certaines conceptions d'APC (*cf.* chapitre 8) et est également un problème pour l'architecture d'ADPC présentée en Fig. 25. Enfin, l'identification expérimentale de coefficients d'amortissement importants remet en cause les

performances de cette architecture d'ADPC.

5 Conclusion

Les travaux présentés dans ce rapport portent sur l'utilisation d'absorbeurs pendulaires centrifuges (APCs) pour réduire les vibrations de torsion rencontrées dans des chaînes de transmission automobiles, qu'elles soient thermiques ou électriques. Le but de ces absorbeurs est de filtrer un couple s'appliquant sur une machine tournante. Les travaux s'orientent autour de deux axes de recherche principaux :

- Augmenter les connaissances sur les absorbeurs pendulaires centrifuges, en se concentrant particulièrement sur leurs limitations actuelles et sur des principes de fonctionnement originaux ;
- Adapter les absorbeurs pendulaires actuellement utilisés dans des véhicules thermiques à des véhicules électriques via la proposition d'architectures originales.

Les principaux résultats sont résumés ci-dessous.

Dans la littérature, la plupart des travaux sur des absorbeurs pendulaires ne considèrent qu'un mouvement de translation des pendules. Cependant, des études récentes ont montré un réel avantage à profiter de la rotation des pendules autour de leur centre de masse. La prise en compte et l'étude approfondie de cette rotation est une contribution importante de cette thèse.

La partie II du manuscrit traite le cas de l'accord classique d'APCs via une approche analytique, numérique et expérimentale. L'étude théorique approfondie du phénomène non-linéaire de localisation d'énergie et du décalage de l'antirésonance du rotor a permis d'accroître la compréhension de ces limitations. Des règles et outils de design ont été proposés afin d'éviter la localisation de la réponse des pendules et de prévenir le décalage de l'antirésonance du rotor, augmentant ainsi la capacité en couple et les performances de filtration du système. Les campagnes d'essai ont permis de valider expérimentalement une partie des modèles théoriques.

L'accord classique est actuellement utilisé dans des véhicules thermiques, mais il n'est cependant pas envisageable dans des véhicules électriques car la filtration d'ordres élevés requiert des tolérances de fabrication trop fines.

La partie III traite le cas de l'accord sous-harmonique d'APCs via une approche analytique, numérique et expérimentale. L'étude théorique approfondie de cette solution purement non-linéaire, du décalage de l'antirésonance du rotor et de l'apparition de solutions localisées a permis d'accroître

la compréhension de cet accord particulier. Des règles et outils de design ont été proposés afin de maximiser la performance du système via l'optimisation de la réponse sous-harmonique et l'évitement de réponses localisées.

Un prototype d'APC basé sur une architecture nouvelle et dédié au fonctionnement sous-harmonique a été conçu durant la thèse. Les campagnes d'essai sur ce prototype ont permis de valider en partie les modèles théoriques et d'observer pour la première fois la filtration sous-harmonique de manière expérimentale.

Il est plus aisé de filtrer des ordres élevés avec des pendules sous-harmoniques qu'avec des pendules classiques car ils peuvent être accordés à la moitié de l'ordre à filtrer. Toutefois, l'accord non-linéaire de pendules sous-harmoniques requiert de très faibles tolérances de fabrication pour des ordres élevés, ce qui empêche actuellement leur adaptation dans des véhicules électriques. La faible capacité en couple du prototype développé, due au glissement des pendules, est un autre frein à l'adaptation d'APCs sous-harmoniques à des véhicules électriques.

La partie IV traite le cas de l'utilisation d'absorbeurs à double pendules centrifuges (ADPCs) plutôt que d'APCs. L'étude théorique approfondie de la réponse linéaire et non-linéaire d'ADPCs, de l'apparition de solutions localisées et du décalage des antirésonances du rotor a grandement amélioré la connaissance de ces systèmes complexes. Des règles et outils de design ont été proposés afin d'éviter la localisation de la réponse des pendules et de prévenir le décalage des antirésonances du rotor, augmentant ainsi la capacité en couple et les performances de filtration de ces systèmes.

Un prototype d'ADPC basé sur une architecture originale a été conçu durant la thèse. Les campagnes d'essai sur ce prototype ont permis de valider en partie les modèles théoriques. Ce sont les premières comparaisons entre la réponse forcée (linéaire et non-linéaire) d'un ADPC obtenue de manière théorique et expérimentale.

Il est plus aisé de filtrer des ordres élevés avec des doubles pendules qu'avec des pendules simples (classique ou sous-harmoniques) car leur accord est plus flexible et nécessite des tolérances de fabrication moins contraignantes. Toutefois, les tolérances requises restent faibles pour un accord satisfaisant. De plus, l'architecture actuelle ne permet pas l'accord non-linéaire de l'ADPC car les pendules suivent des trajectoires circulaires. Ceci pourrait être corrigé en prenant en compte des trajectoires non-circulaires des pendules, comme c'est le cas pour un APC. Une telle étude est laissée pour un travail futur, et il sera nécessaire de vérifier que l'accord non-linéaire requis soit compatible avec des tolérances de fabrication acceptables. Il sera également intéressant d'étudier le glissement des doubles pendules afin de s'assurer que la capacité en couple du système est satisfaisante.

Vincent MAHÉ

Improvements in the design of pendulum absorbers to reduce the vibrations of automotive powertrains

Résumé : Dans le contexte de normes environnementales de plus en plus strictes, les constructeurs automobiles doivent s'adapter pour développer des véhicules moins polluants. Dans ce but, ils proposent de réduire la taille des moteurs thermiques et s'orientent vers les véhicules électriques. Cependant, la réduction de la taille du moteur augmente son acyclisme, provoquant des vibrations de torsion plus importantes de la chaîne cinématique. De plus, l'utilisation de moteurs électriques met en évidence des sources de vibration de torsion auparavant éclipsées par l'acyclisme du moteur. Les absorbeurs pendulaires centrifuges (APCs) sont utilisés depuis près d'un siècle pour contrebalancer l'acyclisme de moteurs thermiques. Ils sont constitués de plusieurs masses (pendules) oscillant par rapport à un rotor. Cependant, ces dispositifs sont soumis à plusieurs sources de non-linéarité qui peuvent réduire drastiquement leur efficacité. Il est donc nécessaire d'optimiser la conception des APCs afin de répondre aux exigences des moteurs thermiques les plus récents et de les adapter aux véhicules électriques. Dans cette thèse, nous nous concentrons sur trois concepts de pendules centrifuges. Le premier est l'APC classique, qui est actuellement utilisé dans l'industrie automobile mais qui requiert des améliorations. Les deuxième et troisième concepts sont les APC sous-harmoniques et les absorbeurs à doubles pendules centrifuges (ADPCs), qui ont été beaucoup moins étudiés que les APC classiques et qui ne sont actuellement pas utilisés dans l'industrie. Nous utilisons principalement des méthodes analytiques pour étudier la réponse non-linéaire des pendules centrifuges. Ces modèles analytiques sont particulièrement utiles car ils fournissent une compréhension approfondie de la dynamique des pendules centrifuges et ils permettent de dériver des règles de design pour optimiser leur efficacité. Ces règles sont étroitement liées au choix de la trajectoire des pendules et à leur rotation par rapport au rotor. Des méthodes numériques sont utilisées pour valider les résultats analytiques. De plus, plusieurs prototypes de pendules centrifuges ont été conçus au cours de la thèse. Ceci a permis de réaliser des analyses expérimentales qui ont validé les modèles théoriques.

Mots clés : pendules centrifuges, absorbeur de vibrations, absorbeur non-linéaire, vibrations de torsion, localisation, sous-harmonique, méthode des échelles multiples, chaîne de transmission.

Abstract: In the context of increasingly stringent environmental standards, automotive manufacturers have to adapt themselves to develop less polluting vehicles. To this aim, they propose to reduce the size of thermal engines and they turn their attention towards electric vehicles. However, the reduction of the engine size increases its acyclism, causing larger torsional vibrations of the drivetrain. Moreover, the use of electric motors brings to the fore sources of torsional vibrations previously hidden by the engine. Centrifugal pendulum vibration absorbers (CPVAs) have been used for nearly a century to balance the acyclism of thermal engines. They consist of several masses (pendulums) oscillating relatively to a rotor. However, these devices are subjected to several sources of nonlinearity that can drastically reduce their efficiency. Hence, there is a need to optimise the design of CPVAs to meet the requirements of the most recent thermal engines and to adapt them to electric vehicles. In this thesis, we focus on three different centrifugal pendulum concepts. The first one is classic CPVAs, which are currently used in the automotive industry but need improvements. The second and third ones are subharmonic CPVAs and centrifugal double pendulums vibration absorbers (CDPVAs), which are been much less studied than classical CPVAs and are currently not used in the industry. We mainly use analytical methods to investigate the nonlinear response of centrifugal pendulums. These analytical models are particularly useful as they provide a deep understanding of the dynamics of centrifugal pendulums and they allow to derive guidelines to optimise their efficiency. These guidelines are related to the choice of the pendulums' path and to their rotation relatively to the rotor. Numerical methods are used to validate the analytical results. Moreover, several centrifugal pendulum prototypes were designed during the thesis. This allowed to perform experimental investigations which validated the theoretical models.

Keywords: centrifugal pendulums, vibration absorber, nonlinear absorber, torsional vibrations, localisation, subharmonic, method of multiple scales, drivetrain.